

4

THE FILE

AFGL-TR-88-0186

## AD-A210 678

LABCEDE Fluorescence Investigations

B. D. Green  
B. L. Upschulte  
W. J. Marinelli  
L. G. Piper  
K. L. Holtzclaw

J. C. Person  
M. E. Fraser  
W. J. Kessler  
H. C. Murphy  
A. T. Lintz

Physical Sciences Inc.  
Research Park  
Andover, MA 01810

August 1988

Final Report  
30 November 1984 - 29 February 1988

Approved for public release; distribution unlimited


AIR FORCE GEOPHYSICS LABORATORY  
AIR FORCE SYSTEMS COMMAND  
UNITED STATES AIR FORCE  
HANSOM AIR FORCE BASE, MASSACHUSETTS 01731-5000

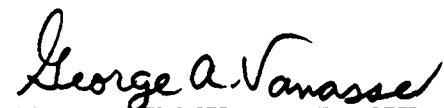
DTIC  
ELECTE  
JUL 21 1989  
S E D  
A

89


2 22 239

"This technical report has been reviewed and is approved for publication"

  
(Signature)  
WILLIAM BLUMBERG  
Contract Manager

  
(Signature)  
GEORGE A. VANASSE  
Branch Chief

FOR THE COMMANDER

  
(Signature)  
R. EARL GOOD  
Division Director

This report has been reviewed by the ESD Public Affairs Office (PA) and is releasable to the National Technical Information Service (NTIS).

Qualified requestors may obtain additional copies from the Defense Technical Information Center. All others should apply to the National Technical Information Service.

If your address has changed, or if you wish to be removed from the mailing list, or if the addressee is no longer employed by your organization, please notify AFGL/DAA, Hanscom AFB, MA 01731. This will assist us in maintaining a current mailing list.

Do not return copies of this report unless contractual obligations or notices on a specific document requires that it be returned.

## REPORT DOCUMENTATION PAGE

1a REPORT SECURITY CLASSIFICATION Unclassified			1b. RESTRICTIVE MARKINGS		
2a SECURITY CLASSIFICATION AUTHORITY			3 DISTRIBUTION / AVAILABILITY OF REPORT Approved for public release; distribution unlimited		
2b. DECLASSIFICATION / DOWNGRADING SCHEDULE			5. MONITORING ORGANIZATION REPORT NUMBER(S) AFGL-TR-88-0186		
4 PERFORMING ORGANIZATION REPORT NUMBER(S) PSI TR-756			7a. NAME OF MONITORING ORGANIZATION Air Force Geophysics Laboratory		
6a NAME OF PERFORMING ORGANIZATION Physical Sciences Inc.		6b OFFICE SYMBOL (if applicable)		7b ADDRESS (City, State, and ZIP Code) Hanscom AFB, MA 01731-5000	
6c ADDRESS (City, State, and ZIP Code) Research Park, P.O. Box 3100 Andover, MA 01810		8b OFFICE SYMBOL (if applicable) OPI		9. PROCUREMENT INSTRUMENT IDENTIFICATION NUMBER F19628-84-C-0057	
8a. NAME OF FUNDING / SPONSORING ORGANIZATION Air Force Geophysics Laboratory		8c ADDRESS (City, State, and ZIP Code) Hanscom AFB, MA 01731		10 SOURCE OF FUNDING NUMBERS	
				PROGRAM ELEMENT NO 61102F	PROJECT NO. 2310
				TASK NO G4	WORK UNIT ACCESSION NO BH
11 TITLE (Include Security Classification) LABCEDE Fluorescence Investigations (U)					
12 PERSONAL AUTHOR(S) B.D. Green, B.L. Upschulte, W.J. Marinelli, L.G. Piper, K.L. Holtzclaw, J.C. Person, M.E. Fraser, W.J. Kessler, H.C. Murphy, and A.T. Lintz					
13a. TYPE OF REPORT Final Report		13b. TIME COVERED FROM 11/30/84 TO 2/29/88		14. DATE OF REPORT (Year, Month, Day) August 1988	
15. PAGE COUNT 554					
16. SUPPLEMENTARY NOTATION					
17 COSATI CODES			18. SUBJECT TERMS (Continue on reverse if necessary and identify by block number)		
FIELD	GROUP	SUB-GROUP	Electron irradiation, fluorescence, cryogenic interferometry		
			circularly variable filter, electronically excited N <sub>2</sub> , ozone, EXCEDE, NH, solar simulator		
19 ABSTRACT (Continue on reverse if necessary and identify by block number)					
<p>This report covers a wide variety of projects to measure and interpret the fluorescence arising from electron excitation of atmospheric gases. Excitation of N<sub>2</sub> B-state is Franck Condon at low pressure but as pressure increases to tens of mtorr, collisional transfer from the A-state into the lowest B-state vibrational levels is observed. The middle levels of the B-state show little variation with pressure even though they strongly coupled to W-state levels.</p> <p>The N<sub>2</sub>a(1Π<sub>g</sub>) state was observed via LBH emission at 0.2 μm. Substantial vibrational redistribution rather than electronic quenching was observed. Again nested electronic states in particular the a'-state are involved in the relaxation. Level-specific investigations of the N<sub>2</sub>a, v=0 relaxation by a variety of gases including N<sub>2</sub> and O<sub>2</sub> is also reported.</p> <p>Electron impact excitation cross sections for N<sub>2</sub> A, v=2-7 were measured at sufficiently low pressures that quenching effects can be removed. Data from two infrared</p>					
20. DISTRIBUTION / AVAILABILITY OF ABSTRACT <input type="checkbox"/> UNCLASSIFIED/UNLIMITED <input type="checkbox"/> SAME AS RPT <input type="checkbox"/> DTIC USERS			21 ABSTRACT SECURITY CLASSIFICATION Unclassified		
22a. NAME OF RESPONSIBLE INDIVIDUAL William Blumberg			22b. TELEPHONE (Include Area Code) (617) 377-2810		22c. OFFICE SYMBOL OPI

spectrometers are used to determine the contributions of various  $N_2$  transitions to the IR spectrum observed in LABCEDE. This data provides the basis for predicting the fluorescence from electron irradiated  $N_2$  which is a necessary basis for disturbed atmospheres code predictions and will serve to guide the analysis of data from field programs. Emission from  $N_2/O_2$  irradiated mixtures were also studied. Changes in production efficiency and state distributions upon variations in electron energy distribution and  $O_2$  addition were small. Oxygen addition resulted in the production of new features,  $N_2$  fluorescence levels were relatively unaltered.

The relative brightness of  $N_2$  First Positive bands depends on the nature of the transition moment variation over a large range of internuclear separations. Emissions from the  $\Delta v=+6$  to  $-2$  sequences was analyzed to deduce a nearly linear transition moment variation. We recommend changes to the B-state and A-state radiative lifetimes.

Ozone fluorescence is observed in cryogenic LABEDE at levels in excess of three body production levels. We report observations of  $O_3$  fluorescence at  $10\text{ }\mu\text{m}$ : spectral distributions and their dependence on parametrical variations. A preliminary review of mechanisms is also presented. With pulsed excitation, the fluorescence spectrum was observed to decay after beam termination at different rates depending upon pressure and composition of the irradiated mix. The vibrational level dependent relaxation is also analyzed.

Laboratory investigations provide insight into mechanisms and efficiencies which can be used to aid in the understanding of field data. An analysis of IR, UV and visible data from the electron-irradiated mesosphere/thermosphere as observed in the EXCEDE mission is presented. Many of the  $N_2$  electronic state transitions described above are observed in that data along with  $CO_2$ ,  $NO$  and other radiators. We briefly describe a radiometer package we are assembling to permit the study of fast atom reactions created by electron impact or in interactions in the environment encountered by orbital missions.

Data from an early field mission seemed to indicate that the auroral fluorescence spectrum was different under sunlit conditions. A laboratory simulation of this phenomenon using a solar simulator and a pulsed electron beam simultaneously incident on  $N_2/O_2$  mixtures produced no detectable difference in the observed fluorescence between  $0.3$  to  $0.8\text{ }\mu\text{m}$  and  $2.2$  to  $6.8\text{ }\mu\text{m}$ .

The LABCEDE Facility was used to provide an understanding of electron/ $N_2$  molecular scattering processes. As pressure is increased, the observed beam width increases due to both elastic and inelastic scattering processes. Our modeling of this data in support of these experiments is presented. NH emission is observed in  $N_2/H_2$  mixtures irradiated by  $40\text{ keV}$  electrons in the small LABCEDE chamber. Quenching rate coefficients can be obtained for NH,  $v=1-3$  by  $N_2$  and  $H_2$  once quenching by beam created species is considered. We present time-dependent modeling of this system for atom production, relaxation, and reaction processes.

It has been postulated that electron-impact on optical elements could produce a detectable signature. The Field Widened Interferometer penetrated an active auroral region and observed unexplained IR features. The emission from clean and contaminated calcium fluoride optical flats irradiated by electrons was obtained. No emission was detected at irradiation levels below optical element damage thresholds. Finally several spectral observations are presented to document and to serve as a guide for potential future projects.



# CONTENTS

Section	Page
1. INTRODUCTION	1
2. EXCITATION AND QUENCHING OF THE VIBRATIONAL LEVELS OF $N_2(B^3\Pi_g)$ STATE IN ELECTRON IRRADIATED NITROGEN	5
2.1 INTRODUCTION	5
2.2 EXPERIMENTAL	7
2.3 RESULTS AND ANALYSIS	9
2.3.1 Vibrational Populations	10
2.3.2 Relative Electronic State Populations	19
2.3.3 Pressure Scaling of Electronic State Populations	21
2.4 DISCUSSION	25
2.4.1 Comparison with Auroral Observations	25
2.4.2 Collisional Energy Transfer and Electronic Quenching	28
2.5 CONCLUSIONS	38
3. VIBRATIONAL RELAXATION AND INTERSYSTEM CROSSING IN $N_2(a^1\Pi_g)$	42
3.1 INTRODUCTION	42
3.2 EXPERIMENTAL	46
3.3 RESULTS AND ANALYSIS	51
3.4 KINETIC MODELING	64
3.5 DISCUSSION	72
3.5.1 Relative Production Efficiencies	72
3.5.2 Vibrational Redistribution	76
3.5.3 Discussion of Field Observations	78
3.5.4 Predictions of Altitude Scaling of Infrared Radiance	83
3.6 CONCLUSIONS	84
4. ELECTRON-IMPACT EXCITATION OF THE $N_2^+$ MEINEL BAND	87
4.1 INTRODUCTION	87
4.2 EXPERIMENTAL	88
4.3 RESULTS AND DISCUSSION	89
4.4 SUMMARY	93

Accession For	
NTIS GRA&I	<input checked="" type="checkbox"/>
DTIC TAB	<input type="checkbox"/>
Unannounced	<input type="checkbox"/>
Justification	
By	
Distribution/	
Availability Codes	
Dist	Avail and/or Special
A-1	



# CONTENTS (CONTINUED)

<u>Section</u>	<u>Page</u>
5. N <sub>2</sub> ELECTRONIC STATES: CVF/INTERFEROMETER MEASUREMENTS IN THE IR	95
5.1 INTRODUCTION	95
5.2 EXPERIMENTAL	96
5.3 ANALYSIS AND RESULTS	97
5.4 CVF SUMMARY	101
5.5 INTERFEROMETER DATA	103
5.6 N <sub>2</sub> ELECTRONIC STATE POPULATIONS	106
6. ROOM AIR FLUORESCENCE INVESTIGATIONS	120
6.1 INTRODUCTION	120
6.2 SURVEY SPECTRA OF LABORATORY AIR	121
6.2.1 The 200 to 300 nm Region	121
6.2.2 The 300 to 400 nm Region	121
6.2.3 The 440 to 800 nm Region	125
6.3 VARIATIONS WITH ELECTRON ENERGY DISTRIBUTION CHANGES	128
6.4 PRESSURE DEPENDENCIES	134
6.5 CONCLUSIONS	139
7. EXPERIMENTAL DETERMINATION OF THE EINSTEIN COEFFICIENTS FOR THE N <sub>2</sub> (B-A) TRANSITION	141
7.1 INTRODUCTION	141
7.2 EXPERIMENTAL	143
7.3 RESULTS	145
7.4 DISCUSSION	149
8. QUENCHING OF N <sub>2</sub> (a <sup>1</sup> Π <sub>g</sub> , v'=0) BY N <sub>2</sub> , O <sub>2</sub> , CO, CO <sub>2</sub> , CH <sub>4</sub> , H <sub>2</sub> , AND Ar	159
8.1 INTRODUCTION	159
8.2 EXPERIMENTAL	163
8.3 RESULTS AND ANALYSIS	165
8.3.1 Quenching by N <sub>2</sub>	168
8.3.2 Quenching by Ar, CO <sub>2</sub> , H <sub>2</sub> , O <sub>2</sub> , and CH <sub>4</sub>	170
8.3.3 Quenching by CO	172
8.4 SUMMARY	172

## CONTENTS (CONTINUED)

<u>Section</u>	<u>Page</u>
9. LOW PRESSURE O <sub>3</sub> PRODUCTION	174
9.1 INTRODUCTION	174
9.2 IR DATA	174
9.3 MECHANISMS	199
9.4 CONCLUSION	201
10. OZONE VIBRATIONAL RELAXATION MEASUREMENTS	202
11. EXCEDE DATA ANALYSIS	212
11.1 INTRODUCTION	212
11.2 DATA HANDLING	214
11.2.1 Spectral Fitting	215
11.2.2 Background Correction	221
11.3 SPECTROSCOPIC IDENTIFICATION	226
11.3.1 Wu-Benesch Emission	228
11.3.2 H <sub>2</sub> O Emission	233
11.3.3 NO Fundamentals	238
11.3.4 Surveys of Other Band Systems	242
11.3.5 Ultraviolet and Visible Interferometer Data	248
11.3.6 Infrared Interferometer Data	256
11.3.7 2.9 $\mu$ m Mystery Emission	261
11.4 CONCLUSIONS	264
12. RADIOMETER EXPERIMENT TO STUDY EMISSIONS RESULTING FROM COLLISIONS WITH HIGH VELOCITY ATOMS	266
13. SOLAR SIMULATOR INVESTIGATIONS	279
13.1 EFFECTS UPON ULTRAVIOLET AND VISIBLE ELECTRON INDUCED FLUORESCENCE	279
13.1.1 Experimental	279
13.1.2 Observations for Air Between 300 and 400 nm	282
13.1.3 Observations for Air Between 440 and 800 nm	283
13.1.4 Conclusion of Visible Experiments	284

## CONTENTS (CONTINUED)

<u>Section</u>	<u>Page</u>
13.2 EFFECTS UPON IR ELECTRON-INDUCED FLUORESCENCE	286
13.2.1 Instrumental	288
13.2.2 Experimental	289
13.2.3 Observations of Fluorescence Changes in the SWIR Wavelength Region	290
13.2.4 Observations in the MWIR Wavelength Region	291
13.3 CONCLUSIONS	294
14. ELECTRON BEAM GROWTH MODELING INCLUDING ELASTIC AND INELASTIC SCATTERING AND CONTRIBUTION FROM FAST SECONDARIES	297
14.1 INTRODUCTION	297
14.2 SIMULATION DESCRIPTION	297
14.3 ABSOLUTE CROSS SECTIONS FOR ELASTIC AND INELASTIC SCATTERING	301
14.4 ELASTIC SCATTERING ANGULAR DISTRIBUTION	301
14.5 INELASTIC SCATTERING ANGULAR DISTRIBUTION	304
14.6 EXCITATION BY FAST SECONDARY ELECTRONS	309
14.7 CROSS SECTIONS FOR EXCITATION OF 391 nm RADIATION BY FAST SECONDARY ELECTRONS	310
14.8 RESULTS	311
14.9 SENSITIVITY TO RELATIVE ANGULAR DISTRIBUTIONS	314
14.10 SENSITIVITY TO ABSOLUTE CROSS SECTIONS	317
14.11 GENERAL FEATURES OF COMPARING THE SIMULATIONS AND THE DATA	318
14.12 OTHER POSSIBLE CAUSES OF FLAT G(r) DISTRIBUTIONS	320
14.13 SUMMARY AND CONCLUSIONS	322
15. MODELING OF THE PRODUCTION OF VIBRATIONALLY EXCITED NH IN N <sub>2</sub> /H <sub>2</sub> MIXTURES	324
15.1 MODEL DESCRIPTION	324
15.2 RESULTS	332
16. ELECTRON IRRADIATION OF CALCIUM FLUORIDE	340
16.1 INTRODUCTION	340
16.2 EXPERIMENTAL	340
16.3 SUMMARY	348

## CONTENTS (CONCLUDED)

<u>Section</u>	<u>Page</u>
17. SPECTRAL SURVEY MEASUREMENTS	351
17.1 UV-VISIBLE SPECTRA OF ELECTRON IRRADIATED NITRIC OXIDE (NO)	351
17.2 FLUORESCENCE FROM Ar/NO MIXTURES	356
17.3 INFRARED EMISSION FROM N <sub>2</sub> /O <sub>2</sub> MIXTURES	357
17.4 MWIR EMISSION FROM Ar/CO <sub>2</sub> MIXTURES	358
17.5 LWIR EMISSION FROM N <sub>2</sub> /CO <sub>2</sub> MIXTURES	362
17.6 OZONE 13 TO 15 $\mu$ m EMISSION	362
REFERENCES	366
APPENDICES	
A. LIST OF JOURNAL PUBLICATIONS AND PRESENTATIONS AT SCIENTIFIC CONFERENCES DURING THIS PROJECT	381
B. LABCEDE STARTUP AND SHUTDOWN PROCEDURES	385
C. COMPUTATION OF ELECTRONIC SPECTRA OF DIATOMIC MOLECULES	395
D. PARTICLE BOMBARDMENT OF ATMOSPHERIC GASES	427
E. O-ATOM EMISSION IN FAIRCEDE	519

## FIGURES

<u>Figure</u>	<u>Page</u>
1. Spectral scan of $N_2$ (B-X) and $N_2$ (C-B) emission excited by electron irradiation at a pressure of 0.15 mtorr.	11
2. Spectral scan of $N_2$ (B-A) and $N_2^+$ (A-X) emission under same conditions as Figure 1.	11
3. Relative vibrational populations of $N_2$ (C) measured at 1.0 mtorr, 10 mtorr, and 70 mtorr.	12
4. Relative vibrational populations of $N_2^+$ (B) measured at 1.0 mtorr, 30 mtorr, and 81 mtorr.	14
5. Spectrum of $N_2$ (B-A) emission excited at 1.0 mtorr pressure (light line) and synthetic fit to spectrum (solid line).	16
6. Spectrum of $N_2$ (B-A) $\Delta v=3$ sequence bands excited at a pressure of 0.15 mtorr showing disequilibrium of the spin components.	16
7. Relative vibrational populations of $N_2$ (B) from electron impact excitation of $N_2$ at 1.0 mtorr, 10.0 mtorr and 70 mtorr.	17
8. Low pressure vibrational distribution for the B-state as observed in LABCEDE is compared to previous auroral and laboratory observations and model predictions.	19
9. Ratio of total B-state population to population of C, $v=0$ as a function of pressure.	23
10. Ratio of population in B( $v=4$ ) to C( $v=0$ ) as a function of pressure.	24
11. Modeled production rate in field of view based on energy deposition, excited state production and cascade.	31
12. Variation in the population ratio $N(B,6)/N(C,0)$ with pressure.	34
13. Energy level diagram for $N_2$ singlets.	43
14. LABCEDE apparatus.	46
15. Variation in $N_2$ (C) state emission intensity with pressure.	49
16. $N_2$ (a) emission spectra at 1.0 and 72 mtorr and spectral fits to data.	52

# FIGURES (CONTINUED)

Figure		Page
17.	Spectral fit to $N_2(C-B)$ $\Delta v=2$ sequence band with $(c_4'-a)$ 0-1 band included.	55
18.	$N_2(a,v)/N_2(C,2)$ population ratios at 1.0 and 72 mtorr obtained from spectral fitting.	57
19.	Stern-Volmer plot for $N_2(a)$ electronic relaxation.	60
20.	Vibrational relaxation analysis decay plots.	65
21.	Comparison of measured electronic relaxation rate data (averaged as solid line) with kinetic model results for selected pressures (open symbols).	68
22.	$N_2(a,V)/N_2(C,2)$ populations at 1.0 mtorr.	69
23.	Kinetic modeling: vibrational distributions at 72 mtorr.	70
24.	Vibrational distributions for $N_2(a^1\Pi_g)$ obtained from fit to data of Huffman et al.	80
25.	VUV nightglow data of Huffman et al. (light line) and spectral fit to data (dark line).	81
26.	Auroral predictions and data.	82
27.	Model predictions for $N_2(a)$ and $N_2(a')$ vibrational distributions at 95 km.	84
28.	Predicted emission spectrum of $N_2$ McFarlane bands at 95 km.	85
29.	Predicted emission spectrum of $N_2$ McFarlane bands at 130 km.	85
30.	Spectrum of electron irradiated $N_2$ at 1 mtorr pressure at beam termination (synthetic spectrum is the heavy line).	98
31.	Spectrum from 5 mtorr $N_2$ at beam termination.	98
32.	Spectrum from 37 mtorr $N_2$ at beam termination.	99
33.	Time evolution of properly fit $N_2$ levels at 1 mtorr pressure.	101
34.	Near IR interferometer data of electron-irradiated $N_2$ (6 mtorr).	104
35.	SWIR interferometer data of electron-irradiated $N_2$ (6 mtorr).	105

# FIGURES (CONTINUED)

Figure		Page
36.	N <sub>2</sub> electronic state populations from LABCEDE visible and IR fluorescence at less than 1 mt pressure compared with high altitude (greater than 110 km) auroral predictions.	108
37.	Vibrational distributions within nitrogen electronic state populations in LABCEDE at 1 mtorr.	109
38.	Vibrational distributions within nitrogen electronic state populations in LABCEDE (15 mtorr).	110
39.	Nitrogen electronic populations Cartwright model.	111
40.	Nitrogen population levels plotted versus level Te for N <sub>2</sub> B, W, a, and w states.	113
41.	Energy level diagram of N <sub>2</sub> electronic-states indicating large number of possible resonances.	114
42.	Total quenching of W <sup>3</sup> Δ, v=3-10 state relative to B <sup>3</sup> Π <sub>g</sub> state.	115
43.	Normalized B-state vibrational populations as a function of pressure.	116
44.	Synthetic spectrum of electron-irradiated nitrogen at 90 km altitude for visible, SWIR/MWIR and LWIR spectral regions.	117
45.	Synthetic spectrum of electron-irradiated nitrogen at 80 km altitude for visible, SWIR/MWIR and LWIR spectral regions.	118
46.	1.2 mtorr room air spectrum taken with a 15.6Å resolution is representative of all data and fits in this spectral region.	122
47.	This figure presents the relative populations of upper state vibrational levels of the observed transitions with and without BPD operative, at a pressure of 1.2 mtorr.	123
48.	The low (1.2 mtorr) and high (20.0 mtorr) pressure (non-BPD) relative populations are presented and compared to the F-C distribution.	125
49.	This figure presents the ratio of total populations of the N <sub>2</sub> (C <sup>3</sup> Π <sub>u</sub> ) state to that in the N <sub>2</sub> (B <sup>2</sup> Σ <sub>u</sub> <sup>+</sup> ) state.	126



# FIGURES (CONTINUED)

<u>Figure</u>		<u>Page</u>
50.	a) 1.2 mtorr BPD data, band assignments, synthetic spectrum b) 1.2 mtorr non-BPD data, synthetic spectrum c) 20 mtorr non-BPD data and synthetic spectrum All the data was taken at a resolution of 15.6Å.	127
51.	Relative populations of band systems observed in the 440 to 800 nm spectral region without BPD, at a pressure of 1.2 mtorr of laboratory air.	129
52.	Relative vibrational populations of the observed band systems $N_2(C-B)$ , $N_2^+(B-X)$ , $N_2^+(A-X)$ at a pressure of 1.2 mtorr with and without BPD operative.	131
53.	Relative vibrational population of the $N_2(B-A)$ band system for 1.2 mtorr air and 1.0 mtorr $N_2$ .	132
54.	Band system distribution at 1.2 mtorr and 20.0 mtorr pressures of air, normalized to the $N_2(B-A)$ relative population.	135
55.	Upper vibrational level distributions in air at 1.2 and 20.0 mtorr pressures for the $N_2(C-B)$ , $N_2^+(B-X)$ , $N_2^+(A-X)$ band systems.	137
56.	Relative populations in the $N_2(B)$ state at 1.2 and 20.0 mtorr of air, 1.0 mtorr of $N_2$ and a prediction from radiative transfer and F-C factors.	138
57.	$\Delta v = 0$ sequence fit for $N_2(B-A)$ and atomic lines.	147
58.	$\Delta v = 0$ sequence fit for $N_2(B-A)$ , $N_2^+(A-X)$ , and atomic lines.	147
59.	$\Delta v = 0$ sequence fit for $N_2(B-A)$ , $N_2^+(A-X)$ , atomic lines with estimated contributions from other $N_2(B-A)$ sequences subtracted out.	147
60.	Variation in the electron-transition moment with r-centroid for the $N_2$ first-positive system.	150
61.	Electronic transition moments for $N_2(B^3\Pi_g - A^3\Sigma_u^+)$ .	152
13.	Energy level diagram for $N_2$ singlets.	160
62.	Schematic diagram of experimental apparatus used in quenching experiments.	163

# FIGURES (CONTINUED)

Figure		Page
63.	Two photon laser induced fluorescence spectrum of $N_2(a-X, 0-0)$ band.	169
64.	Fluorescence decay of $N_2(a^1\Pi_g)$ following laser excitation of $N_2(a, v'=0)$ .	169
65.	Plot of first-order decay rates as a function of $N_2$ density.	170
66.	Stern-Volmer plots for quenching of $N_2(a, v'=0)$ by $O_2$ , $H_2$ and $CO_2$ .	171
67.	Stern-Volmer plot for quenching of $N_2(a, v'=0)$ by $CO$ .	173
68.	$O_3$ fluorescence in $Ar/O_2$ mixture.	175
69.	$O_3$ fluorescence in $N_2/O_2$ mixture.	175
70.	$O_3$ fluorescence and spectral fit of 1 mtorr $O_2/9$ mtorr $N_2$ .	177
71.	$O_3(v=1)$ signal level pressure variation in $O_2/N_2$ with 200/1200 sccm flow.	179
72.	$O_3(v=1)$ signal level pressure variation in $O_2/Ar$ with 200/800 sccm flow.	180
73.	Residence time dependence of $O_3(v=1)$ signal in 1/4: $O_2/Ar$ mixtures at three pressures.	181
74.	Sum of population of $O_3^*$ from spectral synthetic code for 1 mtorr $O_2$ in varying $Ar$ pressure.	184
75.	Residence time normalized $O_3^*$ population versus $Ar$ pressure.	185
76.	$O_3^*(v \geq 2)$ population residence time normalized versus $Ar$ pressure.	186
77.	Population of $O_3^*(v)$ from spectral synthesis code for 1 mtorr $O_2$ in varying $N_2$ pressure.	187
78.	Residence time normalized $O_3^*(v)$ population versus $N_2$ pressure.	188
79.	Residence time normalized $O_3^*(v \geq 2)$ population versus $N_2$ pressure.	189

# FIGURES (CONTINUED)

<u>Figure</u>		<u>Page</u>
80.	Population of $O_3^*(v)$ with varying amounts of $O_2$ in 37 mtorr Ar.	191
81.	Population of $O_3^*(v \geq 2)$ with varying amounts of $O_2$ in 37 mtorr Ar.	192
82.	Temperature dependence of $O_3^*(v=1)$ emission intensity in $N_2$ buffer gas.	193
83.	Temperature dependence of the sum of $O_3^*(v)$ population in a buffer gas.	193
84.	Ozone vibrational distributions at beam termination $O_3^*(0,0,v)$ .	195
85.	Beam termination vibrational distributions of $O_3^*(0,0,v)$ with/without BPD.	196
86.	Pressure variation of rise times of fluorescence intensity upon start of $O_2$ flow to generate a 1/6: $O_2/N_2$ gas mixture.	197
87.	Flow variation of rise times of fluorescence intensity upon start of $O_2$ gas flow to obtain a 1/6: $O_2/N_2$ gas mixture.	197
88.	Flow variation of fall times of fluorescence intensity upon shutoff at $O_2$ gas flow for a 1/6: $O_2/N_2$ gas mixture.	198
89.	Pressure variation of fall times of fluorescence intensity upon shutoff of $O_2$ gas flow for a 1/6: $O_2/N_2$ gas mixture.	198
90.	Temporal behavior of $O_3^*$ fluorescence for a 9 mtorr Ar/1 mtorr $O_2$ mixture.	203
91.	Comparison of relaxation rates using single quantum vibrational and radiative model for a 35 mtorr Ar/1 mtorr $O_2$ mixture.	206
92.	Stern-Volmer plot of $O_3^*(v=1)$ in 1 mtorr $O_2$ and varying Ar pressure.	206
93.	Diffusion corrected Stern-Volmer plot of $O_3^*(v=1)$ in 1 mtorr $O_2$ and varying Ar pressure.	208
94.	Stern-Volmer plot of $O_3^*(v=1)$ for all $O_2/N_2$ mixtures.	209
95.	Stern-Volmer plot of $O_3^*(v=1)$ for $O_2$ /Ar mixtures at 30 mtorr Ar.	210

# FIGURES (CONTINUED)

<u>Figure</u>		<u>Page</u>
96.	Stern-Volmer plot of $O_3^*(v=2)$ for $O_2/Ar$ mixtures at 30 mtorr Ar.	210
97.	EXCEDE SWIR/MWIR spectral scan at 294.9s after launch.	213
98.	EXCEDE MWIR/LWIR spectral scan at 282s after launch.	213
99.	Digitized SWIR scan 524 with linear intensity scale.	218
100.	Digitized MWIR scan 1200 with linear intensity scale.	218
101.	Simulated atomic lines at 3.33 $\mu m$ (a) and 6.67 $\mu m$ (b) convolved with the skewed Gaussian slit function.	222
102.	Simulated atomic lines at 3.33 $\mu m$ (a) and 6.67 $\mu m$ (b) convolved with a Gaussian (FWHM = 0.02 $\lambda_0$ slit function).	223
103.	Uncorrected SWIR scan 490 (TAL = 278.5s, Alt = 89.8 km).	224
104.	Background of the SWIR scans as a function of altitude, normalized to 391 nm photometer emission intensity (L4).	224
105.	Wavelength dependence of the air afterglow emission in the 2 to 5 $\mu m$ region.	225
106.	SWIR scan 524 with background correction (TAL = 294.9s, Alt = 74.6 km).	226
107.	Auroral $N_2$ excited state densities.	228
108.	SWIR scan 524 with fit to $N_2 W^3\Delta_u \rightarrow B^3\Pi_g$ ( $v'=2-5$ ) emission.	230
109.	Corrected scan 524 fit to $N_2(W^3\Delta_u \rightarrow B^3\Pi, v'=2-9)$ at a rotational temperature of 200 K.	231
110.	Determined relative population distribution for $N_2(W^3\Delta)$ normalized at $v'=3$ .	232
111.	$H_2O$ vibrational emission basis sets at 200 K (a) and 400 K (b).	236
112.	Uncorrected SWIR scan 524 fit to 200 K $H_2O$ vibrational basis set.	237
113.	Uncorrected scan 520, TAL = 161.0s, Alt = 125.2s, and fit to 200 K $H_2O$ emission.	237

# FIGURES (CONTINUED)

Figure		Page
114.	Uncorrected MWIR scan 1200 (TAL = 282.0s, Alt = 86.8 km) with fits to NO ( $\Delta v=1$ , $v'=2-12$ ) with independent vibrational variation and with the COCHISE nascent relative vibrational distribution.	239
115.	Relative NO vibrational population distributions at 75.4 km.	240
116.	Relative NO vibrational population distributions at 81.3 km.	241
117.	Relative NO vibrational population distributions at 91 km.	242
118.	Corrected SWIR scan 524 with fit to $N_2(w^1\Delta \rightarrow a^1\Pi$ , $v'=0-2$ ) at a rotational temperature of 200 K.	244
119.	Corrected SWIR scan 524 with fit to $N_2(a^1\Pi_g \rightarrow a'^1\Sigma_u^-$ , $v'=1-5$ ) at a rotational temperature of 200 K.	245
120.	Corrected SWIR scan 524 with fit to $N_2(B'^3\Sigma_u^- \rightarrow B^3\Pi_g$ , $v'=0-3$ ) at a rotational temperature of 200 K.	245
121.	Corrected SWIR scan 524 with fit to $N_2(B^3\Pi_g \rightarrow A^3\Sigma_u^+$ , $v'=0-3$ ) at a rotational temperature of 200 K.	246
122.	Corrected SWIR scan 524 with fit to $N_2(B^3\Pi \rightarrow W^3\Delta_u$ , $v'=2-5$ ) at a rotational temperature of 200 K.	247
123.	Corrected SWIR scan 524 with fit to $N_2^+(A^2\Pi \rightarrow X^2\Sigma$ , $v'=0-3$ ) at a rotational temperature of 200 K.	248
124.	UV spectral scan 149 uncorrected for beam variations.	250
125.	UV spectral scan 116 uncorrected for beam variations.	250
126.	Uncorrected visible scan 47 (TAL = 196s, Alt = 128.3 km).	251
127.	Uncorrected visible scan 73 (TAL = 296s, Alt = 74 km).	251
128.	Comparison of data from scan 116 to $N_2(a-X)$ emission.	252
129.	Determined populations for the indicated $N_2$ and $N_2^+$ states from the UV, Visible, and IR EXCEDE data for the 120 to 128 km range.	253
130.	Determined populations for the indicated $N_2$ and $N_2^+$ states from the UV, Visible, and IR EXCEDE data for the 74 to 79 km range.	254

# FIGURES (CONTINUED)

Figure		Page
131.	Cartwright predictions for several N <sub>2</sub> states (for comparison with Figures 129 and 130).	255
132.	Nitrogen electronic populations in LABCEDE (80 km altitude).	256
133.	IR interferometer data from EXCEDE.	257
134.	Overlay of IR interferometer data with a Wu-Benesch spectrum based on LABCEDE distribution.	259
135.	Comparison of an IR interferometer scan with H <sub>2</sub> O emission.	260
136.	Corrected SWIR scan 524 with fit to OH ( $v'=-13$ ) fundamental emission at a rotational temperature of 200 K.	262
137.	Data (dark line) and fit (light line) to NO fundamental and overtone emission.	263
138.	Data from previous figure with NO fundamental and overtone emission subtracted.	263
139.	InSb detector module assembly.	268
140.	IR detector layout.	269
141.	Background thermal noise in-band with chopping.	271
142.	Radiometer package - cover removed.	272
143.	Radiometer system schematic.	273
144.	Power and control block diagram	274
145.	Schematic InSb amplifier and signal processor.	275
146.	Software structure.	276
147.	These curves show for unfiltered and AMO spectral distributions from the solar simulator.	281
148.	The upper state vibrational level distribution is shown with and without the addition of solar UV-visible radiation.	283
149.	This figure shows the band system distribution obtained with and without solar UV-visible radiation.	285

# FIGURES (CONTINUED)

<u>Figure</u>		<u>Page</u>
150.	This figure presents the upper state vibration level distribution both with and without the presence of solar UV-visible radiation.	286
151.	This figure presents the upper state vibrational level distribution with and without solar-UV, visible radiation.	287
152.	SWIR spectra for 5 mtorr pressure of 20 percent oxygen, 80 percent nitrogen with BPD taken in time dependent data collection mode, performed by chopping the solar simulator photon beam.	291
153.	SWIR spectra under the same conditions as Figure 152 except taken in the manual data collection mode.	292
154.	SWIR spectra with the previous gas conditions, except without BPD ignited, taken in time dependent data collection mode.	293
155.	SWIR spectra at the same gas conditions as before, with BPD ignited, however performed by pulsing the electron beam with the solar simulator off.	294
156.	MWIR spectra at 5 mtorr of a 20/80 percent mixture of O <sub>2</sub> /N <sub>2</sub> , with BPD, taken in time dependent data collection mode, performed by chopping the solar simulator.	295
157.	MWIR spectra at 4 percent O <sub>2</sub> in N <sub>2</sub> without BPD, taken in time dependent data collection mode by pulsing the electron beam with the solar simulator off.	295
158.	Summary of the cross sections for the electron collision with N <sub>2</sub> .	302
159.	Differential elastic cross section at 1 keV.	303
160.	Generalized oscillator strength versus the square of the momentum transfer for 30 eV energy loss.	307
161.	Generalized oscillator strength versus the square of the momentum transfer for 50 eV energy loss.	308
162.	Generalized oscillator strength versus the square of the momentum transfer for 80 eV energy loss.	309
163.	Comparison of simulated and experimental radial distributions for the two N <sub>2</sub> pressures of 30 and 60 mtorr.	312

# FIGURES (CONTINUED)

<u>Figure</u>		<u>Page</u>
164.	Comparison of simulated and experimental radial distributions for the two N <sub>2</sub> pressures of 30 and 50 mtorr.	313
165.	Comparison of simulated and experimental radial distributions for the two N <sub>2</sub> pressures of 30 and 50 mtorr.	314
166.	Comparison of different inelastic angular distributions to simulate a radial distribution for 30 mtorr N <sub>2</sub> pressure at a primary energy of 2 keV.	315
167.	Comparison of simulated and experimental radial distribution for the two N <sub>2</sub> pressures of 30 and 60 mtorr.	316
168.	Effect of increasing the total cross section by 20 percent for the two N <sub>2</sub> pressures of 30 and 60 mtorr at a primary energy of 2 keV.	317
169.	Comparison of simulated and experimental radial distributions for the two N <sub>2</sub> pressures of 30 and 60 mtorr.	319
170.	Comparison of simulated and experimental radial distributions for the two N <sub>2</sub> pressures of 30 and 50 mtorr.	320
171.	Concentrations of major species for the ninth and tenth pulses in a mixture of 7.5 torr of N <sub>2</sub> and 0.2 torr of H <sub>2</sub> .	331
172.	Comparison with LABCEDE experimental data for NHv decay in a mixture of 4.05 torr of N <sub>2</sub> and 0.2 torr of H <sub>2</sub> .	333
173.	Comparison with LABCEDE experimental data for NHv decay in a mixture of 7.5 torr of N <sub>2</sub> and 0.05 torr of H <sub>2</sub> .	334
174.	Comparison with LABCEDE experimental data for NHv decay in a mixture of 7.54 torr of N <sub>2</sub> and 0.4 torr of H <sub>2</sub> .	335
175.	Comparison with LABCEDE experimental data for NHv decay in a mixture of 30.11 torr of N <sub>2</sub> and 0.2 torr of H <sub>2</sub> .	336
176.	Spectrum of CaF <sub>2</sub> (as delivered) irradiated by 2.5 mA of 4.5 keV electrons magnetically confined to irradiate a small portion of the window surface.	343
177.	Spectrum of a 596°C blackbody of 0.65 mm diameter (3.3 x 10 <sup>-3</sup> cm <sup>2</sup> ).	343



# FIGURES (CONTINUED)

Figure		Page
178.	Emission from previously marred $\text{CaF}_2$ (as delivered) irradiated by 1.6 mA of defocussed 4.5 keV electrons.	344
179.	Emission from a blackbody of $150^\circ\text{C}$ with an aperture of $0.33 \text{ cm}^2$ located 1m from interferometer.	344
180.	Spectrum of $\text{CaF}_2$ (as delivered) irradiated by 4 mA of diffuse 4.5 keV electrons striking the edge corner of the window sample.	346
181.	Spectrum of a $1400^\circ\text{C}$ blackbody of $1 \times 10^{-3} \text{ cm}^2$ area.	346
182.	Fluorescence from Apiezon coated $\text{CaF}_2$ irradiated by 3.2 mA of confined electrons.	347
183.	Emission through a $1 \times 10^{-2} \text{ cm}^2$ aperture viewing a $465^\circ\text{C}$ blackbody.	347
184.	Emission from a $\text{CaF}_2$ test sample coated with Cutzol 711 lubricant upon irradiation by 5 mA of diffusion 4.5 keV electrons.	349
185.	SWIR emission from $\text{CaF}_2$ test sampled loaded with Cutzol 711 lubricant upon irradiation by 5 mA of diffusion 4.5 keV electrons.	349
186.	Emission from $\text{CaF}_2$ test sample coated with MolyDee lubricant upon irradiation by 4 mA of 4.5 keV electrons.	350
187.	SWIR emission of same sample as Figure 186.	350
188.	A 1.5 mtorr pure NO spectra at $5.2\text{\AA}$ resolution.	352
189.	Synthetic spectra generated with NO $\gamma$ -bands.	353
190.	a) Synthetic spectrum generated using $1200 \text{ K NO}(A^2\Sigma^+-X^2\Pi)$ , $300 \text{ K N}_2(C^3\Pi_u-B^3\Pi_g)$ , and $300 \text{ K N}_2^+(B^2\Sigma_u^+-X^2\Sigma_g^+)$ ; b) addition of $300 \text{ K NO}(B^2\Pi-X^2\Pi)$ to a); c) addition of $300 \text{ K O}_2^+(A^2\Pi_u-X^2\Pi_g)$ to a); d) addition of both $\text{NO}(B-X)$ and $\text{O}_2^+(A-X)$ to a).	354
191.	Fluorescence from irradiated Ar/NO mixture at 7 mt pressure.	357
192.	MWIR fluorescence from irradiated $\text{N}_2/\text{O}_2$ mixtures ( $p=35\text{mt}$ ) near beam termination.	359

# FIGURES (CONCLUDED)

<u>Figure</u>		<u>Page</u>
193.	MWIR fluorescence from irradiated N <sub>2</sub> /O <sub>2</sub> mixtures (p=35 mt) 20 ms after beam termination.	359
194.	SWIR fluorescence from irradiated N <sub>2</sub> /O <sub>2</sub> mixtures (p=35mt) near beam termination.	360
195.	MWIR fluorescence from irradiated N <sub>2</sub> /O <sub>2</sub> mixtures (p=35 mt) 45 ms after beam termination.	360
196.	MWIR fluorescence from irradiated Ar/trace CO <sub>2</sub> mixtures at 30 mt at beam termination.	361
197.	MWIR fluorescence from Ar/trace CO <sub>2</sub> mixtures 90 ms after beam termination.	361
198.	MWIR fluorescence from Ar/trace CO <sub>2</sub> mixture at 1.9 mt, 10 ms after beam termination.	362
199.	Fluorescence from 36 mt N <sub>2</sub> /trace CO <sub>2</sub> mixture at 25 ms after beam termination.	363
200.	Intensity of CO <sub>2</sub> (v <sub>2</sub> ) R branch fluorescence as a function of time after beam termination for N <sub>2</sub> and N <sub>2</sub> /O <sub>2</sub> bath gases.	364
201.	LWIR emission from Ar/O <sub>2</sub> mixtures 15 ms after beam termination.	364

# TABLES

<u>Table</u>		<u>Page</u>
1.	Ratio of transfer rates from A-state to direct electron production rates.	32
2.	$N_2(a^1\Pi_g-X^3\Sigma_g^+)$ Einstein coefficients, $A_{v',v''}$ ( $s^{-1}$ ) and transition frequency ( $cm^{-1}$ ).	53
3.	$N_2(a,v)/N_2(C,2)$ population ratios.	56
4.	$N_2(a^1\Pi_g-a'^1\Sigma_u)$ Einstein coefficients.	61
5.	$N_2(a,v \rightarrow v-1)$ rate coefficients.	66
6.	Relative Meinel-band excitation rates.	90
7.	Absolute Meinel-band electron-impact excitation cross sections at 100 eV.	93
8.	Normalized populations for B-A $v'=0-7$ used in interferometer data analysis.	106
9.	Emission intensity enhancements upon beam plasma discharge occurrence (1.2 mtorr).	130
10.	Populations of $N_2(C^3\Pi_u)$ , $v'=0,1$ states for a variety of low pressure experiments.	133
11.	Populations of $N_2^+(B^2\Sigma_u^+)$ , $v'=1,2$ states for a variety of low pressure experiments.	133
12.	Populations of $N_2^+(A^2\Pi_u)$ , $v'=2,3,4$ states for a variety of low pressure experiments.	134
13.	Pressure scaling of emission features.	136
14.	Pressure scaling of $N_2^+B$ distributions.	139
15.	$N_2(B^3\Pi_g)$ lifetimes in microseconds.	151
16.	Einstein coefficients and associated data for the nitrogen first-positive system.	153
17.	Measured quenching rate coefficients for $N_2(a,^1\Pi_g)$ , $v'=0$ .	172
18.	Digitized SWIR scans.	216
19.	Digitized MWIR scans.	217

# TABLES (CONCLUDED)

<u>Table</u>		<u>Page</u>
20.	Merged SWIR/MWIR scans.	217
21.	UV and visible interferometer scans.	217
22.	EXCEDE SWIR photometer data.	219
23.	H <sub>2</sub> O IR emission features.	234
24.	OI and NI infrared emission lines.	249
25.	Radiometer detector bandpasses (μm).	270
26.	Components list for radiometers.	277
27.	Estimates of the initial yields of active species, expressed as g-values (number/100 eV).	325
28.	Dose rate estimates for various N <sub>2</sub> pressures.	327
29.	Major reactions considered.	328
30.	Calculated and experimental decay rates and reaction importance for 0.3-ms pulse width.	337
31.	Calculated decay rates and reaction importance for different pulse widths (pulse period 15 ms for a mixture of 15 torr N <sub>2</sub> and 0.2 torr H <sub>2</sub> ).	338
32.	Experimental decay rates and relative NHv concentration for different pulse widths for 15 torr N <sub>2</sub> , 0.2 torr H <sub>2</sub>	338

## 1. INTRODUCTION

This report covers a wide variety of research projects to measure and interpret the fluorescence arising from electron excitation of atmospheric gases. The LABCEDE facility at the Air Force Geophysics Laboratory was used for most of these investigations. The first sections deal with the excitation and energy transfer in electronic states of  $N_2$ . In Section 2, the  $N_2$  B-state behavior is monitored via First Positive fluorescence. Excitation is Franck Condon at low pressure but as pressure increases to tens of mtorr (representative of the mesosphere), collisional transfer from the A-state into the lowest B state vibrational levels is observed. The middle levels of the B-state show little variation with pressure even though they strongly coupled to W-state levels. This is attributed to low production efficiency into the W-state. Thus the shift in B-state populations is not responsible for the formation of a lower red border of aurora. However, the A-state transfer will result in an increase in 0.8 to 2  $\mu m$  emission at lower altitudes.

The  $N_2a(^1\Pi_g)$  state was observed via LBH emission at 0.2  $\mu m$ . Substantial vibrational redistribution rather than electronic quenching was observed. Relaxation out of the highest vibrational levels was nearly gas kinetic. Again nested electronic states in particular the  $a'$ -state are involved in the relaxation. The global measurements performed in LABCEDE are described in Section 3. These observations emphasized the need for level-specific investigations of the  $N_2a, v$  relaxation. The relaxation of  $N_2a, v=0$  by a variety of gases including  $N_2$  and  $O_2$  is reported in Section 8.

Section 4 describes the measurement electron impact excitation cross sections for  $N_2^+ A, v=2-7$  as measured in LABCEDE at sufficiently low pressures that quenching affects can be removed through a Stern-Volmer analysis.  $N_2$  electronic state transitions can also occur in the infrared. In Section 5, data from two infrared spectrometers (a CDF and an interferometer) are used to determine the relative contributions of various transitions to the IR spectrum

observed in LABCEDE. Transitions from  $N_2(W-B)$ ,  $(W-a)$ ,  $(a-a')$ ,  $(B-A)$  and  $N_2^+(A-X)$  all contribute to the low pressure spectrum. In addition changes in relative populations are observed as pressure is varied. This data provides the basis for predicting the fluorescence from electron irradiated  $N_2$  which is a necessary basis for disturbed atmospheres code predictions and will serve to guide the analysis of data from field programs such as EXCEDE. Our analysis of the emission from pure  $N_2$  was completed first to provide a basis for comparison when  $N_2/O_2$  irradiated mixtures were studied as described in Section 6. Changes in production efficiency and state distributions upon variations in electron energy distribution and  $O_2$  addition were small. The fluorescence levels from neutral  $N_2$  are insensitive to large changes in the dosing levels. Oxygen addition resulted in the production of new features,  $N_2$  fluorescence levels were relatively unaltered.

The First Positive emission system is unique in that its transitions span the 0.6 to 3  $\mu m$  wavelength region. The relative brightness of the bands depends on the nature of the transition moment variation over a large range of internuclear separations. In Section 7 we examine First Positive emission detected in several experimental facilities including LABCEDE in order to determine the transition moment variation. Emissions from the  $\Delta V=+6$  to  $-2$  sequences was analyzed to deduce a nearly linear transition moment variation. We recommend changes to the B-state and A-state radiative lifetimes.

Ozone fluorescence is observed in cryogenic LABEDE at levels in excess of three body production levels. We report in Section 9 observations of  $O_3$  fluorescence at 10  $\mu m$ : spectral distributions and their dependence on parametrical variations. A preliminary review of mechanisms is also presented. With pulsed excitation, the fluorescence spectrum was observed to decay after beam termination at different rates depending upon pressure and composition of the irradiated mix. Treatment of the vibrational level dependent relaxation of  $O_3^*$  is described in Section 10.

Laboratory investigations provide insight into mechanisms and efficiencies which can be used to aid in the understanding of field data. In Section 11 we present an analysis of IR, UV and visible data from the electron-irradiated mesosphere/thermosphere as observed in the EXCEDE mission. Many of the  $N_2$  electronic state transitions described above are observed in that data along with  $CO_2$ ,  $NO$  and other radiators. In Section 12 we briefly describe a radiometer package we are assembling to permit the study of fast atom reactions created by electron impact or in interactions in the environment encountered by orbital missions.

Data from an early field mission seemed to indicate that the auroral fluorescence spectrum was different under sunlit conditions. We undertook a laboratory simulation of this phenomenon using a solar simulator and a pulsed electron beam simultaneously incident on  $N_2/O_2$  mixtures. In Section 13 we report on these observations. No detectable difference was observed in the observed fluorescence between 0.3 to 0.8  $\mu m$  and 2.2 to 6.8  $\mu m$  upon solar illumination.

The LABCEDE Facility can be used to provide an understanding of electron/ $N_2$  molecular scattering processes. Using a scanning photometer ( $\lambda = 391$  nm), beam shape is carefully monitored. As pressure is increased, the observed beam width increases due to both elastic and inelastic scattering processes. Our modeling of this data in support of these experiments is presented in Section 14. A separate modeling effort is described in Section 15. NH emission is observed in  $N_2/H_2$  mixtures irradiated by 40 keV electrons in the small LABCEDE chamber. Quenching rate coefficients can be obtained for NH,  $v=1-3$  by  $N_2$  and  $H_2$  once quenching by beam created species is considered. We present time-dependent modeling of this system for atom production, relaxation, and reaction processes. This model has been useful in guiding experiments and the data analysis.

It has been postulated that electron-impact on optical elements could produce a detectable signature. The Field Widened Interferometer penetrated an active

auroral region and observed unexplained IR features. LABCEDE investigated the emission from clean and contaminated calcium fluoride optical flats irradiated by electrons. In Section 16 we report no emission was detected at irradiation levels below optical element damage thresholds. In the last chapter several spectral observations are presented to document and to serve as a guide for potential future projects. Appendices include a) a list of publications and presentations on the research performed under this contract; b) an operations manual for the cryogenic LABCEDE facility; c) a description of the spectral generation code; d) a report by the University of Arizona on heavy ion bombardment of atmospheric gases performed as a subcontract; and e) data analysis of IR atomic emissions from a discharge apparatus.

The numerous sections of this report clearly indicate the versatility and productivity of the LABCEDE Facility in addressing production rate, energy transfer processes, chemiluminescence in electron irradiated air and in performing laboratory screening/simulations, to guide models and field missions.

The authors wish to acknowledge the great assistance of G.E. Caledonia, W.T. Rawlins, S.J. Wolnik, P.F. Lewis, and D. Tremblay in the completion of various phases of this project.



## 2. EXCITATION AND QUENCHING OF THE VIBRATIONAL LEVELS OF $N_2(B^3\Pi_g)$ STATE IN ELECTRON IRRADIATED NITROGEN

### 2.1 INTRODUCTION

The fluorescence which arises from upper atmospheric species when they are excited by precipitating auroral electrons has been studied for many years, both in order to gain an understanding of upper atmospheric composition and key chemical processes, and to determine the efficiency of exciting various molecular states.<sup>1-5</sup> For some excited molecular systems this poses a complex problem because the altitude of peak auroral energy deposition occurs where the atmosphere is undergoing the transition from the radiatively-controlled, collisionless regime (at higher altitudes) to a region where collisional quenching and energy transfer become important. Above this transition altitude photon absorption, direct electron impact, and radiative cascade are the dominant processes. The altitude of the transition is not invariant for every molecular state, but of course depends upon the radiative lifetime of the excited state and its efficiency for being collisionally destroyed.

The most prominent band system of  $N_2$  in the visible aurora is the  $B^3\Pi_g \rightarrow A^3\Sigma_u^+$  "First Positive" transition. The B-state radiative decay lifetimes are relatively short (see Section 3), varying between 4 and 12  $\mu s$ ,<sup>6</sup> and collisional deactivation of this state (even if it occurs at a gas kinetic rate) will not become important until altitudes below the auroral deposition zone. However, the presence of other longer lived electronic states which are nearly resonant with the B-state vibrational levels (such as the high vibrational levels of the  $A^3\Sigma_u^+$  and the nearly degenerate  $W^3\Delta_u$  states) in a nested triplet manifold permits the possibility of enhancing B-state radiances via rapid intersystem energy transfer followed by prompt B-state radiative decay. The effects of such a transfer on the B $\rightarrow$ A spectrum have been suggested by Benesch.<sup>7,8</sup> He predicts that the enhancement would not be uniform, but that the populations of certain vibrational levels of the B-state would be selectively increased as a result of nearly resonant transfer with vibrational levels of the W-state.

He further suggested that laboratory measurements under appropriate conditions, although difficult, would be very useful in defining the importance of these processes.

A laboratory facility which is capable of investigating some of the fundamental chemical and radiative processes which play an important role in the auroral upper atmosphere has been constructed at the Air Force Geophysics Laboratory.<sup>9,10</sup> In this device, fluorescence over the spectral region 0.2 to 15  $\mu\text{m}$  has been observed when gases at pressures between 0.1 and 80 mtorr ( $0.01$  to  $10 \text{ N/m}^2$ ) were irradiated with an electron beam. These gas densities correspond to the ambient at atmospheric altitudes of 105 km down to 67 km.<sup>11</sup> Thus from systematic observations of the spectrally resolved fluorescence in the laboratory, the effects of collisional transfer on the  $\text{N}_2(\text{B})$  state populations can be investigated as the transition from collision-free to collisionally dominated regimes is traversed.

We report here our experimental results of the vibrational creation efficiencies upon electron impact within the  $\text{N}_2$  ionic  $\text{B}^2\Sigma_u^+$  states and the neutral  $\text{C}^3\Pi_u$  as well as the  $\text{B}^3\Pi_g$  states. The vibrational distributions within those states are determined over a range of pressures so as to isolate formation due to direct electron impact from excitation transfer. We postulate that the W-state is created less efficiently than the B-state upon electron-impact, and that transfer from the W- to the B-state occurs radiatively at low pressures and very efficiently in collisions as the pressure increases. At the highest experimental pressures collisional quenching of the B-state is observed. Thus the  $\text{N}_2(\text{W}^3\Delta_u)$  state should play a role as an important energy storage reservoir and contribute to the infrared spectrum of the aurorally disturbed upper atmosphere. Through use of an analytical model we have been able to rationalize the observed behavior of several B-state vibrational levels in a manner which is consistent with most of the relevant literature values of excitation, quenching and radiative decay of the W- and B-states.

A large increase is observed for the lowest vibrational levels (particularly  $v=0$ ), such that the total B-state population increases with pressure. This increase is not due to relaxation of the higher B, $v$  levels into  $v=0$ , but rather is due to transfer from another electronic state. Modeling of energy deposition, excitation cross sections and the flow in the experiment indicate that  $N_2A$ ,  $v=7-12$  levels will build to sufficient densities to transfer into the B-state at the observed rate. Thus, although we see little evidence of changes in the B-state distribution which will cause a "visible" lower red border aurora,  $B \rightarrow A$  emission at  $1-2 \mu m$  and  $W \rightarrow B$  emission at  $2-3 \mu m$  should exhibit a marked altitude dependence.

## 2.2 EXPERIMENTAL

The experiments were conducted at the LABCEDE facility<sup>9,10</sup> at the Air Force Geophysics Laboratory, operated at room temperature for these experiments. Fluorescence was observed in a cylindrical vacuum tank, 3.4m long and 1m in diameter in which an electron beam excites numerous molecular emissions in pure  $N_2$  gas, including the First Positive, Second Positive, First Negative and Meinel bands.<sup>9</sup> An inner liner, which is semi-vacuum tight, permits cryogenic operation. Gases flowing at rates up to 1.6 std. liters per minute were introduced into the reaction chamber through a large porous-tube array located inside one end of the liner enclosure. A plugged flow is developed along the longitudinal axis of the chamber and out through a 32-in. diffusion pump backed by a Roots blower/fore pump combination (effective pumping speed =  $2.6 \times 10^4 \text{ ls}^{-1}$ ). This flow pattern limits the residence time of gaseous species in the electron beam volume to only a few milliseconds at most. Consequently, quenching by electron-beam-created species is negligible. Flow rates can be varied over an order of magnitude at constant target chamber pressure by varying the conductance of the pumping system using a valve.

The electron beam enters the chamber through one side, a little over a meter from the upstream end of tank. The electron gun is in the Pierce configuration and can provide currents up to 25 mA at energies up to 6 kV at its space

charge limit. However, these studies were conducted using 4.5 keV electrons having currents of up to 14 mA with the beam operating continuously or pulsed at 50 percent duty cycle with a period of 4 ms.

These experiments were performed using ultra high purity (99.999 percent) nitrogen, and no further purification was attempted. The leak rate for the entire vacuum chamber (6000 l) was less than  $3 \times 10^{-5}$  std. liter per minute and the blank off pressure was less than  $10^{-6}$  torr. Fluorescent emissions from species other than  $N_2$  were not observed. In order to span the 0.15 to 81 mtorr pressure range,  $N_2$  gas flow rates between 20 and 1600 std. cubic centimeters per minute were required.

Fluorescence is observed through an observation port which views the excitation region from the upstream end of the tank, normal to the electron beam, and about 1.2m from it. Since the apparatus is double walled, the excitation region was viewed through two windows which were  $BaF_2$  and  $CaF_2$  for these observations. A 5 cm diameter, 10 cm focal length suprasil lens collects the fluorescence and focuses it upon the entrance slit of a 0.3m monochromator (McPherson 218). Two different configurations were employed to observe emission from levels  $v=0-12$  of the B-state, a 1200 groove/mm grating blazed at 500 nm, and a 600 groove/mm grating blazed at 1  $\mu m$ . Appropriate order sorting filters (with an out-of-band rejection ratio of  $10^{-6}$ ) were employed. For most of the experimental measurements, data was acquired with a resolution of 1.04 nm. Data with 0.2 nm resolution was acquired to search for the presence of unexpected spectral radiators and unusual rotational distributions. An HTV R955 photomultiplier operated under variable gains up to  $5 \times 10^6$  detects the photons. A fast current amplifier/recorder combination displays the photomultiplier output. The signal is also stored in a laboratory personal computer using a data translation (2801A) D/A converter. When the electron beam was pulsed, phase sensitive detection using a PARC Model 128 Lock-In Amplifier was used in conjunction with the current amplifier. For the infrared observations a IIT-FIS118 PMT with an S-1 response was used to observe fluorescence out to wavelengths of 1.1  $\mu m$ .

The image of the monochromator slit at the excitation region determines the detector's field of view. This image is about  $12 \times 0.5$  cm for viewing from the end of the tank. The field of view of the detector, therefore, is a rectangular slice through the electron beam which has a height larger or comparable to the diameter of the beam but which is narrow compared to the length of the irradiated volume. The mean radiative lifetimes of the  $N_2(C)$ ,  $N_2^+(B)$ ,  $N_2(B)$ , and  $N_2(W)$  states are 37 ns, 63 ns, 6  $\mu$ s, and 100  $\mu$ s respectively,<sup>6</sup> and the mean molecular velocity for a nitrogen molecule at 300 K is  $4.8 \times 10^4$  cm s<sup>-1</sup>. Even the longest lived of these species travels a characteristic distance of only about 5 cm prior to radiating. This distance is short enough to minimize significant diffusive losses out of the field of view in its long dimension. Experiments in which the length of the field of view was varied verified this assumption. Diffusion out of the field of view along the axis of the irradiated volume is balanced by diffusion into the field of view along the beam axis from species excited outside the monochromator field of view. Removal of the imaging lens reduced signal levels by a factor of three, but did not alter the fluorescence distributions observed.

A pair of external electromagnets are located outside the chamber configured so that the electron beam travels through their centers perpendicular to the plane of the magnets. Under high beam current and applied magnetic field conditions, beam-plasma instabilities are observed. These dramatically alter the low-energy "secondary" electron distribution. The majority of our experiments were performed well outside of the operating regime where this instability occurs. A few sets of data were acquired while the observation region was being subjected to this beam-plasma instability excitation in order to determine whether there is a dependence of the observed spectrum on the electron energy distribution.

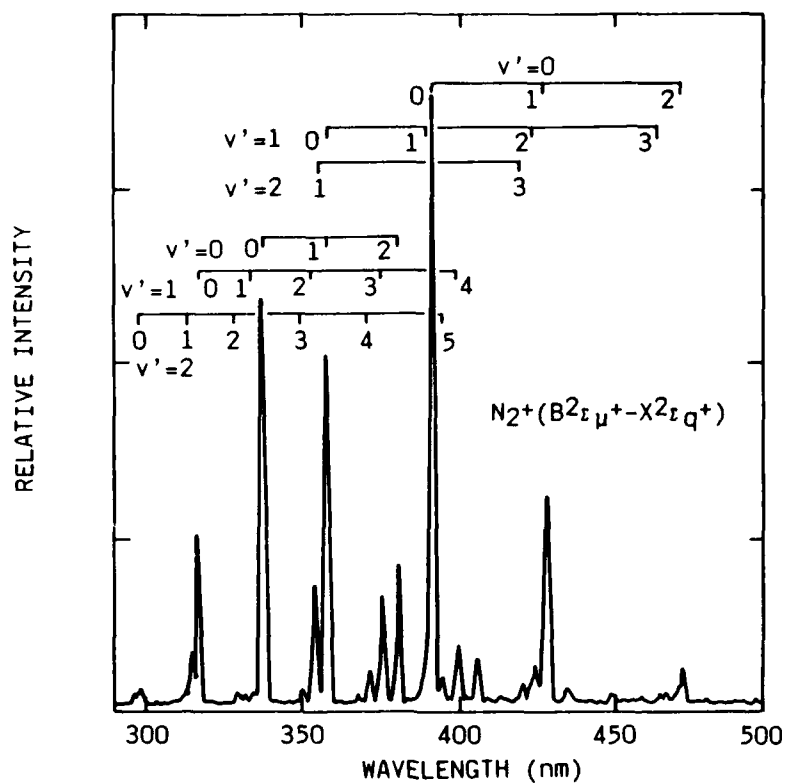
### 2.3 RESULTS AND ANALYSIS

The  $N_2(C-B)$  (Second Positive,  $N_2(B-A)$  (First Positive, and the  $N_2^+(B-X)$  (First Negative) transitions are the dominant radiators observed within the spectral

bandpass of our detection system. The Second Positive and the First Negative bands are spectrally compact and rotational structure within a band is not observed, but adjacent members of a vibrational sequence are clearly resolved under our experimental conditions. A representative spectral scan of these bands, taken at 0.15 mtorr, is shown in Figure 1. A spectrum of the First Positive bands, taken under the same conditions, is shown in Figure 2. The spectrum is much more dispersed, exhibits many overlapping features, and is distorted by the presence of  $N_2^+(A-X)$  (Meinel) bands. In analyzing most of the data which we will present, a simple measurement of peak heights was used to determine relative vibrational populations of the  $N_2(C)$  and  $N_2^+(B)$  states. This approach was found to be accurate since the half-widths of the peaks for each of the systems are similar and since the band systems emit over the same narrow range of wavelengths. Due to the complexity and breadth of the First Positive emission bands, a spectral fitting routine was required to obtain relative vibrational populations in the  $N_2(B)$  state. Specific band features within each system were also graphically integrated by hand to determine the total relative populations of all three electronic states.

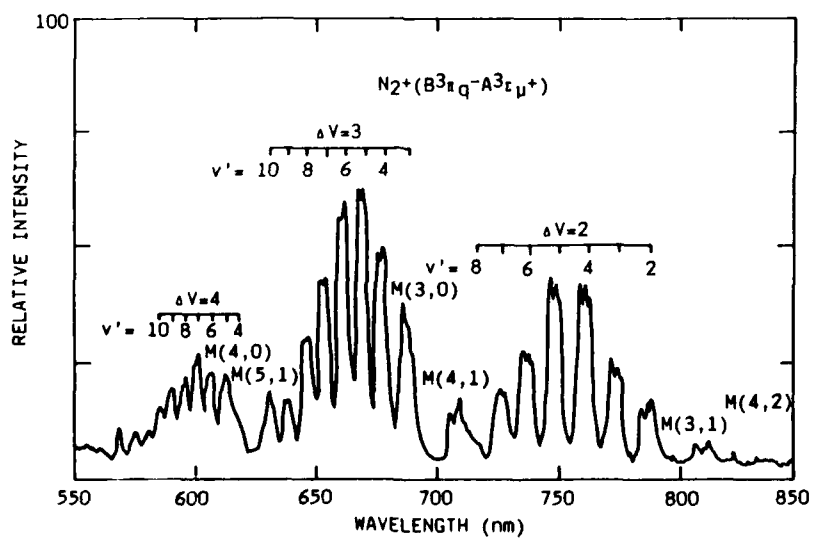
### 2.3.1 Vibrational Populations

The relative vibrational populations of the  $N_2(C)$  state were determined from peak signals of the 0-0, 1-0, 2-1 and 3-2 bands in the Second Positive emission system. The signals were corrected for detection system response and gain, and then converted to relative populations using absolute transition probabilities from Lofthus and Krupenie.<sup>6</sup> Band integrals and comparison with synthetic spectral produced the same distributions. Relative vibrational populations were determined as a function of nitrogen pressure from 0.15 to 81.5 mtorr and under a variety of electron dosings. Populations for three representative pressures are plotted as a function of vibrational level in Figure 3. The corresponding Franck-Condon factors for excitation from  $N_2(X, v=0)$  to  $N_2(C)$  are also plotted as the solid line in that figure. The relative vibrational populations of the C-state are essentially invariant over



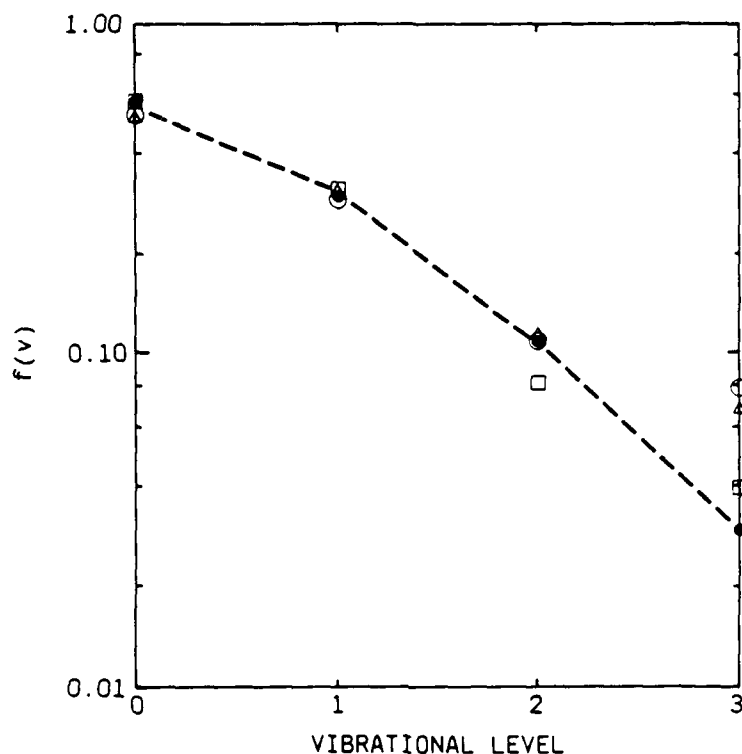
A-8312

Figure 1. Spectral scan of  $N_2^+(B-X)$  and  $N_2(C-B)$  emission excited by electron irradiation at a pressure of 0.15 mtorr. The resolution is 1.05  $\mu m$ .



A-8314

Figure 2. Spectral scan of  $N_2(B-A)$  and  $N_2^+(A-X)$  emission under same conditions as Figure 1.



A-8310

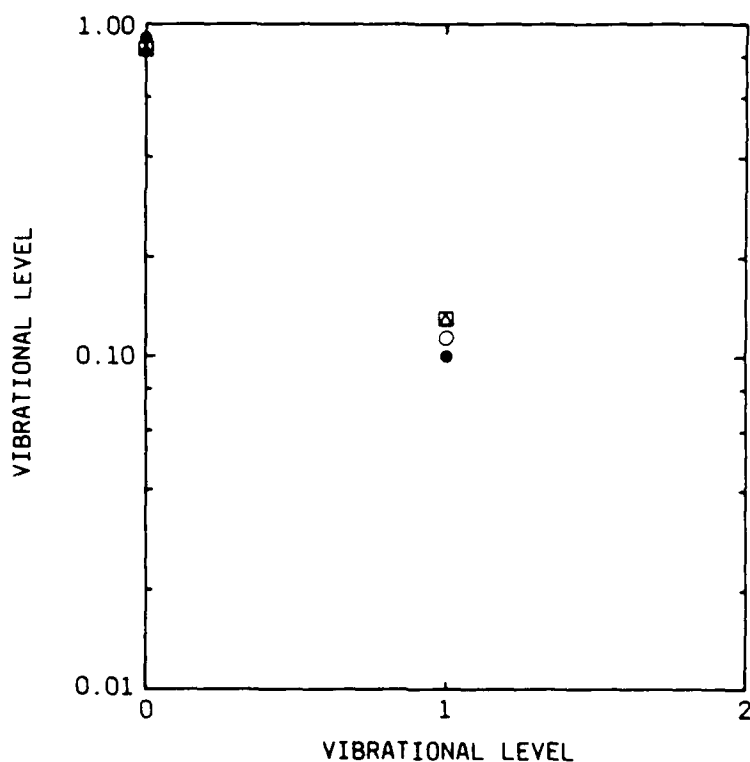
Figure 3. Relative vibrational populations of  $N_2(C)$  measured at  $\bigcirc$ , 1.0 mtorr;  $\triangle$ , 10 mtorr;  $\square$ , 70 mtorr. The filled circles located on the dashed line show the expected Franck-Condon and measured auroral distributions respectively. The estimated relative uncertainties in the populations are 10%.

this pressure range and closely follow the Franck-Condon excitation distribution previously seen in the laboratory.<sup>12</sup> The similarities between the observed populations and the Franck-Condon factors for excitation from ground state nitrogen are a result of the absence of radiative or collisional cascade into the C-state from higher energy electronic states, the uniform radiative lifetimes of all of the lower C-state vibrational levels, and the absence of any quenching due to the radiative lifetime (37 ns)<sup>6</sup> being much shorter than the time between collisions. The relative populations did not change over a wide range of dosing levels (even in a presence of a beam-plasma discharge) and their similarity to those predicted on the basis of Franck-Condon excitation of  $N_2(X, v=0)$  would seem to indicate that there is little vibrationally excited nitrogen present, even under these extreme conditions.



Relative vibrational populations for  $N_2^+(B)$  were determined from the experimental spectra in a similar manner to  $N_2(C)$  using the absolute transition probabilities of Shemansky and Broadfoot.<sup>13</sup> The 0-0 and 1-2 bands were used in the population analysis. The relative vibrational populations for this state were also studied as a function of pressure from 0.15 to 81.5 mtorr. These populations, determined at three representative pressures, are plotted in Figure 4. The corresponding Franck-Condon factors for ionization from vibrationally cold molecular nitrogen, normalized for the variation in  $N_2^+(B)$  radiative lifetime with vibrational level, are also plotted as the dashed line in the figure. These relative populations are also independent of pressure, within experimental error, up to pressures of 81.5 mtorr and agree well with those expected based on a Franck-Condon excitation profile for levels 0 and 1. The population of the  $v=2$  cannot be accurately determined due to underlying spectral features masking emissions from this level, however, the relative population of this level is only a minor fraction of the total ion B-state population. As with the C-state, the radiative lifetimes of these levels (62.5 ns)<sup>6</sup> are all much shorter than the mean time between collisions and radiative or collisional transfer of energy into this state from other electronic states is negligible. Radiative cascade into the ionic B-state has been estimated to be small (Cartwright). If this is the case, then the observed distribution reflects the nascent electronic state vibrational distribution produced by electron-impact excitation.

The spectrum of the  $N_2(B \rightarrow A)$  bands were recorded using both detector configurations so that the relative vibrational populations for the  $N_2(B)$  levels 0-12 could be determined. Emission from the (0-0) transition at  $1.05 \mu m$  was the sole feature observed from the  $B, v'=0$  level. Emission from multiple transitions was used to determine the relative populations of all other vibrational levels. At all pressures some emission due to the Meinel ( $A-X, v'-v'' = 4-0, 5-1, 3-0, 4-1, 2-0, 3-1$ ) transitions is present; however, the  $N_2^+(A)$  state is efficiently quenched by nitrogen<sup>10</sup> and the Meinel band intensities decreased with pressure relative to the First Positive emission.



A-8309

Figure 4. Relative vibrational populations of  $N_2^+(B)$  measured at  $\bigcirc$ , 1.0 mtorr;  $\triangle$ , 30 mtorr;  $\square$ , 81 mtorr. The filled circles show the expected Franck-Condon distribution while the solid line shows the measured auroral distribution. The relative populations are accurate to 10%.

A computer code to create synthetic spectra was developed to permit us to accurately determine relative population of electronically excited states in  $N_2$  under conditions when spectral overlap is severe.<sup>14</sup> Our model is based on the work of Kovacs<sup>15</sup> and is implemented through a major modification and extension of the computer code of Whiting, et al.<sup>16,17</sup> Values of spectroscopic constants ( $\omega_e$ ,  $\omega_e X_e$ ,  $B_v$ , etc.) and transition strengths ( $A_{v',v''}$ ) taken from Lofthus and Krupenie<sup>6</sup> were tabulated as input to the code along with populations and rotational temperature. (Rotational levels are assumed to be in Boltzmann equilibrium).

The calculated line intensities are distributed over wavelength space and then convolved with the appropriate monochromator slit function. The spectra were adjusted for monochromator spectral response. Synthetic spectra with

rotational temperatures of 300 K matched the experimental spectra very closely. Vibrational populations within the excited electronic states were determined by minimizing the square of the difference between the data and the synthetic spectrum. The ability to simultaneously match the intensities of several transitions in different progressions arising from the same emitting state provided confidence in the accuracy of the procedure. The fitting procedure was able to determine populations to  $\pm 10$  percent accuracy. To verify the procedure, populations obtained in this manner agree very well with direct spectral integration.

This code has the ability to create spectra which combine emissions from several different molecular states. Because the Meinel bands ( $N_2^+ A \rightarrow X$ ) underlie the First Positive features, those transitions were included in our spectral fits. Spectroscopic constants were taken from Huber and Herzberg.<sup>18</sup> Einstein coefficients listed by Lofthus and Krupenie<sup>6</sup> were used.

A typical spectrum of the First Positive band emission at 1 mtorr total pressure, and the synthetic fit to that spectrum, is shown in Figure 5 for the range 550 to 820 nm. First Positive  $\Delta v=2, 3$ , and 4 sequences occur in this spectral region. The fits to the spectra were generated assuming a rotational and spin temperature of 300 K and are generally accurate to within 10 percent for vibrational levels 2-10 and 50 percent for levels 0, 1, 11, and 12. This treatment is adequate at pressures of 1 mtorr and above; however, below 1 mtorr there is some evidence of spin disequilibrium. This is seen in Figure 6 where the spectrum recorded at the lowest (as limited by signal levels) experimental pressure, 0.15 mtorr, is presented. At present our spectral fitting routines do not permit the uncoupling of spin and rotational temperature, so our fit at these pressures is slightly less accurate, but a "colder" overall spin/rotational temperature would more closely fit the data. This is an indication that the B state is preferentially formed in lower energy spin states, either by direct electron impact or by radiative cascade. However, comparison with direct spectral integration indicates that the vibrational populations determined under these conditions are still accurate to within 15 percent.

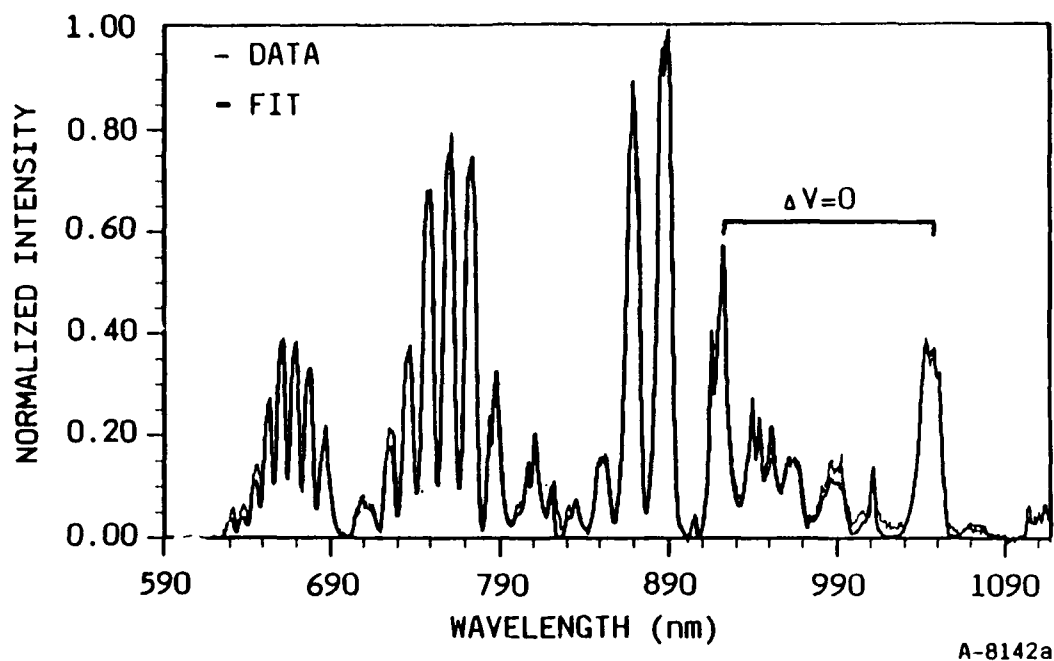


Figure 5. Spectrum of  $N_2(B-A)$  emission excited at 1.0 mtorr pressure (light line) and synthetic fit to spectrum (solid line).

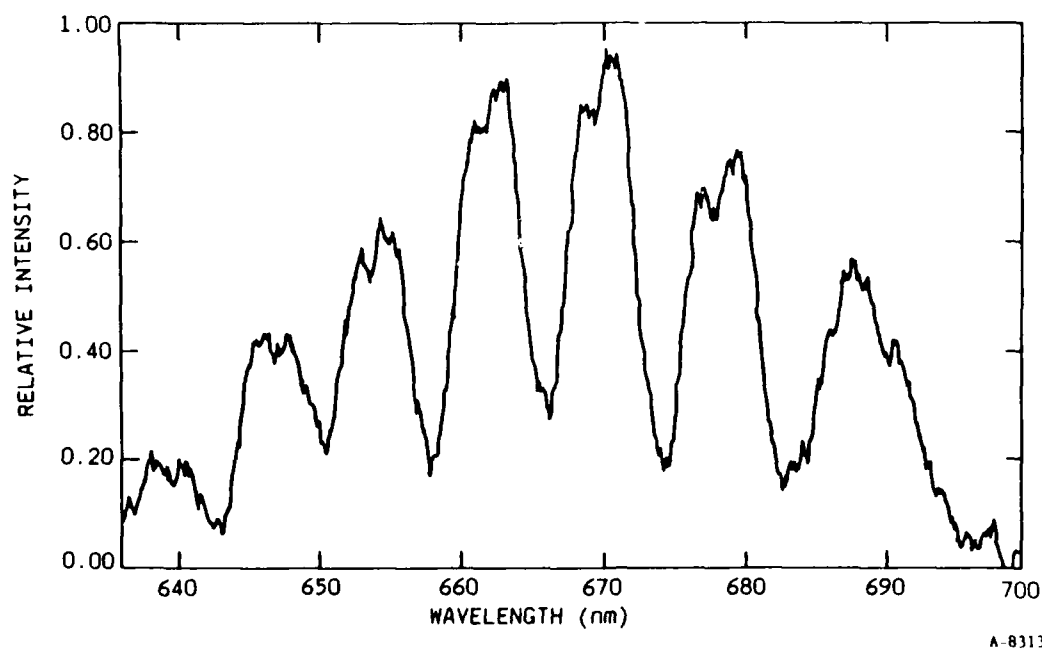


Figure 6. Spectrum of  $N_2(B-A)$   $\Delta v=3$  sequence bands excited at a pressure of 0.15 mtorr showing disequilibrium of the spin components.

The relative vibrational populations for the B-state were determined at many pressures over the range from 0.15 to 81.5 mtorr. At several of the pressures the spectra were recorded for a range of values of the applied magnetic field, nitrogen flow rates through the chamber, and beam currents. In addition spectra were recorded using pulsed and continuous electron excitation, and in the presence of beam-plasma discharges. In varying all of these parameters, the relative vibrational populations for a given pressure remained unchanged within our ability to fit the spectra. The relative vibrational populations measured at 0.15, 10, and 81.5 mtorr are shown in Figure 7 along with the relative populations expected on the basis of Franck-Condon excitation from ground state nitrogen and pure radiative decay.

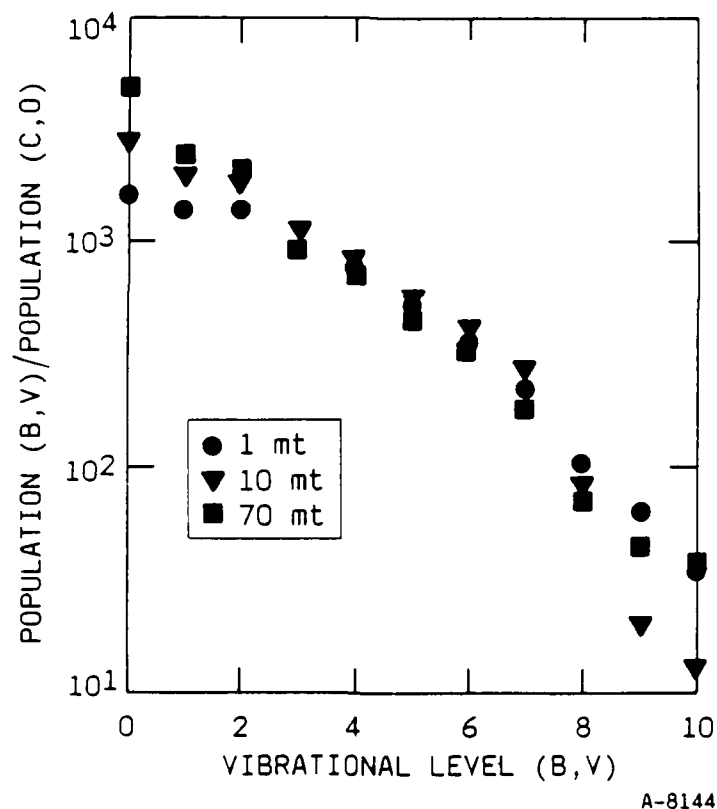
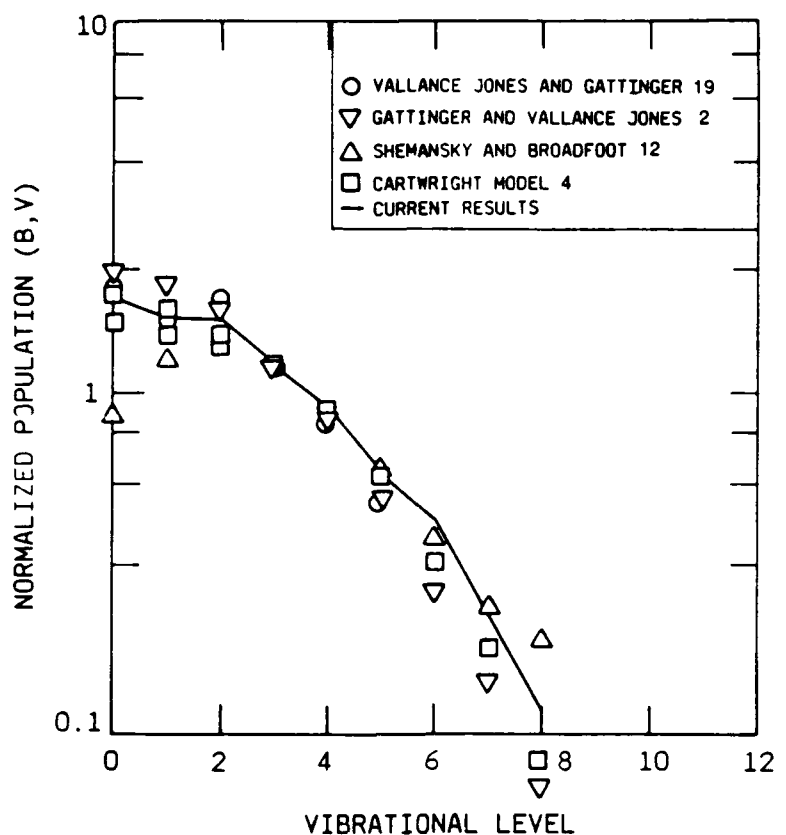


Figure 7. Relative vibrational populations of  $N_2(B)$  from electron impact excitation of  $N_2$  at ●, 1.0 mtorr; ▼, 10.0 mtorr; and ■, 70 mtorr. The total uncertainty in relative vibrational populations is 10% as reflected by the excellent reproducibility in the calculated values.

Additional experiments were done at 3 mtorr total pressure to assess the effects of gas residence time in the chamber on the total population of the B-state. The relative vibrational populations of the B-state remain unchanged when residence time and total pressure are varied. At 3 mtorr we can vary the gas residence time by almost a factor of five while maintaining the same pattern of flow in the irradiation volume. The absolute emission intensity of the First Positive transitions does not change when the residence time is varied over this range; however, there is a 35 to 50 percent increase in the intensity of the  $N_2^+(A-X)$  Meinel bands. This may be evidence for the presence of metastable energy carriers affecting overall formation rates for higher energy states, as will be discussed later.

At 0.15 mtorr the time between collisions is long compared to the radiative lifetimes of all vibrational levels of the B-state and all but the lowest two vibrational levels of the W-state. Therefore, the relative vibrational populations of B-state should be unperturbed by collisional energy transfer from the W-state and by quenching of the B-state. This would seem to be supported by the close agreement between the measured vibrational populations and those calculated based on Franck-Condon excitation for levels 3-10; emission from higher vibrational levels is not observed at these low pressures. Radiative cascade from the W-state is still possible under these conditions. Our low pressure results are compared with previous observations of the B-state distributions in Figure 8. Agreement with both atmospheric<sup>1-3,5</sup> and laboratory observations<sup>12</sup> is quite good.

At pressures above 0.15 mtorr all of the B-state vibrational levels show detectable increases in population relative to  $v=4$ . The magnitude of the increase for  $v=6$ , the level with the smallest energy defect for transfer from any W-state level, is only 20 percent. This is a typical value for levels  $v=3-9$  as well. It is only a factor of two larger than experimental error due to noise and spectral fitting uncertainties. The populations of these levels usually reach a maximum value at about 10 mtorr and decrease slightly at higher pressures. The exceptions to these observations are the lowest levels;  $v=0,1$



A-8143

Figure 8. Low pressure vibrational distribution for the B-state as observed in LABCEDE is compared to previous auroral<sup>2,19</sup> and laboratory<sup>12</sup> observations and model predictions.<sup>4</sup> Agreement is quite good.

and 2 which increase marked in relative population with pressure. Another interesting observation concerns levels 10, 11, and 12, which are weakly observed at pressures below 10 mtorr but rise sharply at higher pressures. This may indicate that there is an additional source mechanism for these levels. The observation of this behavior under pulsed conditions with phase sensitive detection, however, strongly precludes N-atom recombination as that source mechanism. We will address pressure scaling of the B-state populations in Subsection 2.3.3.

### 2.3.2 Relative Electronic State Populations

The relative emission intensities combined with known transition probabilities for each band observed, allows us to calculate the total relative population

in each electronic state. This information is useful for comparison with calculated and measured excitation cross sections and for comparison with measured auroral emission intensities. All of the significantly populated vibrational levels of the  $N_2^+(B)$ ,  $N_2(C)$ , and  $N_2(B)$  states emit somewhere within our detection system bandpass.

The relative vibrational state populations were measured at 1 mtorr pressure for three values of the magnetic field used to confine the primary electron beam and secondary electrons created by scattering. When no external magnetic field is applied, the primary electron beam and any secondary electrons created by scattering act under the influence of the earth's magnetic field and any residual fields present in and around the vacuum enclosure. Under these conditions the range of the typical secondary electron is longer than the width of the field of view of the detection system. These conditions produce relative state populations in which the ion B-state was enhanced relative to the neutral states, when compared with auroral observations. In the presence of low (7 Gauss) and moderate (30 Gauss) confining fields, the relative ion and neutral electronic state populations changed to values comparable to those observed in aurora and were roughly independent of field strength, demonstrating the increased role of the lower-energy secondary electrons. By confining the secondary electrons, their excitations of molecules occur in the field of view. Relative intensities under these laboratory conditions should be closest to auroral observations which, of necessity, contain the effects of complete degradation of the secondary electrons. It should be remembered that the vibrational distributions in these states did not change with applied magnetic field. The implications of these results will be discussed later.

The steady state populations of  $C(v=0-4)$  is about  $1 \times 10^{-3}$  of the B-state ( $v=0-12$ ). The value agrees with the auroral prediction of Cartwright<sup>4</sup> and the observations of Vallence Jones and Gattinger.<sup>2,3</sup> This difference in populations is largely due to the short radiative lifetime of the C-state ( $\tau_C/\tau_B \approx 6 \times 10^{-3}$ ). Because both these states have electron excitation cross sections distributions which peak near the same energy, our laboratory



apparatus is capable of producing distributions comparable to those obtained in the upper atmosphere.

### 2.3.3 Pressure Scaling of Electronic State Populations

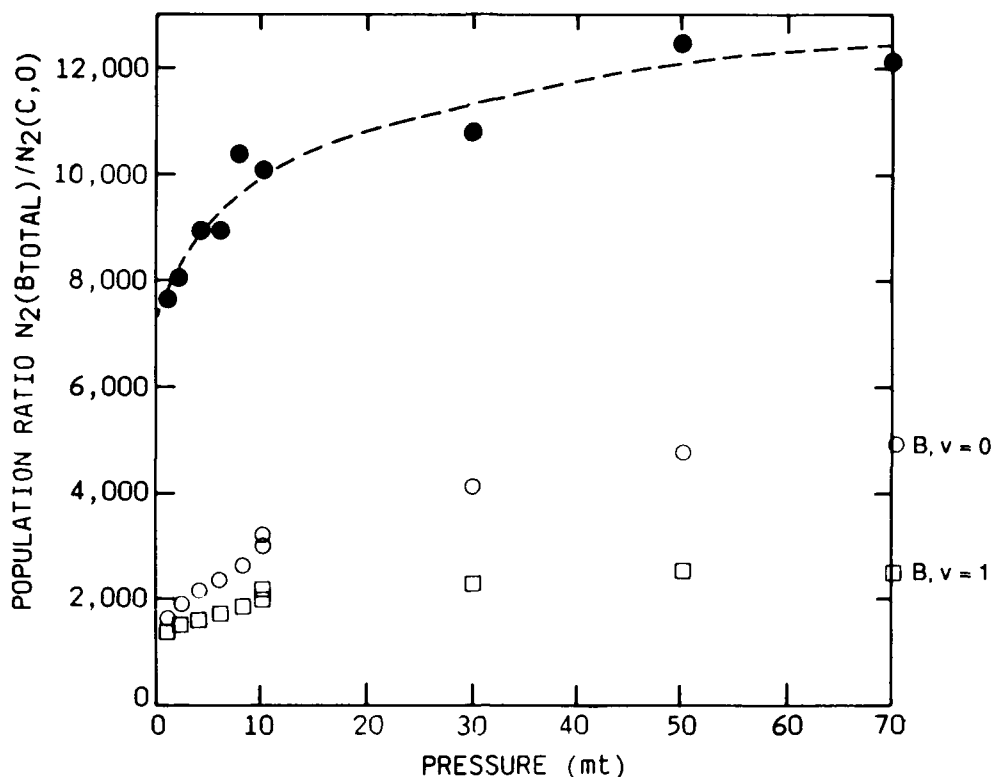
The change in relative state populations with magnetic field described above suggests that secondary electrons play an important role in the excitation process. If they are important, a greater than linear increase in emission intensity with pressure would be expected. The probability of a primary electron-N<sub>2</sub> scattering event increases linearly with pressure (for thin targets). However, if an energetic secondary electron is created by this scattering event, the probability of it undergoing another collision with the field of view to create N<sub>2</sub><sup>\*</sup> also increases with pressure leading to a total intensity scaling of  $p^{>1.0}$ . For all the electronic states the signal increases with pressure to the  $1.3 \pm 0.10$  power and is independent of vibrational level for the First Positive bands. Any variation in the pressure dependence between bands is well within experimental error.

The non-linear growth of signal intensity with pressure makes it difficult to accurately observe additional non-linear increases in intensity due to energy transfer if only a single electronic state is studied. In order to separate the contribution to the non-linear growth due to excitation from the growth due to energy transfer, an experiment was done where the emission intensity of the N<sub>2</sub>(B, 6-3) and the N<sub>2</sub>(C, 0-0) transitions were measured sequentially in the same spectral scan. Because both these states have very similar electron excitation cross sections, the ratio of these intensities from the same spatial volume removes the effects of non-linear excitation as a function of pressure, since diffusion is negligible. The experiments were performed by recording the integrated intensity of the First Positive 6-3 band, centered at 660.8 nm, with the spectrometer in first order and a Corning 3-74 color filter used to block emission below 420 nm. Immediately following that scan, the order sorting filter was changed to a Corning 7-60 UV transmitting but visible blocking color filter, and the spectrum of the Second Positive 0-0 band (337.1 nm) was

recorded in second order at 674.2 nm. Since the  $N_2B \rightarrow A$  emission intensities are within an order of magnitude of the  $N_2C \rightarrow B$  intensities, the latter will not distort the spectrum of the First Positive bands when the filter is in place. Concentrations of  $N_2^+(X)$  and  $N_2(X)$  ground state are sufficiently low that self-absorption of all fluorescence bands is completely negligible (i.e., the gas is optically thin).

The C-state excitation adequately reflects the B-state excitation (as shown by the auroral-like distributions and invariance with experimental dosing parameters). Yet the C-state does not undergo quenching because of its rapid radiative relaxation and thus displays the same vibrational distribution at all our experimental pressures. Consequently, we have ratioed the B-state populations to the C-state so that quenching could be studied with the effects of energy deposition removed.

The total population of the  $B(^3\Pi_g)$  state ( $v=0-12$ ) normalized by the  $C(v=0)$  population is plotted versus pressure in Figure 9. The  $C(v=0)$  level remains a constant fraction (55 percent) of the total C-state population to within  $\pm 5$  percent for all our experiments. The population ratio of  $B_{total}/C(v=0)$  is not constant but increases non-uniformly with pressure, indicating that there exists a net collisional source for creating molecules in the B-state. This feed is dominantly into the lowest three vibrational levels. The population ratio of  $B(v=0)/C(v=0)$  is also plotted in Figure 9. At the lowest pressures,  $v=0$  has barely the highest population of any vibrational level. However, as  $N_2$  pressure increases, the concentration of  $N_2(B, v=0)$  increases dramatically as was seen in Figure 7. From Figure 9 it is seen that it rises in a manner similar to the total B-state and accounts for about 70 percent of the total B-state population increase (relative to  $C(v=0)$ ). The  $B(v=0)$  state population increases by a factor of three relative to  $C(v=0)$  as the  $N_2$  density increases to  $2.5 \times 10^{15}$  molecules/cm<sup>3</sup> (10.3 Pa). Vibrational level 0 is not the only state which undergoes an increase in relative population at all pressures. As seen in Figure 7 the population of  $B(v=0,1,2)/C(v=0)$  all increase with pressure. Level  $v=0$  exhibits the largest increase, but both levels 1 and 2 show

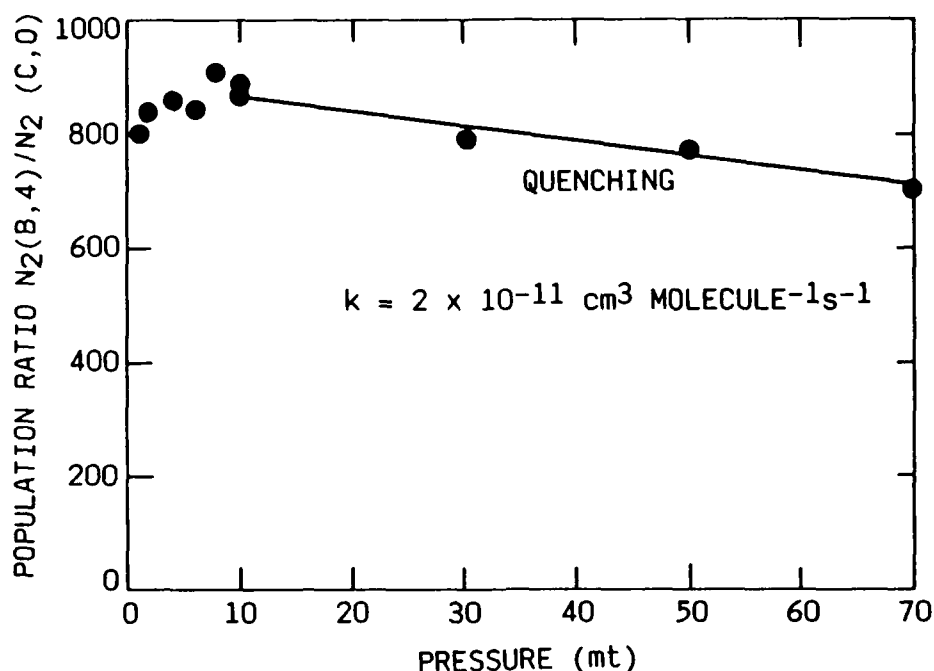


A-8311

Figure 9. Ratio of total B-state population to population of C,  $v=0$  as a function of pressure. Dashed curve is merely to show trend. Also shown as open circles is the ratio of the B,  $v=0$  population to the C,  $v=0$  population. Most of the observed increase in B-state population is attributable to the increase in  $v=0$ . The ratio for level 1 is also plotted as the open squares.

clear trends with pressure. The ratio for level 1 is also plotted in Figure 9. Possible mechanisms which could provide the source of B-state excitation are discussed in the next section.

Level B( $v=3$ ) and most higher levels are nearly invariant with pressure, exhibiting a small increase ( $\leq 20$  percent) in relative population up to 10 mtorr ( $3 \times 10^{14}/\text{cm}^3$ ) followed by a decrease relative to C( $v=0$ ) at higher pressures. We believe the later behavior to be quenching as previously observed by numerous experimenters.<sup>20-23</sup> The ratio of B( $v=4$ )/C( $v=0$ ) is replotted versus pressure in Figure 10. A least squares fit to the population ratios above 8 mtorr has a slope of  $2 \times 10^{-11} \text{ cm}^3/\text{molecule-s}$ . This crude determination is in excellent agreement with the literature values of



A-8197

Figure 10. Ratio of population in B(v=4) to C(v=0) as a function of pressure. There is a slight rise at pressures up to 10 mt which may be attributed to a source term. Above 10 mt quenching occurs at a rate of  $2 \times 10^{-11} \text{ cm}^3 \text{ molecules}^{-1} \text{ s}^{-1}$ .

$2.4 \pm 0.1 \times 10^{-11}$  (Ref. 20),  $1.9 \times 10^{-11}$  (Ref. 21), and  $1.8 \pm 0.2 \times 10^{-11}$  (Ref. 22). For levels 3-8 our quenching values agree with the literature to within 30 percent.

We are unable to clearly determine the fate of the molecules in the excited B-state in levels  $v=3-9$  when they undergo an inelastic collision with another  $N_2$  and are quenched. Vibrational relaxation to a slightly lower level in the B-state ( $\Delta v=1,2$ ) does not appear to be occurring. The population of each level is roughly 60 percent of the level just below it (see Figure 7). Consequently if single quantum vibrational relaxation were occurring exclusively in the B-state, we might expect to see source terms into the  $v-1$  or  $v-2$  levels with an alteration of the vibrational distribution as pressure increases. This effect is not observed. Multiquantum vibrational relaxation within the B-state is another possibility. However, the population decrease in levels

$v=3-9$  (relative to  $C, v=0$ ) between 10 and 70 mtorr is inadequate to explain the rise in  $B(v=0,1,2)$  over that pressure region. (The loss of molecules from state  $B, v=3-9$  is less than 30 percent of the increase observed in  $B, v=0,1,2$ ; less than 40 percent of the increase in  $B, v=0$  alone). The collisional relaxation of the  $B(v=3-9)$  state to  $B(v=0)$  cannot be ruled out, but with the large number of near-resonant levels in other nested electronic states, interstate transfer is the likely route.

The interesting behavior exhibited by higher levels in the  $B(^3\Pi_g)$  state prompted us to develop a simple model based on known rates and likely physical processes which could control the populations of those levels. This model will be discussed in the next section.

## 2.4 DISCUSSION

In the discussion of our electron excitation results we would like to compare our observed spectral distributions and band intensities with those observed in auroral events. We will use this comparison to argue for the presence of the  $N_2(W)$  state in both the LABCEDE experiments and the aurora. Given the presence of the  $W$ -state in significant quantities and our measured  $B$ -state vibrational distributions as a function of pressure, we will discuss the consequences of the radiative and collisional exchange of energy between the  $W$ - and  $B$ -states. Finally, it appears based on our observations that the  $W$ - $B$  collisional energy transfer will not contribute to the creation of the lower red border of a type B aurora as has been previously postulated.

### 2.4.1 Comparison with Auroral Observations

There have been few quantitative measurements of auroral emission spectra. The most extensive measurements have been reported in a series of papers by Gattinger and Vallance-Jones covering the near-UV,<sup>3</sup> visible,<sup>1,2</sup> and near-IR<sup>5</sup> regions. The spectra observed in these measurements were fit using known transition probabilities for various band systems to extract the individual

contributions due to molecular and atomic species. Relative vibrational populations and/or absolute emission intensities were reported for most of the important contributors. Detailed electron impact excitation cross sections have been measured for many nitrogen electronic states by Cartwright, et al.<sup>24,25</sup> Extensive modeling of vibrational populations of  $N_2$  excited states under auroral conditions has been done by Cartwright.<sup>4</sup> The comparison of our data with auroral emission will use observed relative vibrational populations and total electronic state populations. We will also compare measured electronic state populations with those predicted by the Cartwright model.

The relative vibrational populations of the  $N_2(C)$  and  $N_2^+(B)$  states in high altitude auroras, derived from auroral emission intensities of the Second Positive and First Negative bands, were shown in Figures 3 and 4 respectively. These populations agree well with those observed in LABCEDE and those calculated on the basis of Franck-Condon excitation of ground state nitrogen followed by radiative decay. These observations are consistent with the conclusion that these states are not quenched in auroras due to their short lifetimes and that they are not significantly populated by radiative cascade.

The relative vibrational populations of the  $N_2(B)$  state observed in an aurora, shown in Figure 7, agree well with those calculated by Franck-Condon excitation/radiative relaxation for levels 3-12. Levels 0-2 continue to increase in population in an aurora while the excitation model predicts that these levels would decrease. Shemansky and Broadfoot<sup>12</sup> have argued that the increase in population for these levels is entirely due to radiative cascade from the C-state while Cartwright<sup>4</sup> claims that a substantial portion of the increase is due to radiative cascade from the W-state. The source of this discrepancy is a disagreement over the electron impact excitation cross section for the W-state. This will be discussed in detail later.

Relative vibrational populations measured in LABCEDE at 0.15 mtorr agree well with both the auroral and Franck-Condon excitation profiles for B-state levels 2-10. At this pressure collisional processes are not important and we may

consider only direct and radiative cascade excitation. Almost 90 percent of the radiative cascade from the C-state goes into B-state levels 0-2. The close agreement between the three sets of data over this range would seem to exclude any additional formation of the B-state due to radiative cascade from other states. Cartwright, however, has shown that direct excitation and W-B radiative cascade contribute about equally to the total formation of each B-state level from 3-12. Any normalization method which used levels such as 3 or 4 as the reference point would not be very sensitive to this radiative cascade. Hence, little can be said about the role of the W-state based on our low pressure relative vibrational populations.

If radiative decay from the W-state does account for nearly half of the total B-state excitation rate, it should be evident in a comparison of measured relative state populations with those calculated from known excitation cross sections and electron energy distributions. Direct electron impact excitation cross sections for these states at 4.5 kV are small and much of the excitation comes from lower energy secondary electrons created by scattering of the primary beam. The degree and manner in which the energy of the secondary electrons is lost determines the overall excitation efficiency. In LABCEDE the range of the characteristic secondary electron is long compared to the apparatus dimensions; however, the use of the magnetic field confines the secondary electrons and may allow some of their energy to be deposited within the field of view.

The relative electronic state populations measured in LABCEDE are complicated by the effects of the confining field. In the absence of the field the ionic B-state is more prominent because it has a higher cross section for excitation by primary electrons and because many secondary electrons travel out of the detector field of view before they can excite a nitrogen molecule. The relative band populations observed with the applied field are very similar to those seen by Gattinger and Vallance-Jones<sup>2,3</sup> in aurora. They are also consistent with those calculated by the Cartwright<sup>4</sup> model, which includes excitation of the W-state and radiational transfer of the energy to the B-state.

The agreement between the relative vibrational distributions measured in aurora and those observed in LABCEDE suggests that the excitation process in LABCEDE at low pressure is similar to an aurora. The similarity between the relative state populations also supports this conclusion. Both the W- and B-states sample the same range of electron energies and should have similar excitation cross sections. The measurements of Cartwright<sup>19,20</sup> support this argument. We have recently directly observed fluorescence from the W-state at 2 to 4  $\mu\text{m}$  using a circular variable filter spectrometer. No relative calibration exists but there is every reason to believe that  $\text{N}_2(\text{W})$  is present at concentrations comparable to  $\text{N}_2(\text{B})$  in LABCEDE.

#### 2.4.2 Collisional Energy Transfer and Electronic Quenching

The net production of the B-state with increased pressure is perhaps the most intriguing aspect of this study. Production from atom recombination (either directly or through an intermediate state) can be ruled out. The three-body recombination time at mtorr pressures is calculated to be very long. Experimental observations made with a pulsed electron beam (2 ms on/2 ms off) and phase sensitive detection which should effectively discriminate against this source of the B-state yielded a similar pressure dependent vibrational distribution. The remaining most probable source of B-state excitation is via collisional transfer from other states created by direct electron impact. In order to estimate relative production rates into the various states, we rely upon the modeling of Cartwright<sup>4</sup> and Green et al.<sup>26,27</sup> Based on these estimates, significant transfer from many of the states can be ruled out as the B-state source term. The B'-state is resonant with only the higher levels of the B-state and is not produced in sufficient quantities to generate the observed increase in the B-state distribution even for complete transfer. The C-state radiative lifetime is short and will radiatively (not collisionally) decay for all our experimental pressures. Therefore the observed rates of B/C populations can have no pressure dependence due to collisional quenching. Moreover the transfer would most likely be into the higher vibrational levels. The W-state potential surface is shifted to larger internuclear separations

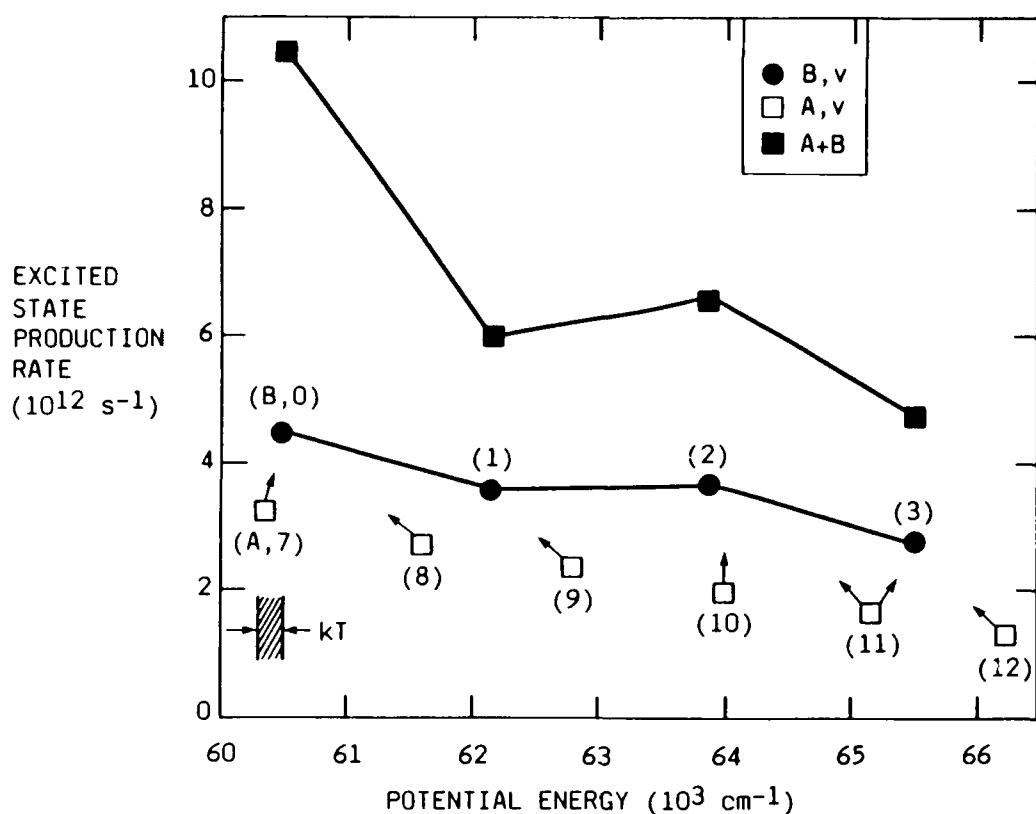


than the ground state. Hence, Franck-Condon direct electron impact excitation favors production of higher vibrational levels in the W state.<sup>4</sup> Thus, level specific feed into B,  $v=0,1,2$  from the W-state is unlikely unless the W-state distribution is totally collapsed into  $v=0,1,2$ . Even then the W-state production based on Cartwright's modeling<sup>4</sup> and the present analysis appears to be insufficient to cause the observed rise in B,  $v=0$ . The W-state levels are strongly mixed with the B-state levels so that near gas-kinetic transfer is possible for specific higher levels. However, the observed transfer into the higher levels alters the B-state population in a level by 20 percent and cannot give rise to the factor of three rise observed for B,  $v=0$ .

The A-state will be considered next. This lowest lying electronically excited state could contribute to B-state population via two mechanisms: energy pooling and direct energy transfer from A,  $v \geq 7$ . In order to assess the magnitudes of this transfer, order of magnitude calculations of the A-state production rates and spatial extent were performed so as to obtain local concentrations. The energy pooling reaction has been extensively studied by Piper et al. in a series of papers.<sup>20,28</sup> When two molecules in the  $N_2(A)$  state collide, one of the molecules is promoted to a more excited electronic state and other presumably is left in the ground state with some degree of vibrational excitation. Excitation of  $N_2C, B$  states has been observed. The Herman Infrared System (states unknown) is also excited. The excitation produced by this transfer depends strongly on the initial A-state vibrational level of each molecule. State specific transfer rate coefficients have been measured. Thus independent of our estimated A-state concentrations we can look for alteration of the C-state distribution due to contributions from energy pooling since the C-state vibrational distributions formed by direct electron impact and energy pooling are significantly different. Experimentally, the C-state vibrational distribution is accurately determined from the spectrum obtained at each pressure. The complete invariance of this distribution over the pressure range studied permits an upper bound to be made for the energy pooling process relative to direct electron impact excitation of the C-state. The energy pooling production rate is less than 20 percent of the direct production rate at

all pressures. Using this bound and the known energy pooling rate coefficients for B- and C-state production, we would expect the pooling rate to be at most 35 percent of the direct production into the B-state even at 70 mtorr. From Figure 9 we observed B/C ratio to increase by 60 percent over this pressure range. In addition, energy pooling would produce molecules in the B-state with a markedly different vibrational distribution than the pressure-dependent excitation observed. As a further check we used the energy deposition modeling of Green et al.<sup>26,27</sup>, coupled with beam growth estimates and experimental mass transport properties to obtain local  $N_2(A)$  state densities. Steady state is established by direct electron impact production and reaction or the pressure dependent diffusion to the walls. We assume: 1) a production rate of 0.5  $N_2(A)$  per ion pair; 2) that  $N_2(A)$  is lost on the walls with unit quenching efficiency; 3) the major gas-phase loss of  $N_2(A)$  was energy pooling. The estimated  $N_2(A)$  concentrations were spatially non-homogeneous but reached several times  $10^9$  molecules/cm<sup>3</sup> at 70 mtorr (4 ppm of total concentration). Even at this substantial concentration, the energy pooling production rate for the  $N_2$  B-state was at most 20 percent of the direct electron production rate. Thus both the vibrational distribution invariance and electron production analysis indicate that energy pooling plays a small role relative to direct production of B-state (< 30 percent and < 20 percent respectively).

This leaves only direct transfer of excitation from molecules in the A-state in vibrational levels greater than six to the B-state. As seen in Figure 11 these levels are substantially populated by electron excitation. In the figure we have used Cartwright's unquenched (130 km) distribution. The quenching of vibrationally excited A-state levels has been measured by Dreyer and Perner.<sup>29</sup> The quenching rate coefficients are very level dependent, increasing rapidly with vibrational level and exhibit a sharp increase at  $v=7$ . Dreyer and Perner suggest that this increase is due to transfer to the B-state  $v=0$ . Their measured rate coefficient for A,  $v=7$  is  $2.4 \times 10^{-12}$  molecule cm<sup>-3</sup> s<sup>-1</sup> which would give a characteristic quenching time of 0.2 ms at 70 mtorr. This process would be rapid enough to follow the variations with pulsed electron beam operation and thus be present in the 4 ms period pulsed data (as



A-8236

Figure 11. Modeled production rate in field of view based on energy deposition, excited state production and cascade.

observed). Also because quenching would be rapid, diffusion of the field of view would be minimal. The magnitude of this source can be estimated by assuming that all molecules produced in levels A,  $v=7-12$  transfer their excitation into B,  $v=0-3$ . From Figure 11 we estimate this would give a net increase in the total B-state production of 50 percent (a value of 60 percent is observed). More specifically we can assume that the level specific transfer from A,  $v$  occurs to the nearest energetically lower level of the B-state; i.e., A,  $v=7-8$  feeds B,  $v=0$ ; A,  $v=9$  transfers to B,  $v=1$ ; A,  $v=10,11$  feed B,  $v=2$  and A,  $v=12$  transfers to B,  $v=3$ . This is certainly an oversimplification but serves to illustrate the level dependence of the magnitude of this transfer. The calculated increases due to A-state transfer are compared to the results from the laboratory for two pressures in Table 1.

TABLE 1. Ratio of transfer rates from A-state to direct electron production rates.

		Transfer Rate (%) Direct Production Rate		Observed Increase (%)	
A Feed Level		p = 10 mtorr	p = 70 mtorr	1-10 mtorr	1-70 mtorr
B, v=0	v=7,8	31	133	59 $\pm$ 12	160 $\pm$ 40
1	9	15	67	29 $\pm$ 14	58 $\pm$ 22
2	10,11	24	100	30 $\pm$ 3	30 $\pm$ 10
3	12	12	48	10 $\pm$ 5	Quenching B

Level B, v=0 suffers the largest enhancement - transfer is comparable to direct production at the highest pressures. The higher levels are less affected; qualitatively agreeing with the trends observed in the data. This rough agreement of our crude model with the experimental data with regard to both the magnitude of the trend with vibrational level and pressure dependence leads us to believe that transfer from the A-state high vibrational levels excites the lower levels of the B-state at significant rates compared to direct B-state production by electrons.

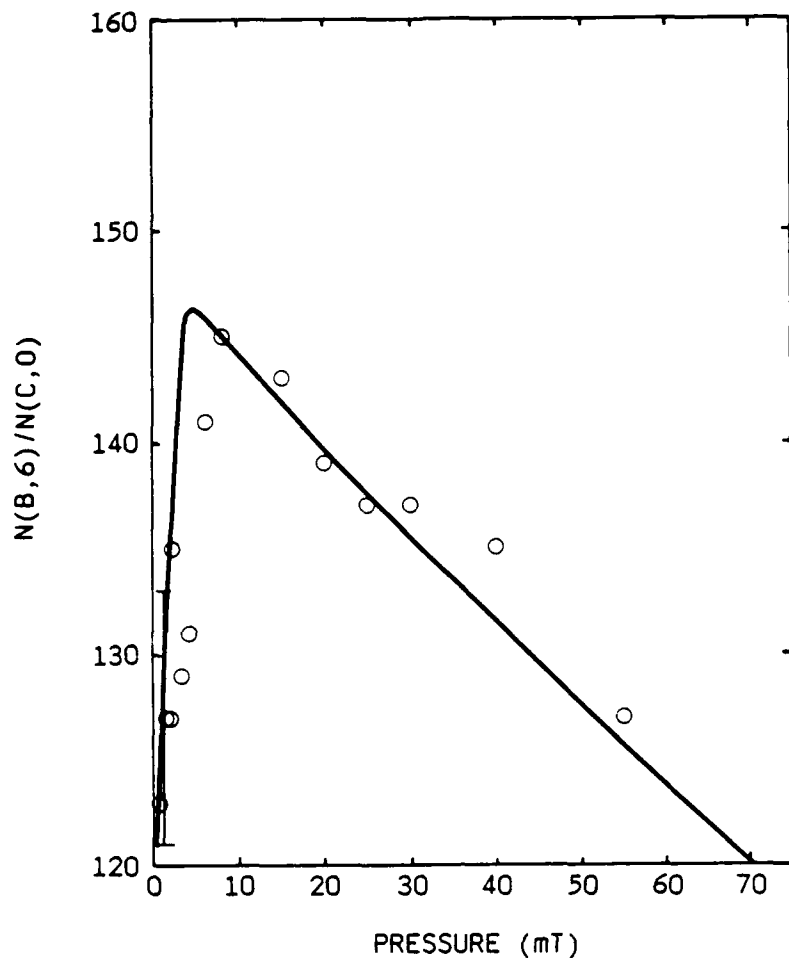
The electronic manifolds we are studying are quite nested permitting a large degree of intersystem transfer. Previous studies have determined the microscopic rates for transfer between specific levels and, as such, often miss related backtransfer and feed processes. We have chosen a more global approach which, while it does not permit detailed examination of such energy transfer processes, does permit observation of the integrated effects of all these processes.

For higher vibrational levels of the B-state, transfer from the W-state is expected to occur. At 10 mtorr there are multiple collisions with other N<sub>2</sub> molecules during a typical W-state radiative lifetime (54  $\mu$ s for v=6) and rapid

collisional processes should begin to dominate over radiation for removal of the W-state. One would expect gross changes in the B-state vibrational distribution to accompany this transformation as collisional channels feed the vibrational levels at different rates than radiative transfer. Simple energy-gap arguments would predict the fastest transfer to occur from W(7) to B(6), which is exoergic by  $129\text{ cm}^{-1}$ . Sadeghi and Setser<sup>30</sup> have measured the rate of this intersystem transfer in Ar and determined the rate coefficient to be  $2.7 \times 10^{-11}\text{ cm}^3\text{ molecule}^{-1}\text{ s}^{-1}$  at ambient temperature. They stated that N<sub>2</sub> should be more efficient than Ar for coupling these levels. Pendleton et al.<sup>31</sup> have measured the rate of collisional coupling for these levels in N<sub>2</sub> to be  $2.5 \times 10^{-10}\text{ cm}^3\text{ molecule}^{-1}\text{ s}^{-1}$  and observed a pronounced change in the vibrational distribution of the B-state. Recently Rotem and Rosenwaks<sup>23</sup> have measured the transfer rate coefficient in N<sub>2</sub> for these channels to be  $2.0 \times 10^{-10}\text{ cm}^3\text{ molecule}^{-1}\text{ s}^{-1}$ .

The N<sub>2</sub>(B) state relative vibrational distributions measured in LABCEDE show only about a 20 percent increase for most of the near resonant levels but larger increases for levels 10-12. When the population in  $v=6$  of the B-state is ratioed to the population in  $v=0$  of the C-state, as shown in Figure 12, a pattern of growth and decay is more evident. We attribute the low pressure increase in the B(6)/C(0) ratio, which peaks at 20 percent at 10 mtorr, to collisional coupling of W(7) to B(6). Higher pressure decay is due to electronic quenching of the B-state. Gas kinetic collisional coupling of W(7) level to B(6) is complete at these pressures and results in a constant contribution to the ratio of B(6) to C(0). Therefore, we can use a simple Stern-Volmer analysis to determine the rate coefficient for quenching of this level. Our value of  $2 \times 10^{-11}\text{ cm}^3\text{ molecule}^{-1}\text{ s}^{-1}$  for  $v=6$  agrees well with the measurements of N<sub>2</sub>(B, $v$ ) quenching by N<sub>2</sub>.<sup>20,21,22</sup>

The careful experimental work of Shemansky and Broadfoot<sup>12</sup> is in good agreement with the present results. They observe only small enhancements of B-state vibrational levels between 2 and 9 as pressure is increased from 0.5 to 10 mtorr. The sole exception is level  $v=6$  which increased by about



A-8308

Figure 12. Variation in the population ratio  $N(B,6)/N(C,0)$  with pressure. Modeled fit to data is shown as solid line. Note that total variation of data is 20%.

15 percent over this pressure range. They also observe a rise in levels  $v=10$ , 11, and 12 at their highest pressures (10 mtorr). The overall vibrational distribution they derive is just slightly "hotter" than Franck-Condon, but is pressure invariant. By contrast, both these sets of observations do not support the intuitively appealing hypothesis of Benesch. Consequently, we undertook the development of a model as an attempt to gain physical insight into our observations.

In order to understand the role of the nested W-state, we constructed a numerical model of excitation and radiative and collisional relaxation in this coupled kinetic system for mid levels of the B-state which are most resonant

with W-state levels. The goal of the modeling effort was to see if our macroscopic experimental observations are consistent with all of the available information on the individual processes which shape the  $N_2(B)$  state vibrational distribution. Only the  $N_2$ , B-, C-, W, and X electronic states were implicitly considered in the model. Electron impact formation of the excited states was treated using relative efficiency factors. The partitioning of the excitation energy over vibrational levels was determined by the Franck-Condon factors for transitions from  $N_2(X, v=0)$  to the vibronic state of interest. The Franck-Condon factors were taken from Lofthus and Krupenie.<sup>6</sup> The rate constant obtained from our Stern-Volmer analysis of the high pressure data was used for pure electronic quenching of  $N_2(B, V)$ , as well as for  $N_2(W, V)$ . Radiative transition probabilities for each of the important excited state transitions were taken from Lofthus and Krupenie,<sup>6</sup> with the exception of the  $N_2(W-B)$  transition. An extensive set of transition probabilities for this system have recently been calculated by Werner et al.<sup>32</sup> These values are approximately three times smaller than those determined by Covey et al.;<sup>33</sup> however, we chose to use the transition probabilities of Covey et al.<sup>33</sup> because the application of their values to our data is consistent with measured electron impact formation rates for the  $N_2(W)$  state. Recent laboratory experiments<sup>34</sup> strongly support the calculations of Werner. The transfer rate coefficients for the levels  $W(7) \rightarrow B(6)$  were taken from Rotem and Rosenwaks<sup>23</sup> and a W-state electronic formation rate was adjusted to best fit the experimental data.

The pressure dependence of the population ratio calculated using the above model is given as the solid line in Figure 12. The ratio of electronic formation rates (W/B) which produced this curve is 0.5. The calculated curve is in good qualitative agreement with the experimental data. The model correctly predicts the magnitude of the initial rise and the pressure at which the data rolls over, as well as the total rate of decay. Variation of the collisional transfer rate coefficient in the model by a factor of 10 showed that the coupling must occur on nearly a per-collision basis to reproduce the trends in the data. The population ratio rises with pressure at a slower rate than the model predicts. This undoubtedly is due to the simple nature of the

model, which neglects transfer into B(6) from levels other than W(7). While this simple model is inadequate to make quantitative predictions about transfer and formation rates, it does show that when reasonable molecular parameters derived from other experimental measurements are used in the calculation, the trends observed in LABCEDE can be explained. Hence, our results seem to be consistent with approximately equal formation rates for the W- and B-states, gas kinetic collisional coupling of near resonant vibrational levels, and radiative coupling of the manifolds in the absence of collisions. It also shows that W-B transfer should not result in large changes in the appearance of the First-Positive spectra, in agreement with our high pressure data.

Application of our model to level B(12), into which there is a significant pressure dependent feed, was unsuccessful. No set of reasonable parameters could reproduce the constant rise in the population of this level with pressure. Thus, we conclude that an additional mechanism for populating these levels is required. Nitrogen atom recombination is known to produce highly vibrationally excited  $N_2(B)$ ; <sup>35</sup> however, we estimate the characteristic N-atom recombination time under our experimental conditions to be on the order hours and hence the rate should be very small. To verify this, the synchronous component of the fluorescence was obtained while rapidly pulsing the electron beam at high frequencies. This spectrum still contained enhanced emissions from levels 10-12 at higher pressures, eliminating recombination and any interaction of metastable species present in low concentration as the source mechanism since their characteristic reaction times are much longer than the beam pulse period. One possible explanation is that high vibrational levels of W-states ( $v=11-13$ ) are formed more efficiently upon electron impact than high levels of the B-state. Thus, as pressure increases, these high levels collisionally feed the  $v=10-12$  levels rather than radiate to B,  $v=5-7$ . Because the B,  $v=10-12$  levels have better radiative feed from very high W-levels ( $v\sim 8$ ), their relative population rises as they are collisionally excited.

An enhancement of B-state vibrational levels 6, 7, 11, and 12 has been observed by Carlson et al.<sup>36</sup> These enhancements were only quantified for  $v=12$  where a



factor of four increase was observed as  $N_2$  pressure increased from 0.6 to 15 mtorr. They propose that the resonant overlap of W- and B-state levels is responsible for their observed enhancements. These various experimental observations<sup>12,36</sup> and the present results are in general agreement. However, the detailed mechanisms have not been specified. The nested electronic states of  $N_2$ : A, B, B', W and even  $a^1\Pi_g$  provide the possibility of coincidental overlaps between vibrational levels leading to level dependent feed and collisional loss rates. Determination of these detailed mechanisms is beyond the scope of our present experiments. Nevertheless, because our observed spectra reflect the global summations of all mechanisms occurring, they are quite useful in unraveling the altitude and dosage scalings of the aeronomic observations. Recently, observations of a low altitude aurora have been reported by Gattinger et al.,<sup>37</sup> They spatially resolved the auroral form and determined altitudes of penetration by means of triangulation. Additionally, they spectrally resolved the fluorescence of these very transitory phenomenon using a TV spectrograph. Their resolution was 100Å which, although coarse, was sufficient to indicate that there was no difference in the spectral shape of emissions originating at 93 and 122 km. Gattinger et al. conclude that no collisional redistribution has occurred down to 93 km in their "pink" bordered aurora. Our laboratory observations seem to preclude these collision changes at any altitude. Recently, Brown et al. have attributed the lower "red" border to quenching of the oxygen atom red line at lower altitudes.<sup>38</sup>

Two attempts were made to alter the observed B-state vibrational distributions by substantially altering the experimental conditions. First, in the LABCEDE apparatus, the flow rate was varied by a factor of five while maintaining constant pressure. This was done using the exit valving port to decrease pumping speed and it resulted in increased recirculation of the gas into the irradiated volume. The spectral intensity of the Meinel bands ( $N_2^+A \rightarrow X$ ) increased significantly (by 35-50 percent) relative to the First Positive emission as the residence time and the probability of re-irradiation of a molecule increased. We attribute this increase to the formation of a metastable state of  $N_2$ . The A-state has been measured<sup>39</sup> to have a large cross

section for ionization with a lower electron energy threshold than for ground state  $N_2$  and the A-state is thus a likely candidate for giving rise to Meinel emission upon re-irradiation. Significantly, no changes were observed in the First Positive spectrum either in total intensity or vibrational distribution.

Secondly, on a separate flow tube apparatus, we looked into a microwave discharge of pure  $N_2$  while varying total pressure between 0.1 and 50 torr and for variety of discharge conditions. The fluorescence spectra observed were also compared with synthetic spectra after correcting for system response and population distributions were determined. The observed distributions are not representative of N-atom recombination but rather at low pressures resemble the 81 mtorr distributions shown in Figure 7. Under certain conditions, the higher vibrational levels could be enhanced, but under no conditions was a spectrum resembling Benesch's<sup>8</sup> observed. The enhancement of the high vibrational levels of the B-state in our discharge experiments may be the result of electron-impact on vibrationally excited ground state  $N_2$ .

The agreement of auroral observations of the  $N_2^+(B)$  and  $N_2(C)$  state vibrational distributions with Franck-Condon excitation of  $N_2(X, v=0)$  demonstrates both in the upper atmosphere under moderate auroral dosing and in LABCEDE, that vibrationally excited ground state  $N_2$  is not present in sufficient concentrations to significantly alter excited state emissions. Our experimental results over a wide range of conditions show that care must be taken to avoid artifacts due to  $N_2(A)$  or  $N_2(X, v)$  which could substantially alter laboratory observations of electron-irradiated  $N_2$ .

## 2.5 CONCLUSIONS

We have reported in this paper experimental results from a large-scale laboratory device capable of reproducing mesospheric/lower thermospheric pressures and auroral dosing levels. Spectrally resolved ultraviolet and visible emissions from electron-irradiated pure  $N_2$  were used to determine relative formation rates of the  $N_2^+(B)$ ,  $N_2(C)$  and B-states. These were found

to be in agreement with aurorally derived values. Vibrational distributions within the  $N_2^+(B)$  and  $N_2(C)$  states were measured to be essentially identical to values expected for Franck-Condon excitation of vibrationally cold ground state  $N_2$ . Agreement between the present laboratory results and observed auroral distributions were excellent. Our distributions were found to be invariant over the pressure range covered (as expected due to the rapid radiative decay of these states) and to be invariant with electron dosing level.

The vibrational distribution of the  $N_2(B)$  state was determined by the comparison of several band sequences of First Positive fluorescence falling between 450 and 1100 nm with synthetic spectra. At low pressures the distribution observed was again in agreement with high-altitude auroral observations. This distribution is representative of Franck-Condon excitation followed by radiative cascade. As the experimental pressure was increased the relative populations of levels  $v=3-9$  (as normalized to  $v=4$ ) varied only slightly up to pressures of 81 mtorr (67 km altitude). Of these levels, the largest change observed was in the  $v=6$  level. The relative population of that level increased by only 20 percent reaching a maximum at 10 mtorr. It should be noted that 85 percent of the B-state molecules have less than six quanta of vibrational excitation. As a result changes in the populations of level 6 and above can have only a relatively small effect on global atmospheric processes. Our observed B-state distributions for  $v=3-9$  and its invariance with pressure are in good agreement with the previously experimental work of Shemansky and Broadfoot<sup>12</sup> and are supported by the recent auroral observations by Gattinger et al.<sup>30</sup> A simple kinetic model was developed which was able to rationalize some of the observed changes in the B-state distribution in terms of the level dependent interplay of radiative and collisional transfer between the  $W^3\Delta_u$  and  $B^3\Pi_g$  states. At the lowest pressures any molecules formed in the W-state upon electronic impact radiatively decay to the B-state (which promptly radiates). As pressure increases, the molecules in the W-state can collisionally exchange their energy into near-resonant vibrational levels of the B-state. As a result the distribution is relatively invariant with pressure. The role of the W-state can only be inferred since it has not been observed in these

measurements. Further experiments aimed at monitoring W-state populations directly are in progress. We have observed emission from several vibrational levels of the W-state between 1.6 and 3.0  $\mu\text{m}$  using a Michelson interferometer.

However, our observations of all B-state levels from 0-12 over a wide pressure range have provided insight into the dynamics of the nested triplet manifold of states in  $\text{N}_2$ . The data show that there is a net production of B-state as pressure increases. Levels above  $v=3$  undergo quenching at rates in agreement with previous observations. However, the lowest levels  $v=0$  (strongly) and  $v=1,2$  (to a lesser extent) exhibit a large feed. Over the pressure range 1 to 70 mtorr the total B-state population increases by 60 percent over direct production as monitored by C-state densities. Based on the agreement of electron energy deposition and electronic state excitation models with experimental data magnitudes and trends, we believe that this additional source of excited B-state is collisional energy transfer from vibrational levels ( $v \geq 7$ ) of the metastable A-state. Excitation of the B and C by energy pooling of two A-state molecules was shown not to contribute significantly under the present experimental conditions. However, at higher experimental dose levels and under special conditions in the strongly disturbed upper atmosphere, energy pooling could contribute substantially to B-state production (and emission) levels. Of great importance, transfer from  $\text{A}, v \gg 0$  to  $\text{B}, v \sim 0$  will occur whenever  $\text{N}_2$  is electron-irradiated.

In this effort we have gained considerable insight into the interplay of the electronic triplets states of  $\text{N}_2$  produced by electron irradiation. Previous studies of particular levels and transitions have carefully determined the microscopic rates for transfer between specific levels but not the ultimate fate of the excitation energy. We have chosen here a more global approach which does not permit detailed examination of each energy transfer rate process. It does permit observation of the integrated effects of all the processes occurring. This approach has allowed us to distinguish small effects (such as transfer into B,6 from W,7 which increases the B,6 population by less

than 20 percent which alters the total B-state population by less than 1 percent) from quite significant transfer effects (such as the additional production of B,  $v=0-2$  which doubles the  $v=0$  population and increases the total B-state excitation by 60 percent).

The invariance of our B-state vibrational distribution with electron-dosing levels, experimental residence times and optical geometry leads us to believe that our low pressure data can support auroral observations and models. The pressure dependence of the populations can be useful in guiding future observations of electron excited air. Our data clearly demonstrates that collisional energy transfer between different electronic states of  $N_2$  does not alter the First Positive emission in the red significantly enough to cause the formation of a lower altitude red border on a deeply penetrating aurora. Substantial changes in the 0.9 to 1.1  $\mu m$  region would be expected due to increased B production in vibrational levels 0-2. The coupling of the W- and B-state could have a large effect on the auroral spectrum between 1.5 and 7  $\mu m$  where the W-state is a dominant emitter.

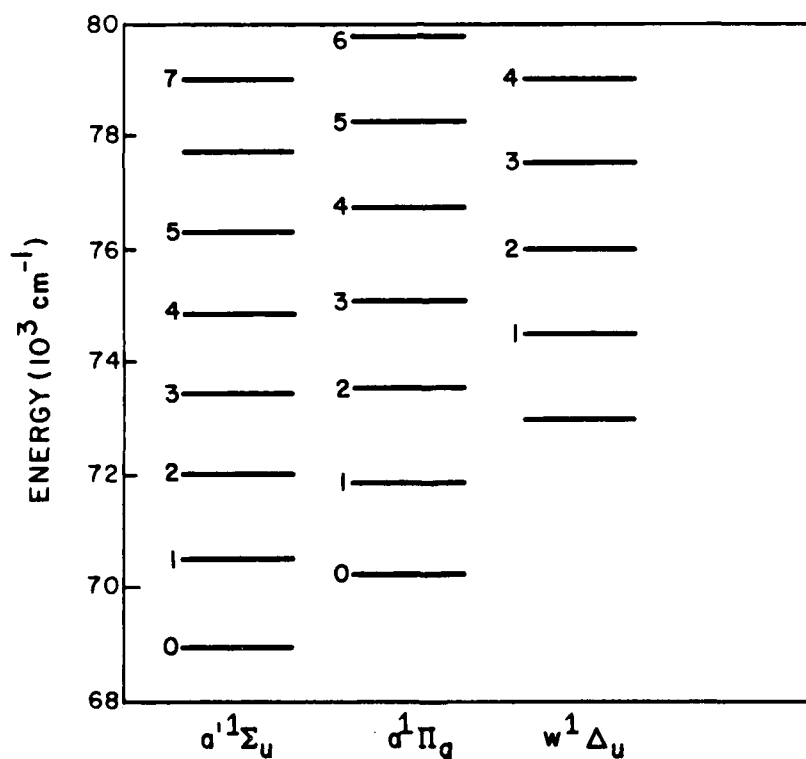
### 3. VIBRATIONAL RELAXATION AND INTERSYSTEM CROSSING IN $N_2(a^1\Pi_g)$

#### 3.1 INTRODUCTION

Emission due to transitions from  $N_2(a^1\Pi_g)$  to  $N_2(X^1\Sigma_g^+)$  ground state (the Lyman-Birge-Hopfield bands) is a prominent feature in the ultraviolet spectrum of the quiescent as well as the aurorally disturbed atmosphere. For high altitude auroras observation of LBH emission<sup>40-45</sup> are consistent with the predictions of models which include Franck-Condon type excitation of ground state molecular  $N_2$  to the  $N_2(a)$  state by energetic electrons followed by radiative relaxation.<sup>46</sup> However, the present study indicates that in penetrating auroras at lower altitudes ( $\sim 100$  km) the observed vibrational distributions of  $N_2(a)$  state molecules are also affected by electronic quenching, vibrational relaxation, and intersystem collision-induced cascade. The altitude dependences of dayglow and nightglow emissions are less well known.<sup>42,47</sup> The excitation of  $N_2(a)$  under sunlit, quiescent conditions is presumably due to collisions with low energy photoelectrons. Although the vibrational level-dependent excitation function has been shown to depend strongly on electron-energy near threshold,<sup>46</sup> the observed dayglow vibrational distribution is too broad to be easily ascribed to a simple steady-state balance between electron-excitation and radiative and collisional relaxation processes. In contrast, nightglow observations of the LBH bands<sup>42,47</sup> reveal an  $N_2(a)$  state vibrational distribution strongly peaked at low vibrational levels. The source, intensity and band shape of this emission is currently unexplained.

In the measurements reported here, the collisional relaxation of  $N_2(a)$  by  $N_2$  has been investigated to characterize electronic quenching, vibrational relaxation, and the effects of collisional and radiative coupling of the  $a$  state to other significant singlet states of  $N_2$ . These measurements provide a global picture of  $N_2(a)$  relaxation both to provide insight into the upper atmospheric LBH band observations, and to provide guidance for state-to-state laser-based investigations of the singlet systems of  $N_2$ .

Collisional processes involving  $N_2(a)$  are complicated by the existence of two other states with comparable term energies: the  $a'^1\Sigma_u^-$  and the  $w^1\Delta_u$ . This trio of electronic states gives rise to a system of nested vibronic levels which are radiatively as well as collisionally coupled. The relative energies of these states is displayed using a ladder diagram in Figure 13. The allowed radiative transitions  $w^1\Delta_u \rightarrow a'^1\Pi_g$  and  $a'^1\Pi_g \rightarrow a'^1\Sigma_u^-$  comprise the McFarlane Infrared System<sup>48</sup> which radiates in the 3 to 8.5  $\mu m$  wavelength range. The transition probabilities for these bands have not been experimentally determined. Moreover, they have not been observed in the upper atmosphere. Radiation from all of these states is dipole forbidden to the ground state; however, emission from  $a'^1\Sigma(v'=0) \rightarrow X^1\Sigma_g^+(v''=3-8)$  (Ogawa-Tanaka-Wilkinson-Mulliken bands) is observed in addition to the (a-X) LBH bands. The  $a'^1\Pi_g$  state is predissociated for vibrational levels above  $v'=6$ . This is indicated by the lack of emission for  $v'=7$  and higher levels. No commensurate broadening of the absorption lines to these levels is observed, indicating that the predissociation is weak.

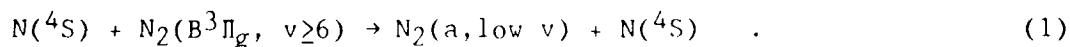


A-2758

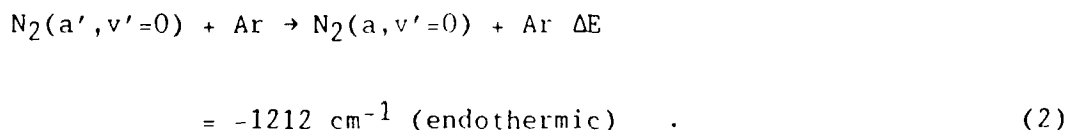
Figure 13. Energy level diagram for  $N_2$  singlets.

Emission from the  $a'^1\Sigma$  state has only been observed for  $v'=0$  to  $v=3-8$  of the ground state.<sup>49,50</sup> No emission from the  $a'$  state has been observed in the McFarlane bands. This would appear to indicate rapid energy transfer out of the  $a'$  state above  $v'=0$ . It is likely that the higher vibrational levels of  $a'$  are strongly coupled to the  $a^1\Pi_g$  state or to other perturbing states. Transitions from the  $w^1\Delta_u$  state to  $a^1\Pi_g$  dominate the McFarlane bands.<sup>48</sup> The transition  $w^1\Delta_u-X^1\Sigma$  has been shown to be pressure dependent.<sup>51</sup> No pre-dissociations of this state have been observed.

The collisional and radiative relaxation of the coupled singlet states have been studied in a series of papers by Golde and Thrush,<sup>52-55</sup> Freund,<sup>56</sup> and van Veen et al.<sup>57</sup> The early work by Golde and Thrush used a discharge flow reactor to create active nitrogen at relatively high pressures (1 to 6 torr). The production of  $N_2(a)$  was shown to occur via two pathways: 1) inverse pre-dissociation to form  $N_2(a, v'=6)$  from ground state N atoms, and 2) intersystem collisional crossing via the reaction



Their observations of  $a'-X$  and  $a-X$  emission showed that  $N_2(a, v=0)$  could be excited by  $N_2(a', v'=0)$  through the process



This conclusion was supported by the observed variation in  $a'/a$  emission intensities with pressure. Electronic quenching of  $N_2(a, v=0)$  by Ar and  $N_2$  was measured to be quite slow,  $k_{Ar} \geq 3 \times 10^{-12} \text{ cm}^3 \text{ molecule}^{-1} \text{ s}^{-1}$  and  $k_{N_2} \geq 1.7 \times 10^{-12} \text{ cm}^3 \text{ molecule}^{-1} \text{ s}^{-1}$ .<sup>55</sup> Quenching by  $CO_2$  was observed to be quite fast ( $k_{CO_2} = 6.5 \times 10^{-11} \text{ cm}^3 \text{ molecule}^{-1} \text{ s}^{-1}$ ) and be strongly dependent on vibrational level.



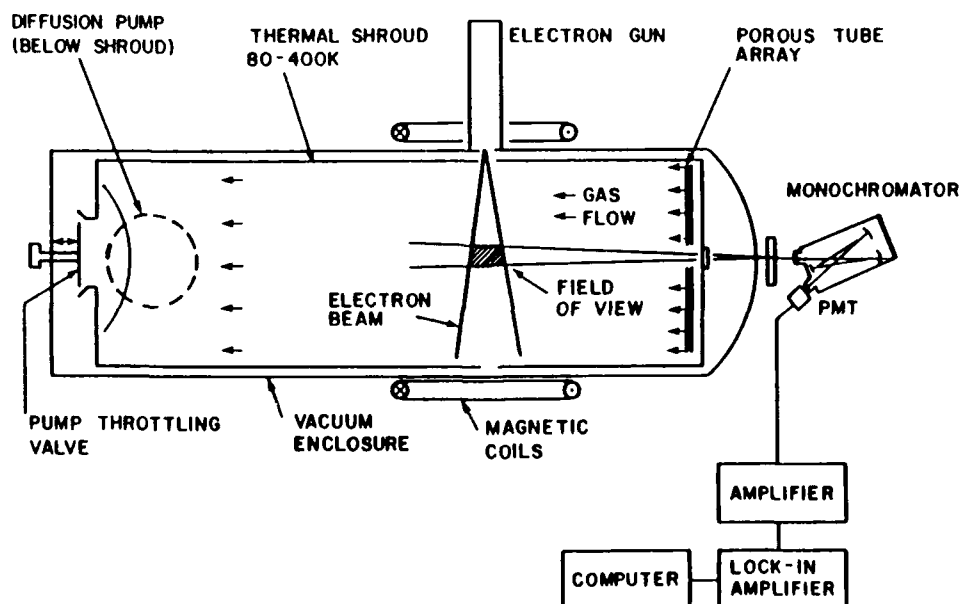
Golde and Thrush observed quenching of high vibrational levels of  $N_2(a)$  by  $N_2$  to be strongly dependent on both vibrational level and temperature, in contrast to  $CO_2$  quenching. Apparent rate coefficients ranging from  $1.6 \times 10^{-12}$  to  $2.7 \times 10^{-11} \text{ cm}^3 \text{ molecule}^{-1} \text{ s}^{-1}$  were observed for levels 0-6. These rates were comparable to Ar quenching suggesting that no resonances are involved and little energy is transferred in the quenching process. This would seem to imply that the relaxation of  $N_2(a, v')$  is primarily vibrational, possibly proceeding via intersystem crossing with the  $a'$  and  $w$ -states.

Model calculations by Freund<sup>56</sup> also indicate that intersystem radiative cascade may play an important role in the apparent lifetimes of the singlet states. His calculations show that the  $a'$ -state is efficiently populated by cascade and that cascade processes affect the apparent  $a$ -state radiative lifetimes. Such a cascade could result in non-exponential population decays and an apparent decrease in the  $a$ -state lifetimes with vibrational level, in contrast with those inferred from absorption oscillator strengths. The calculations also demonstrate that  $a \rightarrow a'$  radiative decay may account for up to 20 percent of the total radiative losses for high vibrational levels of the  $a$  state, with the LBH bands accounting for the remaining losses.

More recently vanVeen, Brewer, Das, and Bersohn<sup>57</sup> used direct two-photon laser excitation of  $N_2(a, v=0,1)$  to measure relaxation rate coefficients for  $N_2$ . They observed regimes of fast exponential (0.05 to 0.2 torr), non-exponential (0.2 to 1.0 torr), and slower exponential (1 to 10 torr) decays. These regimes were ascribed to simple relaxation of the  $a$ -state, partially coupled relaxation of the  $a$  and  $a'$ -states, and fully coupled relaxation of the two manifolds. In the low pressure regime, relaxation rate coefficients of  $2.1 \times 10^{-11}$  and  $2.0 \times 10^{-11} \text{ cm}^3 \text{ molecule}^{-1} \text{ s}^{-1}$  were measured for vibrational levels 0 and 1 respectively. These rate coefficients are the sum of electronic and vibrational relaxation. In the high pressure regimes a decay rate coefficient of  $2.3 \times 10^{-13} \text{ cm}^3 \text{ molecule}^{-1} \text{ s}^{-1}$  is obtained for both  $v=0$  and 1. This rate coefficient is probably a measure of the deactivation of the  $a'$ -state, either through coupling with the  $a$ -state or via relaxation to another manifold.

### 3.2 EXPERIMENTAL

These experiments were performed using the LABCEDE facility at the Air Force Geophysics Laboratory. The LABCEDE chamber is a cylindrical vacuum tank, 3.4m long and 1m in diameter, in which atmospheric species are irradiated by an electron beam. Fluorescence from a number of neutral and ionic electronic bands, including the LBH bands, is observed in irradiated nitrogen. A schematic diagram of the experimental apparatus is shown in Figure 14. The gas to be irradiated enters the reaction chamber at one end through a large porous-tube array, flows under essentially plug-flow conditions along the longitudinal axis of the chamber and out through a 32 in. diffusion pump backed by a Roots blower/fore pump combination (effective pumping speed =  $2.6 \times 10^4 \text{ ls}^{-1}$ ). This flow pattern limits the residence time of gaseous species in the electron beam volume to a few milliseconds at most so that quenching by electron-beam-created species is negligible. The electron beam propagates transverse to the axis of the vacuum tank, a little over a meter from the upstream end of the tank.



A-2757

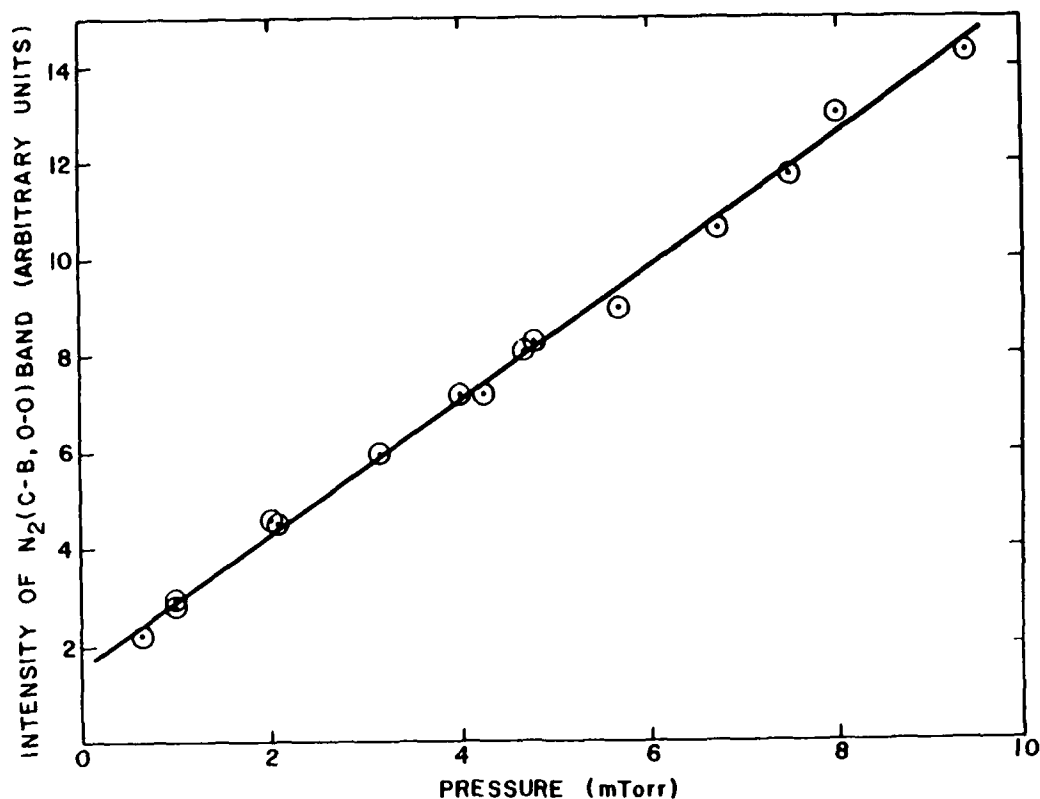
Figure 14. LABCEDE apparatus.

Fluorescence from the electron-irradiated  $N_2$  was observed from the upstream end of the tank perpendicular to the electron beam axis through  $BaF_2$  windows. The emission is spectrally resolved using a McPherson 0.3m monochromator equipped with a 2400 l/mm grating blazed at 150 nm. A partially solar-blind photomultiplier tube (HTV R1220) was used on the monochromator. In the absence of atmospheric attenuation this detection system has good response between 120 and 310 nm. The entire monochromator and light path to the vacuum chamber was purged with  $N_2$  but the effective system wavelength response was limited by residual  $O_2$  absorption to between 175 and 310 nm. The output of the photomultiplier is converted to a voltage in a fast current amplifier (Ithaco Model 1211) and then synchronously detected using a lock-in amplifier (Princeton Applied Research Model 124). A computerized data acquisition system (Compaq/Data Translation DT2801A) was used to record the spectra from the lock-in amplifier. The data was subsequently transferred to a mainframe computer (Prime 450) for further analysis.

The relative wavelength response of the detection system was determined using two techniques. In the region from 175 to 220 nm, the intensities of LBH bands originating from a common upper level of the a-state were compared with the measured fluorescence branching ratios of Shemansky.<sup>58</sup> The ratios of measured to predicted intensities established the response function. In the region from 195 to 310 nm the response was determined using a calibrated deuterium arc lamp (Optronics Laboratories). Additional calibration experiments were performed in which emission from CO(A-X) and NO(A-X) bands in the region from 175 to 290 nm was observed, in situ, from electron excitation of CO and NO. Fluorescence branching ratios for CO(A-X) from Krupenie<sup>59</sup> and NO(A-X) from Piper and Cowles<sup>60</sup> were used to correct observed intensities and obtain relative responses. All calibrations agreed to within 20 percent where they overlapped with the exception of the calibration using the deuterium lamp. From 200 to 230 nm the  $D_2$  lamp deviated from the other calibration by as much as 50 percent. This is potentially due to scattered light. Hence the molecular emissions were used in this wavelength region. The response of the detection system in the 175 to 205 nm region varied by as much as 15 percent

from day to day due to variations in purge efficiency. The response over this region was determined separately for each day's experiments from the LBH branching ratios observed at low pressure.

In these experiments a 50 percent duty cycle pulsed electron beam with a frequency of 195 Hz was used to excite the  $N_2$  (with a high, 99.9999 percent purity grade). Average beam currents of approximately 5.5 to 8.5 mA at an energy of 4.5 keV were employed. The beam current was held constant to  $\pm 0.2$  mA within a given series of experiments. A weak axial magnetic field (7G) was used to confine scattered secondary electrons and enhance excitation efficiency. Observations of  $N_2(C-B)$  emission were used to establish that these excitation conditions were well outside the realm of non-linear beam-plasma interactions. The  $N_2(C)$  state has an electron excitation cross-section function which is similar in shape and magnitude to the  $N_2(a)$  state. Both states sample the same electron energy distribution.<sup>24</sup> The C-state radiative lifetime is sufficiently short (37 ns)<sup>6</sup> that collisional quenching is not important over the pressure range of these experiments. Moreover, there is no experimental evidence for a significant radiative or collisional feed of the C-state from other electronic states. Hence, the population of the C-state represents a balance between direct electron excitation and pure radiative relaxation. The spectrally resolved fluorescence from the  $(C, v=0 \rightarrow B, v=0)$  transition was monitored for a variety of experimental conditions. The C-state populations were observed to increase linearly with electron current at a constant pressure. Additionally, the C-state populations varied linearly with  $N_2$  pressure, for pressures between 0.1 and 10 mtorr. These results are presented in Figure 15. The cascade contribution from higher states such as the E-state appear not to be significant under LABCEDE operating conditions. No (E A) emission (Herman-Kaplan bands) is observed. Based on  $\lambda^3$ -scaling, these bands would be over a hundred times more intense than the E-C transitions, so that C state radiative feed is small. The observed C-state distribution can be ascribed to a Franck-Condon Excitation mechanism so that collisional transfer also seems unlikely. Electron-impact data indicate that the E-state is populated at only 2 percent of the rate of C-state production. The C state was



A-2760

Figure 15. Variation in  $N_2(C)$  state emission intensity with pressure.

thus chosen as a normalization for beam current fluctuations. In the absence of the effects of collisional energy transfer, the ratio of the C-state and a-state populations should be constant.

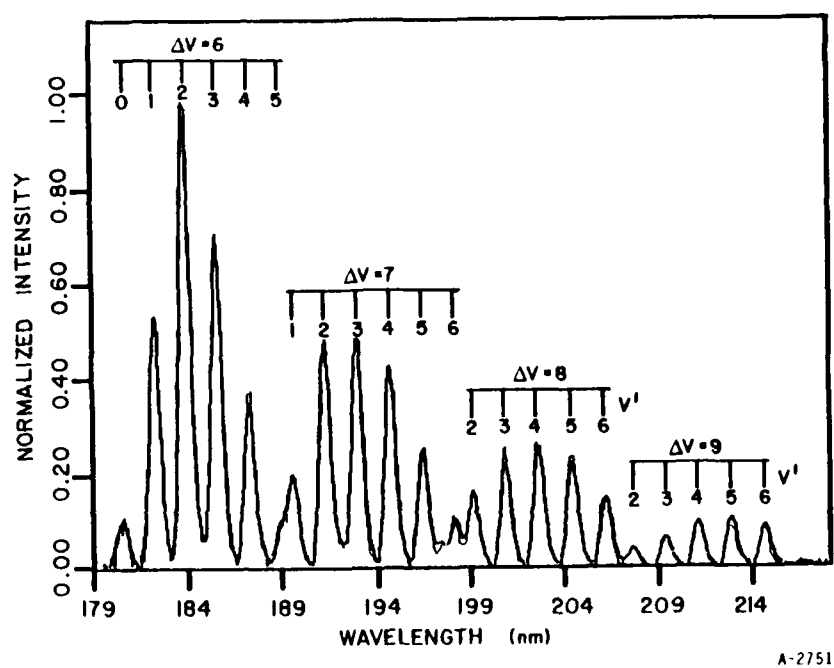
Our experimental approach was to measure the intensities of the LBH bands in the region from 175 to 220 nm and of the  $N_2(C-B)$   $\Delta v=7$  sequence in the region from 292 to 302 nm at pressures from 0.25 to 72 mtorr. The latter was chosen because the  $\Delta v=0$  sequence could not be monitored simultaneously using the solar-blind photomultiplier, which was chosen for good VUV response. Our initial aim was to acquire data at the lowest pressure possible in order to observe the a-state vibrational distribution in the absence of collisional effects. Accordingly, we used the widest slits (coarsest resolution) which still allowed unique spectral feature identification and discrimination of underlying radiators. Slits of 400  $\mu\text{m}$  width provided 5.2Å resolution, which

proved to be more than adequate to resolve the spectrally compact LBH transitions from different vibrational levels. The slit height permitted collection of fluorescence from a 7 cm high slice of the electron-irradiated region perpendicular to the beam axis of propagation.

Because diffusion of  $N_2(\tau = 10^{-4}s)$  molecules out of this field could play a role, data was acquired with different beam geometries. The data presented in this paper was taken with the electron beam defocused so that it was larger spatially than the field of view. The results obtained in this manner did not differ from those obtained with a tightly focused beam, demonstrating that diffusion was not a problem - diffusion into and out of the field of view was balanced to first order. We extracted relative vibrational populations for the bound  $N_2(a)$  levels 0-6 and the C-state levels 2-4 using a linear least-squares spectral fitting code. In addition, we were also able to extract a relative population for the  $N_2(c_4')$  state using emission from the  $C_4'-a, 0-1$  band. This emission occurs in the midst of the  $(C-B)\Delta v=2$  sequence. This linear least squares spectral fitting code uses known line positions and intensities to calculate emission profiles (basis functions) for each vibrational level of a given electronic state. The experimental spectrum is fit using these basis functions in a least-squares sense to minimize the error in the predicted intensities. The outcome of this fit is a set of vibrational populations for each electronic state which can be made absolute if an exact calibration factor is determined. For our experiments absolute calibrations are not required; however, we do obtain a form of absolute calibration by ratioing the measured  $N_2(a,v)$  populations to the  $N_2(C,v=2)$  population determined at the same pressure. Since both states are excited by the same energy electrons, this ratio essentially normalizes the a-state populations for variations in electron beam current from pressure to pressure. More significantly, the C-state is not quenched at any of the pressures we employ. Hence, the ratio of  $N_2(a,v)$  to  $N_2(C,2)$  is independent of pressure in the absence of  $N_2(a)$  vibrational relaxation or feed. It is through an analysis using this ratio that we extract kinetic information.

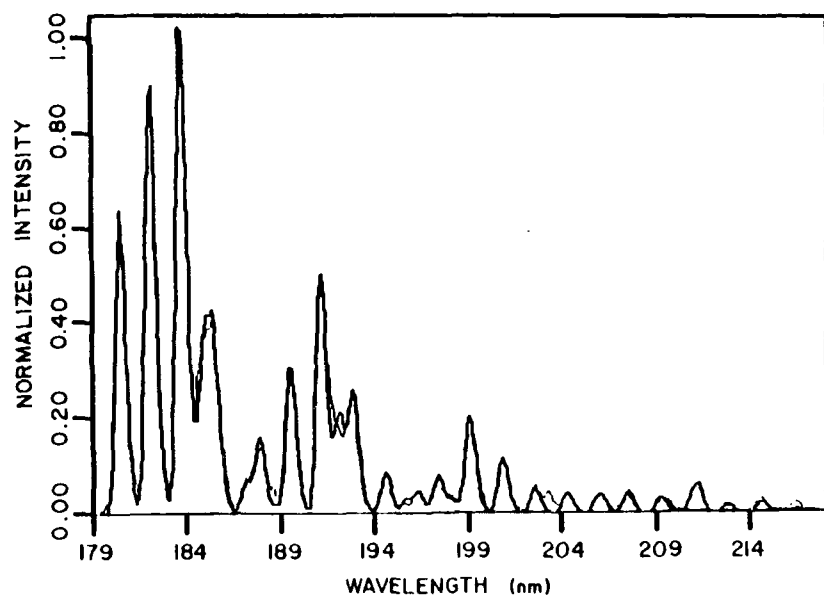
### 3.3 RESULTS AND ANALYSIS

A typical spectrum of the LBH bands recorded at 1 mtorr is shown in Figure 16a along with the least squares spectral fit to the data. The least squares fit used the tabulated spectroscopic parameters from Huber and Herzberg<sup>61</sup> and the modified transition probabilities of Shemansky.<sup>58</sup> These transition probabilities were scaled to match the 80  $\mu$ s lifetimes for  $v=0$  measured by Holland<sup>62</sup> and by Pilling et al.<sup>63</sup> in accordance with the recommendations of Ajello and Shemansky.<sup>46</sup> The transition probabilities used are listed in Table 2. In the 180 to 220 nm spectral region there are several bands originating from each vibrational level except  $v=0$ , and the agreement between the fit and the data is excellent. In addition to the LBH features present, there are also several other emission features which cannot be identified as atomic lines. These features are more evident in the spectrum recorded at 72 mtorr and shown in Figure 16b. These features appear to be a progression from  $a', v=0$  to low vibrational levels of the ground state (Ogawa-Tanaka-Wilkinson-Mulliken Bands). However, the spectral fitting code does not exactly reproduce the exact line positions when the spectral parameters from Huber and Herzberg<sup>61</sup> are used, but instead produces slightly irregularly displaced features from those observed experimentally. The observation of multiple bands in this progression prompt us to believe the  $a'-X$  assignment. The differences between the data and the fit are possibly due to perturbations in the rotational structure of the  $a'$ -state which result in the displacement of peak rotational features to higher  $J$  values and an abnormally large  $Q$  branch.<sup>64</sup> These perturbations have not been included in our spectral fitting code. To account for these features we have generated individual basis functions for each of the emission bands and fit the spectrum using these basis functions. The transitions  $a'-X(v=0 \rightarrow v''6-9)$  are tentatively assigned. A typical spectrum of the  $N_2(C-B)\Delta v=2$  sequence bands in the near UV around 298 nm and the least squares fit to those bands is shown in Figure 17. A basis function for the  $N_2(c_4'-a^1\Pi_g)(0-1)$  band, which falls between the C-B, 2-0, and 3-1 bands, is required to achieve a satisfactory fit. As shown in Figure 14, the  $N_2(C, v=2)$  population does scale linearly with pressure. The non-zero intercept reflects detector dark current levels.



A-2751

(a)



A-2753

(b)

Figure 16. N<sub>2</sub>(a) emission spectra at 1.0 and 72 mtorr and spectral fits to data.



TABLE 2.  $N_2(a^1\Pi_g-X^3\Sigma_g^+)$  Einstein coefficients,  $A_{v',v''}$  ( $s^{-1}$ ) and transition frequency ( $cm^{-1}$ ).

$v'v''$	0	1	2	3	4	5	6
0	732 68950	2116 70617	3360 72255	3865 73866	3616 75449	2929 77005	2129 78533
1	2327 66621	3183 68287	1723 69925	234 71536	127 73119	1018 74675	1972 76203
2	3405 64319	1181 65986	54 67624	1305 69235	1781 70818	921 72373	96 73901
3	3050 62047	7 63713	1556 65352	1063 66962	7 68545	616 70101	1392 71629
4	1880 59803	1072 61469	1090 63108	58 64719	1176 66302	901 67857	43 69385
5	840 57588	1987 59254	5 60893	1209 62504	480 64087	136 65642	1000 67170
6	283 55402	1650 57068	709 58707	709 60317	230 61900	1034 63456	187 64984
7	72 53244	847 54911	1538 56549	5 58160	1060 59743	74 61298	547 62826
8	14 51116	303 52782	1307 54421	758 56032	318 57615	540 59170	600 60698
9	1 49016	78 50683	654 52321	1316 53932	107 55515	785 57071	36 58598
10	0 46946	14 48612	220 50251	983 51862	890 53445	43 55000	750 56528
11	0 44905	1 46571	54 48209	440 49820	1120 51403	349 52959	378 54487
12	0 42892	0 44559	9 46197	132 47808	683 49391	974 50947	29 52475

TABLE 2. Continued.

$v'v''$	0	1	2	3	4	5	6
13	0 40910	0 42576	1 44214	29 45825	260 47408	867 48964	634 50492
14	0 38956	0 40622	0 42261	3 43872	67 45455	420 47010	914 48538
15	0 37032	0 38698	0 40337	0 41948	12 43531	130 45086	587 46614
16	0 35137	0 36804	0 38442	0 40053	1 41636	29 43192	225 44719
17	0 33273	0 34939	0 36577	0 38188	0 39771	3 41327	56 42855
18	0 31437	0 33104	0 34742	0 36353	0 37936	0 39492	9 41020
19	0 29632	0 31299	0 32937	0 34548	0 36131	0 37686	1 39214
Sum	12609	12445	12285	12114	11941	11776	11592

A similar plot of the  $N_2(c_4', v=0)$  population also shows a linear dependence on  $N_2$  pressure. The ratio of  $N_2(C)$   $v=2, 3$ , and 4 populations are constant with pressure and consistent with Franck-Condon type excitation by electrons and radiative relaxation of the excited states. This is further evidence that there are no additional radiative or collisional processes populating the C-state.

The relative vibrational populations of  $N_2(a, v)/N_2(C, v=2)$  which were determined from the spectral fits are given in Table 3 for each pressure studied. Averages are presented when multiple experiments were performed at the same

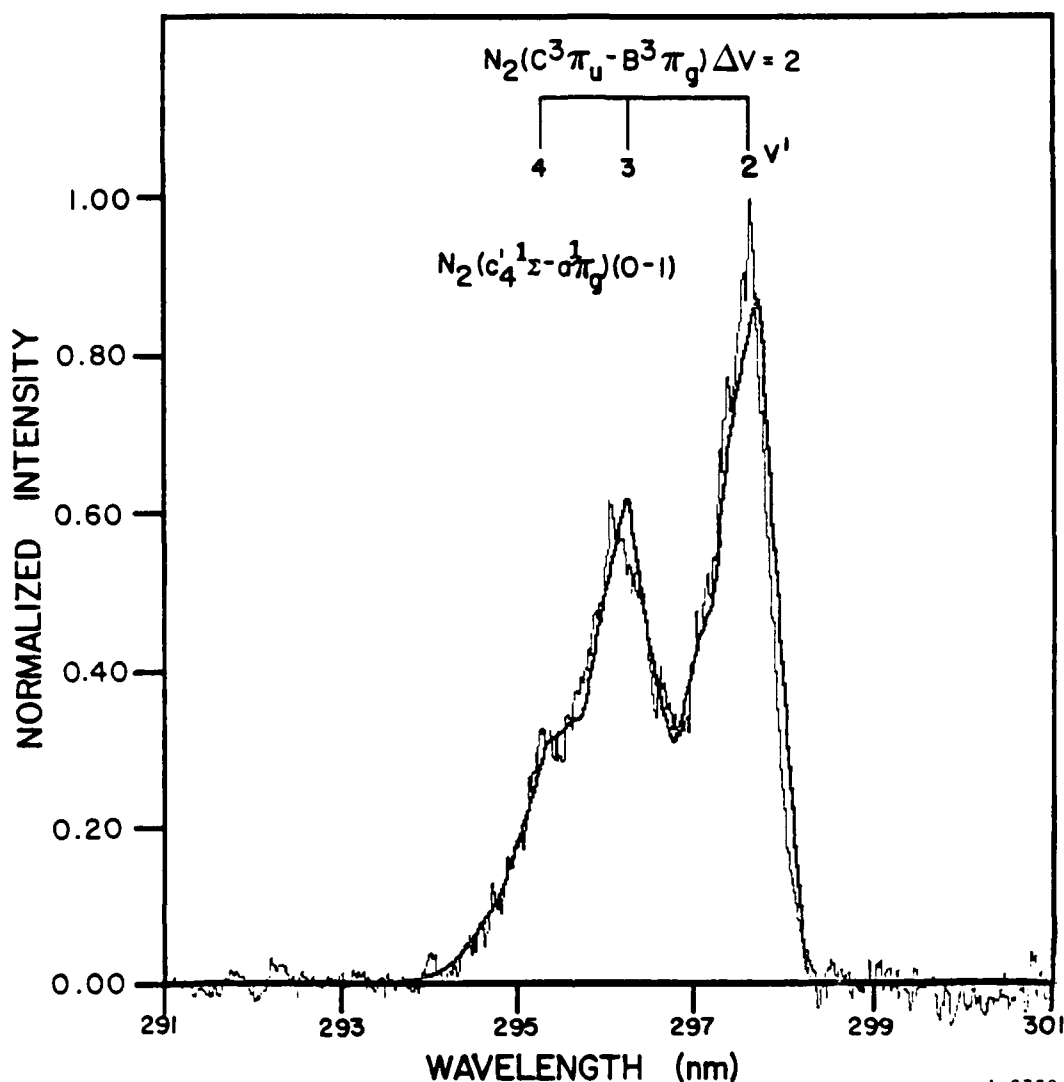


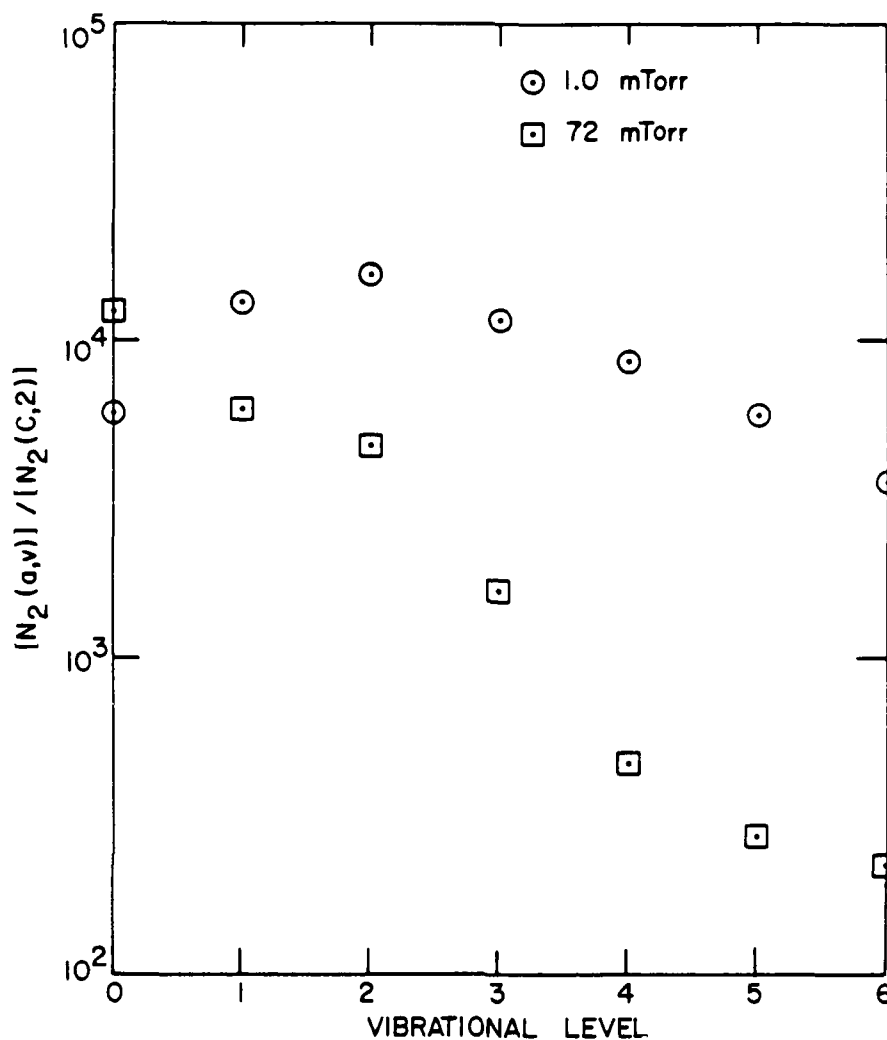
Figure 17. Spectral fit to  $N_2(C-B) \Delta v=2$  sequence band with  $(c'_4-a)$  0-1 band included.

pressure. Agreement was generally better than 20 percent. Plots of the  $N_2(a)/N_2(C,2)$  vibrational population ratios at 1 and 72 mtorr are shown in Figure 18. At 1.0 mtorr less than one collision occurs per a state radiative lifetime on average. The observed vibrational populations agree quite well with those expected from Franck-Condon type excitation of the a and a' manifolds and radiative relaxation of the two states. Details of the model developed for comparison and interpretation of the data will be given in a later section. The vibrational distribution in the a state as observed at

TABLE 3.  $N_2(a,v)/N_2(C,2)$  population ratios.\*

Pressure (mtorr)	Vibrational Level						
	0	1	2	3	4	5	6
0.25	1.18	6.38	8.59	7.35	6.03	3.88	2.48
1.00	3.11	7.30	9.01	6.42	4.92	3.39	2.15
2.00	4.05	6.58	6.91	4.75	3.14	2.15	1.28
3.00	4.92	6.96	7.02	4.26	2.65	1.76	1.13
4.00	6.19	7.94	7.25	3.92	2.40	1.60	1.02
6.00	6.97	8.09	6.94	3.66	1.87	1.26	0.82
8.00	7.93	7.80	6.43	3.07	1.48	0.93	0.66
10.00	7.80	7.90	6.12	2.87	1.36	0.88	0.87
12.50	9.61	8.16	6.17	2.59	1.17	0.71	0.58
15.00	8.57	6.53	5.40	2.22	0.95	0.57	0.36
20.00	9.05	6.62	4.91	1.86	0.76	0.45	0.42
30.00	9.20	5.61	4.06	1.45	0.53	0.31	0.28
40.00	7.97	4.67	3.48	1.15	0.44	0.25	0.25
50.00	7.79	4.21	3.20	1.10	0.34	0.20	0.16
60.00	6.85	3.50	2.75	0.94	0.26	0.16	0.14
72.00	6.30	3.17	2.45	0.86	0.25	0.15	0.14
*All ratios should be multiplied by $10^3$ to obtain actual values.							

72 mtorr is substantially more relaxed than that at 1 mtorr. The populations of levels 5 and 6 have decreased by nearly a factor of ten while the population of  $v=0$  has increased nearly two-fold. In addition to the apparent vibrational relaxation, the total population of  $N_2(a)$  decreases with pressure indicating that electronic deactivation is also occurring at a slower rate.

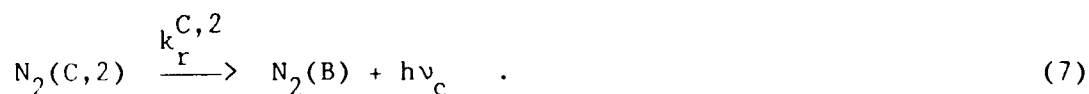


A-2755

Figure 18.  $N_2(a,v)/N_2(C,2)$  population ratios at 1.0 and 72 mtorr obtained from spectral fitting.

An average electronic deactivation rate coefficient for the a-state can be obtained by considering how the total  $N_2(a)$  population, ratioed to the  $N_2(C,v=2)$  population, varies with pressure. The relevant reactions to be considered are:





Both  $N_2(a)$  and  $N_2(C)$  are in steady state and their populations can be written as

$$[N_2(a)] = \frac{k_f^a [N_2]}{k_r^a + k_0 [N_2]} \quad (8)$$

and

$$[N_2(C,2)] = \frac{k_f^{C,2} [N_2]}{k_r^{C,2}} \quad (9)$$

In these expressions  $k_f$  and  $k_r$  represent the formation and radiative rate coefficients,  $k_0$  is the average quenching rate coefficient, and  $[N_2(a)]$  is the total  $N_2(a)$  population obtained by summing over all vibrational levels. As stated above, losses due to diffusion are negligible. Combining expressions (8) and (9) yields the result

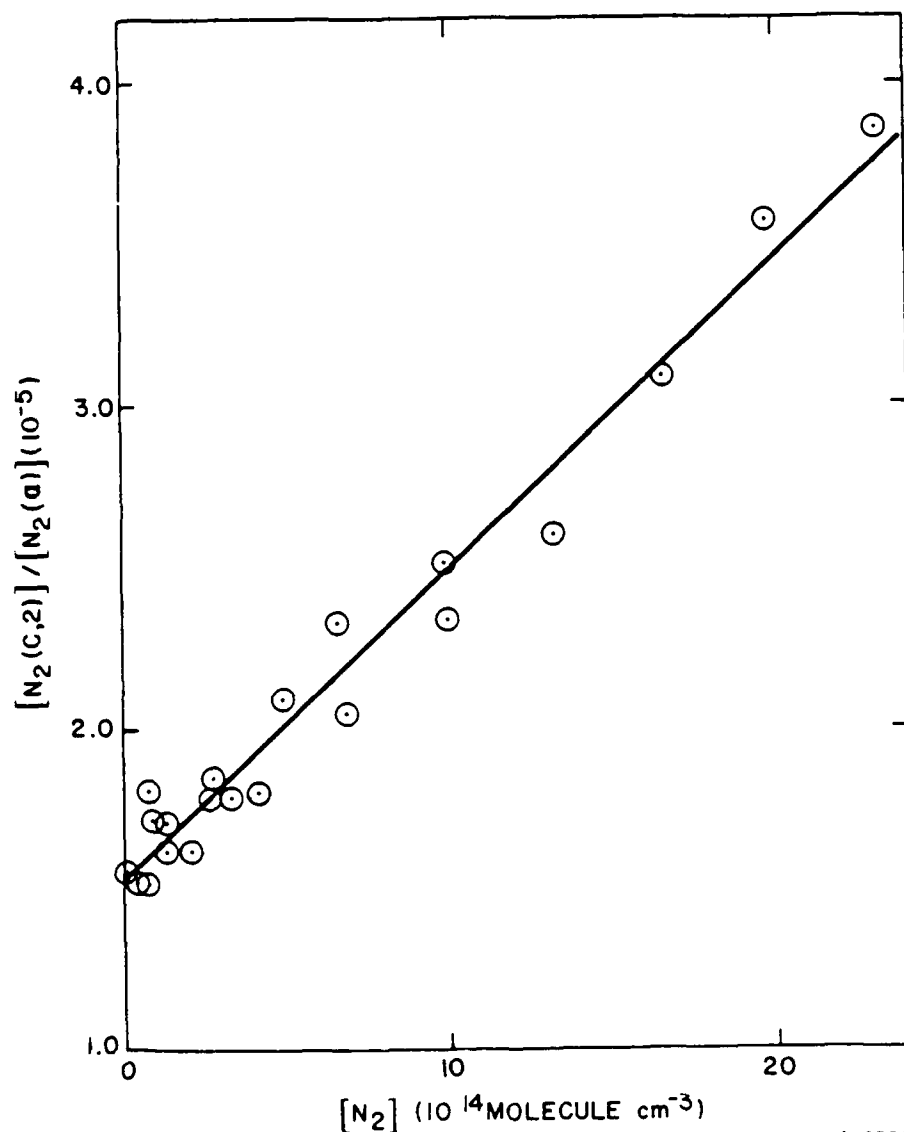
$$\frac{[N_2(C,2)]}{[N_2(a)]} = \frac{\delta k_r^a}{k_r^{C,2}} + \frac{\delta k_q [N_2]}{k_r^{C,2}} \quad (10)$$

where

$$\delta = \frac{k_f^{C,2}}{k_f^a} \quad (11)$$

There is thus a linear relationship between the ratio  $[N_2(C,v=2)]/[N_2(a)]$  and total  $N_2$  pressure. The quenching rate coefficient is simply determined by multiplying the ratio of the slope to the intercept of the line by  $k_r^a$ .

A plot of  $[N_2(C,2)]/[N_2(a)]$  versus  $N_2$  number density is shown in Figure 19. The data does indeed form a straight line with slope  $9.55 \pm 0.44 \times 10^{-21} \text{ cm}^3 \text{ molecule}^{-1}$  and intercept  $1.54 \pm 0.05 \times 10^{-5}$  (statistical error bars only). The radiative rate used in expression (10) is necessarily an average over all of the populated vibrational levels. The a-X transition probabilities vary slowly with vibrational level, hence averaging these values is not a significant source of error. However, radiation from the a-a' transition must also be considered as part of  $k_r^a$  and this component will vary rapidly with  $v$  due to the roughly frequency cubed scaling of the low frequency infrared transitions. We have calculated the transition probabilities for the a-a' transition using the known line positions and Franck-Condon factors<sup>6,61</sup> and the transition moments of Yeager and McKoy.<sup>65</sup> These are summarized in Table 4. When both transitions are considered the averaged transition probability,  $\langle k_r^a \rangle$ , becomes  $13835 \pm 725 \text{ s}^{-1}$ . The results in a value for  $k_0$  of  $8.6 \pm 0.7 \times 10^{-12} \text{ cm}^3 \text{ molecule}^{-1} \text{ s}^{-1}$ , a 15 percent increase over the a-X value. A similar analysis for vibrational level 6 only, which can have no feed from higher levels, yields a larger quenching rate coefficient of  $8.5 \pm 1.8 \times 10^{-11} \text{ cm}^3 \text{ molecule}^{-1} \text{ s}^{-1}$ .



A-2759

Figure 19. Stern-Volmer plot for  $N_2(a)$  electronic relaxation.

The data interpreted in this manner supports the existence of fast vibrational deactivation competing with slow electronic deactivation as the primary pathways for collisional relaxation of  $N_2(a)$  molecules. The absence of any real curvature in the plot of Figure 19 might indicate that radiative and/or collisional feed from either  $N_2(a')$  or  $N_2(w)$  is not a significant source of excitation for  $N_2(a)$ . This prompted us to proceed with a vibrational deactivation analysis of  $N_2(a)$  assuming that the  $a'$  and  $w$  manifolds do not play an



TABLE 4.  $N_2(a^1\Pi_g - a'^1\Sigma_u)$  Einstein coefficients.

$v'v''$	0	1	2	3	4	5	6	Sum( $a'$ )
0	99.74 1211	614.20 2878	351.60 4516	48.44 6127	1.30 7710	0.01 9266	0.00 10793	0.00
1	1.54 -294	33.74 1372	832.70 3010	84.17 4621	161.80 6204	5.37 7759	0.02 9287	1.54
2	118.10 -1776	0.08 -110	2.30 1528	804.80 3138	1325.00 4721	33.20 6277	12.46 7085	118.10
3	206.90 -3235	143.30 -1569	0.01 69	6.22 1679	644.50 3263	1712.00 4818	553.90 6346	350.20
4	164.40 -4671	422.70 -3004	106.60 -1366	0.13 244	35.66 1827	439.90 3382	1996.00 4910	693.70
5	92.23 -6083	467.10 -4417	527.00 -2778	59.40 -1168	0.18 414	76.51 1970	249.80 3498	1146.00
6	42.33 -7473	330.40 -5807	786.00 -4168	499.00 -2557	25.59 -974	0.03 580	114.90 2108	1683.00
7	17.11 -8840	186.70 -7173	697.80 -5535	1003.00 -3924	397.40 -2341	8.42 -786	0.18 741	2311.00
8	6.50 -10184	89.95 -8518	472.20 -6879	1100.00 -5269	1073.00 -3685	275.30 -2130	1.91 -602	3019.00
9	2.31 -11506	39.14 -9840	261.70 -8201	859.70 -6591	1424.00 -5008	988.60 -3452	163.10 -1924	3738.00
10	0.83 -12806	16.27 -11140	129.30 -9501	557.20 -7891	1308.00 -6308	1618.00 -4752	821.10 -3221	4451.00
11	0.31 -14084	6.37 -12418	58.62 -10779	313.10 -9169	946.90 -7586	1716.00 -6030	1625.00 -4502	4667.00
12	0.14 -15341	2.35 -13674	26.76 -12036	157.90 -10425	605.10 -8842	1423.00 -7287	2019.00 -5759	4234.00
13	0.05 -16575	0.99 -14909	10.92 -13270	79.35 -11660	339.20 -10077	101.20 -8521	1901.00 -6993	2432.00

TABLE 4. Continued.

v'v''	0	1	2	3	4	5	6	Sum(a')
14	0.05 -17789	0.99 -16122	10.92 -14484	79.35 -12873	339.20 -11290	626.40 -9734	1465.00 -6993	2310.00
15	0.00 -18981	0.17 -17314	1.94 -15676	15.62 -14065	91.83 -12482	354.60 -10926	1008.00 -9399	1472.00
16	0.00 -20151	0.07 -18485	0.71 -16847	7.66 -15236	41.63 -13653	203.70 -12097	622.80 -10569	876.60
17	0.00 -21301	0.02 -19635	0.30 -17996	3.19 -16386	19.65 -14803	102.60 -13247	358.50 -11719	484.30
18	0.00 -22430	0.00 -20764	0.14 -19125	1.25 -17515	9.79 -15931	48.98 -14376	203.80 -12848	264.00
19	0.00 -23538	0.00 -21872	0.06 -20233	0.49 -18623	4.76 -17040	22.32 -15484	110.40 -13956	138.00
Sum	99.74	647.9	1186.0	943.7	2169.0	2567.0	2927.0	

important role in a-state vibrational relaxation. Kinetic modeling of the a, a-, w system was performed system to assess the magnitude of any errors introduced by this assumption.

The vibronic relaxation of N<sub>2</sub>(a) can be treated as a single quantum vibrational relaxation within the manifold which competes with a deactivation process which removes vibrational quanta entirely from the manifold. At the lowest pressure employed (0.25 mtorr) N<sub>2</sub>(a) only relaxes radiatively. The steady state rate of formation of a given level can be equated to its radiative loss, hence

$$R_v = N_v^0 A_v \quad (12)$$

where  $R_v$  is the rate of information of level  $v$ ,  $N_v^0$  is the ratio of  $N_2(a,v)/N_2(C,2)$  in the collisionless limit, and  $A_v$  is the total emission transition probability for level  $v$ . When normalized by the C-state,  $R_v$  is independent of pressure. At higher pressures collisional feed from higher vibrational levels provides an additional source and collisional quenching becomes an additional loss mechanism. Hence expression (12) becomes

$$R_v = N_v A_v + (k_E^v + k_{v,v-1}^0 N_v [N_2] - k_{v+1,v} N_{v+1} [N_2]) \quad (13)$$

Equating expressions (12) and (13) gives

$$N_v^0 A_v = N_v A_v + (k_E^v [N_2] + k_{v,v-1} [N_2]) N_v - k_{v+1,v} [N_2] N_{v+1} \quad (14)$$

where  $k_v^E$  is the electronic quenching rate coefficient for level  $v$ ,  $k_{v,v-1}$  is the vibrational quenching rate coefficient for level  $v$ , and  $k_{v+1,v}$  is the vibrational quenching coefficient for the level  $v+1$ , which feeds level  $v$ . An equation such as (14) can be written for each vibration level and summed for all levels above the level of interest to extract a vibrational quenching rate coefficient. The resulting expression is given by

$$\frac{N_v^0}{N_v} + \sum_{m=1}^{m=v} \frac{(N_{v+m}^0 - N_{v+m}) A_{v+m}}{N_v A_v} = \frac{[N_2]}{N_v A_v} \sum_{m=1}^{m=v} k_E^v N_{v+m} + \frac{(k_E^{v+m} + k_{v,v-1}^0)}{A_v} [N_2] \quad (15)$$

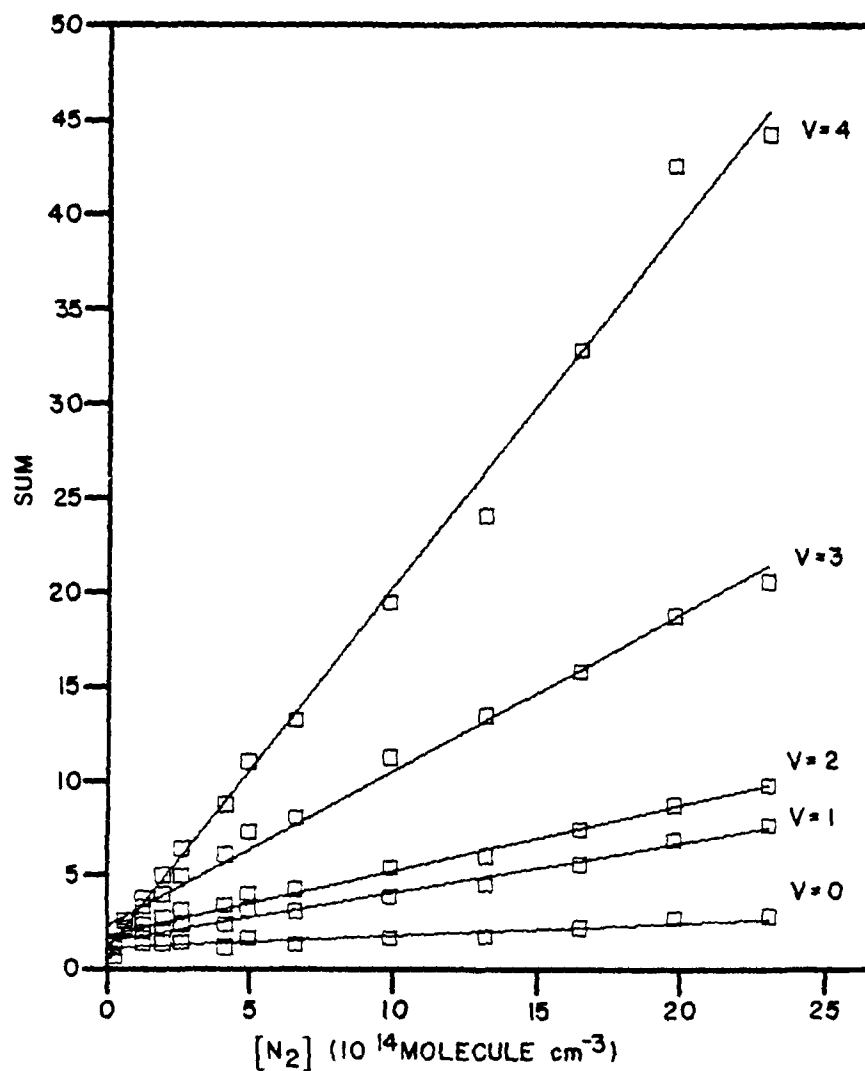
Expression (15) relates a simple sum of experimentally measured vibrational populations and transition probabilities to the  $N_2$  pressure in a linear manner. The model assumes a knowledge of  $k_E^v$  for each level, for which we

substitute our averaged value obtained from the Stern-Volmer analysis presented previously. With this assumption we can obtain vibrational quenching rate coefficient for each bound vibrational level. The predissociation of levels above  $v=6$  provides a convenient upper limit for the sums of expression (15). Plots of the left hand side of expression (15) versus  $N_2$  number density are shown in Figure 20 for vibrational levels 0-4. Levels 5 and 6 are not shown but their rates are somewhat slower. For each of these levels the data clearly defines a straight line with the slope for  $v=0$  being almost flat. This indicates that the average electronic quenching rate coefficient is approximately correct for this level. The intercepts for these lines are generally larger than one by more than the expected experimental error. The intercepts are:  $1.91 \pm 0.18$ ,  $v=0$ ;  $1.88 \pm 0.12$ ,  $v=1$ ;  $2.20 \pm 0.15$ ,  $v=2$ ;  $2.67 \pm 0.34$ ,  $v=3$ ;  $1.35 \pm 0.32$ ,  $v=4$ ;  $1.07 \pm 0.21$ ,  $v=5$ ; and  $1.32 \pm 0.25$ ,  $v=6$ . The errors quoted are  $1\sigma$  limits obtained solely from the fit to the data. This could possibly indicate the presence of an additional source term, perhaps from the  $a'$ -state, or is perhaps due to propagation of experimental errors through the analysis. Both explanations would predict larger deviations from a unit intercept for low vibrational levels: as a result of near resonances in the  $a'$ - $a$  vibrational levels for low  $v$  (see Figure 13) and due to the extended sums required for the calculation of rate coefficients for the lower levels.

The rate coefficients derived from the analysis are given in Table 5. The largest single source of error in these rate coefficients is probably the uncertainty in the radiative transition probabilities, especially for the high vibrational levels where coupling should be small. Of course the values are at least uncertain by the magnitude of the electronic quenching rate coefficient, which may not be constant with vibrational level. These uncertainties are included in the overall estimate of experimental accuracy.

### 3.4 KINETIC MODELING

Kinetic modeling was performed to establish the sensitivity of the measured rate coefficients to intersystem cascade processes. A standard chemical



A-2761

Figure 20. Vibrational relaxation analysis decay plots.

kinetics modeling code was employed in which each vibrational level of the *a* and *a'* states were treated as independent species. The *w* state was not considered in the model because of its poor electron excitation efficiency<sup>24</sup> and because it has no vibrational levels which are near-resonant with any bound *a* state levels (see Figure 13). Two separate criteria were used to judge the effectiveness with which the model reproduced experimental data. The first criterion was how well the model matched the total rate of electronic deactivation of the *a*-state. Secondly, the model was judged on how well it reproduced the measured vibrational distributions at 1 and 72 mtorr.

TABLE 5.  $N_2(a, v \rightarrow v-1)$  rate coefficients.

$v$	$k_{v,v-1}$ ( $10^{-11}$ cm <sup>3</sup> molecule <sup>-1</sup> s <sup>-1</sup> )
1	$2.7 \pm 0.8$
2	$4.0 \pm 1.0$
3	$10.7 \pm 1.1$
4	$26.6 \pm 1.5$
5	$23.0 \pm 1.2$
6	$11.5 \pm 1.3$

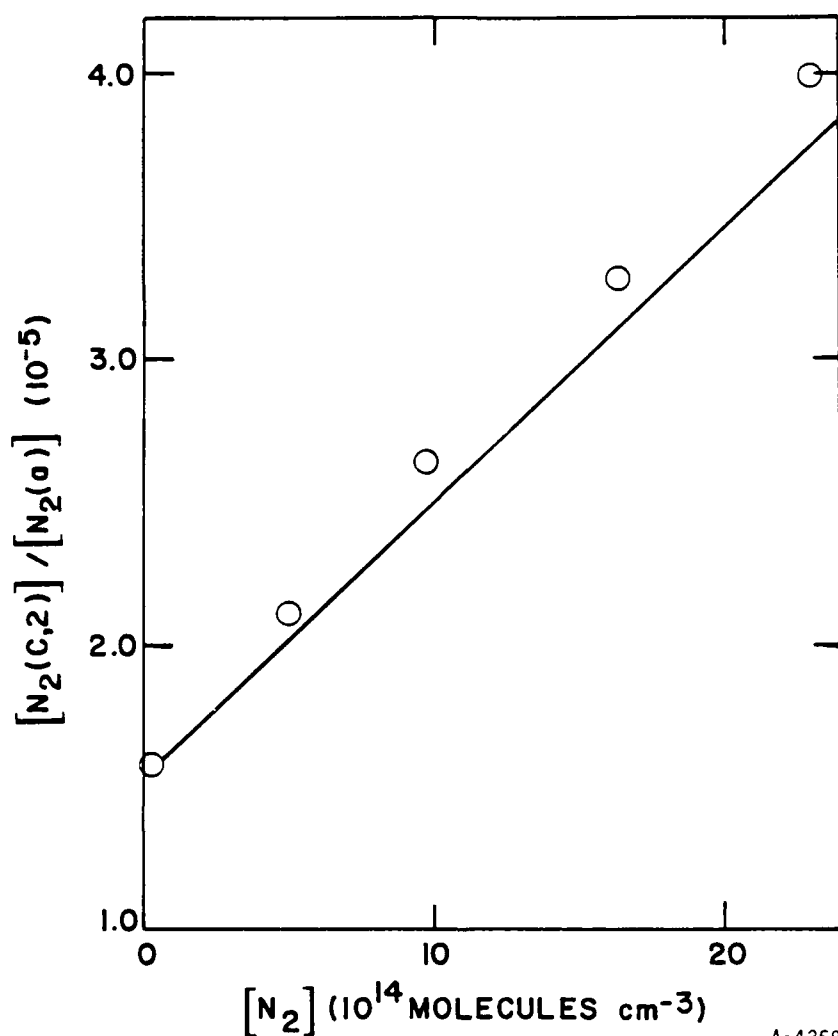
Electronic excitation efficiencies for the  $a$  and  $a'$  states were taken from the work of Cartwright et al.<sup>4</sup> The efficiencies were partitioned between vibrational levels using the Franck-Condon factors between these levels and  $N_2(X, v=0)$  taken from Lofthus and Krupenie.<sup>6</sup> Levels above  $v=6$  of the  $a$ -state were not considered. Radiative transition probabilities (listed in Table 2) for the LBH bands were taken from Shemansky<sup>58</sup> and scaled to match an 80  $\mu$ s lifetime for  $v=0$ , as previously discussed. The transition probabilities for the  $a'-X$  bands were taken from the estimate of Golde<sup>55</sup> and assumed to be independent of vibrational level. The variation of  $a-a'$  emission is much more significant in magnitude. There are no measured transition probabilities for the  $a-a'$  McFarlane Bands. We have calculated transition probabilities using the Franck-Condon factors and  $r$ -centroids from Lofthus and Krupenie,<sup>6</sup> spectroscopic constants from Huber and Herzberg,<sup>61</sup> and transition moments from Yeager and McKoy.<sup>65</sup> These are reproduced in Table 4.

The electronic deactivation rate coefficient for the  $a$ -state was taken from our data to be  $8.6 \times 10^{-12}$  cm<sup>3</sup> molecule<sup>-1</sup> s<sup>-1</sup> and assumed to be independent of vibrational level. Electronic deactivation of  $a'$  vibrational levels was also assumed to be level-independent and assigned a value of  $3 \times 10^{-13}$  cm<sup>3</sup> molecule<sup>-1</sup> s<sup>-1</sup> in accordance with the high pressure deactivation measurements

of van Veen, et al.<sup>57</sup> and Piper.<sup>66,67</sup> This effect of using a faster rate was determined to be negligibly different.

The collisional rate coefficients which couple the  $a'$  and  $a$  vibrational levels were considered for four cases. In Case 1 no collisional coupling was assumed to occur and the  $a$ -state manifold was assumed to vibrationally relax with the same rate coefficients measured from our experiments. In Case 2 the  $a'$  vibrational manifold was allowed to intrasystem relax with the same rate coefficients measured for the  $a$ -state levels. In Case 3 the levels were allowed to couple with rate coefficients given by a gas-kinetic collision coefficient weighted by the exponential of the energy difference between the coupled levels. Vibrational levels of  $N_2(a')$  which couple to  $a$ -state levels above  $v=6$  are assumed to dissociate the molecule. The  $a$  and  $a'$  vibrational levels are assumed to have the same intrasystem relaxation rates as in Case 2. In Case 4 all nearest vibrational levels are allowed to couple with gas kinetic rate coefficients. Predissociating levels are treated the same as in Case 3. The  $a$  and  $a'$  intrasystem vibrational relaxation rate coefficients were set to zero.

In Figure 21 we show a plot of  $[N_2(C2)]/[N_2(a)]$  versus  $[N_2]$  reproduced from our data with the least squares values of Figure 19 substituted for the actual data points. Aside from a slight offset most likely due to calibration errors, the slope of the line in Case 1 does a good job of reproducing the experimental data. In all Cases (1-4), the total deactivation rate was relatively insensitive to vibrational deactivation schemes. This is due to the assumption that electronic deactivation is independent of vibrational level. Thus, vibrational relaxation simply moves populations between vibrational levels which are electronically relaxed with equal efficiency. This agreement with data is seen in Figure 22 where the vibrational population data recorded at 1 mtorr also closely matches the model prediction, aside from the offset. This offset is well within the range of experimental error. The vibrational distribution of  $N_2(a)$  calculated at 1.0 mtorr is identical for all of the



A-4258

Figure 21. Comparison of measured electronic relaxation rate data (averaged as solid line) with kinetic model results for selected pressures (open symbols).

cases tested. This demonstrates that the relaxation processes at this pressure are dominated by radiative mechanisms and collisional coupling of  $a'$  to  $a$ .

The vibrational distribution calculated in Case 1 at 72 mtorr also closely matches the data (Figure 23). The agreement is to be expected since all the assumptions used in analyzing the data are incorporated in the model.



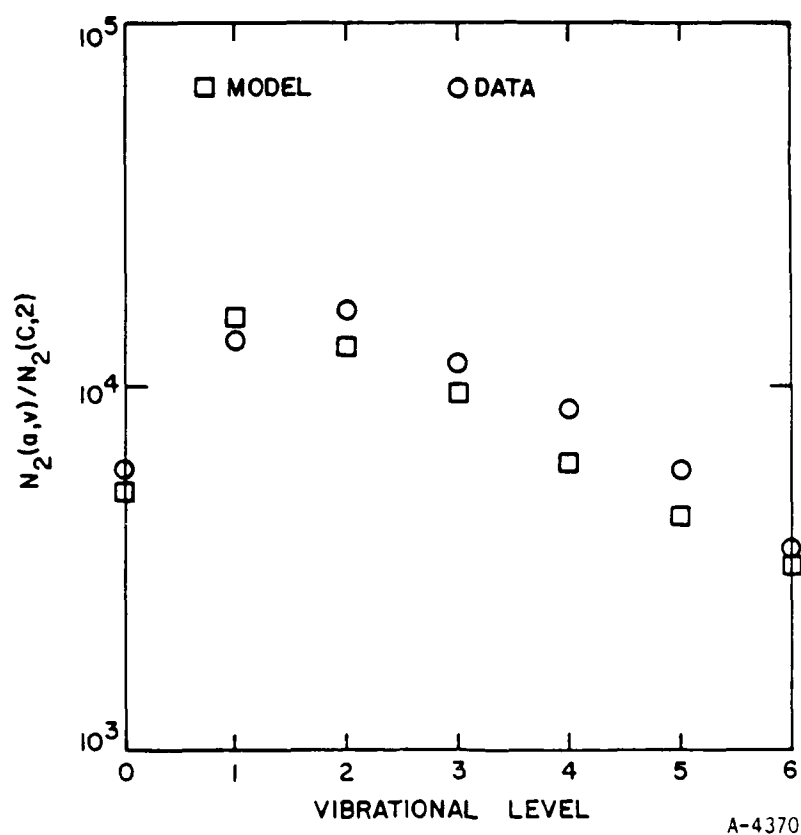
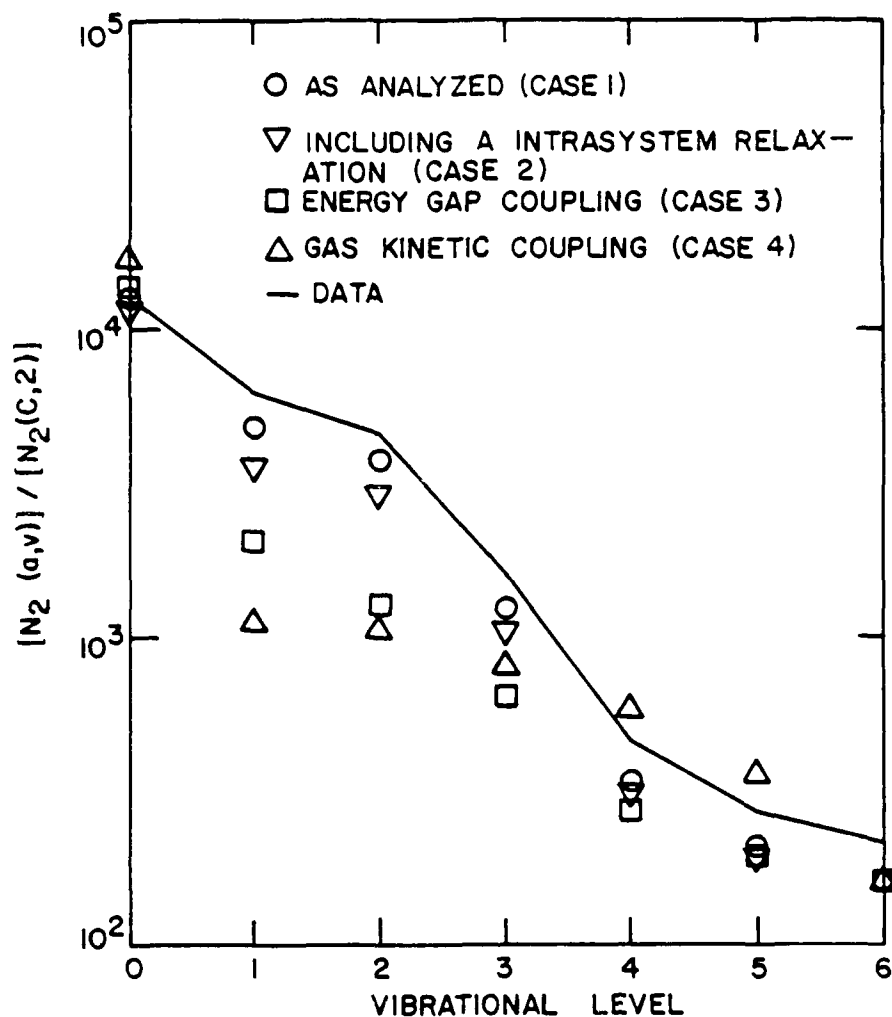


Figure 22.  $N_2(a,V)/N_2(C,2)$  populations at 1.0 mtorr.

The deactivation rate predicted by the Case 2 model is approximately the same as is observed in the data or the Case 1 model. The vibrational distribution predicted at 72 mtorr is significantly more relaxed than observed in the data. If the  $a'$  vibrational levels are not allowed to relax to lower  $a'$  vibrational level, under these coupling conditions, the vibrational distribution at 72 mtorr more closely matches the data. This indicates that strict radiative coupling of the manifolds increases the  $a$  state vibrational relaxation rate by providing another  $v-v$  relaxation channel.

In Case 3 the energy gap type coupling of the  $a'$  and  $a$  vibrational levels results in a large enhancement in the rate of relaxation of the levels most closely coupled, i.e.,  $a$ -state levels 1-3 coupled to  $a'$  state levels 2-4. The higher vibrational levels, which are much more poorly coupled, remain in reasonably good agreement with the data. The modeling clearly shows that the



A-4369

Figure 23. Kinetic modeling: vibrational distributions at 72 mtorr.

total relaxation rate for these levels has been overestimated and some combination of lower inter- and intrasystem relaxation rate coefficients is required to reproduce the data.

In Case 4 (gas-kinetic coupling) the apparent electronic relaxation is again comparable to the data (Figure 23) and the vibrational distribution at 72 mtorr is even more relaxed than under Cases 2 or 3. This result indicates that improved coupling to a second vibrational manifold may efficiently relax the a-state vibrations via intersystem cascade. Inclusion of the intrasystem

vibrational deactivation channels in the  $a'$  and  $a$  manifolds has a minimal effect on the calculated vibrational distribution. Again, the model overpredicts the rate of relaxation for low levels of the  $a$ -state. In this case, the population of high vibrational levels is overestimated by the model, despite the fast intersystem relaxation rates employed. This indicates that the gas kinetic coupling of the levels feeds too much of the populations of higher  $a$  and  $a'$  levels into the level of interest.

Several general conclusions can be drawn from our modeling study. First, the deactivation rate coefficients measured for vibrational levels 4-6 are probably reasonably close to the true values. The modeling shows that the observed populations are relatively insensitive to inter- and intrasystem cascade from higher vibrational energy levels of either state. The acceptor states for the vibrational energy removed from these levels cannot be positively identified. It is clear that if energy is rapidly removed from lower  $a$  state energy levels, then a substantial feed from higher levels is required to account for the measured populations. This would tend to favor an intrasystem vibrational cascade process as the primary loss mechanism for the higher  $a$  state levels. A second conclusion we can draw from the modeling is that our experiments cannot provide a quantitative estimate of the magnitudes of the intersystem and intrasystem cascade processes for the lower vibrational levels. Again, rapid removal of  $a$ -state populations in these levels must be balanced by feed from higher levels or from other electronic manifolds. Feed into these levels from  $N_2(a')$  and  $N_2(w)$  is possible; however, the direct electron impact excitation efficiencies for the resonant levels are quite low. To account for the nearly tenfold increase in population required for the models to match the data, resonant transfer into low levels of the  $a$ -state would have to be the major mode of relaxation for the entire vibrational manifolds of these states. This reasoning also favors intrasystem relaxation as the dominant process.

At low pressures the model does a good job of predicting the observed data. While the model predicts an  $N_2(a', v=0)/N_2(C, v=2)$  population ratio which is

approximately a factor of two greater than observed in our data, this level of error is acceptable, considering the uncertainty in the transition probabilities for the  $a'-X$  transition. The model also provides the populations of higher  $a'$  vibrational levels. These populations are considerably lower than  $v=0$  and hence, given the  $a'-X$  transition probabilities, we would not expect to observe emission from higher levels of the  $a'$ -state. This sharp decrease in  $a'$  state populations with vibrational level is largely due to increases in the  $a'-a$  transition probabilities, which essentially scale as (frequency).<sup>3</sup> Therefore, much of the radiation from these levels occurs in the McFarlane infrared bands. Simultaneous observation of these bands would help to provide an increased understanding of the radiative processes which are occurring.

### 3.5 DISCUSSION

Based on our analysis of the fluorescence from electron irradiated  $N_2$  in the 0.2 to 70 mtorr pressure range, we are able to: a) quantify the relative production efficiencies into several electronic states as well as the vibrational distributions within those states, and b) measure effective vibrational quenching rates for  $N_2(a, v'=0-6)$ . We will discuss these findings in relation to upper atmospheric fluorescence observations. We will also consider in this section the implications of this quenching on atmospheric emission signatures in the VUV and the infrared.

#### 3.5.1 Relative Production Efficiencies

Throughout our analysis we have used the  $N_2(C^3\Pi_u)$  state to normalize the observed populations of the other electronic states. Our fluorescence data indicates that the C-state population scales linearly with the total pressure and beam current (i.e., energy deposition). There appears to be no significant cascade or collisional feed into levels of this short-lived (37 ns) state under our experimental conditions. The vibrational distributions we observe agree well with a Franck-Condon excitation/radiative relaxation model at all pressures, at least up to 80 mtorr. This also indicates that the bulk  $N_2$

molecules have not been substantially vibrationally heated by electron irradiation, since the electron-excited  $N_2$  C-state vibrational distribution is quite sensitive to the parent  $N_2(X,v)$  population. The total electron excitation cross section for the C-state is sharply peaked at electron energies between 11 and 30 eV. The a-state, which lies at lower energy, has a lower excitation threshold (8.6 eV). Its excitation cross section is similar in magnitude to the C state at its peak, but spans a range from 10 to 80 eV resulting in a larger integrated value (electron energy ranges given are for differential cross sections within an e-fold of the maximum).<sup>25</sup> Measurements of the relative electron excitation cross sections for the E- and the C-state by Cartwright<sup>25</sup> indicate that the E-state production rate is approximately 2 percent of the C-state production rate. Moreover, the branching ratio for E-state emission would favor E-A (Herman-Kaplan) transitions by two orders of magnitude. Consequently, population of the C-state by cascade from the E-state and higher lying Rydberg states should be negligible.

At our lowest pressures quenching of the a-state does not occur to any significant extent; moreover, diffusive losses are minimized by using a spatially extended electron beam which overfills the detector field of view. Hence, losses are dominated by radiative decay and will accurately reflect the production rates. Under these conditions, the steady state populations of the  $N_2$  C- and a-states are given by Eqs. (8) and (9). Using  $k_r^C = (37 \text{ ns})^{-1}$  and  $k_r^a = (85 \text{ } \mu\text{s})^{-1}$  (Refs. 6 and 62, respectively), we obtain  $k_f^a/k_f^C = 3.1$ , where  $k_f^a$  includes the sum over all observed vibrational levels 0-6. Inclusion of production into levels above  $v'=6$ , which predissociate, would raise this value by 13 percent to 3.6. Use of a slower radiative rate<sup>58</sup> would increase this ratio further. Cartwright<sup>4</sup> uses a value of 2.1 for this ratio in his model of the auroral upper atmosphere. Green and coworkers<sup>26,27</sup> calculate a value of 2.64 for primary excitation only. We have only observed emission from the  $N_2(a', v'=0)$  level, even though Cartwright's predictions indicate that over 99 percent of the a'-state excitation is into higher vibrational levels at altitudes representative of the low pressures employed in our experiments.

Cartwright shows excitation peaking at  $v'=7$  (from a Franck-Condon type process); however, levels above this may be predissociative.

Our data and kinetic modeling indicate that the  $a'$  and  $a$  states are strongly coupled, radiatively and collisionally ( $a' \rightarrow a$ ) at low pressures, and collisionally ( $a' \rightarrow a$ ) at higher pressures. Consequently, the sum of the  $a$  and  $a'$  formation rates (relative to the C-state) may be more appropriate to compare with Cartwright's excitation cross sections. Cartwright's Table 1 (Ref. 4) yields  $(k_f^a + k_f^{a'})/k_f^C = 3.43$  compared to our corrected value of 3.6. Hence, our results are in agreement with Cartwright's measurements.

Our calculations of the radiative lifetimes of the  $a'$ -state indicate that there is a strong dependence on vibrational level. Radiation from the lowest levels of the  $a'$ -state is dominated by emission to the ground state. For increasingly higher vibrational levels,  $a'$ - $a$  emission initially competes with and eventually dominates emission due to the  $a'$ -X transition. This implies that under collision-free conditions the primary de-excitation mechanism for these states is radiative relaxation of the  $a'$ -state to form the  $a$ -state followed by rapid emission of the  $a$ -X LBH bands.

Our modeling results indicate that the lower vibrational levels of the  $a'$ -state are dominantly collisionally coupled to the  $a$ -state at all pressures encountered in our experiments based on rate coefficients measured by van Veen et al.<sup>57</sup> and Piper.<sup>67</sup> They measured a coupling rate coefficient for  $a'(0)$  to  $a(0)$ , a process which is  $1212 \text{ cm}^{-1}$  endoergic, to be  $2.3 \times 10^{-13} \text{ cm}^3 \text{ molecule}^{-1} \text{ s}^{-1}$ . This rate should reflect a reasonable lower bound for the more resonant and exoergic transfer rates for higher levels of the  $a'$ -state. The clear absence of emission from  $a'$ -state levels greater than  $v'=0$  supports this contention that the collisional rate dominates the emission rate for  $a'$  levels greater than zero. This statement appears to be true even when the lower limit to the coupling coefficient discussed above is used in the model calculations. Our measurement of the  $a$ -state total emission intensity is in good agreement with Cartwright's predictions; however, the details of the

intra- and intersystem relaxation processes must be determined by more specific laser excitation measurements.

In addition to transfer from the  $a'$ -state, cascade excitation of the  $a^1\Pi_g$  state from higher energy electronic states must be considered. Emission from the  $c_4'^1\Sigma_u^+$ ,  $v'=0$  state into  $v'=1$  of the  $a^1\Pi_g$  state is observed in the midst of the  $N_2(C-B)$   $\Delta v=2$  sequence at 296.7 nm (see Figure 17). This state has been observed to have the largest optical emission cross section of all the  $N_2$  electronic states;<sup>68</sup> however, the primary radiative loss mechanism is through the strongly allowed  $c_4'^1\Sigma=X^1\Sigma_g^+$  transition. Hence, the branching ratio between emission on this transition relative to the  $c_4'$ - $a$  transition will determine the cascade contribution to the total  $a$ -state excitation rate. Measurements by Filippelli, Chung, and Lin<sup>69</sup> have established that the branching ratio for emission from these to channels ( $c_4'$ - $a/c_4'$ - $X$ ) has an upper limit of 0.006. When coupled to Cartwright's relative electron excitation cross section for the  $c_4'$  state,<sup>25</sup> cascade from the  $c_4'$  state is calculated to contribute substantially less than one percent of the total excitation of the  $a^1\Pi_g$  state. These results are confirmed by the electron and optical emission cross sections for the  $a^1\Pi_g$  state measured by Ajello and Shemansky.<sup>46</sup> They established an upper limit on the cascade contribution of five percent based on the close agreement between the two cross section measurements. Radiative cascade from other high lying Rydberg states can not be totally precluded. However, they do not appear to be a significant source of excitation of the  $a$  state.

While the  $a$ -state vibrational distributions we observe at low pressures are roughly consistent with a Franck-Condon excitation/radiative relaxation model for the states involved, caution must be exercised in describing the electron excitation process as being entirely Franck-Condon in character. Careful measurements of the relative excitation cross sections for vibrational levels of the  $a^1\Pi_g$  state by Ajello and Shemansky<sup>46</sup> show a strong dependence on electron energy up to energies of approximately 20 eV. At higher energies Franck-Condon excitation profiles are observed. The deviations from Franck-Condon excitation observed in our data are spanned by the variations in cross

sections reported, and our distribution is most closely matched by their excitation efficiencies observed at 13 eV. Our electron beam energy is nominally 4.5 keV, well into the Franck-Condon excitation region. Hence, a sizable fraction of the a-state excitation must come from lower energy electrons created from scattering of the primary beam by the N<sub>2</sub> in the chamber. The uncertain nature of the electron energy distribution in our beam, as it is scattered, makes it difficult to quantify the relative contributions of the high and low energy electrons to the total excitation profile. While the initial N<sub>2</sub>(a) vibrational distribution has no bearing on the subsequent relaxation kinetics, the magnitude of this source will affect the relative excitation efficiency of a-state relative to the C-state.

### 3.5.2 Vibrational Redistribution

The N<sub>2</sub>(a) state vibrational distributions recorded as a function of pressure clearly show that extensive vibrational redistribution is occurring in addition to a slower electronic deactivation process. Our goal in conducting the various kinetic analyses presented is to place bounds on the rate coefficients wherever possible so as to guide later laser-based selective excitation experiments. The electronic quenching analysis for the a-state provides a lower bound on the true average electronic quenching coefficient, since total cascade from the a'-state is not considered as an additional population mechanism. Recent measurements by Piper and coworkers<sup>67</sup> suggest that pure electronic quenching of the a'-state by N<sub>2</sub> is quite slow ( $1.9 \times 10^{-13} \text{ cm}^3 \text{ molecule}^{-1} \text{ s}^{-1}$ ) and hence much of the excitation in the a'-state should decay via coupling to the a-state manifold. The measurements of Piper et al. for quenching of the a'-state are supported by the coupled relaxation measurements of the a-state reported by van Veen and coworkers.<sup>57</sup> In their two-photon excitation measurements of the a-state at high pressures, they observed quenching of the fluorescence from the coupled a'-a system to have a rate coefficient of  $2.3 \times 10^{-13} \text{ cm}^3 \text{ molecule}^{-1} \text{ s}^{-1}$ . The only a'-state level for which we observe fluorescence is a'(0), which lies  $1212 \text{ cm}^{-1}$  below a(0) and is the lowest lying excited singlet vibrational level. This level is poorly coupled to the



a-state and hence we observe its emission in our experiments. Hence, this state may act as a moderately long-lived energy carrier (8.4 eV) in the upper thermosphere or in flow tube studies involving active nitrogen.

The averaged electronic quenching rate coefficient for our experiments also compares reasonably well to the low pressure quenching results of van Veen and coworkers.<sup>57</sup> Their data on relaxation of  $N_2(a, v=0,1)$  at pressures from 0.05 to 0.200 torr give nearly identical rate coefficients of  $2.1 \times 10^{-11} \text{ cm}^3 \text{ molecule}^{-1} \text{ s}^{-1}$ , which are about a factor of two faster than our averaged values. While this result is significantly higher than our data would indicate, it should be stressed that our result is essentially an average over all of the observed vibrational levels and level to level variations in the relaxation rate may be present.

The apparent deactivation rates observed for the a-state increase by nearly a factor of ten over the range of vibrational levels studied. Golde and Thrush<sup>53</sup> in a steady state flow reactor study observed a similar apparent order of magnitude enhancement with vibrational level. Because their observations were made at torr pressures, substantial a-a' coupling may exist.<sup>57</sup> We feel the present observations in the millitorr regime provide a more accurate determination of the deactivation rates. While it is clear that the deactivation analysis is inadequate to obtain kinetic information about the lower vibrational levels of this state, predissociation of a-state levels above  $v'=6$  reduces the amount of cascade into the levels 4-6 significantly and reliable kinetic information can be determined for these higher vibrational levels. Intersystem cascade from high levels of the a'-state can also be ignored because these levels efficiently couple to predissociated levels in the a-state manifold. The deactivation rates we obtain are near gas-kinetic for the higher levels and are significantly faster than what would be expected for a simple V-T relaxation process. The observation of these accelerated rates alone argues that resonant electronic energy transfer between the a and a' states must account for a significant component of the observed relaxation process. Furthermore, the fact that near gas-kinetic relaxation rates are

observed argues that collisional cascade into these upper levels does not occur to a significant extent. If collisional cascade was important then relaxation rates larger than gas kinetic would be required to obtain the apparent rates measured in the laboratory.

The theories for intersystem electronic relaxation where both collision partners have internal degrees of freedom are poorly developed and few conclusions can be drawn about the specifics of the relaxation process from the available data. Simple scalings with vibrational energy level, energy defects with collision partners, or Franck-Condon factors between initial and final states do not seem to readily fit our data. As a result a more detailed comparison with theory does not seem warranted.

### 3.5.3 Discussion of Field Observations

Vibrational distributions for  $N_2(a)$  have been observed in the dayglow via both sounding rocket and satellite<sup>40-45</sup> observations. Recent analysis of this data by Meier et al.<sup>70</sup> and Conway<sup>71</sup> have concluded that the distributions arise from photoelectron excitation, i.e., the results are quite similar to the auroral observations of Feldman et al.<sup>72</sup> and Eastes and Sharp<sup>73</sup>. Differences between the spectra include an apparent depletion of  $N_2(a, v'=3)$  and enhancements in a-state levels 0 and 1. Explanations for the apparent enhancement in the lower levels have included radiative cascade from the  $c_4'$  state (discounted by Ajello and Shemansky<sup>46</sup> and Filipelli et al.<sup>69</sup>) and cascade from the  $a'$ -state. Our data, and our electron excitation model which closely matches our data (Figure 22), does not support radiative and/or collisional feed of these levels from the  $a'$ -state at 1.0 mtorr (95 km) as the mechanism for producing the significant enhancements observed in the a-state lower vibrational levels. Since most of the data available is for higher altitudes this would further preclude the  $a'$ -state cascade mechanism. The threshold effects advanced by Ajello and Shemansky<sup>46</sup> to explain enhancements in the lower vibrational levels do result in an apparent "flattening" of the vibrational distribution, which approaches dayglow measurements for electron energies of 9.5 eV. At these energies

(8.5 to 9.8 eV) the vibrational excitation observed will be a strong function of the photoelectron energy distribution. A careful correlation of simultaneously measured  $N_2(a,v)$  emission intensities and photoelectron distributions are required to accurately evaluate this mechanism.

Observations of LBH emission in the nightglow are poorly understood. The measurements by Huffman et al.<sup>42</sup> and subsequent reanalysis of the data by Meier and Conway<sup>74,75</sup> indicate an a-state vibrational distribution which is quite strongly peaked for low vibrational levels (Figure 24). The measurements were conducted aboard a polar orbiting, nadir viewing satellite with a viewing altitude which ranged from 160 to 260 km. Subsequent higher resolution data reported by Torr et al.<sup>47</sup> from Spacelab I does show spectra in the 1200 to 1800Å region which have been labeled as LBH bands. Our analysis of this published data using the spectral synthesis techniques used to analyze the laboratory data reported here indicates that there is no consistent assignment of the bands observed in the data to LBH spectral features. In particular, we find that bands occurring in a progression originating from a common a-state vibrational level are often missing. This leads us to conclude that this data is not dominantly due to LBH band emission and is potentially contaminated by near-field effects. No further analysis of this data has been attempted.

Our analysis of the data of Huffman et al.<sup>42</sup> confirms previous analyses which showed only fair agreement between the spectrum and a pure LBH spectrum at the quoted resolution. Meier and Conway<sup>75</sup> showed that absorption of LBH emission by atmospheric  $O_2$  could not account for the deviations from the expected emission profile. Our analysis of the 1304Å O-atom line from this data indicates the actual spectral resolution of the data is closer to 30Å than the 25Å quoted spectral resolution. This factor alone does not significantly improve the fit. Our experimental observations of  $N_2(a',v'=0)$  emission in this region has indicates that the a'-state could be an important radiator. Addition of transitions arising from the  $N_2(a'-X,v'=0)$  state and well known N-atom lines to the fit results in further improvement. Finally, addition of CO(A-X) (Fourth Positive) bands to the fit produces the fit obtained in

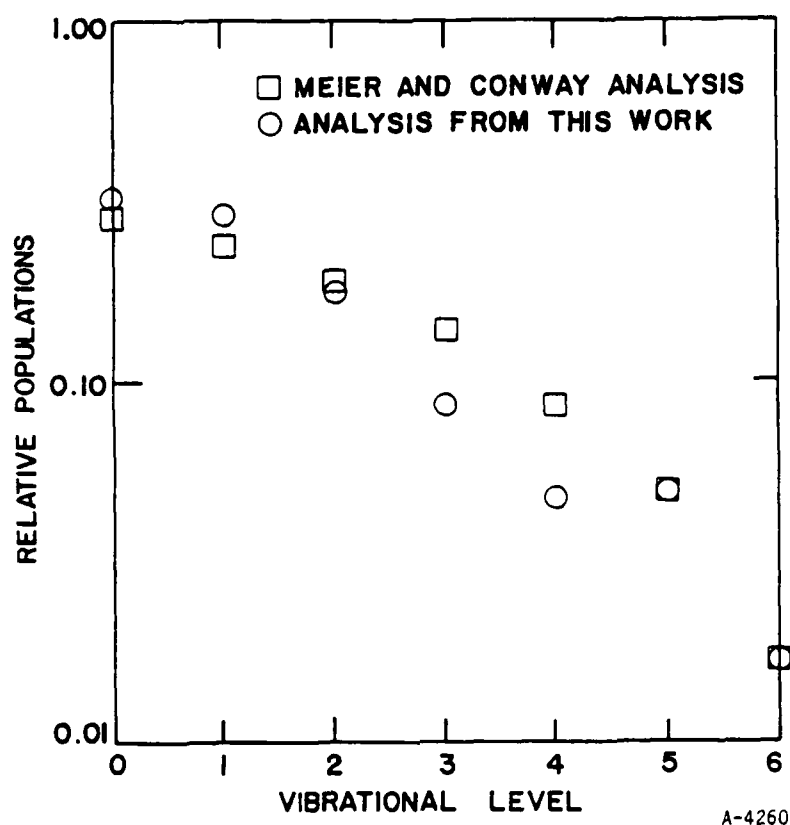
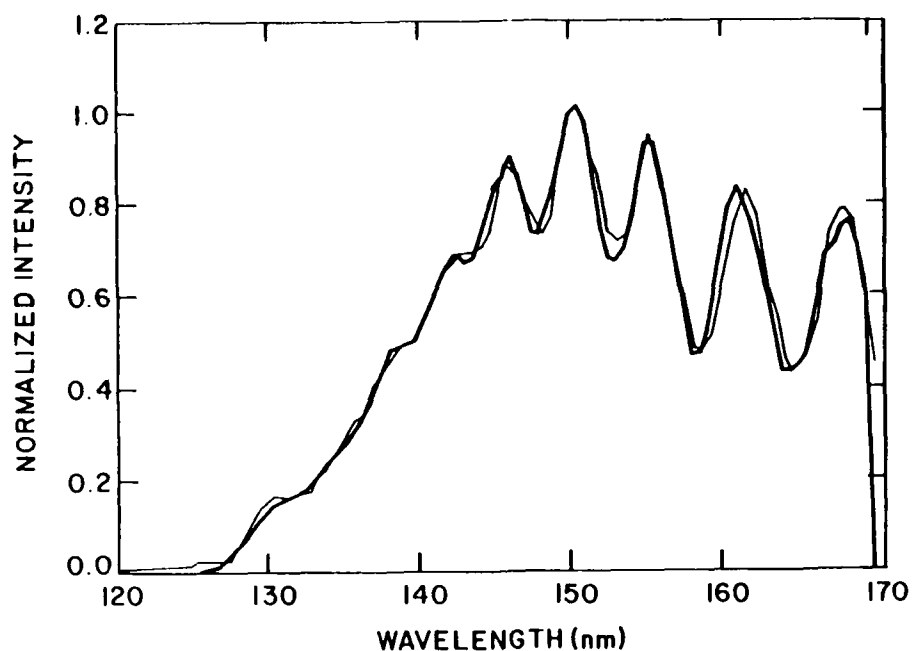


Figure 24. Vibrational distributions for  $N_2(a^1\Pi_g)$  obtained from fit to data of Huffman et al.<sup>42</sup>

Figure 25. The vibrational distributions obtained from these fits are shown in Figure 24. These distributions do indeed show an  $N_2(a)$  state vibrational distribution which is peaked at low  $v$  and somewhat insensitive to the addition of other radiators. The  $CO(A)$  state vibrational distribution obtained from the fit is non-physical and illustrates the limitations of trying to fit data of such coarse resolution with a large number of basis functions. Further efforts to spectrally fit data in order to obtain populations which may elucidate the production mechanism must await higher resolution data from which distinct band systems can be conclusively identified.

Comparison of our data with auroral data and modeling predictions provides some insight into the role of radiative and collisional coupling of the  $a'$ -state to the  $a$ -state. The primary controversy concerns the degree to



A-4068

Figure 25. VUV nightglow data of Huffman et al.<sup>42</sup> (light line) and spectral fit to data (dark line).

which  $a'$ -state cascade contributes to the lower vibrational levels of the  $a$  state under auroral conditions. Our  $a$ -state vibrational distributions for 1.0 mtorr of  $N_2$  (95 km), Cartwright's auroral model predictions for 110 km,<sup>4</sup> and Meier et al.'s<sup>70</sup> analysis of the data of Feldman and Gentieu<sup>72</sup> (160 to 180 km) are shown in Figure 26. The largest differences between the three vibrational distributions are clearly in the prediction for  $v'=0$  where Cartwright predicts a value 2.2 times greater than observed by Meier and coworkers, while our data gives a value 44 percent larger. From this discrepancy Meier and coworkers concluded that radiative cascade did not play an important role in the production of the  $a$ -state. This disagreement is most likely a result of Cartwright's use of  $N_2 B \leftrightarrow A$  transition probabilities to estimate the  $a' \leftrightarrow a$  intersystem radiative cascade rates. Our calculations, based on the transition moments of Yeager and McKoy,<sup>65</sup> clearly show significantly lower transition probabilities for these bands. Hence, the radiative cascade contribution to the  $a$ -state population rate is significantly smaller.

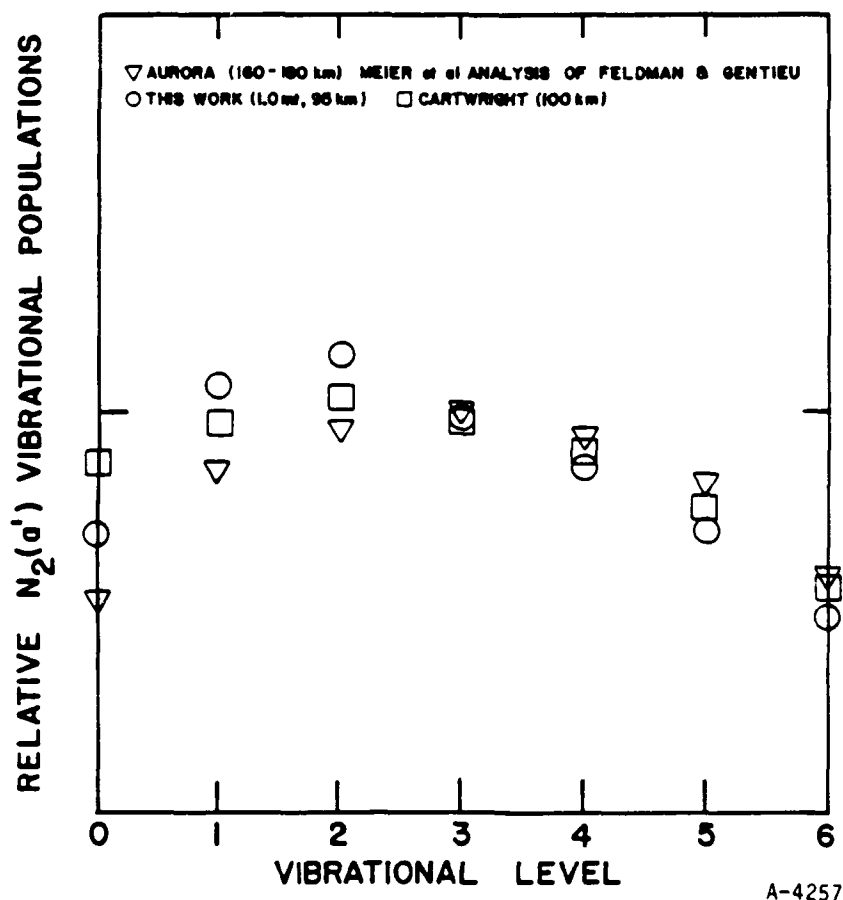


Figure 26. Auroral predictions and data.

Our data for  $a'$ -state levels 1 and 2 also show enhanced population over both the higher altitude auroral data and the radiative cascade model of Cartwright. This discrepancy can be explained if additional collisional coupling of the lower levels of the  $a'$ -state is allowed. Recent estimates place the radiative lifetime of the lower levels of the  $a'$ -state at approximately 25 ms.<sup>67</sup> At 95 km only a modest collisional rate coefficient of  $1.2 \times 10^{-12} \text{ cm}^3 \text{ molecule}^{-1} \text{ s}^{-1}$  is required to couple  $a'(2)-a(1)$  and  $a'(3)-a(2)$ . The ladder diagram of Figure 13 shows these levels to be resonant, while coupling for higher levels is increasingly non-resonant and endoergic. If collisional coupling is gas kinetic, this process must be considered important up to altitudes of approximately 130 km. This also implies that few laboratory measurements of  $a'$ -state kinetics can be made in a regime in which

coupling to the a-state is negligible. Furthermore, it explains why emission from a'-state levels greater than  $v=0$  are not observed in our experiments. At all pressures attainable, the lower a'-state vibrational levels are collisionally coupled to the a-state while the higher a'-state levels are radiatively coupled to the a-state at rates which dominate over emission on the a'-X Ogawa-Tanaka-Wilkinson-Mulliken Bands.

#### 3.5.4 Predictions of Altitude Scaling of Infrared Radiance

The application of our observed rates, as well as a variety of possible inter-system energy transfer rates, provides some insight into the implications of collisional and radiative coupling of the a and a' states. As previously stated, the long radiative lifetimes of the lower vibrational levels of the a'-state allow for collisional coupling of these levels to low levels of the a state at altitudes as high as 130 km (for gas kinetic coupling rate coefficients.) The model predictions for the a and a' state vibrational distributions at 95 km (Figure 27) clearly show a dip in the near-resonant a'-state vibrational populations and a corresponding increase in the a state receptor level populations. Using our spectral synthesis codes we are able to predict the spectral signature of the a-a' and a'-a bands for this set of vibrational distributions (Figure 28). The spectrum is most intense in the 2 to 4  $\mu\text{m}$  range where the a-a' $\Delta v=1$  sequence bands and the a'-a $\Delta v=3,4$  sequence bands are prominent. At altitudes greater than 130 km the relaxation of the a'-state is dominated by radiation. Hence, the level dependent depletion of the a'-state levels due to resonant transfer is eliminated. This results in enhanced emission from lower a'-state vibrational levels, as shown in Figure 29 where the  $\Delta v=2$  sequence bands in the 5.5 to 7.0  $\mu\text{m}$  region are increased in intensity. This emission occurs in a region where little infrared emission occurs in the quiescent atmosphere and hence should be observable in the high altitude regions of most aurora. The ratio of emission intensities of these bands (2 to 8  $\mu\text{m}$ ) to the  $\text{N}_2(\text{C-B}, 0-0)$  transition at 3371Å is estimated to be 11.4 at an altitude of 130 km. These predictions point out the need for improved IR

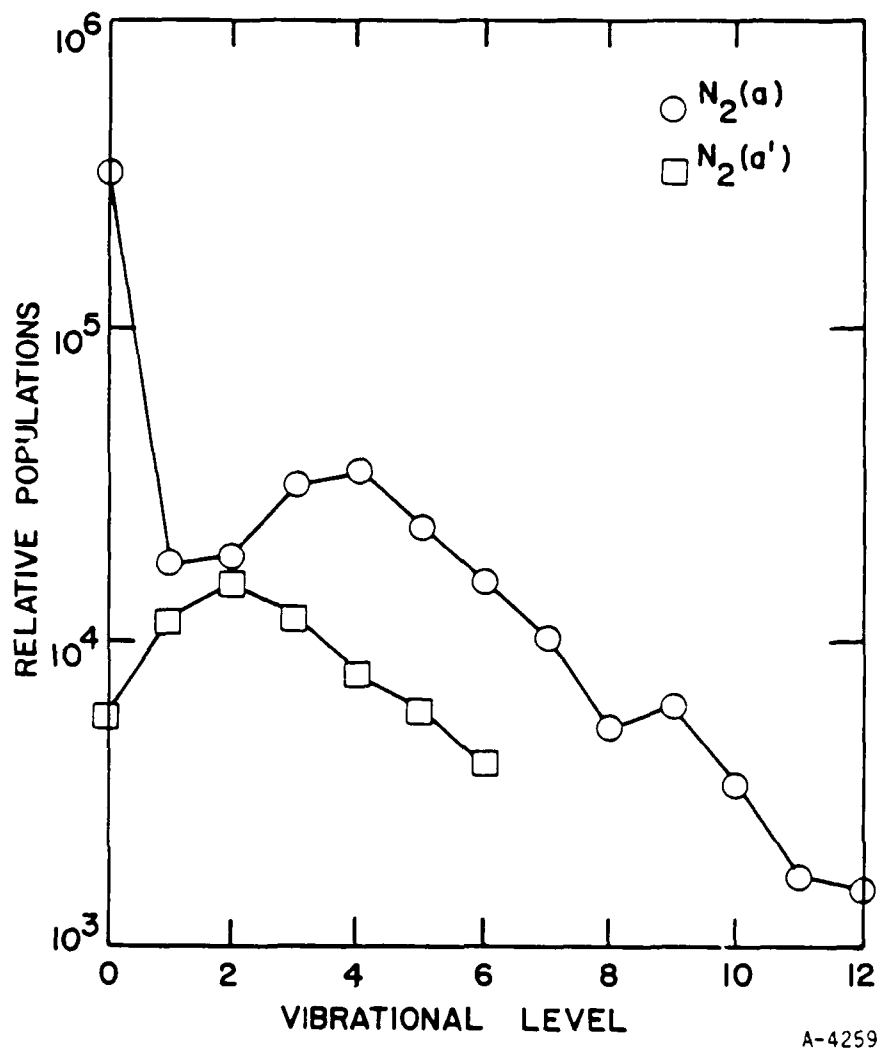


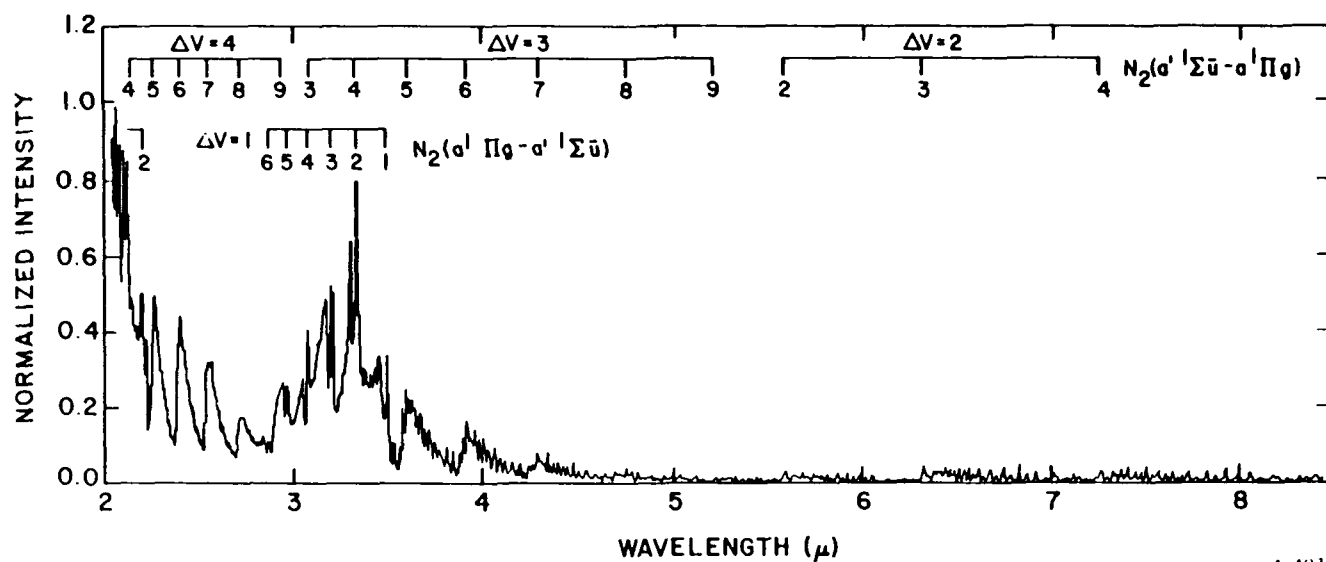
Figure 27. Model predictions for  $N_2(a)$  and  $N_2(a')$  vibrational distributions at 95 km.

field observations of the aurorally disturbed atmosphere to correlate laboratory measurements and models with actual dynamical processes.

### 3.6 CONCLUSIONS

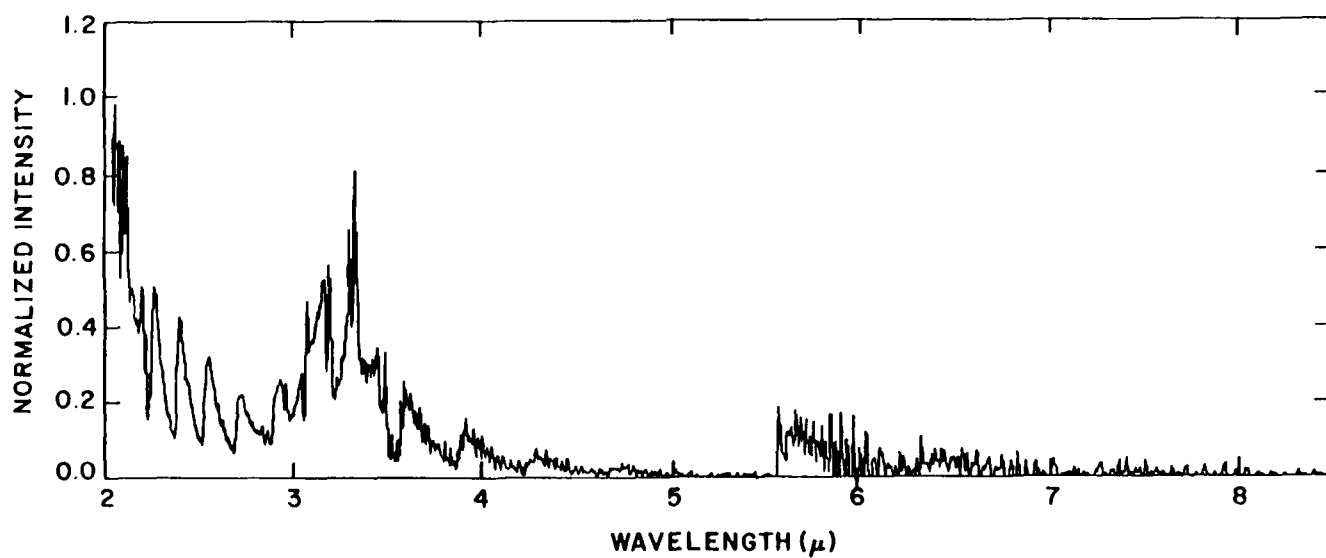
The global deactivation rate for loss of  $N_2(a^1\Pi_g)$  molecules by electronic quenching has been experimentally determined to be greater than or equal to





A-4071

Figure 28. Predicted emission spectrum of N<sub>2</sub> McFarlane bands at 95 km.



A-4072

Figure 29. Predicted emission spectrum of N<sub>2</sub> McFarlane bands at 130 km.

$8.9 \times 10^{-12} \text{ cm}^3 \text{ molecule}^{-1} \text{ s}^{-1}$ . Feed into the a-state from higher electronic states does not appear to be significant based on spectral surveys and  $\text{N}_2(\text{C})$  state normalization. A substantial redistribution of the vibrational populations within the a-state as a function of pressure is observed. Total quenching rate coefficients for vibrational levels 4-6 approach gas kinetic values. Intersystem energy transfer from the  $\text{N}_2(\text{a}'^1\Sigma_u^-)$  state to lower vibrational levels of the a-state cannot be distinguished from intrasystem vibrational relaxation within the a-state manifold. An analytical model developed in light of these observations indicated that a-state intrasystem vibrational relaxation could not be distinguished from intersystem collisional cascade. Future state specific laser excitation experiments are required to distinguish these competing pathways. The observed vibrational redistribution within the a-state indicates that there should be an altitude dependence of LBH band emission intensities in an auroral arc. Furthermore, at the highest altitudes (above 130 km) both a' and a-state emission may be observed. The relative intensities of the band systems will exhibit markedly different altitude dependences. Bands arising from the a' state, high  $v$  levels of the a state and low  $v$  levels of the a state, will be quenched at successively lower altitudes. We are presently trying to observe the a and a' infrared in the laboratory. We have also started laser excited state-specific relaxation studies to test some of the hypotheses suggested by the more global observations reported here.

#### 4. ELECTRON-IMPACT EXCITATION OF THE $N_2^+$ MEINEL BAND

##### 4.1 INTRODUCTION

The  $N_2^+(A^2\Pi_u)$  state plays an important role in the aurora or disturbed upper atmosphere. Because  $N_2^+(A^2\Pi_u)$  is efficiently produced in the ionization of  $N_2$  (Vallance Jones and Gattinger;<sup>19</sup> Gattinger and Vallance Jones<sup>3</sup>) the  $N_2^+(A^2\Pi_u - X^2\Sigma_g^+)$  Meinel bands are bright features in the auroral spectrum. Radiative and collisional loss of the  $N_2^+(A)$  state leads to vibrationally excited  $N_2^+$ . Thus the distribution of vibrational excitation of  $N_2^+(X^2\Sigma_g^+)$  in the aurora depends, in part, on the excitation and relaxation of the  $A^2\Pi_u$  state. The relative electron-impact excitation rates of the lower vibrational levels of the  $A^2\Pi_u$  state are reasonably well established.<sup>3,12,13,76,77</sup> However, reported values for the absolute electron-impact excitation cross section differ by an order of magnitude.<sup>12,77-83</sup>

The discrepancies in absolute cross sections result, in part, from past difficulties in determining the effects of quenching of the  $A^2\Pi_u$  state. We have reported recently the quenching rate coefficients for the ionic A state by air,  $N_2$ , and  $O_2$ .<sup>84</sup> In the present study we have measured relative rates for electron-impact excitation of vibrational levels 2-7 of the  $N_2^+(A^2\Pi_u)$  state by determining the relative intensities of Meinel-band emission from vibrational levels 2-7 at pressures for which quenching is negligible. By combining the relative intensities of the Meinel bands with an extrapolation to zero pressure of the ratio intensities of the  $N_2^+$  First Negative band to the Meinel bands, we have determined the ratio of the cross sections for electron impact ionization into the  $A^2\Pi_u$  state to that into the  $B^2\Sigma_u^+$  state. From this ratio, and the known cross section for electron-impact ionization of  $N_2$  into the  $B^2\Sigma_u^+$  state,<sup>85</sup> we can infer the total cross section for producing the  $N_2^+(A^2\Pi_u)$  state by the impact of 3 to 6 keV electrons on  $N_2$ .

## 4.2 EXPERIMENTAL

These measurements were made using the Air Force Geophysics Laboratory's LABCEDE facility as described previously. This apparatus consists of a cylindrical vacuum chamber measuring 1m in diameter by 3.4m long in which beams of 3 to 6 keV electrons with currents up to 20 mA irradiate atmospheric species. The gas samples flow under plug flow conditions along the axis of the chamber sufficiently rapidly to eliminate the effects of quenching by electron-beam-created species. Fluorescence was observed both perpendicular to the electron beam and at an acute angle of 19 deg to the electron beam, both viewing geometries giving identical results. A 0.3m (McPherson 218) monochromator operated with a 1200 groove/mm grating blazed at 500 nm resolved the fluorescence. A Corning 3-71 colored glass filter eliminated second order spectra to the red of 500 nm. The second order rejection ratio was  $10^{-6}$ , more than sufficient to prevent contamination of the Meinel (2,0) band fluorescence at 782 nm by the second order of the First Negative (0,0) band at 391 nm. An HTV 955 photomultiplier tube, biased to provide a gain of  $5 \times 10^6$ , detected the signal. A picoammeter/recorder combination amplified and displayed the photomultiplier output.

The fluorescence was resolved spatially by collecting the fluorescence with a 5 cm diameter, 10 cm focal length Suprasil lens and focussing it onto the slits of the monochromator. The slit height was adjusted to limit the field of view of the monochromator to only the central region of the fluorescing volume excited by the electron beam. The spatial resolution permitted discrimination of the Meinel bands from the First Positive bands. Approximately 80 percent of the Meinel (and First Negative band) excitation is due to primary electrons in the beam, whereas 90 percent of the nitrogen First Positive band excitation is due to secondary electrons.<sup>26</sup> The primary electrons in the beam are confined to a narrow and well defined central core of the electron beam as it traverses the chamber. On the other hand, the secondary electrons created in the ionization processes scatter at preferred angles between 45 and 90 deg to the incident primaries.<sup>86</sup> In effect, therefore the

secondaries will appear to be distributed uniformly around the primary beam. Thus by limiting the field of view to the central core of the primary beam, Meinel emissions are observed preferentially. At the same time the field of view was kept sufficiently large to eliminate effects of diffusion of  $N_2^+(A)$  out of the field of view. Of course, at the lowest pressures ( $\leq 1$  mtorr) where the number of secondary electrons created is small and their range is very large compared to the size of the primary beam, the degree of First Positive band excitation relative to the Meinel band excitation is only a few percent at most. At higher pressures, however, the effects of excitation by secondary electrons grow much more rapidly than the effects of primary excitation. Thus spatial discrimination becomes imperative. The operating pressures always represented thin target conditions; i.e., very little of the beam energy was deposited in the gas and little beam spread occurred.

#### 4.3 RESULTS AND DISCUSSIONS

The relative excitation rates of the Meinel bands were measured by scanning the spectrum of the Meinel bands between 600 and 850 nm at pressures sufficiently low ( $\sim 0.70$  mtorr) to minimize the effects of quenching and of secondary electron excitation. Correcting the integrated intensities of the various emission features by the appropriate transition probabilities<sup>3,87</sup> and the monochromator response function gives the relative populations in each of the observed emitting states. In most cases at least two different bands from the same upper levels,  $v'=2-7$ , were observed in the spectral range. All such redundant observations agreed to better than 7 percent. Table 6 lists the present results normalized to the population in  $v'=2$ . The relative populations of  $v'=0$  and 1 were estimated by taking the ratio of the relevant Franck-Condon factors<sup>6</sup> for excitation of these levels to that of  $v'=2$ .

The values for the relative electron-impact excitation rates of vibrational levels  $v=2-7$  of the  $A^2\Pi_u$  state reported here agree quite well with both the auroral observations of Gattinger and Vallance-Jones<sup>3</sup> and the laboratory measurements of Mendelbaum and Feldman,<sup>76</sup> Shemansky and Broadfoot,<sup>12</sup> and

TABLE 6. Relative Meinel-band excitation rates.

Level	Present Results	Auroral Data		Lab Data		Franck-Condon
		Gattinger and Vallance Jones (Ref. 3)	Mandelbaum and Feldman (Ref. 76)	Shemansky and Broadfoot (Ref. 12)	Skubenich and Zapesochnyy (Ref. 77)	Lofthus and Krupenie (Ref. 6)
0	(1.28)	1.4	1.42	1.07		1.28
1	(1.49)	1.59	1.44	1.46	1.41	1.49
2	1.0	1.0	1.0	1.0	1.0	1.0
3	0.51	0.61	0.52	0.53	0.52	0.52
4	0.26	0.23	0.24	0.25	0.25	0.23
5	0.105				0.110	0.092
6	0.047				0.051	0.035
7	0.036					0.013

Skubenich and Zapesochnyy.<sup>77</sup> The relative excitation-rate measurements also agree with Franck-Condon factors for excitation of the  $A^2\Pi_u$  state by ionization of the ground state of the  $N_2$  molecule. Katayama et al.<sup>88</sup> have shown that collisional coupling between the  $N_2^+(X^2\Sigma_g^-)$  state and the  $N_2^+(A^2\Pi_u)$  state is rapid even at fairly low pressures. The question arises, therefore, whether the relative electron-impact excitation rates reported here are actually excitation rates into high vibrational levels of the X state with the A state being populated only by collisions. This collisional coupling is not important in these studies, however. At the electron energies used in this investigation, electron-impact ionization is a Franck-Condon process, and produces a vibrational distribution proportional to the appropriate Franck-Condon factors.

The measured A state vibrational level distribution agrees well with the relative Franck-Condon factors. The Franck-Condon factors for X state production of vibrational levels with energies comparable to the A-state energies observed here (i.e.,  $v''=6-12$ ) are 6 to 7 orders of magnitude smaller than those for producing the A state levels.<sup>6</sup> Additionally no change in the relative distribution was observed as pressure was slowly increased. Our quenching studies have already defined the range of pressures below which collisional effects are minimal.<sup>84</sup> Cross sections for exciting higher lying states of  $N_2^+$  which could then produce  $N_2^+(A^2\Pi_u)$  via radiative cascade are too small to affect the present results. For example, no  $D^2\Pi_g - A^2\Pi_u$  (Janin - d'Incan System) emission was observed between 200 and 300 nm.

The Stern-Volmer analysis used in the quenching measurements<sup>84</sup> showed that the ratio of the First Negative band emission intensity  $I_B$  to the Meinel band emission intensity  $I_A$  is given by

$$\frac{I_B}{I_A} = \frac{1}{\alpha} + \frac{k_Q[Q]}{\alpha k_r} \quad , \quad (16)$$

where  $\alpha$  is the ratio of the Meinel band excitation rate to the First Negative band excitation rate,  $k_Q$  is the rate coefficient for quenching by species Q,  $[Q]$  is the number density of Q, and  $k_r$  is the total radiative rate for the given vibrational level of the A state.

When corrected for monochromator response and the appropriate factors to convert the peak height measurements used in the quenching runs to band areas, the intercepts of the quenching plots give the cross section ratios  $\sigma_{B,v'=0 \rightarrow X,v''=0}/\sigma_{A,v' \rightarrow X,v''}$  of 1.7, 2.5, and 8.0 for the 2,0, 3,1, and 4,1 bands respectively. The uncertainty in each of these ratios is  $\pm 10$  percent. These ratios were invariant for electron beam energies between 2.5 and 6 kV and beam currents between 6 and 21 mA. If we correct these values for the fraction of total  $N_2^+(B)$  production appearing in the 0,0

transition<sup>6,13,81,89-91</sup> and the branching fraction of total  $N_2^+(A)$  emission from a given upper level to that from the observed bands,<sup>3,87</sup> and then use the relative Meinel excitation rates determined here to correct further for total  $N_2^+(A)$  production, we find that the ratio of the cross section for total A state production to that for B state production is  $4.1 \pm 0.7$ . This ratio concurs moderately with the ratio of  $5.7 \pm 2.0$  determined by Gattinger and Vallance Jones<sup>2,3</sup> from auroral observations. Their measurement is subject to substantial uncertainty because it involves estimates of absolute auroral intensities made in different wavelength regions at different times. In theory our laboratory observations and the auroral observations ought to agree on the ratio of A-state to B-state excitation because both systems involve excitation by electrons primarily in the keV range where the excitation cross section ratio is invariant with energy.<sup>26,83</sup> Meinel quenching in aurorae is generally negligible, although some quenching occasionally appears in deeply penetrating aurorae.<sup>19</sup>

Given that the ratio of the A state to B state cross sections is invariant with electron energy down to below 100 eV, an absolute A state excitation cross section can be determined using Borst and Zipf's measurement<sup>85</sup> of the 391.4 nm excitation cross section at 100 eV,  $(1.74 \pm 0.17) \times 10^{-17} \text{ cm}^2$ , the peak of the excitation-function curve. This results in excitation cross sections of  $(10.1 \pm 1.4)$ ,  $(7.0 \pm 1.0)$ , and  $(2.2 \pm 0.3) \times 10^{-18} \text{ cm}^2$  for excitation of the Meinel 2,0, 3,1, and 4,1 bands respectively. From the total cross section ratio given above, we infer a total electron-impact excitation cross section for  $N_2^+A$  production of  $(1.15 \pm 0.23) \times 10^{-16} \text{ cm}^2$ . Table 7 compares the present measurements with other reported values. The great range in the values reported for the electron-impact excitation cross section of the Meinel bands is somewhat disturbing. The present results agree with the molecular-beam measurements of Holland and Maier,<sup>78,79</sup> and with Pendleton and Weaver<sup>83</sup> and Shemansky and Broadfoot.<sup>13</sup> The agreement with this last group is fortuitous since their analysis depends upon lifetime measurements which are low by about a factor of two. Pendleton and Weaver<sup>83</sup> corrected their results for quenching and for first-positive emission contamination as in the case of the



TABLE 7. Absolute Meinel band electron-impact excitation cross sections at 100 eV.

( $10^{-18} \text{ cm}^2$ )

Group	Band 2,0	Band 3,1	Band 4,1	Band 3,0
Simpson and McConkey <sup>80</sup>	$2.1 \pm 0.6$		$0.60 \pm 0.17$	$0.65 \pm 0.19$
Stanton and St. John <sup>81</sup>	$4.5 \pm 0.2$	$2.9 \pm 0.2$	$1.0 \pm 0.1$	
Srivastava and Mizra <sup>82,92</sup>	$6.0 \pm 1.2$	$2.4 \pm 0.5$	$0.7 \pm 0.1$	
Holland and Maier <sup>78,79</sup>	$11.4 \pm 4.0$	$7.3 \pm 2.6$	$2.6 \pm 0.9$	
Shemansky and Broadfoot <sup>12</sup>	$>11.0$	$>7.9$	$>2.5$	
Pendleton and Weaver <sup>83</sup>	$7.5 \pm 1.5$	$5.0 \pm 1.0$	$2.4 \pm 0.5$	
Skubenich and Zapesochnyy <sup>77</sup>	$5.7 \pm 0.9$	$3.8 \pm 0.8$	$1.3 \pm 0.3$	$1.4 \pm 0.3$
Present Work	$10.1 \pm 1.4$	$7.0 \pm 1.0$	$2.2 \pm 0.3$	

present measurements. The molecular-beam measurements of Holland and Maier<sup>78,79</sup> require no such corrections. The other groups listed in Table 7 do not appear to have applied such corrections. That probably accounts for their being substantially below the present results.

#### 4.4 SUMMARY

Relative electron-impact excitation rates for vibrational levels 2-7 of the  $A(^2\Pi_u)$  state of  $N_2^+$  have been measured. The present results agree with auroral observations, other laboratory measurements, and relative Franck-Condon factors for production by ionization of the  $N_2$  ground state. The absolute cross section for production of the  $N_2^+(A^2\Pi_u)$  state by 100 eV electron impact on  $N_2$  has also been inferred. The new value is among the larger

values obtained for this cross section. We have been careful, however, to eliminate quenching effects. These measurements, together with the quenching rate coefficient measurements reported in Piper et al.<sup>84</sup> should permit a more detailed understanding of the role the  $N_2^+(A^2\Pi_u)$  plays in the dynamics of the aurora and the disturbed atmosphere.

## 5. N<sub>2</sub> ELECTRONIC STATES: CVF/INTERFEROMETER MEASUREMENTS IN THE IR

### 5.1 INTRODUCTION

Detection of the IR fluorescence of nitrogen was performed in the wavelength region from 2.3 to 6.9  $\mu\text{m}$  using a liquid helium cooled circular-variable-filter (CVF).<sup>93,94</sup> The CVF was mounted to the LABCEDE tank with a series of silicon O-ring flanges and compression fittings designed to provide vacuum-type seals at reduced temperatures. The fluorescence from the electron excited nitrogen was viewed through a KRS 5 window at the upstream end of the LABCEDE tank and normal to the electron beam. Signals from the As:Si detector in the CVF were first processed with a PAR Model 113 preamplifier then digitized, averaged, and stored on the hard disc of a PDP 11 computer system. Synchronous detection was performed by pulsing the electron beam with a General Radio Model 1217B pulse/waveform generator. Both time-dependent and time-averaged spectra could be collected using the PDP 11. Time-dependent spectra, uncorrected for detector response, were displayed on the screens of the laboratory Apollo computer following a data file transfer to that device. Magnetic tapes of raw data were generated on the Apollo computer and transferred to Physical Sciences Inc. (PSI) for data reduction and analysis.

Data collection in the time averaged mode of operation was performed using the PDP 11 as a lock-in amplifier and manually rotating the CVF filter wheel through the appropriate wavelength segments. In the time-dependent mode of data collection, the PDP 11 commanded the wavelength scans via a stepping motor and associated controller attached to the filter wheel. The minimum step size ranged from 1/3 to 1/5 of a resolution element in the 2.3 to 3.6  $\mu\text{m}$ , and 4.0 to 6.8  $\mu\text{m}$  wavelength regions (hereafter referred to as the SWIR, MWIR regions, respectively). Resolutions in the SWIR, MWIR wheel segments were determined from the FWHM of O-atom lines to be 2.0 and 4.6 percent of the wavelength, respectively.

Because of the sensitivity of the CVF, the detector is saturated by the emission from warm surfaces. Thus the LABCEDE shroud was cooled from 300 K to ~ 90 K with a slow flow of liquid nitrogen through tubing welded to the shroud walls. The nitrogen gas was cooled in the liquid nitrogen heat exchanger prior to entering the shroud volume. The CVF-detector and filter wheel must be cooled to liquid helium temperature to permit sensitive detection of the weak emission from the irradiated gases. The cooling of the CVF is performed in two stages. The filter wheel and detector are cooled with liquid nitrogen overnight, then with liquid helium on the morning prior to afternoon data collection.

## 5.2 EXPERIMENTAL

A variety of experimental conditions have been surveyed. The lowest pressure providing detectable signal was 0.15 mtorr. Spectral scans with pressures up to 37 mtorr at cryogenic temperatures have been collected. This upper pressure limit was determined from the total gas throughput necessary to overload the diffusion pump, and corresponds to a flow of 1.7 slm of N<sub>2</sub> with the throttling valve closed. Peak electron current was held constant in each experiment, but has been varied in the range of 12.0 to 33.0 mA. Pulse repetition rates have varied across the range from 11 to 38 Hz with duty cycles from 15 to 50 percent. The electron energy was maintained at 4500 eV throughout. Spectra taken with the magnetic field off reflected about a 50-fold decrease in signal level. Most experiments were performed with the B-field in the high current range with a dial reading between 20 to 40, i.e., approximately 26 to 45 gauss at the center of the tank - the region viewed by the CVF. The amplifier was only linear to a gain of 2000. Commonly gains ranging from 100 to 2000 were employed. Frequency bandwidths for data collection were commonly 1 to 100 Hz.

### 5.3 ANALYSIS AND RESULTS

The initial analysis on the  $N_2$  fluorescence was performed on the SWIR and MWIR wavelength regions independently. The SWIR spectra are very complex. The complexity arises from the fact that multiple bands may be contributing to a particular spectral feature and the resolution of the CVF, i.e.,  $\sim 2$  percent of the wavelength in the SWIR, cannot distinguish the contributors even with the aid of the spectral synthesis code. For example, a relatively strong spectral feature is observed between 3.2 and 3.4  $\mu m$  at all nitrogen pressures at a resolution of 0.07  $\mu m$ . Possible contributors to this feature include the  $N_2(W^3\Delta_u - B^3\Pi_g)$   $v'=2$  to  $v''=0$  band at 3.32  $\mu m$  and  $v'=8$  to  $v''=5$  band at 3.33  $\mu m$ , the  $N_2(a^1\Pi_g - a'^1\Sigma_u)$   $v'=2$  to  $v''=1$  band at 3.32  $\mu m$ , the  $N_2(B'^3\Sigma_u - B^3\Pi_g)$   $v'=1$  to  $v''=3$  band at 3.32  $\mu m$  and the  $N_2(B^3\Pi_g - A^3\Sigma_g^+)$   $v'=10$  to  $v''=19$  band at 3.33  $\mu m$ . In an effort to deconvolute these complex spectra, the SWIR and MWIR wavelength regions under identical experimental conditions) were combined using the appropriate gain and response normalizations. Combining the spectra places constraints on the possible band system contributors, i.e., features arising from common upper levels but fluorescing to different lower levels must be observed with the proper branching ratio or ratio of Einstein coefficients.

Figures 29, 31, and 32 present experimental spectra (shown as the narrow line) and synthetic spectral (heavy line) obtained in 1, 5, and 37 mtorr of  $N_2$  just after termination of the electron beam. The synthetic spectra were obtained for the  $N_2(W-B)$ ,  $N_2(a-a')$  band systems and Figure 30 shows the relevant band origin positions. These spectra and synthetic counterparts are representative of the level of agreement which can be obtained between theory and experiment. Unfortunately, the overlap of band system emissions does not allow the spectral fitting code to make a unique determination of the emitting species. (This code is described in Appendix C.)

Synthetic spectral fits were performed using each possible contributing band system alone, then in all possible combinations to determine which combinations

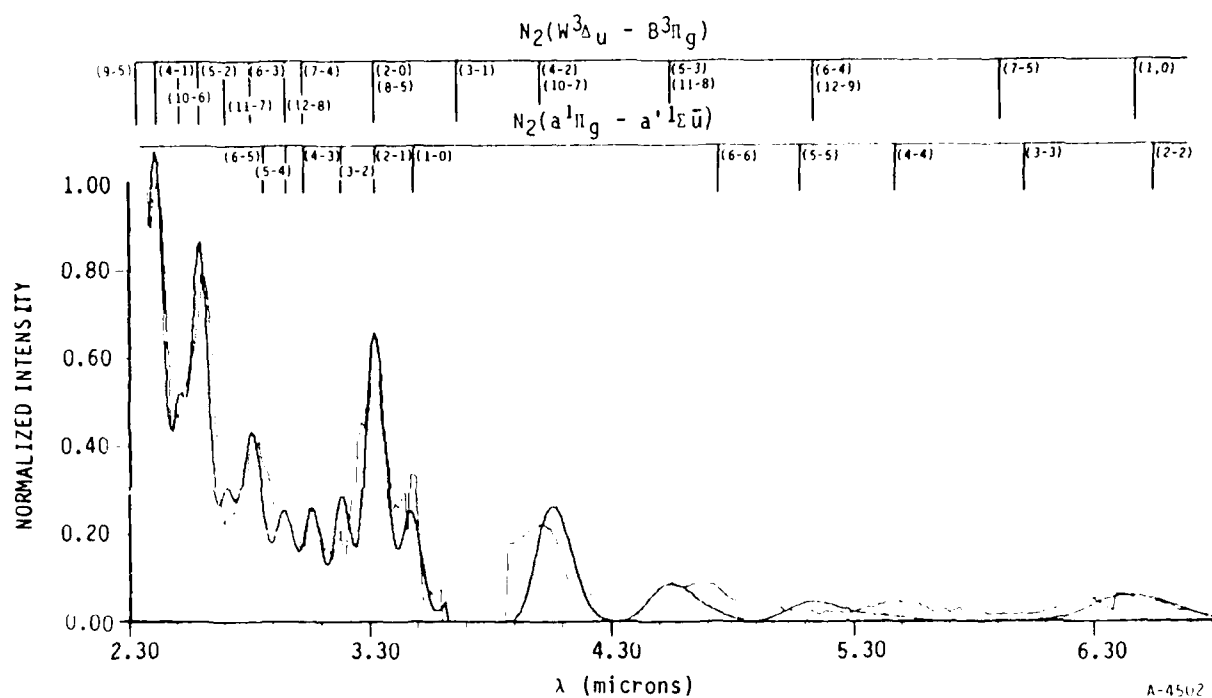


Figure 30. Spectrum of electron irradiated  $N_2$  at 1 mtorr pressure at beam termination (synthetic spectrum is the heavy line).

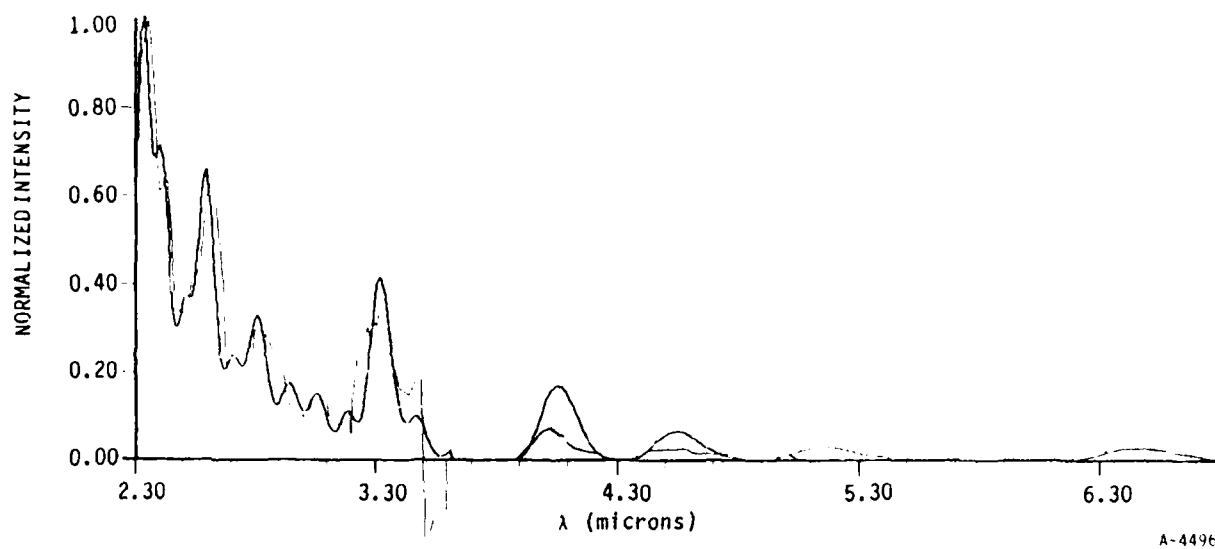


Figure 31. Spectrum from 5 mtorr  $N_2$  at beam termination.

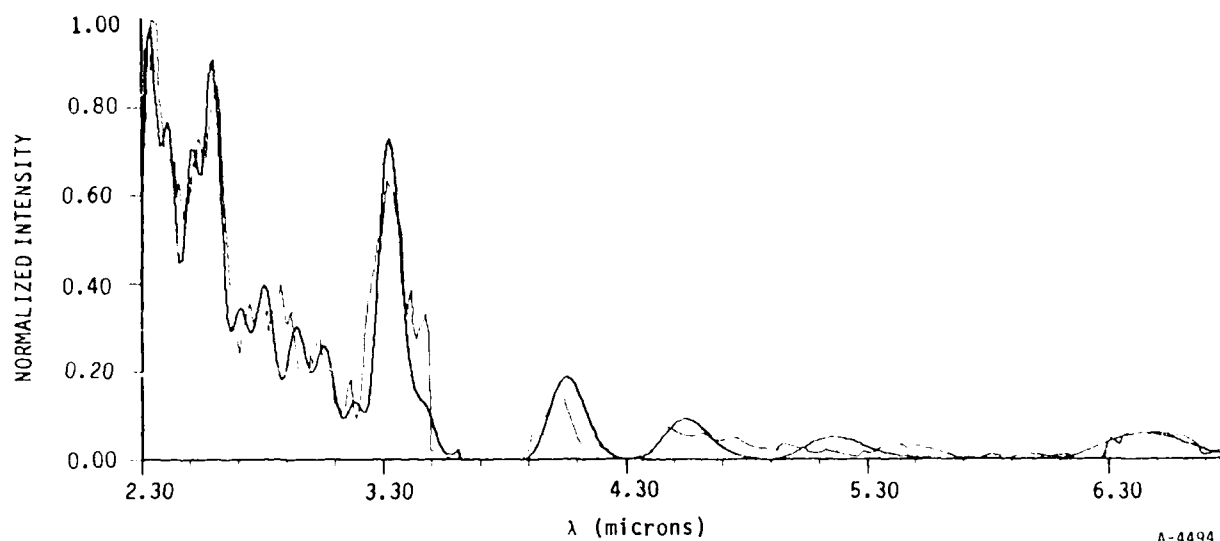


Figure 32. Spectrum from 37 mtorr  $N_2$  at beam termination.

provided reasonable agreement with the experimental spectra. The band systems used in the analysis included:  $N_2(W-B)$ ,  $N_2(a-a')$ ,  $N_2(w-a)$ ,  $N_2(B-A)$ ,  $N_2(B'-B)$ , and  $N_2^+(A-X)$ . The analysis was performed on 1, 5, and 37 mtorr nitrogen data at electron beam termination and for several 5 ms time intervals thereafter, until the signal fell into the noise and no further reasonable comparisons could be made.

In the initial analysis the vibrational distributions had been allowed to vary unconstrained in order to obtain the best fit of the experimental spectrum. In the next stage of analysis, the vibrational distributions of the  $N_2(W^3\Delta_u)$ ,  $N_2(a^1\Pi_g)$ ,  $N_2(B^3\Pi_g)$ , and  $N_2(w^1\Delta_u)$  states have been set to the high altitude atmospheric model predictions.<sup>4</sup> In addition, the ratio of population in the  $N_2(B^3\Pi_g)$  to the  $N_2(a^1\Pi_g)$  states was set to agree with both the visible<sup>95</sup> and model results.<sup>4,32</sup> The comparison of these predictions to 1 mtorr  $N_2$  data at electron beam termination illuminated several inconsistencies. First, the relative population of  $N_2(w^1\Delta_u)$  necessary to provide the best fit of the

experimental spectrum was  $\sim 150$  times larger than the model would predict. Second, the model  $N_2(W^3\Delta_u)$  vibrational distribution did not produce a good fit to the obvious  $N_2(W-B)$  spectral features. Third, the model's poor under-prediction of the experimental spectrum would require the inclusion of an additional band system: most likely the  $N_2(B'-B)$ . However, to make any significant contribution to the observed experimental spectrum, the relative population of the  $N_2(B')$  state would necessarily need to be about 100 times greater than predicted by the model. One possible conclusion to be drawn from this analysis is that important physical processes are occurring which have not been included in the modeling.

The analysis has also been applied to the time-dependent spectra. Anomalous results were encountered. The prominent feature at  $3.3\ \mu\text{m}$  can be fit to the  $N_2(W-B)\ v'=2$  to  $v''=0$  transition. The persistence of this level at long times for the 5, 37 mtorr data is not consistent with the 1.22 ms radiative lifetime of the  $N_2(W^3\Delta_u)\ v'=2$  state calculated by Werner.<sup>32</sup> In addition, the 1 mtorr  $N_2$  signal decay corresponds to about a 3 ms time constant which is shorter than the expected detector time constant of 5 to 6 ms.<sup>93,94</sup> A careful re-evaluation of the time-dependent data shows a signal saturation artifact when the CVF filter wheel scan makes the transition from the mask region to the filtering region. The saturation effect is only observed in the SWIR from  $\sim 3.1$  to  $3.6\ \mu\text{m}$ . This artifact can be eliminated by starting the wavelength scans near the edge of the mask, but securely in the filter segment of the wheel. This artifact represents less than a 5 percent correction to the 1 mtorr  $N_2$  data at beam termination in the  $3.1$  to  $3.6\ \mu\text{m}$  region. This makes the correction insignificant for the previous conclusions drawn from the beam termination spectra. Figure 33 shows the 1 mtorr  $N_2$  decay curves for three upper states corresponding to relatively well behaved spectral features outside the  $3.1$  to  $3.6\ \mu\text{m}$  region. The time decay of these states define the time constant of the CVF detector since each of their respective radiative lifetimes is much less than 1 ms. A 5.8 ms detector time constant is consistent with documentation suggesting it would be between 5 and 6 ms.<sup>93,94</sup> Unfortunately, these results suggest our ability to measure radiative lifetimes, and/or



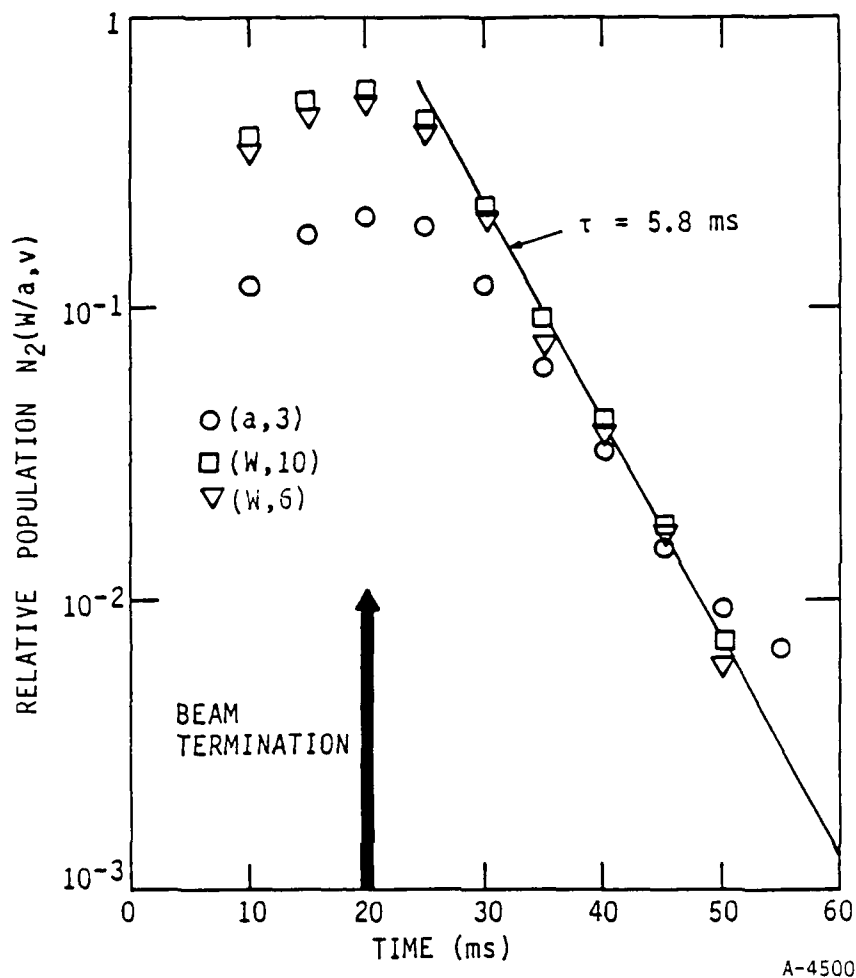


Figure 33. Time evolution of properly fit  $N_2$  levels at 1 mtorr pressure.

collisional quenching is limited by the CVF detector to the 10 ms time regime (rates of less than  $100 \text{ s}^{-1}$ ).

#### 5.4 CVF SUMMARY

Infrared emission of electron impact excited nitrogen has been observed with a cryogenic circular-variable-filter in the wavelength regions from 2.3 to  $3.6 \mu\text{m}$  and 4.0 to  $6.9 \mu\text{m}$ . Comparisons with synthetically generated spectra identify the dominant emissions as the  $N_2(W^3\Delta_u-B^3\Pi_g)$  Wu-Benesch system and  $N_2(a^1\Pi_g-a'^1\Sigma_u^-)$  McFarlane Infrared system. Minor contributions may arise from

$N_2(w^1\Delta_u-a^1\Pi_g)$  and  $N_2(B^3\Pi_g-A^3\Sigma_u^+)$  First Positive transitions. No definitive evidence is observed for emissions from the  $N_2^+(A^2\Pi_u-X^2\Sigma_g^+)$  Meinel system or from the  $N_2(B'^3\Sigma_u^--B^3\Pi_g)$  Infrared Afterglow system.

Analysis of 1 mtorr  $N_2$  spectra at electron beam termination suggests the relative population of the  $N_2(W^3\Delta_u)$  state is approximately two times larger than predicted by modeling.<sup>4</sup> In addition, the vibrational distribution in the  $N_2(W^3\Delta_u)$  state providing the optimum fit of the 1 mtorr  $N_2$  data does not match the predicted vibrational distribution. Fixing the vibrational distributions of the  $N_2(W^3\Delta_u, B^3\Pi_g, w^1\Delta_u)$  states to the model predictions and the  $N_2(a^1\Pi)$  vibrational distribution to match visible observations produced unexpected results. The combination of these basis sets underpredicts the experimental spectrum. The relative population of the  $N_2(w^1\Delta_u)$  state is  $\sim 150$  times larger than predicted and the relative population of  $N_2(B'^3\Sigma_u^-)$  that would be required to make a significant intensity contribution is  $\sim 100$  times greater than predicted by the model.

Time-dependent spectra have shown artifacts in the SWIR 3.1 to 3.6  $\mu m$  region, which have been traced to a transient detector response when rotating the CVP wheel from a mask region to filtering segment. Population decays outside this wavelength region have been used to evaluate the detector time constant, giving a value of 5.8 ms, which is within the documentation estimates of 5 to 6 ms.<sup>93,94</sup> An instrumental decay constant of 5.8 ms will inhibit the measurement of many rapid IR radiative lifetimes and quenching rates.

Much of the uncertainty in the analysis, and conclusions, stems from the inability to resolve overlapping or closely spaced spectral features.

Data from the CVP confirmed the speculation that  $N_2(W^3\Delta_u-B^3\Pi_g)$  Wu Benesch bands would dominate the SWIR. However, the poor resolution of this device prohibited the identification of weaker emitters. Previous interferometer data obtained on warm LABCEDE was reanalyzed to support and compliment the CVP observations.

## 5.5 INTERFEROMETER DATA

This data set was acquired using a cooled PbS detector viewing the electron-irradiated volume through the room temperature Michelson interferometer. The LABCEDE apparatus was operated at room temperature (298 K) for these observations. Data was acquired on every interference fringe zero crossing of the reference laser so that emission into the visible (632.8 nm) could be observed. Beam splitter efficiency decreases in the visible as does detector responsivity so that the first positive  $\Delta v=2$  sequence was the shortest wavelength observed feature. Responsivity across the entire spectrum (3000 to 15,800  $\text{cm}^{-1}$ ) is very non uniform. This data was not accurately response corrected and consequently can only be used to qualitatively assign spectral radiators. More exact determinations must await a dedicated measurements program.

Emission from five electronic transitions appears to be present in the infrared interferometer data. These were the First Positive ( $B^3\Pi_g-A^3\Sigma_u^+$ ), Wu Benesch ( $W^3\Delta_u-B^3\Pi_g$ ),  $a^1\Pi_g-a'^1\Sigma_u$ , and  $w^1\Delta_u-a^1\Pi_g$  systems of nitrogen and the Meinel system ( $A^2\Pi_O-X^2\Sigma_g^+$ ) of  $N_2^+$ . Relative population levels were determined using the general spectral fitting code which was first modified to fit data linear in wavenumber. Several details considered in analyzing the data will now be described.

The computer data files were modified by increasing the number of data points by a factor of four via simple linear interpolation (this did not alter the appearance of the spectra). This was done since the resolution in this data is defined as the point spacing ( $\text{cm}^{-1}/\text{point}$ ). With only one point per resolution interval, it was found that the appearance of the rotational contours was not well reproduced by the code. The finer point spacing gave better agreement between calculated and experimental spectra. Resolution was assumed to be  $15.4 \text{ cm}^{-1}$ , the point spacing of the original data. A triangular slit function was assumed. A rotational temperature of 400 K was used in creating the basis sets for all systems except Wu-Benesch where a temperature of 300 K was used. These were estimated by fitting isolated bands of the Meinel, First Positive,

and Wu-Benesch systems in several spectra. Future improvements will include larger Fourier transforms for improved point spacing and utilization of a sinc slit function.

Band integrated Einstein coefficients were taken from several sources and are crucial in determining the populations given in figures 34 and 35. Those assumed for the First Positive and Wu-Benesch systems were calculated by Werner et al.<sup>32</sup> Although there exist experimentally determined Einstein coefficients for the First Positive system,<sup>6</sup> they are derived from transitions whose  $r$  centroids are larger than those for the transitions in the region 1.5 to 3.5  $\mu\text{m}$ . They were thus created by extrapolation of the  $r$  centroid versus  $R_e$  curve and are of uncertain reliability. Efforts to characterize this region of the  $r$ -centroid curve culminating in a new set of Einstein coefficients have since been performed and are described in Section 7 of this report. Implications are discussed in a subsequent paragraph. No experimentally determined Einstein coefficients exist for the Wu-Benesch system.

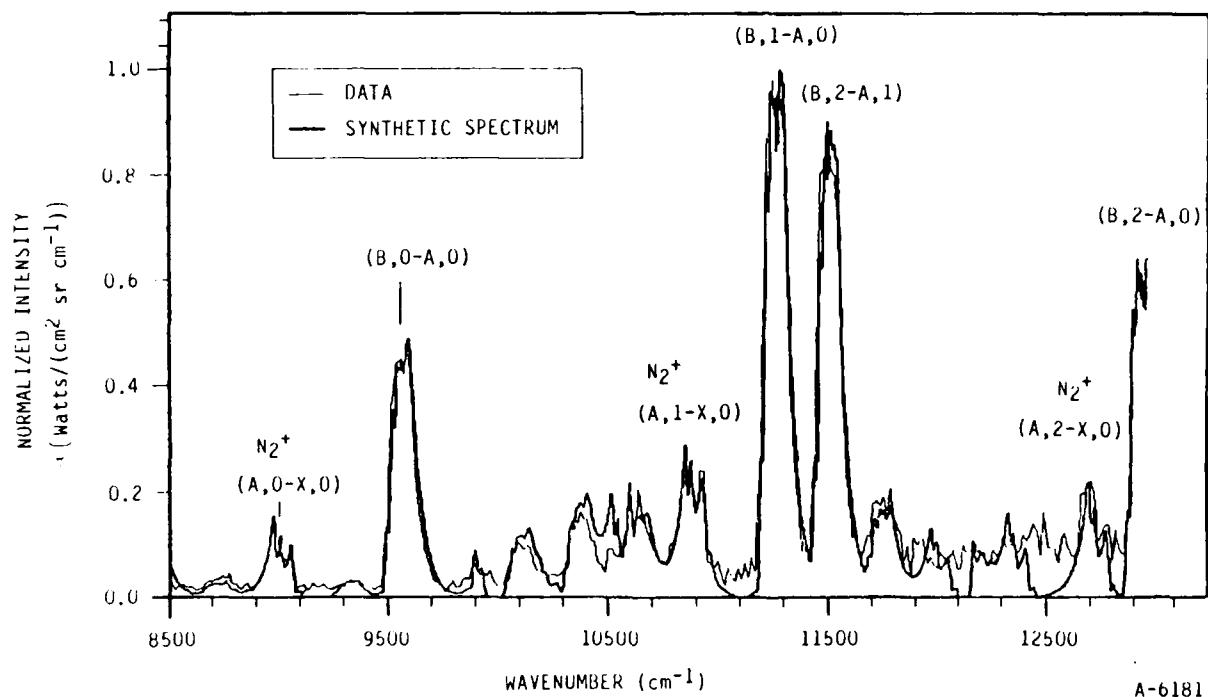


Figure 34. Near IR interferometer data of electron-irradiated  $\text{N}_2$  (6 mtorr).

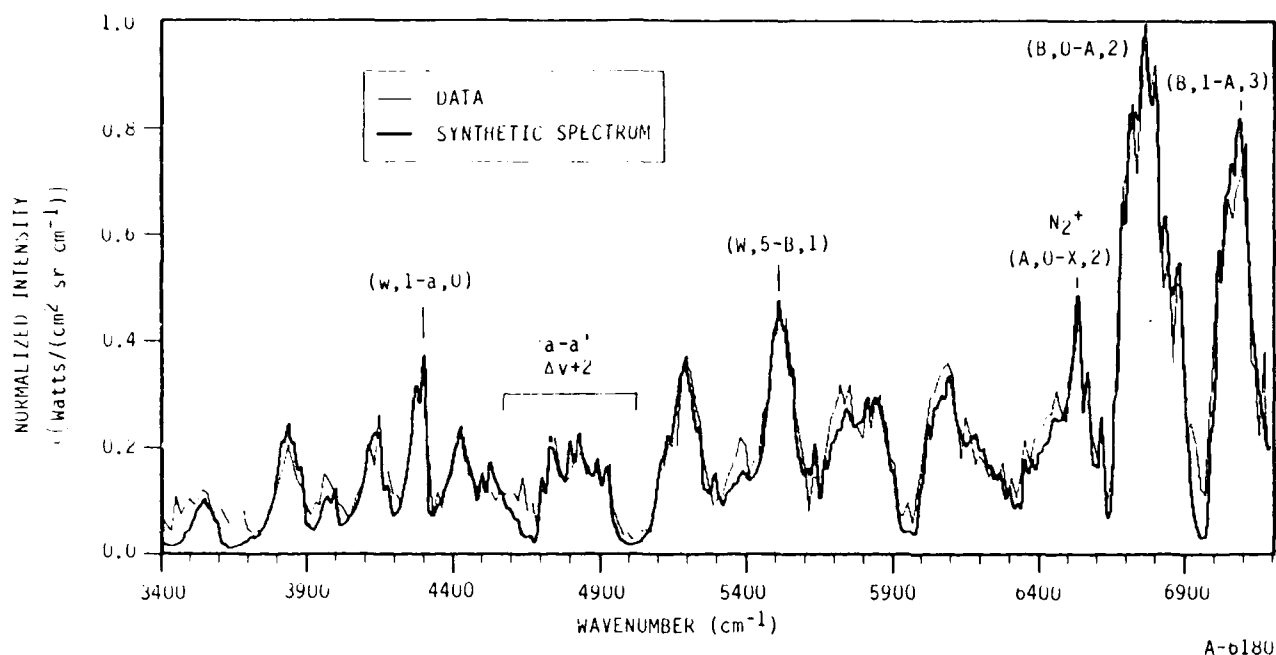


Figure 35. SWIR interferometer data of electron-irradiated  $N_2$  (6 mtorr).

Experimentally determined Einstein coefficients for the Meinel system were taken from Ref. 6 in the absence of experimental data for the w-a and a-a' systems, Einstein coefficients for both were calculated using Franck-Condon factors from Ref. 6 and the transition moment functions of Yeager and McKoy.<sup>65</sup>

Previously determined relative vibrational state distributions were used where possible to simplify the analysis by reducing the degrees of freedom in the fit. This was desirable given the experimental resolution and significant band overlap. A single distribution was assumed for the Meinel system.<sup>96</sup> This distribution corresponds to the relative rates of excitation as determined in the LABCEDE facility. Vibrational state distributions for the  $a^1\Pi_g$  state have been determined in LABCEDE for all pressures investigated<sup>95</sup> in this work as have those for the  $B^3\Pi_g$  state (see Section 2). The latter were determined by fitting First Positive data in the visible region of the spectrum and are summarized in Table 8. In all cases combined basis sets were created reflecting

TABLE 8. Normalized populations for B-A  $v'$  0-7 used in interferometer data analysis (based on Section 2).

$v'$	Pressure (mtorr)				
	1.0	3.0	6.0	10.0	15.0*
0	0.18	0.24	0.27	0.28	0.29
1	0.19	0.19	0.19	0.20	0.20
2	0.19	0.19	0.19	0.19	0.19
3	0.14	0.13	0.12	0.12	0.11
4	0.11	0.11	0.10	0.09	0.08
5	0.07	0.07	0.06	0.06	0.05
6	0.05	0.05	0.05	0.04	0.04
7	0.03	0.03	0.03	0.03	0.03
*Extrapolated from the trends found in data taken at pressures of 1.0, 2.0, 3.0, 4.0, 6.0, 8.0, and 10.0 mtorr					

these ratios and a single electronic state population was determined. Individual populations for the constituent levels were then calculated as the fraction of this population given from the normalized vibrational distribution.

#### 5.6 N<sub>2</sub> ELECTRONIC STATE POPULATIONS

The combined CVF and interferometer data have allowed us to evaluate reasonable levels of population in specific states. Figure 36 shows the results for an altitude of 90 km in comparison to the model predictions of Cartwright<sup>4</sup> and observations made from visible fluorescence under similar experimental conditions.<sup>95</sup> The scale is relative and the population of the N<sub>2</sub>(C<sup>3</sup>Π<sub>u</sub>) state has been used for normalization. The same vibrational level summations have been used throughout. The population levels of the N<sub>2</sub>(a<sup>1</sup>Π<sub>u</sub>)

state have been used to normalized the different data sets. The infrared measurement of the  $N_2(B^3\Pi_g)$  state population is significantly higher than predicted by Cartwright or observed in the visible measurement. This disagreement may arise from two different sources. As portrayed in Figure 36, the higher  $N_2(B^3\Pi_g)$  state population level depends upon R-centroid values of Werner<sup>32</sup> extrapolated to smaller  $R_e$  values for these IR transitions. Using the higher resolution data obtained with the interferometer, we have been able to calculate a different set of R-centroid values which provide a better fit to the observed  $N_2(B^3\Pi_g-A^3\Pi_u)$  First Positive spectral features. The lower level of  $N_2(B^3\Pi_g)$  population indicated in Figure 36 is that obtained using these calculated  $R_e$  values.

The population levels of the  $N_2(W^3\Delta)$  state are also in reasonable agreement. Note the infrared data was obtained at 1 to 2 mtorr hence collisional relaxation effects in these long-lived states (must be considered since radiative lifetimes range from 100 to 600  $\mu$ s, whereas mean collision times are order of 10  $\mu$ s). Data obtained at 15 mtorr show very similar population levels, suggesting that relaxation to lower vibrational levels in that state is slow. Therefore, the comparison is at the extreme only slightly worse than presented in Figure 36. The discrepancies observed for both the  $w^1\Delta_u$  and  $B'^3\Sigma_u$  states are surprising. Transitions arising from these states are minor ( $\leq 10$  percent) contributors to the overall infrared spectra and are often overlapped with much stronger  $N_2(W-B)$ ,  $N_2(a-a')$ ,  $N_2(B-A)$  spectral features. Even though our determination of their population levels is much less accurate, the discrepancy is outside our estimated uncertainty. These discrepancies warrant further investigation.

The compilation of the vibrational level dependent populations are presented in Figures 37, 38 and 39. Figures 37 and 38 represent our most accurate determination of the relative distribution of excited electronic-vibronic states. In general, UV-visible data was used wherever possible as this data base has been more extensively studied and the spectral constants have been

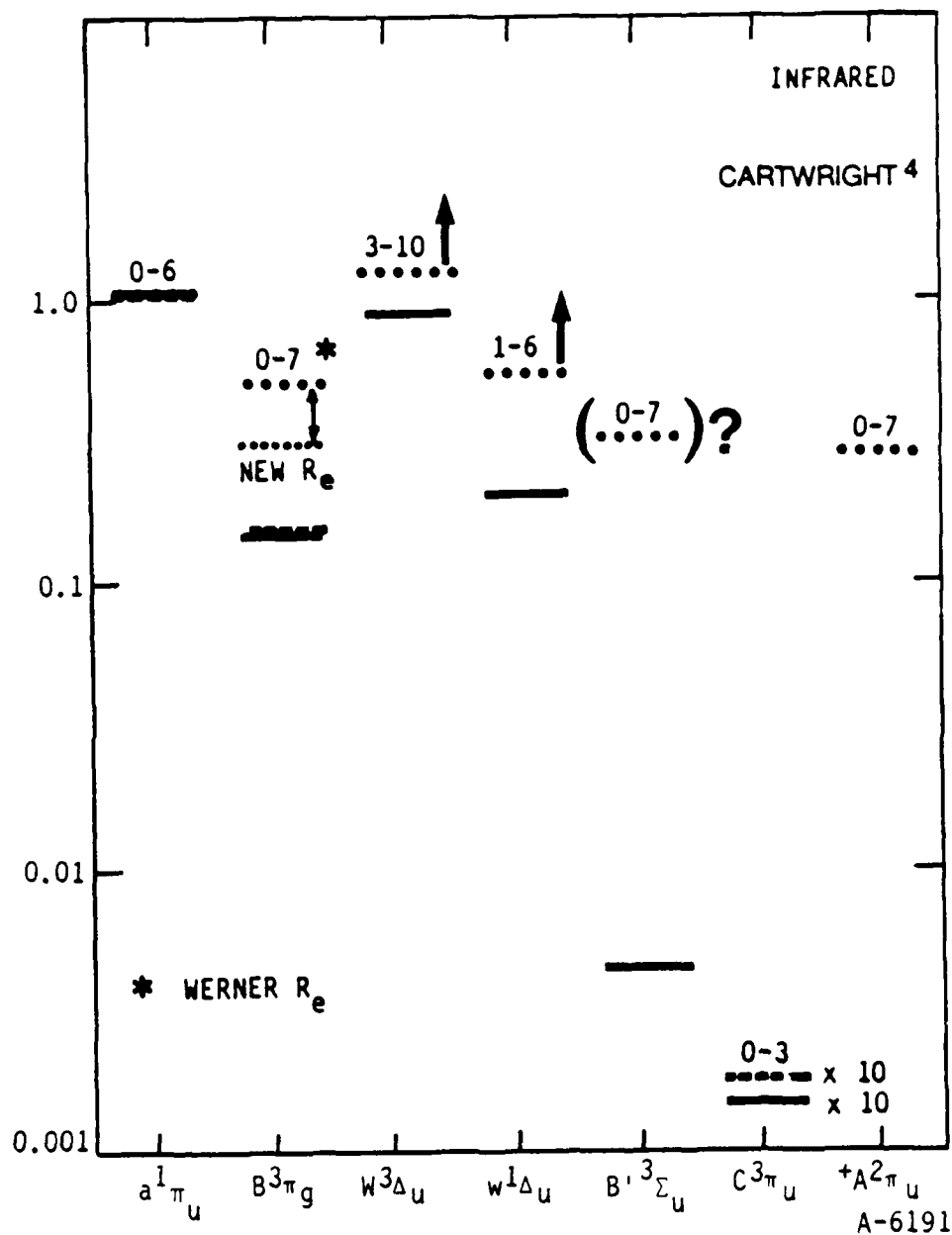


Figure 36. N<sub>2</sub> electronic state populations from LABCEDE visible and IR fluorescence at less than 1 mt pressure compared with high altitude (greater than 110 km) auroral predictions. Population determined from visible (---) and infrared (···) fluorescence data are compared to modeled predictions (—) for high altitude aurora.<sup>4</sup>



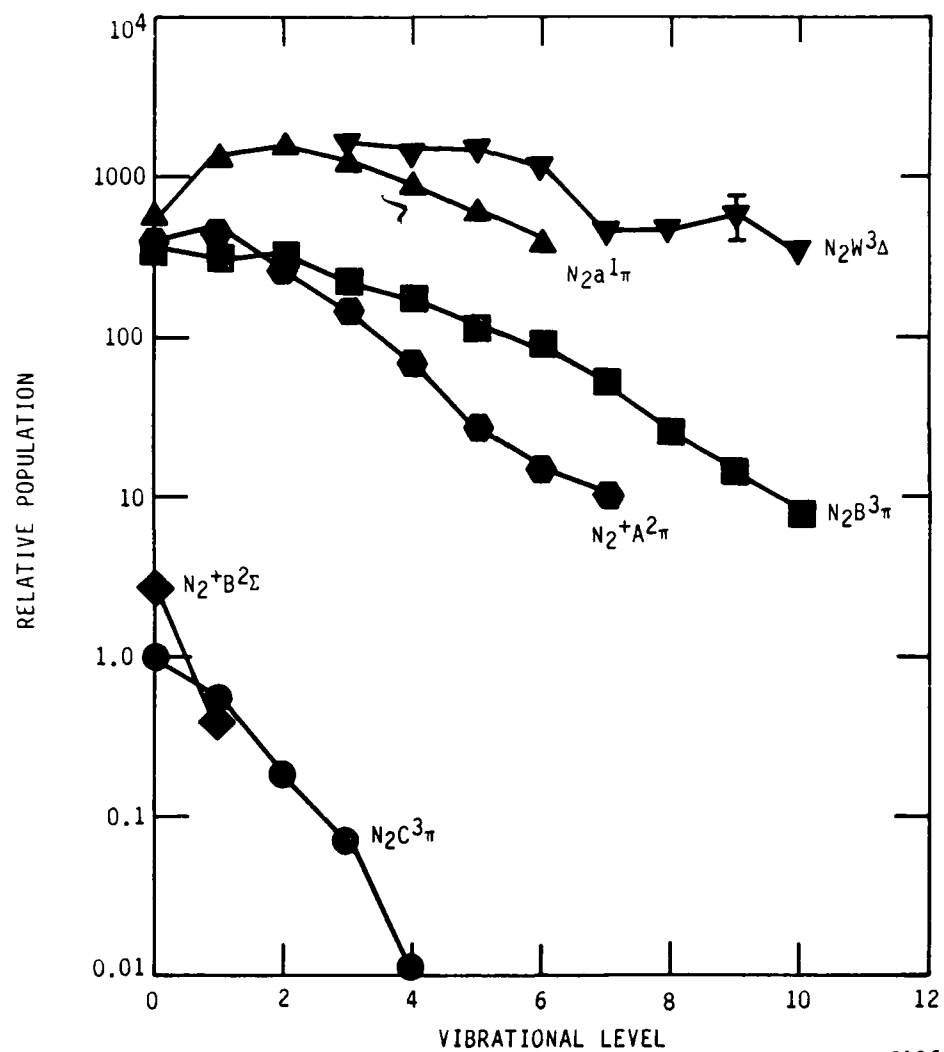
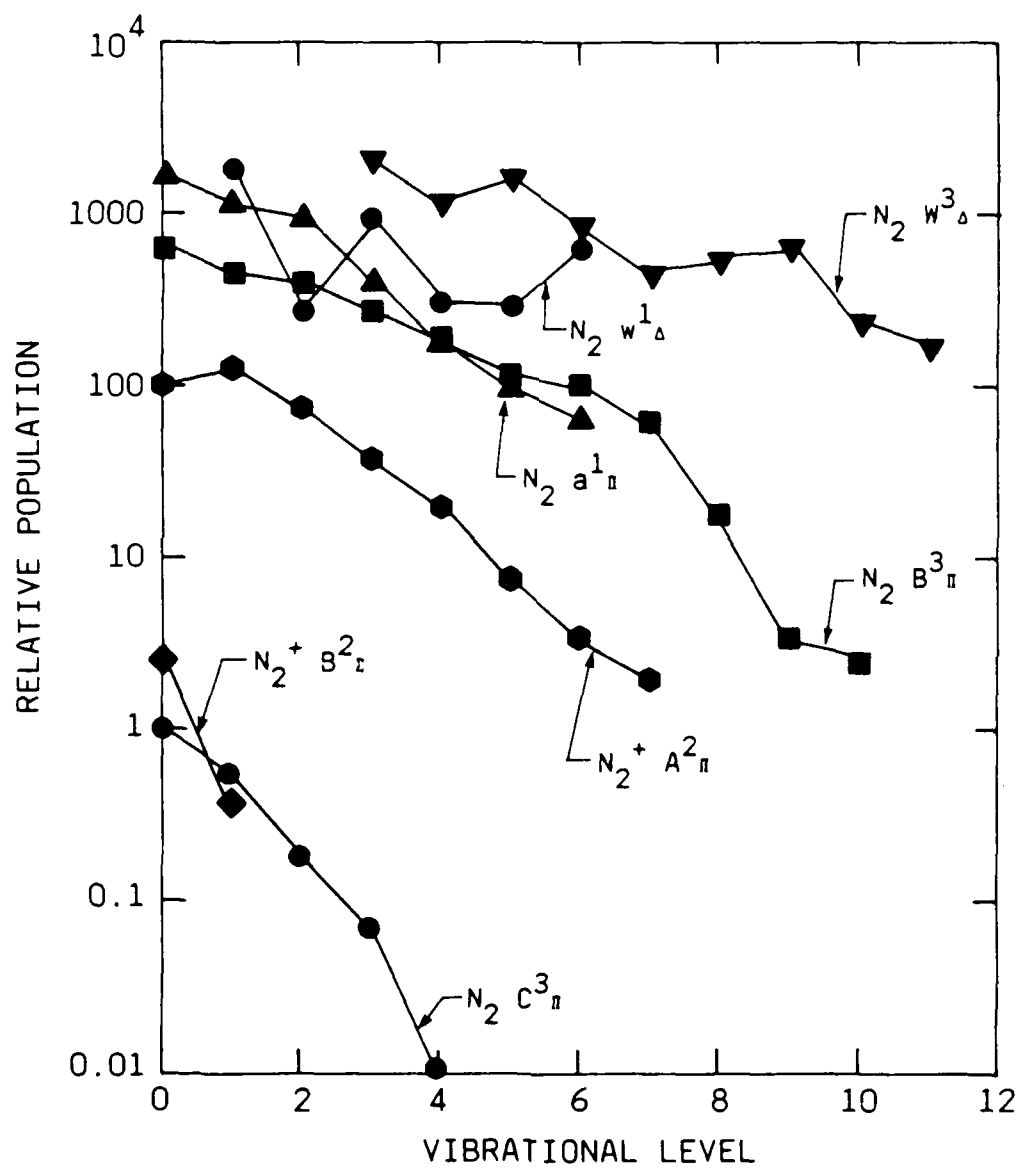


Figure 37. Vibrational distributions within nitrogen electronic state populations in LABCEDE at 1 mtorr.



A-6565

Figure 38. Vibrational distributions within nitrogen electronic state populations in LABCEDE (15 mtorr).

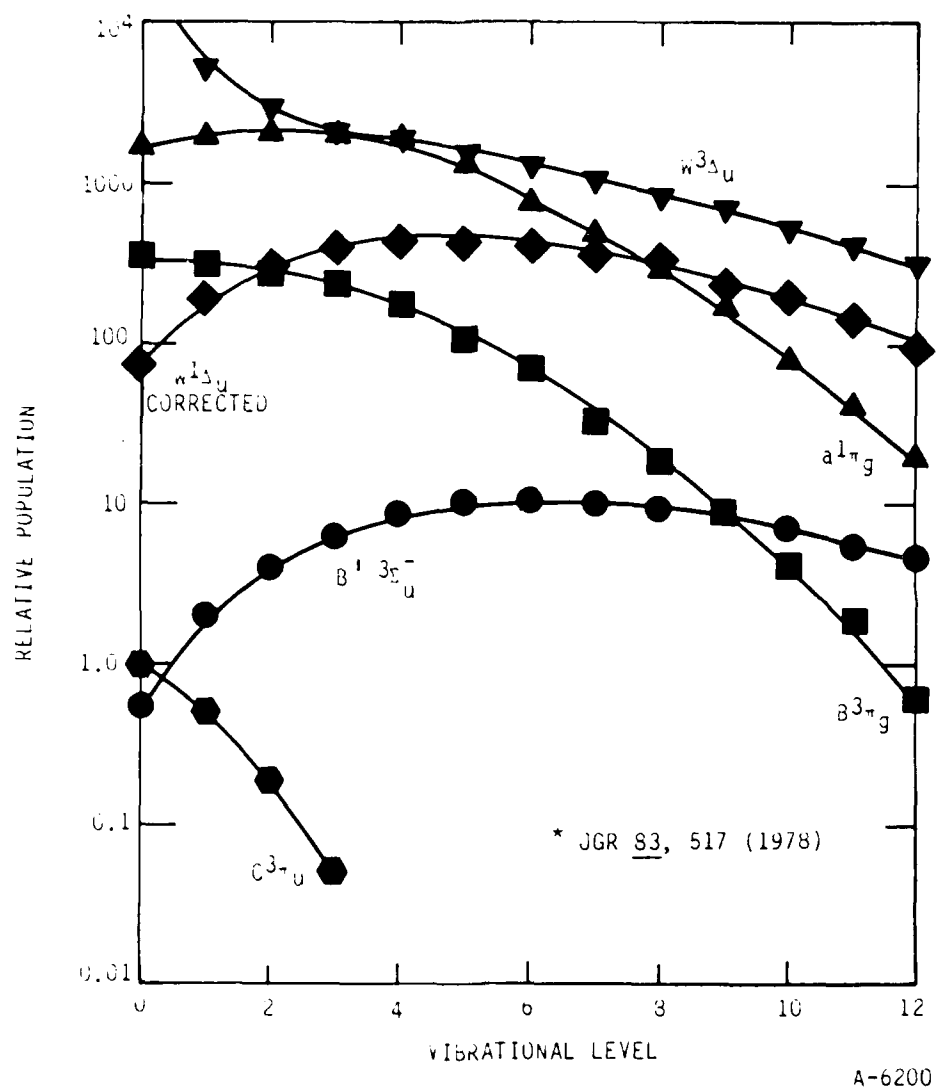
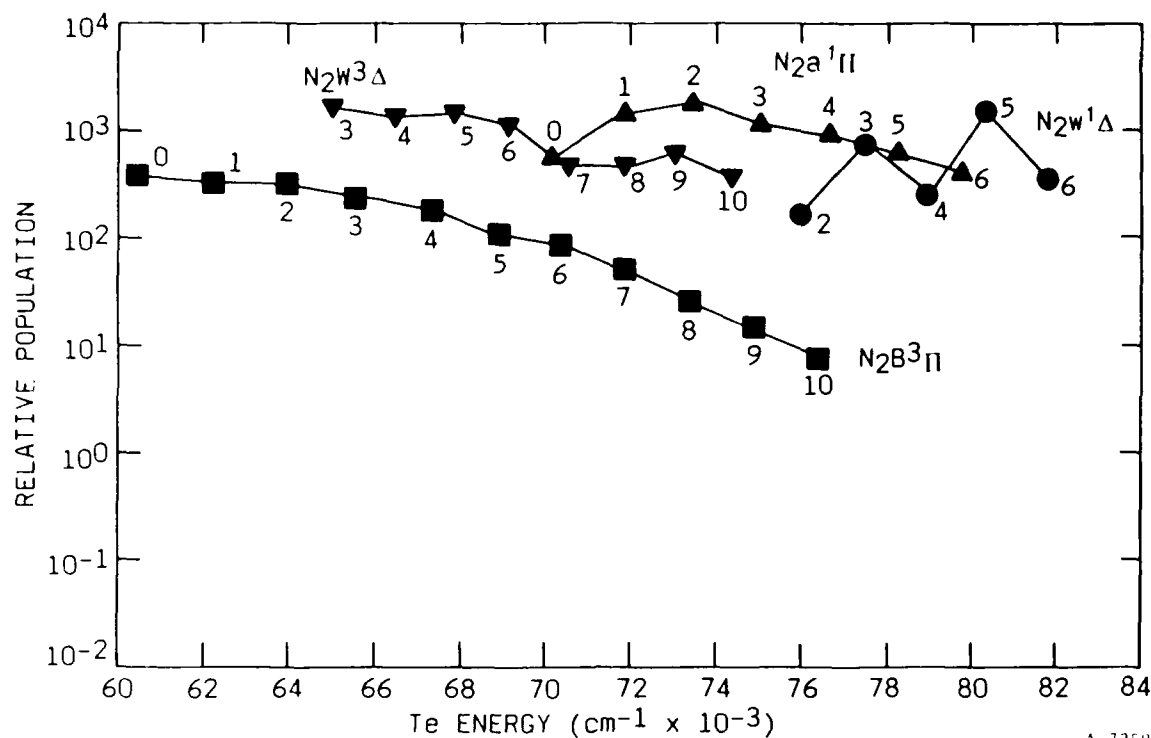


Figure 39. Nitrogen electronic populations Cartwright model.<sup>4</sup>

more accurately determined. The states whose populations are determined exclusively from the infrared measurements are the  $N_2(W^3\Delta)$ ,  $N_2(w^1\Delta)$ . In all cases, the populations have been normalized to the  $N_2(C^3\Pi_u, v=0)$  level. At 1 mtorr pressure, these populations closely represent the relative production efficiencies for generation by 4.5 KeV electrons. At 15 mtorr, (Figure 38), we observe changes in population levels attributable to collisional energy transfer. Figure 39 presents the predictions of Cartwright<sup>4</sup> for comparison to our 1 mtorr data. One difference arises from our  $N_2(W^3\Delta, v=7,8,9)$  levels which show a drop then a slight rise in population by comparison. This same decrease and rise in population appears at 15 mtorr. Figure 40 shows the relative population at 1 mtorr of the  $N_2(W^3)$ ,  $N_2(B^3)$ ,  $N_2(a^1)$ ,  $N_2(w^1)$  vibrational levels plotted versus the total potential energy (electronic plus vibrational) for each level. A chance resonance occurs between the  $N_2(a^1\Pi, v=1)$ ,  $N_2(W^3\Delta, v=8)$ , and  $N_2(B^3\Pi, v=7)$  states. The decrease in population between  $v=6$  and  $v=7$  of the  $N_2(W^3\Delta)$  state is not matched by a discontinuous increase in either the  $N_2(a^1\Pi, v=0)$  or  $N_2(B^3\Pi, v=6)$  level populations. Figure 41 shows an energy level diagram of additional states which are near resonant with  $N_2(W^3\Delta, v=7)$ . It is an intriguing possibility that population transfer into one of these states may be occurring.

The possible quenching/relaxation of  $N_2(W^3\Delta)$  levels can be explored via an analysis of higher pressure interferometer data. In order to remove the effects of electron energy deposition we again ratio the populations of two states. To unravel the effects of quenching the preferred reference state would be short lived and suffer negligible feed and sample the same energy electrons. Previously we have utilized the  $N_2^+(B)$  and  $N_2(C)$  for these reference states. Unfortunately, these states are not detectable in the interferometer spectrum and we must choose the  $N_2(B)$  state which is short lived and has a similar electron excitation cross section function. As described in Section 2, this state suffers a collisional transfer increase in population as pressure increases. Figure 42 shows the  $N_2(W)$  state population relative to  $N_2(B)$  for pressures 1 to 15 mtorr. A decline is observed which could be due to 1) vibrational relaxation of  $N_2(W)$  into levels 0-2 which are



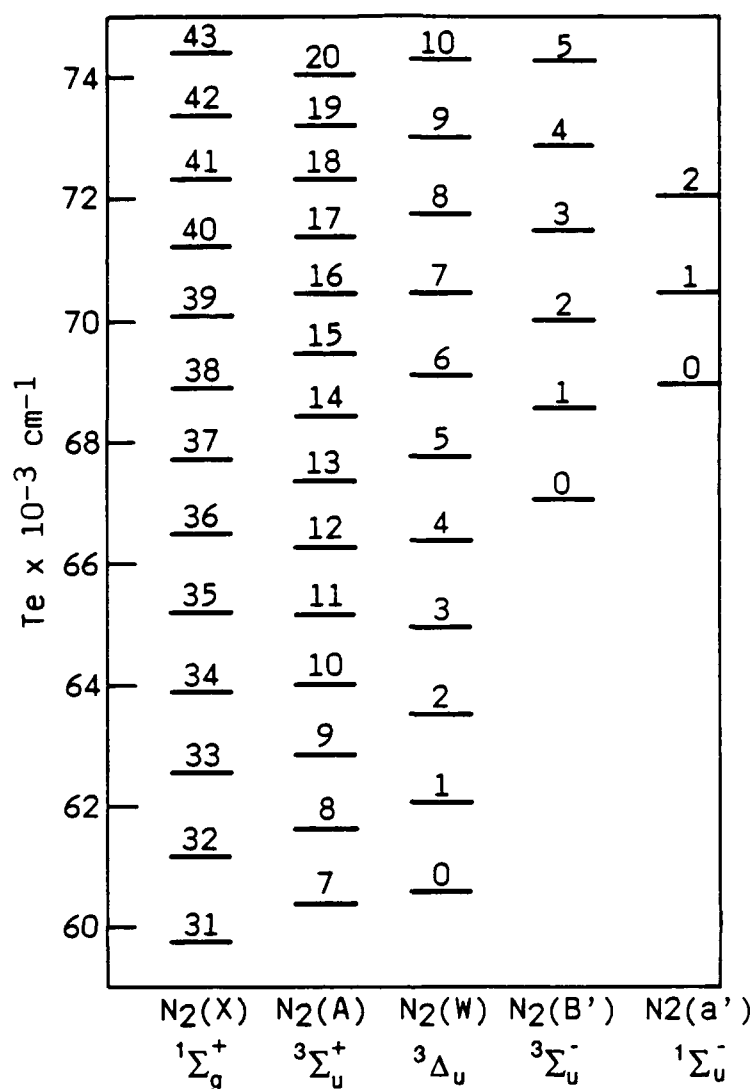
A-7358

Figure 40. Nitrogen population levels plotted versus level Te for N<sub>2</sub>B ( ), W (▼), a (▲), and w (●) states.

not detectable in this experiment; 2) electronic quenching of N<sub>2</sub>(W); or 3) net feed of population into N<sub>2</sub>(B).

Figure 43 presents the vibrational populations of the N<sub>2</sub>(B) for several pressures as referenced to the unquenched N<sub>2</sub>(C,0) population. The net increase is into vibrational levels resonant with W state levels 0-2 not included in Figure 42. The observed decrease in W state population is twice as large as the increase in B, and a decrease in W state populations occurs even after the increase in B is included in the analysis. Thus W state relaxation or quenching is occurring. In general the W state vibrational distribution is not altered substantially between 1 and 15 mtorr. Further data is needed to more accurately determine the fate of the W state.

An intriguing observation relates to (W,v=7). In Section 3 we observed that N<sub>2</sub>(a,v=0) increased relative to the other vibrational levels and in absolute



A-7359

Figure 41. Energy level diagram of N<sub>2</sub> electronic-states indicating large number of possible resonances.

concentration as pressure increases. (Here N<sub>2</sub>(C) was used as the reference state.) At 15 mtorr, Figure 38 tells us that a significantly larger fraction of the total N<sub>2</sub>(a<sup>1</sup>Π) population resides in v=0. This may arise by two different mechanisms: 1) vibrational relaxation from higher levels of a-state and 2) a feed of population from other nested states as is observed for N<sub>2</sub>(B). The near resonance of the N<sub>2</sub>(W, v=7), N<sub>2</sub>(a, v=0) states and the precipitous drop in population at the N<sub>2</sub>(W, v=7) level may be indicative of a collisional energy transfer.

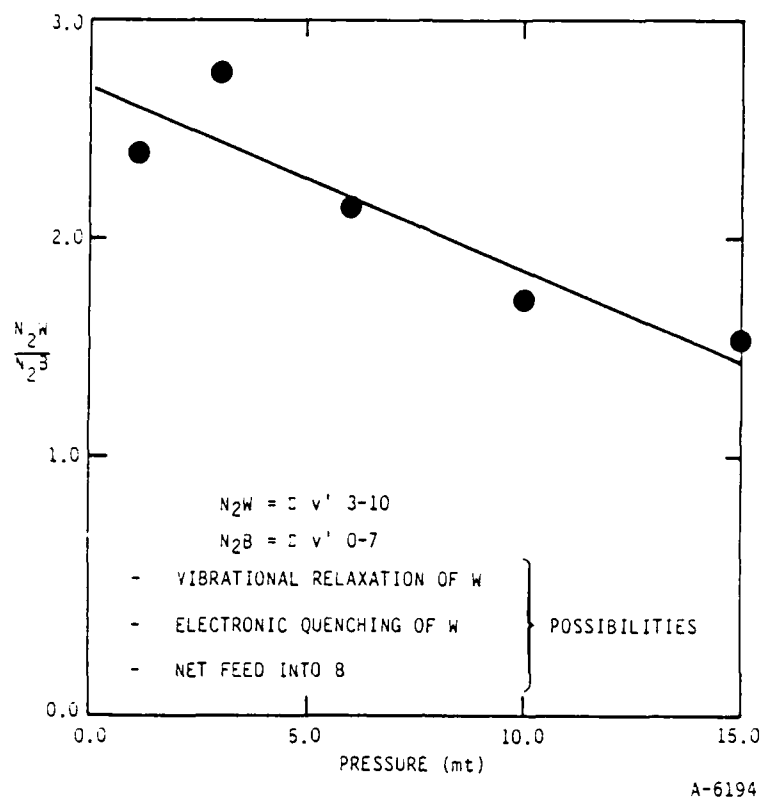
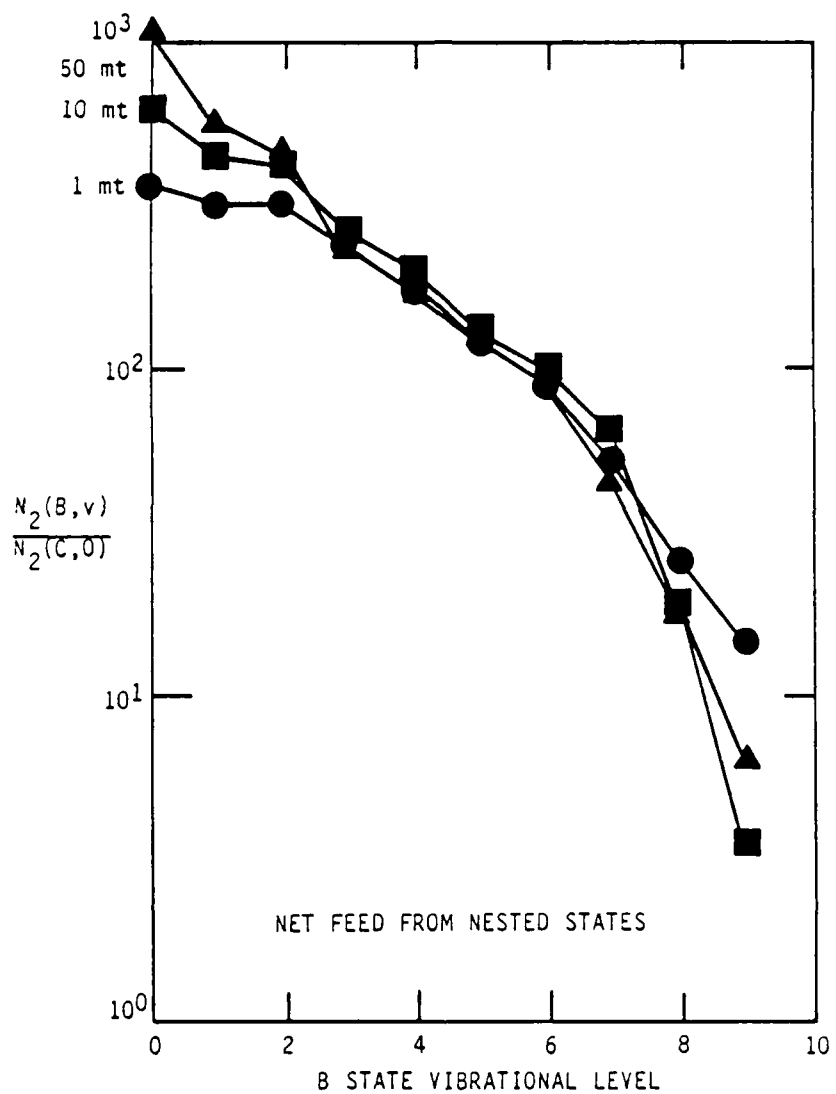


Figure 42. Total quenching of  $W^3\Delta$ ,  $v=3-10$  state relative to  $B^3\Pi_g$  state.

The summary of our efforts to measure the vibrational level dependent production into excited electronic (and ionic) states of nitrogen by electron irradiation is portrayed in Figures 44a-c and Figures 45a-c. These are relative spectral intensity predictions based upon our population measurements. The spectral intensity is predicted from 150 nm to 9  $\mu$ m in a series of three figures, i.e., a,b,c with a resolution of 50Å by generating basis functions (triangular slit) with experimentally determined vibrational distributions for all the observed band systems. The change in magnitudes of intensity between figures in the series a,b,c accurately predicts spectral intensities.

Figure 44 corresponds to an altitude of 90 km and Figure 45 to 80 km. A comparison of the same wavelength regions between Figures 44 and 45 accurately represents redistribution of population levels hence spectral emission intensity, but absolute signal level differences are not portrayed here. Relative minima ( $\sim 1$  percent of peak intensity) occur in the UV between 185 and 270 nm, in the visible between 465 and 565 nm. The spectrum in the near IR is very



A-6195

Figure 43. Normalized B-state vibrational populations as a function of pressure.

rich with no observable minima, however, at 880 nm the emission intensity begins to fall monotonically until 3.5  $\mu\text{m}$ . A minimum is observed between 3.5 and 3.6  $\mu\text{m}$ , another between 4.3 and 4.4  $\mu\text{m}$ . The wavelength region beyond 4.5  $\mu\text{m}$  remains much less than 1 percent of the emission levels of the UV, visible and near IR. At 6.0  $\mu\text{m}$  the emission intensities approach one millionth ( $10^{-6}$ ) of the UV-Vis-IR peak emission levels. Emission is considered only from levels detected in this project. Emission from other levels (notably W,



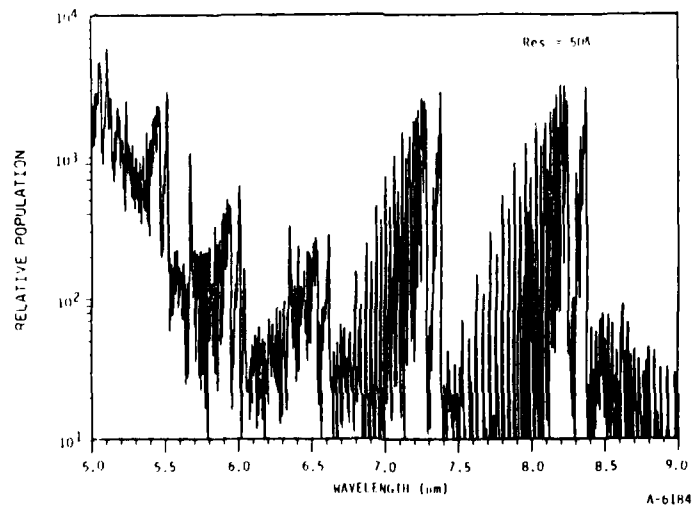
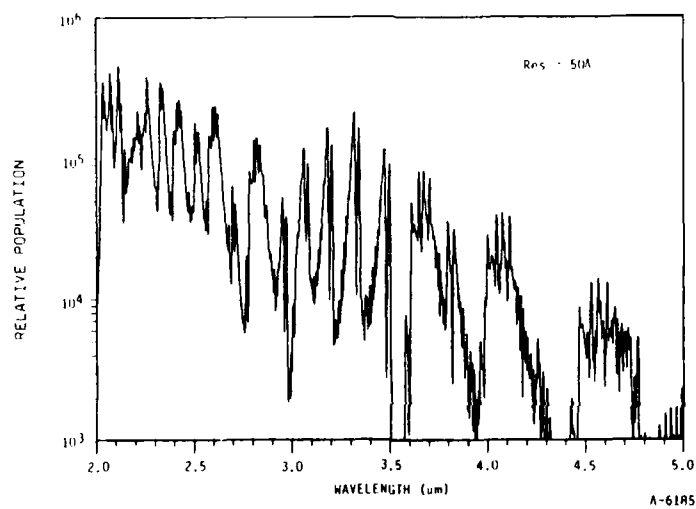
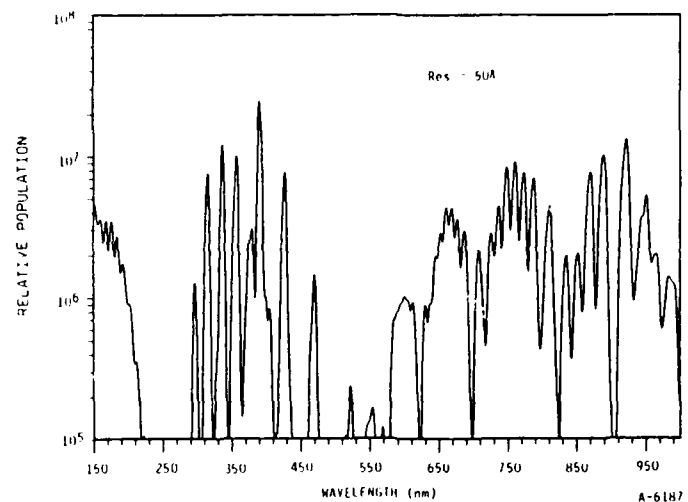


Figure 44. Synthetic spectrum of electron-irradiated nitrogen at 90 km altitude for three spectral regions: a) visible; b) SWIR/MWIR; and c) LWIR.

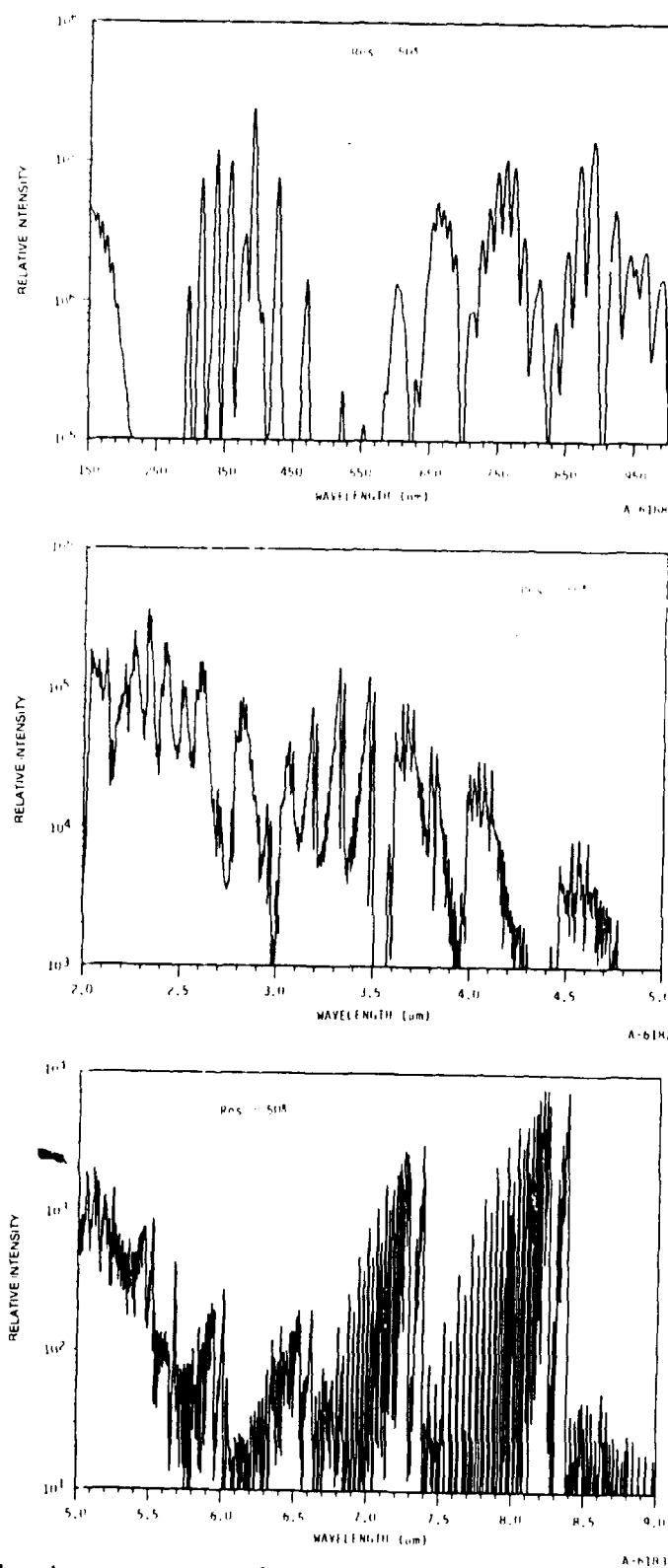


Figure 45. Synthetic spectrum of electronic irradiated nitrogen at 80 km altitude for three spectral regions: a) visible; b) SWIR/MWIR; and c) LWIR.

$v=0-2$  and  $w, v=0,1$ ) will contribute particularly in the MWIR and LWIR. A more careful determination of the  $N_2$  electronic state radiance levels must await the cryogenic interferometer.

This project is intended to provide guidance for the interpretation of electron-irradiated atmospheres and in particular for the EXCEDE field mission. These electronic state populations as a function of altitude provide a basis for comparison so that an understanding of mission performance can be arrived at more quickly and so that new unexpected radiators can be more clearly highlighted.

## 6. ROOM AIR FLUORESCENCE INVESTIGATIONS

### 6.1 INTRODUCTION

The fluorescence from electron excited room temperature  $N_2/O_2$  mixtures was viewed through the  $BaF_2$  window from the upstream end of the LABCEDE tank and normal to the electron beam. A 0.3m McPherson Model 218 scanning monochromator equipped with a 1200 line/mm grating blazed at 500 nm dispersed the radiation from 200 to 800 nm onto a HTV R955 photomultiplier (a Corning Glass Corporation 3-74 order sorting filter was used in scans including wavelengths greater than 450 nm). Synchronous detection of the fluorescence from the pulsed electron beam was performed. The modulated component of the signal from the photomultiplier was processed with an Ithaco Model 1211 current pre-amplifier and a P.A.R Model 124 lock-in amplifier. The amplified fluorescence signal was displayed and recorded on a chart recorder and digitized on a Compaq personal computer. The digitized spectra were transported to PSI via floppy disks for further quantitative analysis.

Experimental conditions were chosen to be similar to previous experiments performed on pure nitrogen. The electron beam characteristics were: 4500 eV energy, 5 to 15 mamp current, and a 200 Hz square wave beam pulse rate. Gas was introduced through one of three MKS Model mass flow meters and was introduced into the chamber via a porous plug array of inlets. Ultra high purity gases were used: (99.999 percent minimum) nitrogen ( $N_2$ ) and (99.99 percent minimum) nitric oxide (NO). Laboratory air was introduced via an unconnected (open to the room air) flexible hose leading to the mass flow meter. Gas flows range from 40 to 387 sccm of nitrogen equivalents, i.e., mass flow was uncorrected for gas identity. In conjunction with the variable position throttling valve, these gas flows provided selectable experimental pressures between 1.0 and 20.0 mtorr. The majority of experiments were performed with a monochromator slit width of 600  $\mu m$ , providing a resolution of 15.6Å. The HTV R955 PMT was operated at bias voltages between 720 and 950V. Preamplifier gains ranged from  $10^5$  to  $10^7$  V/amp with a raise time of 0.1 ms. The lock-in

amplifier was operated at a gain between 20 and 1000, with a time constant of 1 to 3s. Computer data sampling occurred at 1 to 3 Hz.

## 6.2 SURVEY SPECTRA OF LABORATORY AIR

### 6.2.1 The 200 to 300 nm Region

Survey spectra of laboratory air in the 200 to 300 nm were collected at low (1.2 mtorr) pressure with and without Beam Plasma Discharge occurring, and at high (20 mtorr) pressure without BPD. The electron energy was 4500 eV with a current of 12.5 mamp. When BPD was ignited, the signal to noise was significantly better. However, the same features were observed and the spectra could be overlayed precisely. The 20.0 mtorr air spectrum in this region showed a slight increase in the relative intensity of the 234 nm feature but was otherwise unchanged. Several band systems,  $N_2(a^1\Pi_g-X^1\Sigma_g^+)$  LBH,  $N_2(D^3\Sigma_u^+-B^3\Pi_g)$  Fourth Positive,  $NO(A^2\Sigma^+X^2\Pi)$   $\gamma$ -bands,  $NO(B^2\Pi-X^2\Pi)$   $\beta$ -bands,  $NO(C^2\Pi-X^2\Pi)$   $\delta$ -bands,  $O_2^+(A^2\Pi_u-X^2\Pi_g)$  Second Negative were observed. Combinations of these were utilized in an attempt to fit the observed spectra.

All attempts to synthetically generate the experimental spectra failed. A search and review of previous work performed on this detection system showed a Wood's anomaly in the 200 to 300 nm region, making quantitative spectral analysis of this experimental data impossible.

### 6.2.2 The 300 to 400 nm Region

Spectra in the 300 to 400 nm region were collected at a pressure of 1.2 mtorr with and without BPD and at 20.0 mtorr without BPD. Figure 46 is representative of the experimental spectra and the synthetic spectra which were obtained. The exact same features are observed at all the experimental conditions that were sampled. The main features are assigned to the electronic bands  $N_2(C^3\Pi_u-B^3\Pi_g)$  and  $N_2^+(B^2\Sigma_u^+-X^2\Sigma_g^+)$ . For the synthetic spectra, the  $N_2(C^3\Pi_u-B^3\Pi_g)$   $v'=0-4$  levels were utilized, although  $v'=3,4$  were found to

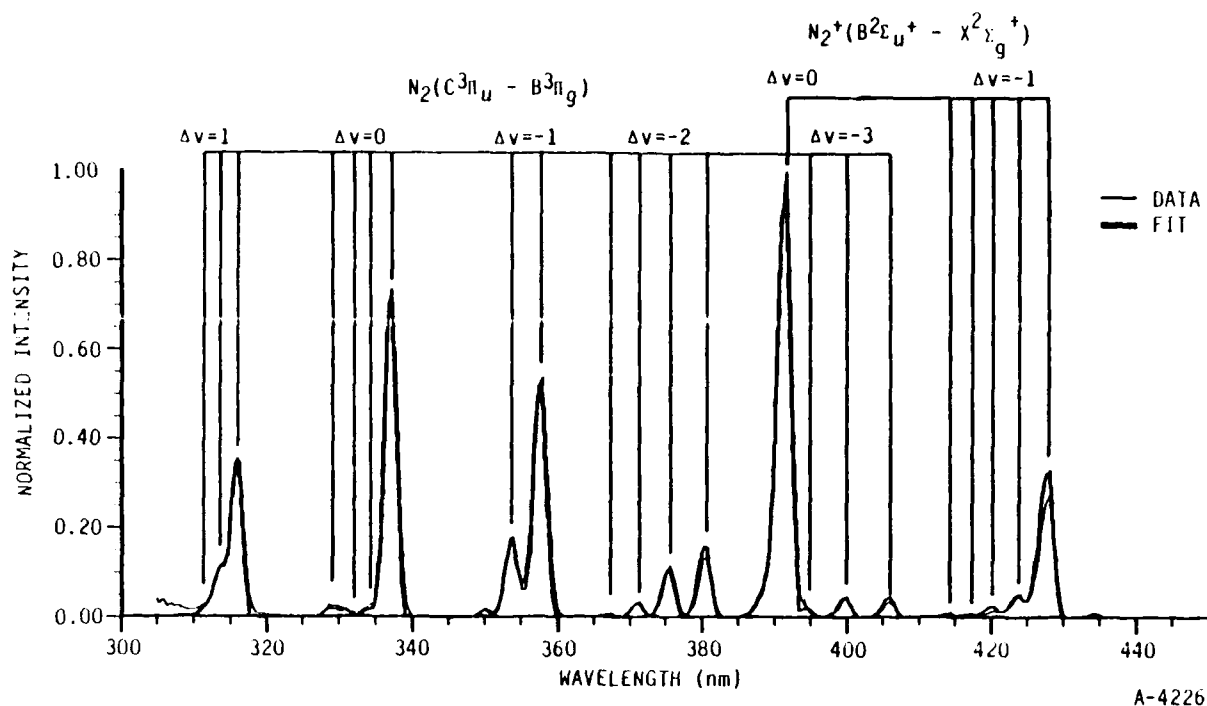


Figure 46. 1.2 mtorr room air spectrum taken with a 15.6Å resolution is representative of all data and fits in this spectral region.

be only marginally present due to the weak signal of transitions originating from these levels. In the case of  $N_2^+(B^2\Sigma_u^+ - X^2\Sigma_g^+)$ ,  $v'=0-4$  were utilized in the synthetic spectral generation, but  $v'=2,3,4$  proved to be relatively weak and inaccurately determined. Figure 47 shows the relative populations of the upper state vibrational levels, as calculated from the spectral generation code (see Appendix C). The data points are for 1.2 mtorr of laboratory air, and the dashed lines represent the predicted distributions based on the Franck-Condon (F-C) factors for excitation from ground state molecular nitrogen,  $N_2(X^1\Sigma_g^+)$ .<sup>6</sup> In each case the F-C distributions has been normalized to the  $v'=0$  BPD data points. The  $N_2(C^3\Pi_u - B^3\Pi_g)$   $v'=0,1$  distribution matches the Franck-Condon distribution. The population ratio  $v'=1$  to  $v'=2$  for  $N_2(C^3\Pi_u)$  state with and without BPD is  $\sim 2.3$ , whereas F-C factors would predict a ratio of 2.9. The population ratio  $v'=2$  to  $v'=3$  for  $N_2(C^3\Pi_u)$  with and without BPD is  $\sim 3.0$ , where F-C factors would predict 3.6. These discrepancies are felt to be within the experimental uncertainty. For  $N_2^+(B^2\Sigma_u^+ - X^2\Sigma_g^+)$   $v'=0,1$  there

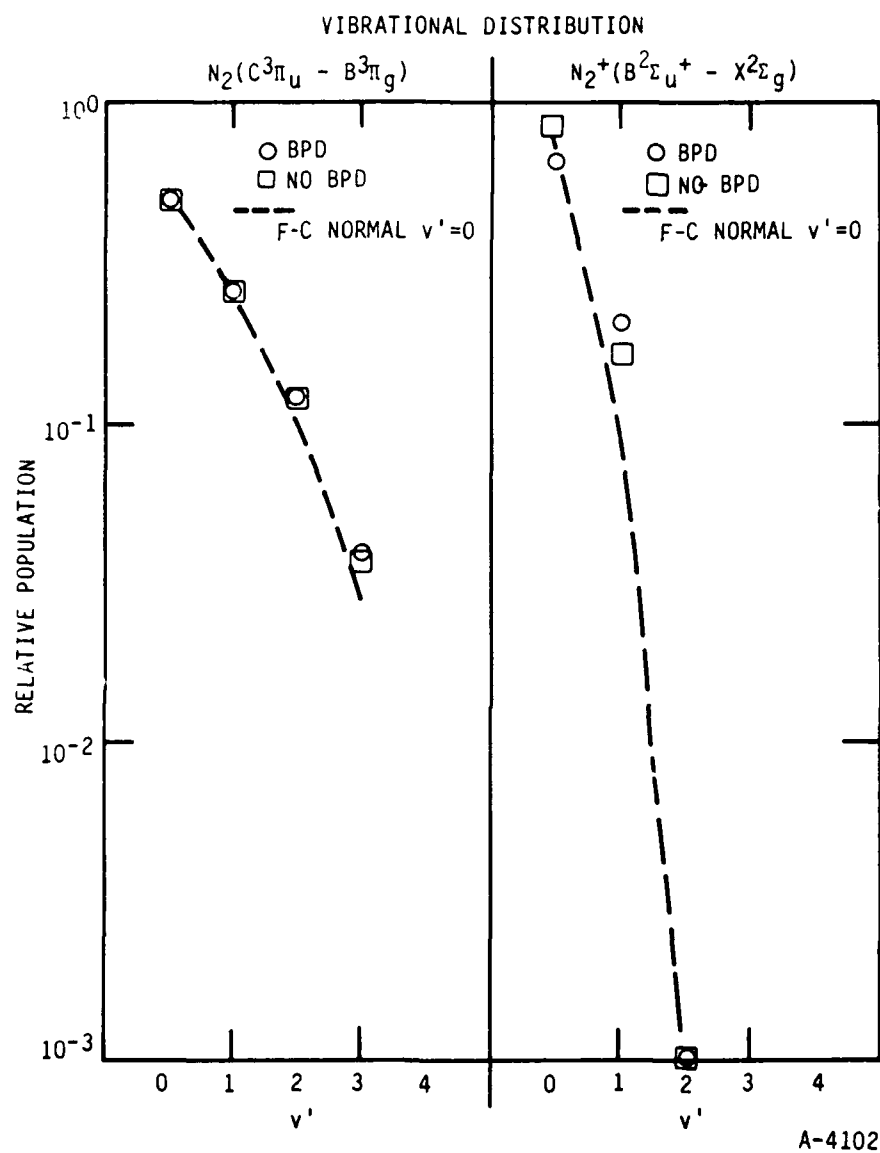


Figure 47. This figure presents the relative populations of upper state vibrational levels of the observed transitions with and without BPD operative, at a pressure of 1.2 mtorr. The distribution predicted by the relevant Franck-Condon factors is plotted for comparison.

is a hint that the vibrational population distribution is shifted to higher  $v'$ . This might be indicative of the target gas being vibrationally excited. Franck-Condon factors<sup>6</sup> would predict a  $v'=0$  to  $v'=1$  population ratio in  $N_2^+(B^2\Sigma_u^+)$  of 8.0, however, the data without BPD gives a ratio of  $\sim 4.5$  which drops to  $\sim 3.2$  when BPD is ignited. This discrepancy would imply that a combination of processes feed population to the  $N_2^+(B^2\Sigma_u^+)$  state or more likely that an underlying radiator has distorted the populations predicted by the spectral generation code. For  $N_2^+(B^2\Sigma_u^+)$ , it is interesting to compare the ratio of  $v'=0$  to  $v'=1$  populations at those two pressure extremes. At 1.2 mtorr  $n[N_2^+(B, v'=0)]/n[N_2^+(B, v'=1)]$  has been evaluated previously and is  $\sim 4.5$ . At 20 mtorr this ratio is  $\sim 4.4$ . Thus the expected invariance with pressure is achieved.

A comparison of low (1.2 mtorr) and high (20.0 mtorr) pressure population distributions without BPD is available from Figure 48. The F-C distributions (dashed lines) have been normalized to the low pressure  $v'=0$  data points. For  $N_2(C-B)$  the  $v'=0,1,2,3$  low pressure populations reproduce the F-C distribution nicely. The same is true for the  $N_2(C^3\Pi_u)$   $v'=0,1,2$  high pressure populations. The  $N_2(C^3\Pi_u)$   $v'=3$  population at 20 mtorr appears uncharacteristically high.

Figure 49 presents the ratio of total population in the  $N_2(C^3\Pi_u)$  state to the total population in the  $N_2^+(B^2\Sigma_u^+)$  state as calculated by the spectral generation code. At 1.2 mtorr without BPD operative, this ratio is 0.64 and jumps to a value of 0.82 when BPD is ignited. At 20 mtorr (non-BPD), this ratio has returned to a value of 0.69. The gain in intensity of the  $N_2(C^3\Pi_u-B^3\Pi_g)$  and  $N_2^+(B^2\Sigma_u^+-X^2\Sigma_g)$  bands was  $\sim 103$  and  $\sim 80$  respectively upon ignition of BPD at 1.2 mtorr pressure. The points to reiterate before proceeding to the next spectral region are that the relative populations of the  $N_2C$  and  $N_2^+B$  states are largely unaffected by the occurrence of BPD or pressure variations, and the magnitude of emission for both C and ionic B states increased approximately 100 fold upon BPD ignition.



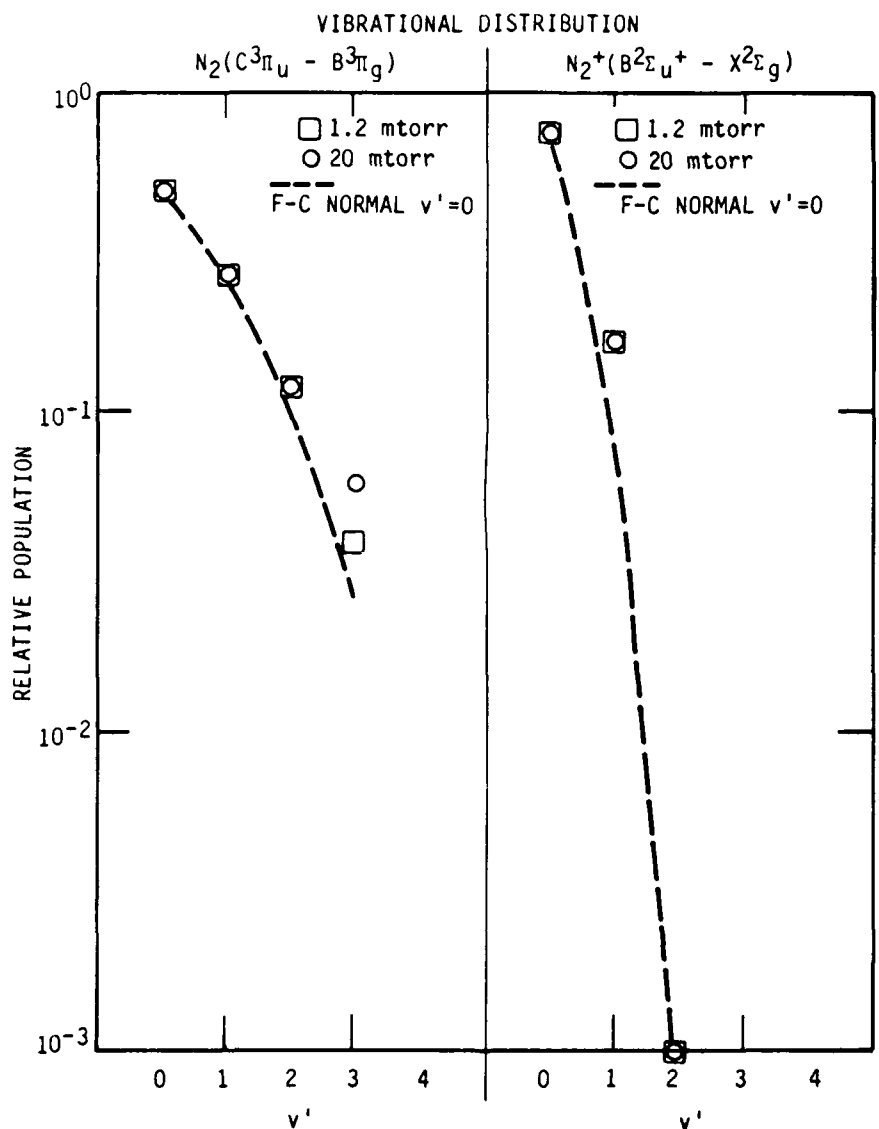
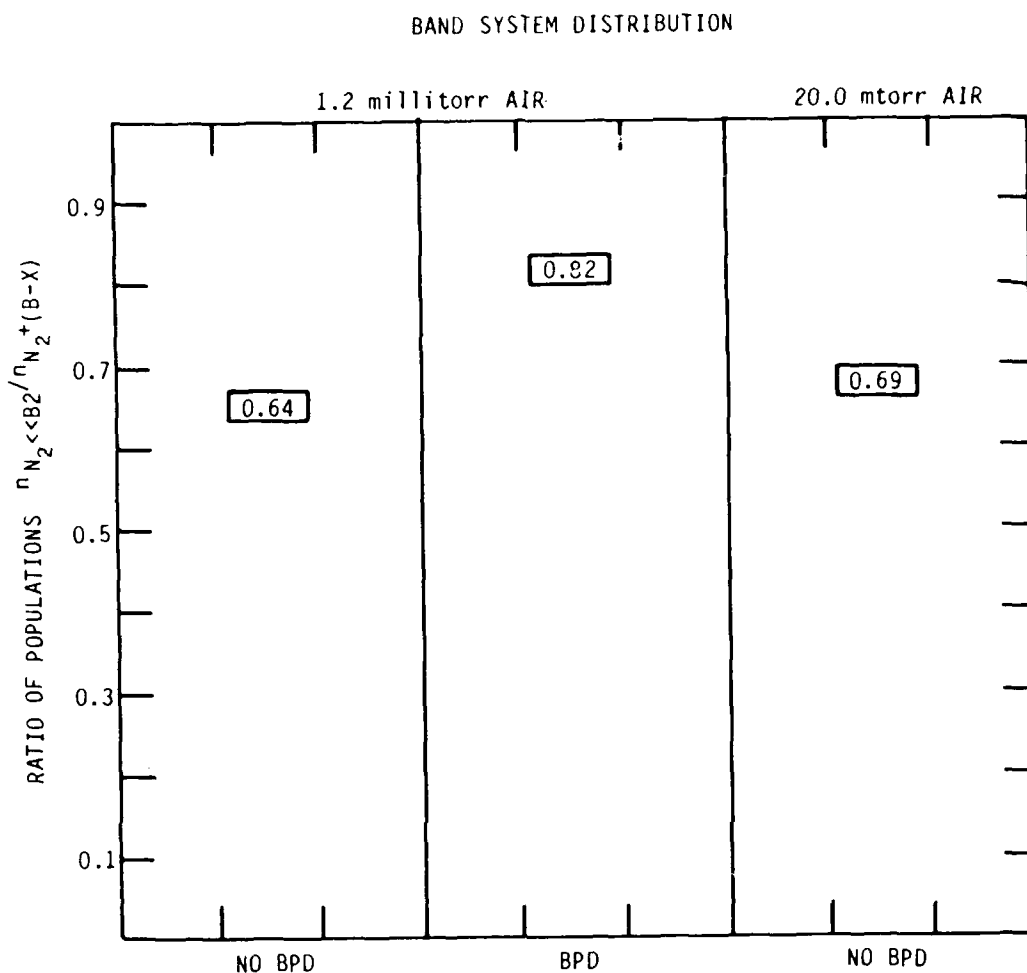


Figure 48. The low (1.2 mtorr) and high (20.0 mtorr) pressure (non-BPD) relative populations are presented and compared to the F-C distribution.

### 6.2.3 The 440 to 800 nm Region

In the 440 to 800 nm region data was collected at three sets of conditions: low pressure (1.2 mtorr) with and without BPD and at high pressure (20.0 mtorr) without BPD operative. The electron current in these experiments ranged from 12.0 to 12.9 mamp and the electron energy was held constant at 4500 eV. Low pressure gas flow was 176 sccm and high pressure gas flow was 387 sccm. The



A-4108

Figure 49. This figure presents the ratio of total populations of the  $N_2(C^3\Pi_u)$  state to that in the  $N_2(B^2\Sigma_u^+)$  state.

resolution of these experiments was 15.6Å. Figure 50a-c shows data sets, band system assignments, and the computer generated synthetic spectra. Every feature with a peak intensity above 5 percent is assignable to at least one of the following band systems:  $N_2^+(A-X)$ ,  $N_2^+(B-X)$ ,  $N_2(B-A)$ ,  $N_2(C-B)$ ,  $O_2^+(b-a)$ , and/or the OI1, NII, NII atomic/ionic multiplets. The overlap of  $O_2^+(b-a)$   $\Delta v=0$  and  $N_2(B-A)$   $\Delta v=4$  bands in the region between 570 and 620 nm makes discrete transition assignment very difficult. The assignments of the

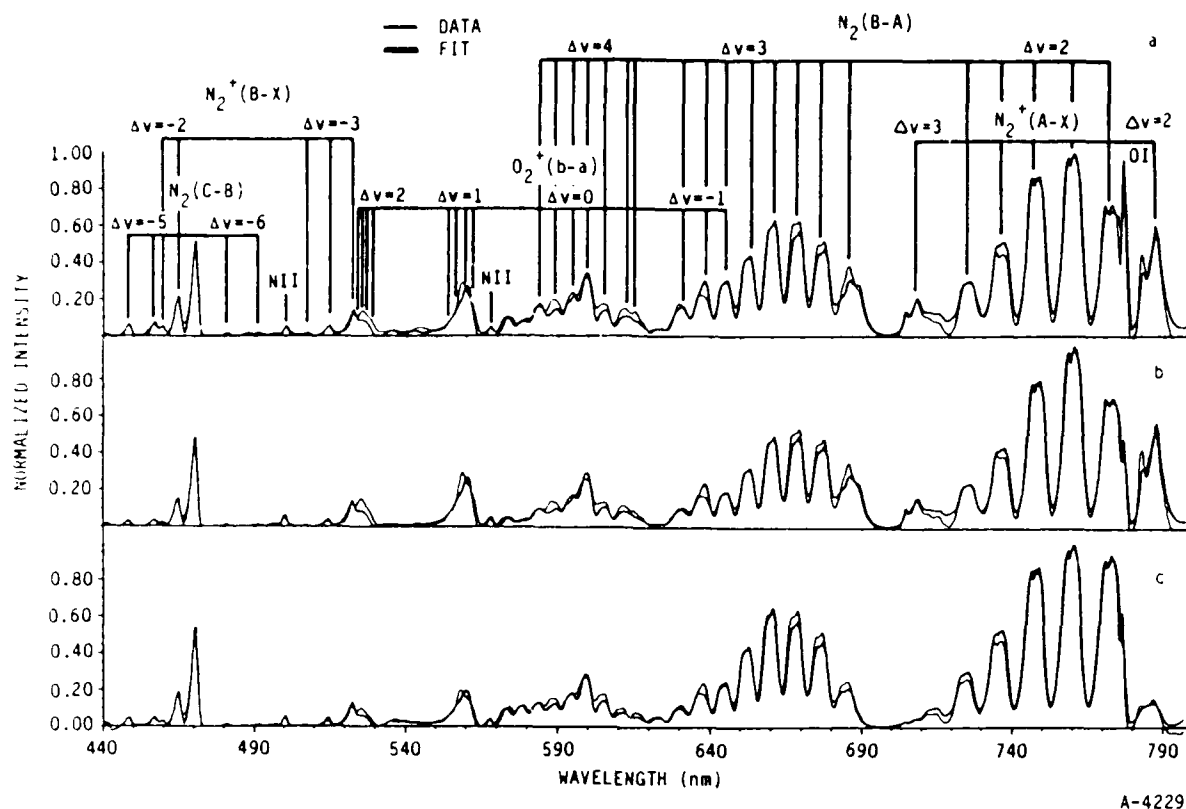


Figure 50. a) 1.2 mtorr BPD data, band assignments, synthetic spectrum  
 b) 1.2 mtorr non-BPD data, synthetic spectrum  
 c) 20 mtorr non BPD data and synthetic spectrum  
 All the data was taken at a resolution of 15.6Å.

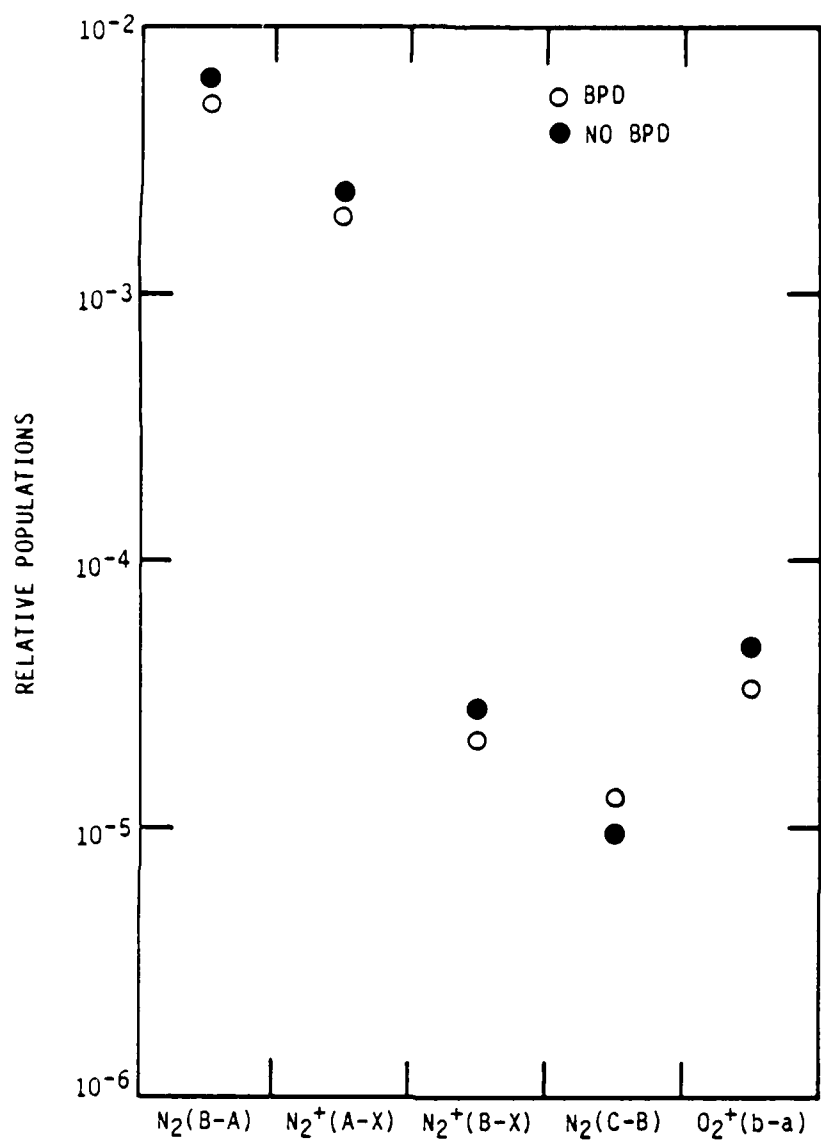
$O_2^+(b\ a)$  transitions was performed with the assistance of spectra taken by Fink and Welge.<sup>97</sup> (The band shapes are extraordinarily similar.) The synthetic spectrum reproduces the data very well and provides a high level of confidence in the band system assignments.

The First Negative system of  $O_2^+$  is a quartet system which cannot currently be created by the synthetic generation code. In this case, five singlet systems were generated, representing transitions originating from  $O_2^+(b)$   $v'=0$  to  $v'=4$ . The Einstein coefficients were calculated (for  $v'=0$  to 4,  $v''=0-7$ ) from the oscillator strengths of Erman and Larsson<sup>98</sup> using the band heads of Gattinger

and Jones.<sup>2</sup> To compensate for the lack of width of these singlet transitions, the temperature was artificially increased to 900 K. The band shapes are still not properly reproduced with this procedure. The intent of this process was to introduce spectral transitions representative of the observed  $O_2^+(b-a)$  features to improve the fit and allow more accurate determination of populations of states which have overlapping features with  $O_2^+(b-a)$  features. In this way the trends, as experimental conditions are varied, will be more accurately represented.

### 6.3 VARIATIONS WITH ELECTRON ENERGY DISTRIBUTION CHANGES

The populations determined by analysis of the spectra of Figure 50 are presented in Figure 51 which shows the relative populations of each observed band system before and after BPD was ignited in 1.2 mtorr of air. The intensity changes upon ignition of BPD is presented in Table 9. No band system showed a decrease in intensity and as suggested from Figure 51, the  $N_2(C^3\Pi_u-B^3\Pi_g)$  system underwent a larger increase in intensity than the other molecular band systems. In the 300 to 400 nm spectral region the increase upon ignition of BPD for  $N_2(C^3\Pi_u-B^3\Pi_g)$  was determined for the strongest transitions, and thus represents a more accurate determination. The nitrogen ion features increased approximately 20 percent less than the molecular systems. The oxygen atom feature increased 2.3 times more than the molecular features. The relative vibrational level populations at 1.2 mtorr with and without BPD are shown in Figures 52 and 53. In Figure 53 the dashed line represents the net effect of F-C excitation and  $N_2(C^3\Pi_u)$  and  $N_2(W^3\Delta_u)$  state radiative relaxation into the  $N_2(B^3\Pi_g)$  levels. For  $N_2(C^3\Pi_u)$   $v'=1,2$  the distribution is approximately F-C in form, both with and without BPD. The  $N_2(C^3\Pi_u)$   $v'=3$  level deviates from the F-C distribution. This arises due to the weak signal from that level. Recall, in the 300 to 400 nm region the  $N_2(C^3\Pi_u)$   $v'=1$  to  $v'=2$  population ratio was  $\sim 2.3$ ; here, the  $v'=1$  to  $v'=2$  population ratio is  $\sim 2.5$ . F-C factors predict this ratio to be 2.89. A review of pure nitrogen data gives a  $N_2(C^3\Pi_u)$   $v'=1$  to  $v'=2$  population ratio of  $\sim 2.7$ . This information is compiled in Table 10. For  $N_2^+(B^2\Sigma_u^+)$  the  $v'=2$  population is less reliable due



A-4109

Figure 51. Relative populations of band systems observed in the 440 to 800 nm spectral region without BPD, at a pressure of 1.2 mtorr of laboratory air.

to weak signal levels. Statistics for the  $v'=0/v'=1$  population ratio in  $N_2^+(B^2\Sigma_u^+)$  are compiled in Table 11. Also shown are the ratios measured in the 300 to 400 nm spectral region. The data consistently predicts a population shift to high  $v'$  levels of  $N_2^+(B^2\Sigma_u^+)$  when BPD is ignited. The pure  $N_2$  data agrees fairly well with the no-BPD air data in the 440 to 800 nm region.

TABLE 9. Emission intensity enhancements upon beam plasma discharge occurrence (1.2 mtorr).

System	Intensity Change Ignition of BPD	
NII (5004Å)	58	
NII (5680Å)	61	
O <sub>2</sub> <sup>+</sup> (b-a)	66	
N <sub>2</sub> (B-A)	74	
N <sub>2</sub> <sup>+</sup> (B-X)	75	80*
N <sub>2</sub> <sup>+</sup> (A-X)	86	
N <sub>2</sub> (C-B)	125	103*
OI (7773Å)	177	
*increase in 300-400 nm region		

Both data sets show the  $v'=0/v'=1$  N<sub>2</sub><sup>+</sup>(B<sup>2</sup>Σ<sub>u</sub><sup>+</sup>) population ratio to be around 6.1, significantly lower than predicted by F-C factors. The poor agreement with no-BPD air data in the 300 to 400 nm spectral region is not explicable. Transitions originating from  $v'=2,3,4$  for the N<sub>2</sub><sup>+</sup>(A-X) band system were observed. The ratio of vibrational level populations is computed in Table 12. The N<sub>2</sub><sup>+</sup>(A<sup>2</sup>Π)  $v'=4/v'=2$  population ratios are all in excellent agreement. The discrepancy in the  $v'=3/v'=2$  population ratio most likely arises due to the additional overlap of the O<sub>2</sub><sup>+</sup>(b-a) 0-2 transition at 6822Å to the already crowded N<sub>2</sub><sup>+</sup>(A-X) 3-0 and N<sub>2</sub>(B-A) 3-0 transitions between 6800 and 6900Å.

The N<sub>2</sub>(B-A) First Positive are by far the dominant spectra features throughout this region. Figure 53 shows the B-state vibrational distributions for the air data with and without BPD at 1.2 mtorr, and pure N<sub>2</sub> data without BPD at 1.0 mtorr. The dashed line represents the F-C excitation factors coupled with radiative relaxation processes from the N<sub>2</sub>(C,W) states which feed population

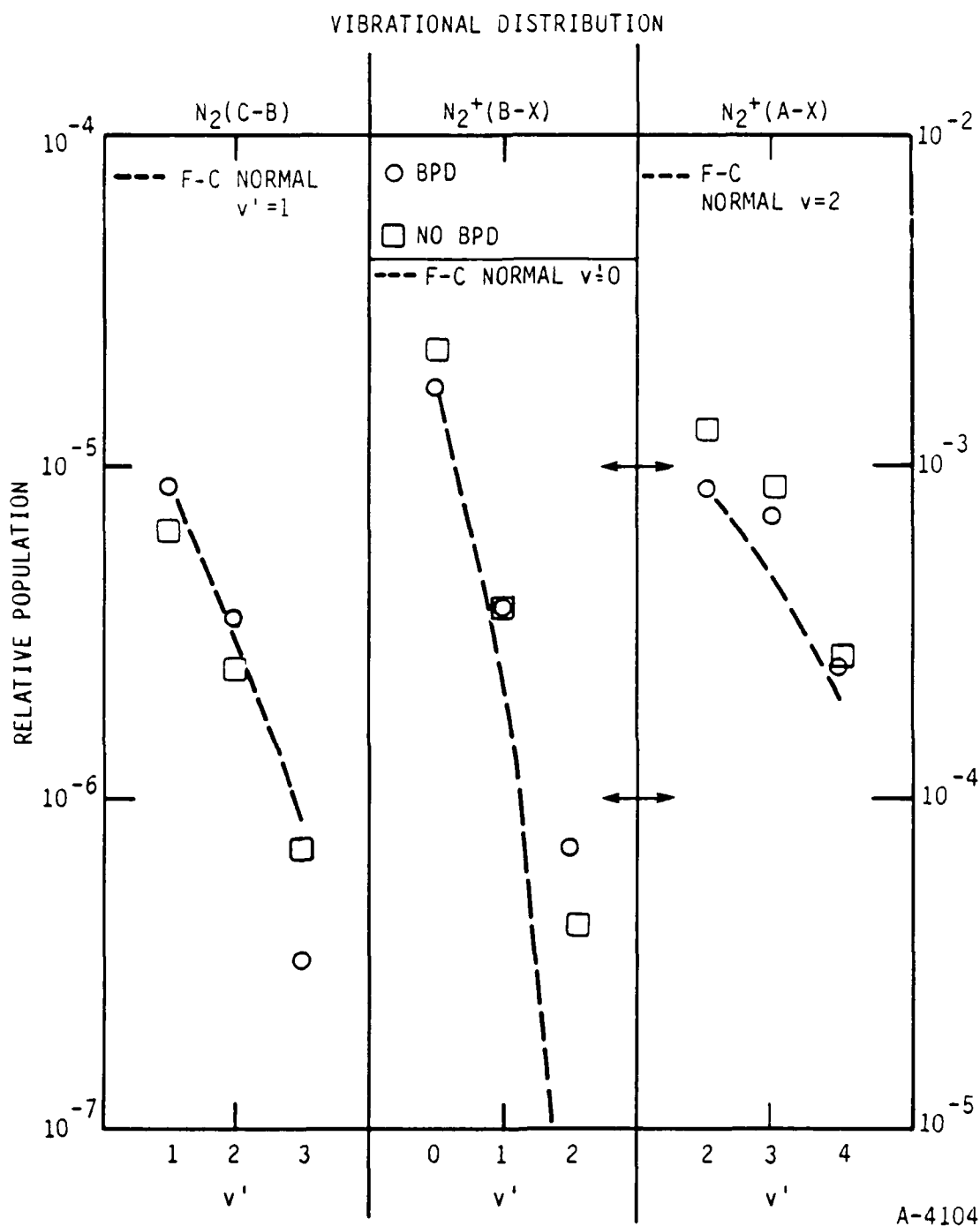
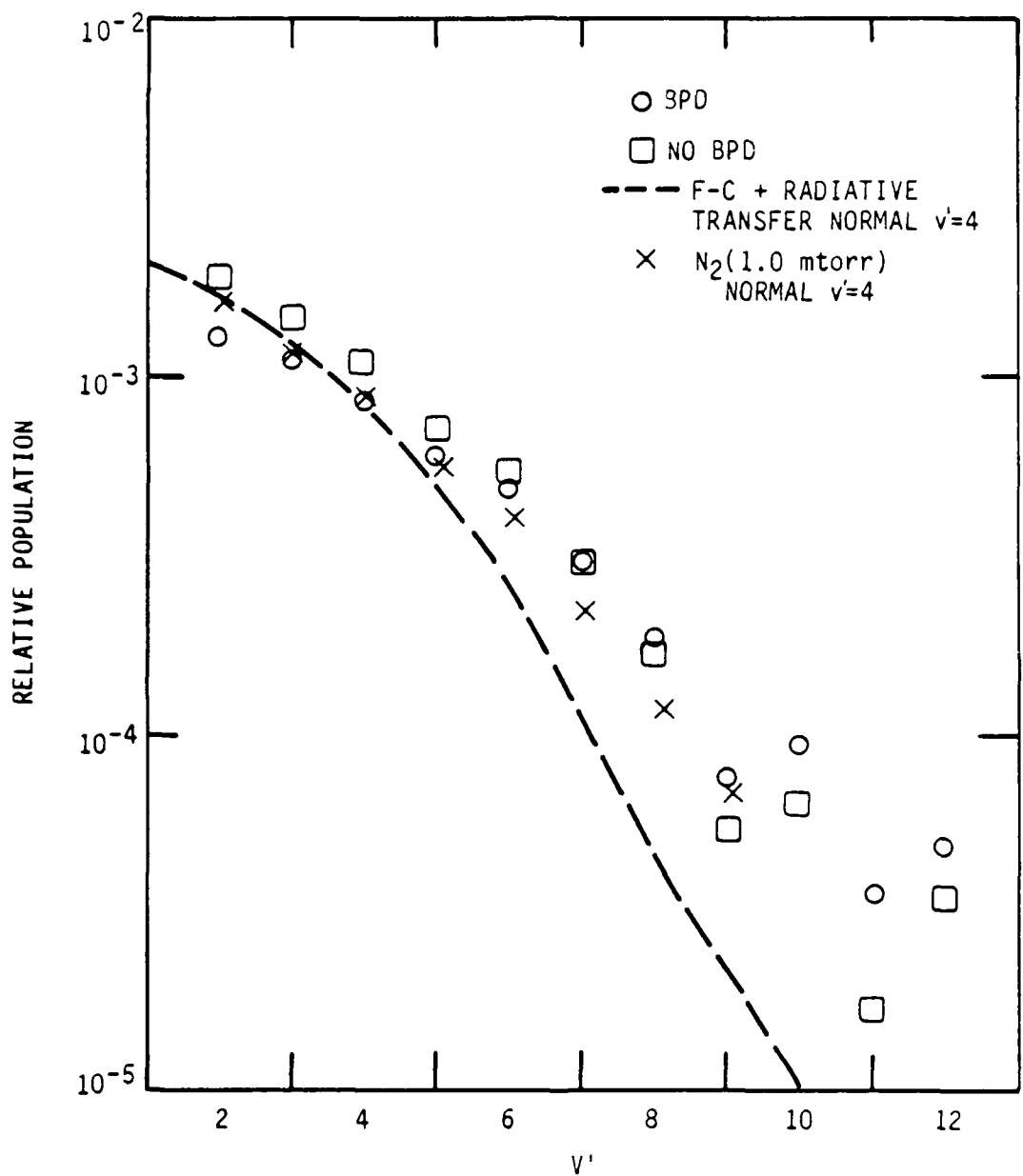


Figure 52. Relative vibrational populations of the observed band systems  $N_2(C-B)$ ,  $N_2^+(B-X)$ ,  $N_2^+(A-X)$  at a pressure of 1.2 mtorr with and without BPD operative.



A-4107

Figure 53. Relative vibrational population of the N<sub>2</sub>(B-A) band system for 1.2 mtorr air and 1.0 mtorr N<sub>2</sub>. The dashed line includes FCF's and radiative relaxation processes from N<sub>2</sub>(C,W) states into the N<sub>2</sub>(B) levels.



TABLE 10. Populations of  $N_2(C^3\Pi_u)$ ,  $v'=0,1$  states for a variety of low pressure experiments.

Population Ratio $N_2(C^3\Pi_u)$ $v'=1/v'=2$	Conditions	Gas/Pressure (mtorr)	Spectral Region (nm)
2.5	BPD	Air (1.2)	440-800
2.5	no-BPD	Air (1.2)	440-800
2.3	BPD	Air (1.2)	300-400
2.3	no-BPD	Air (1.2)	300-400
2.7	-	$N_2$ (1.0)	-
2.89	FCF <sup>6</sup>	-	-

Table 11. Populations of  $N_2^+(B^2\Sigma_u^+)$ ,  $v'=1,2$  states for a variety of low pressure experiments.

Population Ratio $N_2^+(B^2\Sigma_u^+)$ $v'=1/v'=2$	Conditions	Gas/Pressure (mtorr)	Spectral Region (nm)
6.1	no-BPD	Air (1.2)	440-800
4.7	BPD	Air (1.2)	440-800
4.5	no-BPD	Air (1.2)	300-400
3.2	BPD	Air (1.2)	300-400
6.2	-	$N_2$ (1.0)	300-450
8.0	FCF <sup>6</sup>	-	-

into the  $N_2(B)$  state. The  $N_2$  (1.0 mtorr) and air (1.2 mtorr) distributions without BPD are in excellent agreement. Once again the ignition of BPD has slightly shifted the population to larger  $v'$ .

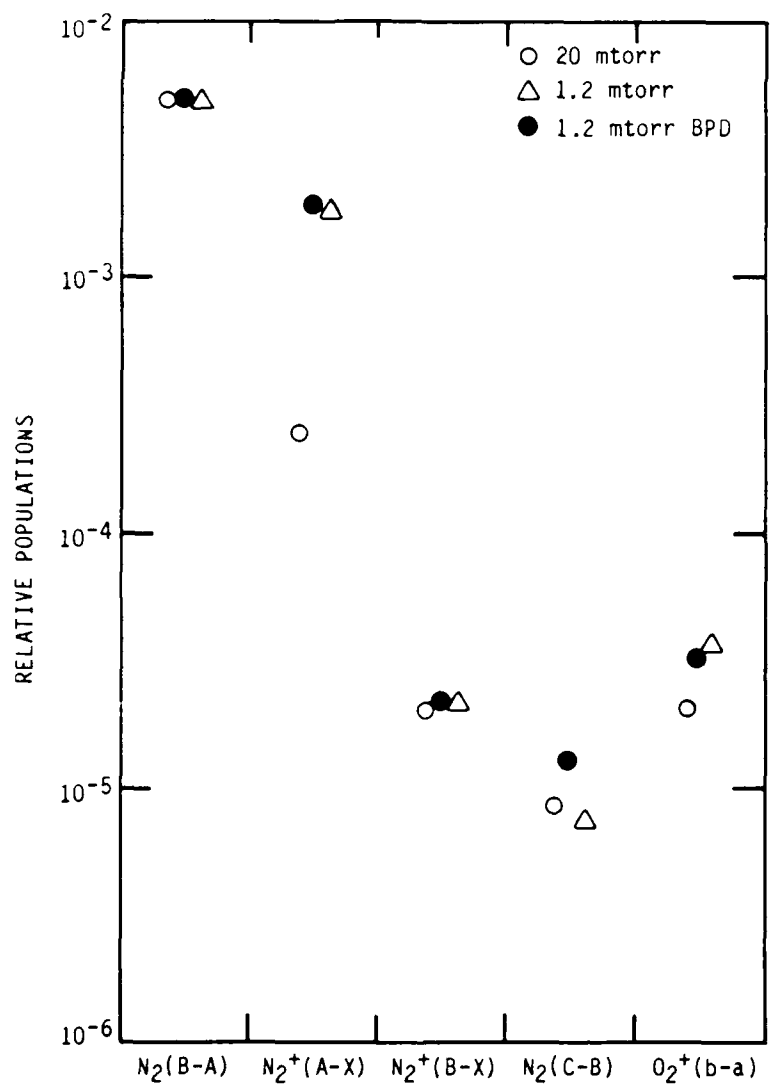
TABLE 12. Populations of  $N_2^+(A^2\Pi_u, v'-2,3,4)$  states for a variety of low pressure experiments.

Population Ratio $N_2^+(A^2\Pi_u)$		Conditions	Gas/Pressure (mtorr)	Spectral Region (nm)
$v'=3/v'=2$	$v'=4/v'=2$			
0.70	0.23	no-BPD	Air (1.2)	440-800
0.82	0.28	BPD	Air (1.2)	440-800
0.51	0.26	-	$N_2$ (1.0)	500-850
0.52	0.23	FCF <sup>6</sup>		

#### 6.4 PRESSURE DEPENDENCIES

The next set of comparisons to be made will focus on the effect of increasing the pressure from 1.2 to 20.0 mtorr, as shown in Figure 54. The data is normalized with respect to the  $N_2(B-A)$  relative population. It is clear that both  $N_2^+(B-X)$  and  $N_2(C-B)$  undergo approximately the same change as does  $N_2(B-A)$  upon this pressure increase, but  $N_2^+(A-X)$  and to a lesser extent  $O_2^+(b-a)$  undergo a decrease upon this pressure increase. Table 13 shows the magnitude of the signal intensity change upon increasing the pressure. Every system gained signal by increasing the pressure. The  $O_2^+(b-a)$  and  $N_2^+(A-X)$  systems gained less than did the other systems. The third column of Table 13 show the effective power dependence of signal intensity on pressure based on these two pressures for each observed band system. A power dependence of  $p^{1.3}$  is observed in pure  $N_2^{99}$  based on a prompt emitting state which undergoes no feed or quenching. The  $N_2C$  fits the specification.  $O_2^+b$  and  $N_2^+A$  are quenched at 20 mt pressure.

Figures 55 and 56 show the relative vibrational distributions at these two pressures. For  $N_2(C-B)$  the distributions, both 1.2 and 20.0 mtorr, are



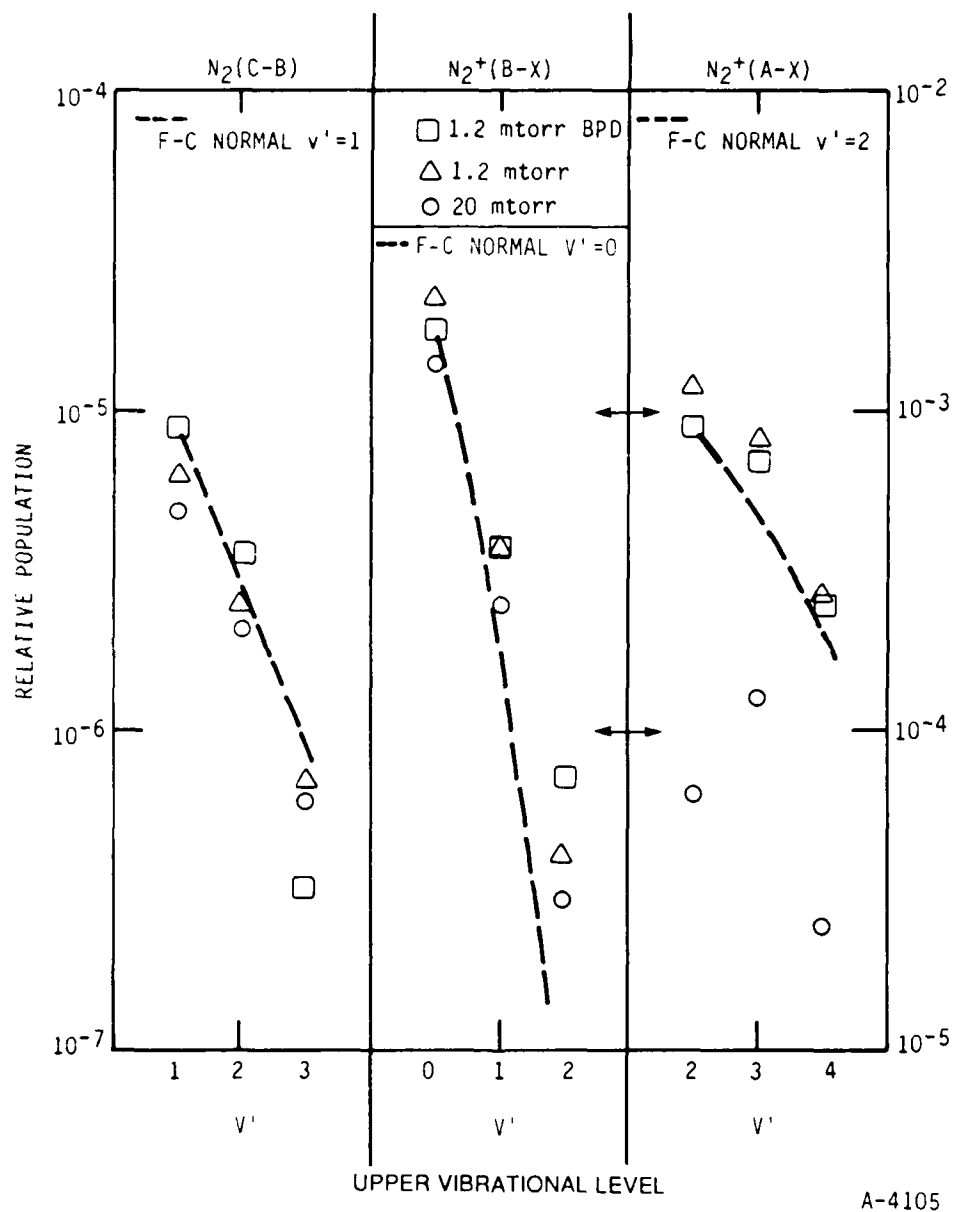
A-4110

Figure 54. Band system distribution at 1.2 mtorr and 20.0 mtorr pressures of air, normalized to the  $N_2(B-A)$  relative population.

TABLE 13. Pressure scaling of emission features.

System	Signal Gain Upon the Pressure Rise from 1.2 mtorr to 20.0 mtorr	X Assuming $I \propto p^X$
N <sub>2</sub> (C-B)	37.0	1.3
N <sub>2</sub> (B-A)	31.0	1.2
O I (7773Å)	30.0	1.2
N <sub>2</sub> <sup>+</sup> (B-X)	29.0	1.2
N II (5004Å)	24.0	1.1
N II (5680Å)	21.0	1.1
O <sub>2</sub> <sup>+</sup> (b-a)	18.0	1.0
N <sub>2</sub> <sup>+</sup> (A-X)	4.4	0.53

within experimental uncertainty equal to the distribution predicted by Franck-Condon factors. Recall, the N<sub>2</sub>(C-B)  $v'=3$  population is more uncertain due to weak signal levels. The population distribution for N<sub>2</sub>(C<sup>3</sup>Π<sub>u</sub>) in pure N<sub>2</sub> has been determined to be Franck-Condon in form. For N<sub>2</sub><sup>+</sup>(B-X) the  $v'=2$  population is more uncertain due to weak signal levels. The N<sub>2</sub><sup>+</sup>(B<sup>2</sup>Σ<sub>u</sub><sup>+</sup>)  $v'=0$  to  $v'=1$  population ratio at various conditions is compiled in Table 14. The 1.2 mtorr, 20 mtorr air (440 to 800 nm spectral region) and 1 mtorr N<sub>2</sub> values are in excellent agreement ( $\pm 10$  percent), but differ from the predicted Franck-Condon ratio by about 36 percent. The N<sub>2</sub><sup>+</sup>(B<sup>2</sup>Σ<sub>u</sub><sup>+</sup>)  $v'=0$  to  $v'=1$  population ratios measured in the 300 to 400 nm region at 1.2 and 20 mtorr of air agree well with each other but are  $\sim 25$  percent low of the values measured in the 440 to 800 nm region. In the case of N<sub>2</sub><sup>+</sup>(A-X) the distributions at low and high pressures of air are dramatically different. It is clear that N<sub>2</sub><sup>+</sup>(A<sup>2</sup>Π)  $v'=2,4$  are reduced significantly more than is  $v'=3$ . The N<sub>2</sub><sup>+</sup>(A<sup>2</sup>Π)  $v'=2-4$  quenching rate coefficients in pure N<sub>2</sub> are  $7.0 \pm 0.4$ ,  $7.5 \pm 1.0$ , and  $7.0 \pm 1.0 \times 10^{-10}$  cm<sup>3</sup> molecule<sup>-1</sup> s<sup>-1</sup>,



A-4105

Figure 55. Upper vibrational level distributions in air at 1.2 and 20.0 mtorr pressures for the  $N_2(C-B)$ ,  $N_2^+(B-X)$ ,  $N_2^+(A-X)$  band systems. The dashed lines are predictions of F-C factors.

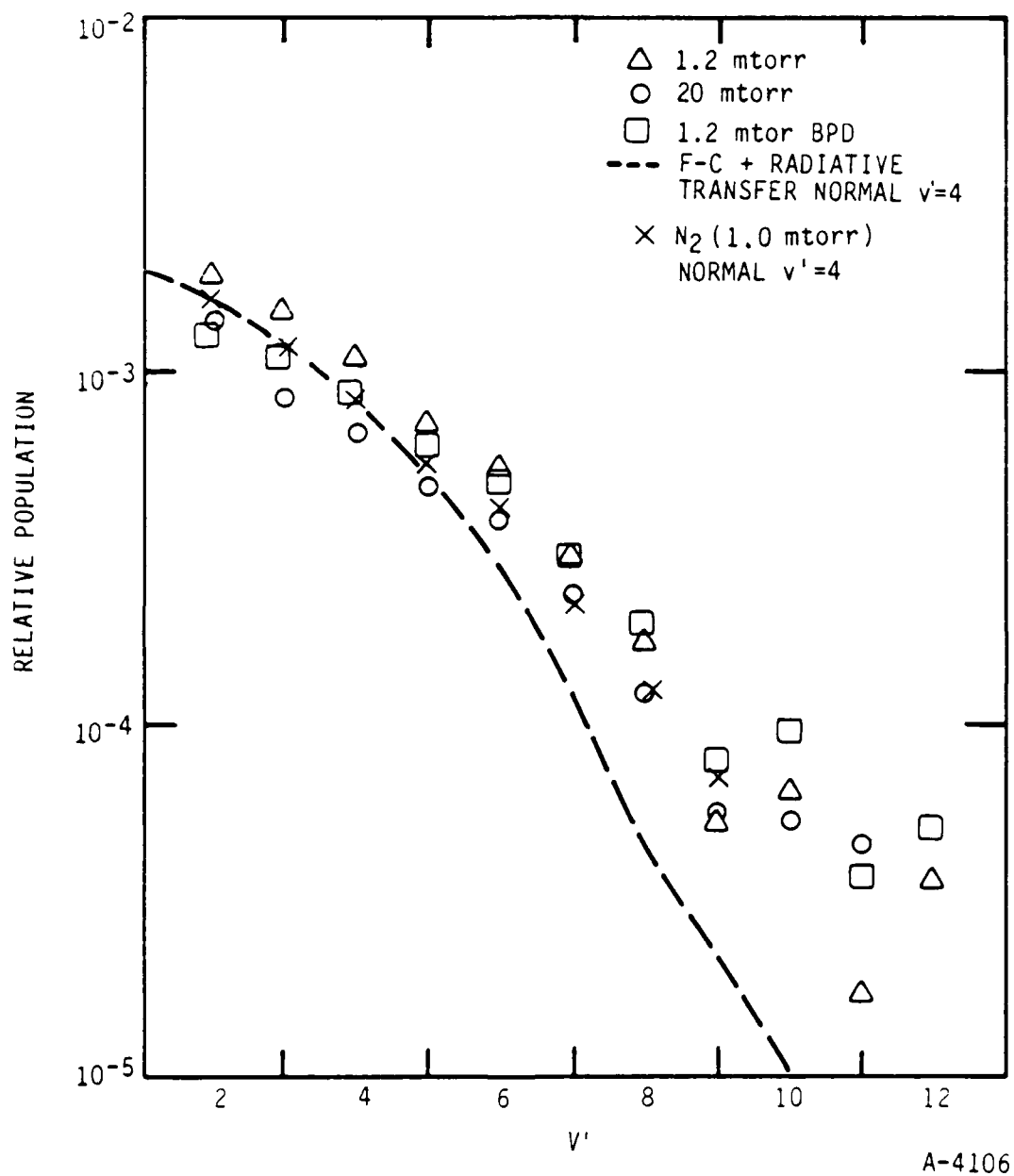


Figure 56. Relative populations in the  $N_2(B)$  state at 1.2 and 20.0 mtorr of air, 1.0 mtorr  $N_2$  and a prediction from radiative transfer and F-C factors.

TABLE 14. Pressure scaling of  $N_2^+B$  distributions.

$N_2^+(B^2\Sigma_u^+)$ State Population Ratio $v'=0$ to $v'=1$	Gas (Pressure)	Spectral Region (nm)
6.1	Air (1.2 mtorr)	440-800
5.6	Air (20.0 mtorr)	440-800
4.5	Air (1.2 mtorr)	300-400
4.4	Air (20.0 mtorr)	300-400
6.2	$N_2$ (1 mtorr)	-
8.0	FCF <sup>6</sup>	

respectively<sup>10</sup> suggesting in this data the anomalously large relative population in  $N_2^+(A^2\Pi)$   $v'=3$  is an artifact of multiple radiators and overlapping spectral features. Certainly the overlap of the (3-1) Meinel band with the (3-0) First Positive feature complicated previous analysis of this system. Additional underlying features due to oxygen further cloud an accurate determination here. Figure 56 shows the relative population distribution of  $N_2(B,v')$  levels at 1.2 and 20.0 mtorr of air, 1.0 mtorr  $N_2$  and the radiative transfer/Franck-Condon factor prediction. The 1.2 mtorr air and 1.0 mtorr  $N_2$  distributions are in relatively good agreement. The 20 mtorr air distribution shows some small deviations from the low pressure data. These deviations can be attributed to both quenching and population distortion by underlying radiators.

## 6.5 CONCLUSIONS

These experiments were aimed at determining the effect of  $O_2$  on altering electronic state production and distributions in electron-irradiated mixtures. Clear evidence of  $O_2^+$  First Negative and atomic lines were obtained. A comparison of  $N_2$  and  $N_2^+$  emissions from air and from pure  $N_2$  show no dramatic

differences or energy repartitioning. The presence of oxygen merely adds spectral features across the visible region.



## 7. EXPERIMENTAL DETERMINATION OF THE EINSTEIN COEFFICIENTS FOR THE $N_2(B-A)$ TRANSITION

### 7.1 INTRODUCTION

Several years ago we observed that the rate coefficient for exciting  $NO(A^2\Sigma^+)$  in the electronic energy transfer reaction between  $N_2(A^3\Sigma_u^+)$  and  $NO$  was apparently about 40 percent larger than the total quenching rate coefficient.<sup>100</sup> A detailed error analysis indicated that the most likely reason for this discrepancy was that the accepted value for the lifetime of  $N_2(A^3\Sigma_u^+)$  was too short.<sup>101</sup> Further investigation revealed that the accepted experimental value of  $N_2(A)$  lifetime was based upon Shemansky and Carleton's<sup>102</sup> analysis of Carleton and Oldenberg's<sup>103</sup> experimental determination of the absolute photon emission rate of the 0,6 Vegard-Kaplan band coupled with a determination of the absolute number density of  $N_2(A, v'=0)$  by an absorption measurement on the 1,0 band of the first-positive system of nitrogen. Knowing the population in the emitting state and the absolute photon-emission rate allows one to calculate the Einstein coefficient for the transition. This analysis hinges, then, upon knowing the transition probability of the 1,0 first-positive band accurately. Recent theoretical calculations indicate that the value used for the 1,0 B $\rightarrow$ A transition probability is quite likely to be 25-40 percent too large.<sup>32,65,104</sup> We thus felt it imperative to reinvestigate the transition probabilities of the  $N_2(B - A)$  system experimentally.

The currently accepted experimental values for the  $N_2(B-A)$  Einstein coefficients rests upon the relative variation in the transition moment as a function of  $r$ -centroid as measured by Shemansky and Broadfoot<sup>13</sup> tied to the lifetime of the  $v'=3$  level of  $N_2(B)$  which they also determined by measuring real-time decays following excitation of  $N_2$  by a pulsed electron beam. The results from this procedure are consistent with the recent theoretical calculations for vibrational levels above  $v'=3$ . The Einstein coefficients from the three lowest vibrational levels of  $N_2(B)$ , however, result from extrapolations of the transition-moment curve well outside the region of the measurements used

to establish it. We thus undertook to re-determine the relative transition moment variation as a function of  $r$ -centroid, using a procedure similar to that used by Shemansky and Broadfoot, but with measurements extending much farther to the long-wavelength side of the curve.

The  $r$ -centroid approximation was first put forth by Fraser<sup>105</sup> and has been used extensively over the last three decades to describe the Einstein coefficients of a large number of molecular systems. The intensity of a molecular emission is given by

$$I_{v',v''} = N_{v'} A_{v',v''} \quad (17)$$

where  $N_{v'}$  is the number density in the upper-state vibrational level and  $A_{v',v''}$  is the Einstein coefficient which is

$$A_{v',v''} = \frac{64\pi^4 \nu_{v',v''}^3}{3h} |\langle v' | R_e(r) | v'' \rangle| \quad (18)$$

Here  $\nu_{v',v''}$  is the transition frequency in  $\text{cm}^{-1}$ , the integral is of the wave functions over the electric dipole-moment operator, and the constants have their usual meanings. Fraser showed that this matrix element could be separated reasonably well into two parts. One part represents the overlap of the wavefunctions of the two levels with each other, and is called the Franck-Condon factor. Fraser showed that the other, the electronic transition moment, could generally be represented adequately by a function (usually polynomial or exponential) of the  $r$ -centroid. This quantity is defined as

$$\bar{r}_{v',v''} = \frac{\langle v' | r | v'' \rangle}{\langle v' | v'' \rangle} \quad (19)$$

by measuring the relative intensities of a number of bands with a common upper vibrational level, one can map out how the electronic transition moment varies with r-centroid. For a given band intensity we have

$$I_{v',v''} = \frac{64\pi^4 \nu_{v',v''}^3}{3h} N_{v'} q_{v',v''} |R_e(\bar{r})|^2 \quad (20)$$

where the Franck-Condon factor is

$$q_{v',v''} = |\langle v' | v'' \rangle|^2 \quad (21)$$

Ratioing measured band intensities to the product of the Franck-Condon factor times the cube of the transition frequency then gives a set of reduced intensities which should vary one from the other in the same way that the electronic transition moment varies with r-centroid:

$$\frac{I_{v',v}/q_{v',v} \nu_{v',v}^3}{I_{v',v''}/q_{v',v''} \nu_{v',v''}^3} = \frac{|R_e(\bar{r}_{v',v})|^2}{|R_e(\bar{r}_{v',v''})|^2} \quad (22)$$

We have measured the intensities of a number of first-positive bands over the wavelength region between 500 and 1700 nm. This set of sequences covers the  $\Delta v=6$  through  $\Delta v=2$  sequences and encompasses an r-centroid range between about 1.2 and 1.7 Å.

## 2.2 EXPERIMENTAL

Three different monochromator/detector systems and three different excitation sources were used in these studies. This allowed us to make careful cross checks of the data in the regions of spectral overlap. In addition, different

excitation sources emphasize the formation of different vibrational levels. This allowed matching the source to the most appropriate wavelength region.

One system consisted of looking at the excitation of nitrogen, at pressures on the order of a few millitorr, by a high energy electron beam of 4.5 kV and about 15 mA. A 0.3 m monochromator with an S-1 photomultiplier was used for these observations which spanned a spectral region between 570 and 1050 nm, or the  $\Delta v=4$  through  $\Delta v=0$  sequences of the nitrogen first-positive system. This system, the LABCEDE facility at AFGL, has been described in detail previously in this report.

The second system which emphasized the short-wavelength region of the spectrum, consisted of a 0.5 m monochromator coupled to a thermoelectrically cooled photomultiplier with a GaAs photocathode. It covered the spectral region between 500 and 850 nm, covering principally the  $\Delta v=6$  through  $\Delta v=2$  sequences of the first-positive system. The excitation source in this instance was atomic nitrogen recombination in a He/N<sub>2</sub> discharge afterglow. This source tends to emphasize excitation of the highest levels of N<sub>2</sub>(B).

The third system employed a 0.5 m monochromator with an intrinsic Ge detector. This system covered the spectral region between 700 and 1700 nm, covering the  $\Delta v=2$  through  $\Delta v=-2$  sequences of the nitrogen first-positive system. In this instance, the excitation source was a low pressure (0.1-20 Torr), low power (10-20 Watts) microwave-discharge lamp in nitrogen.

All systems were calibrated for relative spectral response against a standard quartz-halogen lamp. In the latter two systems, the light from the lamp was reflected off a BaSO<sub>4</sub> screen into the entrance slit of the monochromator in order to ensure that the optics were filled. The BaSO<sub>4</sub> screen is uniformly reflecting to within  $\pm 2$  percent between 300 and 1300 nm.<sup>106,107</sup> The drop off in reflectivity beyond 1300 nm is only a few percent, but was included in the calculation of the calibration curves. The relative response of the latter two systems was cross checked by comparison with the O/NO air afterglow

continuum. Good agreement with published air afterglow intensities was found in the region between 400 and 650 nm,<sup>108-110</sup> but not in the infrared.<sup>111,112</sup> We further checked our response function with a second quartz-halogen lamp and with a 1250 K black body. We think that most published values for the air afterglow intensities in the infrared are erroneous. Recent observations by Bradburn and Lilienfeld<sup>113</sup> over this same spectral region result in a similar conclusion.

The procedure, therefore, was to scan the first-positive spectra over the appropriate spectral region under several different sets of conditions.

### 7.3 RESULTS

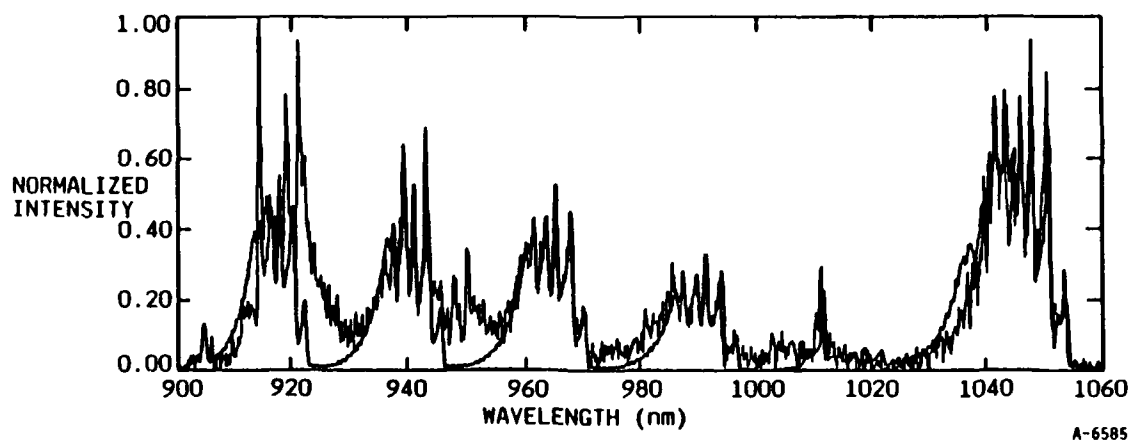
The individual band intensities were determined with the use of the PSI spectral fitting code. This code enables the determination of vibronic level number densities from the resolved emission spectra of diatomic molecules, even when there is significant overlap of the features of interest with other bands. The general procedure involves calculating synthetic spectra whose magnitudes correspond to unit population for the bands of interest. The populations of these emitters are then adjusted in a linear least-squares fitting routine in order to best reproduce the observed spectrum. The synthetic spectra were calculated at the instrumental resolution and assumed a Boltzmann distribution of rotation levels best matching the observed rotational contours. The band intensities were calculated from effective populations determined from fitting spectral regions containing only one band from the level of interest, i.e., fitting individual band sequences.

Often significant spectral overlap occurs between bands of interest and others. Generally bands from higher vibrational levels of the  $\Delta v=n-1$  sequence overlap with the lower vibrational levels in the  $\Delta v=n$  sequence. This problem is particularly severe for the  $\Delta v=+3, 2, 1, 0$  sequences. The infrared afterglow system ( $B'^3\Sigma_u^- - B^3\Pi_g$ ) and several sets of atomic-nitrogen lines contaminate the microwave discharge spectra. The infrared afterglow system also

affects the atom-recombination data. In addition, overlap with  $\Delta v=n-1$  first-positive bands is particularly severe in these data due to the larger relative populations of the high  $v'$  levels. The  $N_2^+$  Meinel bands ( $A^2\Pi_u-X^2\Sigma_g^+$ ) are strong in electron-impact excitation spectra.

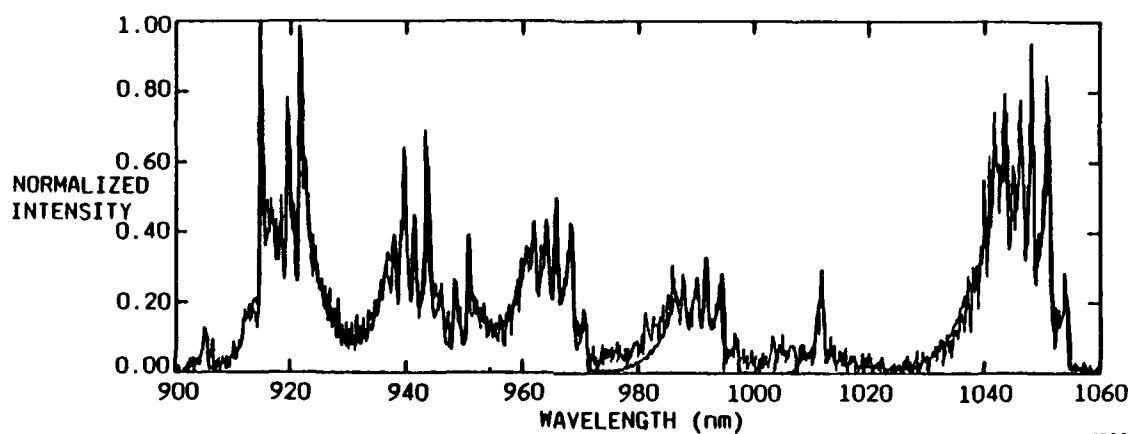
Where such overlap occurs, it's extent determined the strategy used to fit the spectrum. In instances where the overlap is only partial, the code determined the populations of all emitting species directly. Where more complete overlap is present or where bands from more than one system overlap those of interest, populations of the contaminating species were estimated by fitting adjacent regions of the spectrum where more reliable estimates could be made. These populations were then used to generate a synthetic spectrum that was computer subtracted from the data, thus reducing the overlap. Number densities were not used in instances where the relevant feature coincides with another band of comparable or greater intensity or is severely overlapped with a significant band for which no independent population estimate could be made.

Figures 57 to 59 illustrate the power of the spectral fitting procedure. They show successive approximations in the fitting of the  $\Delta v=0$  sequence in the data taken on LABCEDE. In Figure 57 only the  $v'=0-5$  levels of  $N_2(B)$  and some atomic lines were included in the fit. Large discrepancies are evident in the fit, particularly around 920 and 950 nm. These regions contain the 1,0 and 2,1 Meinel bands. Including the Meinel bands in the fit gives the result displayed in Figure 58. The region between 910 and 950 nm now is fit excellently in addition to some improvement at 1040 nm. Some problems still exist at 970 to 980 nm and between 1000 and 1010 nm. The 7,8 and 6,7 first-positive bands appear in these regions. Estimating their intensities from fits at shorter wavelengths, and subtracting the estimates from the experimental spectrum gives the result in Figure 59. We now see that the entire spectral region is fit excellently, and we can be confident our fits will result in accurate intensity determinations.



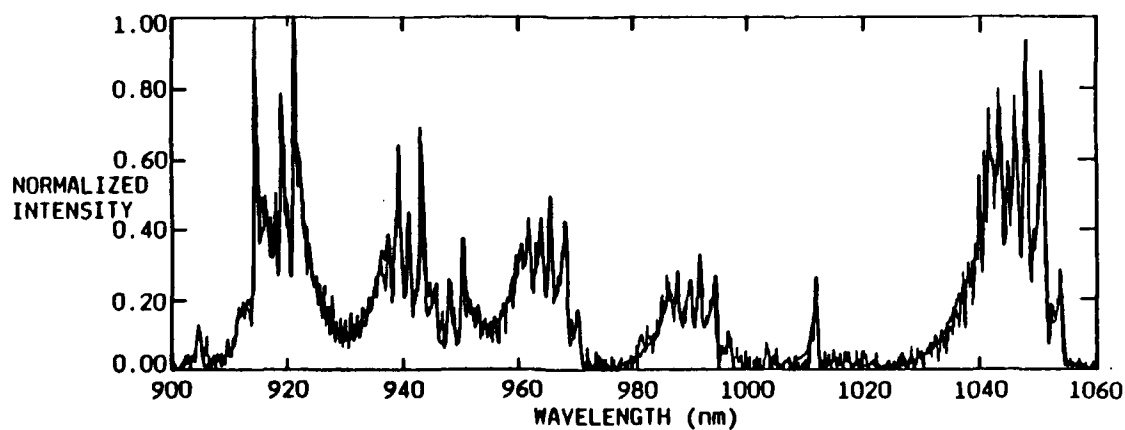
A-6585

Figure 57.  $\Delta v = 0$  sequence fit for  $N_2(B-A)$  and atomic lines.



A-6586

Figure 58.  $\Delta v = 0$  sequence fit for  $N_2(B-A)$ ,  $N_2^+(A-X)$ , and atomic lines.



A-6584

Figure 59.  $\Delta v = 0$  sequence fit for  $N_2(B-A)$ ,  $N_2^+(A-X)$ , atomic lines with estimated contributions from other  $N_2(B-A)$  sequences subtracted out.

We note that systematic errors are possible in this analysis, particularly when subtraction was performed since the particular Einstein coefficients determine the magnitudes of the spectra to be subtracted.<sup>114</sup> In regions of the spectrum where such subtraction has the potential to produce significant errors, there is overlap of data using at least two excitation methods that produce spectra with markedly different characteristics. Thus systematic errors should be manifest as differing trends in the  $R_e(\bar{r})$  curves from the different data. The lack of these discrepancies is evidence for the absence of such errors.

The  $r$ -centroids and Franck-Condon factors necessary for the evaluation of the reduced intensities and the construction of the  $R_e(\bar{r})$  curve were calculated using the procedure outlined previously<sup>115</sup>. Rydberg-Klein-Rees potentials were first calculated for both electronic states using the spectroscopic constants of Roux et al.<sup>116</sup> and the approach of Tellinghuisen<sup>117</sup>. The numerical eigenfunctions were then evaluated using the Numerov-Cooley procedure<sup>118</sup> to solve the radial Schrodinger equation. The overlap integrals in the  $r$ -centroid and Franck-Condon factor calculations were evaluated using Simpson's Rule.

The reduced intensities were averaged for all spectra taken with a given excitation method. A total of four spectra were analyzed for the discharge data, three for the atom-recombination data, and two for the data taken with the LABCEDE facility. The data were then combined to form the relative transition moment curve by minimizing the sum of the squares of the differences of each  $v'$  sequence from the analytical expression which best represented all the data. In practice, we determined the best fit of a given analytical form to one  $v'$  sequence, e.g.,  $v'=2$  or  $v'=10$ , and then adjusted each of the other  $v'$  sequences to obtain the minimum least squares deviation from that analytical expression. We then recomputed the best fit analytical expression to the adjusted  $v'$  sequences. This defines a new line, and the individual  $v'$  sequences were adjusted to match this line best. Generally, after several iterations, none of the  $v'$  sequences could be adjusted significantly to



improve the fit between all of the data and the analytical form which best represented them.

We tried both linear and quadratic expressions to represent  $R_e$  as a function of  $\bar{r}_{v',v''}$ . The fitting procedure showed the quadratic term not to be statistically significant. The best linear fit was

$$R_e(\bar{r}_{v',v''}) = (1.67 \pm 0.04) - (0.654 \pm 0.030) \bar{r}_{v',v''} \quad (23)$$

Figure 60 shows the relationship between this line and the experimental data.

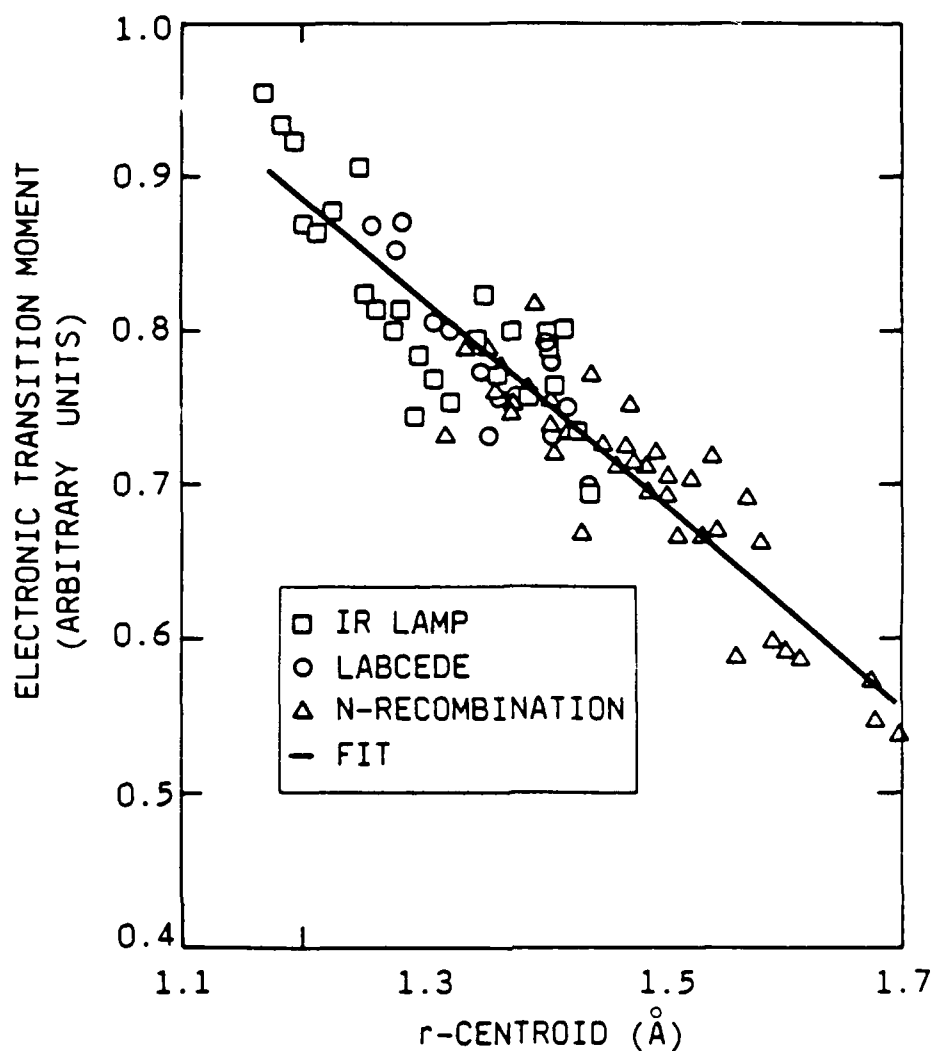
The relative transition-moment curve shown in Figure 60 was placed upon an absolute basis by multiplying it by the average of the ratio

$$\frac{1/\tau_{v'}}{\sum_{v''} q_{v',v''} v_{v',v''}^3 \left| R_e(\bar{r}_{v',v''}) \right|_{\text{rel}}^2} = (1.89 \pm 0.03) \times 10^{-7} \quad (24)$$

for  $v'=5-12$ . We used the radiative lifetimes of Eyler and Pipkin<sup>119</sup> in the normalization. In principle, these should be the most accurate values because they were determined by laser-induced fluorescence in a molecular beam under collision-free conditions. We note, however, that this set of lifetimes appear to be 10-15 percent shorter than those determined in the most reliable of the other experimental<sup>36,120,121</sup> or theoretical studies.<sup>32,65,104</sup>

#### 7.4 DISCUSSION

Table 15 compares lifetimes calculated from the present results with those of Shemansky and Broadfoot<sup>13</sup> as well as the recent measurements of Eyler and Pipkin<sup>119</sup> and the theoretical calculations of Werner et al.<sup>32</sup> In the final column we list the theoretical results of Werner et al. scaled to match the lifetimes of Eyler and Pipkin. The scaling involved fitting Werner et al.'s



A-8234

Figure 60. Variation in the electron-transition moment with r-centroid for the  $N_2$  first-positive system.

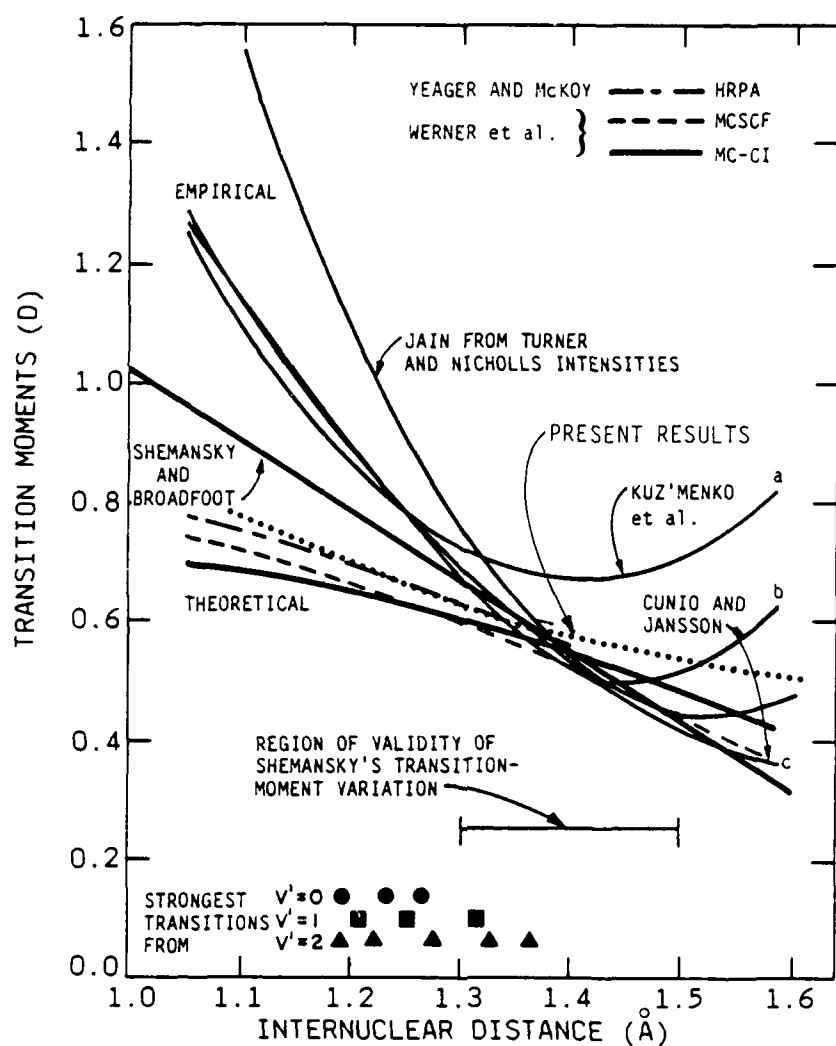
transition-moment variation to a quadratic function. This quadratic function was then used as a relative  $R_e$  function to calculate relative transition probabilities. The relative probabilities were then made absolute by applying the procedure given by Eq. (24). This resulted in a 9 percent increase in Werner et al.'s transition-moment curve at every point. This scaling procedure results in a set of lifetimes which agree excellently with the ones we have calculated. The maximum discrepancy is about 5 percent for the lowest vibrational levels.

TABLE 15.  $N_2(B^3\Pi_g)$  lifetimes in microseconds.

$v'$	This Work	Shemansky and Broadfoot <sup>13</sup>	Eyler and Pipkin <sup>119</sup>	Werner, Kalcher and Reinsh <sup>32</sup>	Werner et al. Scaled
0	12.1	8.9		13.4	11.6
1	9.7	7.8		11.0	9.2
2	8.5	7.0		9.3	8.1
3	7.3	6.5		8.2	6.9
4	6.5	6.1		7.3	6.3
5	5.9	5.8	5.9 $\pm$ 0.2	6.6	5.7
6	5.5	5.5	5.3 $\pm$ 0.2	6.2	5.3
7	5.1	5.3	5.0 $\pm$ 0.2	5.8	5.0
8	4.8	5.1	4.7 $\pm$ 0.2	5.5	4.7
9	4.5	5.0	4.4 $\pm$ 0.2	5.2	4.5
10	4.3	4.8	4.3 $\pm$ 0.2	5.0	4.3
11	4.1	4.7	4.2 $\pm$ 0.2	4.9	4.2
12	4.0	4.6	4.1 $\pm$ 0.2	4.8	4.2

Figure 61 compares our transition-moment function with other proposed transition-moment functions, both experimental<sup>120,122-125</sup> and theoretical.<sup>32,65,104</sup> Our results clearly agree moderately well, both in terms of slope and magnitude, with the various theoretical calculations. Previous empirical estimates, however deviate markedly from our results.

Our results indicate a lifetime for  $N_2(B, v'=0,1)$  that is at least 36 and 24 percent longer, respectively, than that given by Shemansky and Broadfoot. The discrepancy could be even greater since Shemansky and Broadfoot's values for the highest vibrational levels are 10-15 percent longer than ours. Scaling their results down accordingly would lead to a discrepancy of about 40 percent.



A-2156b

Figure 61. Electronic transition moments for  $N_2(B^3\Pi_g - A^3\Sigma_u^+)$ .

This 25-40 percent discrepancy in the lifetime for  $N_2(B, v'=1)$  is in keeping with our expectations based upon our analysis of the  $N_2(A)$  lifetime issue.

Table 16 summarizes our results completely. It gives  $r$ -centroids, Franck-Condon factors, the electronic transition moment in Debye and the Einstein coefficients for all important transitions in the nitrogen first-positive bands.

TABLE 16. Einstein coefficients and associated data for the nitrogen first-positive system.

$v' = 0$	$v''$	wavelength	$Qv'v''$	$r(v'v'')$	$Re(r)$	Branching	$Av'v''$
		nm		Angstroms	Debye	Ratio	$s^{-1}$
	0	1046.94	0.3987	1.253	0.661	0.5766	4.756E+04
	1	1231.72	0.3222	1.215	0.680	0.3031	2.500E+04
	2	1489.53	0.1732	1.183	0.696	0.0966	7.966E+03
	3	1874.06	0.0691	1.154	0.711	0.0202	1.664E+03
	4	2508.56	0.0251	1.126	0.725	0.0032	2.620E+02
	5	3752.82	0.0081	1.098	0.739	0.0003	2.621E+01
	6	7293.42	0.0025	1.070	0.753	0.0000	1.138E+00
	7	94436.64	0.0008	1.045	0.766	0.0000	1.649E-04
		FCF sum=	0.9996			$Av'v''$ sum=	8.248E+04
						lifetime=	1.212E-05
$v' = 1$	$v''$						
	0	888.35	0.4104	1.297	0.638	0.7243	7.481E+04
	1	1017.92	0.0032	1.315	0.629	0.0037	3.802E+02
	2	1187.83	0.1585	1.227	0.674	0.1304	1.347E+04
	3	1420.21	0.1888	1.191	0.692	0.0959	9.902E+03
	4	1756.99	0.1276	1.161	0.707	0.0357	3.692E+03
	5	2288.41	0.0648	1.134	0.721	0.0085	8.817E+02
	6	3250.67	0.0287	1.110	0.733	0.0014	1.409E+02
	7	5521.57	0.0114	1.086	0.745	0.0001	1.175E+01
	8	17407.73	0.0042	1.063	0.757	0.0000	1.431E-01
		FCF sum=	0.9976			$Av'v''$ sum=	1.033E+05
						lifetime=	9.682E-06
$v' = 2$	$v'' =$						
	0	773.21	0.1557	1.348	0.612	0.3353	3.962E+04
	1	869.55	0.2737	1.309	0.632	0.4417	5.218E+04
	2	990.59	0.0690	1.258	0.658	0.0816	9.642E+03
	3	1147.12	0.0230	1.249	0.663	0.0178	2.099E+03
	4	1357.25	0.1264	1.202	0.686	0.0633	7.473E+03
	5	1653.94	0.1430	1.170	0.703	0.0414	4.896E+03
	6	2104.11	0.1026	1.142	0.717	0.0150	1.776E+03
	7	2867.47	0.0573	1.117	0.730	0.0034	4.058E+02
	8	4442.93	0.0280	1.095	0.741	0.0005	5.496E+01
	9	9588.11	0.0126	1.073	0.752	0.0000	2.535E+00
		FCF sum=	0.9913			$Av'v''$ sum=	1.182E+05
						lifetime=	8.464E-06

TABLE 16. Continued.

$v' = 3$	$v'' =$	wavelength	$Qv'v''$	$r(v'v'')$	$Re(r)$	Branching	$Av'v''$
		nm		Angstroms	Debye	Ratio	s-1
	0	685.85	0.0311	1.408	0.582	0.0743	1.024E+04
	1	760.59	0.2843	1.356	0.608	0.5443	7.500E+04
	2	851.61	0.0958	1.323	0.625	0.1380	1.901E+04
	3	964.79	0.1526	1.271	0.651	0.1642	2.262E+04
	4	1109.23	0.0054	1.198	0.688	0.0043	5.884E+02
	5	1299.79	0.0418	1.218	0.678	0.0199	2.748E+03
	6	1562.50	0.1073	1.181	0.697	0.0311	4.288E+03
	7	1947.50	0.1092	1.151	0.712	0.0171	2.353E+03
	8	2565.31	0.0788	1.125	0.726	0.0056	7.708E+02
	9	3716.99	0.0474	1.102	0.737	0.0011	1.574E+02
	10	6614.82	0.0248	1.082	0.747	0.0001	1.501E+01
	11	27571.11	0.0120	1.063	0.757	0.0000	1.029E-01
		FCF sum=	0.9905			$Av'v''$ sum=	1.378E+05
						lifetime=	7.257E-06
$v' = 4$	$v'' =$						
	0	617.32	0.0038	1.468	0.551	0.0101	1.541E+03
	1	677.23	0.0971	1.413	0.579	0.2152	3.292E+04
	2	748.46	0.2964	1.366	0.603	0.5275	0.069E+04
	3	834.49	0.0075	1.367	0.603	0.0096	1.471E+03
	4	940.41	0.1514	1.282	0.646	0.1557	2.382E+04
	5	1073.89	0.0509	1.235	0.670	0.0378	5.783E+03
	6	1247.13	0.0022	1.272	0.651	0.0010	1.508E+02
	7	1480.78	0.0552	1.193	0.691	0.0166	2.547E+03
	8	1812.72	0.0943	1.161	0.707	0.0162	2.484E+03
	9	2320.85	0.0901	1.135	0.720	0.0077	1.174E+03
	10	3194.72	0.0653	1.111	0.733	0.0022	3.372E+02
	11	5047.68	0.0406	1.090	0.743	0.0004	5.472E+01
	12	11601.26	0.0226	1.070	0.753	0.0000	2.578E+00
		FCF sum=	0.9774			$Av'v''$ sum=	1.530E+05
						lifetime=	6.537E-06
$v' = 5$	$v'' =$						
	0	562.17	0.0003	1.504	0.533	0.0010	1.707E+02
	1	611.42	0.0168	1.478	0.546	0.0407	6.883E+03
	2	668.89	0.1684	1.421	0.575	0.3455	5.842E+04
	3	736.77	0.2444	1.378	0.597	0.4042	6.835E+04
	4	818.13	0.0105	1.330	0.621	0.0137	2.323E+03
	5	917.32	0.0956	1.296	0.639	0.0938	1.585E+04
	6	1040.83	0.0951	1.249	0.663	0.0687	1.162E+04
	7	1198.67	0.0086	1.191	0.692	0.0044	7.502E+02
	8	1407.28	0.0143	1.215	0.680	0.0044	7.440E+02
	9	1695.46	0.0598	1.173	0.701	0.0112	1.892E+03
	10	2118.86	0.0809	1.144	0.716	0.0081	1.367E+03
	11	2800.76	0.0736	1.120	0.728	0.0033	5.571E+02
	12	4079.41	0.0539	1.098	0.739	0.0008	1.361E+02
	13	7339.16	0.0343	1.079	0.749	0.0001	1.527E+01
	14	32830.76	0.0202	1.061	0.758	0.0000	1.029E-01
		FCF sum=	0.9767			$Av'v''$ sum=	1.691E+05
						lifetime=	5.914E-06

TABLE 16. Continued.

$v' = 6$	$v'' =$	wavelength	$Qv'v''$	$r(v'v'')$	$Re(r)$	Branching	$Av'v''$
		nm		Angstroms	Debye	Ratio	s-1
	0	516.84	0.0000	1.601	0.484	0.0000	6.917E+00
	1	558.17	0.0016	1.543	0.513	0.0042	7.606E+02
	2	605.68	0.0381	1.487	0.542	0.0863	1.579E+04
	3	660.81	0.2293	1.431	0.570	0.4430	8.105E+04
	4	725.52	0.1561	1.390	0.591	0.2448	4.479E+04
	5	802.47	0.0580	1.321	0.626	0.0754	1.380E+04
	6	895.42	0.0352	1.314	0.630	0.0333	6.097E+03
	7	1009.82	0.1043	1.261	0.656	0.0748	1.369E+04
	8	1153.91	0.0392	1.218	0.678	0.0201	3.683E+03
	9	1340.78	0.0000	1.200	0.687	0.0000	1.636E-01
	10	1592.42	0.0255	1.188	0.694	0.0052	9.529E+02
	11	1949.06	0.0599	1.156	0.710	0.0070	1.279E+03
	12	2492.80	0.0713	1.131	0.722	0.0041	7.537E+02
	13	3421.41	0.0621	1.109	0.734	0.0014	2.618E+02
	14	5362.46	0.0460	1.088	0.744	0.0003	5.185E+01
	15	11930.70	0.0307	1.070	0.753	0.0000	3.219E+00
FCF sum=			0.9573			$Av'v''$ sum=	1.830E+05
						lifetime=	5.465E-06

$v' = 7$	$v'' =$			$r(v'v'')$	$Re(r)$	Branching	$Av'v''$
		wavelength	$Qv'v''$				
	0	478.94	0.0000	1.700	0.434	0.0000	1.020E-01
	1	514.23	0.0001	1.641	0.464	0.0002	3.174E+01
	2	554.28	0.0043	1.564	0.503	0.0101	2.002E+03
	3	600.10	0.0729	1.495	0.538	0.1546	3.060E+04
	4	652.99	0.2650	1.441	0.565	0.4817	9.536E+04
	5	714.67	0.0748	1.407	0.582	0.1101	2.180E+04
	6	787.46	0.1064	1.337	0.618	0.1318	2.610E+04
	7	874.60	0.0031	1.300	0.637	0.0030	5.893E+02
	8	980.66	0.0817	1.275	0.649	0.0579	1.146E+04
	9	1112.43	0.0674	1.233	0.671	0.0349	6.910E+03
	10	1280.29	0.0103	1.183	0.696	0.0038	7.461E+02
	11	1501.12	0.0042	1.180	0.698	0.0010	1.896E+02
	12	1804.22	0.0326	1.170	0.703	0.0043	8.598E+02
	13	2245.28	0.0556	1.142	0.717	0.0040	7.920E+02
	14	2944.79	0.0607	1.118	0.729	0.0020	3.964E+02
	15	4220.86	0.0529	1.098	0.739	0.0006	1.206E+02
	16	7275.87	0.0397	1.079	0.749	0.0001	1.813E+01
	17	24268.39	0.0269	1.062	0.758	0.0000	3.388E-01
FCF sum=			0.9586			$Av'v''$ sum=	1.980E+05
						lifetime=	5.051E-06

TABLE 16. Continued.

$v' = 8$	$v'' =$	wavelength	$Qv'v''$	$r(v'v'')$	$Re(r)$	Branching	$Av'v''$
		nm		Angstroms	Debye	Ratio	s-1
	0	446.80	0.0000	1.800	0.383	0.0000	7.219E-04
	1	477.36	0.0000	1.700	0.434	0.0000	6.508E-02
	2	511.69	0.0003	1.643	0.463	0.0006	1.253E+02
	3	550.49	0.0102	1.572	0.499	0.0227	4.769E+03
	4	594.67	0.1102	1.506	0.532	0.2216	4.655E+04
	5	645.40	0.2724	1.452	0.560	0.4738	9.952E+04
	6	704.19	0.0201	1.436	0.568	0.0277	5.819E+03
	7	773.07	0.1282	1.349	0.612	0.1551	3.259E+04
	8	854.78	0.0046	1.300	0.637	0.0045	9.367E+02
	9	953.19	0.0450	1.290	0.642	0.0320	6.714E+03
	10	1073.83	0.0769	1.245	0.665	0.0410	8.606E+03
	11	1224.98	0.0326	1.206	0.684	0.0124	2.606E+03
	12	1419.59	0.0009	1.200	0.687	0.0002	4.405E+01
	13	1679.12	0.0106	1.189	0.693	0.0016	3.374E+02
	14	2041.85	0.0353	1.153	0.711	0.0031	6.582E+02
	15	2583.39	0.0516	1.129	0.723	0.0023	4.915E+02
	16	3476.93	0.0536	1.108	0.734	0.0010	2.156E+02
	17	5225.32	0.0459	1.089	0.744	0.0003	5.584E+01
	18	10157.87	0.0350	1.072	0.752	0.0000	5.931E+00
FCF sum=			0.9333			$Av'v''$ sum=	2.100E+05
						lifetime=	4.761E-06

$v' = 9$	$v'' =$	wavelength	$Qv'v''$	$r(v'v'')$	$Re(r)$	Branching	$Av'v''$
		nm		Angstroms	Debye	Ratio	s-1
	0	419.23	0.0000	2.000	0.281	0.0000	2.023E-02
	1	446.02	0.0000	1.900	0.332	0.0000	1.950E-01
	2	475.84	0.0000	1.800	0.383	0.0000	1.153E+00
	3	509.22	0.0006	1.675	0.446	0.0013	2.982E+02
	4	546.80	0.0191	1.583	0.493	0.0401	8.910E+03
	5	589.40	0.1559	1.514	0.528	0.2998	6.661E+04
	6	638.04	0.2471	1.463	0.554	0.4121	9.158E+04
	7	694.07	0.0002	1.400	0.586	0.0003	6.120E+01
	8	759.24	0.1198	1.363	0.605	0.1413	3.140E+04
	9	835.89	0.0291	1.299	0.637	0.0286	6.347E+03
	10	927.24	0.0136	1.280	0.647	0.0101	2.239E+03
	11	1037.81	0.0661	1.258	0.658	0.0361	8.033E+03
	12	1174.19	0.0524	1.221	0.677	0.0209	4.651E+03
	13	1346.30	0.0122	1.179	0.698	0.0034	7.644E+02
	14	1569.91	0.0005	1.174	0.701	0.0001	1.831E+01
	15	1871.55	0.0158	1.169	0.703	0.0017	3.739E+02
	16	2299.71	0.0358	1.141	0.717	0.0021	4.753E+02
	17	2953.31	0.0466	1.119	0.729	0.0014	3.013E+02
	18	4070.46	0.0470	1.099	0.739	0.0005	1.193E+02
	19	6405.63	0.0407	1.082	0.747	0.0001	2.713E+01
	20	13929.36	0.0320	1.066	0.755	0.0000	2.120E+00
FCF sum=			0.9345			$Av'v''$ sum=	2.222E+05
				156		lifetime=	4.500E-06



TABLE 16. Continued.

$v' = 10$	$v'' =$	wavelength nm	$Qv'v''$	$r(v'v'')$ Angstroms	$Re(r)$ Debye	Branching Ratio	$Av'v''$ s-1
	0	395.32	0.0000	2.100	0.231	0.0000	1.620E-03
	1	419.05	0.0000	2.000	0.281	0.0000	1.688E-01
	2	445.27	0.0000	1.900	0.332	0.0000	3.920E-03
	3	474.37	0.0000	1.800	0.383	0.0000	5.170E+00
	4	506.82	0.0015	1.676	0.446	0.0031	7.185E+02
	5	543.21	0.0327	1.593	0.488	0.0651	1.524E+04
	6	584.26	0.1981	1.525	0.522	0.3633	8.506E+04
	7	630.90	0.2063	1.475	0.548	0.3304	7.736E+04
	8	684.28	0.0101	1.400	0.586	0.0145	3.395E+03
	9	745.93	0.0902	1.377	0.598	0.1040	2.435E+04
	10	817.83	0.0590	1.317	0.628	0.0570	1.335E+04
	11	902.66	0.0003	1.300	0.637	0.0002	4.842E+01
	12	1004.09	0.0423	1.273	0.650	0.0237	5.545E+03
	13	1127.34	0.0590	1.233	0.671	0.0248	5.812E+03
	14	1280.00	0.0292	1.200	0.687	0.0088	2.064E+03
	15	1473.65	0.0031	1.149	0.713	0.0007	1.546E+02
	16	1726.80	0.0030	1.198	0.688	0.0004	8.664E+01
	17	2070.94	0.0185	1.154	0.711	0.0014	3.302E+02
	18	2564.48	0.0339	1.130	0.723	0.0014	3.296E+02
	19	3329.09	0.0417	1.110	0.733	0.0008	1.906E+02
	20	4628.34	0.0417	1.092	0.742	0.0003	7.270E+01

FCF sum= 0.8706

 $Av'v''$ sum= 2.341E+05  
lifetime= 4.271E-06

$v' = 11$	$v'' =$	wavelength nm	$Qv'v''$	$r(v'v'')$ Angstroms	$Re(r)$ Debye	Branching Ratio	$Av'v''$ s-1
	0	374.40	0.0000	2.500	0.028	0.0000	9.082E-05
	1	395.63	0.0000	2.300	0.129	0.0000	6.753E-02
	2	418.92	0.0000	2.100	0.231	0.0000	9.077E-02
	3	444.57	0.0000	2.000	0.281	0.0000	1.979E-01
	4	472.95	0.0000	1.893	0.336	0.0000	1.002E+01
	5	504.49	0.0028	1.697	0.435	0.0053	1.291E+03
	6	539.71	0.0502	1.603	0.483	0.0959	2.336E+04
	7	579.26	0.2325	1.536	0.517	0.4117	1.003E+05
	8	623.96	0.1526	1.490	0.540	0.2362	5.752E+04
	9	674.81	0.0375	1.393	0.589	0.0546	1.330E+04
	10	733.12	0.0533	1.395	0.588	0.0603	1.470E+04
	11	800.56	0.0791	1.332	0.620	0.0765	1.862E+04
	12	879.34	0.0057	1.250	0.662	0.0048	1.157E+03
	13	972.44	0.0196	1.293	0.640	0.0113	2.741E+03
	14	1083.96	0.0520	1.249	0.663	0.0231	5.623E+03
	15	1219.69	0.0431	1.215	0.680	0.0141	3.444E+03
	16	1388.11	0.0145	1.182	0.697	0.0034	8.253E+02
	17	1602.13	0.0003	1.170	0.703	0.0000	9.417E+00
	18	1882.39	0.0061	1.157	0.709	0.0006	1.443E+02
	19	2264.09	0.0198	1.143	0.716	0.0011	2.747E+02
	20	2798.32	0.0321	1.121	0.728	0.0010	2.433E+02

FCF sum= 0.8012

 $Av'v''$ sum= 2.435E+05  
lifetime= 4.106E-06

TABLE 16. Concluded.

$v'=12$	$v''=$	wavelength nm	$Qv'v''$	$r(v'v'')$ Angstroms	$Re(r)$ Debye	Branching Ratio	$Av'v''$ s <sup>-1</sup>
	0	355.97	0.0000	2.500	0.028	0.0000	3.170E-07
	1	375.10	0.0000	2.300	0.129	0.0000	9.905E-04
	2	395.98	0.0000	2.100	0.231	0.0000	1.075E-02
	3	418.82	0.0000	2.000	0.281	0.0000	6.761E-02
	4	443.91	0.0000	1.900	0.332	0.0000	2.374E-02
	5	471.58	0.0001	1.840	0.363	0.0002	3.775E+01
	6	502.22	0.0051	1.706	0.431	0.0093	2.324E+03
	7	536.30	0.0722	1.615	0.477	0.1335	3.338E+04
	8	574.39	0.2592	1.546	0.512	0.4496	1.124E+05
	9	617.21	0.0968	1.506	0.532	0.1463	3.657E+04
	10	665.63	0.0713	1.450	0.561	0.0953	2.383E+04
	11	720.75	0.0198	1.424	0.574	0.0218	5.461E+03
	12	783.99	0.0827	1.346	0.613	0.0810	2.025E+04
	13	857.16	0.0231	1.288	0.643	0.0190	4.754E+03
	14	942.64	0.0026	1.275	0.649	0.0016	4.107E+02
	15	1043.64	0.0349	1.265	0.654	0.0165	4.126E+03
	16	1164.54	0.0467	1.230	0.672	0.0168	4.192E+03
	17	1311.52	0.0276	1.200	0.687	0.0073	1.814E+03
	18	1493.56	0.0063	1.167	0.704	0.0012	2.942E+02
	19	1724.19	0.0001	1.162	0.707	0.0000	3.974E+00
	20	2017.51	0.0076	1.157	0.709	0.0006	1.461E+02
FCF sum=			0.7561			$Av'v''$ sum=	2.500E+05
						lifetime=	4.000E-06

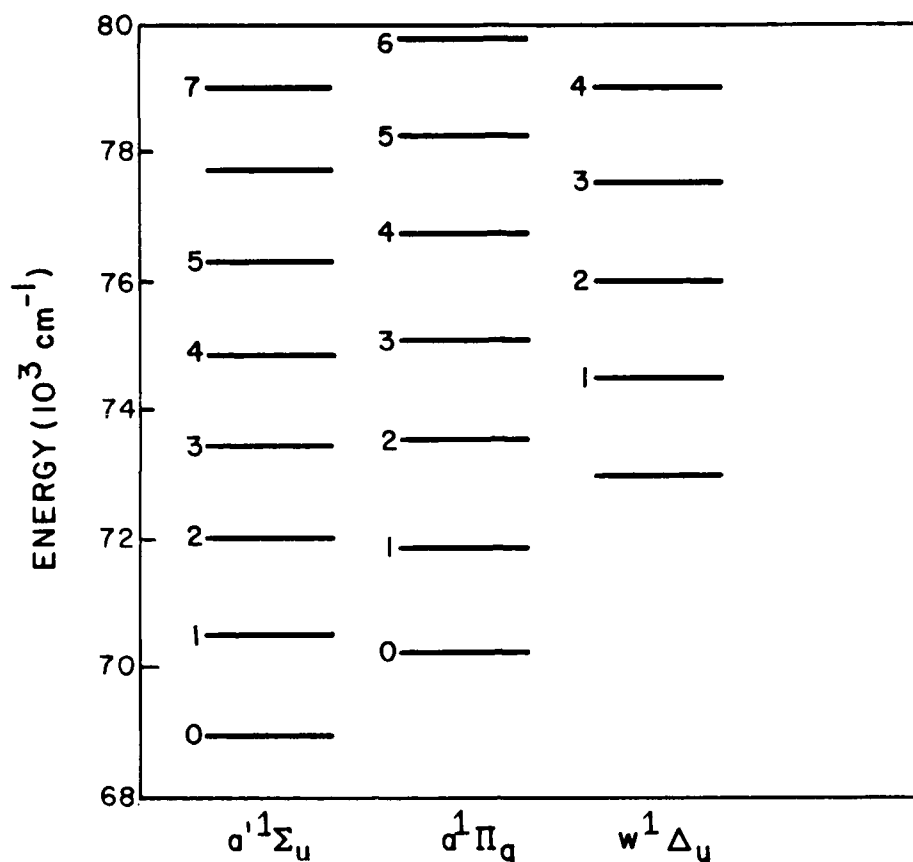
## 8. QUENCHING OF $N_2(A^1\Pi_g, V'=0)$ BY $N_2$ , $O_2$ , $CO$ , $CO_2$ , $CH_4$ , $H_2$ , AND $Ar$

### 8.1 INTRODUCTION

One of the most examined areas in molecular energy transfer is the exchange of energy between near-resonant states in different molecules. Extensive experimental and theoretical attention has been given to the atom-atom and atom-diatom transfer processes. Electronic-to-vibrational energy transfer in atom-diatom and diatom-diatom collisions has also been intensively investigated. A much less well investigated area is the competition between radiative, intramolecular, and intermolecular electronic relaxation processes. A theoretical treatment of such processes is complex, since information about two electronic potential curves and the intermolecular interaction potential must be available. Nonetheless, studies of such processes are extremely important, especially when the excited state is metastable and may act as an energy storage reservoir. These states may play an important role in chemical laser kinetics, atmospheric background emissions, and plasma kinetics.

An example of such a coupled system is found in the lowest lying singlet states of  $N_2$ . The  $a^1\Pi_g$ ,  $a'^1\Sigma_u^-$ , and  $w^1\Delta_u$  states all have term energies of approximately 8.5 eV and are metastable with respect to radiation to the ground  $X^1\Sigma_g^+$  state. An electronic energy level diagram of these states, shown in Figure 13, and is repeated here. It highlights the many opportunities for near-resonant energy exchange within the singlet manifold.

These states may be coupled via emission of infrared radiation. The  $w$ - $a$  and  $a'$ - $a$  transitions comprise the well-known McFarlane Infrared Transitions in  $N_2$ . These transitions were observed in  $N_2$  laser cavities by McFarlane<sup>48</sup> and the  $w$ - $a$  transition has been most recently observed by Fraser, Rawlins, and Miller.<sup>126</sup> The  $a$ - $a'$  transition has been recently probed in absorption using diode laser spectroscopy by Hirota.<sup>127</sup> Transition probabilities for the  $a$ - $a'$  transition have been calculated by Freund<sup>128</sup> and have recently been reinvestigated by Marinelli, Green, DeFaccio, and Blumberg.<sup>95</sup> Radiative coupling of



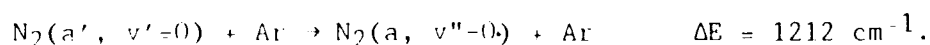
A-2758

Figure 13. Energy level diagram for N<sub>2</sub> singlets.

these states to the ground state is via forbidden transitions. The well known  $a'1\Pi_g - X'1\Sigma_g^+$  (Lyman-Birge Hopfield) bands have been the subject of numerous studies,<sup>6</sup> although the radiative lifetime of the  $a'1\Pi_g$  state remains a subject of much controversy. Measurements of the lifetime center around a value of  $80^{+40}_{-20}$  us.<sup>58,62-64</sup> The  $a'1\Sigma_u^- - X'1\Sigma_g^+$  transitions (Ogawa-Tanaka-Wilkinson-Mulliken Bands) have been observed in absorption. Only  $v'=0$  of this state has been observed in emission.<sup>6,95</sup> The radiative lifetime of the  $a'1\Sigma_u^-$  state is also quite uncertain,<sup>129,130</sup> although the latest work of Piper<sup>66</sup> appears to have established a lower bound on the lifetime of  $23^{+11}_{-6}$  ms. The  $w'1\Delta_u - X'1\Sigma_g^+$  transition has only been observed in absorption in high pressure N<sub>2</sub>.<sup>6</sup>

The collisional relaxation of the coupled singlet states has been investigated in a series of papers by Golde and Thrush,<sup>52-55</sup> Freund,<sup>128</sup> van Veen and coworkers,<sup>57</sup> and Piper.<sup>66</sup> Collisional quenching of the  $a^1\Pi_g$  state by CO has been investigated by Filseth<sup>131</sup> and Sha, Proch, and Kompa.<sup>132</sup> Rotational relaxation of the  $a^1\Pi_g$  state has also been investigated by Kompa and coworkers.<sup>132</sup> Most recently, vibrational relaxation of  $N_2(a)$  and intersystem crossing with the  $a'$ -state has been investigated by Marinelli, Green, DeFaccio, and Blumberg.<sup>95</sup>

The early work by Golde and Thrush used a discharge flow reactor to create active nitrogen in Ar at pressures from 1-6 Torr. Their observation of  $a'-X$  and  $a-X$  emissions showed that  $N_2(a, v=0)$  could be excited by  $N_2(a', v=0)$  through the endothermic process



This conclusion was supported by the observed variation in  $a'/a$  emission intensities with pressure and temperature. Electronic quenching of  $N_2(a, v=0)$  by Ar and  $N_2$  was measured to be quite slow ( $k_{Ar} \geq 3 \times 10^{-12} \text{ cm}^3 \text{ molecule}^{-1} \text{ s}^{-1}$  and  $k_{N_2} \geq 1.7 \times 10^{-12} \text{ cm}^3 \text{ molecule}^{-1} \text{ s}^{-1}$ ).<sup>55</sup> The quenching rate coefficient for  $CO_2$  was measured to be  $6.5 \times 10^{-11} \text{ cm}^3 \text{ molecule}^{-1} \text{ s}^{-1}$  and is strongly dependent on the  $a$ -state vibrational level.

Golde and Thrush also observed quenching of high vibrational levels of  $N_2(a)$  to be strongly dependent on both vibrational level and temperature. The high levels of the  $a$ -state were produced via N atom recombination. They measured quenching rate coefficients ranging from  $1.6 \times 10^{-12}$  to  $2.7 \times 10^{-11} \text{ cm}^3 \text{ molecule}^{-1} \text{ s}^{-1}$  for vibrational levels 0-6. Quenching by Ar was observed to have similar rates, suggesting that little energy is transferred in the process and that transfer to the  $a'$  and/or  $w$  states is the dominant quenching mechanism.

Direct two-photon excitation of  $N_2(a, v'=0,1)$  was used by van Veen and coworkers<sup>57</sup> in their quenching studies. They observed both simple quenching of the a-state at low pressures and coupled relaxation of the a-a' states at higher pressures. Quenching rate coefficients of  $2.1 \times 10^{-11}$  and  $2.0 \times 10^{-11} \text{ cm}^3 \text{ molecule}^{-1} \text{ s}^{-1}$  were measured for  $N_2(a)$  levels 0 and 1 respectively. At higher pressures a decay rate coefficient of  $2.3 \times 10^{-13} \text{ cm}^3 \text{ molecule}^{-1} \text{ s}^{-1}$  was measured for the coupled system. They concluded that this rate was due to the rate-limiting relaxation of  $N_2(a', v=0)$ .

These conclusions are supported by the measurements of Piper.<sup>66</sup> In his study of  $N_2(a')$  quenching by a range of gases he measured a rate coefficient for relaxation by  $N_2$  of  $1.9 \pm 0.5 \times 10^{-13} \text{ cm}^3 \text{ molecule}^{-1} \text{ s}^{-1}$ . Quenching by NO,  $CH_4$ , CO, and  $N_2O$  was observed to be approximately gas kinetic while quenching by  $H_2$ ,  $O_2$ , and  $CO_2$  was observed to be roughly tenth gas kinetic. Quenching by Ar was observed to be quite slow ( $k \leq 2 \times 10^{-14} \text{ cm}^3 \text{ molecule}^{-1} \text{ s}^{-1}$ ).<sup>66</sup> Quenching by CO was observed to efficiently produce CO(A-X) emission. Energy transfer from  $N_2(a)$  to CO was also observed to produce A-X emission by Kompa and coworkers.<sup>132</sup> They measured a quenching rate coefficient a factor of 3 to 4 greater than gas kinetic for the total relaxation process. The energy mismatch between  $N_2(a)$  and CO(A) vibrational levels was observed to be the controlling factor in the partitioning of energy to CO(A,v).

Quenching of high vibrational levels of  $N_2(a)$  by  $N_2$  was observed to be nearly gas kinetic by Marinelli and coworkers.<sup>95</sup> The lower vibrational levels were measured to relax at rates nearly tenth gas kinetic but coupling to the a'-state in their electron-beam excitation experiment made an exact determination of these rate coefficients quite difficult. Electronic relaxation of the vibrational manifold was measured to have an average rate coefficient of  $8.9 \times 10^{-12} \text{ cm}^3 \text{ molecule}^{-1} \text{ s}^{-1}$ , somewhat lower than the results for  $v=0,1$  measured by van Veen et al.<sup>57</sup>

The present study extends our previous work. We now use two-photon excitation of  $N_2(a, v=0)$  to examine quenching of this level by a variety of species. Our

hope is to provide more detailed insight into the global observations in the previous study.<sup>95</sup>

## 8.2 EXPERIMENTAL

These experiments were conducted using a standard laser-induced fluorescence apparatus consisting of a flow cell, Nd:YAG pumped dye laser system, and time resolved fluorescence detection equipment. A schematic diagram of the apparatus is shown in Figure 62 and each of the components is described in detail below.

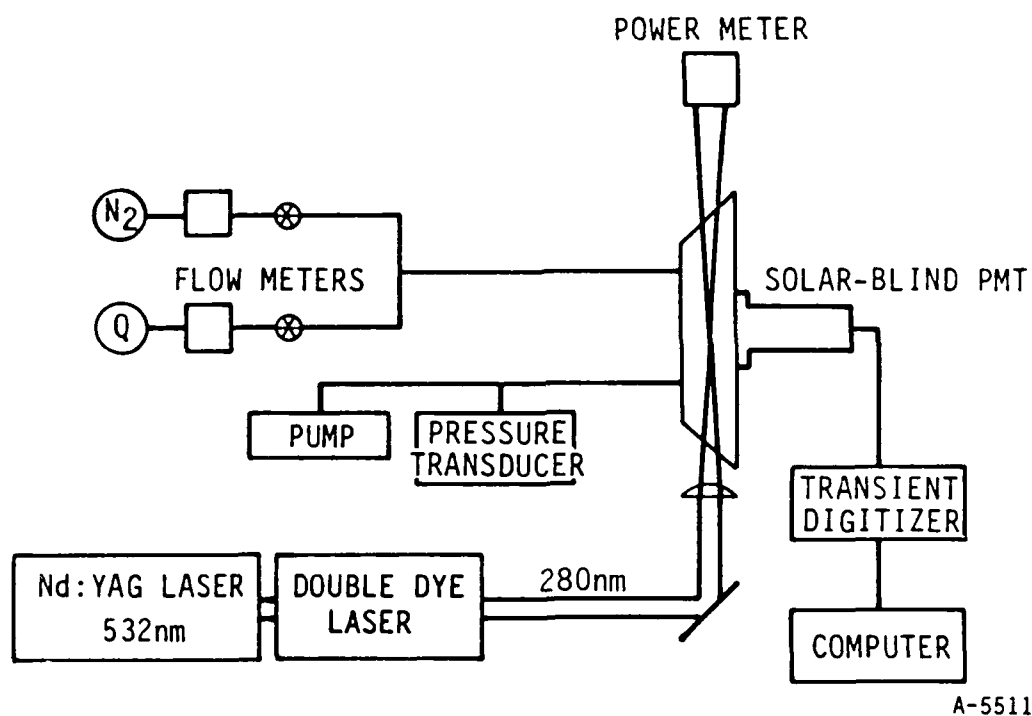


Figure 62. Schematic diagram of experimental apparatus used in quenching experiments.

The quenching experiments were performed in a 2.5 cm diameter flow reactor pumped by a 17 cfm rotary pump. Flow velocities in excess of  $1000 \text{ cm s}^{-1}$  are achieved in this system. A flowing system was employed to eliminate the possibility of interference in the kinetic measurements due to quenching by laser

produced species or reaction products. Flow rates for  $N_2$  and other quenching species were measured using calibrated mass flow meters (Teledyne-Hastings) and total cell pressures were determined using capacitance manometers (MKS). All gases were standard reagent grade and were used without further purification. The kinetic measurements were performed in a section of the flow reactor consisting of a teflon coated (Dupont Ploy TFE) and internally-blackened six-way cross. One axis of the cross was utilized for gas flow while a second axis was equipped with baffled S1-UV quartz windows for introduction of the laser beam. The third axis of the cross was fitted with a PMT to view the fluorescence.

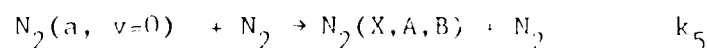
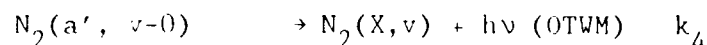
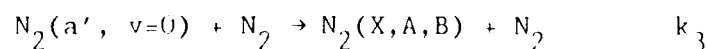
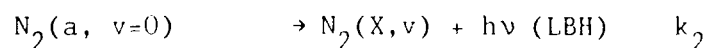
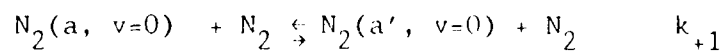
The  $N_2(a^1\Pi_g, v'=0)$  state was excited using a pulsed Nd:YAG pumped dye laser (Quintel International YG 581C/TDL 50). The output from a 50 percent mixture of R590/R610 was frequency doubled to obtain approximately 10 mJ at 290 nm in a 7 ns Q-switched pulse. The UV output of the laser system was maximized using servo-tracking of the non-linear KDP crystal phase matching angle. A Pellin-Brocha prism was used to separate the fundamental and second harmonic output of the laser system. Right-angle prisms were used to direct the beam to a 10 cm focal S1-UV quartz lens which focused it to a spot in the center of the cell. The laser power was monitored at the exit window of the cell using a surface-absorbing power meter (Scientech).

Fluorescence was observed from the  $N_2(a-X)$  transition using a solar-blind PMT (EMR 542G-17) located approximately 6 cm from the laser focal volume. A flow of  $N_2$  was used to purge the region between the  $CaF_2$  window of the fluorescence cell and the PMT photocathode. This technique has been shown to effectively eliminate  $O_2$  absorption at wavelengths above 145 nm. No fluorescence collection optics were employed (effective  $f/3.2$ ) and the distance from the center of the cell to the exit window was limited to 4 cm to minimize absorption of fluorescence by some of the quenching gases. Fluorescence signals from the PMT were captured using a 200 MHz transient digitizer and stored on an IBM-PC for analysis (LeCroy TR8828C/CATALYST). A standard linear least squares analysis package was employed to obtain kinetic rates from the fluorescence decays.



### 8.3 RESULTS AND ANALYSIS

The quenching of  $N_2(a, v'=0)$  is complicated by the possibility of collisional coupling to  $N_2(a', v''=0)$ . For the case of quenching by  $N_2$  the relevant kinetic processes are described by



where creation of  $N_2(a, v'=0)$  by the laser occurs on a time scale rapid compared with relaxation. The rate equations describing relaxation of  $N_2(a, v=0)$  are given by

$$\frac{d[N_2(a)]}{dt} = -((k_1 + k_5)[N_2] + k_2)[N_2(a)] + k_{-1}[N_2(a')] [N_2] \quad (25)$$

where

$$\frac{d[N_2(a')]}{dt} = ((k_1 + k_3)[N_2] + k_4)[N_2(a')] + k_1[N_2(a)] [N_2] \quad (26)$$

The treatment of this coupled system, neglecting activation from the ground state, has been reviewed for the case of vibrational energy transfer by Yardley.<sup>133</sup> The solution to these equations for the behavior of  $N_2(a, v=0)$  is given by

$$[N_2(a)]_t = [N_2(a)]_0 \left[ \frac{(\lambda_2 - C_{11})}{\lambda_2 - \lambda_1} e^{-\lambda_1 t} + \frac{(C_{11} - \lambda_1)}{\lambda_2 - \lambda_1} e^{-\lambda_2 t} \right] \quad (27)$$

where

$$C_{11} = (k_1 + k_5) [N_2] + k_2$$

$$C_{12} = k_{-1} [N_2]$$

$$C_{21} = k_1 [N_2]$$

$$C_{22} = (k_{-1} + k_3) [N_2] + k_4$$

The two decay constants,  $\lambda_1$  and  $\lambda_2$ , are given by the relations

$$\lambda_1, \lambda_2 = \frac{1}{2} \left\{ (C_{11} + C_{22}) \pm \left[ (C_{11} + C_{22})^2 - 4(C_{11}C_{22} - C_{12}C_{21}) \right]^{1/2} \right\} \quad (28)$$

$$\lambda_1 \lambda_2 = C_{11}C_{22} - C_{21}C_{12} \quad (29)$$

$$\lambda_1 + \lambda_2 = C_{22} + C_{11} \quad (30)$$

In our experiments,  $N_2(a, v=0)$  is produced by the laser and decays initially to reach a coupled equilibrium with  $N_2(a', v=0)$ . The system subsequently decays at a rate determined by a weighted average of the relaxation rates to the ground or other excited states. The weighting factor is simply the Boltzmann distribution of total population in  $N_2(a)$  and  $N_2(a')$ . An additional relation between  $\lambda_1$  and  $\lambda_2$  gives the ratio of the amplitude components of the fast (initial) and slow (final) decays; S:

$$S = \frac{\lambda_2 - C_{11}}{C_{11} - \lambda_1} \quad (31)$$

For the coupled system  $N_2(a, v=0)/N_2(a', v=0)$  the amplitude ratio is given by

$$S = \left( \frac{k_1}{k_{-1}} \right) \left( \frac{k_5 [N_2]}{k_3 [N_2]} + \frac{k_2}{k_3} \right) \quad (32)$$

where

$$\frac{k_1}{k_{-1}} = \frac{1}{2} e^{1212/kT} \quad (33)$$

which has a value of 168 at 300K. Previous results for the values in the second term of expression (32) show that this term is also unity or greater under our experimental conditions. Hence,  $S \gg 1$ . The results of van Veen and coworkers<sup>57</sup> show that

$$\lambda_1 = C_{11} = (k_1 + k_5) [N_2] + k_2 \quad (34)$$

and hence, from expression (30)

$$\lambda_2 = (k_1 + k_3) [N_2] + k_4 \quad (35)$$

Thus,  $\lambda_1$  is related to the loss of a state via  $N_2$  quenching to any state and radiative decay, while  $\lambda_2$  is related to loss of a state to  $a'$  followed by decay of that state.

Our experiment employs an 8 bit digitizer (resolution =  $4 \times 10^{-3}$  of full scale). Hence, the ratio of fast to slow amplitudes in our experiment is such that the slow component of the decay is much smaller than the resolution of

the data acquisition system. Thus we are only able to determine  $\lambda_1$  and equation (27) reduces to

$$[N_2(a, v=0)]_t = [N_2(a, v=0)]_0 e^{-[(k_1 + k_5)[N_2] + k_2]t} \quad (36)$$

This is classical first order kinetics in which the magnitude of  $k_1 + k_5$  may be determined from a Stern-Volmer type analysis.

### 8.3.1 Quenching by $N_2$

A typical two photon laser-induced fluorescence spectrum of the  $N_2(a-X, 0-0)$  band is shown in Figure 63. All fluorescence decay experiments were performed by exciting the S-branch band head of this transition ( $J=7-9$ ). At the  $N_2$  pressures employed in these experiments sufficient collisions are available to thermalize the rotational population of  $v'=0$  prior to quenching by other species. Though we did not attempt to observe any dependence of quenching rate on rotational level excited, we believe these experiments would not be able to detect such an effect.

The decay of  $N_2(a, v=0)$  emission intensity as a function of time for an  $N_2$  density of  $1.3 \times 10^{16}$  molecules  $\text{cm}^{-3}$  is shown in Figure 64. The log of the emission intensity is clearly linear for in excess of three e-folding lifetimes in this plot (only four are practically possible). A plot of first-order rate coefficients determined as a function of  $N_2$  density is shown in Figure 65. The slope of this line gives the value of  $k_1 + k_5$ , the total quenching rate coefficient for this level by  $N_2$ . A least-squares analysis of the data gives a value for the rate coefficient of  $2.2 \pm 0.1 \times 10^{-11} \text{ cm}^3 \text{ molecule}^{-1} \text{ s}^{-1}$  in excellent agreement with the results of van Veen and coworkers.<sup>57</sup>

The intercept of the line indicates a zero-pressure decay rate of  $1 \times 10^5 \text{ s}^{-1}$ . This is approximately an order of magnitude faster than the reported lifetimes

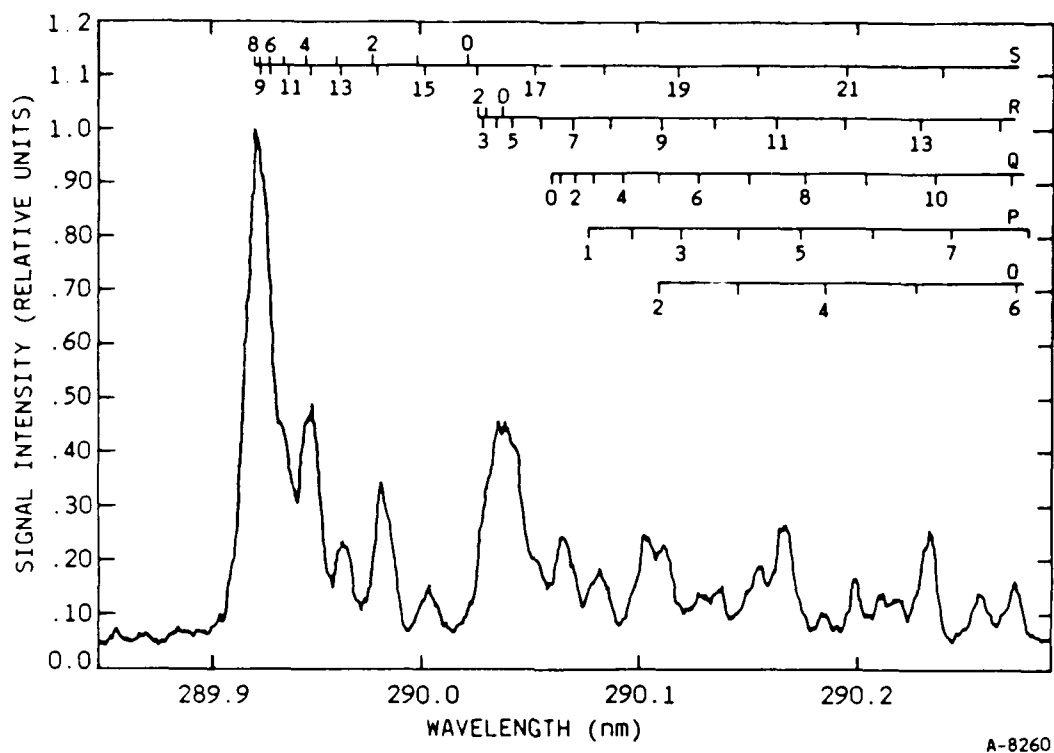


Figure 63. Two photon laser induced fluorescence spectrum of  $N_2(a-X, 0-0)$  band.

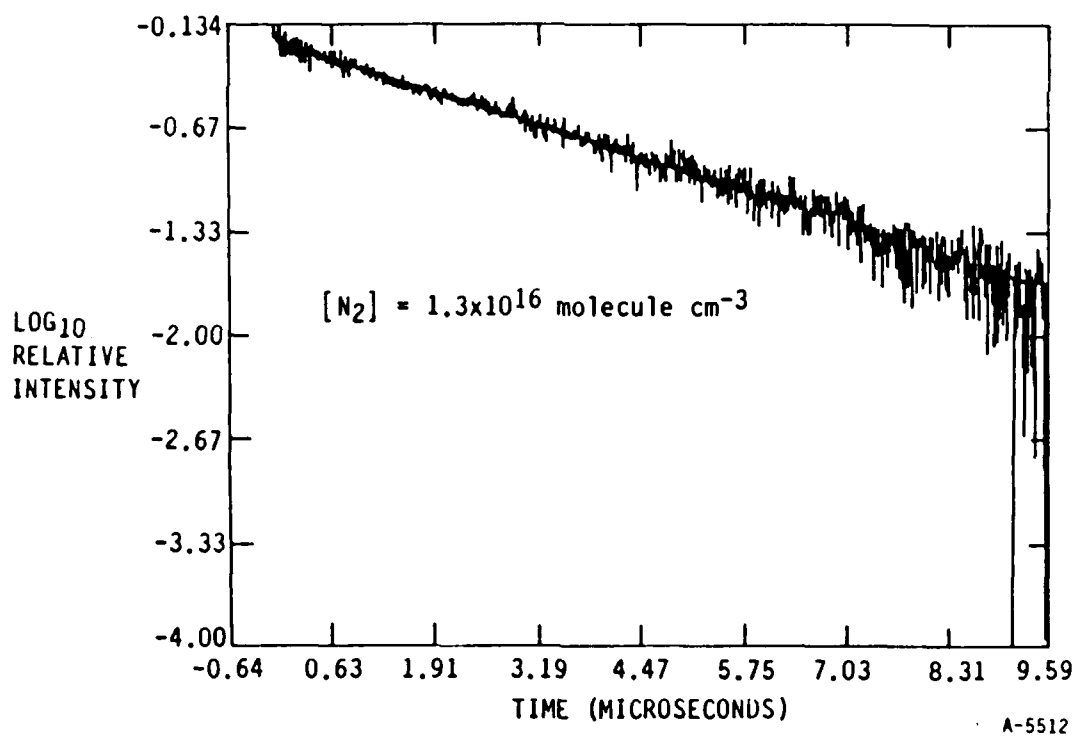


Figure 64. Fluorescence decay of  $N_2(A^1\Pi_g)$  following laser excitation of  $N_2(a, v'=0)$ .

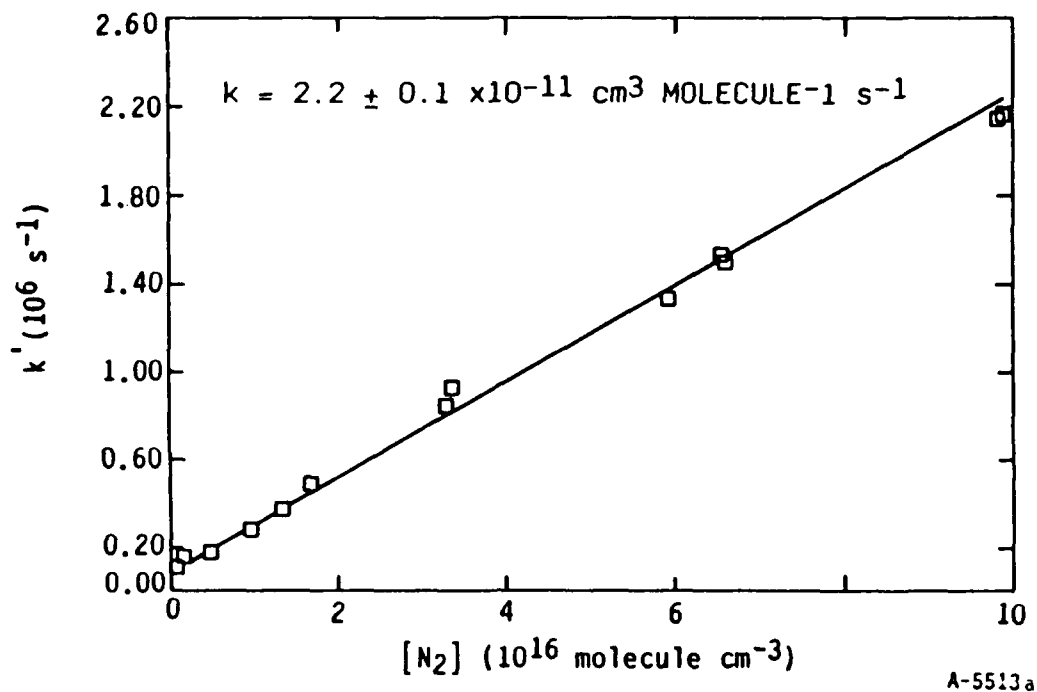


Figure 65. Plot of first-order decay rates as a function of  $N_2$  density. The slope of this line gives the quenching rate coefficient.

for  $N_2(a)$ <sup>58,62-64</sup> and can be simply explained by considering diffusion out of the field of view of our detection system. Of course the diffusion rate is inversely proportional to pressure this should result in some curvature in the plot of Figure 65 at low pressure. However, quenching by  $N_2$  is sufficiently rapid that the diffusion component of the decay represents only a minor contribution to the total decay rate at all but the lowest  $N_2$  densities. No curvature can be effectively discerned from this plot.

### 8.3.2 Quenching by Ar, CO<sub>2</sub>, H<sub>2</sub>, O<sub>2</sub>, and CH<sub>4</sub>

Addition of other species to a fixed amount of  $N_2$  enables the determination of total quenching rate coefficients for these species. In these experiments approximately 1 Torr of  $N_2$  was employed in order to produce the  $N_2(a)$ . At this pressure the decay of  $N_2(a)$  is dominated by  $N_2$  quenching and the contribution due to diffusion is not important. First-order decay rates were

determined as a function of quencher density for each species. The contribution due to quenching by  $N_2$  was subtracted from each rate, using the rate coefficient reported above, in order to account for variations in  $N_2$  density as the quencher density was varied. Stern-Volmer type plots for quenching of  $N_2(a)$  by  $O_2$ ,  $CO_2$  and  $H_2$  are shown in Figure 66. A summary of measured rate coefficients is given in Table 17.

An attempt was made to determine the quenching rate coefficient for  $N_2O$ ; however,  $N_2O$  is efficiently excited by the laser at the wavelength used to excite  $N_2(a, v=0)$  and VUV emission was observed in the bandpass of our detection system. Nitrous oxide is transparent at the 290 nm wavelength of our excitation laser and absorbs into a structured continuum at 145 nm via a two-photon process. Absorption at 145 nm does not produce products which radiate in the VUV.<sup>134</sup> No further attempt has been made to explore this process.

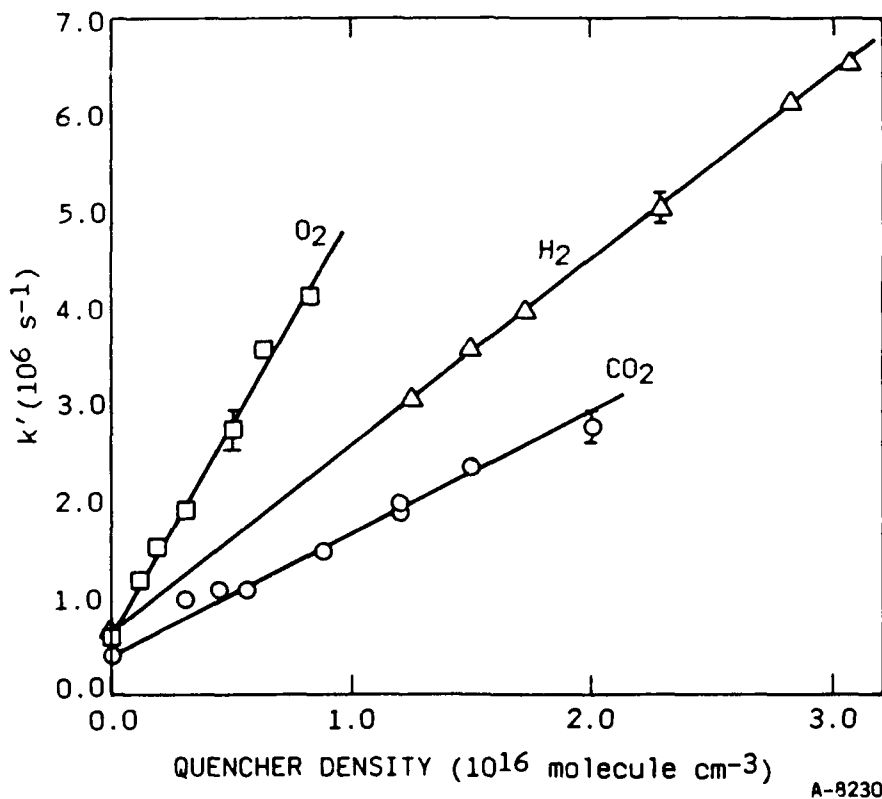


Figure 66. Stern-Volmer plots for quenching of  $N_2(a, v'=0)$  by  $O_2$ ,  $H_2$ , and  $CO_2$ .

TABLE 17. Measured quenching rate coefficients for  $N_2(a, {}^1\Pi_g, v'=0)$ .

Species	$k_1 + k_5$ ( $10^{-10}$ cm <sup>3</sup> molecule <sup>-1</sup> s <sup>-1</sup> )
Ar	$0.13 \pm 0.01$
N <sub>2</sub>	$0.22 \pm 0.02$
O <sub>2</sub>	$4.3 \pm 0.2$
CO	$2.8 \pm 0.2$
H <sub>2</sub>	$2.0 \pm 0.1$
CO <sub>2</sub>	$1.30 \pm 0.05$
CH <sub>4</sub>	$5.2 \pm 0.2$

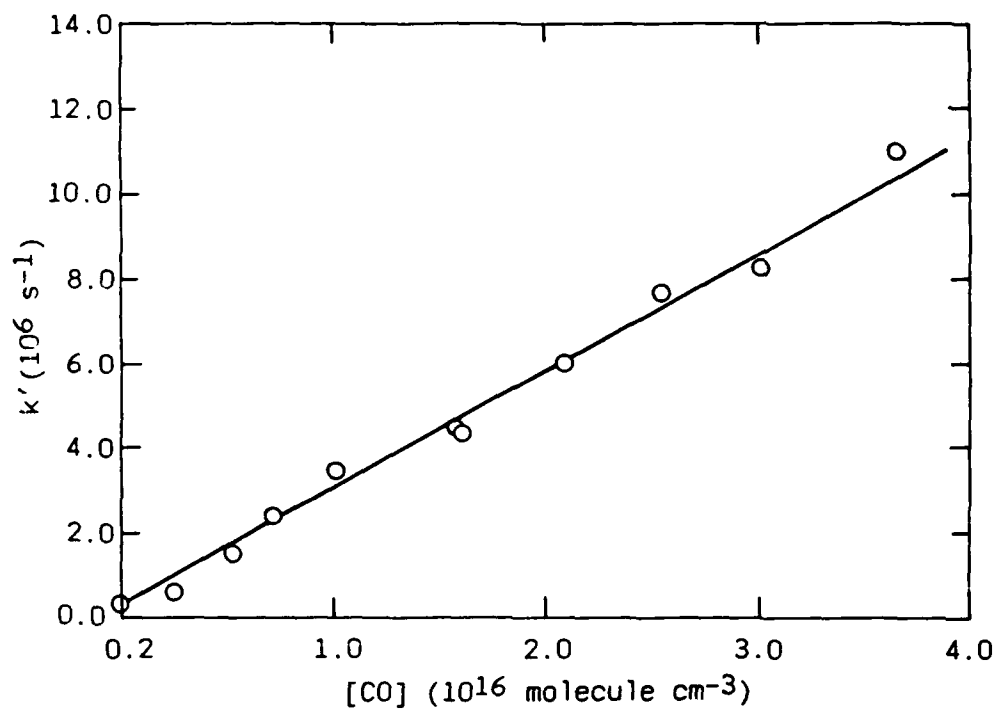
### 8.3.3 Quenching by CO

The quenching of  $N_2(a)$  by CO produced strong emission in the 130-190 nm bandpass of our detection system. This is of course due to the excitation of  $CO(A^1\Pi)$  via energy transfer. Since the radiative lifetime of the  $CO(A)$  state is approximately 10 ns<sup>134</sup> and the kinetic decays occur on the microsecond time scale,  $CO(A)$  is in steady state during the decay and its emission can be used as a tracer for the  $N_2(a)$  density. Hence, this emission can be used, exactly as the direct emission from  $N_2(a)$  was employed, to obtain the quenching rate coefficient for CO. The Stern-Volmer analysis of the decay rates shown in Figure 67 yields a rate coefficient of  $2.8 \pm 0.2 \times 10^{-10}$  cm<sup>3</sup> molecule<sup>-1</sup> s<sup>-1</sup>. This is approximately a factor of two slower than observed by Kompa and coworkers.<sup>132</sup>

### 8.4 SUMMARY

These preliminary observations provide a basis for future measurements. The rapid transfer rates out of  $N_2(a)$  are perhaps due to near-resonant energy transfer (E-E) for several partners such as CO and O<sub>2</sub>. The rate for argon is more puzzling. The rate for  $N_2$  quenching partner is slower than expected. Hydrogen presents a real enigma. Transfer to H<sub>2</sub> would result in dissociation





A-8231

Figure 67. Stern-Volmer plot for quencher of  $N_2(a, v'=0)$  by CO.

producing fast moving H atoms. Future spectrally resolved measurements of the fluorescence will provide additional insight into the energy transfer pathways.

## 9. LOW PRESSURE $O_3$ PRODUCTION

### 9.1 INTRODUCTION

In the quiescent atmosphere ozone production below 100 km occurs via

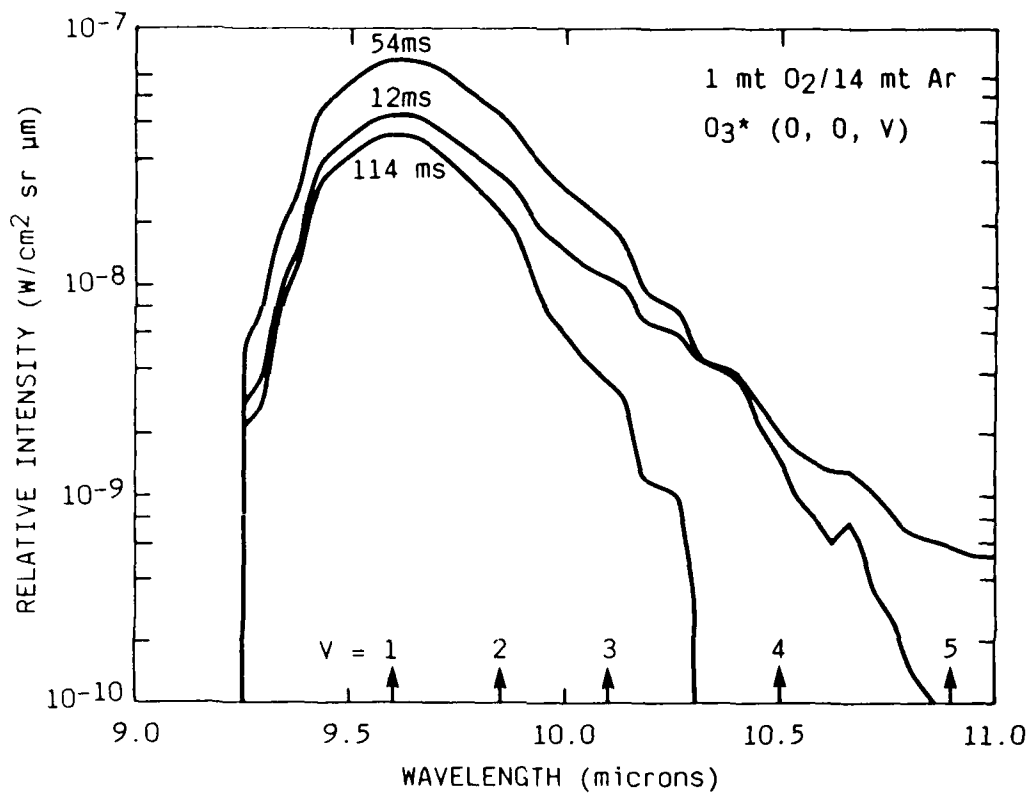


the three-body recombination mechanism. This mechanism has been studied extensively<sup>135-142</sup> both in the laboratory (COCHISE) and in field experiments (SPIRE). Our motivation in studying  $O_3$  in the LABCEDE facility arose from several field observations of potentially enhanced  $O_3(v)$  production under disturbed atmospheric conditions, i.e., both aurora and electron gun dosing. Our goals were to look for  $O_3(v_3)$  emission in electron irradiated  $O_2/N_2$  mixtures, evaluate the IR emission intensity to ascertain the dominant production mechanism at low pressure, and measure  $O_3(v_3)$  collisional relaxation kinetics.

Measurements of  $O_3(v_3)$  emission were obtained in the cryogenic LABCEDE facility using a CVF. The electron beam acceleration potential was 4.5 kV for all of these measurements. The electron-beam was operated in both a DC and pulsed mode with peak currents up to 30 mA. In pulsed mode, the repetition rates ranged from 2.9 to 4.5 Hz and utilized a 20 ms electron beam pulse width. The CVF was controlled by a laboratory computer, PDP 11/03, to obtain both spectrally resolved,  $\sim 2.5$  percent  $\lambda$ , and temporally resolved,  $\sim 6$  ms, fluorescence intensities. Gas mixtures of both  $O_2/Ar$ ,  $O_2/N_2$  were irradiated. Studies of  $O_3(v_3)$  emission were performed with constant partial pressures of  $O_2$  varying buffer gas pressure and with constant buffer gas pressure and varying  $O_2$  partial pressures.

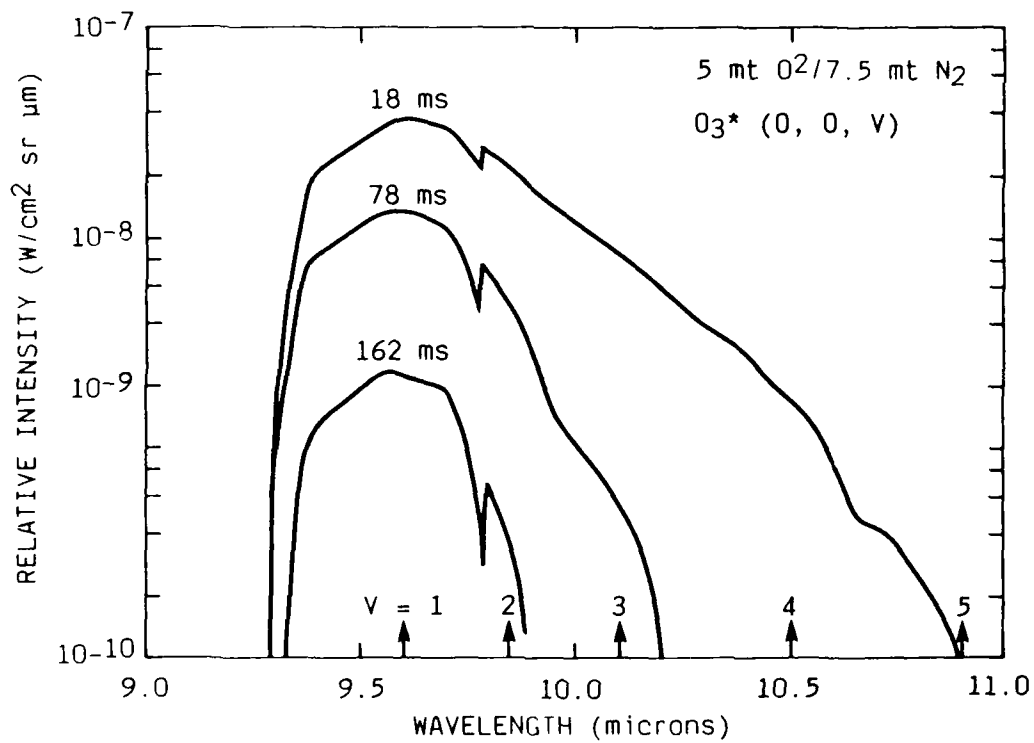
### 9.2 IR DATA

Figures 68 and 69 present examples of the  $O_3(v_3)$  emission observed in Ar and  $N_2$  buffer gas respectively. These figures show population into vibrational



A-7540

Figure 68.  $O_3$  fluorescence in Ar/ $O_2$  mixture.



A-7538

Figure 69.  $O_3$  fluorescence in  $N_2$ / $O_2$  mixture.

levels up to  $v=5$ . The time dependent emission in Ar buffer gas shows evidence of vibrational redistribution (note, the radiative decay lifetime ranges from  $\sim 100$  ms for  $v=1$  to  $\sim 25$  ms for  $v=5$ ) from the upper vibrational levels feeding population into the lower vibrational levels. By contrast the time dependent emission in  $N_2$  buffer shows decay of population from even the lowest vibrational levels. This alone suggests either  $N_2$  or  $O_2$  or both are more efficient at collisionally relaxing  $O_3(v_3)$  than is Ar.

To obtain vibrational level population information, the  $O_3(v_3)$  spectra were analyzed by a least-squares fitting procedure whose details<sup>138,139</sup> have been described previously. For  $v=1,2$  detailed information on the rotational line positions and strengths were obtained from the AFGL absorption line parameter compilation<sup>143,144</sup> and convolved with the instrumental slit function to generate a vibrational basis function for a Boltzmann distribution of rotational levels,  $T_r$ . For  $v \geq 3$  the bandshapes were calculated using the rotational line spacings and relative strengths for the (001)-(000) band convolved with the instrumental slit function. Combining the bandshape and bandcenter transition frequencies,  $\nu_{0v}$ , obtained from the perturbation treatment of Adler-Golden and Armstrong,<sup>145</sup> we were able to generate basis functions for the upper vibrational levels. To transform spectral fits into molecular number densities required band-integrated Einstein coefficients,  $A_{v' \rightarrow v''}$ . For  $v=1,2$  these were available from the line compilation of the AFGL.<sup>143,144</sup> For  $v \geq 3$  the Einstein coefficients were scaled from the values for (001) $\rightarrow$ (000) via

$$A_{v',v''} = v' A_{10} \left( \frac{\nu_{v',v''}}{\nu_{10}} \right)^3 \quad (38)$$

where 10 denotes the (001)-(000) transition. Figure 70 presents the level of agreements that was routinely obtained between the experimental data and spectral fit. The individual vibrational basis functions are presented with

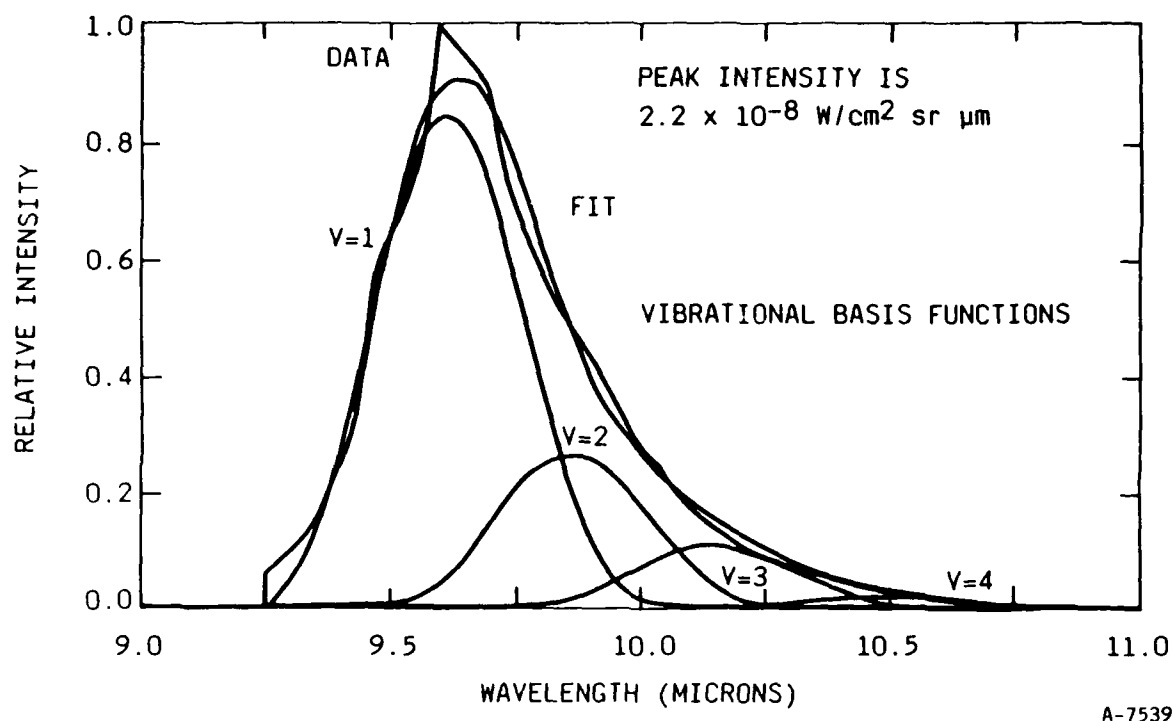


Figure 70.  $O_3$  fluorescence and spectral fit of 1 mtorr  $O_2$ /9 mtorr  $N_2$ .

the correct relative contribution to the theoretical spectral fit. Molecular number densities,  $N_{v'}$ , were determined from

$$N_{v'} = I_{v'} / h \nu_{0v'} A_{v' \rightarrow v''} \quad (39)$$

where  $I_{v'}$  is the contribution to the total integrated intensity due to each  $v' \rightarrow v''$  band calculated from

$$I_{v'} = C_{\lambda} F(v) 4\pi \Delta\lambda / L \quad (40)$$

utilizing the measured intensity calibration (p. 104-114 of Ref. 99), where  $C_{\lambda}$  is the CVF spectral response function,  $F(v)$  is the non-linear response correction factor,  $\Delta\lambda$  is the CVF resolution, and  $L$  is the emitter line thickness. Using steady state arguments we estimated what concentration of atomic oxygen,  $[O]$  would be necessary to produce the observed concentration of ozone,  $[O_3(v)]$  via the three-body mechanism:

$$[O] = \frac{[O_3^*] \cdot \text{Loss Rate}}{k_{3\text{-body}} [O_2] [M]} \quad (41)$$

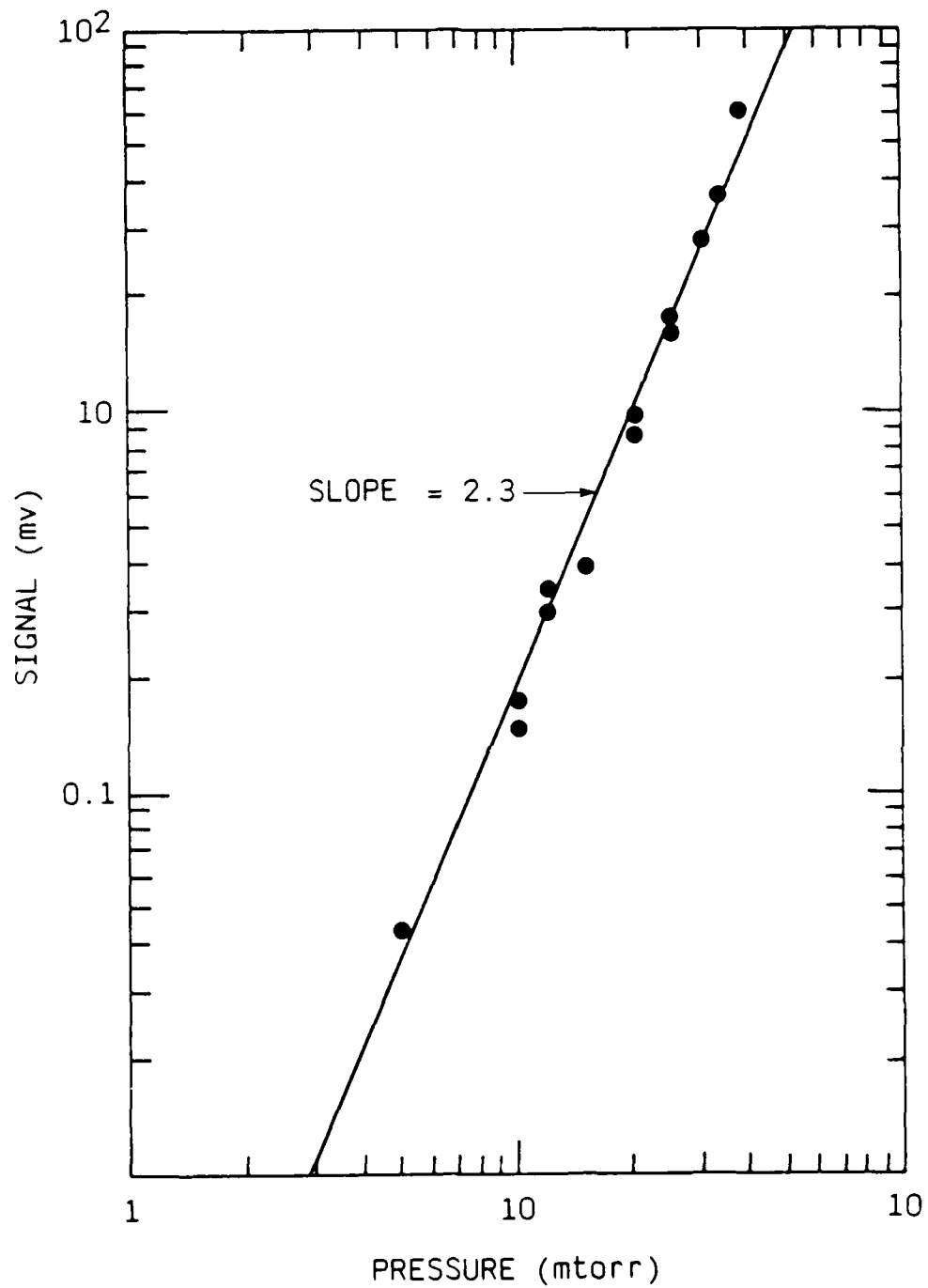
Using the fitting code described previously, the integral kinetics code to be described later and a  $k_{3\text{-body}} = 3 \times 10^{-33} \text{ cm}^6 \text{ molecule}^{-1} \text{ s}^{-1}$  (Ref. 142) we calculated a concentration of  $[O]$  which would be required to explain the fluorescence intensity observed. Only at very high pressures of  $1/4:O_2/Ar$  mixtures could obtain  $[O] < 2[O_2]$ . The conclusion being that even if nearly all the  $O_2$  were dissociated, there would be insufficient  $O_3$  production to explain the observed  $O_3(v)$  concentration via a three-body mechanism.

The observed pressure dependence of  $O_3(v=1)$  emission at  $9.65 \mu\text{m}$  for  $1/4:O_2/Ar$  and  $1/6:O_2/N_2$  mixtures is presented in Figures 71 and 72. The data obtained in nitrogen suggests a pressure dependence of  $p^{2.3}$ , however the pressure dependence in argon is very complex. Between 10 and 30 mtorr the pressure dependence is  $p^{2.1}$ . At low pressure it scales as  $p^{1.1}$ , and above 40 mtorr we may be observing the onset of an even larger pressure dependence. Additional pressure dependence measurements and analysis were performed to understand these pressure dependence variations. Many parameters were checked and evaluated to assist us in our interpretation. Residence time within the tank provided an interesting set of results (see Figure 73). We calculated the residence time phenomenologically via,

$$\text{Residence Time (s)} = \frac{\text{Volume (cc)}}{\text{Pump Speed (cc/s)}} \quad (42)$$

At constant pressure the effective pump speed can be related to the flow of gas into the tank with

$$\text{Pump Speed } \left( \frac{\text{cc}}{\text{s}} \right) = \frac{\text{Gas Flow (molecules/s)}}{\text{Gas Density (molecules/cc)}} \quad (43)$$



A-7541

Figure 71.  $O_3(v=1)$  signal level pressure variation in  $O_2/N_2$  with 200/1200 sccm flow.

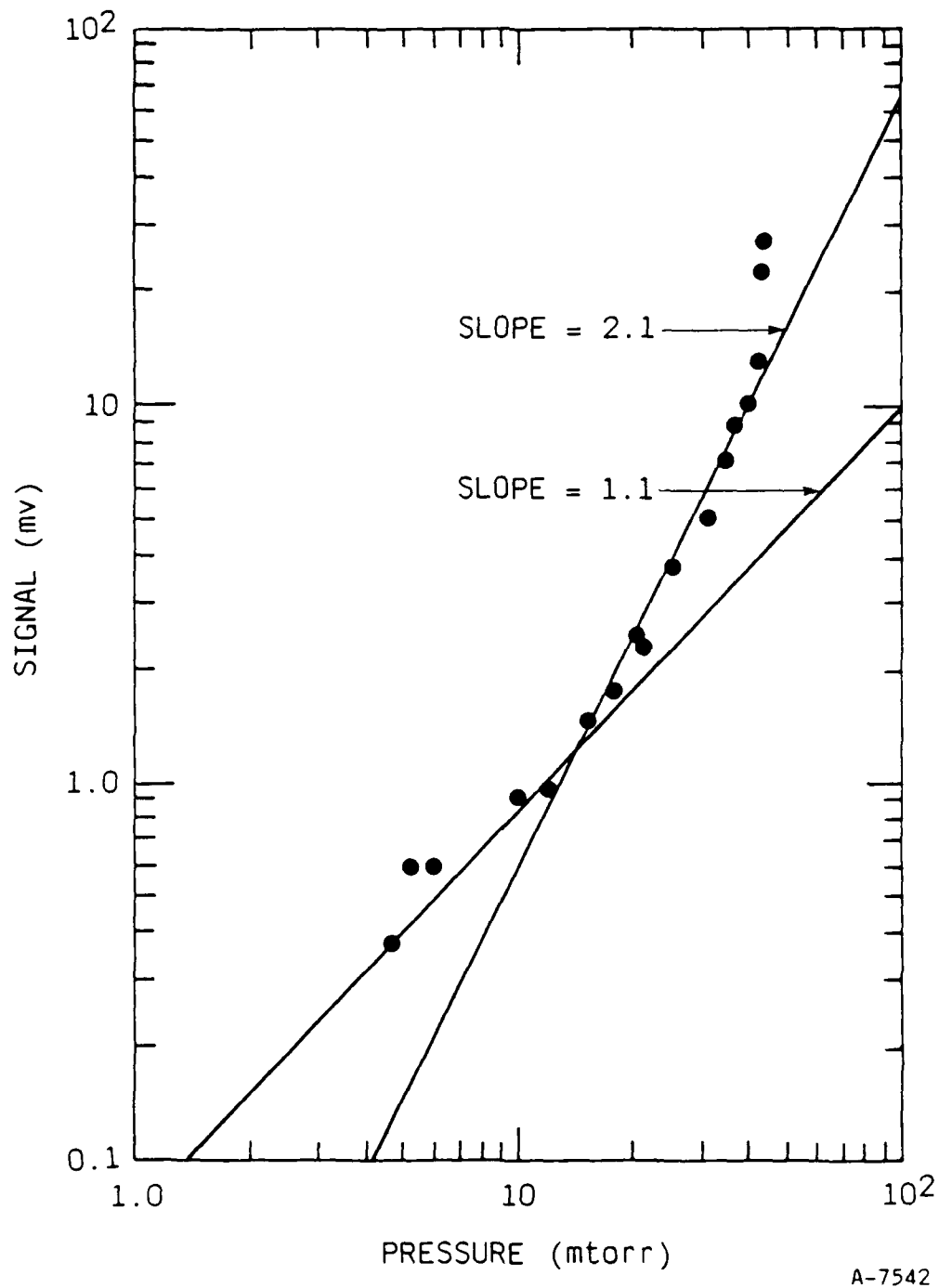
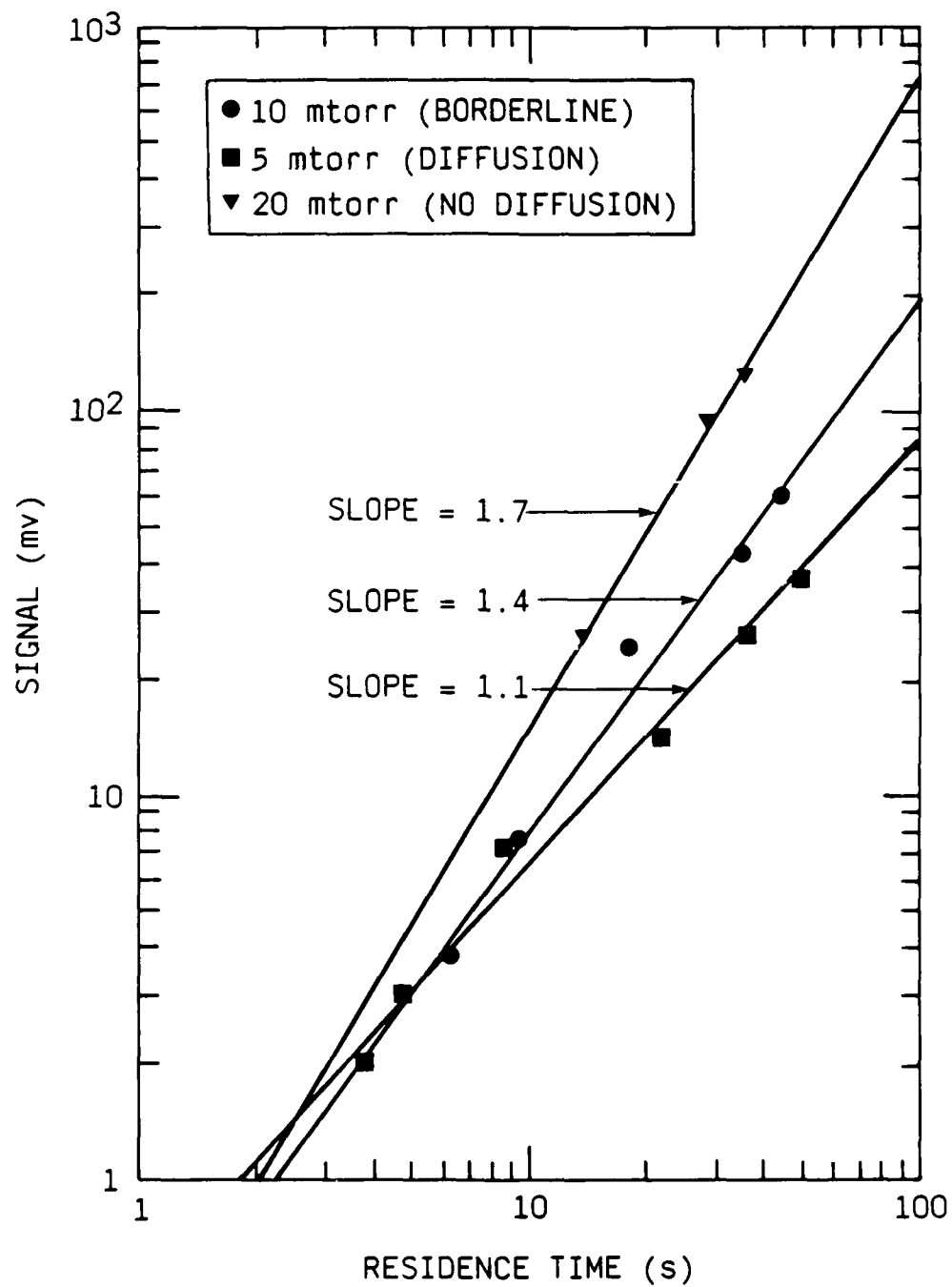


Figure 72.  $O_3(v=1)$  signal level pressure variation in  $O_2/Ar$  with 200/800 sccm flow.





A-7543

Figure 73. Residence time dependence of  $O_3(v=1)$  signal in 1/4:O<sub>2</sub>/Ar mixtures at three pressures.

We used the shroud volume of approximately  $2 \times 10^6$  cc in these calculations. Because this value is approximate, the absolute residence times may be slightly different. The three curves in Figure 73 represent three different pressures. The data points on any one curve are obtained by changing the gas flow,  $F(\text{scm})$ , then adjusting the gas conductance value (coupling the shroud volume and the LABCEDE diffusion pump) to obtain the predetermined pressure for that curve. These results allow us to draw three conclusions. First, the  $\text{O}_3(v-1)$  signal depends rather dramatically on residence time, i.e., gas flow rate, at constant pressure. Second, the power dependence of the signal on residence time varies with pressure, ranging from  $(\text{Residence Time})^{1.1}$  at 5 mtorr to  $(\text{Residence Time})^{1.7}$  at 20 mtorr. Third, the pressure dependence, i.e., any vertical line comparison of data points, varies with residence time. At low pressure there appears to be much a smaller pressure effect than at higher pressures. Note the residence time effect can be significant, less than or equal to a factor of 100, whereas the maximum pressure dependence corresponds to about a factor of 8.

Unfortunately this coupling of pressure and residence time makes it impossible to evaluate a single signal level pressure dependence. Referring back to Figures 71 and 72, the total flow of gas is constant in each figure and the pressure is varied by changing the pump conductance value. Since residence time is proportional to the ratio of pressure to flow rate,  $P/F$ , and since Figure 73 suggests the residence time power dependence of 1.1 to 1.7, it becomes unclear whether the pressure dependences observed in Figures 71 and 72 are due to pure pressure effect, pure residence time effect, or a convolution of these two.

Prior to recognition of the strong residence time effect, we collected a large volume of time dependent data leaving the conductance valve set and varying gas flow rates to effect a pressure variation, and observing the resulting signal level change. Our initial intentions were to use steady state arguments,

$$[O_3^*(v)] = \frac{\text{Volumetric Production Rate} \left( \frac{\text{molecules}}{\text{cc s}} \right)}{\text{Total Loss Rate} \left( \frac{\text{molecules}}{\text{s}} \right)} \quad (44)$$

and the observed pressure dependence of  $O_3^*$  emission with the pressure dependence of the total loss rate, i.e., either the diffusion limited pressure dependence of  $1/p$  at low pressure or the  $p^{1.0}$  dependence at high pressure due to collisional relaxation, to evaluate the pressure dependence of the production rate and determine conclusively whether the mechanism was two or three body. Figure 74 presents the total population derived from the spectral fitting code at electron beam termination for 1 mtorr of  $O_2$  and a variety of Ar pressures. Only a slight variation with Ar pressure is observed. To augment the analysis we normalized these data points to expected residence time effect by dividing the sum of population by  $(P/F)^n$  where  $n$  ranged from 1.1 at low pressure to 1.7 at high pressure. Based upon our earlier observations, there was no reason to believe this would provide any physical insight. However the plot of normalized data, Figure 75, shows a clear trend. Upon closer inspection we noticed that the  $P/F$  factors (proportional to residence time) varied from 0.037 to 0.081, roughly a factor of 2.2. By comparison in Figures 71, 72, and 73 the residence times were varied by an order of magnitude. The conclusion being, if we perform experiments in a narrow range of residence times, we may obtain an approximate measure of the pure pressure dependence of the steady state concentration of  $O_3^*(v)$ .

The sum of population determined by the spectral fitting code is dominated by the  $v=1$  contribution. To ascertain if the upper vibrational level populations have the same pressure dependence, we replotted the excluding  $v=1$  (see Figure 76). Within the data scatter we believe that all the vibrational levels possess the same pressure dependence.

Figures 77, 78 and 79 present this same analysis for 1 mtorr  $O_2$  over range of diluent  $N_2$  pressures. Within scatter of the data, we believe that all the vibrational levels possess a pressure dependence of  $p^2$  for  $N_2$  buffer gas as

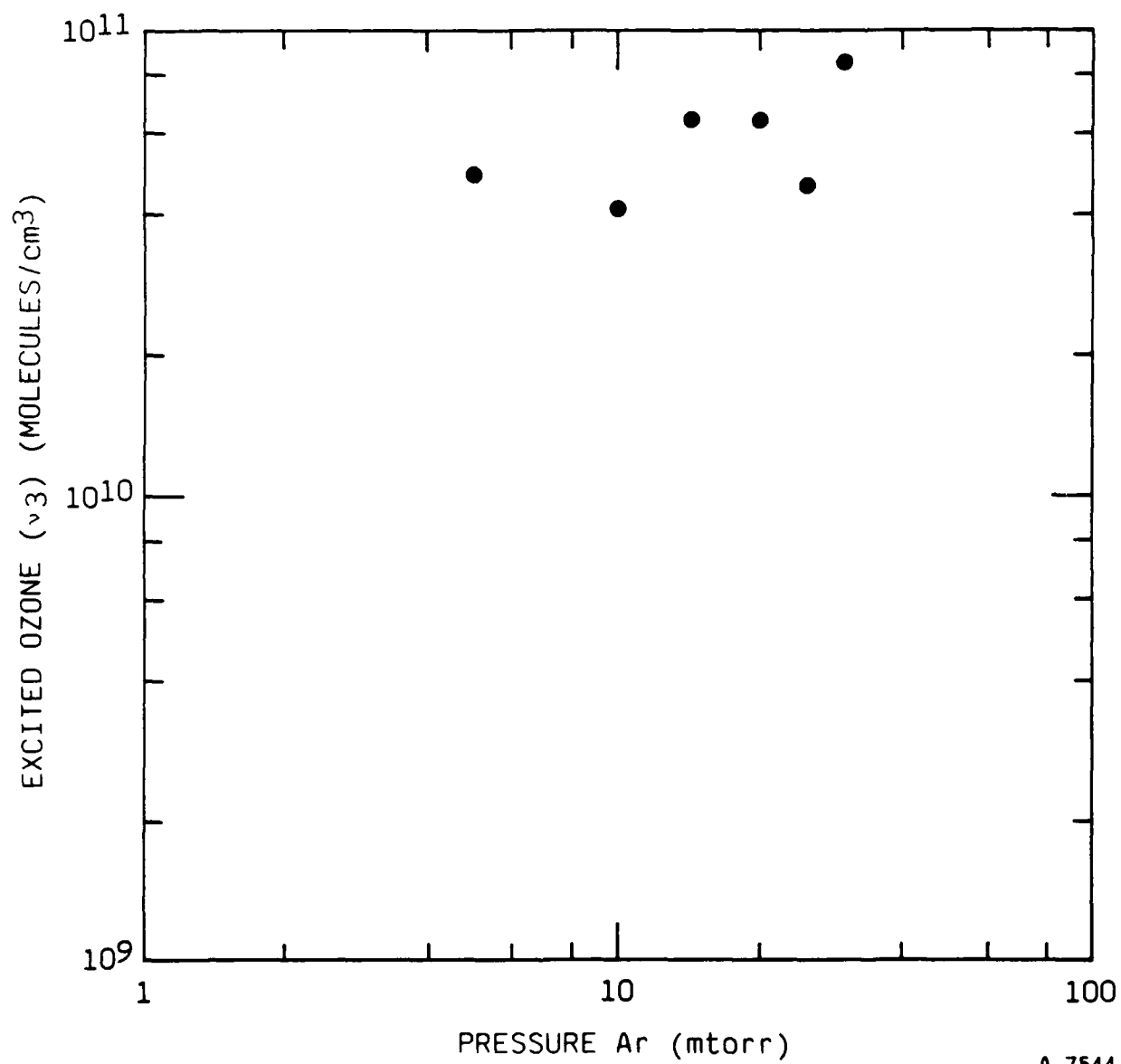
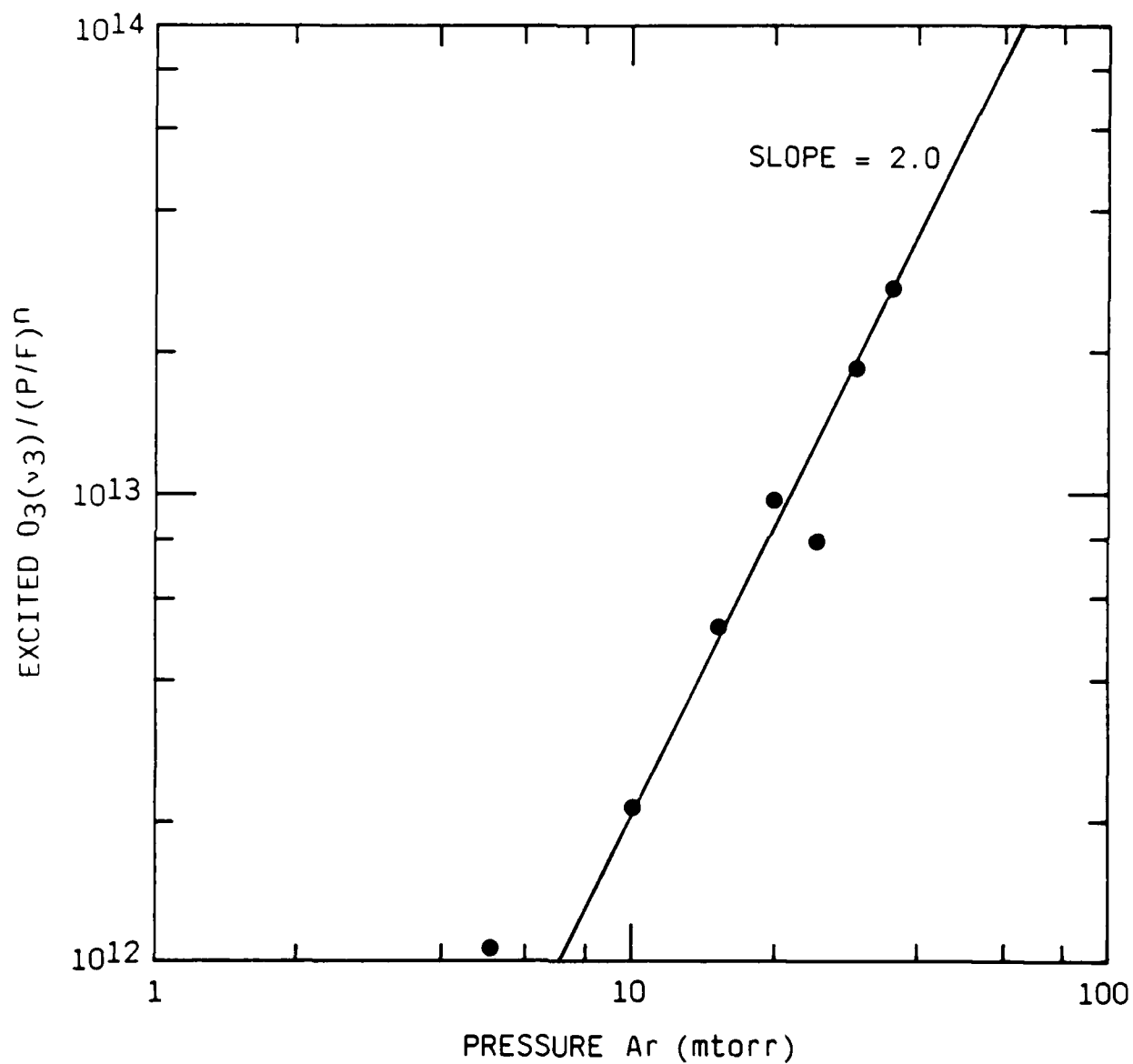


Figure 74. Sum of population of  $O_3^*$  from spectral synthetic code for 1 mtorr  $O_2$  in varying Ar pressure.



A-7545

Figure 75. Residence time normalized  $O_3^*$  population versus Ar pressure.

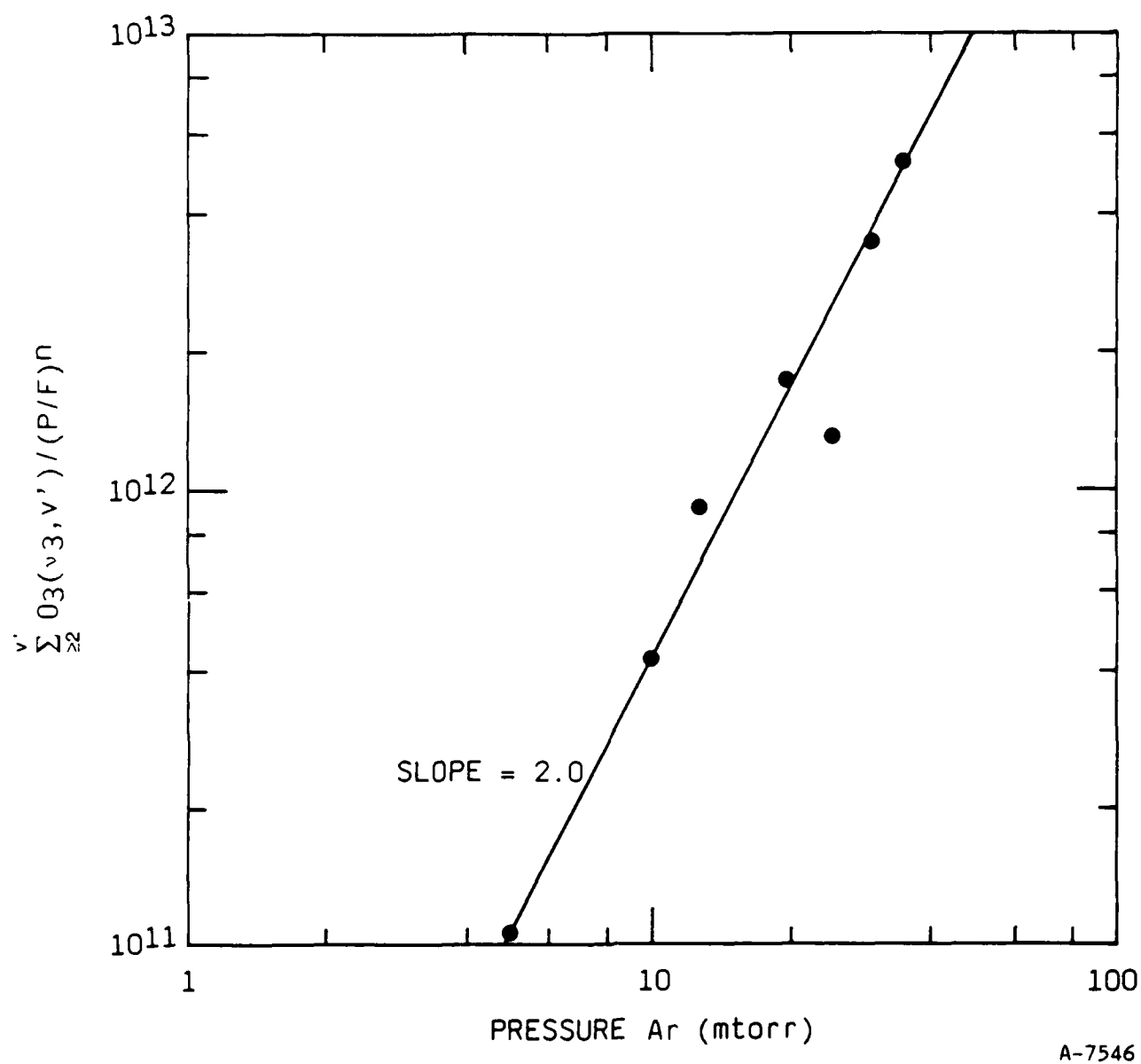
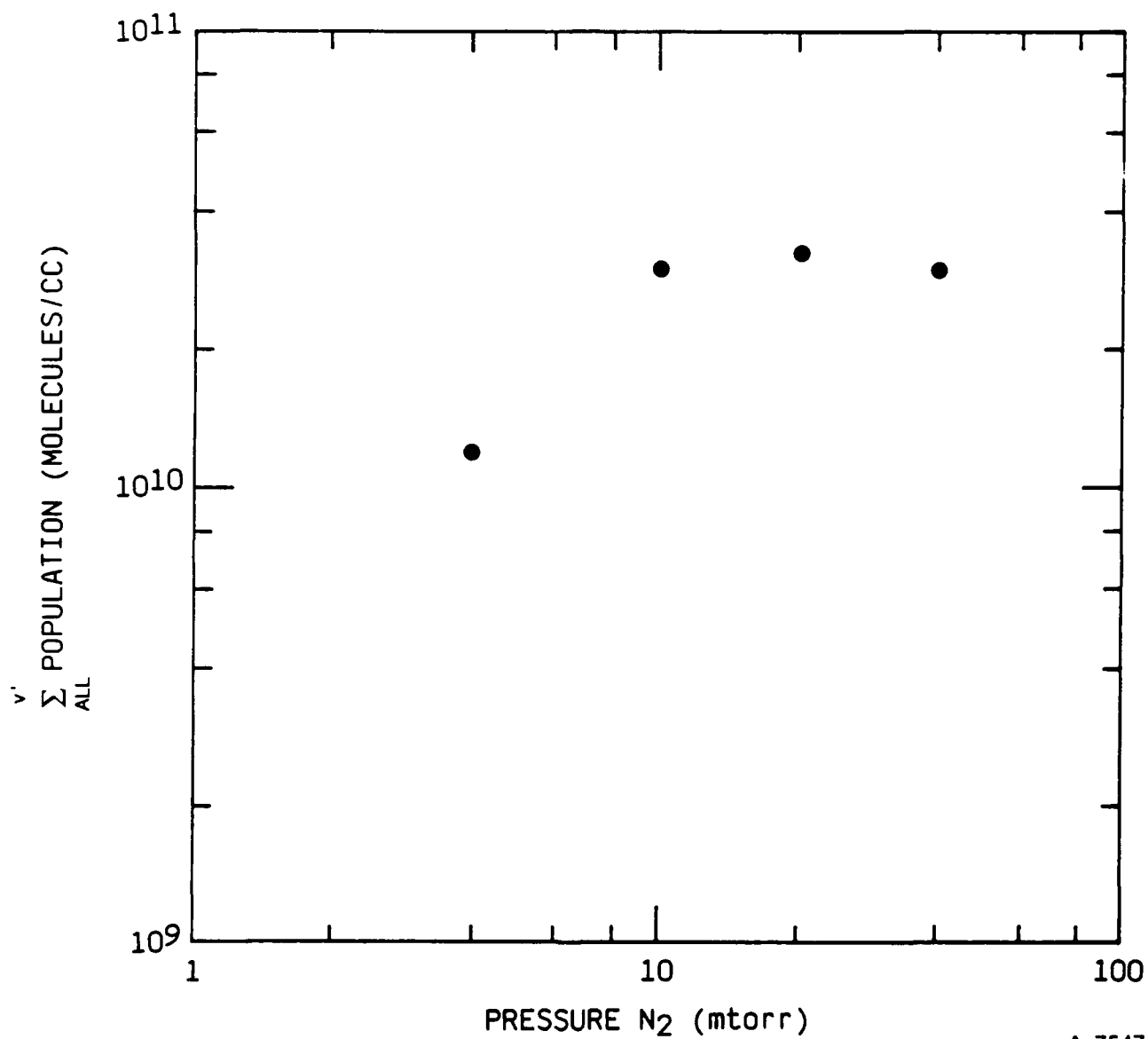


Figure 76.  $O_3^*(v \geq 2)$  population residence time normalized versus Ar pressure.



A-7547

Figure 77. Population of  $O_3^*(v)$  from spectral synthesis code for 1 mtorr  $O_2$  in varying  $N_2$  pressure.

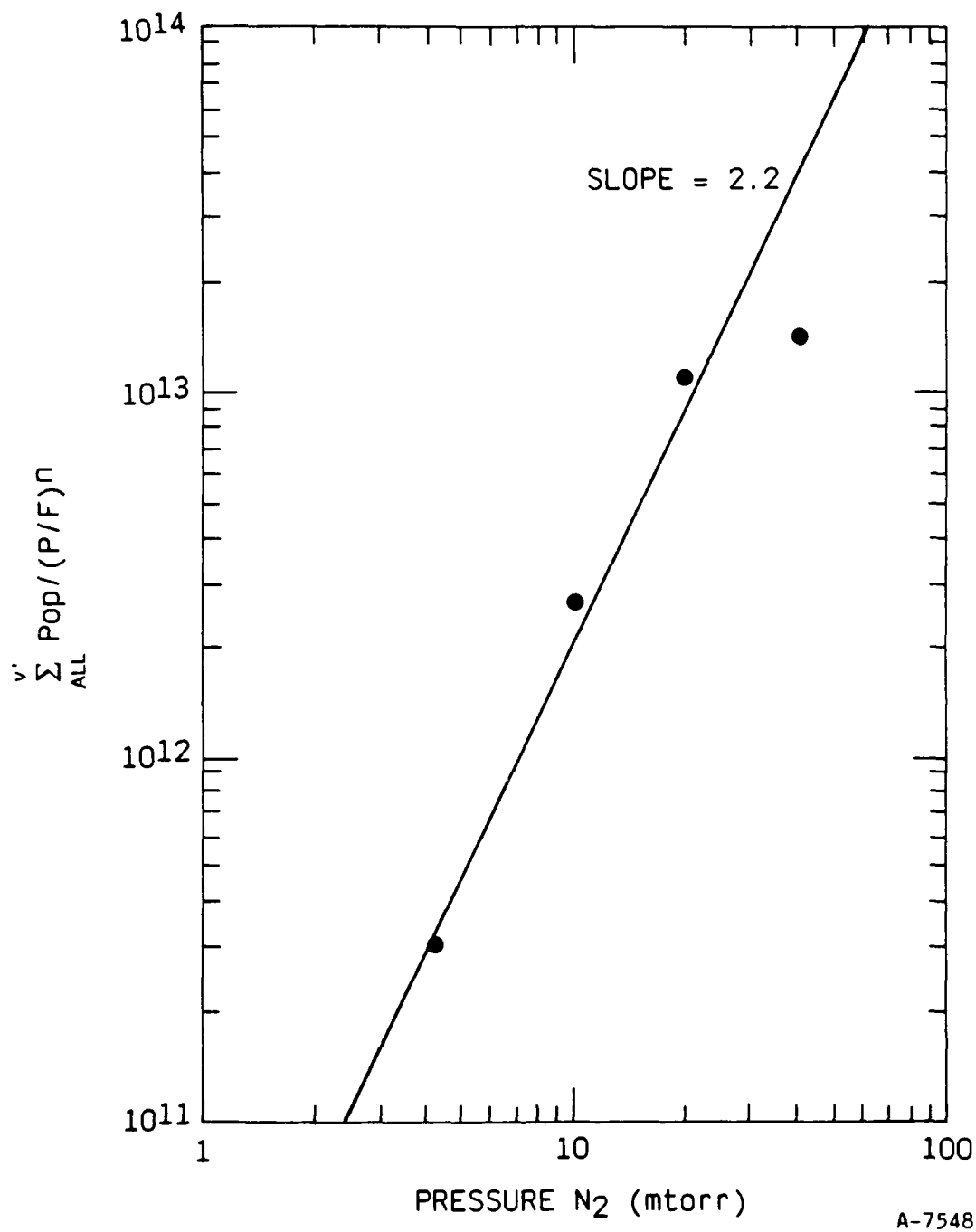
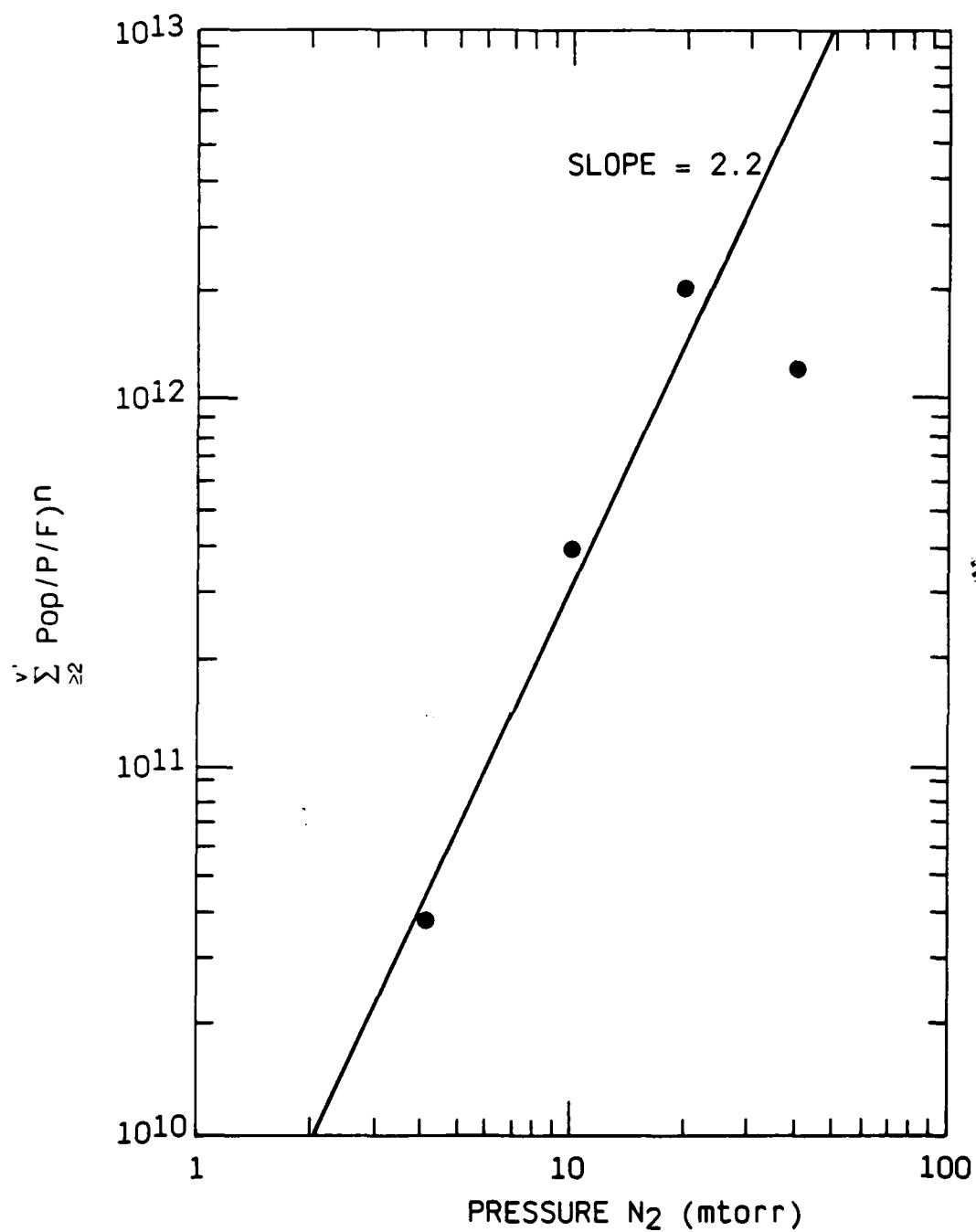


Figure 78. Residence time normalized  $O_3^*(v)$  population versus  $N_2$  pressure.





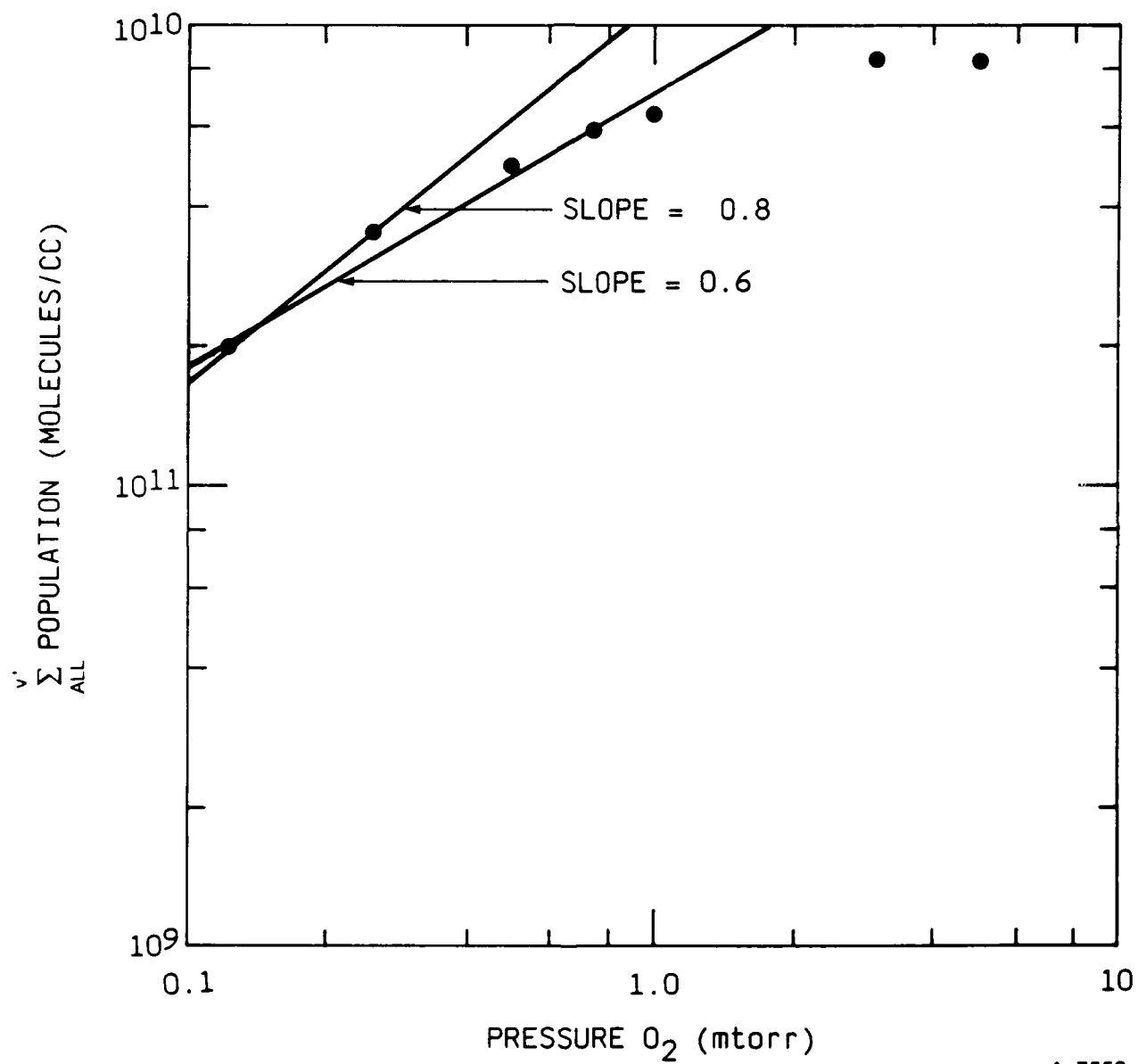
A-7549

Figure 79. Residence time normalized  $O_3^*(v \geq 2)$  population versus  $N_2$  pressure.

well once normalization by residence time occurs. For most pressures of  $N_2$ , collisional relaxation of  $O_3^*(v)$  clearly dominates the loss rate. This observation coupled with the population pressure dependence just described suggests a production mechanism whose overall dependence on  $N_2$  buffer gas pressure is linear. Although less dramatically, Ar collisional relaxation also dominates the loss rate and leads to the conclusion that the production mechanism dependence on Ar buffer gas pressure is also linear.

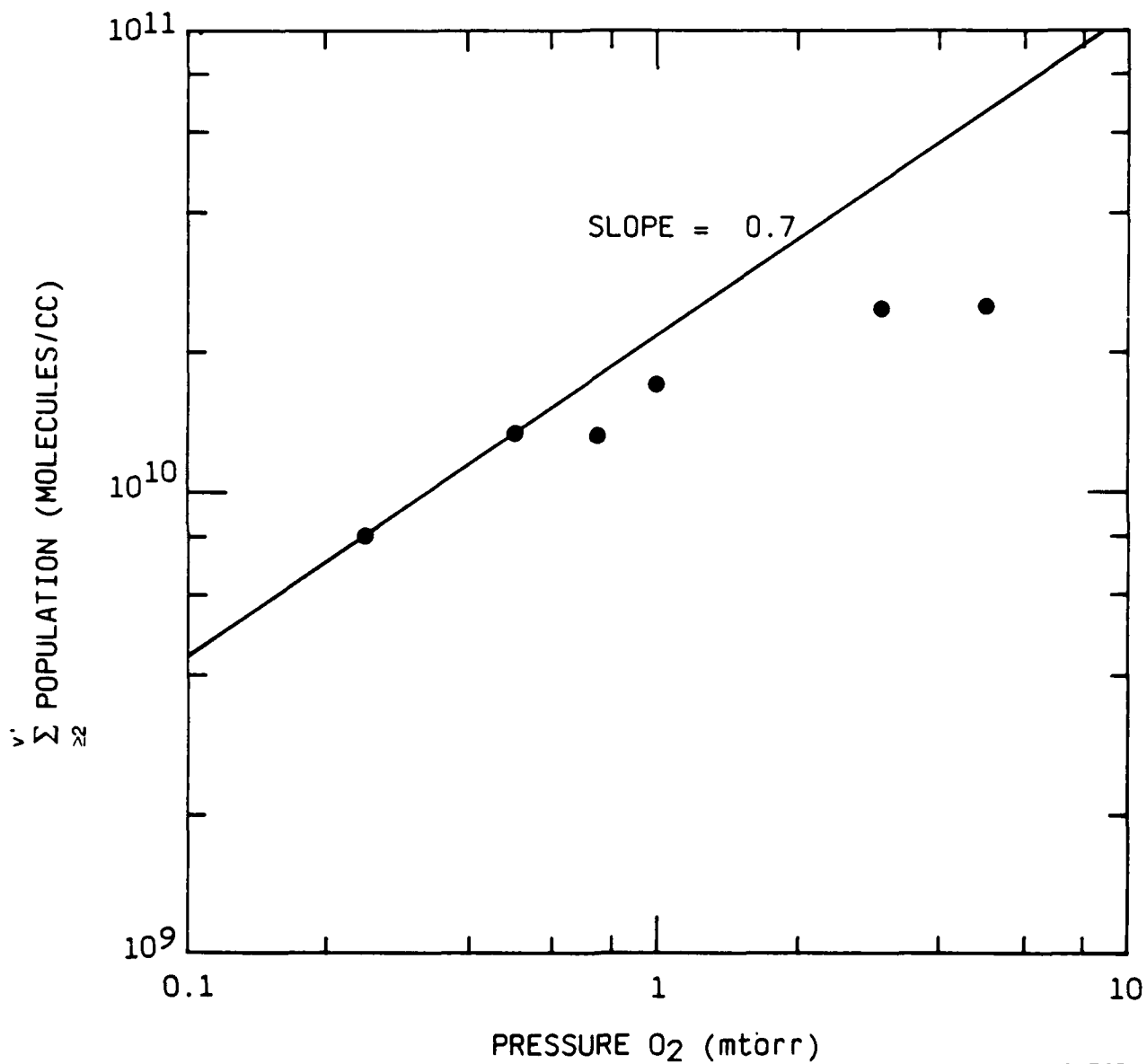
Experiments to determine the  $[O_3^*(v)]$  dependence on  $O_2$  pressure were performed with 0.15 to 5 mtorr of  $O_2$  diluted in 35 to 37 mtorr of Ar buffer gas. In this case the total pressure and total flow rates, hence residence time is not changing significantly. Figures 80 and 81 present the  $O_2$  pressure dependence of the  $[O_3^*(v)]$  at electron beam termination. Calculations based on the collisional relaxation rate constant described in the next section predicts that at 0.2 mtorr  $O_2$ , the Ar collisional relaxation rate is 59 times larger than the  $O_2$  rate. At 1.2 mtorr  $O_2$ , the  $O_2$  collisional relaxation approaches 10 percent of the Ar collisional relaxation rate. Based on these observations the total loss rate would not be changing significantly. The observed roll-over in the pressure dependence at  $O_2$  pressures between 1 and 2 mtorr, however, indicates that a relatively complex production mechanism is occurring.

The temperature dependence of the  $O_3^*(v=1)$  emission intensity was measured in both Ar at  $\sim 39$  mtorr and at  $\sim 10$  mtorr, and in  $N_2$  at  $\sim 36$  mtorr and at  $\sim 8.5$  mtorr. The temperature in  $N_2$  ranged from 104 to 153 K and in Ar from 94 to 123 K. The log-log plots of signal versus temperature are shown in Figures 82 and 83. In Argon the temperature dependences at high and low pressure agree rather well giving a value of  $T^{-n}$  where  $n=5$ . In  $N_2$  the temperature dependence at high and low pressure differ significantly, i.e.,  $T^{-n}$  where  $n=4$  at low pressure and  $n=6$  at high pressure. Compared to the  $T^{-2}$  dependence observed for the three-body recombination reaction, these values are larger than expected. Data obtained in COCHISE at a variety of  $O_2$  mole fractions gave a  $T^{-3.2}$  temperature dependence. Collisional relaxation processes would



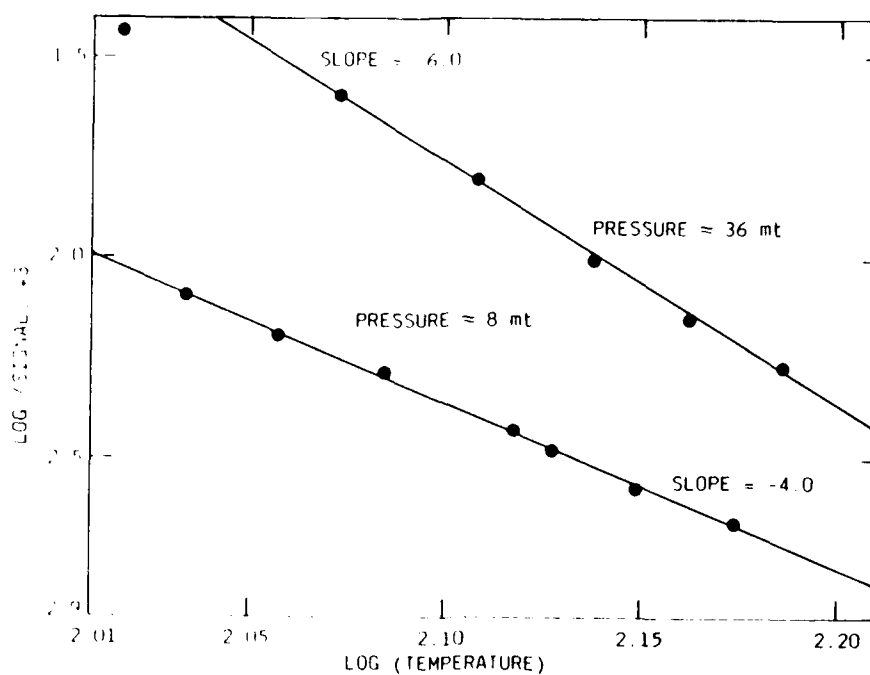
A-7550

Figure 80. Population of  $\text{O}_3^*(v)$  with varying amounts of  $\text{O}_2$  in 37 mtorr Ar.



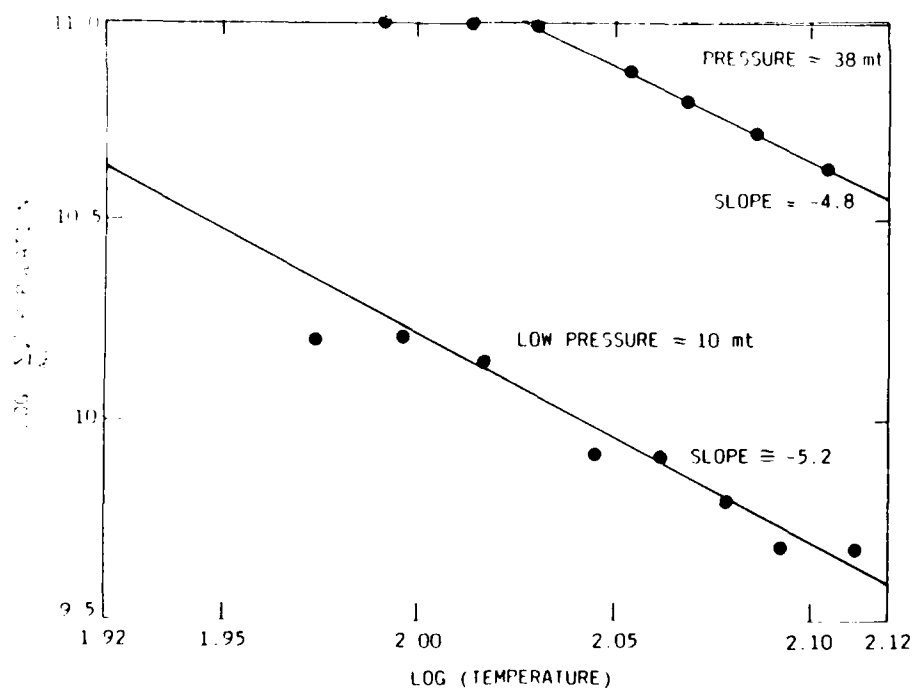
A-7551

Figure 81. Population of O<sub>3</sub>\* (v ≥ 2) with varying amounts of O<sub>2</sub> in 37 mtorr Ar.



A 7537

Figure 82. Temperature dependence of  $0_3^*(v=1)$  emission intensity in  $N_2$  buffer gas.



A 7536

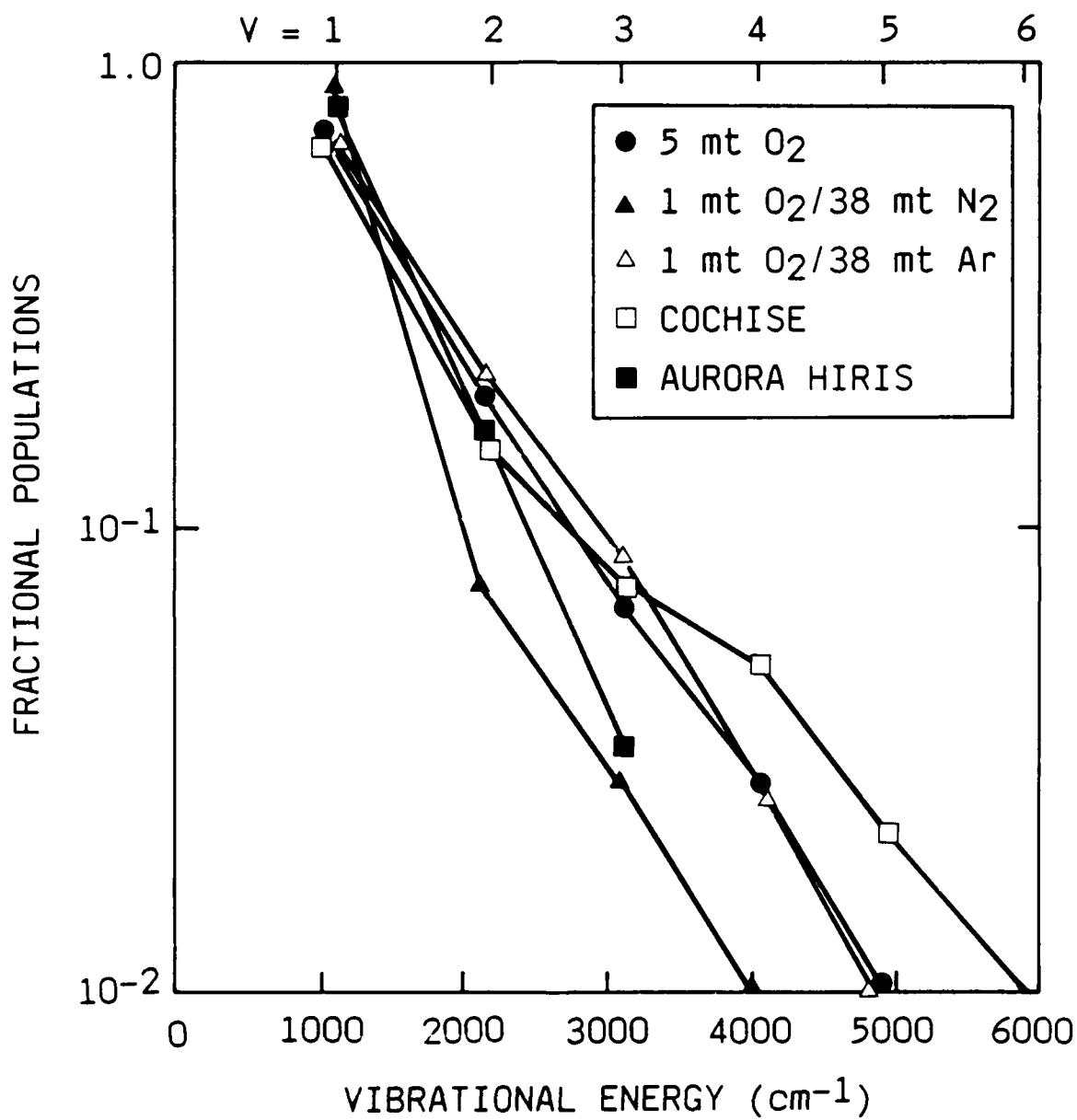
Figure 83. Temperature dependence of the sum of  $0_3^*(v)$  population in a buffer gas.

processes would contribute at most a  $T^{1/2}$  factor, leaving our production temperature dependence significantly larger than previously observed. Recent observations of the role of wall passivation on  $O_3$  fluorescence intensities suggests that some of the observed reduction at higher temperatures can be attributed to passivation loss.

The spectral synthesis code was utilized to determine  $O_3^*(0,0,v)$  vibrational distributions at electron beam termination. Figure 84 presents a comparison of these distributions with COCHISE observations and the bright arc observed in HIRIS auroral measurements. The COCHISE data at higher pressure represents the expectation for the three-body recombination mechanism and matches the distribution obtained from SPIRE measurements of the quiescent upper atmosphere. In general our measurements and the HIRIS aurora measurements are "colder" than that obtained from a three-body recombination mechanism.

Figure 85 shows that Beam Plasma Discharge can substantially alter the vibrational distribution. This is not a contributing factor in either the high pressure (38 mtorr) Ar or  $N_2$  data of Figure 84, since we were unable to sustain a BPD above 15 mtorr total pressure. However, this effective secondary electron heating may contribute to the fact that the aurora data is hotter than the 38 mtorr  $N_2$  LABCEDE measurements.

Peculiar to all these  $O_3^*$  observations was the fact that even though the fluorescence intensity was synchronous with the electron beam pulse, the initial signal intensity approached a steady state value very slowly. The rise/fall time of both the  $O_3^*(v)$  at  $9.65 \mu m$  and OI at  $2.89 \mu m$  upon addition or shutoff of  $O_2$  gas flow were measured. The CVF was operated in a hybrid mode where the signal level to the PDP/11 computer was temporally resolved but not spectrally resolved. Experiments presented in Figures 86 through 89 were performed with a 21 ms wide electron beam pulse at a pulse repetition rate of 37 Hz. Time constants,  $T_c$ , were calculated based on the time for the signal level to change one e-fold, i.e., a drop of 63 percent from the steady state value or the time to rise to 63 percent of the steady state value. The data



A-7552

Figure 84. Ozone vibrational distributions at beam termination  $0_3^*(0,0,v)$ .

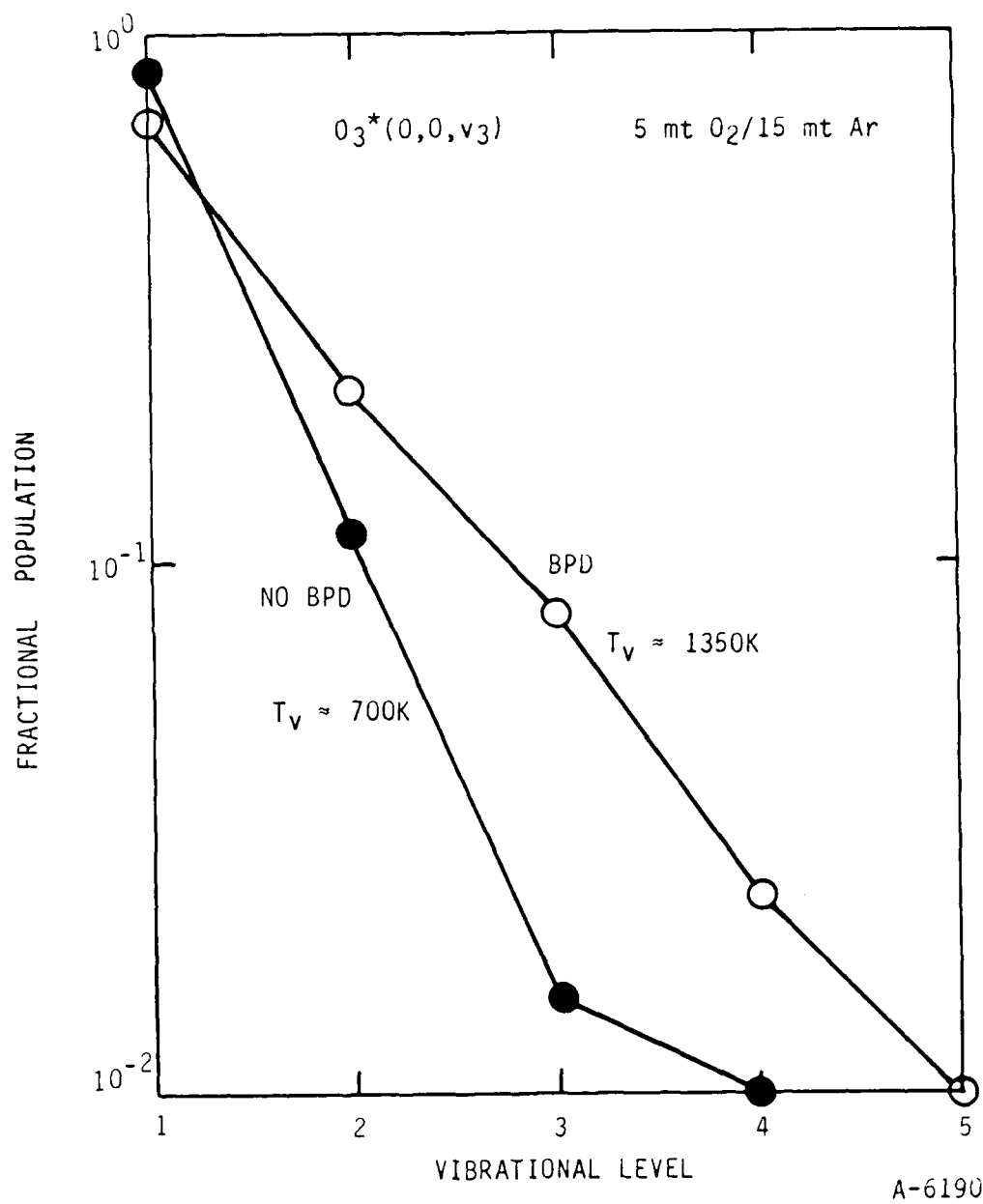


Figure 85. Beam termination vibrational distributions of  $O_3^*(0,0,v)$  with/without BPD.



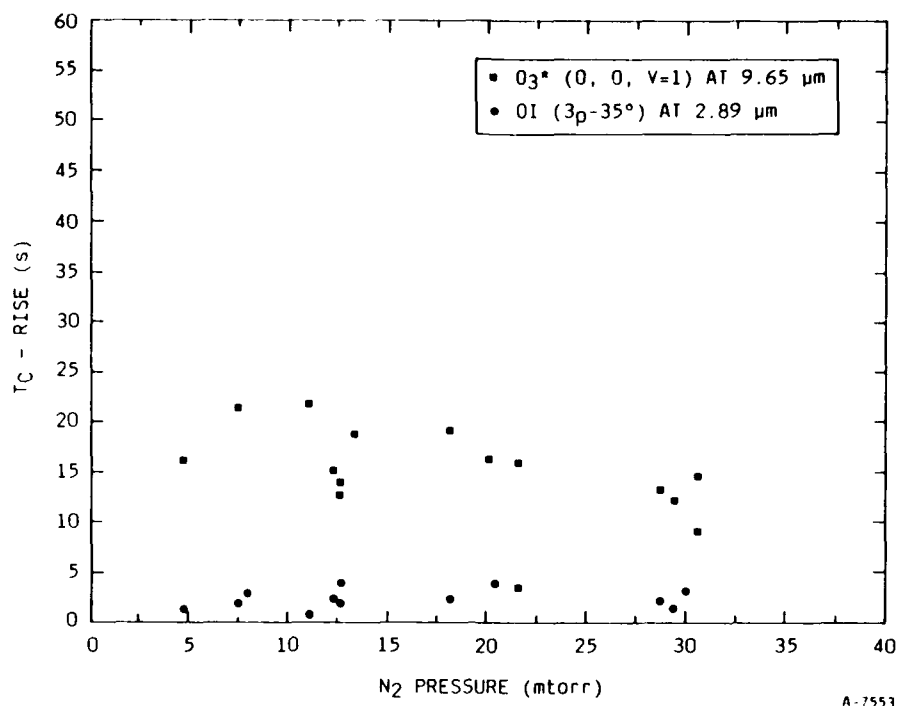


Figure 86. Pressure variation of rise times of fluorescence intensity upon start of  $O_2$  flow to generate a  $1/6:O_2/N_2$  gas mixture.

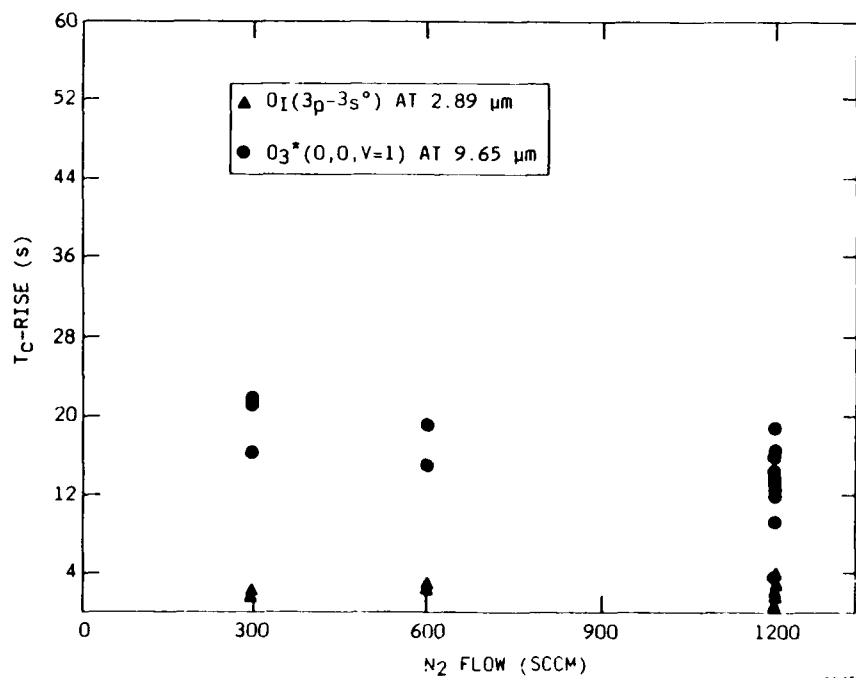
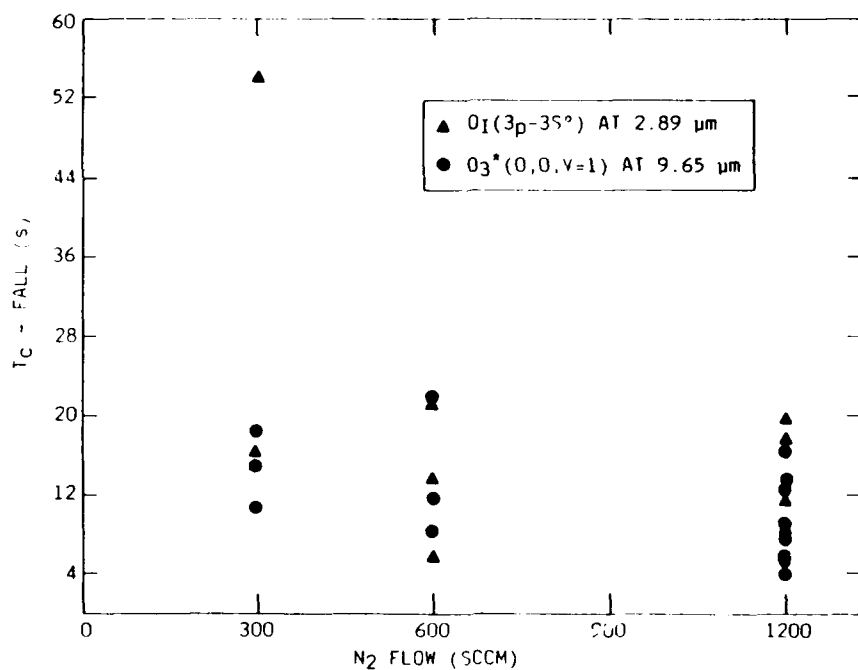
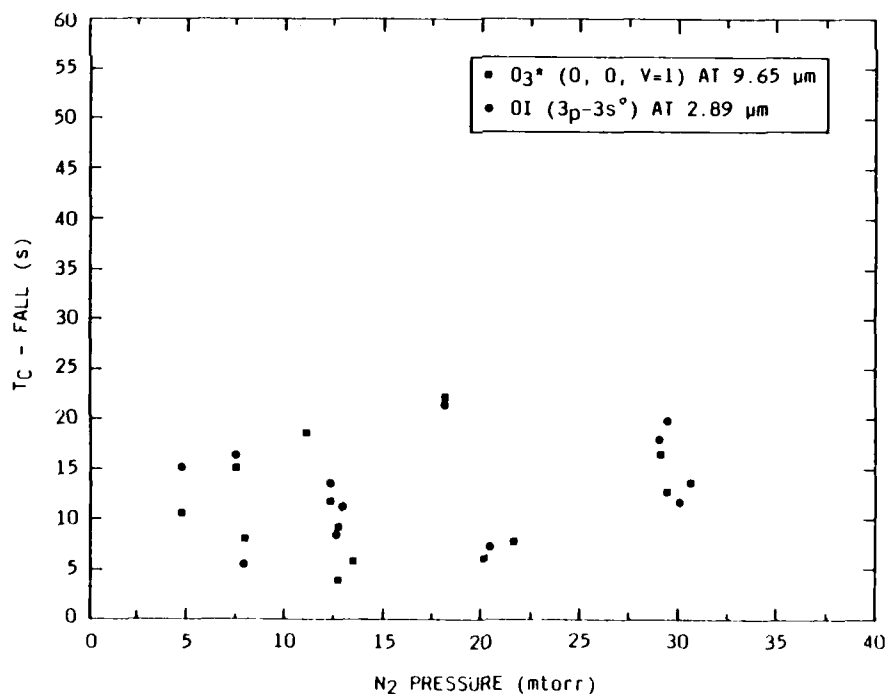


Figure 87. Flow variation of rise times of fluorescence intensity upon start of  $O_2$  gas flow to obtain a  $1/6:O_2/N_2$  gas mixture.



A-7534

Figure 88. Flow variation of fall times of fluorescence intensity upon shutoff at  $O_2$  gas flow for a  $1/6:O_2/N_2$  gas mixture.



A-7554

Figure 89. Pressure variation of fall times of fluorescence intensity upon shutoff of  $O_2$  gas flow for a  $1/6:O_2/N_2$  gas mixture.

is plotted without regard to gas residence time in the tank. The rise time data, Figures 86 and 87, shows a dramatic difference in time for observation of the OI emission and  $O_3^*$  emission upon initiating the  $O_2$  flow. The  $T_c \sim 2s$  for observation of OI emission is attributed to the flow time from the mass flow control valve to the point of interaction with the electron beam. The time constant for observation of  $O_3^*(v=1)$  emission,  $T_c \sim 15s$ , can only be attributed to the slow buildup of a long-lived metastable species involved in the formation of  $O_3^*$ . Figures 88 and 89 do not show time separations for decay of OI and  $O_3^*$  emission. Note that these decay time constants are consistent with our residence time values presented earlier, and thus gas residence in the tank control the  $O_2$ , O and  $O_3$  removal rates.

### 9.3 MECHANISMS

The experimental observations permit some preliminary speculation about the observed  $O_3^*$  production processes. Three body processes such as



are unable to produce sufficient  $O_3$  to explain the observed intensity levels. Moreover the vibrational distributions created by these processes has been measured previously in the COCHISE facility.<sup>138,139</sup> They do not resemble the distribution in LABCED. Radiative association



would have to occur with a rate coefficient of  $10^{-16} - 10^{-17} \text{ cm}^3 \text{ molecule}^{-1} \text{ s}^{-1}$  to produce the observed levels, yet the most rapid radiative association rates measured are an order of magnitude slower. The ozone appears to require the build up of a long lived state since the fluorescence signal does not reach a steady state value until after many beam pulses. However, the observed fluorescence time history is synchronous with the electron beam. This suggests processes such as



where  $O_2^{**}$  is a long lived metastable and  $O_2^*$  can be a very reactive state. Thermochemistry demands that the total internal energy of the reactants be at least 4 eV (in addition to the energy of any barrier in the reaction channel). Thus at least one of the reagents would have to be in the  $C^1\Sigma$ ,  $A^3\Sigma$ , or  $A'^3\Delta$  states. The other reaction partner could then be any bound  $O_2$  state including vibrationally excited ground state. However, we must use future experiments to determine that the walls do not play a significant role in the  $O_2^{**}$  production or even produce  $O_3$  directly. In that case



would provide the beam synchronous fluorescence signal. Our rough modeling indicates that for process (47) to explain the observed intensity levels: 1) ozone is produced efficiently at the walls, nearly every oxygen atom produced by the beam eventually is transformed into  $O_3$ ; 2) ozone leaves the walls upon formation and can return to the beam irradiated volume; and 3)  $O_3^*$  is efficiently produced upon electron impact of  $O_3$ , dissociation is not a major process. All these criteria must be met.

Although process (47) appears unlikely we will direct future experiments to quantitatively address the role of the walls on ozone formation either by  $O_3$  or  $O_2^{**}$  production. These experiments will observe fluorescence levels as a function of gas residence time and flow rates, electron irradiation time, level and duty cycle. Obviously an active  $O_3$  monitor would permit total ozone production to be measured and related to the excited fraction,  $O_3^*$ . Time-resolved infrared laser based diagnostics may need to be implemented in order to unravel the details of the production process.

#### 9.4 CONCLUSIONS

To summarize, we observe significantly more ozone fluorescence intensity than can be attributed to the three-body recombination process; the steady state vibrational distribution of  $O_3^*(v)$  more closely matches that observed in aurora measurements than that obtained from the three-body recombination mechanism; a steep temperature dependence of the fluorescence intensity is observed in Ar and in  $N_2$ . Both scalings are larger than the  $T^{-3.2}$  dependence observed for three-body recombination. All of these observations suggest the recombination mechanism is at best a minor contribution to the production of  $O_3^*(v)$  in the LABCEDE tank. Further observations including: 1) a 30s rise time; 2) a quadratic buffer gas pressure dependence for  $N_2, Ar$ ; 3)  $p^n$  where  $0.5 \leq n \leq 1$  for  $O_2$  gas; and 4) a pressure dependent residence time  $\tau^n$  where  $1.1 \leq n \leq 1.7$ , of the fluorescence intensity suggesting a complex production mechanism.

## 10. OZONE VIBRATIONAL RELAXATION MEASUREMENTS

While performing the pressure dependence studies of  $O_3^*(v)$  fluorescence intensity, we acquired a large data base of time dependent spectra. Nominally, 40 spectra were obtained at 6 ms time intervals for each of five or six pressure settings of  $O_2$ ,  $N_2$ , Ar. In addition, data sets were often repeated to check experimental reproducibility, to check for B-field effects, etc. Upon review, in excess of 3000 spectra of  $O_3^*(v)$  were obtained. Spectral fitting was performed on approximately two-thirds of these spectra to obtain time dependent vibrational level population distributions. Figure 90 shows an example of the population time histories determined from the spectral fitting code. These temporal histories of  $O_3^*(v)$  may be interpreted in terms of quenching by the reactant gases. For the case of  $O_2/N_2$  gas mixtures, the total quenching rate for each level  $v$ ,  $R_v$ , may be written as a sum of these processes

$$R_v = \sum_M k_M(v) [M] + A_{v \rightarrow v-1} + R_{Diff} \quad (48)$$

where  $M$  represents the quenching partner (i.e.,  $N_2$ ,  $O_2$ ,  $O$ ),  $k_M(v)$  is the rate coefficient for single quantum vibrational relaxation of  $O_3^*(v \rightarrow v-1)$ ,  $A_{v \rightarrow v-1}$  is the Einstein coefficient for the single quantum relaxation of  $O_3^*(v)$  and  $R_{Diff}$  is the net rate of loss of  $O_3^*(v)$  out of the field of view of the CVF.  $R_{Diff}$  is normally negligible at high pressure with Eq. 48 being dominated by the quenching terms. At low pressure it will be important for long lived species, but have no significant variation with vibrational level.

Changes in the observed population of a vibrational level as a function of time is a balance between feed via relaxation of the level above and losses by relaxation into the next lower level.

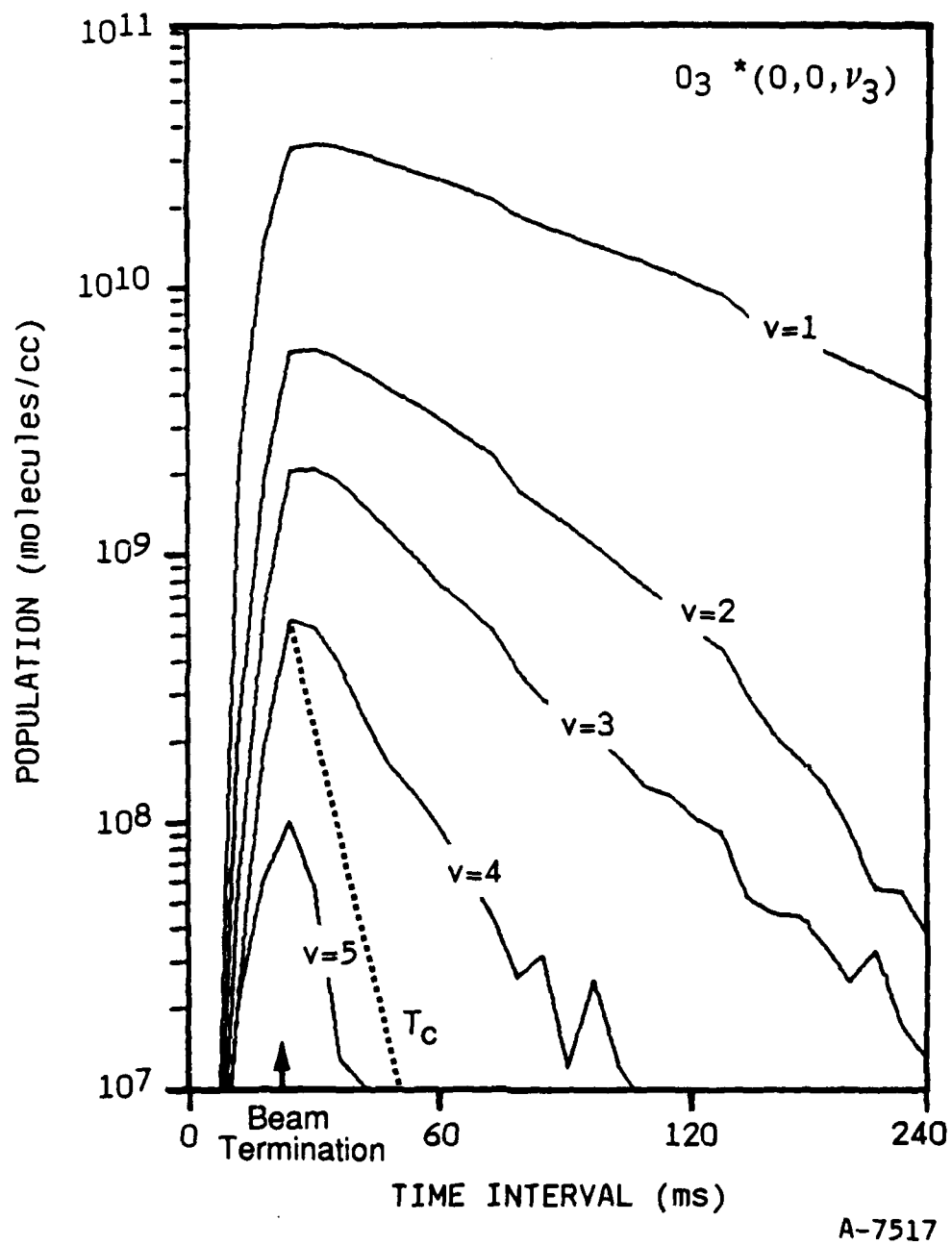


Figure 90. Temporal behavior of  $O_3^*$  fluorescence for a 9 mtorr Ar/1 mtorr  $O_2$  mixture.

The master equations which describe the time rate of change of the coupled vibrational populations may then be written:

$$\begin{aligned}
 \frac{dn_1}{dt} &= -R_1 n_1 + R_2 n_2 \\
 &\cdot \\
 &\cdot \\
 &\cdot \\
 \frac{dn_m}{dt} &= -R_m n_m + R_{m+1} n_{m+1} \\
 &\cdot \\
 &\cdot \\
 &\cdot \\
 \frac{dn_N}{dt} &= -R_N n_N ,
 \end{aligned}
 \tag{49}$$

where  $n$  represents the most highly excited vibrational level and  $n_m$  is the relative population of vibrational level  $m$ . Determination of the  $R_m$  values is complicated by the numerical inaccuracies, introduced upon evaluating the slopes  $dn_m/dt$  of the experimental data. A time integrated approach, developed previously for CO and NO relaxation measurements,<sup>146</sup> improves the accuracy of the deduced values of  $R_m$ . Integrating Eq. (49) over all times between  $t_1$  and  $t_2$ , we obtain

$$\Delta n_m = n_m(t_1) - n_m(t_2) = R_{m+1} a_{m+1} - R_m a_m ,
 \tag{50}$$

where

$$a_m = \int_{t_1}^{t_2} n_m dt .
 \tag{51}$$

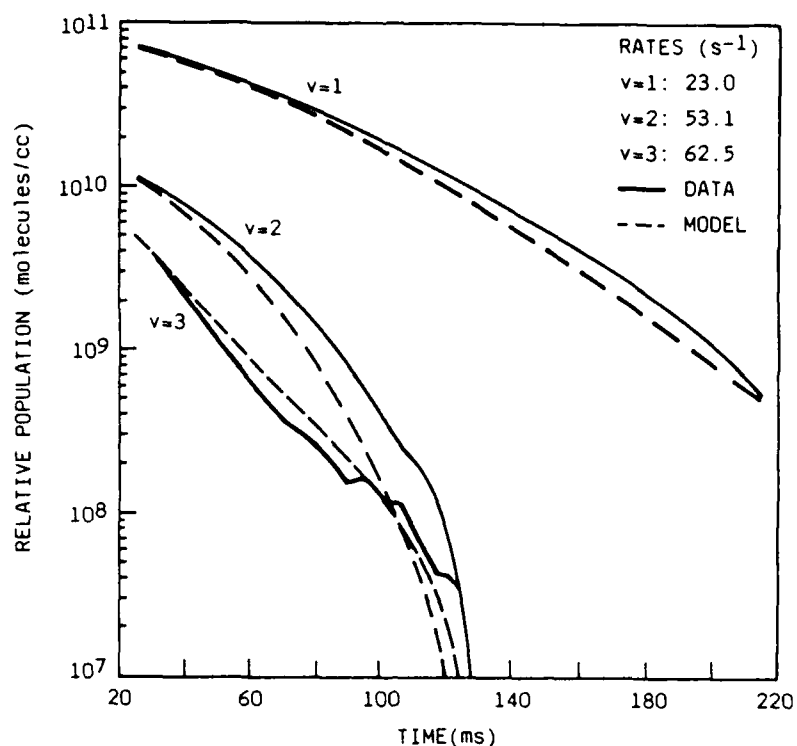


This integral form of the master equations is particularly useful in that it not only eliminates the need for derivative values but also allows determination of the best value of  $R_m$  over a specified time interval, effectively filtering random fluctuations in the population histories introduced in the curve fitting process. Rearranging Eq. (50) permits direct specification of the rates  $R_m$  in terms of measured quantities

$$R_m = \sum_{v=m}^n \Delta n_v / a_m \quad . \quad (52)$$

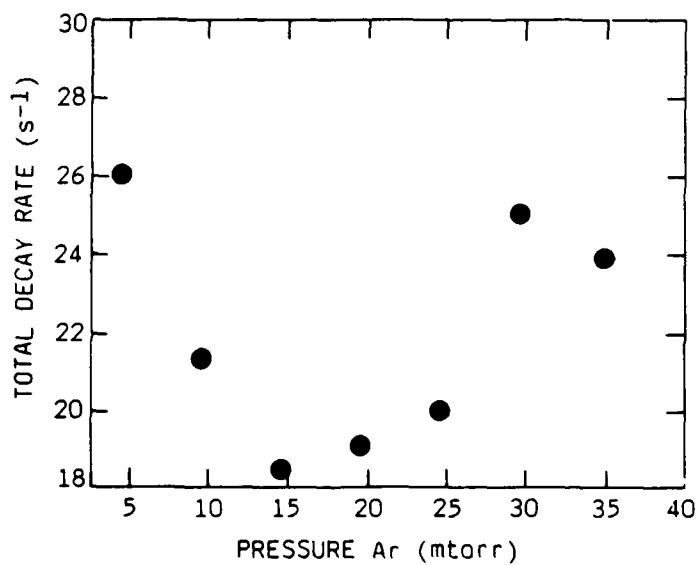
The deactivation rates  $R_m$  have been deduced from the measured vibrational population histories (such as shown in Figure 90) through use of Eq. (52). The populations were typically integrated over 100 ms, starting just after beam termination (populations were measured at 6 ms intervals). Variation of the time interval chosen for integration has only a small effect on the deduced rates. The populations of the highest vibrational levels tend to be the least accurately determined; primarily because the rapid relaxation out of these levels causes the populations at all times to decrease with increasing  $v$  (see Figure 90), thus resulting in signal-to-noise limitations being more important for the higher levels. Accordingly, the rates could generally be evaluated for only the lowest three vibrational levels even though emission from five levels was observed under the best conditions. It was found that inclusion of the more poorly determined populations in the analysis produced only 5 to 10 percent changes from the rate values determined without the high  $v$  data. The aim of the analysis is not to deduce the rates  $R_m$  but to separate the effects of the competing relaxation process [the different terms in Eq. (48)]. Figure 91 shows the typical level of agreement that was obtained between the kinetic model and population time histories.

The second step of the data interpretation is to subject the total relaxation rates from the different experiments with varying pressures of one of the components of the gas mixture to a Stern-Volmer type analysis. Figure 92 shows



A-7518

Figure 91. Comparison of relaxation rates using single quantum vibrational and radiative model for a 35 mtorr Ar/1 mtorr  $O_2$  mixture.



A-7369

Figure 92. Stern-Volmer plot of  $O_3^*(v=1)$  in 1 mtorr  $O_2$  and varying Ar pressure.

the Stern-Volmer plot of total decay rate versus pressure of Ar buffer gas for  $O_3^*(v=1)$  while maintaining a 1 mtorr  $O_2$  pressure. The rise in total decay rate below 15.0 mtorr Ar is evidence of diffusive losses of  $O_3^*(v=1)$  from the CVF field of view.

A careful mapping of the field of view was not undertaken. Without this information, and given the complex geometric coupling of the field of view and cylindrical electron beam volumes, an accurate determination of the diffusion loss rate is nearly impossible. However to determine whether this careful mapping would be warranted in future more accurate measurements, we applied a crude correction to calculate the effective diffusive loss rate via a simple gas kinetic formula and optimize the size of the field of view to obtain an Stern-Volmer plot intercept which matches the best available data for the Einstein coefficient of  $O_3^*(v=1 \rightarrow v=0)$ . We used

$$R_{\text{Diff}} = \lambda \bar{v} / 3r^2 \quad (53)$$

where  $\lambda$  is the mean free path,  $\bar{v}$  is the thermal velocity at  $\sim 90$  K, and  $r$  the field of view radius at the electron beam plane. To optimize the data, we utilized the best signal to noise data for both  $N_2$ , Ar buffer gas and the  $O_3^*(v=1)$  decay rate since the  $A_1$  radiative rate is the most agreed upon value. However, the Stern-Volmer intercept in our case represents the sum of:  $A_1$ , the contribution of  $k_{O_2}$  [ $O_2$ ], and  $k_M[M]$  where  $m$  may be any species other than the buffer gas molecule whose pressure variation is mapped out in the Stern-Volmer analysis. From later measurements,  $k_{O_2}$  [ $O_2$ ] represents less than a 10 percent increase in the intercept compared to  $A_1$ . To account for these contributions, an intercept of  $12 \text{ s}^{-1}$  was decided upon. Using these assumptions we obtained an effective radius of the field of view of 13.7 cm. From the diffusion corrected Stern-Volmer plot in Figure 93, we see that the high pressure data is affected by less than 5 percent but the low pressure has been forced to fit the intercept criteria. The slope of this line, albeit somewhat uncertain, corresponds to a quenching rate coefficient.

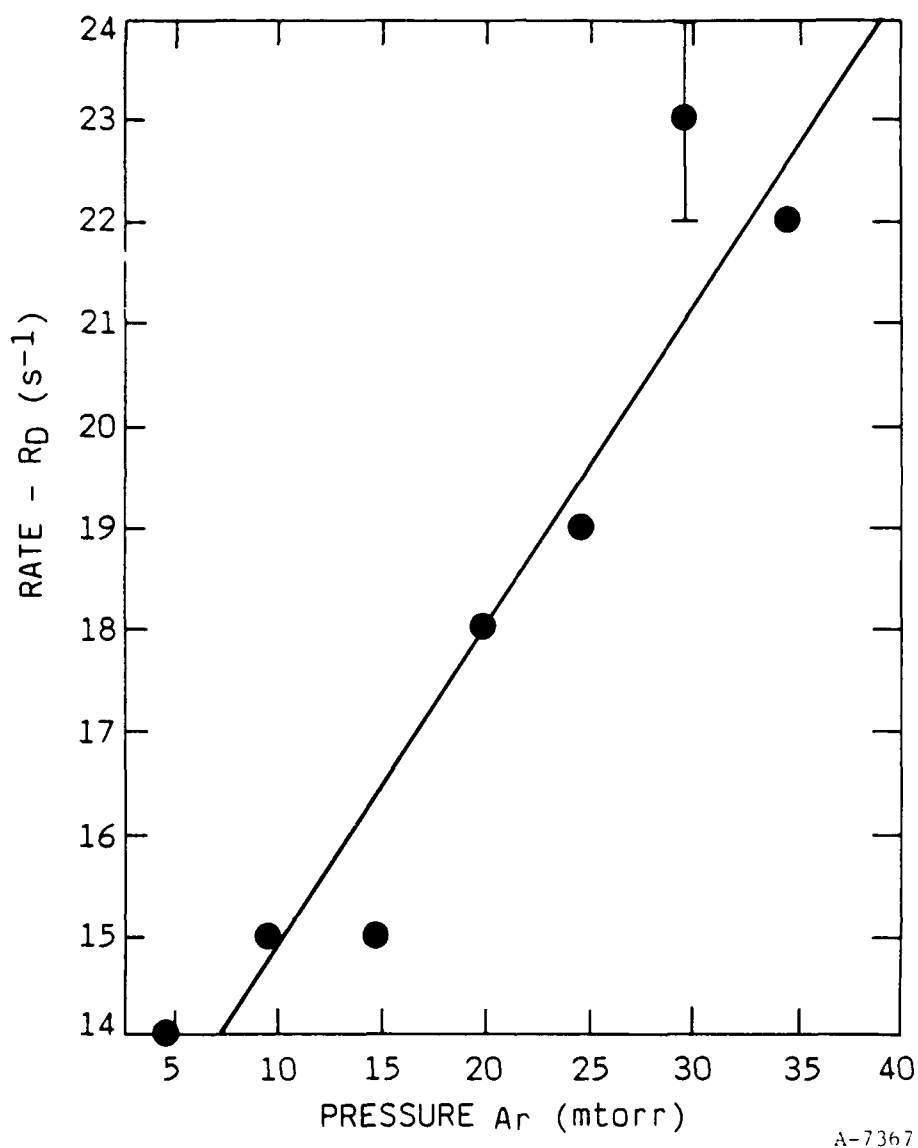
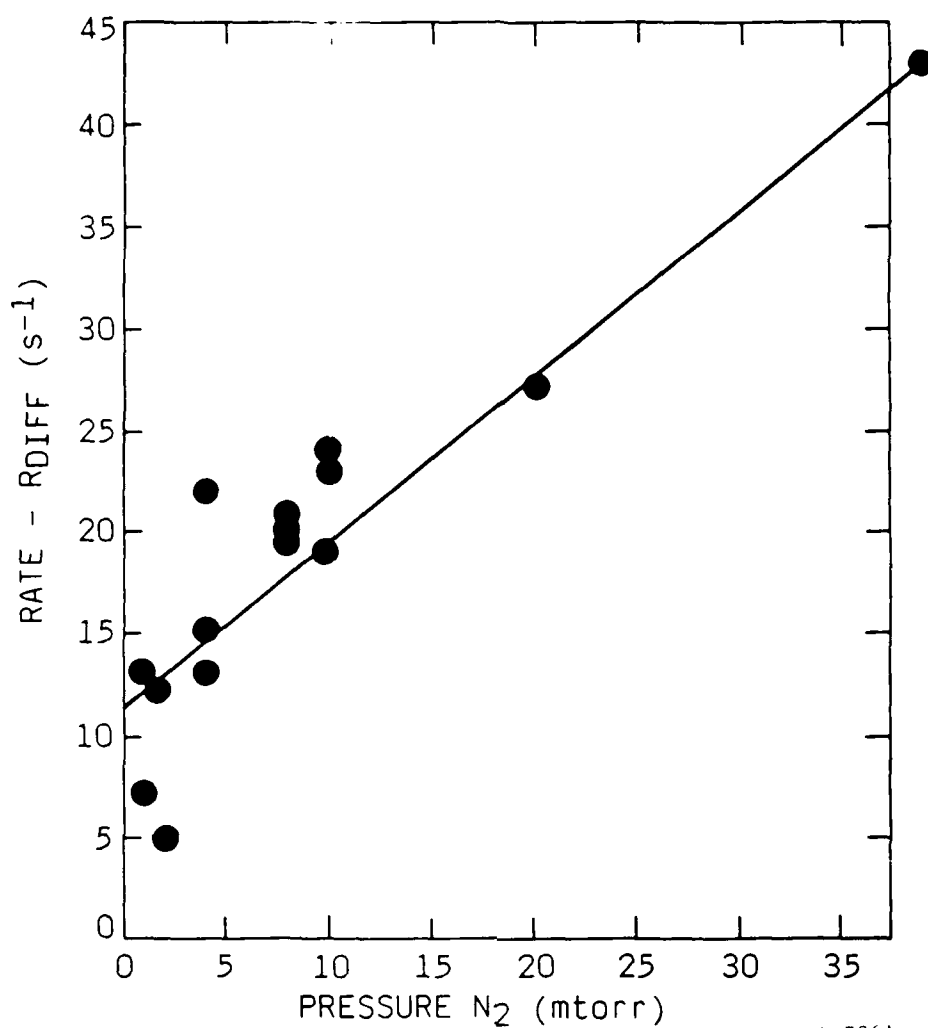


Figure 93. Diffusion corrected Stern-Volmer plot of  $O_3^*(v=1)$  in 1 mtorr  $O_2$  and varying Ar pressure.

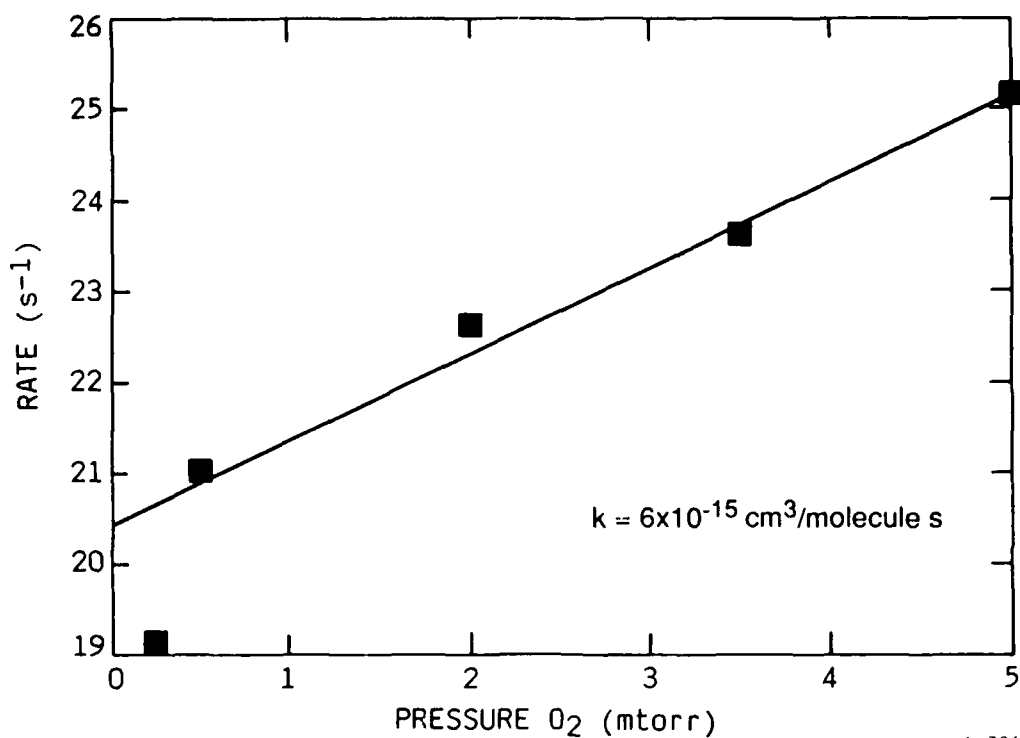
For  $O_2/N_2$  mixtures a range of  $O_2$  pressures from 0.5 to 2 mtorr were used. A Stern-Volmer plot for all these mixtures is shown in Figure 94. The data is crudely corrected for diffusive losses as described previously. Part of the data scatter at lower pressure is attributed to the range of  $k_{O_2}[O_2]$  contribution at different  $O_2$  partial pressures. The intercept for  $v=1$  is in reasonable agreement with the literature. Clearly,  $O_2/N_2$  mixtures require further investigation in future measurements.



A-7361

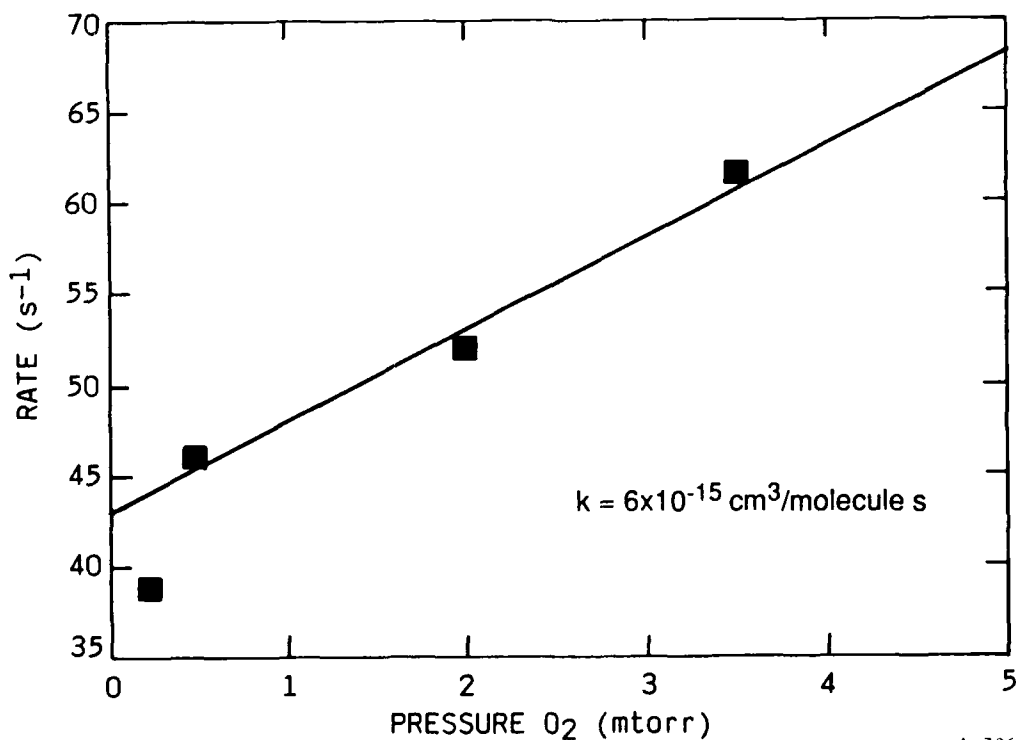
Figure 94. Stern-Volmer plot of  $O_3^*(v=1)$  for all  $O_2/N_2$  mixtures.

Measurements of  $O_3^*(v)$  vibrational relaxation by  $O_2$  were performed in a different fashion. In this case a partial pressure of Ar was maintained at 30 mtorr and the  $O_2$  partial pressure was varied between 0.2 and 5 mtorr. Diffusional corrections are less important. Figure 95 presents the Stern-Volmer plot of  $O_2/Ar$  mixtures with 30 mtorr Ar for  $O_3^*(v=1)$ . The  $k_{Ar}[Ar]$  contribution to the intercept is about  $11 \text{ s}^{-1}$  suggesting a  $A_1$  of  $9.5 \text{ s}^{-1}$ , about 10 percent below the literature values. Figure 96 presents the Stern-Volmer plot of  $O_3^*(v=2)$ . The  $k_{Ar}[Ar]$  contribution to the intercept is



A-7365

Figure 95. Stern-Volmer plot of  $\text{O}_3^*(v=1)$  for  $\text{O}_2/\text{Ar}$  mixtures at 30 mtorr Ar.



A-7364

Figure 96. Stern-Volmer plot of  $\text{O}_3^*(v=2)$  for  $\text{O}_2/\text{Ar}$  mixtures at 30 mtorr Ar.

$\sim 39 \text{ s}^{-1}$ , which implies a  $A_2$  value of  $4 \text{ s}^{-1}$ . This is significantly lower than the expected value of  $\sim 19 \text{ s}^{-1}$ . This gives an estimate of the error in the intercept for  $v=2$  data.

In summary, this preliminary data review indicates that time resolved fluorescence from  $O_3^*$  at  $10 \text{ }\mu\text{m}$  can be analyzed to extract level-dependent quenching rate coefficients for relaxation of  $O_3 v_3(v=1,2,3)$  by Ar,  $N_2$  and  $O_2/O$  partners. Moreover once diffusional losses are more accurately modeled, the low pressure data may be used to extract radiative decay rates  $A_{v \rightarrow v-1}$ . To our knowledge this would be the first experimental measurement of these values in emission.

## 11. EXCEDE DATA ANALYSIS

### 11.1 INTRODUCTION

The EXCEDE:Spectral mission was an auroral simulation experiment launched from Poker Flat, Alaska on 19 October 1979 into the aurorally inactive night-time atmosphere. The scientific purpose of the EXCEDE experiment was to investigate the detailed production and loss processes of various excited and vibrational states that result in optical and infrared emission as energetic electrons interact with the atmosphere. A thorough description of the mission and the current status of the data analysis is presented elsewhere.<sup>147</sup> Only those mission aspects relevant to these investigations will be discussed here.

At approximately 155 km on the upleg the four electron guns were initiated (7 to 8 amps each at 3 kV) and the electron deposition region was observed by several spectrometers and photometers. Electron deposition and data collection continued to 70 km on the downleg. The data channels of interest to this study are those principally from the LN<sub>2</sub> CVF spectrometer which obtained data over the 2.07 to 5.28  $\mu$ m region and the LHe CVF spectrometer which obtained data over the 4.04 to 6.74 and 13.05 to 22.43  $\mu$ m regions. The 13.05 to 22.43  $\mu$ m data has been analyzed elsewhere<sup>147-149</sup> and will not be considered here. Although not a major focus of these investigations, we have also examined some UV, Vis, and IR interferometer data in order to assist in the interpretation of the CVF data.

Two sample spectra from the LN<sub>2</sub> and LHe CVF spectrometers are shown in Figures 97 and 98. The goals of this research effort were to identify the major and minor radiators in these spectra and determine their relative vibrational distributions and altitude dependences. Determination of absolute number densities are not possible owing to the variability in the electron deposition region, however, relative number densities have been obtained.



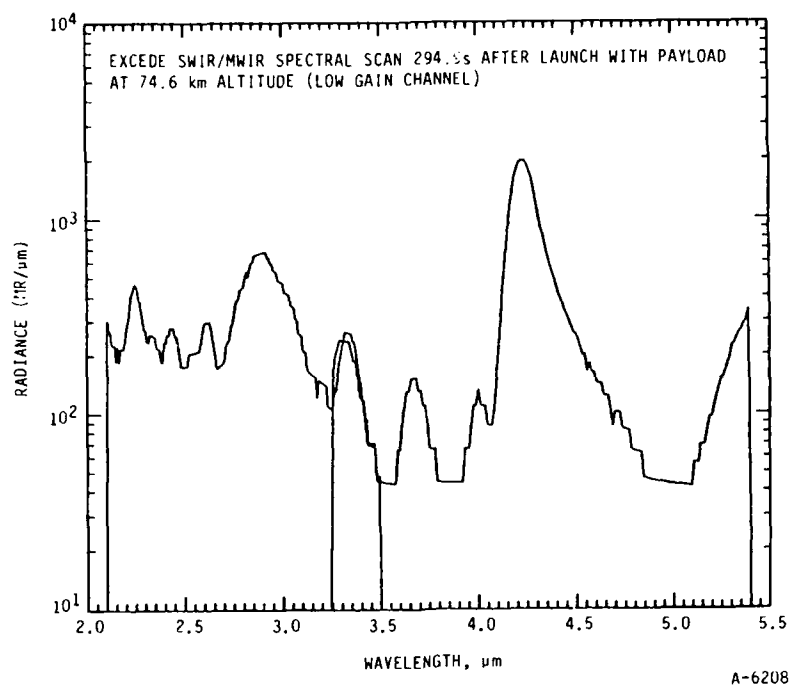


Figure 97. EXCEDE SWIR/MWIR spectral scan at 294.9s after launch.

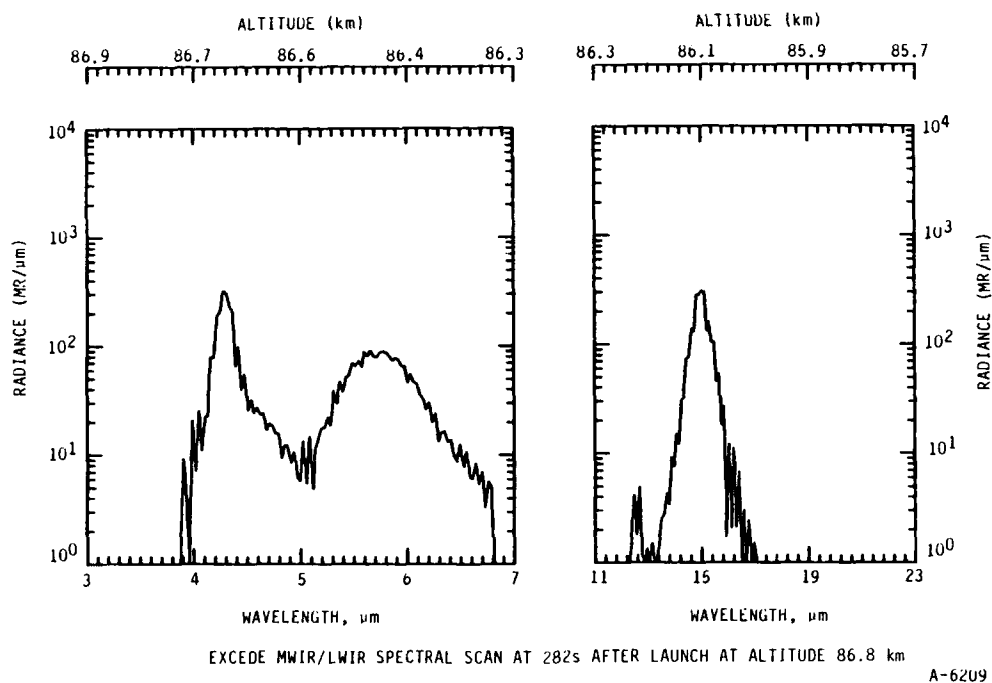


Figure 98. EXCEDE MWIR/LWIR spectral scan at 282s after launch.

Several of the features in Figures 97 and 98 are well-known auroral emissions. For example, the intense feature at 4.3  $\mu\text{m}$  in both figures is the  $\text{CO}_2\text{v}_3$  emission and the feature at 5.4  $\mu\text{m}$  in Figure 98 is probably NO fundamental emission arising from the reaction of  $\text{N}(^2\text{D}) + \text{O}_2$ . These emissions have been previously identified in the HIRIS mission<sup>150,151</sup> and the NO fundamentals have been extensively studied with the COCHISE apparatus.<sup>152</sup> These are the only spectroscopic features which were unambiguously identified prior to start of the current analysis. Several other band systems were suspected, however, including the  $\text{N}_2(\text{W}^3\Delta \rightarrow \text{B}^3\Pi)$ ,  $\text{N}_2(\text{a}^1\Pi \rightarrow \text{a}'^1\Sigma)$ , and  $\text{H}_2\text{O}$  vibrational emission which are known to radiate in the 2 to 4  $\mu\text{m}$  spectral range. Emission from  $\text{H}_2\text{O}$  was suggested owing to the high column densities of water ( $\leq 10^{16} \text{ cm}^{-3}$ ) known to have outgassed from the vehicle during the course of the mission.<sup>148</sup> Unambiguous identification of these band systems and determination of their vibrational distributions had not yet been performed and, therefore, were the principal goals of these studies.

## 11.2 DATA HANDLING

In order to obtain the data files in usable form (i.e., as digitized files on the PSI Microvax computer system) we were presented with two alternatives - digitize hard copies of the files by hand or attempt to read the tapes. Since the total number of files used in these studies was low ( $< 50$ ), the former method was chosen. Digitization was performed with a digitizing board and pen which were controlled by software on an IBM PC. For the CVF data 700 data points (15 digitized points per 600Å resolution element) were taken for each spectrum. The digitization procedure typically required less than 0.5 hr per data file. The resulting x,y data pairs were then stored on floppy disk and downloaded to the Microvax for further treatment. Software was written on the Vax which then performed the following operations: 1) all the data points were first passed through a simple filter which discarded spurious points; 2) an interpolation routine was passed over the remaining array to provide a uniform point spacing (typically, 40Å was used) and 3) the resulting file was then written out in a format compatible with our spectral analysis routines and

stored. Once digitization was complete, each finished file was compared to the original hard copy to check for errors.

A summary of the digitized data is presented in Tables 18 through 21. Table 18 lists the 2.07 to 5.4  $\mu\text{m}$  (SWIR) spectra; Table 19 the 4 to 6.8  $\mu\text{m}$  (MWIR) spectra; Table 20 the merged SWIR and MWIR spectra; and Table 21 the UV and visible spectrometer data files. Two samples of the digitized files are shown in Figures 99 and 100. They are the same files as in Figures 97 and 98 but are shown with a linear intensity scale. Since several of the SWIR and MWIR spectra corresponded closely in time, they were merged by normalizing using the intensities of the  $\text{CO}_2\text{v}_3$  feature. These files are listed in Table 20. The parameters also shown in these tables, where relevant, include altitude, time after launch, the identities of the operating electron guns, and the intensity of the  $\text{CO}_2\text{v}_3$  emission in Megarayleighs. The identities of operating guns shown in Tables 18 and 19 were taken from the compilation in Grieder and Foley.<sup>153</sup>

The extent of the electron deposition changed dramatically with altitude.<sup>147</sup> Therefore, in order to compare data from different altitudes, some normalization is required. This was performed using the photometer intensities shown in Table 22 for each digitized SWIR scan. Predominantly, L4, the photometer operating at 5581 $\text{\AA}$ , was used. This radiometer observed emission from  $\text{O}(^1\text{S})$  features. This system was chosen as it is formed by similar processes and electron energies as the neutral band systems examined here.

#### 11.2.1 Spectral Fitting

The spectral analysis technique used for these studies has also been successfully applied to the analysis of  $\text{NO}(A^2\Sigma)$ .<sup>60</sup>  $\text{N}_2$  electronic emission<sup>100</sup> including  $\text{W}^3\Delta \rightarrow \text{B}^3\Pi$  emission,<sup>126</sup> and  $\text{IF}(\text{B}^3\Pi_{0+})$ .<sup>154</sup> The synthetic spectra are generated by a computer code based upon the work of Kovacs<sup>15</sup> and implemented through major modification of a program written by Whiting, et al.<sup>16,17,155</sup> The program considers singlet-singlet, doublet-doublet, and triplet-triplet

TABLE 18. Digitized SWIR scans.

Scan No.	TAL (s)	Alt (km)	Channel	Gun (s)	I(CO <sub>2</sub> ), MR
213	143.0	119.2	High gain	4	18.9
247	159.6	124.8	High gain	4	9.8
249	160.5	125.1	High gain	4	10.0
250	161.0	125.2	High gain	4	10.0
319	195.1	128.3	High gain	4	4.0
417	243.2	114.1	High gain	4	13.3
425	247.0	112.0	High gain	4	5.3
430	249.5	110.6	High gain	4	6.6
454	261.1	103.3	Low gain	3,4	133.0
461	264.4	100.9	Low gain	3	213.0
464	265.9	99.8	Low gain	3	188.0
488	277.5	90.7	Low gain	3,4	1868.0
490	278.5	89.8	Low gain	1,3,4	1740.0
496	281.4	87.3	Low gain	1,4	1580.0
508	287.2	82.1	Low gain	1	1653.0
512	289.1	80.2	Low gain	1	1640.0
513	289.6	79.8	Low gain	1	-
514	290.1	79.3	Low gain	1	1520.0
521	293.5	76.0	Low gain	1,3	3784.0
523	294.4	75.0	High gain	3	-
524	294.9	74.6	Low gain	3	1887.0
524	294.9	74.6	High gain	3	-
525	295.4	74.1	Low gain	3	3243.0
525	295.4	74.1	High gain	3	-
526	295.8	73.6	High gain	3	-
Observed intensity ratio: high gain/low gain = 0.80					

TABLE 19. Digitized MWIR scans.

Scan No.	TAL (s)	Alt (km)	Guns
1195	276.0	92.0	3,4
1196	277.2	91.0	3,4
1197	278.4	90.0	1,3,4
1200	282.0	86.8	1,4
1202	284.4	84.6	1,3
1204	286.8	82.4	1
1205	288.0	81.3	1
1206	289.2	80.2	1
1209	292.8	76.6	1
1210	294.0	75.4	1,3
1211	295.3	74.2	3

TABLE 20. Merged SWIR/MWIR scans.

SWIR Scan	Alt (km)	MWIR Scan	Alt (km)
524	74.6	1211	74.2
512	80.2	1206	80.2
490	88.8	1197	90.0

TABLE 21. UV and visible interferometer scans.

UV or VIS	Scan No.	TAL (s)	Alt (km)
UV	149	290	79.0
UV	116	230	120.0
VIS	47	196	128.3
VIS	73	296	74.0

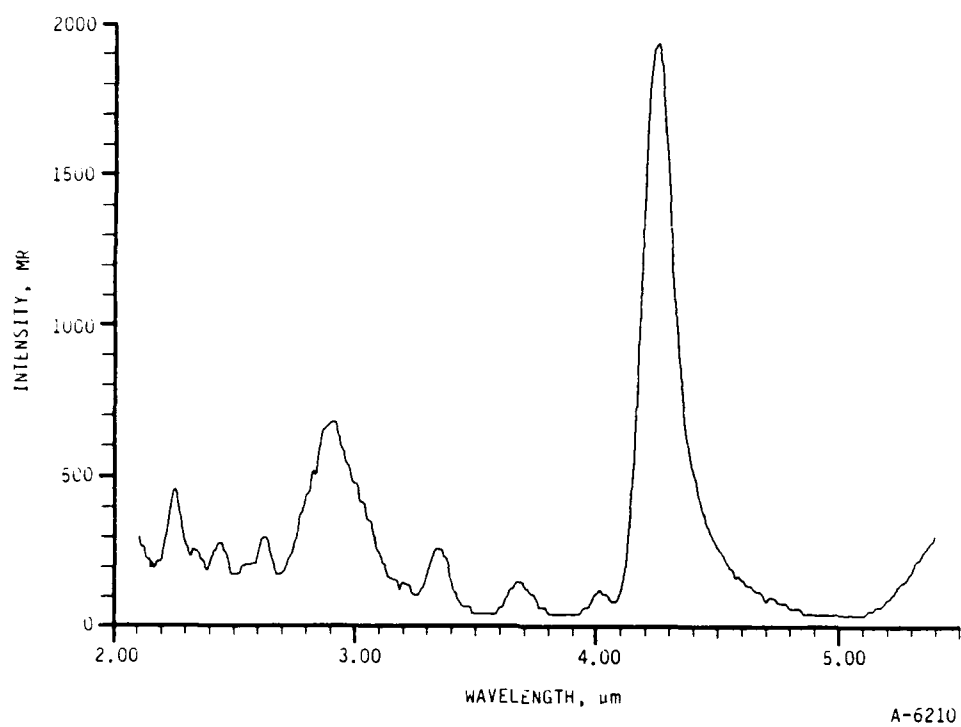


Figure 99. Digitized SWIR scan 524 with linear intensity scale.

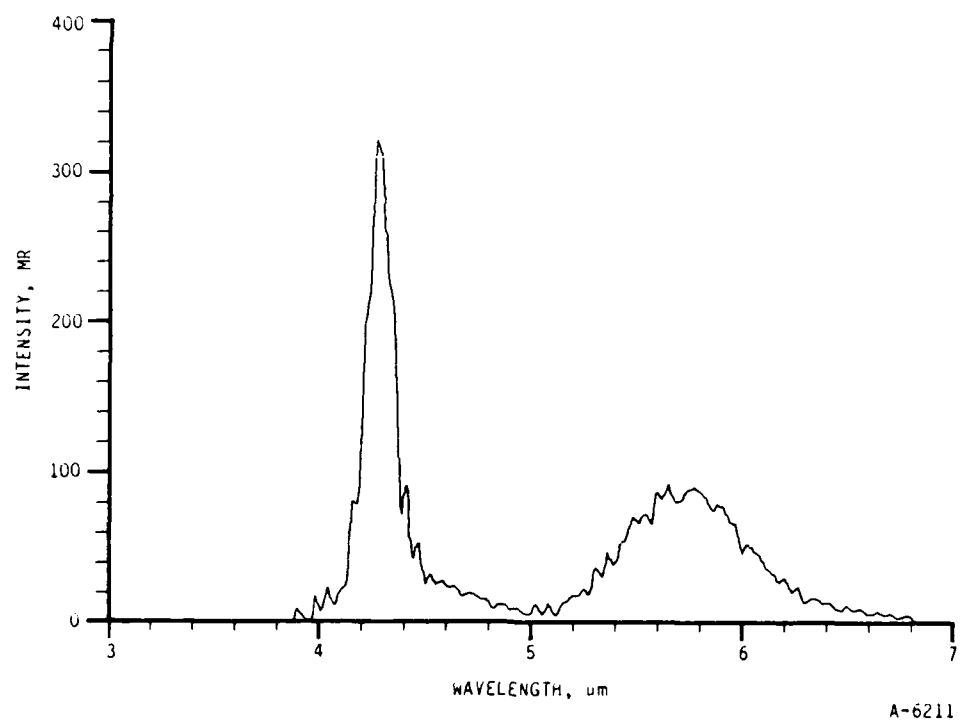


Figure 100. Digitized MWIR scan 1200 with linear intensity scale.

TABLE 22. EXCEDE SWIR photometer data.

Scan No.	TAL	Alt	Channel	Guns	2° Field of View L1 I (MR)	4° x 4° L2 I (MR)	L4 I (MR)	L7 I (MR)
					3913Å	3912Å	5581Å	5579Å
213	143.0	119.2	H.G.	4	$1 \times 10^1$	$5 \times 10^0$	$3 \times 10^{-1}$	$3.2 \times 10^{-1}$
247	159.6	124.8	H.G.	4	$7 \times 10^0$	$3 \times 10^0$	$1.9 \times 10^{-1}$	$1.9 \times 10^{-1}$
249	160.5	125.1	H.G.	4	$7 \times 10^0$	$3 \times 10^0$	$1.9 \times 10^{-1}$	$1.9 \times 10^{-1}$
250	161.0	125.2	H.G.	4	$7 \times 10^0$	$3 \times 10^0$	$1.9 \times 10^{-1}$	$1.9 \times 10^{-1}$
319	19.51	128.3	H.G.	4	$4.5 \times 10^0$	$2 \times 10^0$	$1.2 \times 10^{-1}$	$1 \times 10^{-1}$
417	243.2	114.1	H.G.	4	$5.5 \times 10^0$	$2.8 \times 10^0$	$1.5 \times 10^{-1}$	$1.4 \times 10^{-1}$
425	247.0	112.0	H.G.	4	$5.5 \times 10^0$	$2.8 \times 10^0$	$1.5 \times 10^{-1}$	$1.5 \times 10^{-1}$
430	249.5	110.6	H.G.	4	$5.5 \times 10^0$	$2.8 \times 10^0$	$1.7 \times 10^{-1}$	$1.6 \times 10^{-1}$
454	261.1	103.3	L.G.	3,4	$2.3 \times 10^1$	$1 \times 10^1$	$7.5 \times 10^{-1}$	$7.5 \times 10^{-1}$
461	264.4	100.9	L.G.	3	$3 \times 10^1$	$1.5 \times 10^1$	$1 \times 10^0$	$9 \times 10^{-1}$
464	265.9	99.8	L.G.	3	$3 \times 10^1$	$1.5 \times 10^1$	$1 \times 10^0$	$9 \times 10^{-1}$
488	277.5	90.7	L.G.	3,4	$1 \times 10^2$	$4.2 \times 10^1$	$2.2 \times 10^0$	$2 \times 10^0$
490	278.5	89.8	L.G.	1,3,4	$2.5 \times 10^2$	$1.3 \times 10^2$	$6 \times 10^0$	$5.5 \times 10^0$
496	281.4	87.3	L.G.	1,4	$2 \times 10^2$	$1 \times 10^2$	$4 \times 10^0$	$3.5 \times 10^0$
508	287.2	82.1	L.G.	1	$1.6 \times 10^2$	$8 \times 10^1$	$3.5 \times 10^0$	$3 \times 10^0$
512	289.1	80.2	L.G.	1	$1.6 \times 10^2$	$8 \times 10^1$	$3.5 \times 10^0$	$3 \times 10^0$
513	298.6	79.8	L.G.	1	$1.6 \times 10^2$	$8 \times 10^1$	$3.5 \times 10^0$	$3 \times 10^0$
514	290.1	79.3	L.G.	1	$1.6 \times 10^2$	$8 \times 10^1$	$3.5 \times 10^0$	$3 \times 10^0$
521	293.5	76.0	L.G.	1,3	$4.1 \times 10^2$	$3 \times 10^2$	$1.2 \times 10^1$	$1.2 \times 10^1$
523	294.4	75.0	H.G.	3	$2.3 \times 10^2$	$1.4 \times 10^2$	$4.2 \times 10^0$	$3.5 \times 10^0$
524	294.9	74.6	L.G.	3	$2.1 \times 10^2$	$1.2 \times 10^2$	$3.8 \times 10^0$	$3.2 \times 10^0$
524	294.9	74.6	H.G.	3	$2.1 \times 10^2$	$1.2 \times 10^2$	$3.8 \times 10^0$	$3.2 \times 10^0$
525	295.4	74.1	L.G.	3	$2.1 \times 10^2$	$1.2 \times 10^2$	$3.8 \times 10^0$	$3.2 \times 10^0$
525	295.4	74.1	H.G.	3	$2.1 \times 10^2$	$1.2 \times 10^2$	$3.8 \times 10^0$	$3.2 \times 10^0$
526	295.8	73.6	H.G.	3	$2.1 \times 10^2$	$1.2 \times 10^2$	$3.8 \times 10^0$	$3.2 \times 10^0$

dipole transitions for diatomic molecules in the optically thin limit. Line-by-line transition frequencies are computed from energy eigenvalues determined by exact solution of the Schrödinger equation, where the matrix elements of the upper and lower state Hamiltonians are specified from tabulated spectroscopic constants. Following well-established procedures,<sup>15,156</sup> the eigenfunctions of the states are described as linear combinations of eigenfunctions of hypothetically pure Hund's case (a) eigenstates. The transition amplitudes are given by the transformation of the dipole moment function between the upper and lower states.<sup>15,156</sup> The computed infinite resolution emission spectrum is convolved with the instrument scan function to create basis sets for each vibrational level which are then fit to the experimental spectrum using a linear least squares method. The fitting procedure yields a determination of the product of the upper state number density and the spontaneous emission coefficient of the transition. Rotational distributions are treated by simple Boltzmann expressions, so that band-integrated vibrational state number densities and transition probabilities may be used.

Lambda doubling, which is on the order of  $1\text{ cm}^{-1}$  for the  $W^3\Delta \rightarrow B^3\Pi$  system,<sup>157</sup> is not treated in this analysis. Despite the complexities of the systems to which this code has been applied, comparison of the line positions of synthesized spectra (in this case the  $2,0\text{ }W^3\Delta \rightarrow B^3\Pi$  feature)<sup>126</sup> to high resolution data<sup>157</sup> indicates the principal lines are reproduced to generally within  $1\text{ cm}^{-1}$ . The agreement determined for the singlet systems such as  $w^1\Delta \rightarrow a^1\Pi$  is excellent,  $\leq 0.1\text{ cm}^{-1}$ . Since the CVF data examined here exhibit a resolution of  $\sim 600\text{Å}$  ( $\sim 60\text{ cm}^{-1}$ ) at  $3\text{ }\mu\text{m}$ , deficiencies in the spectral synthesis program on the order of  $1\text{ cm}^{-1}$  or less are too small to be observed.

Most of the spectroscopic data has been drawn from Huber and Herzberg<sup>18</sup> or Lofthus and Krupenie.<sup>6</sup> Data from Roux<sup>158</sup> et al. has been used for the  $w^1\Delta$  state of  $N_2$ , and Cerny<sup>159</sup> et al. for  $W^3\Delta$  and Effantin<sup>160</sup> for  $B^3\Pi$ . The Einstein coefficients used for the triplet states of nitrogen are those determined by Werner<sup>32</sup> et al.

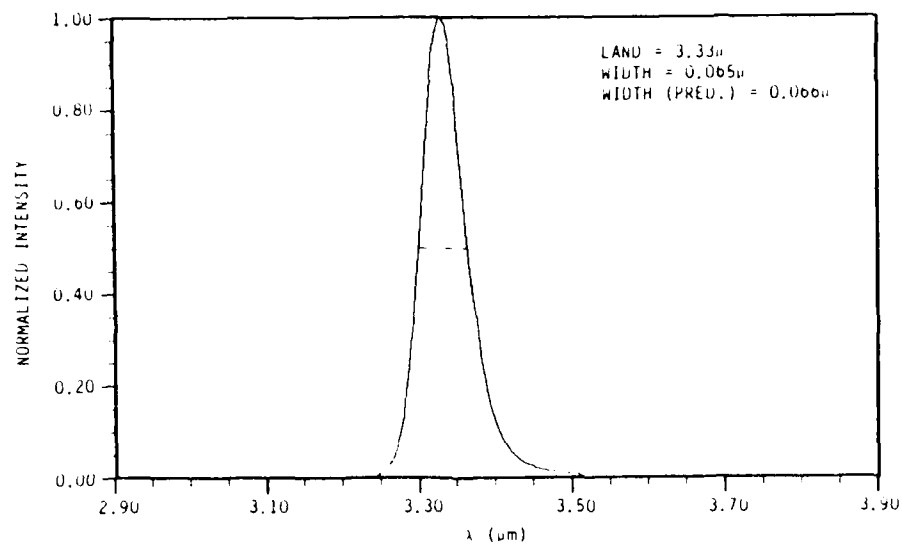


In order to fit the data, the synthetic spectra must be convolved with the experimental slit function. Post flight calibration of the EXCEDE spectrometers was precluded due to the loss of the payload. Therefore, the nature of the CVF slit function is not absolutely known. In order to fit the data, the slit function of an analogous instrument, that of SPIRE,<sup>141</sup> was used. This slit function is a skewed Gaussian with a full width at half maximum 2 percent of the wavelength center. This slit function was incorporated into our spectral fitting routines for use with EXCEDE data. Shown in Figures 101a and b are simulated atomic lines at 3 and 6  $\mu\text{m}$ , respectively, convolved with the skewed Gaussian slit function. Close inspection of this slit function indicates there to be only small differences to a Gaussian slit function with FWHM of 2 percent. This function is shown for comparison in Figures 102a and b. Most of the data has been fit to basis functions incorporating the skewed Gaussian slit function, but some have utilized the simpler Gaussian function.

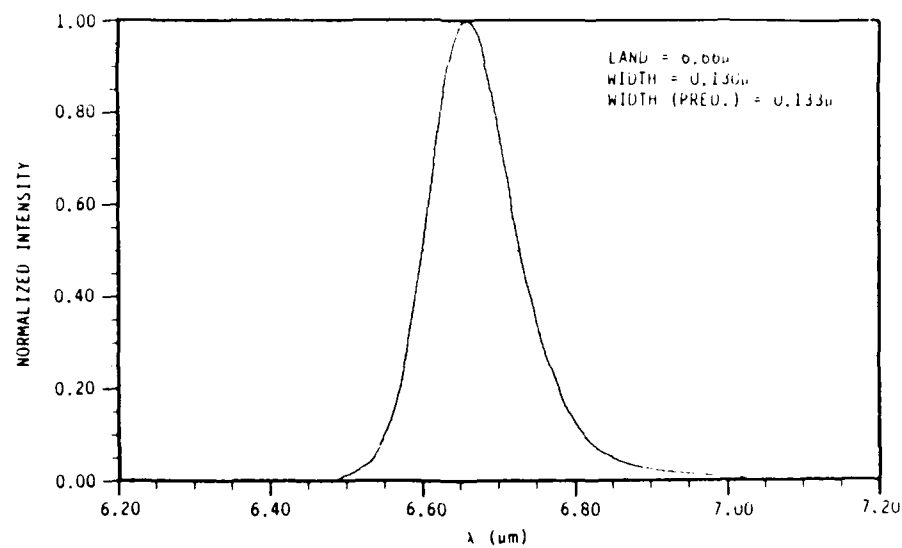
#### 11.2.2 Background Correction

All of the SWIR (2.1 to 5.4  $\mu\text{m}$ ) files exhibit an apparent background that is quite significant at 2.1  $\mu\text{m}$  and decays into the noise at 3.5  $\mu\text{m}$ . The absolute magnitude of the background varies from low values at low and high altitudes to high values at the mid-altitude region. An example (scan number 490 for 89.8 km) is shown in Figure 103. Background of this type is also seen in Figure 99, scan 524 at 74.6 km. We have ruled out detector recovery from the intense NO fundamental band as the source of the background by comparison of adjacent scans. The nature of this background IR emission is not clear but we have determined its altitude dependence and described its spectral distribution. In addition, this background has been observed on scans where the NO fundamental band is not as intense.

Figure 104 shows the altitude dependence of the background. The background intensity was measured at 2.14  $\mu\text{m}$  and normalized using the intensity



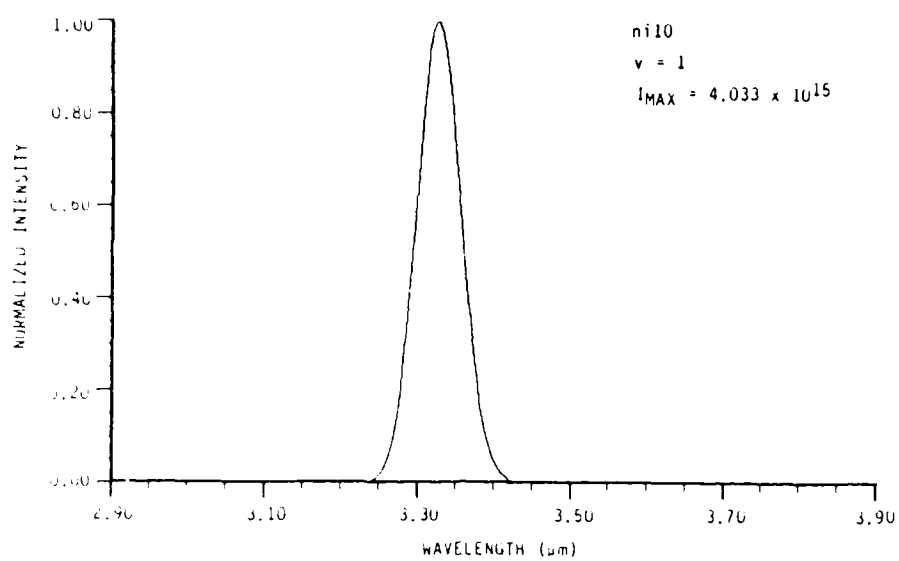
(a)



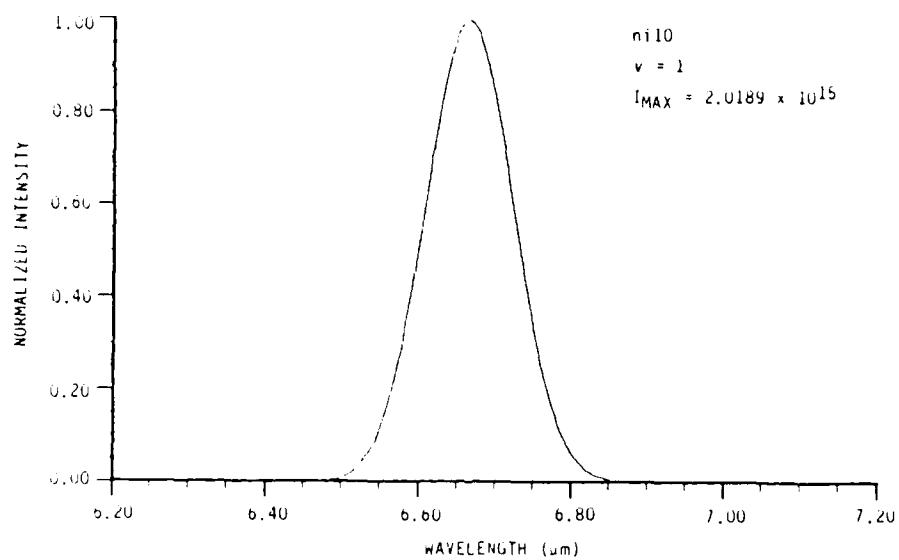
A-6212

(b)

Figure 101. Simulated atomic lines at  $3.33 \mu\text{m}$  (a) and  $6.67 \mu\text{m}$  (b) convolved with the skewed Gaussian slit function.



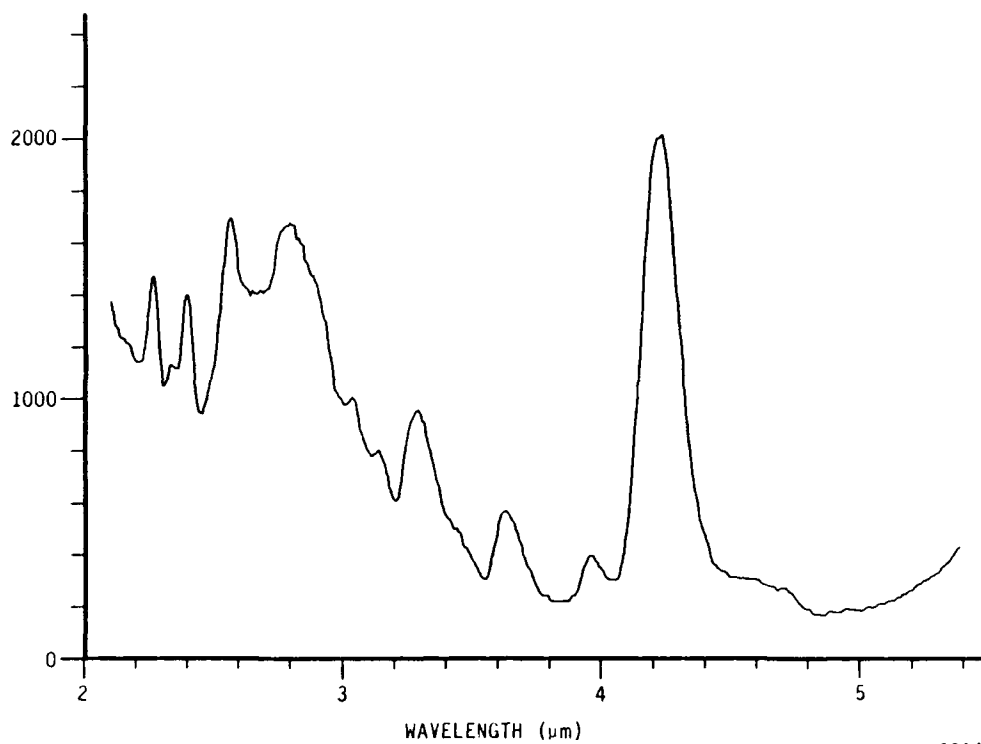
(a)



(b)

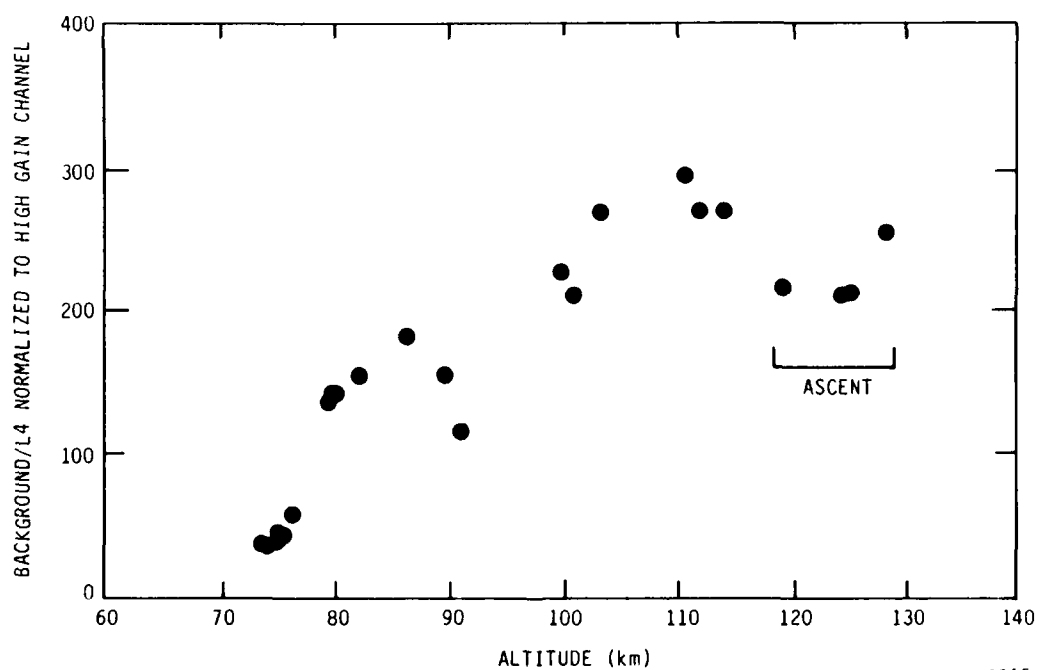
A-6213

Figure 102. Simulated atomic lines at 3.33  $\mu\text{m}$  (a) and 6.67  $\mu\text{m}$  (b) convolved with a Gaussian (FWHM =  $0.02 \lambda_0$  slit function).



A-6214

Figure 103. Uncorrected SWIR scan 490 (TAL = 278.5s, Alt = 89.8 km).



A-6215

Figure 104. Background of the SWIR scans as a function of altitude, normalized to 391 nm photometer emission intensity (L4).

of the L4 photometer. The resulting curve shows that normalized background increases by a factor of six from 75 to 120 km.

The spectral distribution of the emission is closely matched by the air afterglow emission.<sup>111,112</sup> Figure 105 shows the intensity decay of the air afterglow emission over the 2 to 5  $\mu\text{m}$  region. Figure 106 shows scan 524 corrected for the background (after normalization at 2.14  $\mu\text{m}$ ). This correction has been applied to most of the SWIR data files.

The visible interferometer data shows no evidence of  $\text{NO}_2$  air afterglow emission which would have to be present at wavelengths  $\geq 380$  nm. In addition, calculation of the required NO and O number densities produced by the discharges indicates that these species are insufficient by about an order of magnitude to account for the observed background intensities. Although the

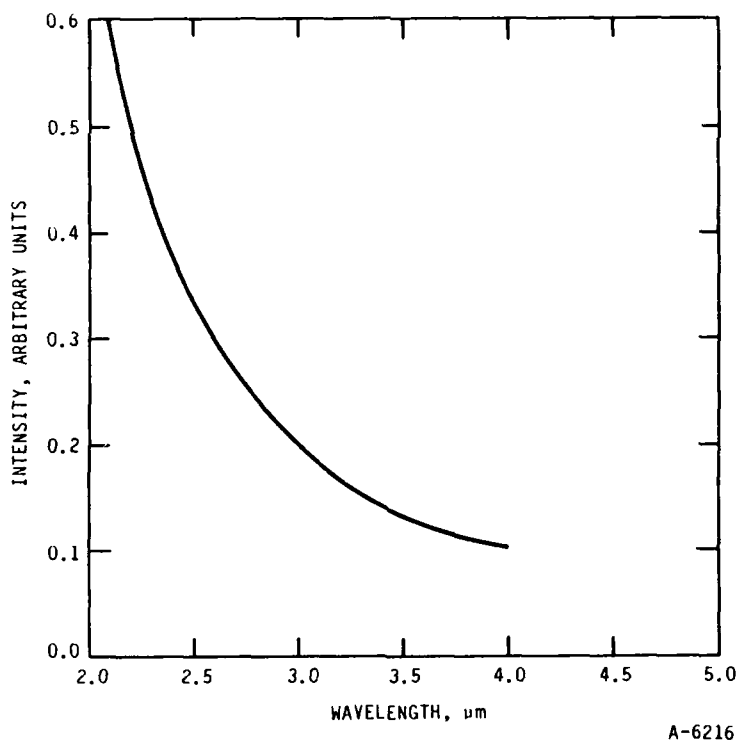


Figure 105. Wavelength dependence of the air afterglow emission in the 2 to 5  $\mu\text{m}$  region.

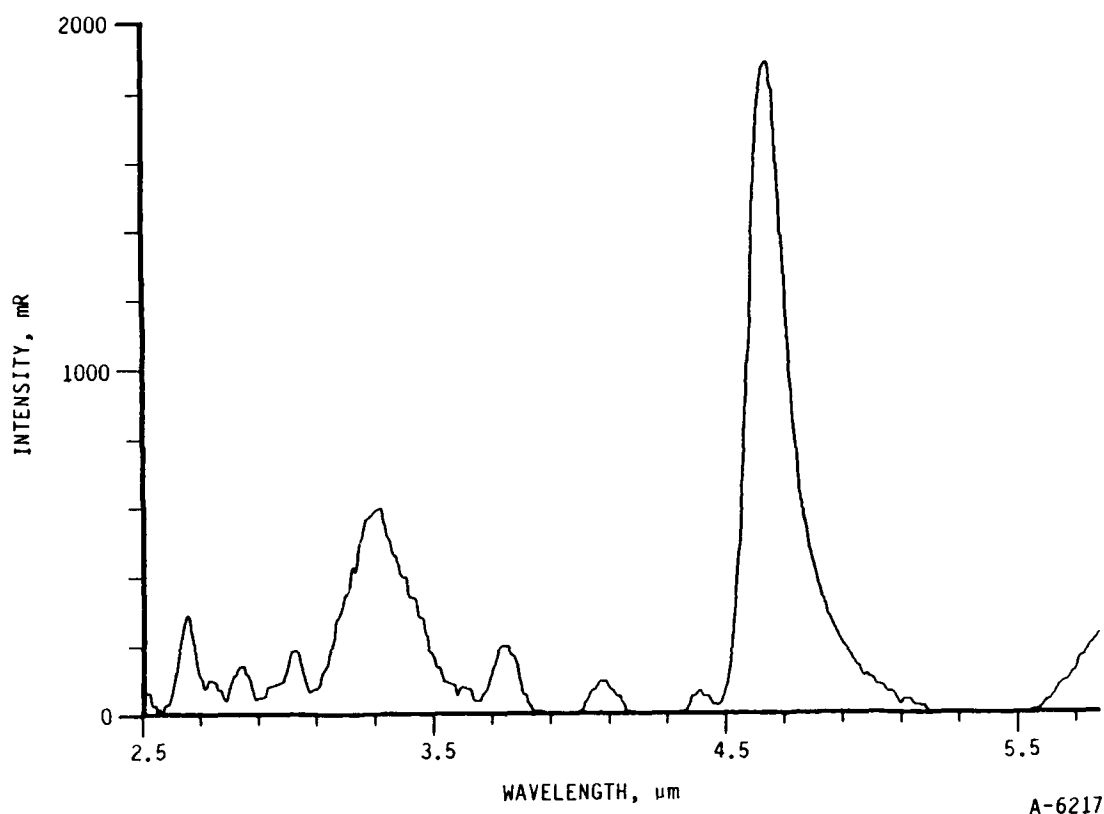


Figure 106. SWIR scan 524 with background correction (TAL = 294.9s, Alt = 74.6 km).

nature of the background is unknown, the functional form of the continuum has been applied to all the data so that further quantitative analysis of the spectrally structured features is possible.

### 11.3 SPECTROSCOPIC IDENTIFICATION

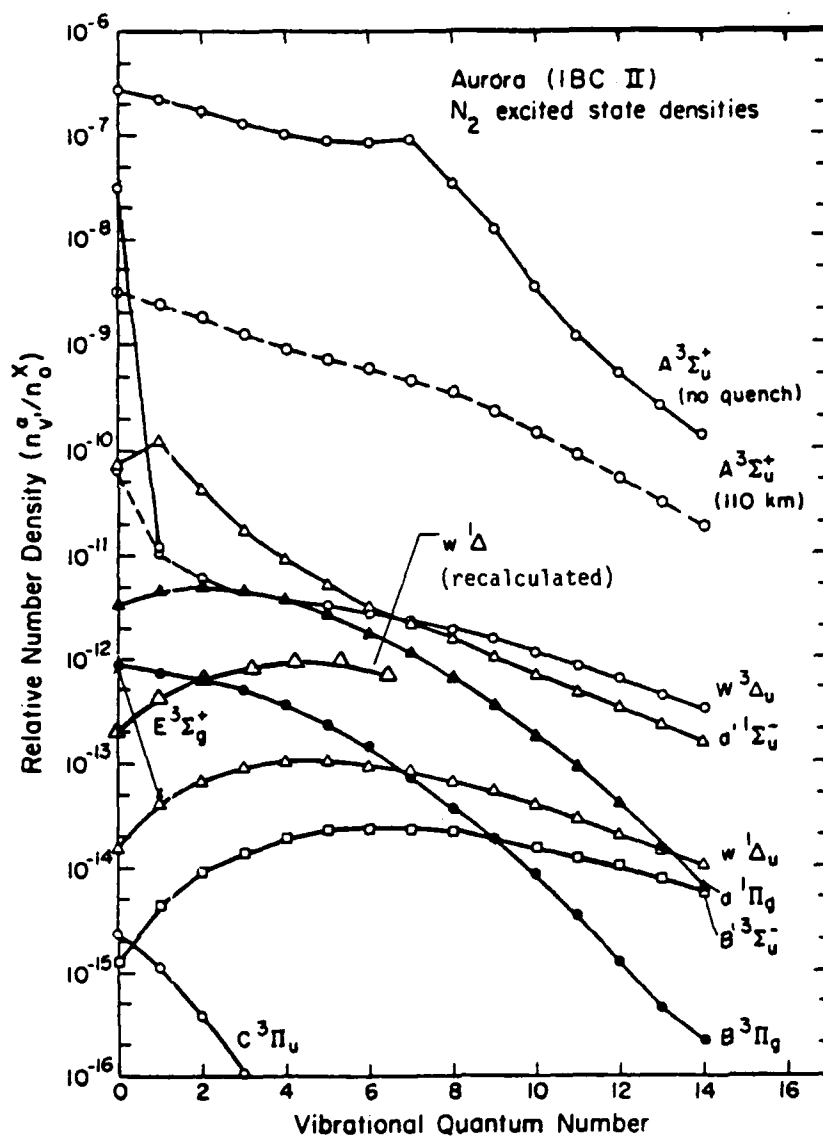
Many of the emission features in these spectra have been previously identified. For example, the intense feature at 4.3  $\mu\text{m}$  is due to the  $\text{CO}_2(\nu_3)$  band created by the interaction of energetic electrons with ambient  $\text{CO}_2$ .<sup>9</sup> The broad feature at 5.4  $\mu\text{m}$  has been previously assigned<sup>147</sup> to the NO fundamental emission from vibrational levels as high as  $v=12$  arising from the reaction,



The  $N(^2D)$  arises from electron induced dissociation of nitrogen. Reaction (54) has been studied in the laboratory.<sup>152,161</sup> The relative population distributions as well as the fundamental/overtone ratios have been determined.<sup>162</sup> However, the EXCEDE spectral data will provide production efficiencies, the altitude dependence of the vibrational distribution, and the relative contribution of the NO overtones to the emission feature at 2.9  $\mu m$ .

There are several features in the 2 to 4.1  $\mu m$  region which have not been cleanly identified prior to this project. The band centers of many of the features align with emission from several  $N_2$  electronic states, specifically the  $W^3\Delta \rightarrow B^3\Pi$ ,  $a^1\Pi \rightarrow a'^1\Sigma$ , and  $w^1\Delta \rightarrow a^1\Pi$  band systems. The coarse resolution of the CVF and observed wavelength "jitter" in some of the spectra prevented their unambiguous assignments previously. We detail below a spectral fitting approach which permits their identification. Only those band systems which exhibit credible vibrational distributions for all levels and transitions will be considered to be positively identified.

The relative importance of the  $N_2$  electronic states in an aurora have been modeled by Cartwright.<sup>4</sup> He used measured or inferred electron excitation cross sections, radiative relaxation and cascade, and quenching estimates to determine the relative number densities of the nitrogen electronic states in an aurora. His results are shown in Figure 107. The  $A^3\Sigma$ ,  $W^3\Delta$ , and  $a'^1\Sigma$  states are indicated to be present at the highest concentrations due to their long radiative lifetimes. Because of the flow around the EXCEDE payload, residence time in the field of view of the spectrometers will be a function of mission time. Residence times of less than 10 ms are expected for most of the data. Thus these longest lived states will not have concentrations as high as the Cartwright model due to diffusive (field of view) loss time. Of these long lived states only the  $W^3\Delta$  state emits in the infrared in the  $W^3\Delta \rightarrow B^3\Pi$  system. Several of the other states shown in Figure 107 should also emit in the infrared, including  $w^1\Delta \rightarrow a^1\Pi$ ,  $a^1\Pi \rightarrow a'^1\Sigma$  and some bands in the  $B'^3\Sigma \rightarrow B^3\Pi$  and  $B^3\Pi \rightarrow A^3\Sigma$  systems.



A-6218

Figure 107. Auroral  $N_2$  excited state densities.

### 11.3.1 Wu-Benesch Emission

Electron irradiation of nitrogen is well-known to produce extensive emission from the  $N_2(W^3\Delta \rightarrow B^3\Pi)$  system.<sup>163,164</sup> This emission system has recently been examined in the laboratory using the LABCEDE and COCHISE apparatus<sup>126,165</sup> and these experiments<sup>126</sup> verified the W-B branching ratios over the 2 to 4  $\mu m$  region and observed the previously unidentified 1-0 and 2-1 features in the 6 to 8  $\mu m$  region. Emission from the  $N_2(w^1\Delta \rightarrow a^1\Pi)$  system was also examined. We

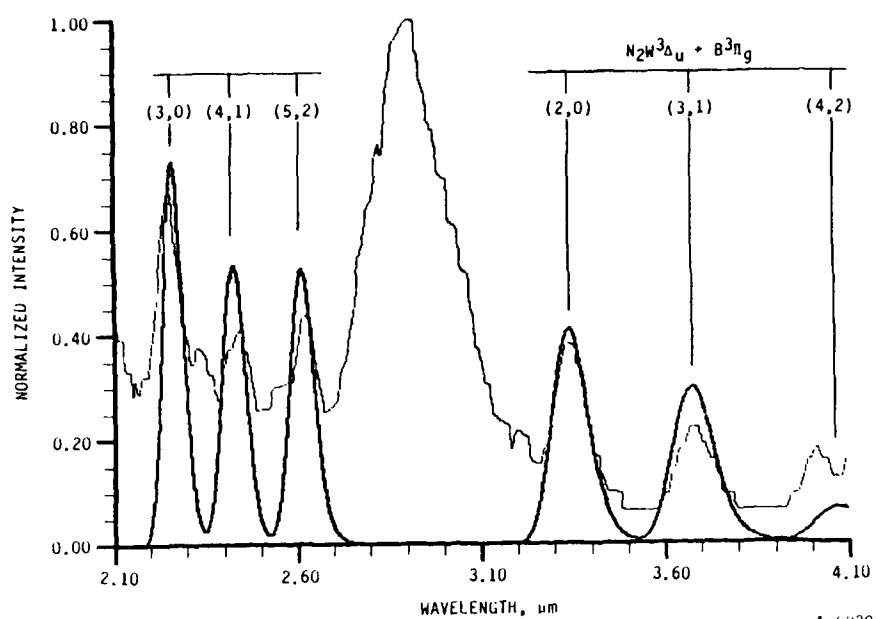


have calculated the Einstein coefficients for this transition system using the transition moment function of Yeager and McKoy.<sup>65</sup> The results predict the auroral density of the  $w^1\Delta$  state to be greater by an order of magnitude over Cartwright's initial estimates. The corrected predictions for the  $w^1\Delta$  state are shown in Figure 107.

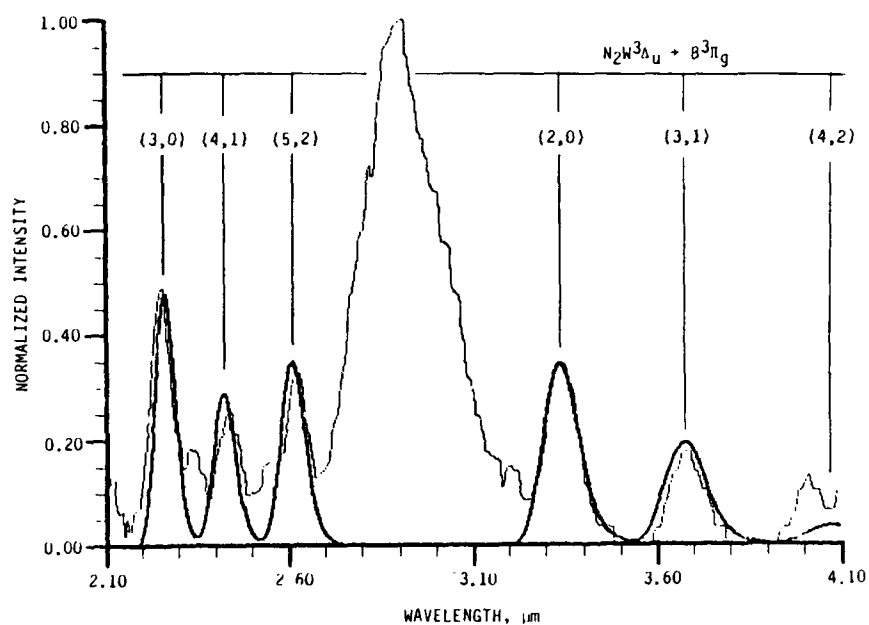
The COCHISE apparatus employs microwave discharges operating at 1 torr pressure with the viewing region maintained at 3 to 5 mtorr. The results, therefore, can be applied to aeronomy and provide a useful spectroscopic data base. LABCEDE, which excites atmospheric gases at densities equivalent to 65 to 105 km altitudes, is a more direct system to understand the aurora. This experiment has recently examined the infrared emission from the electron irradiation of nitrogen over the 0.8 to 6.5  $\mu\text{m}$  region.<sup>165</sup> The identified band systems are  $\text{N}_2(W^3\Delta \rightarrow B^3\Pi)$ ,  $\text{N}_2(a^1\Pi \rightarrow a'^1\Sigma)$ ,  $\text{N}_2(B^3\Pi - A^3\Sigma)$ ,  $\text{N}_2^+(A^2\Pi - X^2\Sigma)$ , and  $\text{N}_2(w^1\Delta - a\Pi)$ .

Comparisons of the digitized files to synthetic Wu-Benesch emissions have been performed for all low altitude data ( $< 90$  km). Two typical results are shown in Figures 108a and b. The vibrational levels used in these basis sets are  $v'=2-5$ . Figure 108a shows the fit to uncorrected data in the 2.1 to 4.1  $\mu\text{m}$  region and Figure 108b shows the fit to the same data file corrected for background. In both figures, the fit to the W-B (2,0), (3,1), (4,2), (3,0), (4,1) and (5,2) features is excellent. The band positions are well reproduced and with background subtraction, as shown in Figure 108b, the relative intensity distributions are also reproduced. The feature at 4.0  $\mu\text{m}$  is not fully matched by the W-B (4,2) emission. Since we have previously verified the W-B branching ratios<sup>126</sup> and Figure 108b shows a good match of the (3,0) and (3,1) relative intensities, failure to reproduce the 4.0  $\mu\text{m}$  feature indicates that it is likely due in part to another radiator.

Fits to higher vibrational levels in the Wu-Benesch manifold have also been performed. Figure 109 shows a fit of the uncorrected data to W-B  $v'=2-9$ .

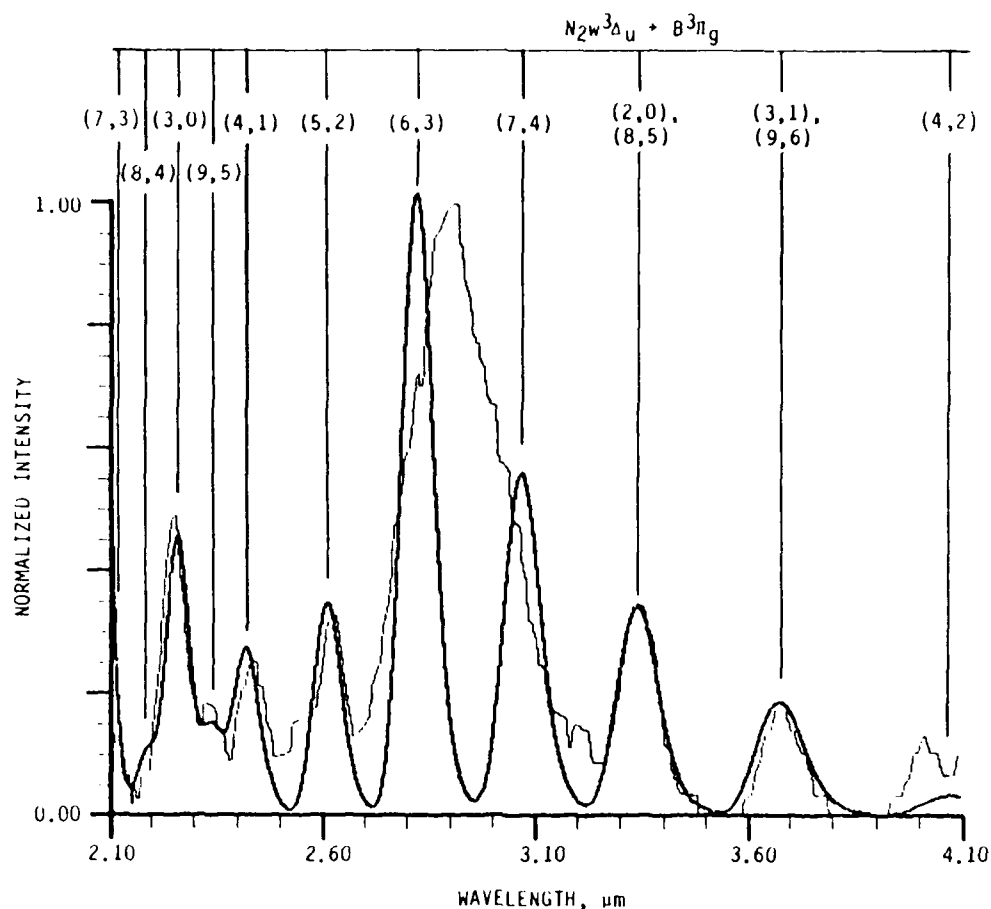


(a)



(b)

Figure 108. SWIR scan 524 with fit to  $N_2W^3\Delta_u \rightarrow B^3\Pi_g$  ( $v'=2-5$ ) emission. The data is shown only for 2.1 to 4.1 μm. (a) is the uncorrected file and (b) has background correction. The rotational temperature used was 200 K.



A-6222

Figure 109. Corrected scan 524 fit to  $N_2(W^3\Delta_u \rightarrow B^3\Pi, v'=2-9)$  at a rotational temperature of 200 K.

Emission from the (9,6) and (8,5) transitions underlie the (3,1) and (2,0) features respectively. This prevents clear assignment. The (9,5) feature may be present just at the noise level. Levels W,7 and 6 are masked by the filter wheel (7,3) and (6,3) by the strong 2.9  $\mu\text{m}$  emission. The W state levels greater than five are thus compromised in some manner. The EXCEDE data cannot clearly prove their presence. Vibrational level 9 is a possible assignment but cannot be seriously considered without positive identification of emissions from  $v' = 6-8$  which are absent. Only the lower vibrational levels,  $v' \leq 5$ , are clearly observed at all altitudes. At the highest altitudes the (5,2) feature is masked by  $\text{H}_2\text{O}$  emission and the (2,0) and (3,1) features are strongly overlapped by the same system but the (4,1) and (3,0) bands remain distinguishable over all altitudes.

The determined population distributions at several altitudes are shown in Figure 110. Also shown for comparison is the distribution predicted by Cartwright<sup>4</sup> normalized at  $v'=3$ . This figure indicates the observed W-B distributions to be "colder", i.e., more relaxed than Cartwright. Because of the large degree of overlap in the CVF data, particularly at the higher altitudes, we do not believe the apparent vibrational effects to reflect a true altitude variation.

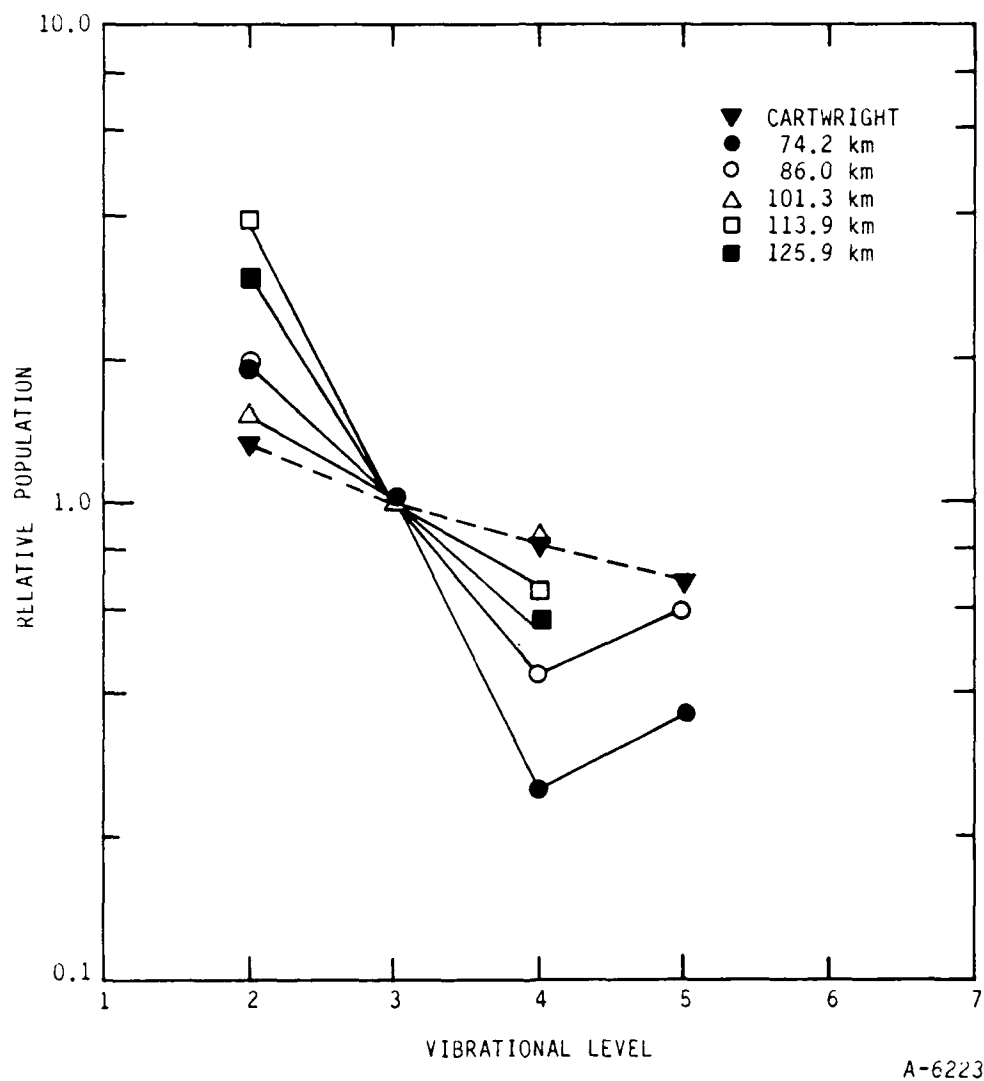


Figure 110. Determined relative population distribution for  $N_2(W^3\Delta)$  normalized at  $v'=3$ .

### 11.3.2 H<sub>2</sub>O Emission

The immediate environment around the payload was strongly contaminated by outgassing water, with contamination decreasing with mission time.<sup>148</sup> The column density was sufficiently large (up to  $10^{16}$  cm<sup>2</sup>) that OH rotational emission was detected in the 11 to 18  $\mu$ m region.<sup>148,149</sup> Thus, emission from vibrationally excited H<sub>2</sub>O in the 2 to 8  $\mu$ m region seemed likely. The low altitude 2.9  $\mu$ m feature was given this preliminary assignment by previous investigators. Careful inspection, however, indicates that this low altitude feature cannot be due to water. H<sub>2</sub>O emission has been unambiguously identified in the higher altitude data, however.

Table 23 shows the principal H<sub>2</sub>O vibrational transitions in the 1.4 to 7  $\mu$ m range. The table shows the  $2\nu_2$ ,  $\nu_1$ , and  $\nu_3$  features to be the principal emissions in the 2.9  $\mu$ m region. Although none of these bands centers fall at 2.9  $\mu$ m, synthesis of a basis set was deemed necessary to verify or rule out the contribution of water emission in the EXCEDE data. Synthetic spectral generation of emission from polyatomics is difficult but was achieved by conversion of a compilation of absorption line strengths. Such a compilation for water and other polyatomics (such as CO<sub>2</sub>, N<sub>2</sub>O, and O<sub>3</sub>) have been performed by Rothman et al.<sup>143,144,166</sup> and is available on magnetic tape.

The AFGL tape is organized by frequency. Each line contains the frequency, absorption strength, energy of the upper level, the involved vibrational levels, a code for the isotope, and a code for the identity of the molecule. This tape was read, the molecule and isotope of interest were selected, the absorption line strengths were converted to emission intensities, and an infinite resolution spectrum compatible with our spectral fitting codes was generated.

Two simple computer codes were written, the first performed the search and line intensity conversion and the second performed the slit function convolution. The absorption line intensities in the AFGL tape were compiled

TABLE 23. H<sub>2</sub>O IR emission features.

Transition	$\nu_0$ (cm <sup>-1</sup> )	$\lambda$ (μm)
010-000	1594.736	6.27
020-000	3151.631	3.17
100-000	3657.054	2.734
001-000	3755.924	2.662
030-000	4666.720	2.143
110-000	5234.981	1.91
011-000	5331.245	1.876
120-000	6775.10	1.476

for 296 K rotational temperatures. Conversion to a temperature of interest was achieved by adjusting the line strength as follows

$$S_J(T) = S_J(296) \frac{Q_v(296)}{Q_v(T)} \frac{Q_R(296)}{Q_R(T)} \exp \left[ \frac{E''}{k} \left( \frac{1}{296} - \frac{1}{T} \right) \right] \quad (55)$$

where  $E'$  is the energy of the lower state. For H<sub>2</sub>O,

$$\frac{Q_v(296)}{Q_v(T)} = 1.0$$

and

$$\frac{Q_R(296)}{Q_R(T)} = \left( \frac{296}{T} \right)^{3/2}.$$

Emission intensities are calculated from the relationship

$$A_J = 2.8 \times 10^{-8} \nu^2 L_0 S_J(T) e^{E''/kT} \quad (56)$$

where  $L_0$  is Loschmidt's number

$$L_0 = \frac{9.66 \times 10^{18}}{T} \cdot 760 \quad .$$

Computation of individual line intensities is then straightforward,

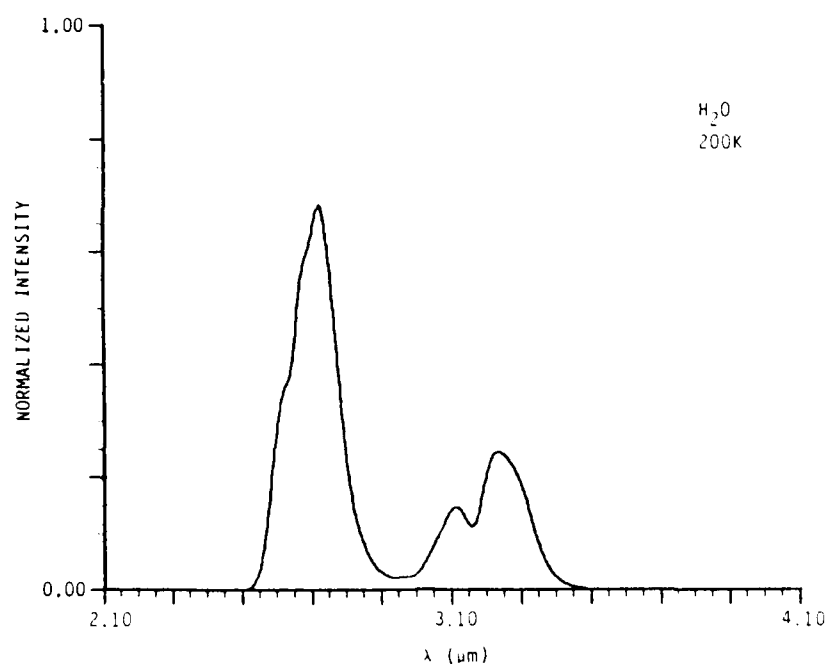
$$I_J = hc \nu A_J N_V e^{-E_R'/kT} \quad (57)$$

where  $N_V$  is the population in the vibrational level of interest and  $E_R'$  is the rotational energy level origin within the vibrational level and is equal to

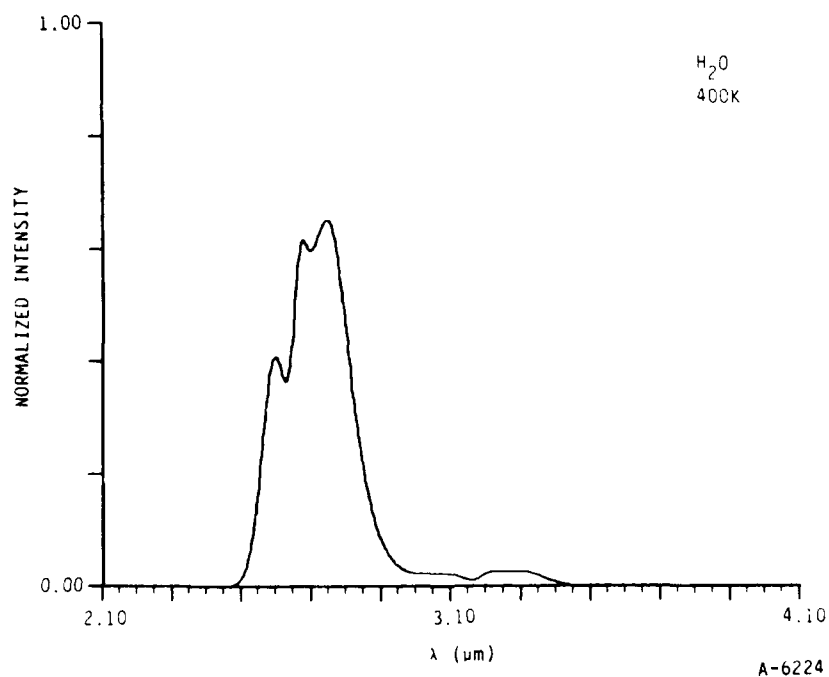
$$E_R' = \nu + E'' - E_0^{v'}$$

where  $E_0^{v'}$  is the energy of the vibrational level  $v'$  at the ground rotational level.

In the spectral generation and fitting programs in use for diatomics, the vibrational population is a dependent variable and is determined by the fit since each vibrational level is created as an independent basis set. For this application we want to determine the expected bandshape in the region 2.6 to 3.4  $\mu\text{m}$  and contrast this with the low and high altitude data. Thus, an assumed vibrational distribution of equal populations was chosen. The resulting basis sets at rotational temperatures of 200 to 400 K are shown in Figures 11a and b, respectively. A fit of the 200 K basis set to a low altitude spectrum is shown in Figure 112. Clearly, the 2.9  $\mu\text{m}$  feature evident in the low altitude data is not attributable to  $\text{H}_2\text{O}$  emission. A fit to higher altitude data is shown in Figure 113. Here the agreement is improved, indicating the 2.7  $\mu\text{m}$  emission at these altitudes is due to water emission.



(a)



(b)

Figure 111. H<sub>2</sub>O vibrational emission basis sets at 200 K (a) and 400 K (b).



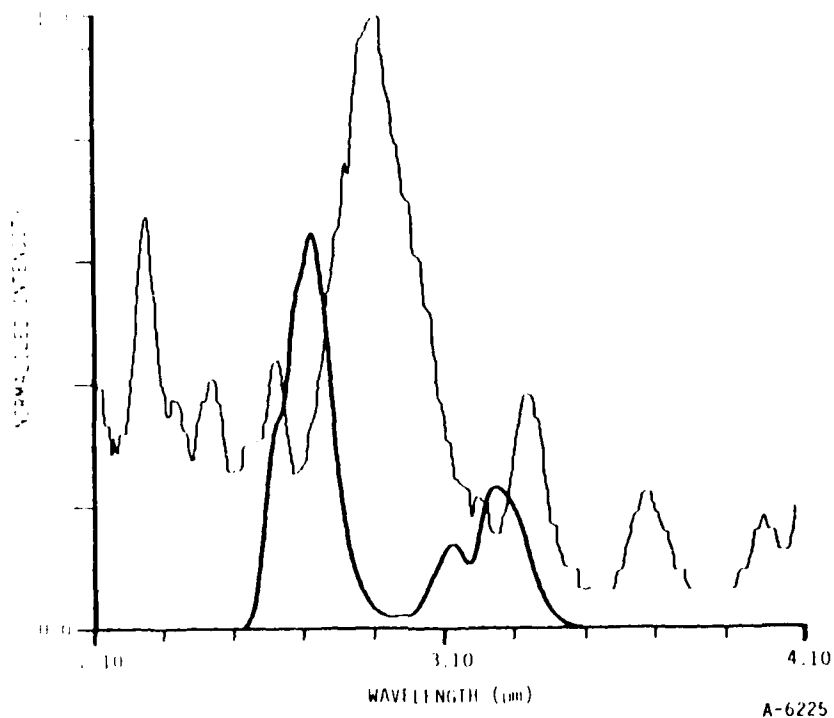


Figure 112. Uncorrected SWIR scan 524 fit to 200 K H<sub>2</sub>O vibrational basis set.

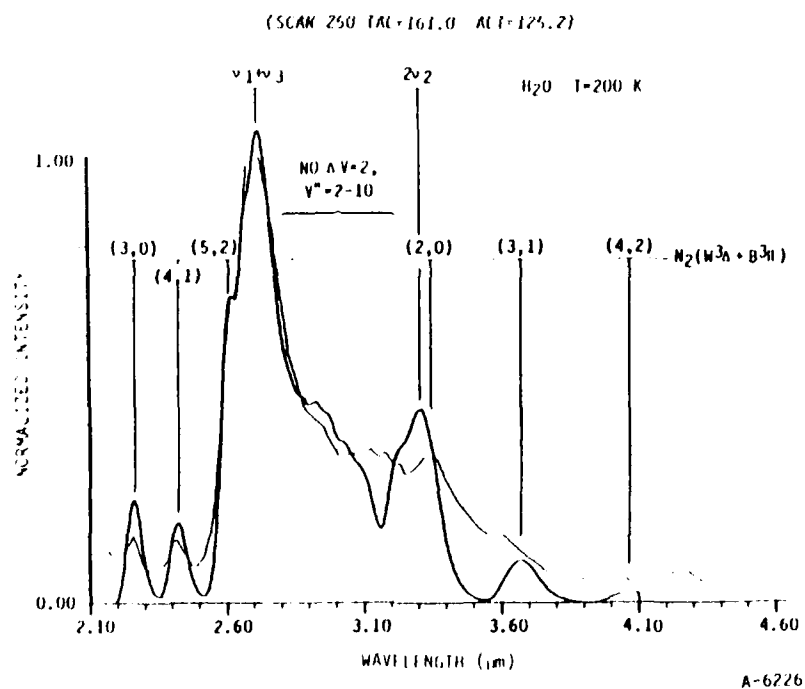


Figure 113. Uncorrected scan 520, TAL = 161.0s, Alt = 125.2 s, and fit to 200 K H<sub>2</sub>O emission. Also included in the fit is emission for N<sub>2</sub>(W<sup>3</sup>Δ<sub>u</sub> + B<sup>3</sup>Π<sub>g</sub>, v' = 2-5) and NO Δv = 2. The NO overtones were determined to be a minor constituent.

H<sub>2</sub>O emission at 2.7  $\mu$ m peaked at  $\sim 100$  km exceeding  $10^3$  MR. At higher altitudes the spectra are clearly dominated by H<sub>2</sub>O but the peak intensity is reduced. At lower altitudes the H<sub>2</sub>O emission steadily decreases such that below 80 km it is no longer observable.

### 11.3.3 NO Fundamentals

The 5.4  $\mu$ m band system in the MWIR data has been identified in a previous analysis<sup>147</sup> as NO fundamentals. At a single altitude, the vibrational distribution was determined to be similar to the nascent  $N(^2D) + O_2 \rightarrow NO(v) + O$  vibrational distribution as determined from COCHISE experiments.<sup>152</sup> Verification of this conclusion as well as examination of the entire data base was the goal of this work.

Only eleven MWIR scans exhibited sufficient signal to noise to warrant analysis. The scan numbers and relevant data are listed in Table 19. Although the data set is limited, they do represent an almost 20 km height profile (74.2 to 92 km). It was hoped that these files would be sufficient to indicate altitude variation and thus quenching effects.

Figure 114 shows the 4.8 to 6.8  $\mu$ m portion of MWIR scan 1200 with a baseline emission level subtracted. The radiance between 4.95 to 5.00  $\mu$ m was taken as this background level. The data has not been smoothed. Although the resolution element is large in this wavelength range (0.1  $\mu$ m FWHM at 5.0  $\mu$ m), smoothing was not performed to avoid introducing any systematic errors. Figure 114 also shows two synthetic spectra; one with vibrational levels adjusted to give a best fit and the other with the relative vibrational populations fixed in the COCHISE nascent distribution. When we allow the vibrational distribution to be varied freely in the fitting process, an excellent match to the data is obtained.

Some of the best data is shown in Figure 114. The noise in the data was found to cause observable fluctuations in the determined relative population

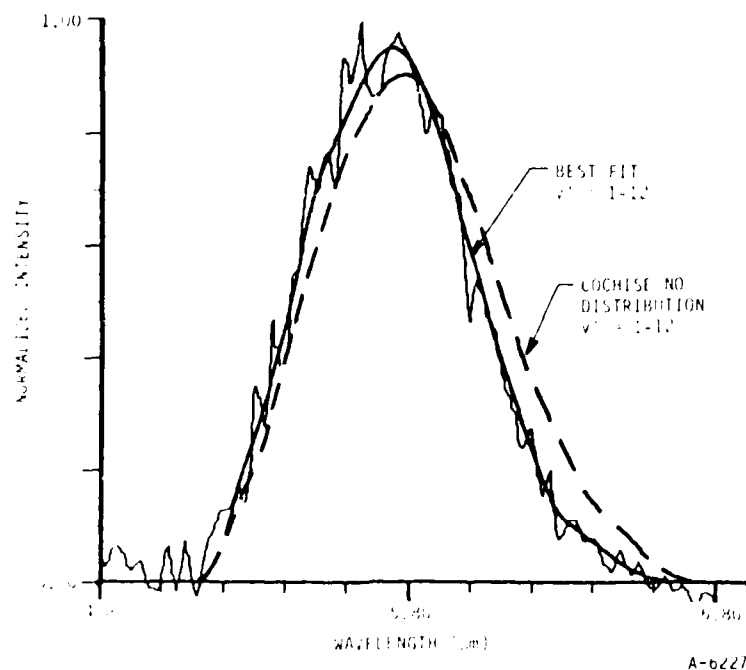
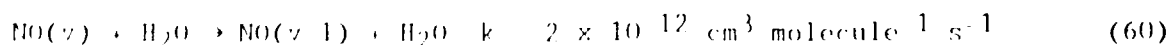
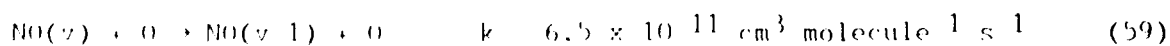
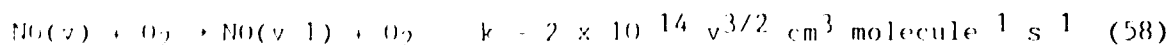


Figure 114. Uncorrected MWIR scan 1200 (TAL = 282.0s, Alt = 86.8 km) with fits to NO ( $\Delta v=1$ ,  $v''=2-12$ ) with independent vibrational variation and with the COCHISE nascent relative vibrational distribution.

distributions. Thus, the population distribution from several appropriate altitudes were averaged; files 1195-1197 taken near an altitude of 91 km were averaged, as were 1204-1206 (81.3 km), and 1209-1211 (75.4 km). These populations with one standard deviation error bars are shown in Figures 115 through 117. For comparison the NO nascent distribution is also plotted. The EXCEDE data follows the nascent distributions at all altitudes.

Quenching of NO( $v$ ) may occur by atomic and molecular oxygen and water via the quenching reactions shown below:



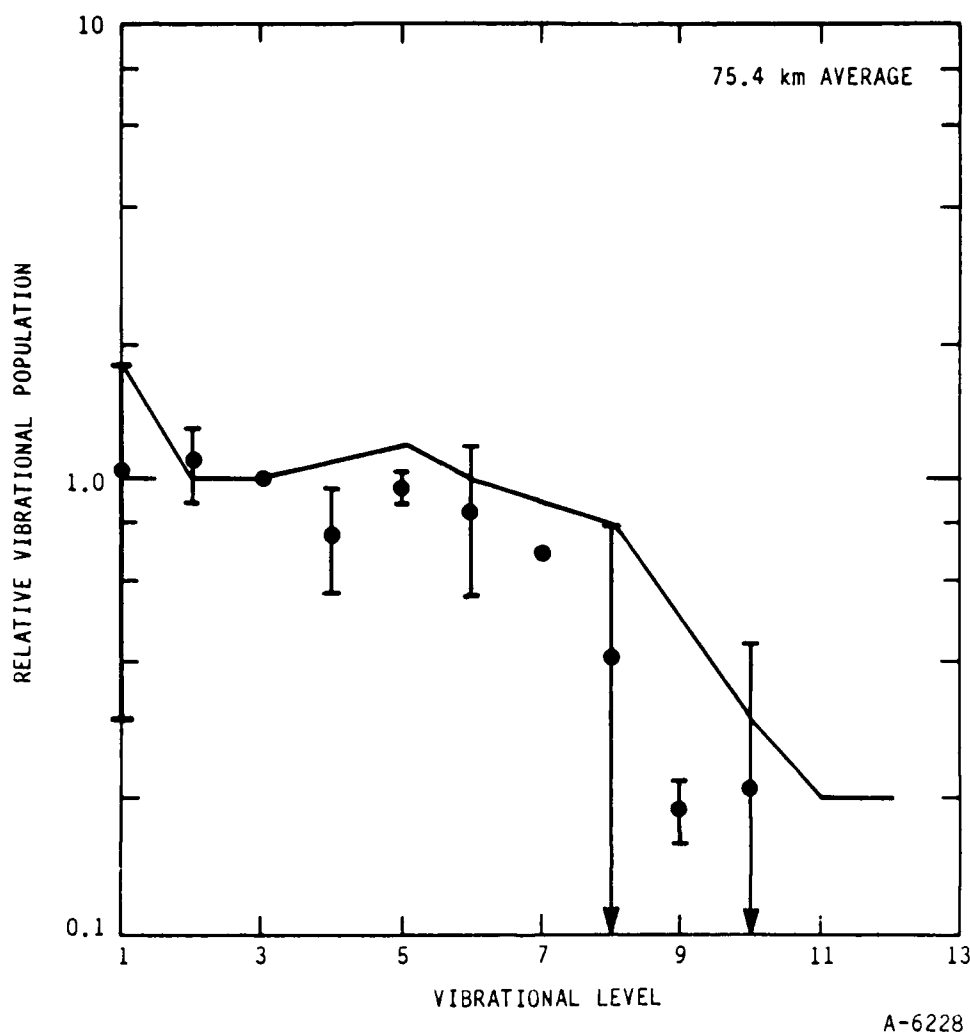


Figure 115. Relative NO vibrational population distributions at 75.4 km. Also shown in solid line is the COCHISE nascent distribution. The data have been averaged from fits to MWIR files 1209 1211 and are shown with one standard deviation error bar.

The observation of the measured nascent distribution unrelaxed by collisions or radiation strongly indicates that the observed emission is due to  $N(^2D) + O_2$  and there is a rapid NO(v) removal mechanism. From Reactions (58) and (59) above we have calculated the NO(v) quenching rates by O and  $O_2$  over the altitudes of interest for typical atmospheric densities and find that the quenching rates are of the same order as the radiation rate over all altitudes. For  $H_2O$  quenching to contribute, the concentration must have been in excess of

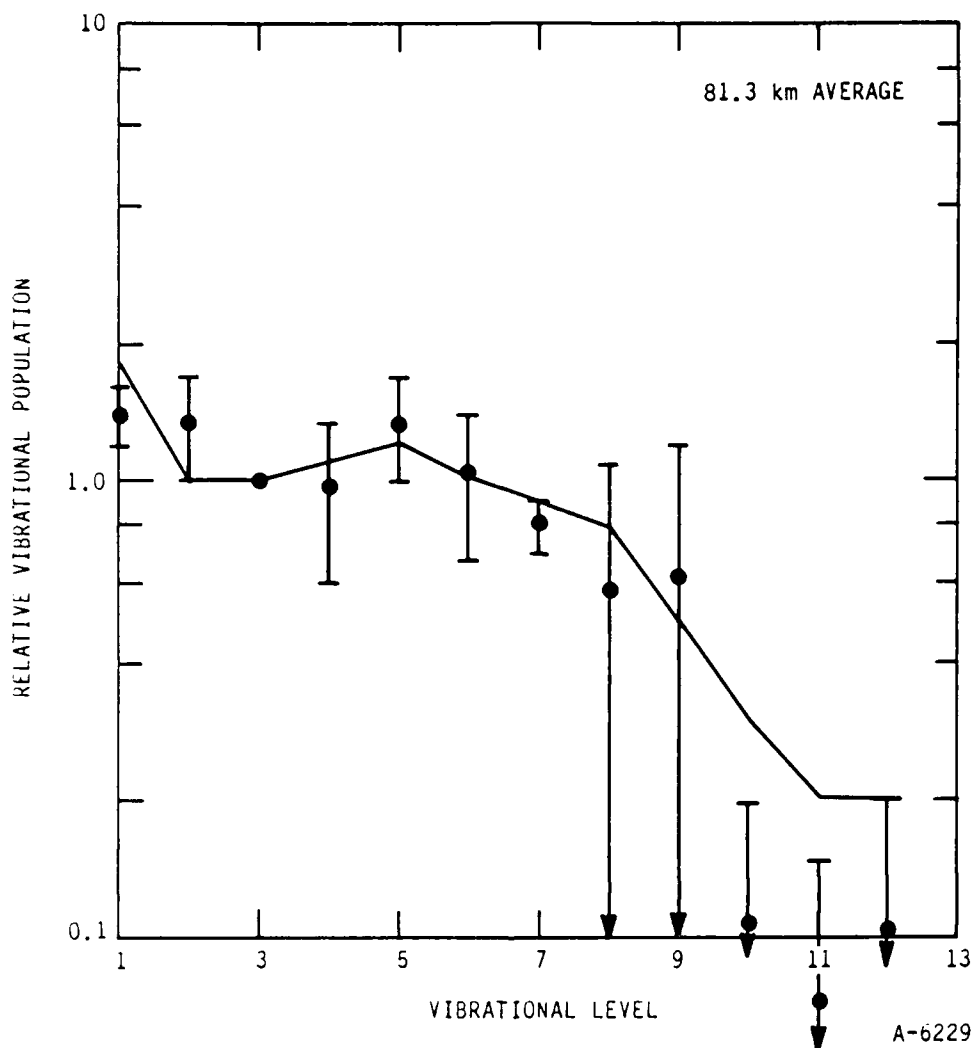
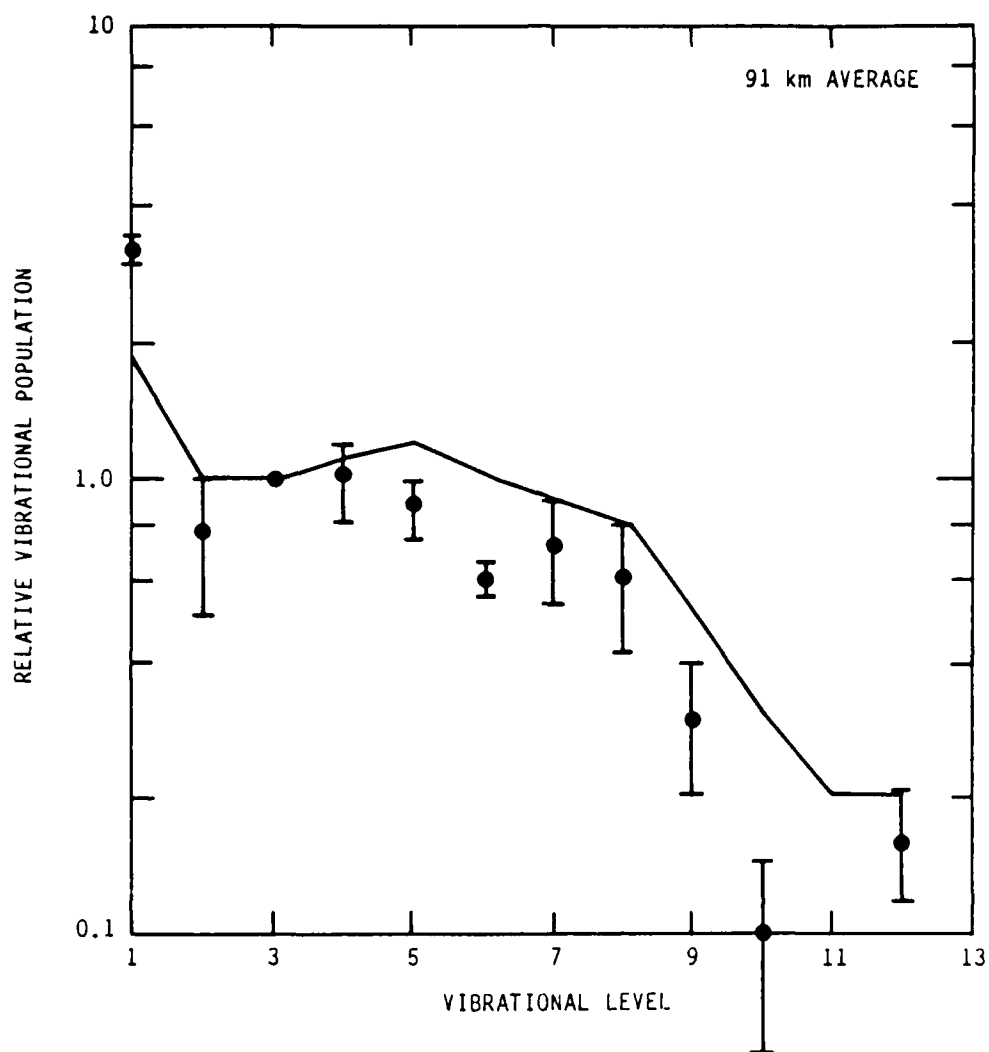


Figure 116. Relative NO vibrational population distributions at 81.3 km. Also shown is the COCHISE nascent distribution. The data have been averaged from fits to MWIR files 1204-1206 and are shown with one standard deviation error bar.

$10^{13} \text{ cm}^{-3}$ . Clearly, quenching is too slow to have modified the nascent distribution. The likely cause is rapid removal from the field of view. The reported residence time in the field of view is 10 ms.<sup>147</sup> In comparison to the NO radiation and quenching rates, this is sufficiently rapid to cause a nascent distribution to be observed. Thus, quenching effects of NO(v) were not observed in the EXCEDE data down to 75 km altitudes. The short residence time in the field of view limits quenching observations to lower altitudes still.



A-6230

Figure 117. Relative NO vibrational population distributions at 91 km. Also shown as a solid line is the COCHISE nascent distribution. The data have been averaged from fits to MWIR files 1195-1197 and are shown with one standard deviation error bar.

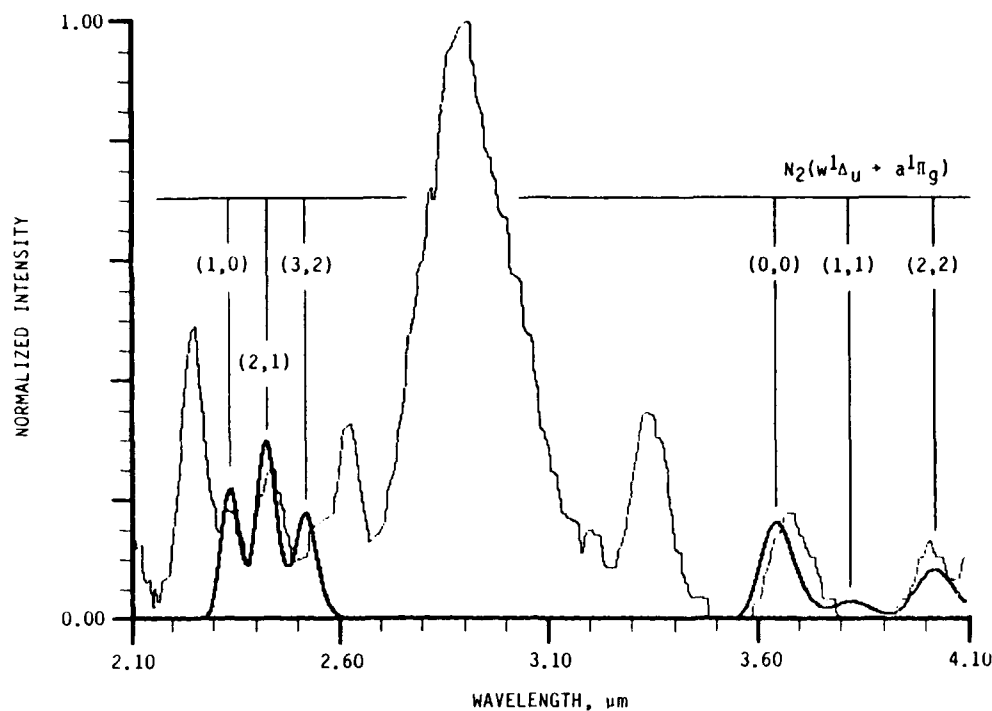
#### 11.3.4 Surveys of Other Band Systems

Previous sections have covered investigation of the EXCEDE 2 to 5  $\mu\text{m}$  data for Wu-Benesch and NO fundamental emission. In this section we attempt to find evidence for emission from the other band systems. Most systems considered did not appear to be present in the EXCEDE data. Transitions considered include: the other possible  $\text{N}_2$  IR emission systems,  $w^1\Delta \rightarrow a^1\Pi$ ,  $a^1\Pi \rightarrow a'^1\Sigma$ ,

$B^3\Pi \rightarrow A^3\Sigma$ , and  $B'^3\Sigma \rightarrow B^3\Pi$ ; the  $N_2^+$  Meinel system,  $A^2\Pi \rightarrow X^2\Sigma$ ; and OH vibronic emission and NI and OI Rydberg emission.

The corrected low gain scan at 74.6 km has been chosen to present the results of the spectral comparisons. Since the  $CO_2$   $v_3$  emission dominates the low altitude scans, only the 2.1 to 4.1  $\mu m$  region will be shown for purposes of contrast. Owing to the low resolution of the data, spurious assignments are possible. The criteria used for positive identification are: overlap of features in the data with a synthetic spectrum and simultaneous overlap of all branches arising from the same upper state; the fit should produce a rational vibrational distribution; the determined upper state populations should be indicative of an auroral distribution as shown in Figure 107.

The results of the spectral survey are shown in Figures 118 through 123. Figure 118 shows a fit to  $N_2(w^1\Delta \rightarrow a^1\Pi, v'=0-3)$ . This emission system has been observed to be severely overlapped with Wu-Benesch emission in the COCHISE apparatus<sup>126</sup> at equivalent number densities. The individual transitions are marked. Although several of the bands exhibit overlap with features in the data, we believe this emission system does not contribute significantly to the observed spectra. The (0,0) band overlaps with the feature at 3.7  $\mu m$ , a feature that is well reproduced by the (2,0) Wu-Benesch transition. Since the transition probabilities for the w-a and W-B system are similar,<sup>126</sup> observation of w-a emissions is inconsistent with the order of magnitude difference in auroral number densities predicted by reinterpretation of Cartwright's data (see Figure 107). If background correction is applied, as shown in Figure 118, then there is no evidence for the w-a (1,1) band. Therefore, we believe the overlap between the data and the predicted w-a band system is coincidental; there is no firm evidence in the CVF data for this emission system. This conclusion is supported by fits of the interferometer data to simulated w-a spectra; no evidence for this system could be found in the interferometer data as well.



A-6231

Figure 118. Corrected SWIR scan 524 with fit to  $N_2(w^1\Delta_u + a^1\Pi_g)$ ,  $v'=0-2$ ) at a rotational temperature of 200 K.

Figure 119 shows a fit of the  $N_2(a^1\Pi \rightarrow a'^1\Pi, v'=1-5)$  system to the data. The transitions that occur in the wavelength region are from the  $\Delta v=+1, +2$  sequences. The (1,0) band falls at 3.5  $\mu\text{m}$  and does not overlap with any feature in the data. Since none of the bands of the  $a-a'$  system exhibit sufficient overlap with features in the data, we conclude there to be no evidence for the presence of this emission system.

The next emission considered was the  $N_2(B'^3\Sigma \rightarrow B^3\Pi, v'=0-3)$  system as shown in Figure 120. Although the (2,3) and (3,4) transitions overlap nicely with the data in the 2.2 to 2.4  $\mu\text{m}$  region, the (2,4) and (3,5) features do not correspond well with the data in the 3.4 to 3.8  $\mu\text{m}$  region. The feature at 3.7  $\mu\text{m}$  has been previously assigned as the W-B (3-1) transition. The predicted column densities of the  $B'$  state are only a factor of two to three less than those determined for the  $W^3\Delta$  state. Cartwright predicts the  $B'^3\Sigma$  number densities to be more than two orders of magnitude less than the  $W^3\Delta$  state. For these reasons, emission from the  $B'-B$  system has been ruled out.



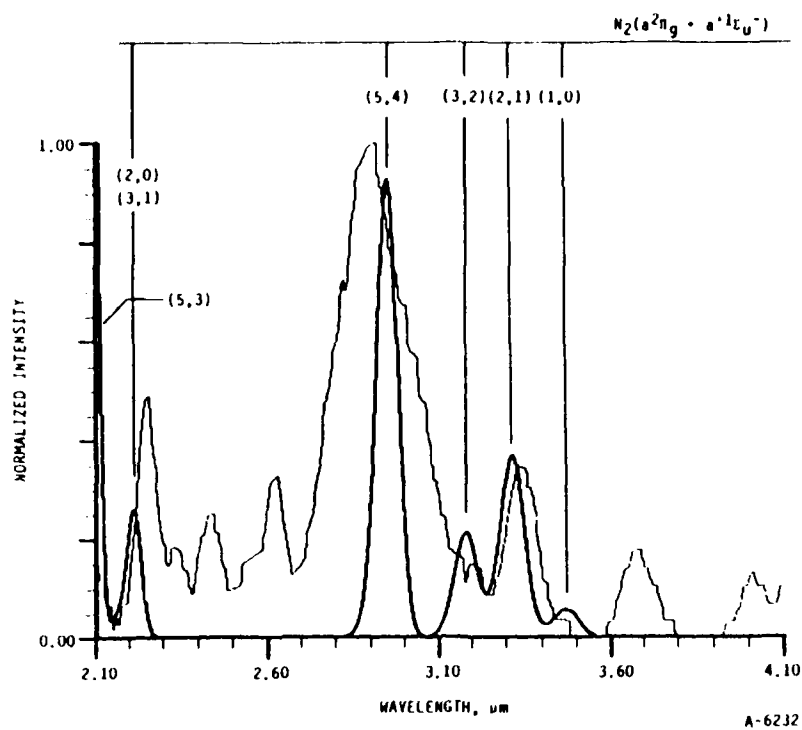


Figure 119. Corrected SWIR scan 524 with fit to  $N_2(a^1\Pi_g \rightarrow a'^1\Sigma_u^-, v'=1-5)$  at a rotational temperature of 200 K.

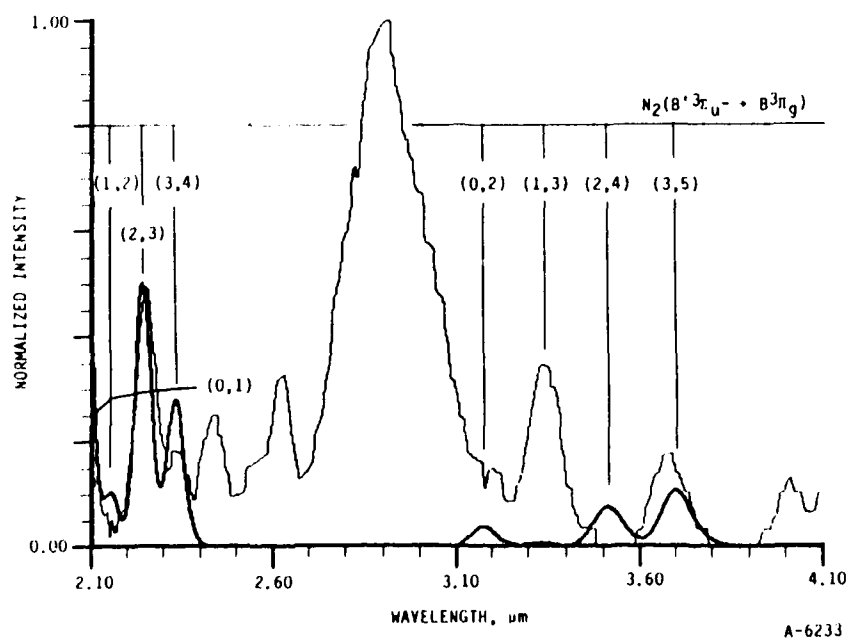


Figure 120. Corrected SWIR scan 524 with fit to  $N_2(B'^3\Sigma_u^- \rightarrow B^3\Pi_g, v'=0-3)$  at a rotational temperature of 200 K.

Emission from the First Positive system,  $N_2(B^3\Pi \rightarrow A^3\Sigma)$ , is commonly observed from discharged nitrogen. Figure 121 shows a fit to  $v'=0-3$  of the First Positive band system. The bands that occur in this spectral region are due to the  $\Delta v=+4,+5,+6$  sequences. The poor correspondence between the fit and data indicates that this emission system is an unlikely contributor to the EXCEDE spectra.

The last neutral nitrogen band system investigated was the  $(B_3\Pi \rightarrow W^3\Delta, v'=2-5)$  as shown in Figure 122. Several of the transitions align with features in the data but the predicted column densities (roughly twice  $W^3\Delta$ ) are far too large. Cartwright predicts  $B^3\Pi$  number densities to be an order of magnitude lower than the  $W^3\Delta$  state at the lower vibrational levels. In addition, there was no indication of the strongest  $B \rightarrow A$  First Positive band which must be observed if  $B \rightarrow W$  emission is present. Thus, despite the agreement between the fit and the data, it is unlikely that  $B-W$  emission is present in the EXCEDE spectra.

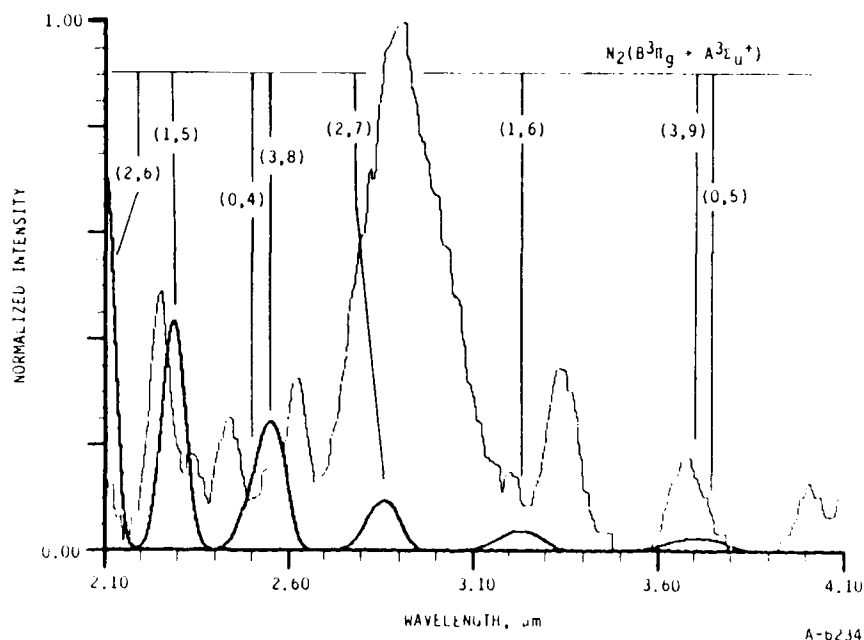


Figure 121. Corrected SWIR scan 524 with fit to  $N_2(B^3\Pi_g \rightarrow A^3\Sigma_u^+, v'=0-3)$  at a rotational temperature of 200 K.

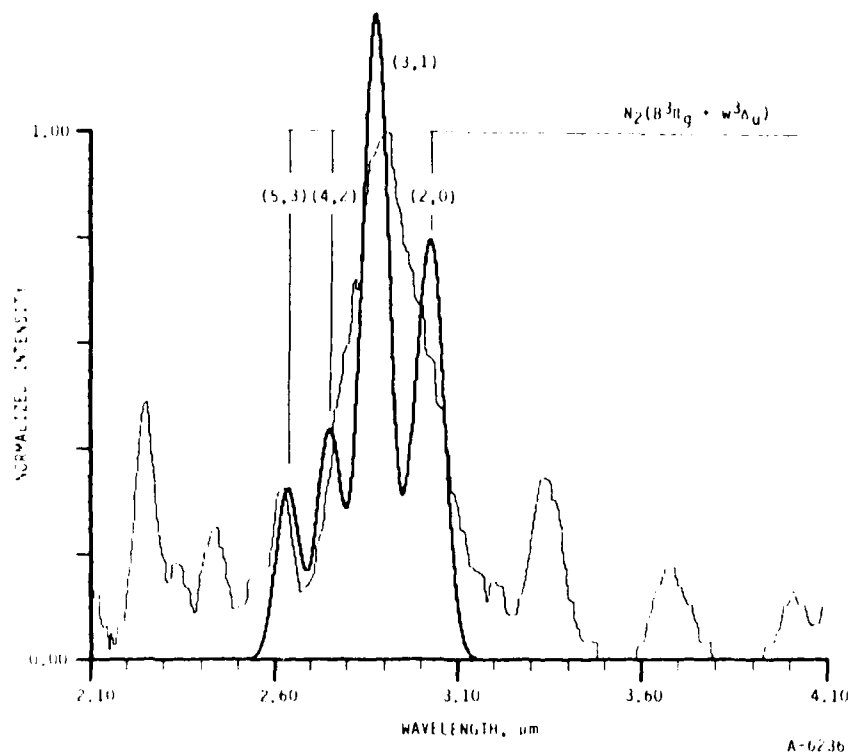


Figure 122. Corrected SWIR scan 524 with fit to  $N_2(B^3\Pi_g + w^3\Delta_u, v' = 2-5)$  at a rotational temperature of 200 K.

The  $N_2^+$  Meinel system has been observed in auroral<sup>2,5</sup> and electron impact on  $N_2$ .<sup>96</sup> Figure 123 shows a fit of this band system to the data. Only the (1,3) feature aligns with the data and this has been previously assigned to the (3,0) Wu Benesch transition. There is, therefore, no clear evidence for the presence of  $N_2^+(A'^2\Pi + X^2\Sigma)$  emission.

Spectra of discharged air at reduced pressures often exhibit OI and NI Rydberg emissions (Refs. 164, 167, and Appendix E). Table 24 presents a list of commonly encountered atomic lines in the 2 to 4  $\mu\text{m}$  region. Synthetic spectra of atom emission compared to these data indicate possible participation of OI lines at 2.65, 2.76, 2.89, and 3.10  $\mu\text{m}$ . If present, an atomic line at 2.65  $\mu\text{m}$  may help explain the anomalous population from W B (5,3). An NI line at 4.0  $\mu\text{m}$  is the likely source of that observed emission. No other nitrogen atomic lines correspond well with unidentified features in the data.

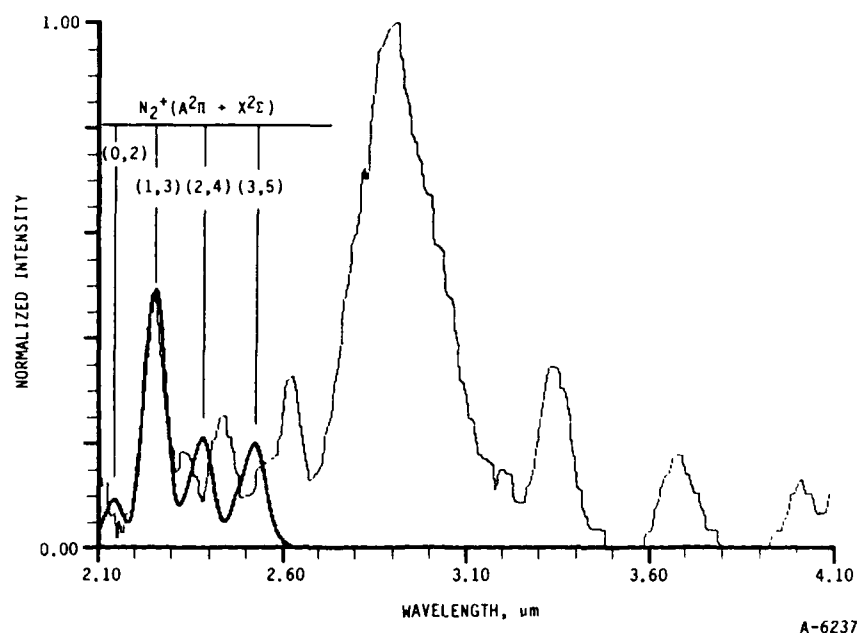


Figure 123. Corrected SWIR scan 524 with fit to  $N_2^+(A^2\Pi \rightarrow X^2\Sigma, v'=0-3)$  at a rotational temperature of 200 K.

#### 11.3.5 Ultraviolet and Visible Interferometer Data

Examination of this portion of the EXCEDE data was not part of the original goals of this research effort. However, the data has not been previously analyzed and it was felt that a preliminary examination may aid interpretation of the IR data as well as provide a quick comparison of EXCEDE results to auroral data.

Two pairs of UV and visible spectra were chosen, one at low altitude and one at high altitude. These spectra file numbers and altitude data of the chosen files are shown in Table 21.

These spectra have been digitized and fit to determine the emitting column densities in the following states:  $N_2 a^1\Pi$ ,  $B^3\Pi$ ,  $C^3\Pi$ , and  $N_2^+ A^2\Pi$ ,  $B^2\Sigma$ . All four data files are shown in Figures 124 through 127. Figure 128 shows a portion of a fit of scan number 116 to  $N_2(a^1\Pi_g \rightarrow X^1\Sigma_g^+)$  emission. The reproduction of the observed features is good but not perfect.

TABLE 24. OI and NI infrared emission lines.

Species	Transition	Wavelength ( $\mu\text{m}$ )
OI	$4d^3D^0 - 4p^5P$	2.65
OI	$4p^2P - 4s^5S^0$	2.76
OI	$4p^3P - 4s^3S^0$	2.89
OI	$4d^3D^0 - 4p^3P$	3.10
NI	$4p^4S^0 - 4s^4P$	2.621
NI	$4p^4S^0 - 4s^4P$	2.693
NI	$4p^4P^0 - 4s^4P$	3.027
NI	$5fF(4)^0 - 4d^2D$	4.004
NI	$5fG(3) - 4d^2F$	4.006
NI	$5fF(3) - 4d^2D$	4.007
NI	$5d^4D - 4fG(4)$	4.015
NI	$5d^2F - 4fD(2)^0$	4.022
NI	$5s^4P - 4p^4S^0$	4.032
NI	$5fD(2)^0 - 4d^4P$	4.035
NI	$5d^4F - 4fG(3)^0$	4.036
Data from Linus experiment <sup>167</sup> and Saum and Benesch. <sup>164</sup>		

The relative determined populations are shown in Figures 129 and 130 for altitudes of 74 to 78 km and 120 to 128 km, respectively. For comparison, Figure 131 shows the Cartwright distributions for the neutral states.

We examined the data in Figures 129 and 130 in spite of the potential uncertainties present in the uncorrected data such as source variations with time, intensity variations between the UV and visible spectrometers and even between bands during a scan. Nevertheless, based on only a preliminary analysis, several important conclusions can be drawn. The spectral fitting to the

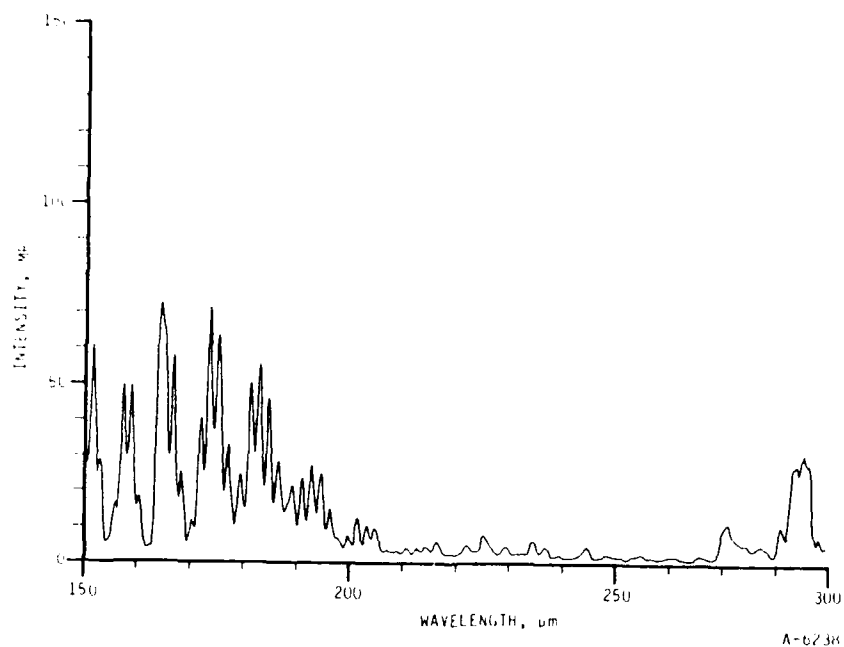


Figure 124. UV spectral scan 149 uncorrected for beam variations.  
(TAL = 290s, Alt = 79 km)

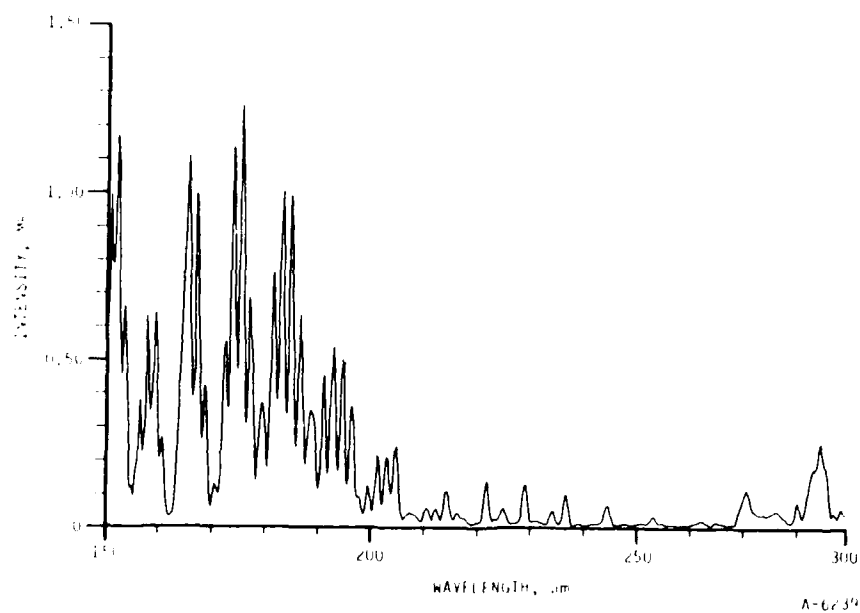


Figure 125. UV spectral scan 116 uncorrected for beam variations.  
(TAL = 230s, Alt = 120 km).

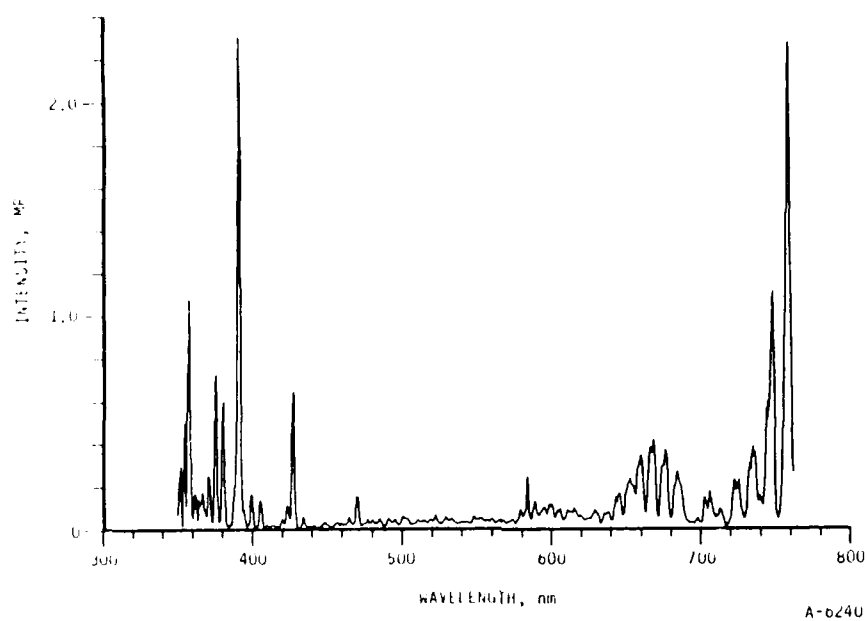


Figure 126. Uncorrected visible scan 47 (TAL = 196s, Alt = 128.3 km).

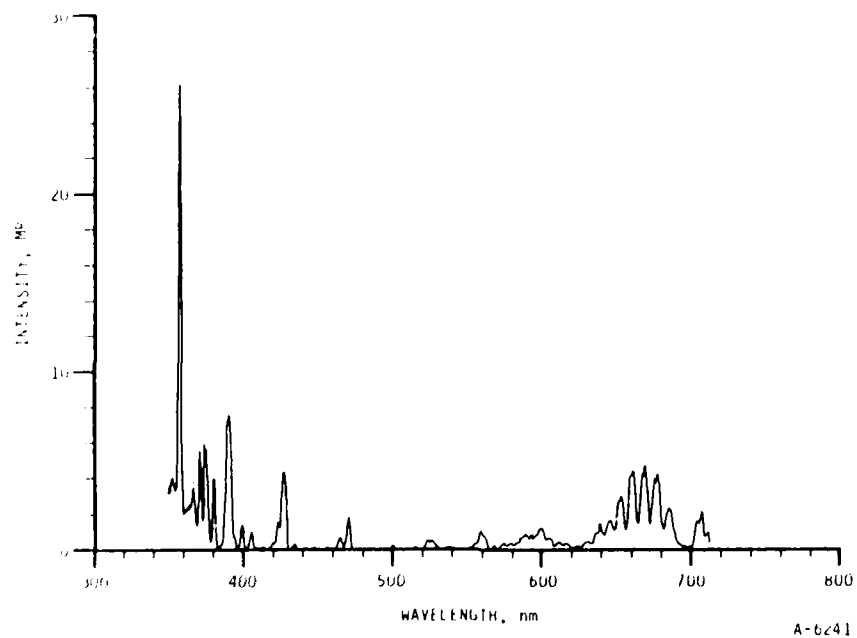


Figure 127. Uncorrected visible scan 73 (TAL = 296s, Alt = 74 km).

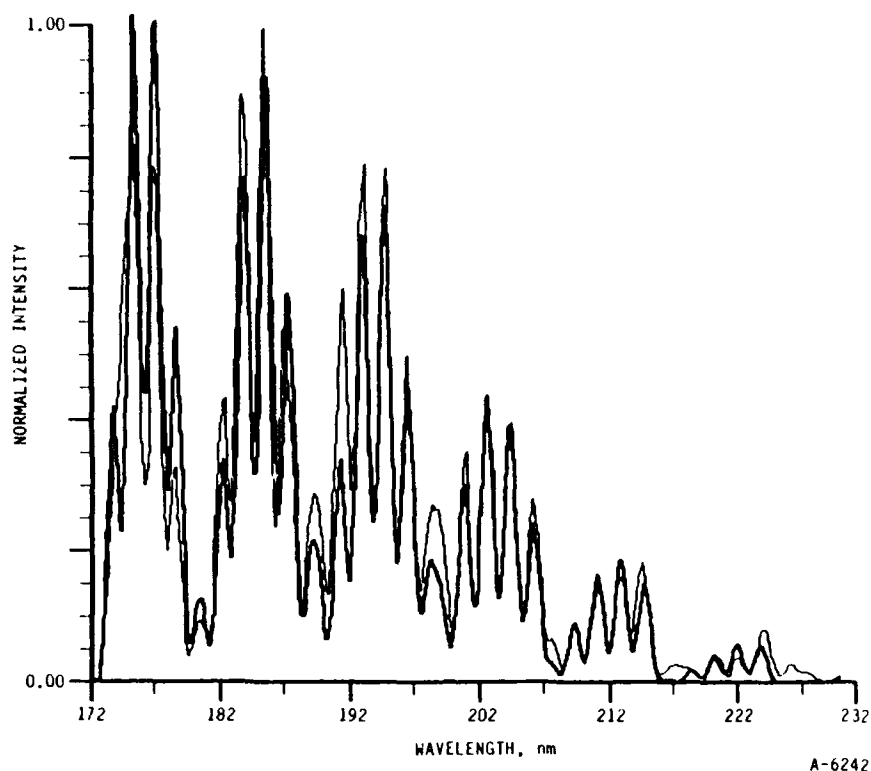


Figure 128. Comparison of data from scan 116 to  $N_2(a-X)$  emission.

data is sufficiently adequate that we may conclude the electronic state vibrational distributions derived from the high altitude EXCEDE data have the same shape as predicted by Cartwright. His model was based on electron impact excitation laboratory data and theoretical calculations. Recent LABCEDE observations support much of his modeling. The high altitude data exhibit a ratio of the C-state to B-state populations which is the same as Cartwright's value. The concentration of these states compared to the a-state in the EXCEDE data is a factor of four below the model. This ratio depends upon the relative spectrometer calibrations and beam intensity invariance. The W-state populations from the EXCEDE data (relative to the C- and B-state) are a factor of five below the ratio in the model.

The radiative lifetime of the  $N_2$  C-state is 37 ns and consequently this state should radiatively (not collisionally) decay at all altitudes where EXCEDE data exists. The lower altitude EXCEDE data (74 to 79 km) possesses an excited state column density in the spectrometer field of view only ten times



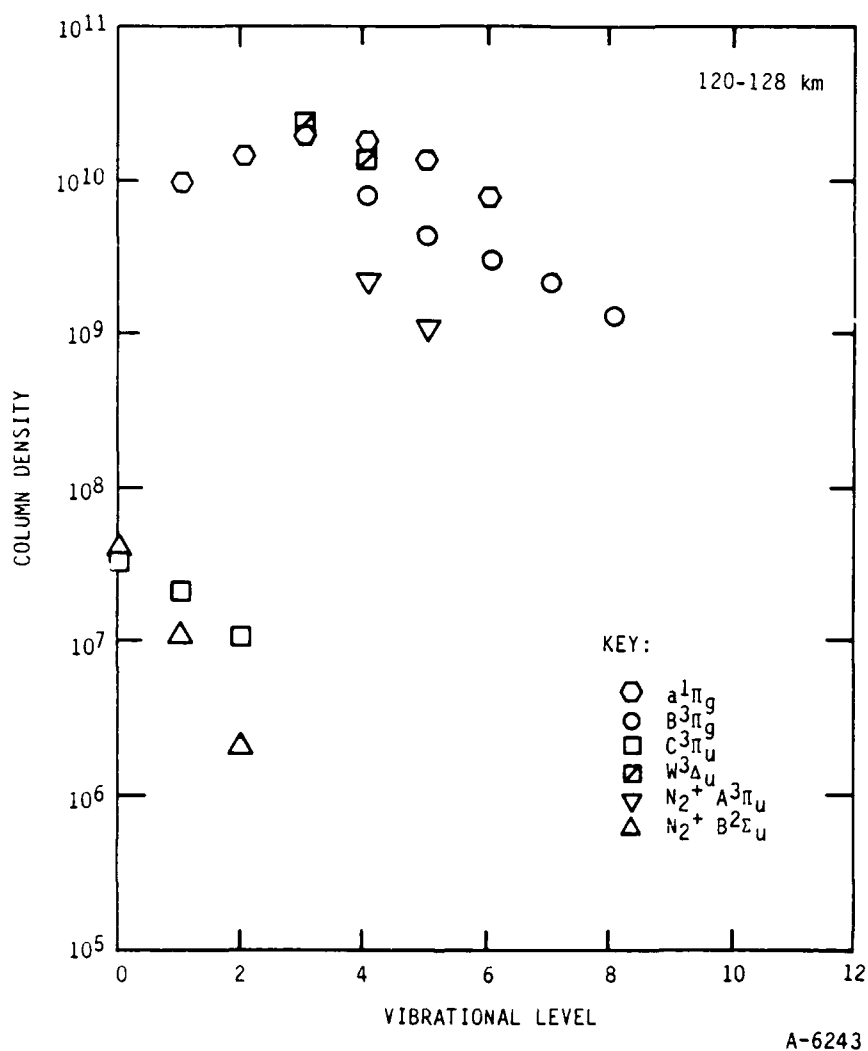


Figure 129. Determined populations for the indicated  $N_2$  and  $N_2^+$  states from the UV, Visible, and IR EXCEDE data for the 120 to 128 km range.

greater than the 125 km data. Over this altitude range the atmospheric  $N_2$  density increases by a factor of a thousand. This emphasizes that caution must be exercised when drawing conclusions from data which is incompletely characterized. Many parameters must be considered including the electron range for both primaries and secondaries, their distribution within the field of view of each spectrometer, and the line of sight of each instrument relative to the beam and the location of the previously dosed regions.

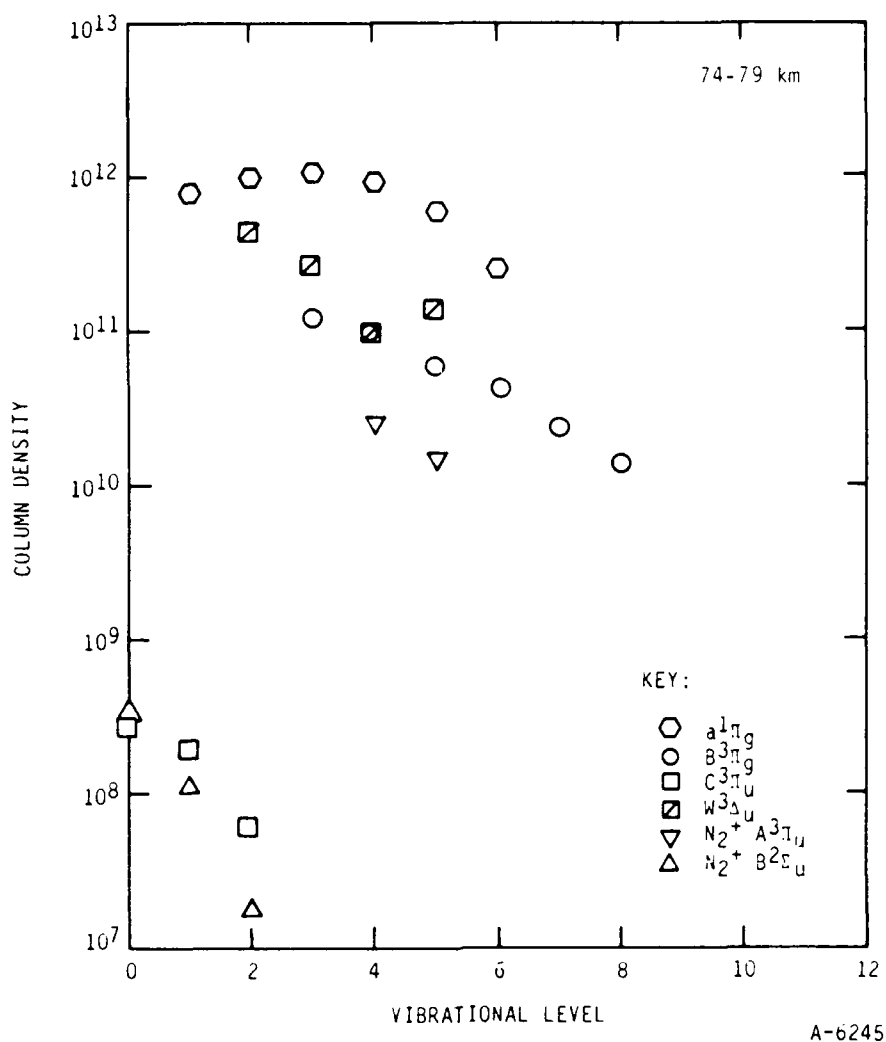


Figure 130. Determined populations for the indicated  $N_2$  and  $N_2^+$  states for the UV, Visible, and IR EXCEDE data for the 74 to 79 km range.

For the lower altitude data, the ratio of the C- and B-state populations differs from Cartwright's prediction by 50 percent. We consider this good agreement giving the assumptions in the analysis. The a-state populations are greater than expected relative to the normalizing C- and B-states. Moreover, the LABCEDE data taken at a pressure corresponding to 80 km altitude (plotted in Figure 132) indicates that quenching of the a-state should occur. The EXCEDE data is too bright by an order of magnitude. The W-state populations clearly determined from the low altitude EXCEDE data are a factor of five below the LABCEDE populations (relative to the C-state).

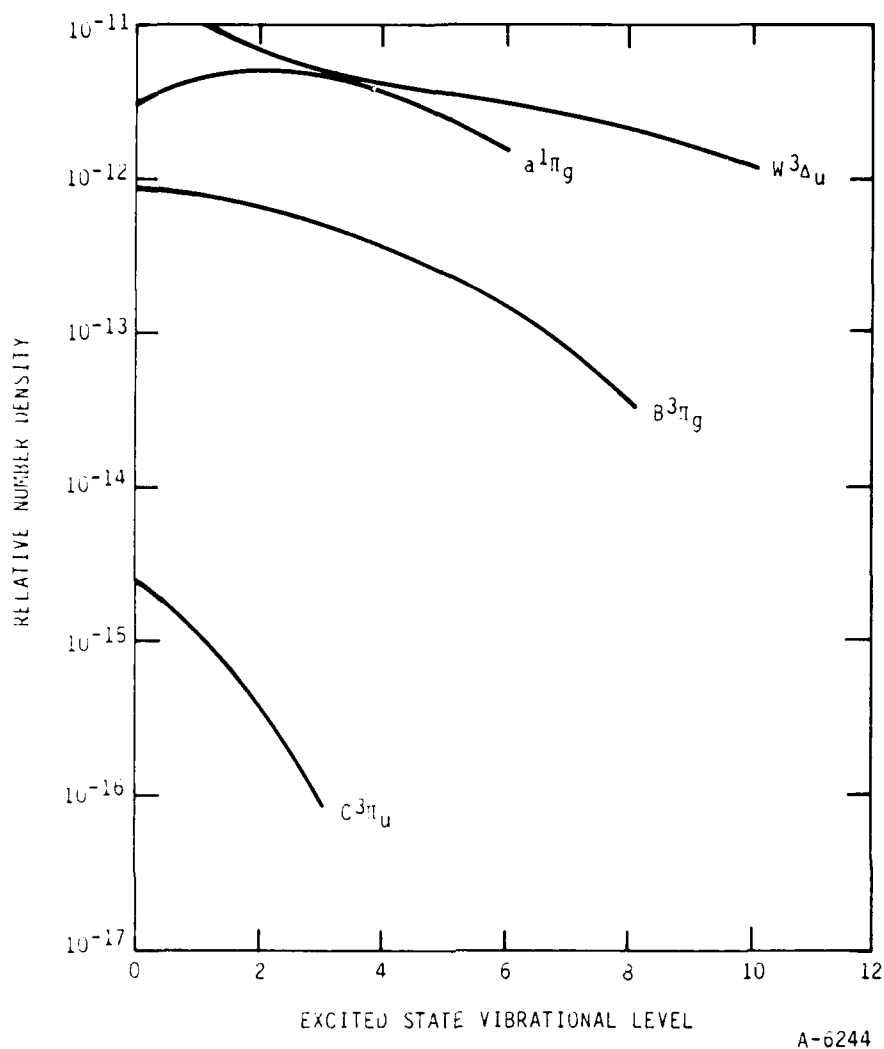


Figure 131. Cartwright predictions for several  $N_2$  states (for comparison with Figures 129 and 130).

This analysis is very preliminary and clearly has not reached a satisfactory level of sophistication. Nevertheless, this exercise has proved that data from a field observation of electron irradiation of the upper atmosphere should permit fluorescence efficiencies and quenching effects to be obtained to first order. A more accurate determination will result from a more careful analysis.

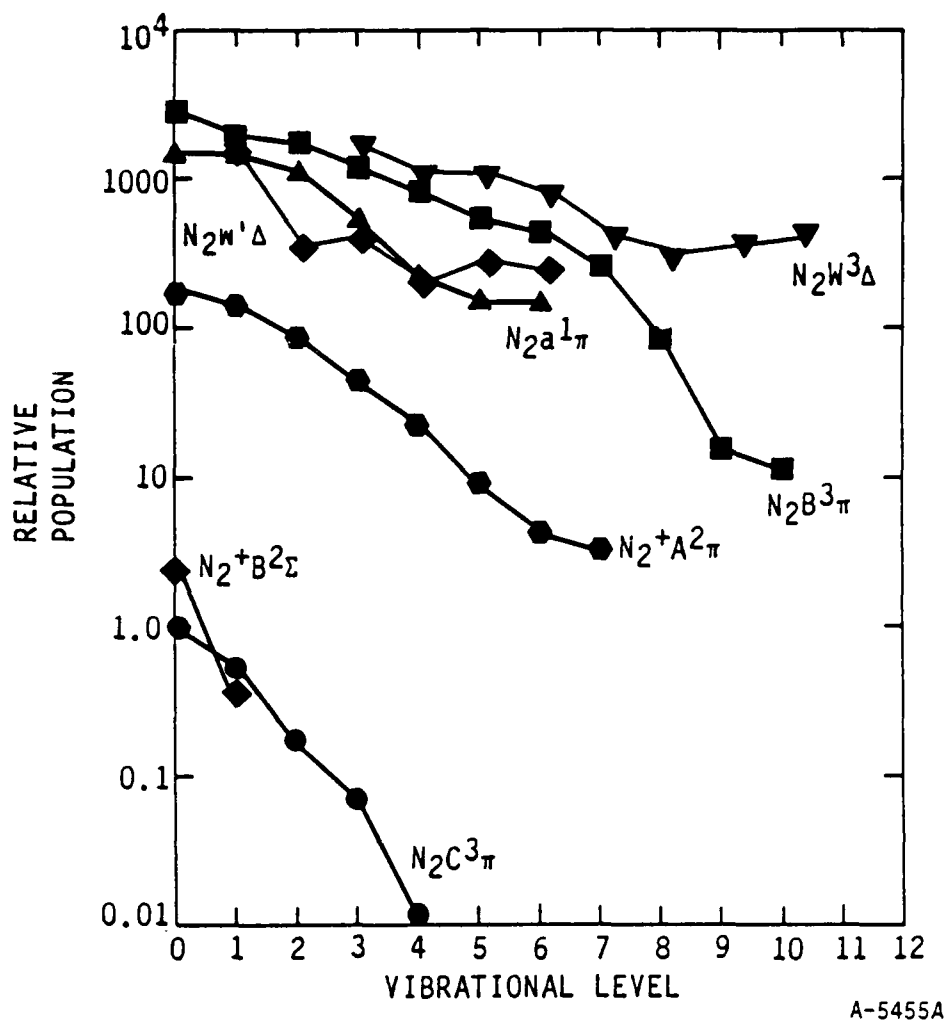


Figure 132. Nitrogen electronic populations in LABCEDE (80 km altitude).

#### 11.3.6 Infrared Interferometer Data

None of the infrared interferometer spectra were digitized, rather overlays of relevant simulated spectra were created to aid in spectral identification of features of the CVF data. Four of the interferometer spectra are shown in Figure 133. These spectra exhibit similar trends as have been observed with the CVF data; i.e., a prevalence of discrete emission features at low altitudes and principally a broad spectral emission at  $2.9 \mu\text{m}$  ( $\sim 3400 \text{ cm}^{-1}$ ) at higher altitudes.

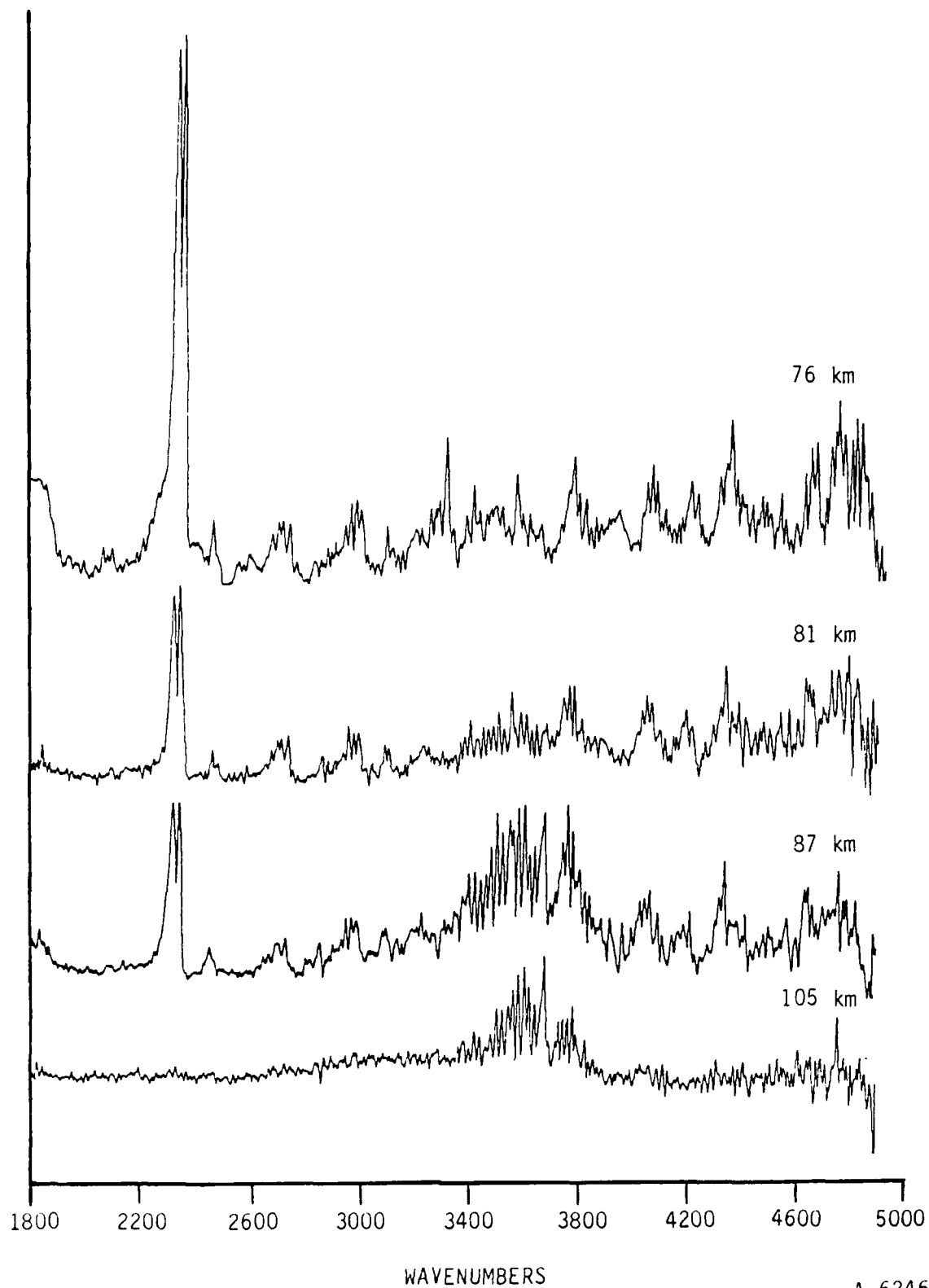


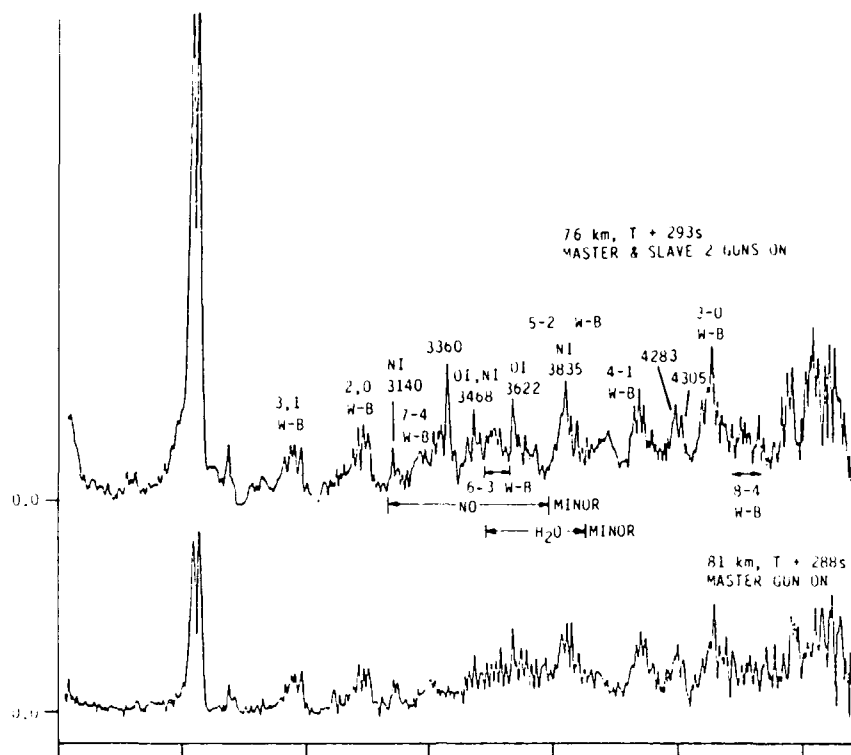
Figure 133. IR interferometer data.

Upon examination of these spectra, we have determined that the interferometer tracing shown in Figure 133, EXCEDE: Spectral Final Report<sup>147</sup> is from a much higher altitude (87 km) rather than 74 km as stated in the text. This figure creates the impression that the 2.9  $\mu\text{m}$  feature in the CVF data is due to  $\text{H}_2\text{O}$ , which as will be discussed later, is not the case.

Since the interferometer data is much higher resolution than the CVF, spectroscopic identification should be much less ambiguous. Overlays of  $\text{H}_2\text{O}$  vibrational emission,  $\text{N}_2(\text{W}^3\Delta \rightarrow \text{B}^3\Pi)$ ,  $(\text{w}^1\Delta \rightarrow \text{a}^1\Pi)$ , and  $(\text{a}^1\Pi \rightarrow \text{a}'^1\Sigma)$  were created to determine the contribution of these emission systems to the observed interferometer data. Figure 134 shows an overlay of an interferometer scan with Wu-Benesch spectra. The vibrational distributions are from LABCEDE studies for  $v'=3-10$  (as shown in Figure 132) with the  $v'=2/v'=3$  ratio set in the distribution determined from the CVF data and the Cartwright distribution. This comparison confirms the presence of Wu-Benesch emission in the interferometer data but the vibrational distribution cannot be determined. The (5,2) band is clearly observed at  $3800\text{ cm}^{-1}$ . The (6,3) and (7,4) bands at  $3550$  and  $3250\text{ cm}^{-1}$ , respectively, are difficult to distinguish from the other features present in the region. The two sharp features at  $4300\text{ cm}^{-1}$  do not have the proper shape to be the (9,5) W-B transition. Thus, as with the CVF, we have no firm evidence from the interferometer data for W-B emissions from  $v'>5$ . The interferometer data do not support creation of  $\text{N}_2$  W-states above  $v=5$ .

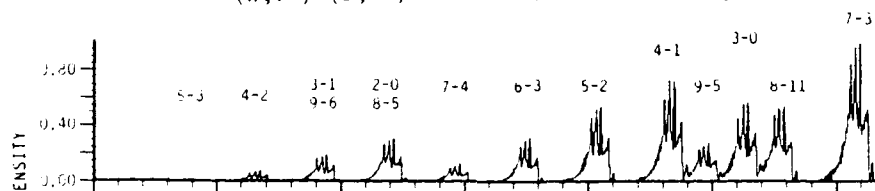
Comparison of the  $\text{N}_2(\text{w}^1\Delta \rightarrow \text{a}^1\Pi)$  and  $(\text{a}^1\Pi \rightarrow \text{a}'^1\Sigma)$  systems with the interferometer data yields no clear indication of the presence of these emissions. Figure 135 shows a comparison of a high altitude interferometer scan with  $\text{H}_2\text{O}$  emission. The similarity is quite striking and confirms the presence of water emission at these altitudes. Comparison of the water emission spectrum with lower altitude interferometer scans indicates little or no contribution of  $\text{H}_2\text{O}$  emission at the lower altitudes on the downleg part of the mission.

A surprising omission is lack of NO fundamental band emission. In the 76 km spectrum, the rise beyond  $1900\text{ cm}^{-1}$  is due to detector response fall off

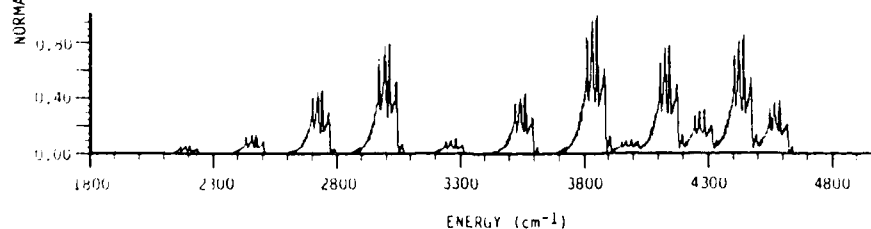


THE ASSIGNMENTS MADE FOR THE 76 km DATA SHOWN ABOVE WERE PERFORMED BY OTHER INVESTIGATORS IN A PREVIOUS STUDY

$(W, v') \rightarrow (B, v'')$  CARTWRIGHT DISTRIBUTION



$W, v' \rightarrow B, v''$  LABCEDE DISTRIBUTION



A-6247

Figure 134. Overlay of IR interferometer data with a Wu-Benesch spectrum based on LABCEDE distribution.

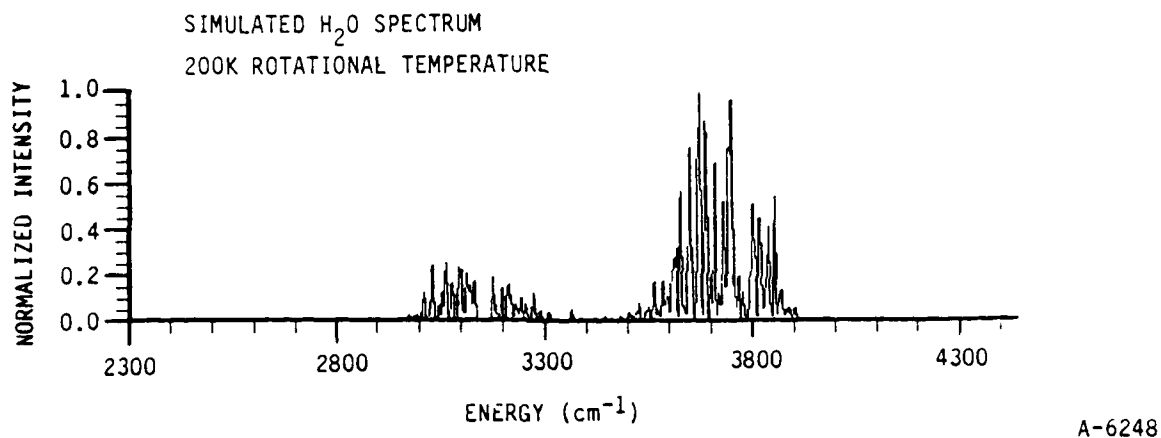
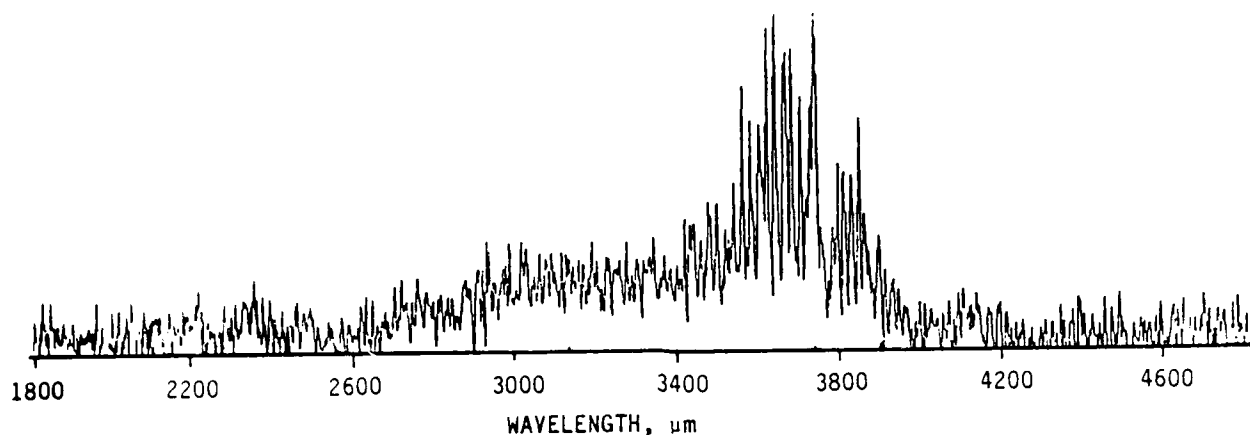


Figure 135. Comparison of an IR interferometer scan with H<sub>2</sub>O emission.

and response correction. At best a vague hint of NO(1→0) emission is present in this rise. The lack of overtone emission is also surprising. The small features between 1950 and 2010 cm<sup>-1</sup> roughly line up with NO rotational band-heads, but we do not believe this is a convincing assignment. Perhaps the interferometer's smaller field of view favors the more prompt electronic state from N<sub>2</sub> over the NO vibrational bands so that the NO emission falls below detection threshold. We have no further explanation at the present time.



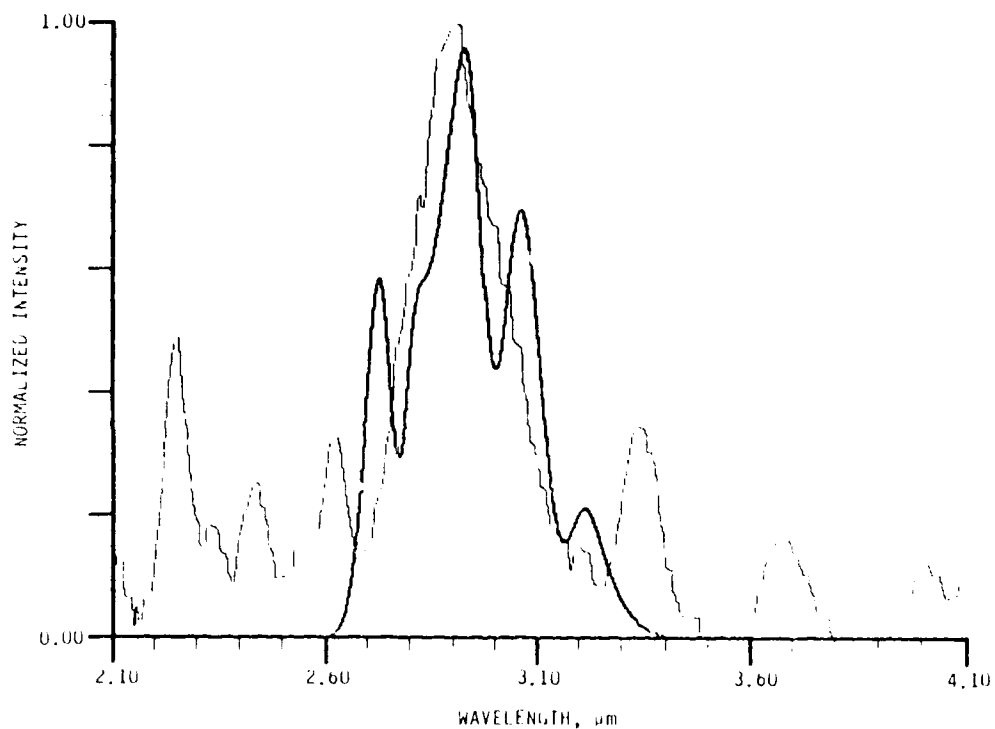
### 11.3.7 2.9 $\mu$ m Mystery Emission

It is difficult to discuss the SWIR data without addressing the most prominent feature in the 2.1 to 4.1  $\mu$ m region. At low altitudes, the CVF data exhibit an intense, broad peak centered at 2.9  $\mu$ m. At high altitudes there is a peak centered at 2.7  $\mu$ m. We have previously demonstrated that the 2.7  $\mu$ m feature at high altitudes is due to water. This emission system is inadequate to describe the observed emission at low altitudes, however. In addition, the interferometer data just discussed provides no evidence for H<sub>2</sub>O emission at low altitudes whereas it is prominent at higher altitudes. Clearly, the low altitude CVF 2.7  $\mu$ m feature is not due to water emission. We have also ruled out CO<sub>2</sub> combination bands from spectral comparisons.

Several diatomic band systems were investigated to account for this emission. The emission from the fundamental band of OH falls in this wavelength region. Figure 136 shows a fit of OH fundamental emission from  $v'=1-3$  at a rotational temperature of 200 K. Even at the EXCEDE CVF resolution element the P and R branches are evident whereas no such structure can be seen in the data. Increasing the rotational temperature does not improve the fit.

N<sub>2</sub>(B<sup>3</sup> $\Pi$ →W<sup>3</sup> $\Delta$ ) emission falls in this wavelength region as well. A fit of the B-W spectrum to the data has already been presented in Figure 122. Although several of the transitions occur in the proper wavelength region, the shape of the observed feature is not reproduced by this band system. In addition, the required column densities in the B<sup>3</sup> $\Pi$  state are far in excess of the Cartwright predictions.

This peak cannot be entirely attributable to NO overtone emission. Although the 2.7  $\mu$ m emission may be adequately fit to the NO overtone, the resulting distribution is vibrationally "colder" than the COCHISE nascent distribution observed for the fundamentals. If this feature is attributed solely to NO overtones, the peak intensity is far in excess of that predicted for the overtones from the intensities observed from the fundamentals. To test this,



A-6249

Figure 136. Corrected SWIR scan 524 with fit to OH ( $v'--13$ ) fundamental emission at a rotational temperature of 200 K.

the merged SWIR/MWIR spectra were used. These files were created by using the  $\text{CO}_2$  ( $v_3$ ) emission to normalize the two spectrometers data. Figure 137 shows the merged file for 74.6 km altitude. Superimposed on this figure is a simultaneous fit of both the overtones and fundamentals using the COCHISE nascent distribution<sup>152</sup> and Einstein coefficient ratios measured in the laboratory.<sup>162,168</sup> The fit to the fundamental re. . is adequate, as previously discussed, but the reproduction of the 2.9  $\mu\text{m}$  feature is inadequate. This figure indicates that no more than 50 percent of the observed emission intensity in this feature can be attributed to the NO overtones. In addition the peak of the NO overtones is red-shifted relative to the data, the data peaks at 2.9  $\mu\text{m}$  while the overtone emission peaks at 2.95  $\mu\text{m}$ . In order to determine the residue not attributable to the NO overtones, spectral subtraction has been performed and the result is shown in Figure 138. The result is a much narrower peak centered at 2.9  $\mu\text{m}$ . We have not been able to identify the origin of this feature.

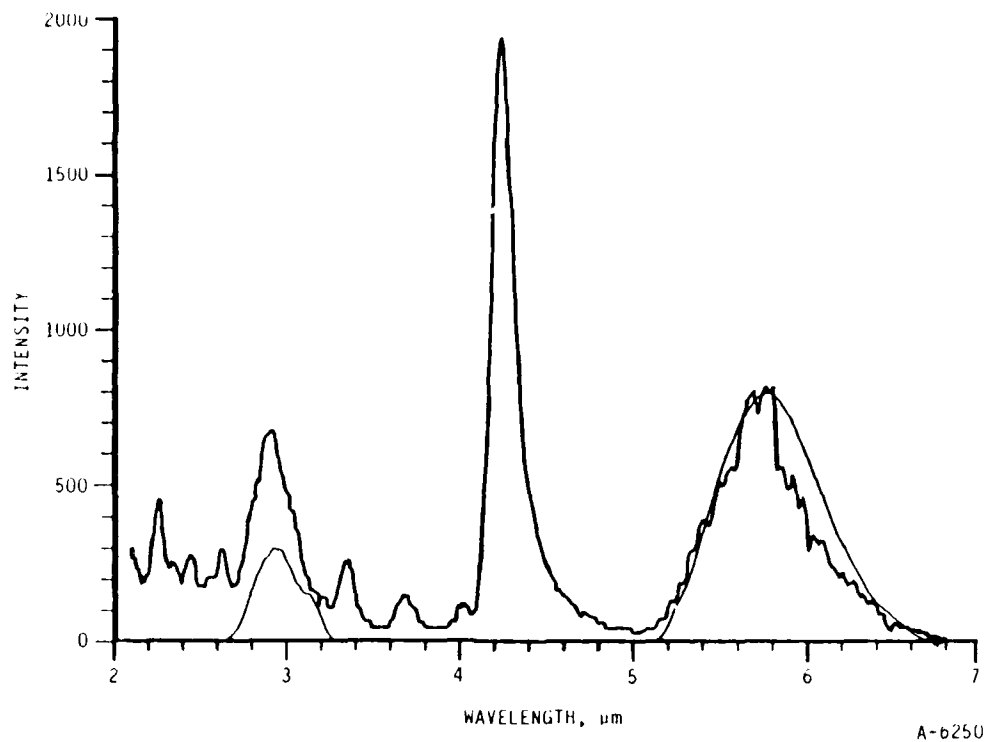


Figure 137. Data (dark line) and fit (light line) to NO fundamental and overtone emission.

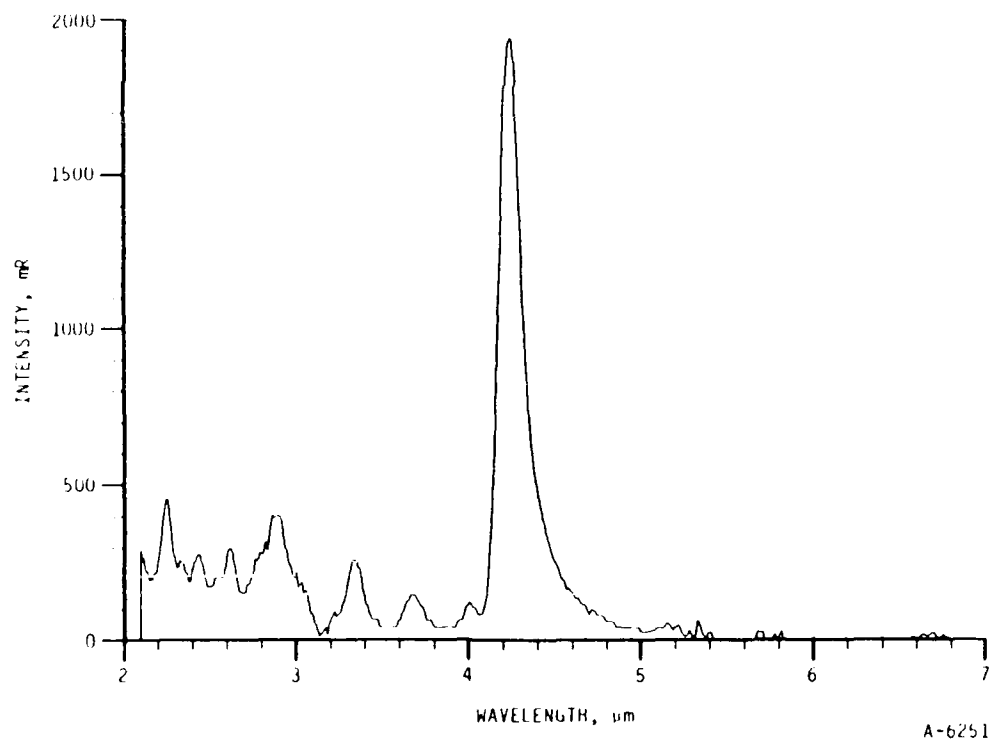


Figure 138. Data from previous figure with NO fundamental and overtone emission subtracted.

#### 11.4 CONCLUSIONS

Nitrogen Wu-Benesch ( $W^3\Delta \rightarrow B^3\Pi$ ) emission has been positively identified in the CVF data. The interferometer data indicates the possible presence of vibrational levels greater than five but further analysis will be required to quantify the distribution. Wu-Benesch emission is observed at all altitudes, even under those conditions in which the water emission intensity is strong. The vibrational distribution is more relaxed than the predictions of Cartwright and the recent LABCEDE results.

No other nitrogen electronic band system has been positively identified in the IR data, including both CVF and interferometer data. The band systems considered include  $w^1\Delta \rightarrow a^1\Pi$ ,  $a^1\Pi \rightarrow a'^1\Sigma$ ,  $B^3\Pi \rightarrow A^3\Sigma$ ,  $B'^3\Sigma \rightarrow B^3\Pi$ , and the  $N_2^+$  Meinel system,  $A^2\Pi \rightarrow X^2\Sigma$ . There is some evidence for atomic oxygen emission, particularly at 2.65, 2.76, and 3.1  $\mu\text{m}$ . Atomic nitrogen lines may be responsible for part of the intensity at 4.0  $\mu\text{m}$ .

The SWIR data exhibits a background which decays from 2.1 to 3.5  $\mu\text{m}$ . The spectral distribution of the background is similar to the  $O + NO$  air afterglow emission but is far too intense to be attributed to ambient air afterglow. Nevertheless, the data have been corrected for background using the  $O + NO$  spectral distribution.

The  $NO$  fundamental emission observed matches the COCHISE nascent distribution and is clearly due to  $N(^2D) + O_2$ . No evidence for quenching was observed over the 75 to 91 km region since the time scales for quenching for  $O_2$ ,  $O$ , and  $H_2O$  are long at these altitudes compared to residence time in the field of view ( $\sim 10$  ms).

The 2.7  $\mu\text{m}$  high altitude feature is clearly  $H_2O$ ,  $v_1$  and  $v_2$  vibronic emission. This feature disappears at lower altitudes and is replaced by a broad 2.7  $\mu\text{m}$  feature which is not due to water. This feature is only observed in the CVF data, it is not reproduced in the interferometer spectra. The CVF feature can

be only partially attributed to the NO overtones. An anomalous fundamental/overtone ratio and a more relaxed distribution must be invoked to force NO to be the sole source of that emission. We believe that more than 50 percent of the emission intensity at 2.9  $\mu\text{m}$  is attributable to the NO overtones.

In the visible and ultraviolet spectral regions, nitrogen electronic state transitions dominate the spectrum. Preliminary analysis show that the vibrational distributions within these electronic states and relative production levels agree with model and laboratory observations to first order. The differences which exist can be resolved in future, more careful analyses.

The major conclusion of this study is that flight data from the artificially electron dosed upper atmosphere can be analyzed to identify atmospheric radiators and their vibrational and electronic state distributions. Effects of nearfield contamination can be removed from the data permitting atmospheric band emission efficiencies and distributions and processes to be quantified.

## 12. RADIOMETER EXPERIMENT TO STUDY EMISSIONS RESULTING FROM COLLISIONS WITH HIGH VELOCITY ATOMS

A variety of atmospheric processes can produce high velocity atoms. Photo-dissociation of molecular  $O_2$  in the thermosphere by solar Lyman  $\alpha$  emission (1216 nm) has been suggested as a potential source for fast moving O since a photon at Lyman  $\alpha$  wavelengths has 5 eV of energy in excess of the  $O_2$  binding energy. Dissociative recombination of  $N_2^+$  should produce N-atoms with several eV of translational energy. Collisions of these fast moving atoms with atmospheric species can potentially give rise to excitation and emission processes not previously included in atmospheric models. In this section we describe the design of a radiometer package to observe emission from these high velocity collisional processes. This radiometer package could find application in both laboratory (LABCEDE) or as part of a field experiment.

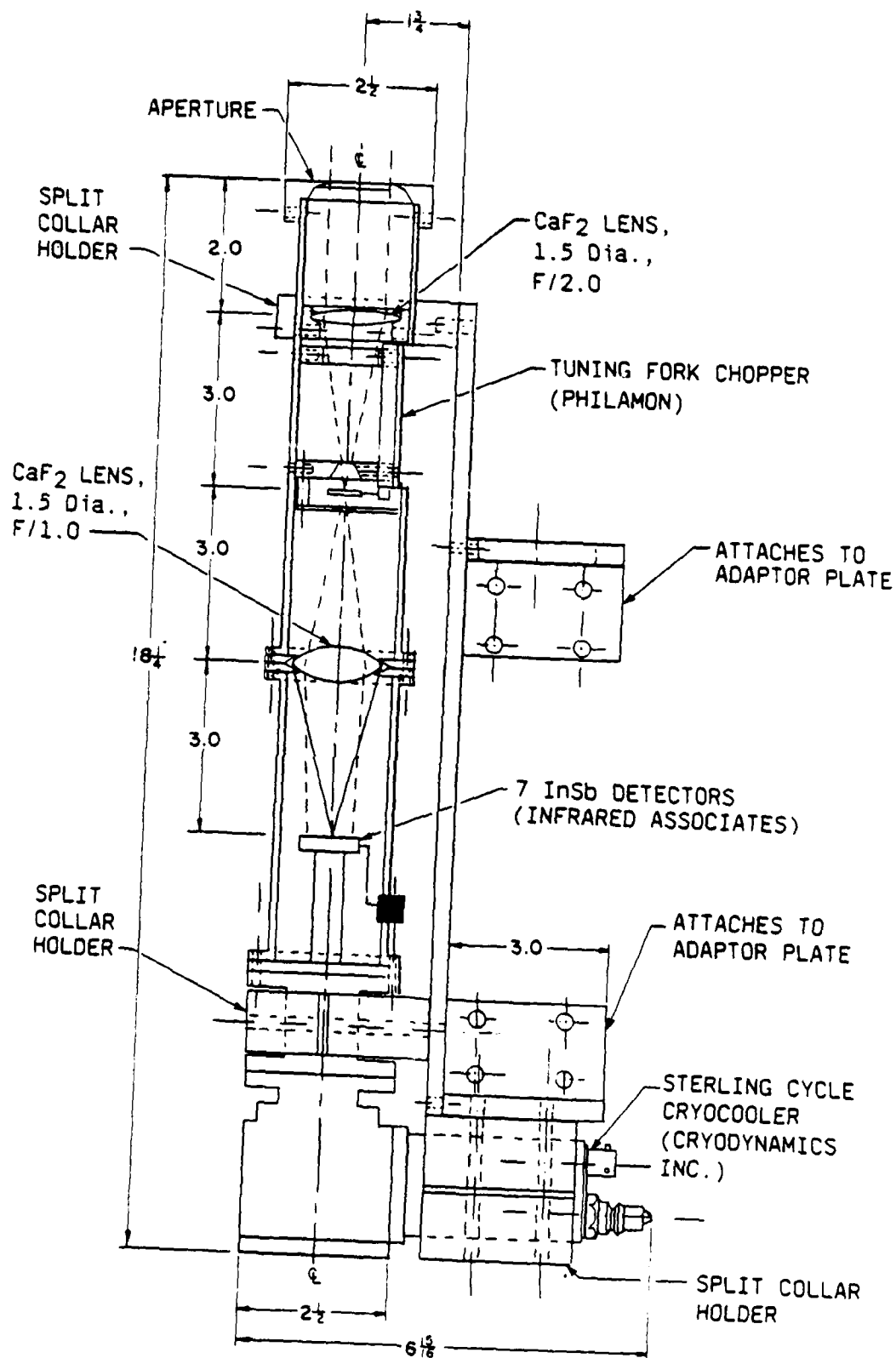
Our goal is to observe emission from these collisional processes across a wide spectral region to monitor translation to vibration excitation and even translation to electronic state conversion. LABCEDE operates at sufficiently low pressure conditions that any high velocity atoms produced will not be slowed completely in the experiment field of view. A spacecraft-borne experiment would also provide an excellent test ground for these processes due to the orbital translational velocity of 8 km/s. Thus in the frame of reference of the spacecraft, atmospheric thermal velocity oxygen atoms possess a directed translational energy of over 5 eV. Molecular nitrogen possesses 9.3 eV. Moreover, the variable environment surrounding spacecraft (particularly the Shuttle) permits the observation of  $O + N_2$  collisions as well as collisions with outgassed or generated species such as  $CO_2$ ,  $H_2O$ , and  $NO$ . Collisions of fast oxygen atoms with these gases will provide insight into the interaction of fast atoms (transfer energy or reaction) with trace gases present in the lower thermosphere.

Our suggested approach is to use rugged bandpass filtered detectors with good time resolution. This will permit activity-induced radiances to be removed

from the collisional interaction data. Also, attitude dependence will permit gas phase emission to be separated from collision-induced surface generated radiances (glow). The detectors in the radiometer package should span the 0.2 to 5.2  $\mu\text{m}$  range and possess a variety of bandpasses to isolate emitters. High sensitivity in the infrared (SWIR/MWIR) will be achieved by cooling InSb detectors using Sterling cycle cryocoolers. Passively cooled PbS and PbSe detectors will also be used to provide dynamic range and redundancy. The detectors will view the interaction region through a simple two-lens optical system to achieve good off-axis rejection and a well defined field of view. The collisional emission would be chopped by a reflective tuning fork chopper located at the focal point between the lens pair. The optics would be configured to match component thermal emissions in the optical train. This will minimize the absolute and synchronous signals arising from the radiometer itself. A schematic of the cooler, detector array, and optical network is given in Figure 139. Seven bandpass filtered detectors could reside at the focal plane of this system as shown in Figure 140.

A total of 71 detectors are required to provide full spectral coverage and sufficient spectral resolution to isolate radiators and excitation processes. The optimum detectors and bandpasses are listed in Table 25. Note that several bandpasses are shared by different detectors. This will permit real time relative calibrations to be made. In order to isolate rapidly varying emissions, eight broadband spectral channels covering the entire 0.2 to 5  $\mu\text{m}$  region will be sampled at 8.3 samples/s. The remainder of the channels could be completed and recorded more slowly, every 1.7s. The bandpasses were chosen to distinguish emission from particular molecules in this environment.

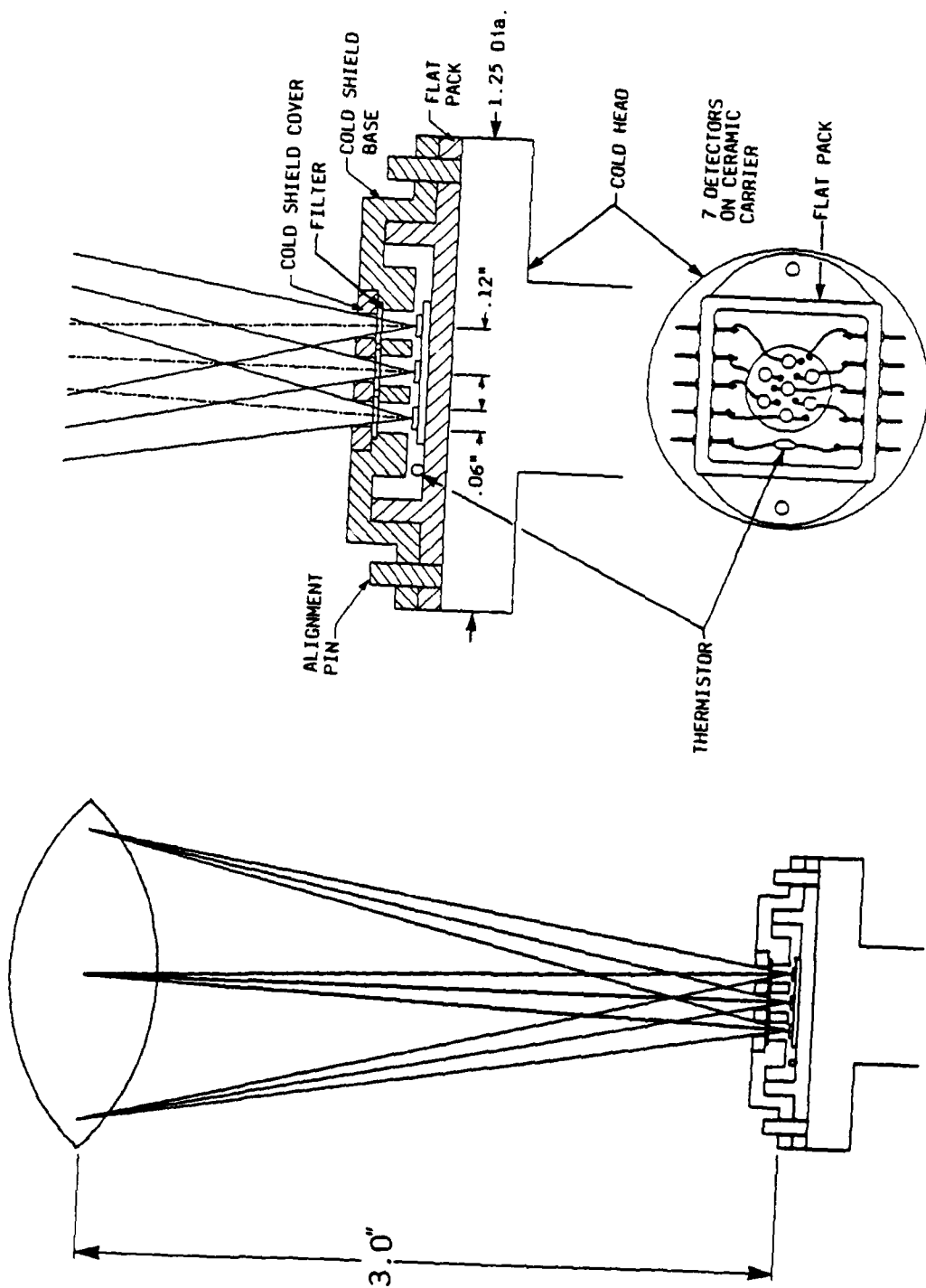
Using this radiometer configuration noise levels have been calculated based on thermal design analysis and optical geometry including component and wall emissions. The synchronous noise levels for the actively cooled radiometers are shown for several bandpasses in Figure 141. Also shown in that figure is an estimate of the collisional excitation of  $\text{H}_2\text{O}$  ( $v_1, v_3$ ) by oxygen atoms. Because cross sections for collisional excitation are unknown at these



A-8024

Figure 139. InSb detector module assembly.





A-8023

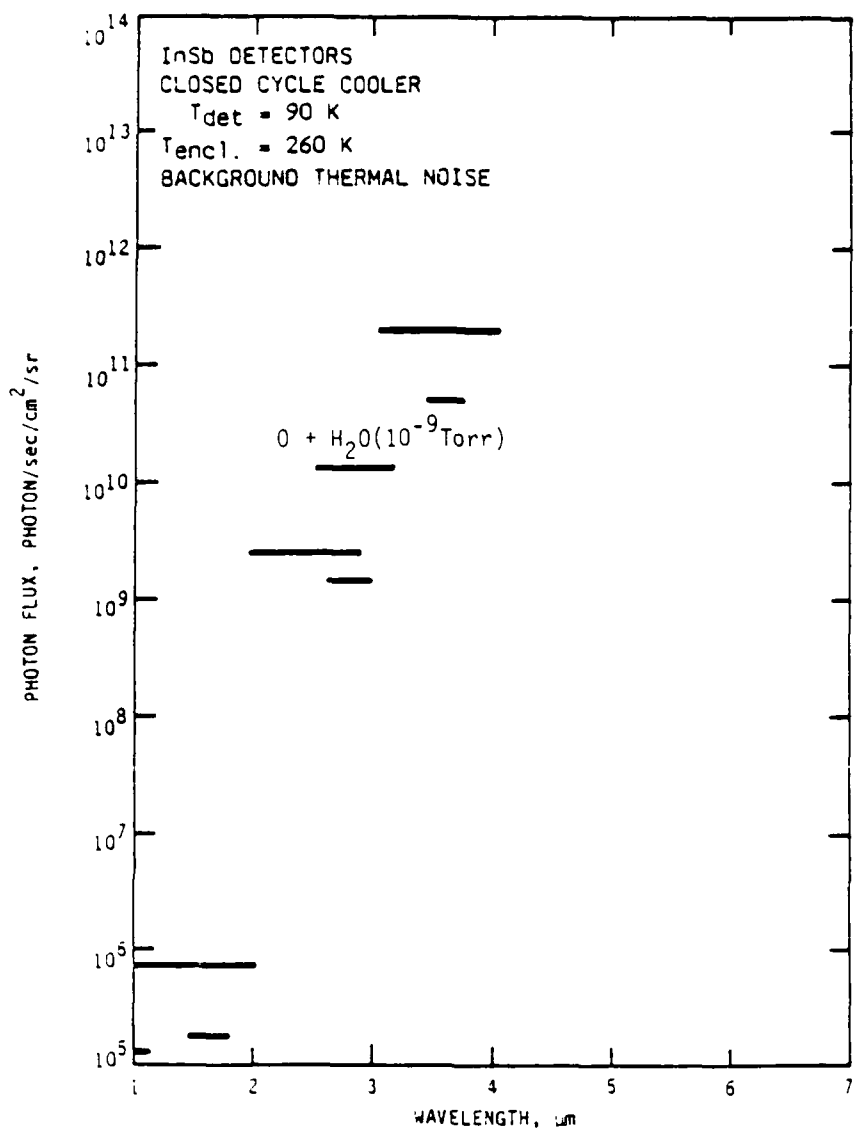
Figure 140. IR detector layout.

TABLE 25. Radiometer detector bandpasses ( $\mu\text{m}$ ).

Silicon	Lead Sulfide	Indium Antimonide
0.2-0.5; $\Delta\lambda = 0.5 \rightarrow 6$	1.5 -1.8 OH <sup>+</sup>	1.5 -1.8
0.5-1.1; $\Delta\lambda = 0.025 \rightarrow 24$	2.0 -3.0 Whitteborn	2.0 -3.0 Fast
0.2-0.4 Fast	2.73-2.79 NO	3.0 -4.0 Fast
0.4-0.6 Fast	2.80-2.90 OH	4.0 -L.P Fast
0.6-0.8 Fast	2.3 -2.5 CO	2.3 -2.5 CO
0.8-1.0 Fast	2.5 -3.1 H <sub>2</sub> O	2.73-2.79 NO
<u>1.0-1.1</u>	<u>2.0 -2.3 Background</u>	2.80-2.90 OH
35 Si detectors	7 PbS detectors	3.5 -3.7 NO <sub>2</sub>
		4.20-4.32 CO <sub>2</sub>
		4.35-4.6 NO <sup>+</sup>
Germanium	Lead Selenide	4.6 -5.0 CO
1.0-1.1	2.8 -2.9 OH	5.0 -L.P NO
1.1-1.3 x 2	3.0 -4.0	3.7 -4.1 background
1.3-1.5 x 2	3.5 -3.7	<u>3.1 -3.5 NO<sub>2</sub></u>
1.5-1.8	4.35-4.6 NO <sup>+</sup>	14 InSb detectors
1.0-2.0	4.20-4.32 CO <sub>2</sub>	
<u>1.0-2.0 Fast</u>	4.60-5.00 CO	
8 Ge detectors	<u>4.0 -5.0</u>	TOTALS:
	7 PbSe detectors	71 detectors
		(8 fast)

energies and because chemiluminescent emission from reactive channels which can occur only at suprathreshold energies have not been considered, the plotted emission levels are extremely uncertain.

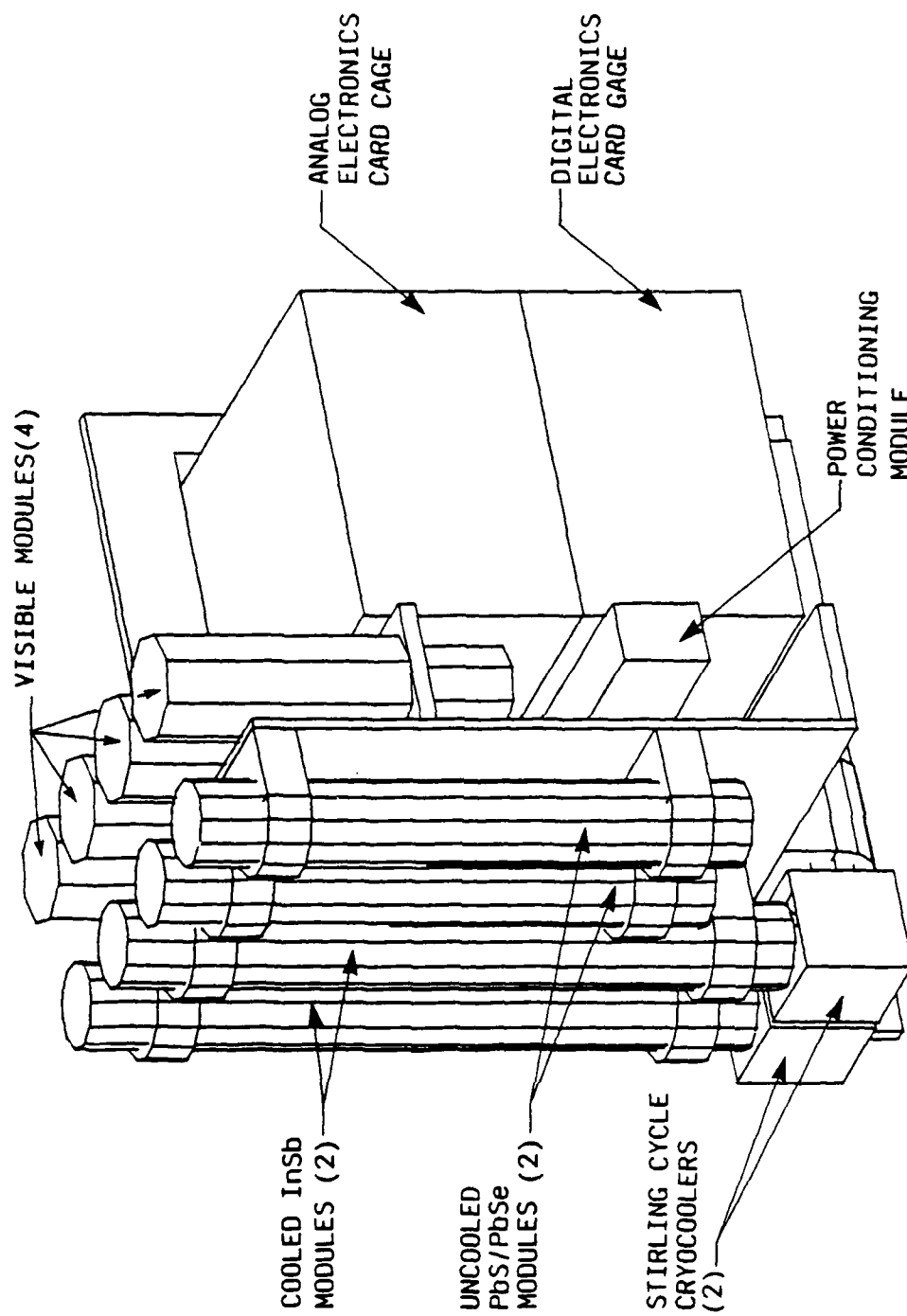
The physical package of the radiometer system design is shown in Figure 142. Figure 143 outlines the relation of the components of overall system as configured for a Shuttle payload. Figure 144 provides a schematic of the



A-8021

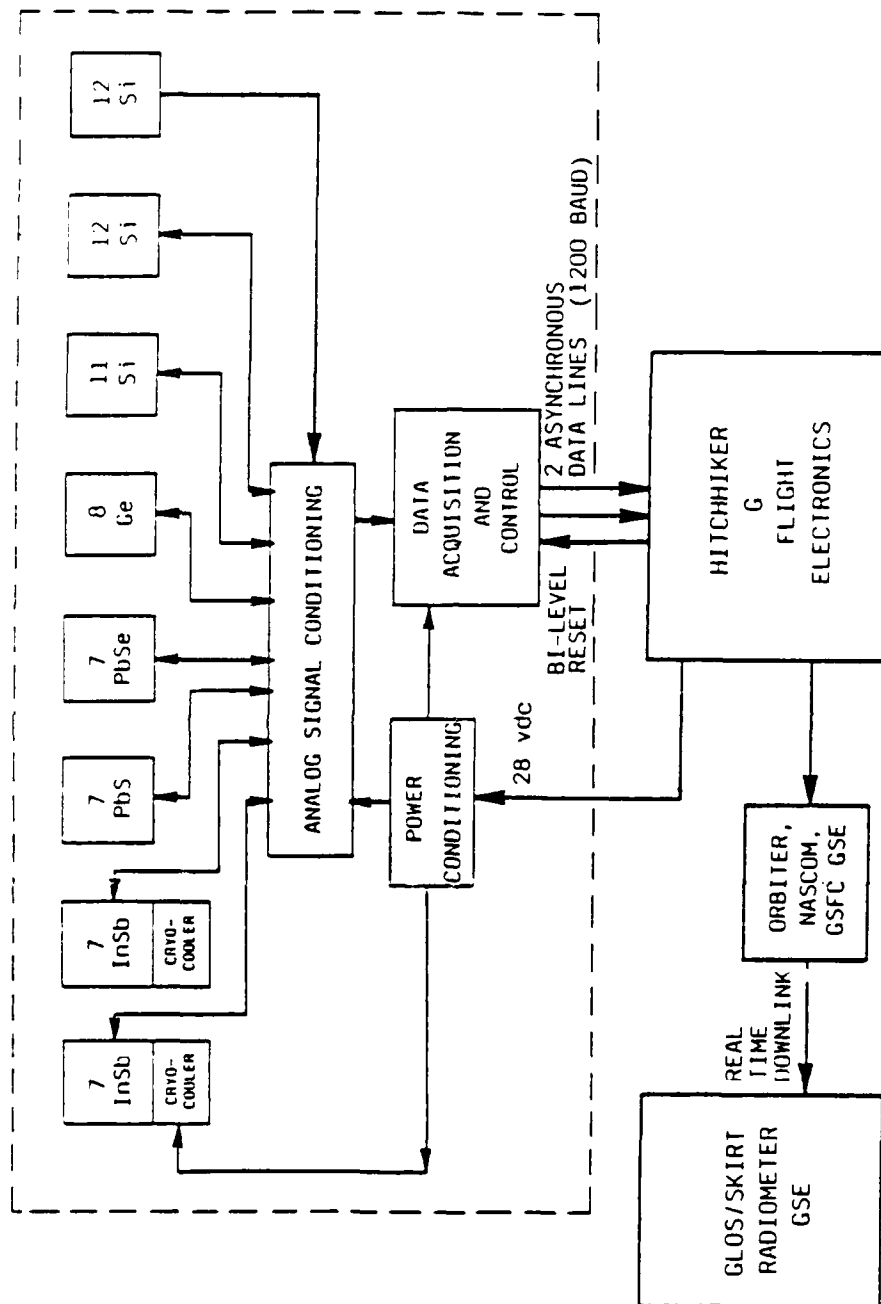
Figure 141. Background thermal noise in-band with chopping.

power and control network for the radiometers. Each radiometer channel will have its own amplification and signal processing circuits so as to minimize the effects of single component failure. A diagram for a InSb signal channel is given in Figure 145. The flowchart for the software to be developed to drive radiometer sequencing is shown in Figure 146. Finally a list of the major components selected for inclusion in the radiometer package is given in Table 26.



A-8022

Figure 142. Radiometer package - cover removed.



A-8020

Figure 143. Radiometer system schematic.

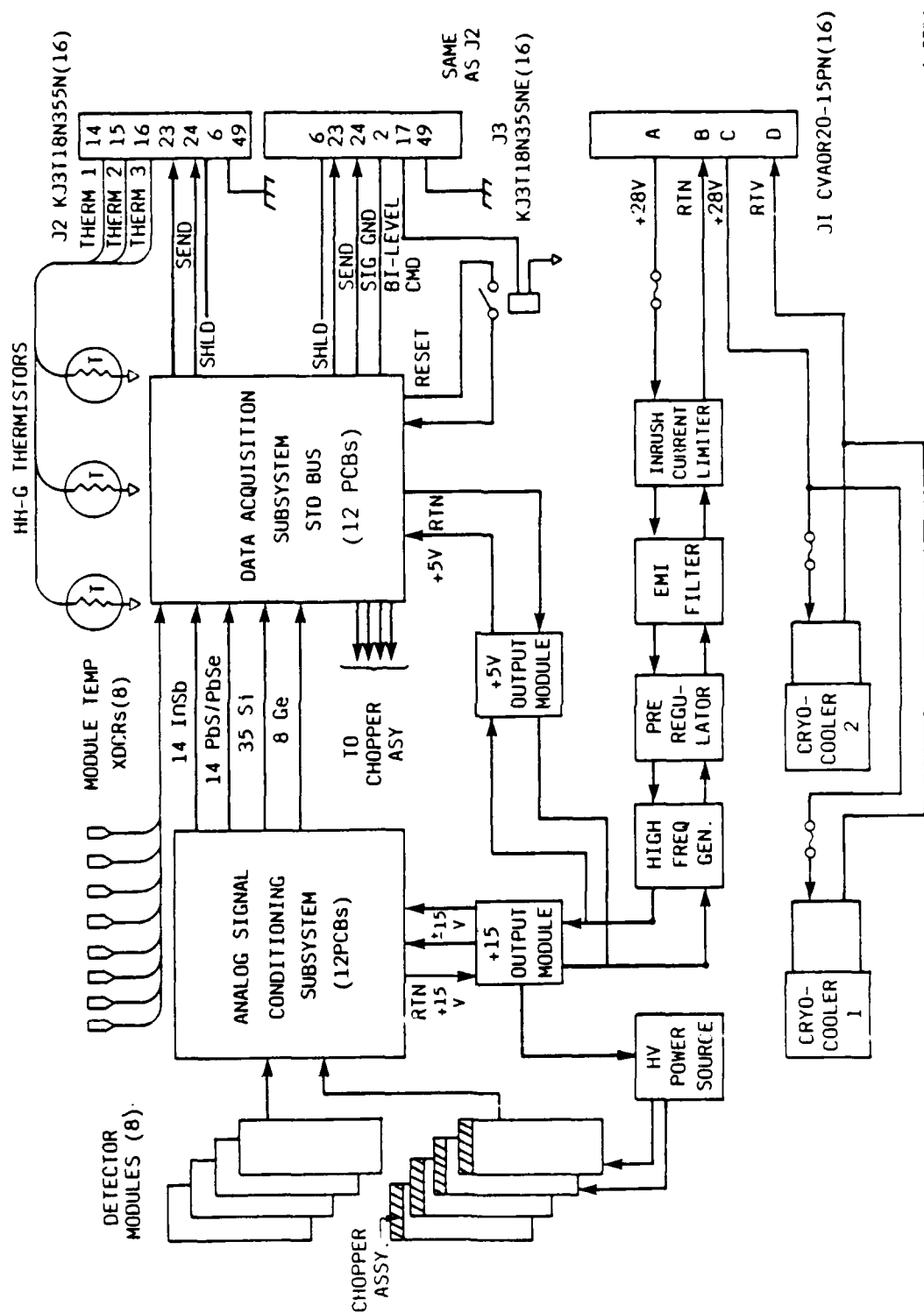
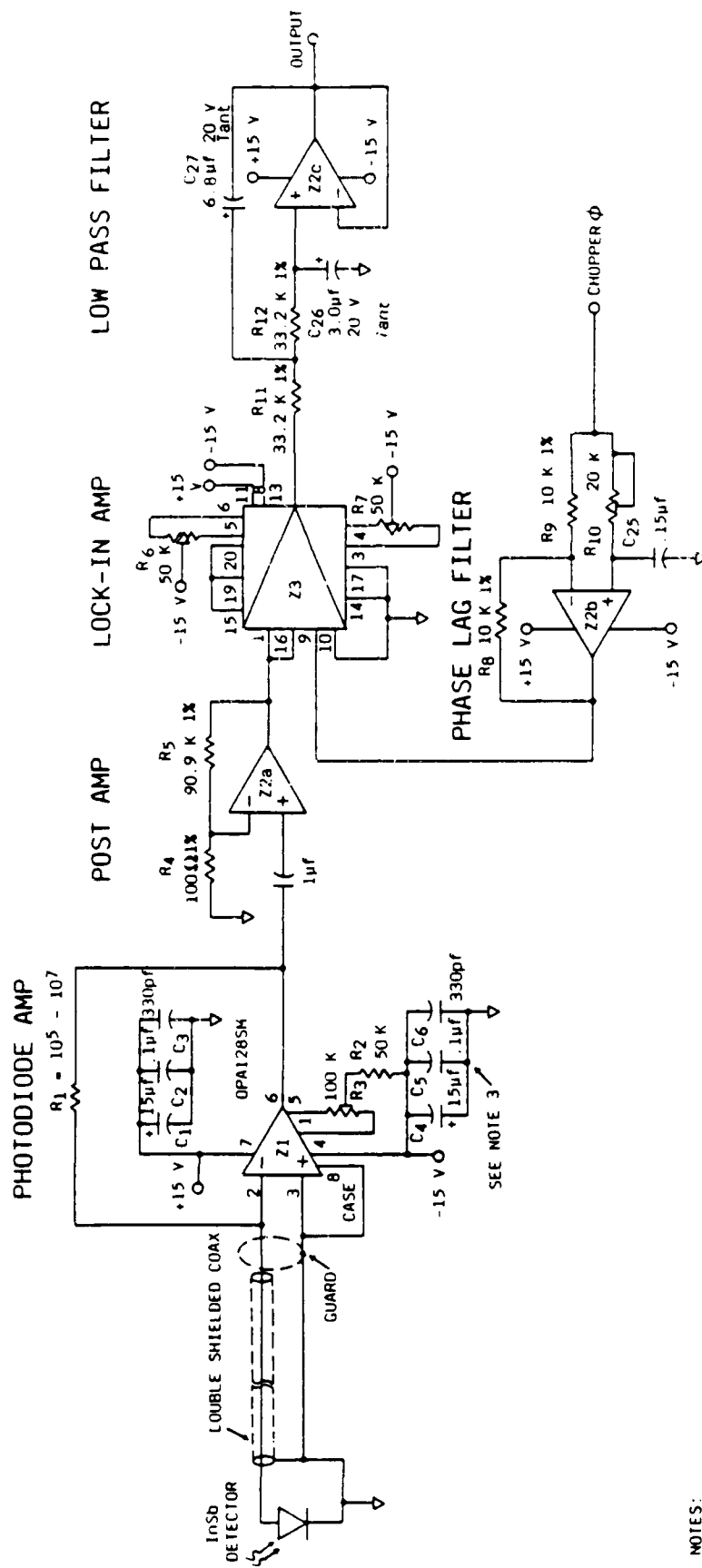


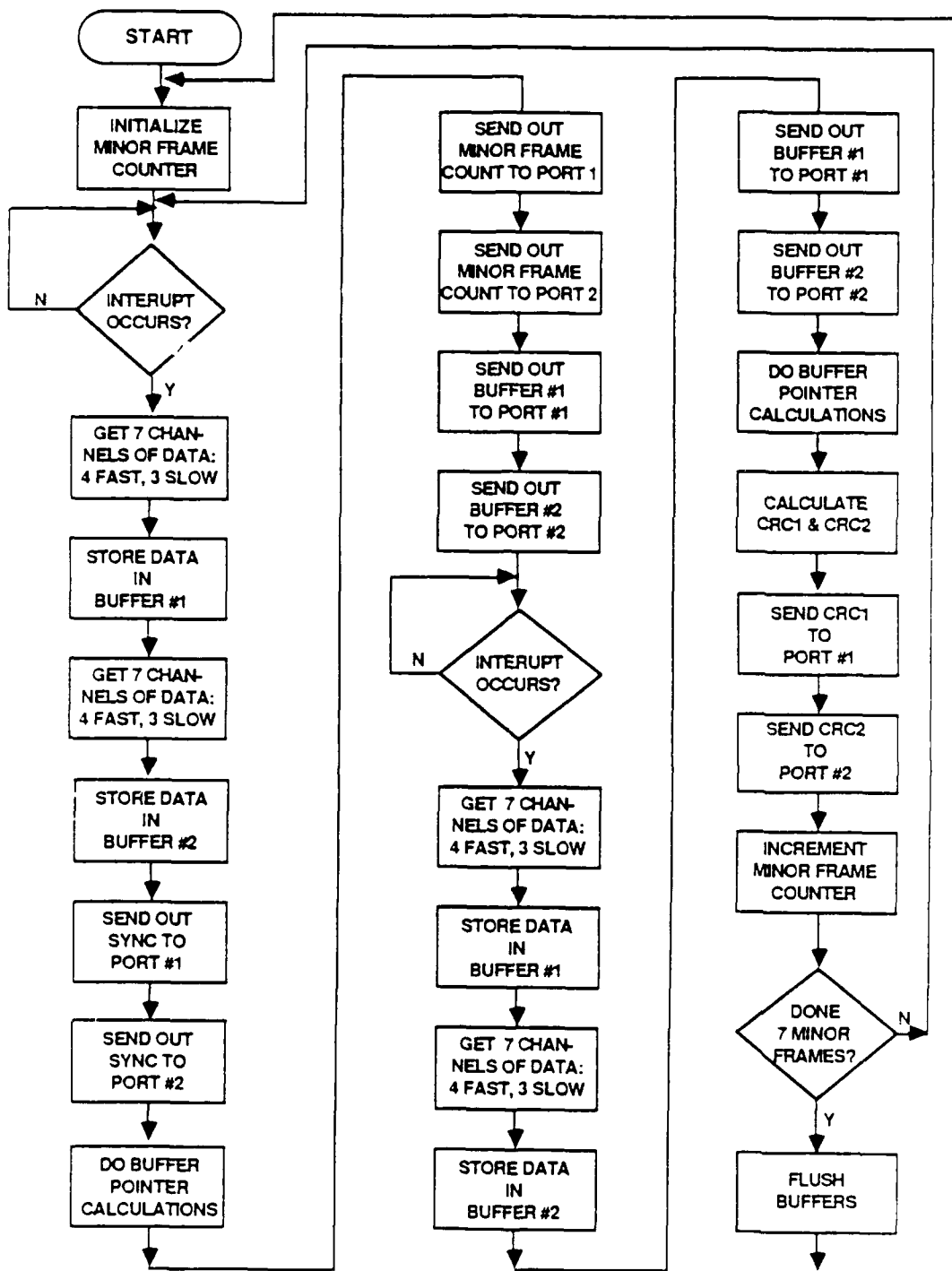
Figure 144. Power and control block diagram.

A-7736



A-8019

Figure 145. Schematic InSb amplifier and signal processor.



Note: Interrupt occurs every 120 ms.

A-8018

Figure 146. Software structure.



The radiometers should be turned on as early as possible during a Shuttle mission. At early times the outgassing levels are the highest and the largest signal levels are expected. Data late in the mission will be essential for study of collisions of  $O + N_2$  and baseline isolation. Continuous operation is preferred so that sufficient data can be gathered to isolate the many potential competing processes which could be occurring simultaneously. This highlights the need for auxiliary laboratory studies. The optimum flight experiment would be at as low an altitude as possible to maximize atom concentration.

TABLE 26. Components list for radiometers.

Optical Part List

Device	Model Number	Qualification
Stirling cycle cooler	Cryodynamics M15-R	MIL and NASA spec compliance-flown on STS61C
Tuning fork chopper	Philamon 30A5	Rocket and Shuttle
InSb detectors PbS/PbSe detectors Si/Ge detectors	IR Associates Custom IR Associates Custom UDT PIN-3DP	GOES, INSAT, TYCOS, etc. GOES, INSAT, TYCOS, etc. Industrial grade
CaF <sub>2</sub> lenses	Infrared Optics 38115-CF 38215-CF	
Silicon lenses	ESCO Products A120040	UV Grade A fuses silicon
Filters (55 required)	Microcoatings Corion OCLI Ealing Spectragan	39 standard "stock" filters plus 16 custom-made filters

TABLE 26. Concluded.

Principal Components

Device	Model Number	Qualification
Processor board RS-422 serial I/O board Analog data Card cage	Prolog 7890 Model A Prolog 7313  Analog Devices RTI-1280 Prolog BX-12R	Severe industrial Severe industrial  Severe industrial Severe industrial
Low voltage power	Powercube cold-line circuit blocks	
Inrush current limiter	XIA609	Mil/Space
EMI filter	XF614	Mil/Space
Pre-regulator	18SP50-S1/S2	Mil/Space
High frequency generator	18G75W40	Mil/Space
+5V output module	5TR30	Mil/Space
±15V output module	15TRC10	Mil/Space
High voltage power (100V)	Venus Scientific C2T	MIL-STD-810
<u>Integrated Circuits</u>		
Low noise op-amp	Burr-Brown OPA128SM	MIL-STD-883
Precision quad op amp	Precision monolithics OP-400AY	MIL-STD-883
Lock-in amplifier	Analog Devices AD630BD	MIL-STD-883
Instrumentation amp	Analog Devices AD624C	MIL-STD-883

### 13. SOLAR SIMULATOR INVESTIGATIONS

#### 13.1 EFFECTS UPON ULTRAVIOLET AND VISIBLE ELECTRON INDUCED FLUORESCENCE

The LABCEDE facility was utilized to investigate the effects of solar UV and visible light upon fluorescence from electron impact excited laboratory air. Air fluorescence was detected between 300 and 800 nm. Solar UV-visible light was supplied by a commercially available (ORIEL) solar simulator. Qualitative and quantitative comparisons of fluorescence spectra with and without solar UV visible irradiation have been performed. This experimental effort was undertaken to determine if solar UV visible light produces any significant effects in the fluorescence signatures observed in the disturbed upper atmosphere.

##### 13.1.1 Experimental

The fluorescence from the electron excited room temperature air was viewed through the BaF<sub>2</sub> window located at the upstream end of the LABCEDE tank. The detection system optical axis was perpendicular to the electron beam. A 0.3m McPherson Model 218 monochromator equipped with a 1200 line/mm grating blazed at 500 nm dispersed the radiation from 300 to 800 nm to a HTV R955 photomultiplier. A Corning 3 74 order sorting filter was used in scans at wavelengths greater than 450 nm. Synchronous detection was performed by pulsing the electron beam with a Wavetek Model 132 square wave pulse generator. The AC component of the photomultiplier signal was first processed with a P.A.R. Model 113 current preamplifier and a P.A.R. Model 124 lock-in amplifier. The in-phase signal was displayed and recorded on a chart recorder. A digitized spectrum was simultaneously recorded on a Compaq personal computer system.

The original configuration of the Oriel Solar Simulator Model 8551-7, 1000 watt lamp, was not immediately adaptable to the LABCEDE experiment. The simulator was designed to produce the desired irradiance at a maximum working distance, lens to target plane, of only a few inches. Beyond this distance

the photon beam diverged rapidly from a beam waist of a few inches in diameter to approximately two feet in diameter at 1.5m (the diameter of the vacuum chamber). Furthermore, the photon beam uniformity worsened, showing bright spots due to the focusing of each individual cylindrical lens within the fly's eye collimation lens pair. This element was a double array of cylindrical lenses, which could be adjusted to slightly modify beam focus and quality. The solar simulator was modified by PSI and AFGL personnel so as to project a horizontal photon beam and bench tested to produce a collimated uniform beam. Initial testing involved setting up a display screen to determine visually the photon beam shape, uniformity and collimation. In stage two of bench testing the display screen was replaced with a Scientech surface absorbing laser power meter for more quantitative measure of beam properties. A variety of lens combinations were also tested.

From this exhaustive bench testing it was determined that the solar simulator provided the most collimated, highest power photon beam by removing the internal fly's eye lenses, and moving the lamp off center in order to image the bright arc region of the lamp onto the output coupling lens of the simulator. A 3 in. diameter quartz lens with a 6-1/2 in. focal length was then utilized to further collimate the beam. This arrangement could propagate 90 percent of the lamp exit plane output power to a 6 ft distance. Using the air mass zero filter, which simulates the solar UV-visible distribution outside earth's atmosphere, a power density of  $95 \text{ mW/cm}^2$  could be obtained in the center 1.5 in. diameter beam, with a total beam diameter of 3 in. A one sun equivalent air mass zero power density is approximately  $130 \text{ mW/cm}^2$ . Figures 147a and b show the unfiltered and AM0 spectral distribution from the solar simulator. The photon flux assuming an average wavelength of  $5000\text{\AA}$  is approximately  $2.5 \times 10^{17} \text{ photons/cm}^2\text{s}$  in the central 1.5 in. diameter beam. For comparison, the electron flux ranges from  $2.5 \times 10^{16}$  to  $1 \times 10^{18} \text{ electrons/cm}^2\text{s}$ . The interface to LABCEDE involved the design and fabrication of a stand for the solar simulator, and an adjustable lens mount. The solar simulator photon beam was introduced into the LABCEDE tank through a quartz window.

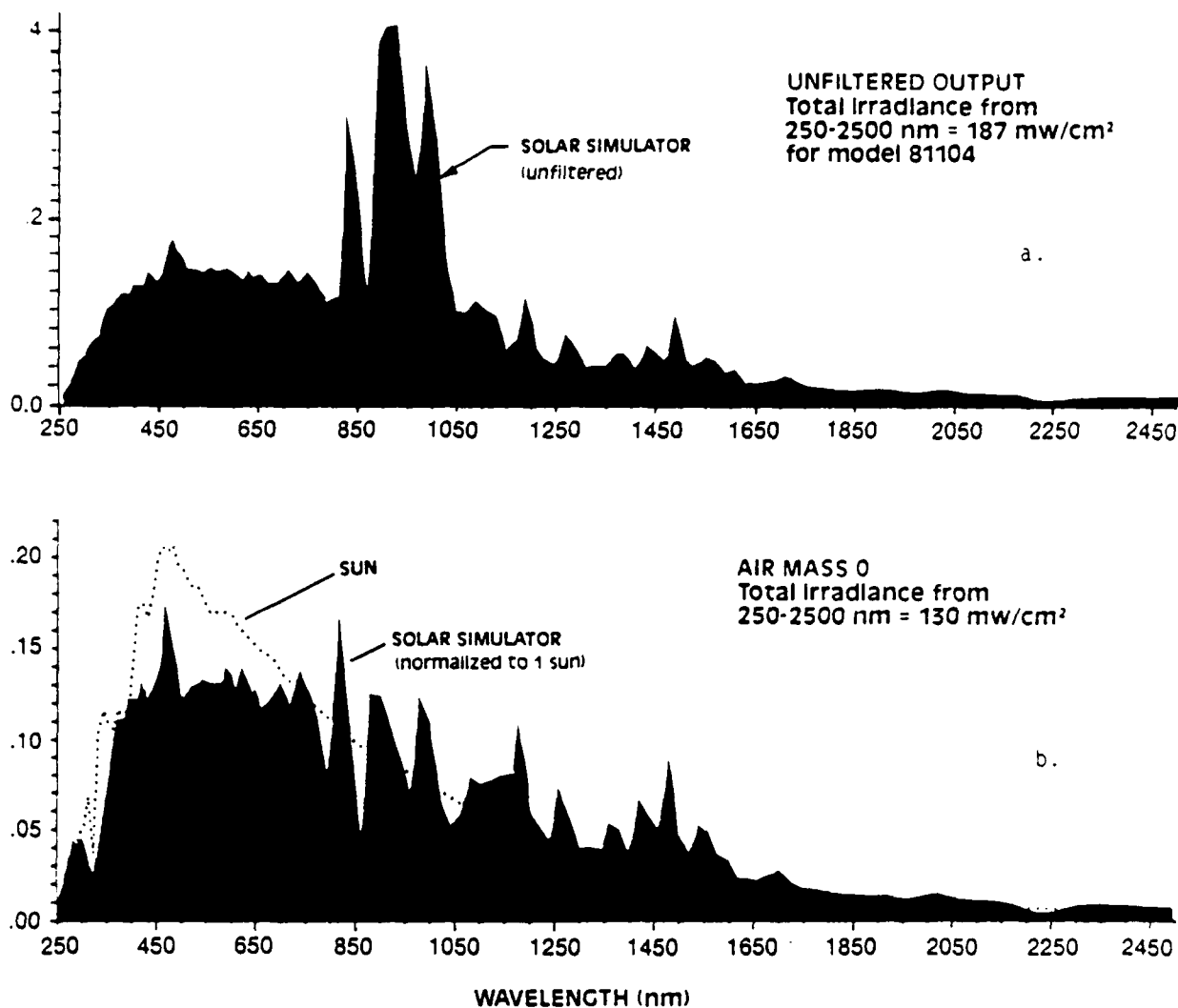


Figure 147. These curves show for unfiltered and AMO spectral distributions from the solar simulator.

The photon beam crossed the electron beam at an angle of about 20 deg near the chamber center, and emerged out of the vacuum chamber through a quartz window parallel and opposite the first window. Two types of experiments were performed using the solar simulator. One series of experiments were performed by collecting the full spectrum with (then without) the photon beam. A second series of solar simulator experiments were performed with the electron beam on continuously (20 mA) and the photon beam being chopped at 40 Hz. Synchronizing the lock-in amplifier with the chopping frequency of the photon beam provided more than an order of magnitude greater sensitivity. Laboratory air was introduced by opening the inlet line to a mass flow meter calibrated for N<sub>2</sub>, to the

room. Air mass flows of 176 and 387 sccm, N<sub>2</sub> equivalent, provided an operating pressure of 1.2 and 20.0 mtorr, respectively. The electron energy for every experiment was 4500 eV; the current ranged from 5 to 20 mA and was either continuous or square wave pulsed at 200 Hz.

### 13.1.2 Observations for Air Between 300 and 400 nm

In this spectral region the N<sub>2</sub><sup>+</sup>(B<sup>2</sup>Σ<sub>u</sub><sup>+</sup>-X<sup>2</sup>Σ<sub>g</sub><sup>+</sup>) Δv=1,0 and N<sub>2</sub>(C<sup>3</sup>Π<sub>u</sub>-B<sup>3</sup>Π<sub>g</sub>) Δv= 3,-2,-1,0,1 bands are observed. The spectrum obtained by pulsing the electron beam without either BPD or solar simulator operative, at a pressure of 1.2 mtorr air and a resolution of 15.6Å was shown previously. Every spectrum in this region obtained by pulsing the electron beam showed the same spectral features; the effects of igniting BPD and irradiating with solar UV-visible radiation upon the vibrational level distributions at 1.2 mtorr produced no detectable changes. The populations determined from the theoretical fit are presented in Figure 148. N<sub>2</sub>(C<sup>3</sup>Π<sub>u</sub>) v'=4 and N<sub>2</sub><sup>+</sup>(B<sup>2</sup>Σ<sub>u</sub><sup>+</sup>) v'=4 levels are less accurately determined due to their weak signals in the spectrum. The vibrational level distributions in the spectra with and without photon irradiation are identical within experimental error.

Two spectra were obtained by chopping the photon beam at 40 Hz, one spectrum at 1.2 mtorr with BPD operative and one spectrum at 20.0 mtorr without BPD. Neither experiment showed a meaningful spectral feature above the noise level. Since the photon and electron fluxes are approximately equal, a comparison of the signal intensities between chopping the photon beam and pulsing the electron beam provides an approximate upper bound on the cross section for photon excitation relative to electron excitation. In this spectral region we calculate

$$\frac{\sigma_{\text{photons}}}{\sigma_{\text{electrons}}} < 2 \times 10^{-4} .$$

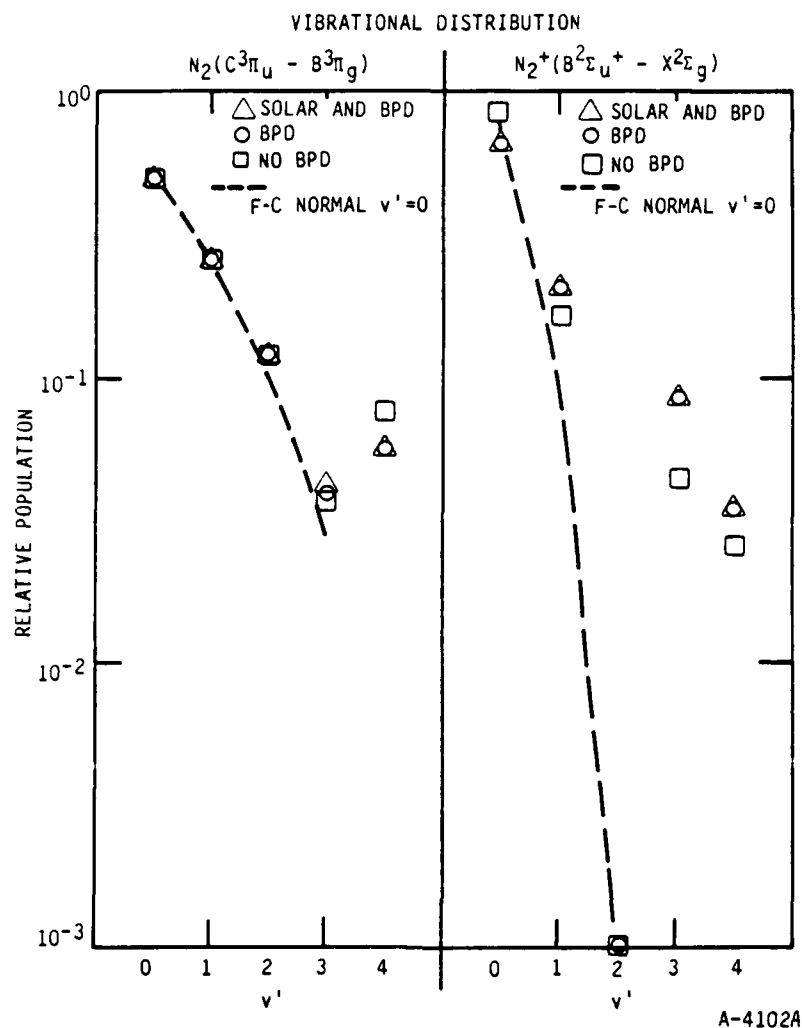


Figure 148. The upper state vibrational level distribution is shown with and without the addition of solar UV-visible radiation. The data was obtained in 1.2 mtorr air in the 300 to 400 nm region with a resolution of 1.56 nm. The electron beam was pulsed for these observations.

### 13.1.3 Observations for Air Between 440 and 800 nm

Six spectra were collected in this region. Four spectra were taken at 1.2 mtorr pressure and two spectra at 20.0 mtorr. The low pressure spectra varied by having no BPD, BPD, BPD and solar simulator irradiation while pulsing the electron beam and a spectrum with both BPD and solar simulator present while chopping the photon beam. At 20.0 mtorr without BPD one spectrum was

obtained by pulsing the electron beam and one was obtained by chopping the photon beam.

The band system distributions obtained with and without solar-UV, visible radiation at 1.2 mtorr with BPD and electron beam pulsing is presented in Figure 149. The corresponding vibrational level distributions are presented in Figures 150 and 151. In every case, the distributions are identical with and without solar UV-visible irradiation. The one spectrum obtained at low pressure while chopping the photon beam contained no features above the noise level. The high pressure spectrum obtained with electron beam pulsing shows the same features as observed at low pressure, and once again the photon beam chopped spectrum contained no meaningful features. A comparison of signal intensities at low and high pressure with electron beam pulsing and photon beam chopping gives a cross section ratio

$$\frac{\sigma_{\text{photons}}}{\sigma_{\text{electrons}}} < 0.1 \quad .$$

Recall, that in the 300 to 400 nm region that ratio

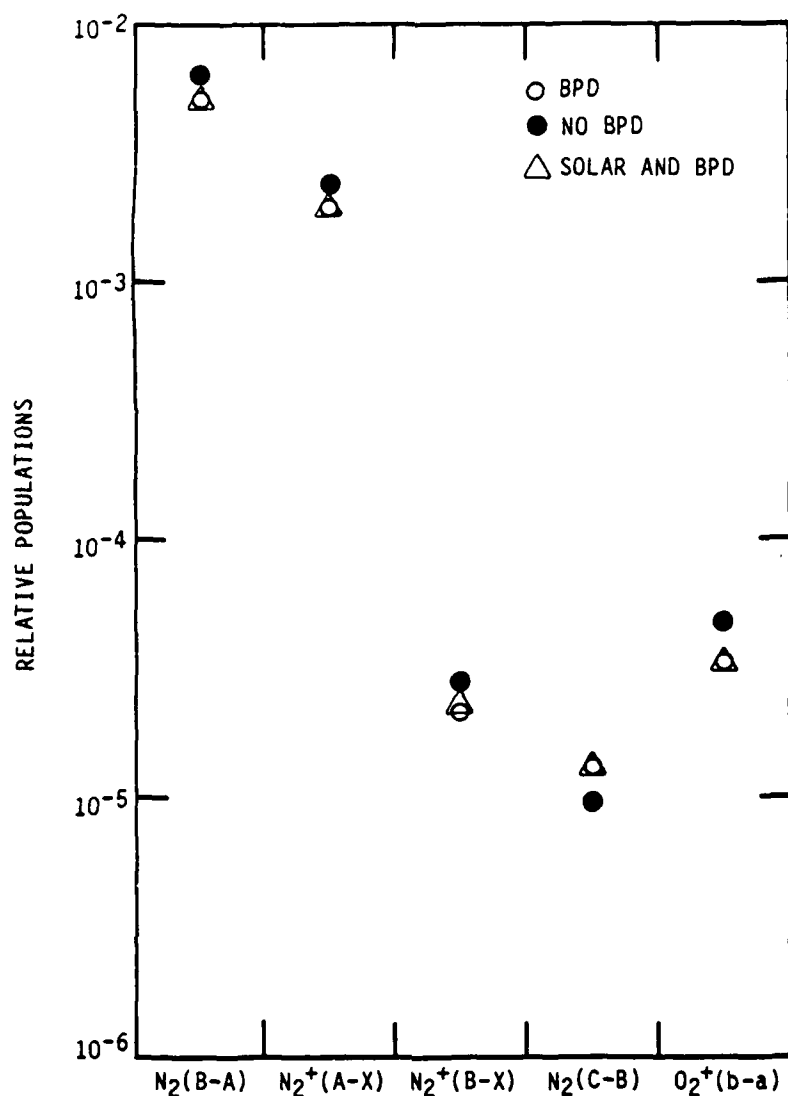
$$\frac{\sigma_{\text{photons}}}{\sigma_{\text{electrons}}} < 2 \times 10^{-4} \quad .$$

This does not represent a discrepancy between the two spectral regions because different band systems, i.e., excitation pathways, dominate in the two spectral regions. No solar effects were observed in either region; signal levels in the UV region allowed a stronger lower bound to be established.

#### 13.1.4 Conclusion of Visible Experiments

Clearly, the conclusion to be drawn from this set of experiments is the effect of solar UV-visible light on the fluorescence arising from air irradiated by





A-4109A

Figure 149. This figure shows the band system distributions obtained with and without solar UV-visible radiation. The data was obtained in 1.2 mtorr air in the 440 to 800 nm region with a resolution of 1.56 nm. The electron beam was pulsed for these observations.

electrons is small. A comparison of electron pulsing experiments with photon chopping experiments in the two spectral regions sampled provide an upper bound for the ratio of the photon excitation cross section,  $\sigma_{\text{photon}}$ , to the electron excitation cross section,  $\sigma_{\text{electron}}$ . This ratio was calculated to be  $2 \times 10^{-4}$  and  $1 \times 10^{-1}$  in the 300 to 400 nm and 440 to 800 nm regions, respectively. Although no significant effect of solar-UV, visible light

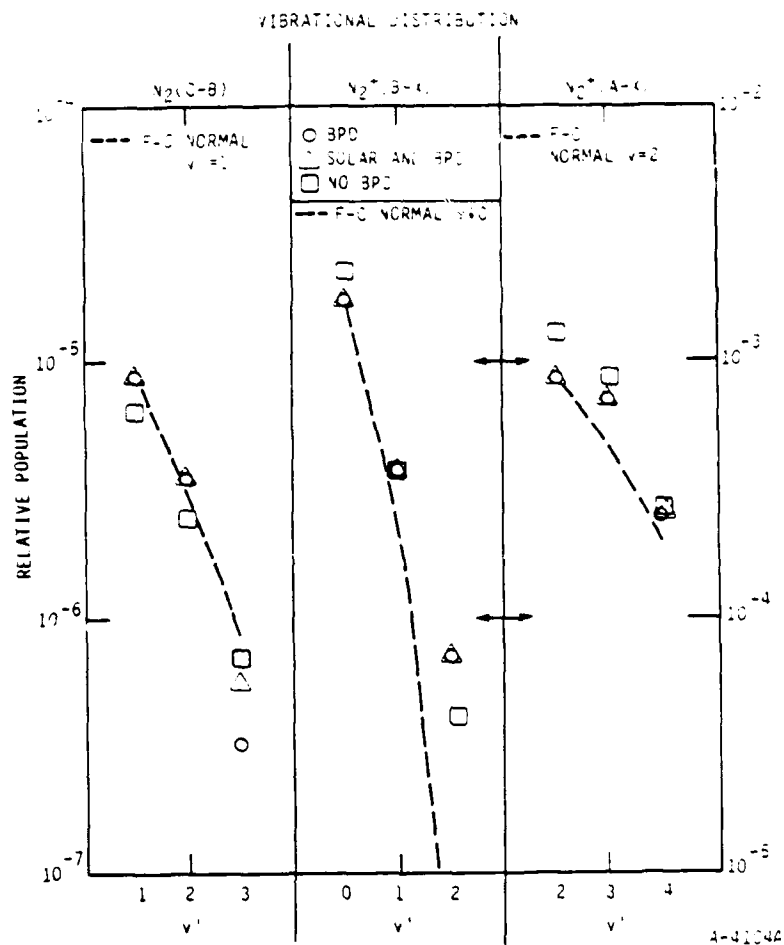


Figure 150. This figure presents the upper state vibration level distribution both with and without the presence of solar UV-visible radiation. The data was obtained by irradiating 1.2 m'torr of air with a pulsed electron beam. The spectrum covers the 440 to 800 nm region and has a resolution of 1.56 nm.

was observed in the visible fluorescence of electron-impact excited air, it may still play an important role in the fluorescence observed in the infrared region.

### 13.2 EFFECTS UPON IR ELECTRON-INDUCED FLUORESCENCE

The LABCEDE facility was also utilized to investigate the effects of solar UV and visible light upon infrared fluorescence from electron impact excited

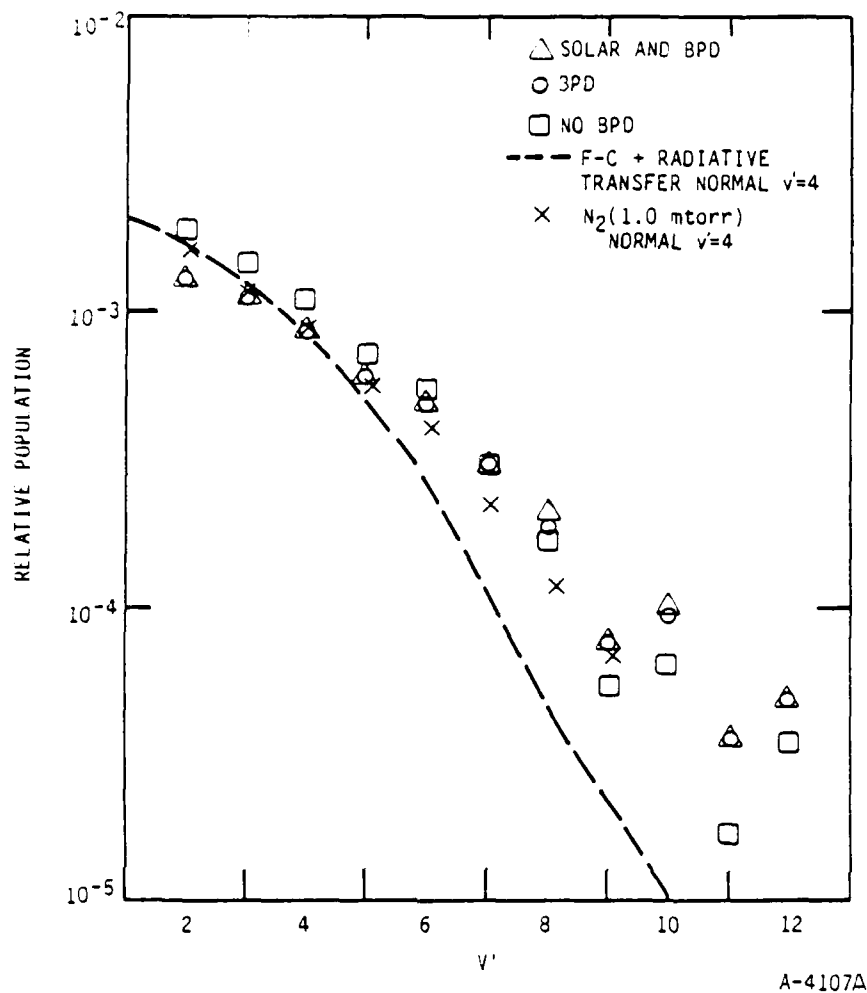


Figure 151. This figure presents the upper state vibrational level distribution with and without solar-UV, visible radiation. The data was obtained by irradiating 1.2 mtorr of air with a pulsed electron beam. The populations are determined by a least-squares fitting of theoretical spectra to the data in the visible region.

nitrogen/oxygen mixtures. Detection of the air fluorescence was performed in the infrared from 2.3 to 6.5  $\mu\text{m}$  using a liquid helium cooled circular-variable-filter (CVF).<sup>93,94</sup> The solar UV-visible light was generated with the Oriel solar simulator described previously. This effort was undertaken to determine if solar UV-visible light will produce any significant effects in the fluorescence signatures observed in the disturbed upper atmosphere.

### 13.2.1 Instrumental

The fluorescence from the photon/electron excited liquid nitrogen cooled gas mixtures was viewed through a KRS-5 window located at the upstream end of the LABCEDE tank. The detection system optical axis was perpendicular to the electron beam, and the solar simulator photon beam crossed the electron beam at an angle of about 20 deg near the tank center, emerging out of the tank through a quartz window parallel and opposite the first window. The CVF was mounted to the LABCEDE tank with a series of silicon O-ring flanges and compression fittings designed to provide vacuum-tight seals at reduced temperatures. In order to make use of the liquid helium temperature CVF, it is necessary to cool all surfaces in the entire field of view of the CVF to liquid nitrogen temperatures. The LABCEDE shroud was cooled from 300 K to ~ 90 K with a slow flow of liquid nitrogen through the shroud cryogen recirculation system. The gases are cooled in a liquid nitrogen temperature heat exchanger prior to entering the shroud volume. The CVF detector (As:Si) and filter wheel are cooled with liquid nitrogen overnight then with liquid helium on the morning prior to afternoon data collection. It was feared that the quartz windows would admit sufficient thermal emission to saturate the CVF detector in the short wavelength infrared. This was not the case. The CVF wheel contains four filter segments corresponding to the wavelength regions 2.3 to 3.6  $\mu\text{m}$ , 4.0 to 6.8  $\mu\text{m}$ , 9.3 to 11.1  $\mu\text{m}$ , and 13.4 to 15.0  $\mu\text{m}$ , hereon referred to as the SWIR, MWIR, LWIR (10  $\mu\text{m}$ ), and LWIR (14  $\mu\text{m}$ ) regions, respectively.

The resolution in the CVF SWIR and MWIR wheel segments was determined from the FWHM of O-atom lines to be 2.0 and 4.6 percent of the wavelength, respectively. Synchronous, time dependent detection was performed by chopping the photon beam with a variable speed mechanical chopper or pulsing the electron beam with a General Radio Model 1217B pulse/waveform generator. Signal from the CVF detector was first processed with a P.A.R. Model 113 preamplifier then digitized, averaged, and stored on the disc of a PDP 11 computer system. Time dependent spectra, uncorrected for detector response, were displayed on the

screen of the laboratory Apollo computer following a data file transfer to that device. This data file transfer provided access to a magnetic tape drive for transporting the data to PSI for reduction and analysis. Wavelength selection and scans were performed on command from the PDP 11 to a stepping motor and associated controller attached to the CVF. The minimum step size ranges from one-third to one-fifth of a resolution element in the SWIR, MWIR wavelength regions.

Using the air mass zero filter, which simulates the solar UV-visible distribution outside earth's atmosphere, a power density of 95 mW/cm<sup>2</sup> could be obtained in the center 1.5 in. diameter beam, with a total beam diameter of 3 in. A one sun equivalent, air-mass zero power density is approximately 130 mW/cm<sup>2</sup>. The photon flux assuming an average wavelength of 5000Å is approximately  $2.5 \times 10^{17}$  photons/cm<sup>2</sup>s in the central 1.5 in. diameter beam. For comparison, the electron flux ranges from  $2.5 \times 10^{16}$  to  $1 \times 10^{18}$  electrons/cm<sup>2</sup>s.

#### 13.2.2 Experimental

Two types of experiments were performed using the solar simulator. First, the PDP 11 computer was used as a lock-in signal averager while the CVF wheel was manually rotated through the SWIR, MWIR wavelength regions. Second, the PDP 11 computer was utilized to command the CVF wavelength scans, signal average, and record time dependent spectra. In both cases the experiments were performed by chopping the solar simulator photon beam, and triggering the data collection with the response from a photodiode synchronized to the chopper. The chopper frequencies ranged from 12 to 13 Hz with a symmetric square wave pulse width of 77 or 41 ms. In all experiments the electron beam was run D.C. at constant conditions with an energy of 4.5 KeV and a current in the range of 13.0 to 19.6 mA. A series of experiments were performed with 20 percent oxygen, 80 percent nitrogen at a total pressure of 5.0 mtorr, and a relatively fast flow. Spectral scans were performed in the SWIR and MWIR regions with and without BPD occurring and also in time dependent and non time-dependent

data collection modes. A second series of experiments were performed at a later date with 4 percent oxygen, 96 percent nitrogen at a total pressure of 15.5 mtorr, and slow flow conditions. Control experiments were performed by pulsing the electron beam at the same rate and experimental conditions with the solar simulator shutter closed. Peak electron current was similar to the D.C. electron current.

### 13.2.3 Observations of Fluorescence Changes in the SWIR Wavelength Region

Figures 152 through 154 show the SWIR spectra collected with 20 percent oxygen, 80 percent nitrogen at 5 mtorr pressures for fast flow: 1) utilizing time dependent collection with BPD; 2) manual scan with BPD; and 3) time dependent without BPD, respectively. The only significant spectral signature in the range from 2.3 to 2.8  $\mu\text{m}$  can be attributed to scattered light from the solar simulator. The signal intensity cutoff at 2.8  $\mu\text{m}$  corresponds to the wavelength transmission cutoff for the UV grade quartz windows providing access for the solar simulator photon beam. Figure 155 presents an SWIR spectra for a 20/80 mixture of  $\text{O}_2/\text{N}_2$  under similar experimental conditions when pulsing the e-beam without using the solar simulator. Two aspects are evident. Scattered room light out to the 2.8  $\mu\text{m}$  window cutoff is insignificant in comparison to the real spectral features. Because no-window-transmitted emission is observed in the normal fluorescence data, any contribution from photon excitation effects is smaller than the above mentioned scattered room light. A comparison of absolute signal levels suggests the ratio of cross sections for photon excitation to electron excitation must be less than or equal to  $8 \times 10^{-2}$

$$\frac{\sigma_{\text{photons}}}{\sigma_{\text{electrons}}} \leq 0.08 \quad .$$

Corrections for electron current differences have been taken into account. SWIR data for 4 percent  $\text{O}_2$  in  $\text{N}_2$  is identical to the 20 percent  $\text{O}_2$  in  $\text{N}_2$  data and gives essentially the same cross section ratio.

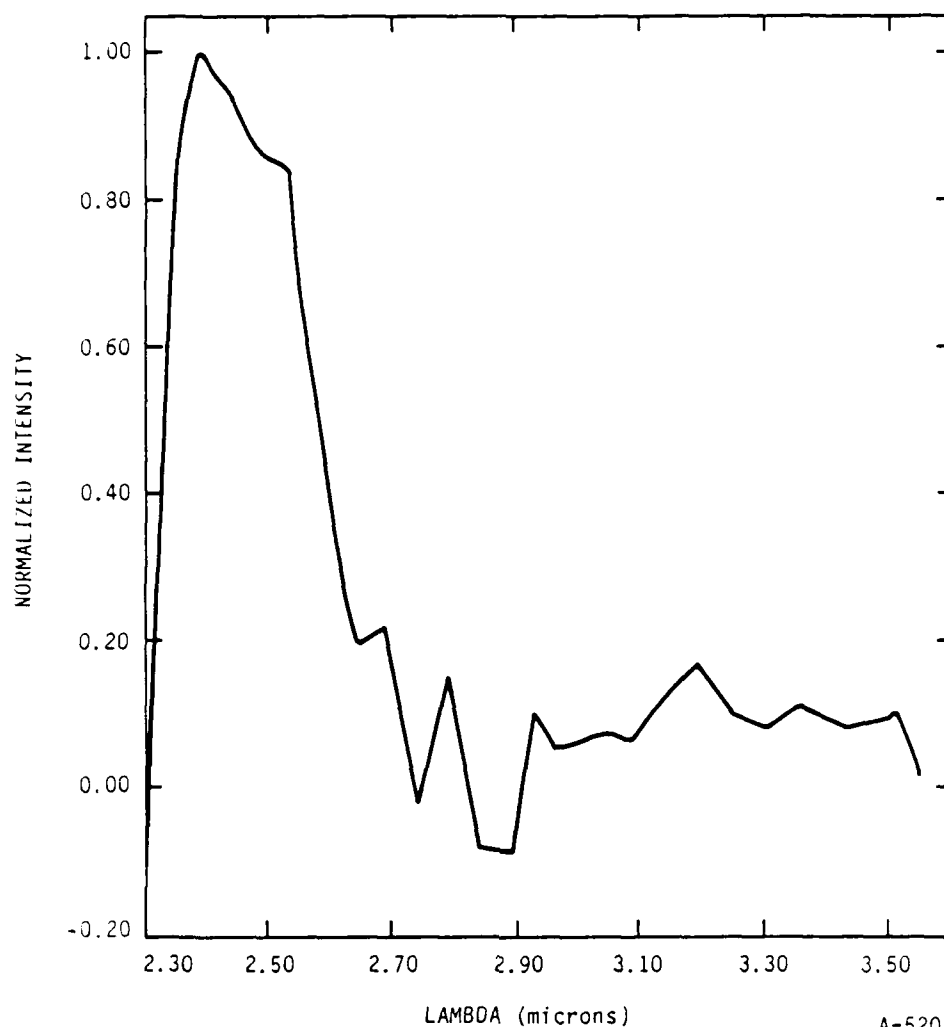


Figure 152. SWIR spectra for 5 mtorr pressure of 20 percent oxygen, 80 percent nitrogen with BPD taken in time dependent data collection mode, performed by chopping the solar simulator photon beam. Peak intensity is  $\sim 2.8 \times 10^{-8} \text{ W/cm}^2 \text{ sr } \mu\text{m}$ .

#### 13.2.4 Observations in the MWIR Wavelength Region

Figure 156 shows a typical spectra in the MWIR for a 5 mtorr 20/80 mixture of  $\text{O}_2/\text{N}_2$  taken by chopping the solar simulator. No significance can be placed on any feature. A comparison with 20/80 mixtures of  $\text{O}_2/\text{N}_2$  at similar conditions by pulsing the electron beam without using the solar simulator suggests the cross section ratio for photon versus electron excitation is less than or equal to  $3 \times 10^{-2}$ , when corrected for electron current differences

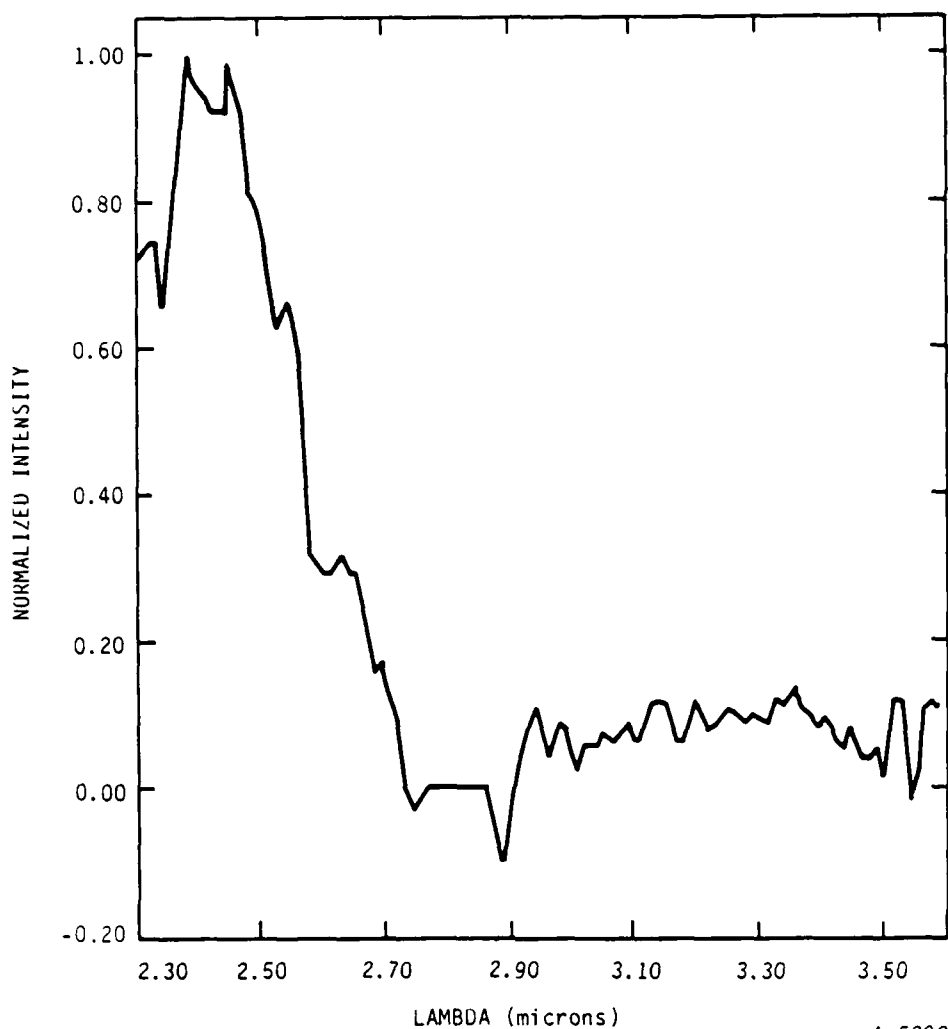
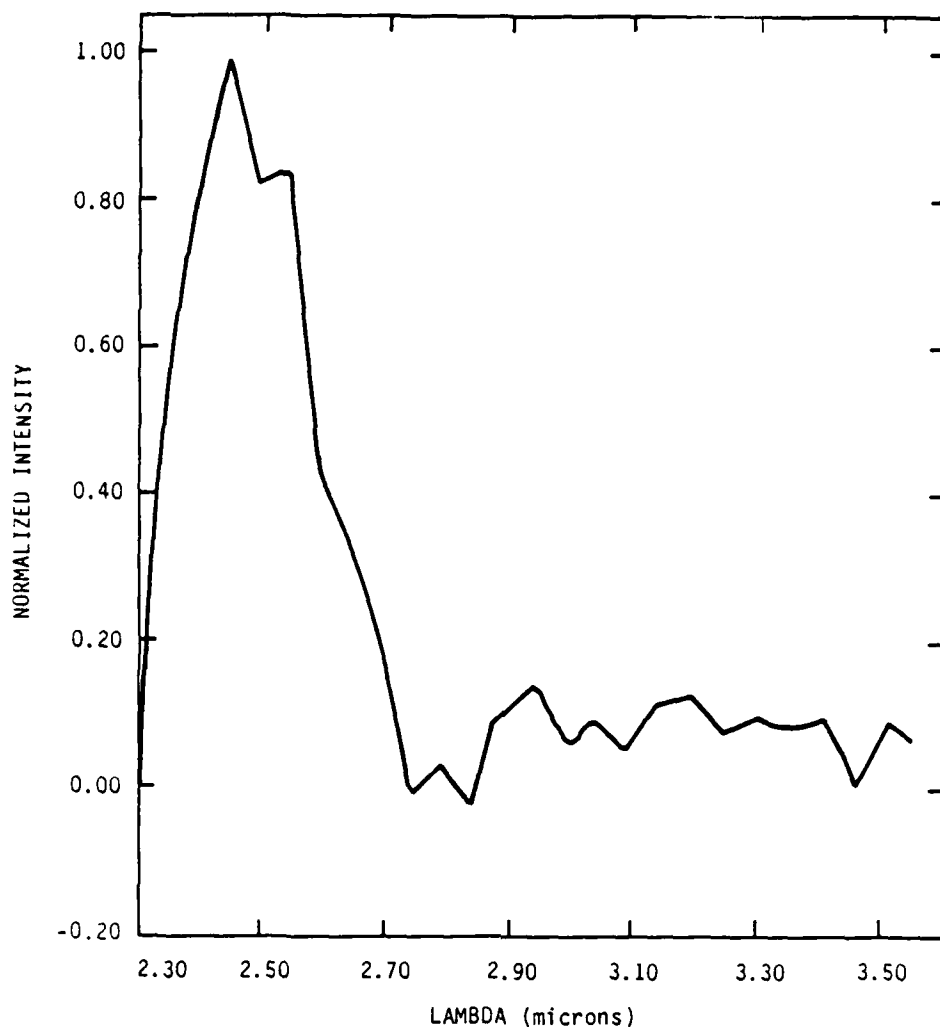


Figure 153. SWIR spectra under the same conditions as Figure 152 except taken in the manual data collection mode. Peak intensity is  $\sim 5.8 \times 10^{-7}$  W/cm<sup>2</sup> sr  $\mu$ m.

$$\frac{\sigma_{\text{photon}}}{\sigma_{\text{electron}}} \leq 0.03 \quad .$$

The MWIR air spectrum obtained by electron beam pulsing is dominated by NO fundamental emission at 5.7  $\mu$ m. Figure 157 shows this emission for the 4 percent O<sub>2</sub> in N<sub>2</sub> data set. The spectra obtained by chopping the photon beam for 4 percent O<sub>2</sub> in N<sub>2</sub> is once again unassignable. A comparison of signal intensities suggests the cross section ratio



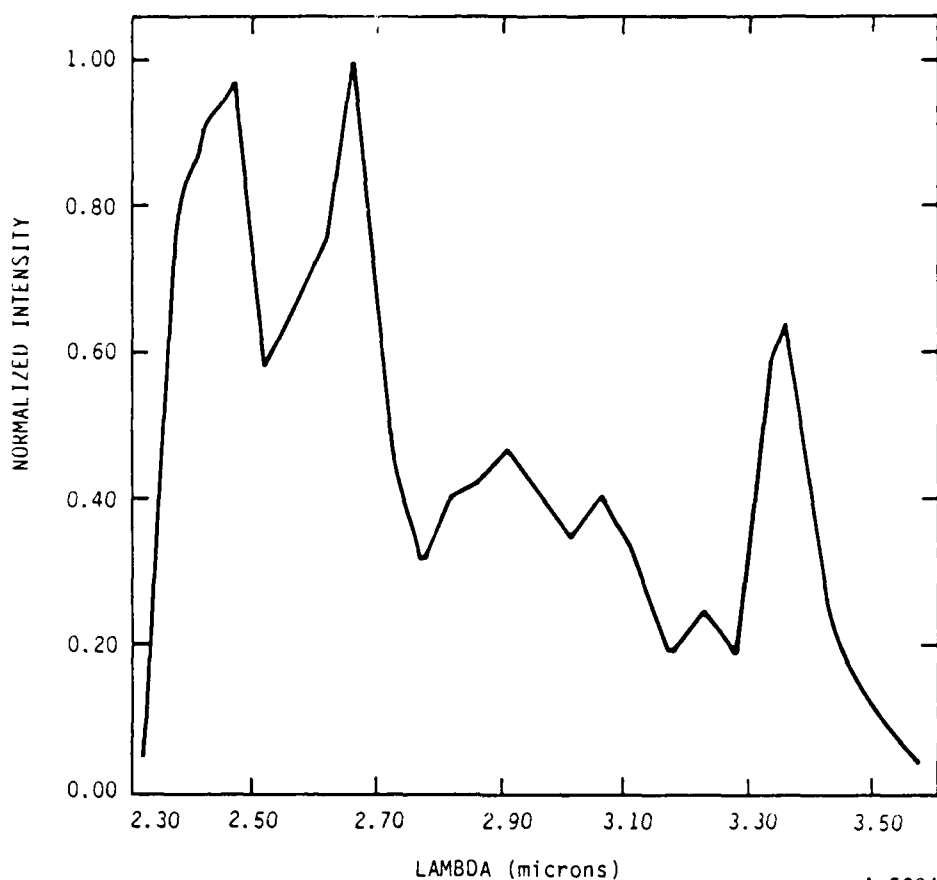


A-5203

Figure 154. SWIR spectra with the previous gas conditions, except without BPD ignited, taken in time dependent data collection mode. Peak intensity is  $\sim 2.9 \times 10^{-8} \text{ W/cm}^2 \text{ sr cm}^2$ .

$$\frac{\sigma_{\text{photon}}}{\sigma_{\text{electron}}} \leq 0.009$$

to be less than  $9 \times 10^{-3}$ . The lowering of this cross section ratio for 4 percent  $\text{O}_2$  in  $\text{N}_2$  is believed to be due to changes in noise levels of the detector from data set to data set and the difference in NO production rates by lowering the  $\text{O}_2$  fraction. Future work may be required to fully elucidate the relevant factors.



A-5204

Figure 155. SWIR spectra at the same gas conditions as before, with BPD ignited, however performed by pulsing the electron beam with the solar simulator off. Peak intensity is  $\sim 8.5 \times 10^{-8} \text{ W/cm}^2 \text{ sr } \mu\text{m}$ .

### 13.3 CONCLUSIONS

A comparison of electron pulsing experiments with photon chopping experiments in the SWIR, MWIR spectral regions provide an upper bound for the ratio of the photon excitation cross section,  $\sigma_{\text{photon}}$ , to the electron excitation cross section,  $\sigma_{\text{electron}}$ . This ratio was calculated to be  $8 \times 10^{-2}$  and 0.009 to 0.03 in the SWIR and MWIR regions, respectively. (The upper bound for the

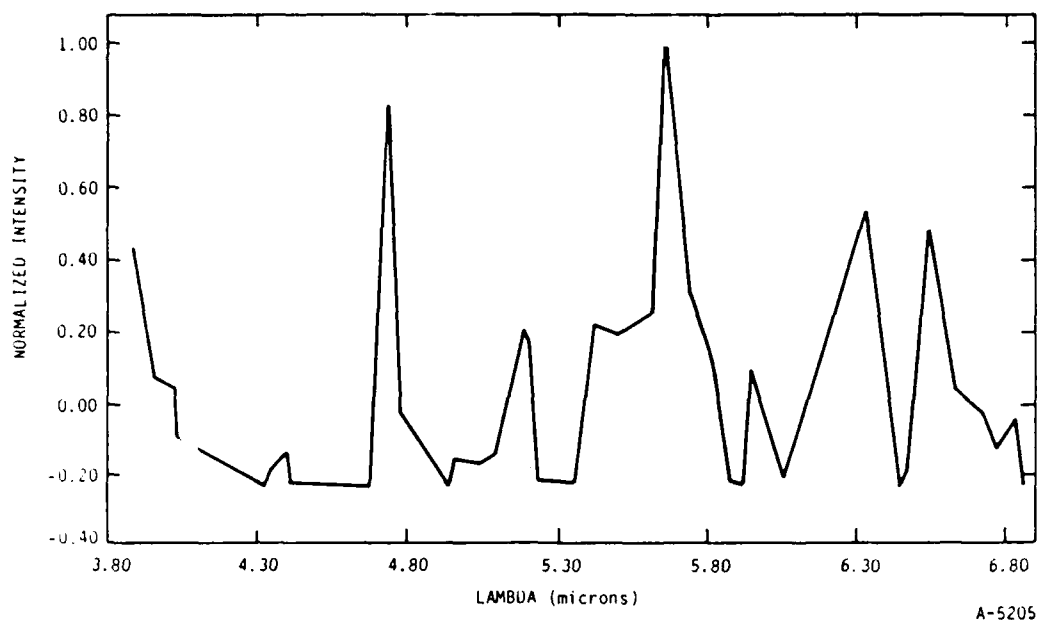


Figure 156. MWIR spectra at 5 mtorr of a 20/80 percent mixture of  $O_2/N_2$ , with BPD, taken in time dependent data collection mode, performed by chopping the solar simulator. The peak intensity is  $\sim 5.9 \times 10^{-10} \text{ W/cm}^2 \text{ sr } \mu\text{m}$ .

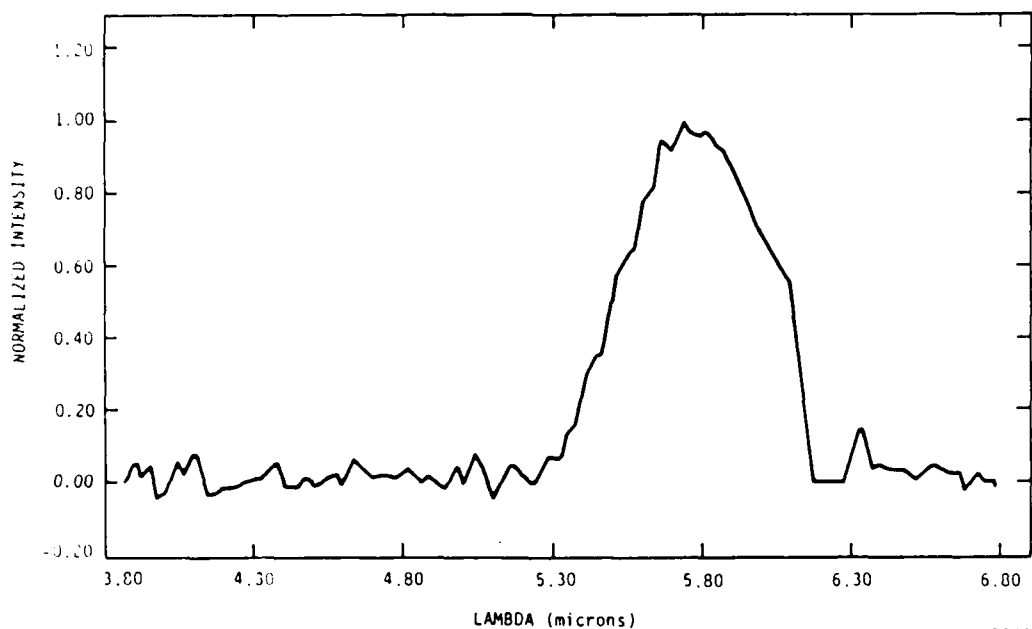


Figure 157. MWIR spectra at 4 percent  $O_2$  in  $N_2$  without BPD, taken in time dependent data collection mode by pulsing the electron beam with the solar simulator off. The dominant feature can be assigned to NO fundamental emission.

ratio of cross sections into the SWIR may be even smaller than measured since the scattered light from the solar simulator prohibited us from using the full sensitivity range of the CVP detector in this wavelength region.) The only conclusion to be drawn from these observations is that the effect of solar UV-visible light on the air fluorescence generated by electron impact excitation in the IR up to 6.9  $\mu\text{m}$  is small.

Between 0.3 to 6.0  $\mu\text{m}$ , no solar induced effect on molecular fluorescence was observed. Only upper bounds on excitation cross sections could be made. They were found to be less than 10 percent,  $2 \times 10^{-2}$  percent, 8 percent, 0.9 percent in the 0.3 to 0.4  $\mu\text{m}$ , 0.44 to 0.8  $\mu\text{m}$ , SWIR, MWIR regions in comparison to electron excitation cross sections.

## 14. ELECTRON BEAM GROWTH MODELING INCLUDING ELASTIC AND INELASTIC SCATTERING AND CONTRIBUTION FROM FAST SECONDARIES

### 14.1 INTRODUCTION

When an electron beam passes through nitrogen gas, the beam will spread radially as a result of elastic and inelastic collisions of the electrons. The total cross section for inelastic collisions is comparable with the cross section for elastic collisions for electrons with energies of 2 to 6 keV incident upon nitrogen gas. Thus we may expect that inelastic collisions will contribute to the spreading of the electron beam as it passes through the gas. In addition some of the secondary electrons produced will have enough energy to excite 391 nm radiation. In this section we shall discuss how a numerical simulation was undertaken to assess the relative importance of these processes. We shall give details of the cross section and angular distribution calculations, and present a comparison of the simulation results with the experimental data. In this manner we shall assess the ability of previous measurements and calculations to reproduce the trends observed in our experimental measurements.

### 14.2 SIMULATION DESCRIPTION

For each primary electron energy the simulation is done in two parts. First we estimate the contribution to 391 nm excitation from fast secondary electrons, and then we find the contribution from the scattering of the primary beam. In a Monte Carlo simulation, we find the contribution from the primary beam by following the trajectories of some 8000 primary electrons. Each primary electron is assumed to start with an energy equal to the primary energy at  $z=0$  and  $r=(x^2+y^2)^{0.5} = 0$ , with the electron traveling directly down the  $z$  axis. The total cross section,  $\sigma_{\text{tot}} = \sigma_{\text{in}} + \sigma_{\text{el}}$ , is the sum of the inelastic and elastic cross sections calculated for an electron with an energy  $E_0$ . This total cross section is used with the nitrogen number density  $n_{\text{N}_2}$  to find the

path length traveled before the next collision. This length is found by using a random number  $R$  from a uniform distribution between 0 and 1 in the relation

$$1 - \ln(R)/(\sigma_{\text{tot}} n_{\text{N}_2}) \quad . \quad (61)$$

This length is used with the direction cosines of the electron velocity vector to find the  $x, y, z$  coordinates of the collision. At each collision, another random number between 0 and 1 is selected to determine the nature of the collision. If this number is less than the fraction of collisions that is elastic (which is equal to  $\sigma_{\text{el}}/\sigma_{\text{tot}}$ ), then the collision is taken as elastic. If the number is larger, then the collision is taken as inelastic and the random number is used to select the inelastic channel is excited. Here  $\sigma_{\text{tot}}$  is considered to be given by

$$\sigma_{\text{tot}} = \sigma_{\text{el}} + \sum \sigma_j (E_0, E_j) \quad , \quad (62)$$

where  $\sigma_j (E_0, E_j)$  is the inelastic cross section for transfer of an energy  $E_j$  to the nitrogen molecule. In practice we only used a limited number of  $E_j$  values, with one value (12 eV) to simulate excitation and several values to represent ionization. These values were taken to be the ionization potential ( $I = 15.6$  eV) plus representative secondary electron energies of 2, 10, 18, 24, 30, 45, 80, 120, 180, 400, 900, and 2000 eV. The maximum secondary electron energy in a collision of an electron with an initial energy of  $E_0$  is given by  $0.5 (E_0 - I)$ .

If the collision is elastic, we find the new direction cosines of the electron by taking two more random numbers, one to give the azimuthal scattering angle  $\phi$  (which is uniformly distributed between 0 and  $2\pi$ ), and one to give the deviation from the original direction  $\theta$ . The  $\theta$  angle is found by integrating the angular distribution  $\sigma_{\text{el}} (E_0, \theta)$  times  $2\pi \sin(\theta)d\theta$  to give a uniform probability between 0 and the total elastic cross section. The integrated

distribution is used with a random number to select the value of the scattering angle  $\theta$  corresponding to the fraction of  $\sigma_{e1}$ . In this way we allow backscattering to occur, since  $\theta$  varies between 0 and  $\pi$ . This sequence represents the study of one collision. A new path length is then found, and the trajectory is followed until the electron passes outside the range of interest. The range of interest is  $z$  values from -8 cm to  $z_{\max}$ , where  $z_{\max}$  is 50, 70, 80, or 90 cm for  $E_0$  values < 2, 2, 4.5, or 6 keV, respectively.

If the collision is inelastic, we find the new direction cosines in a similar manner, except we use the inelastic angular distribution  $\sigma_j(E_0, E_j, \theta)$  for scattering by an inelastic collision that transfers an energy  $E_j$ . In addition, we recalculate  $\sigma_{\text{tot}}$  at the new value of  $E_0$  for use in finding the path length between collisions. If the electron energy decreased significantly in the collision (i.e., if it has lost approximately 30 percent of the initial energy), then the angular distributions for elastic and inelastic scattering are changed to correspond to the smaller  $E_0$  value.

The contribution of fast secondary electrons to excitation of 391 nm radiation is estimated by finding the contribution produced by a limited number (100 to 800) of primary electrons. For these primary electron trajectories, we find the direction cosines of the secondary electron and the coordinates of the point of formation. The direction cosine is selected from the collision and the angular distribution for production of secondaries, which is evaluated from the values of  $E_0$  and  $E_j$  used at each collision. The effect of this fast secondary is found using the results of the previous calculation where the primary energy was the same as this fast secondary. That is, in an earlier calculation we determined the excitation of 391 nm radiation as a function of  $z$  and  $r$ , and this result gives the contribution for a fast secondary electron. We do this by finding the  $z', r'$  coordinates (in the cylindrical coordinate system along the direction of the fast secondary) of each region of  $r$  in the  $z=50$  cm plane (of the primary beam), where we want to compare with data. In practice we compute this contribution and the primary contribution at a series of planes

for  $z$  values from -4 to 50 cm. We start the calculation using primary electrons that have low energies. For each higher primary energy we add the effect of secondaries with lower energies to that of the primaries. Thus the secondary electron contribution will include the contribution of the tertiary (and higher order) electrons produced by the secondaries. This is because we only consider secondary electrons with fixed initial energies and we calculate the combined effect of those primary electrons plus the secondaries (with energies of 24 eV or more) produced by the primaries. Thus the calculation for 80 eV primaries includes contributions from the 24 and 30 eV secondaries, so when we later form an 80 eV secondary, the contribution we use will include the effects of the 24 and 30 eV tertiaries.

At each primary electron energy, we calculate the  $G(r)$  distribution of the 391 nm excitation from both the primary electron and the fast secondaries. This contribution is calculated at  $z$  values of -4, -1, -0.001, 0, 1, 2, 4, 6, 10, 15, 20, 30, and 50 cm. At each  $z$  value the contribution to  $G(r)$  per incident primary electron is found for  $r$  values in rings 5 mm wide. These data are stored by keeping the individual values for the four rings with  $r < 20$  mm, and the data for the larger  $r$  values are fit by three lines, where  $\log(G)$  is fitted as a linear function of  $r$  for the three ranges of 15 to 60, 45 to 105, and 85 to 150 mm. When the primary electron is calculated, the range of the excitation of 391 nm radiation is found for both the  $z$  and  $r$  coordinates. This range is taken as the point at which the excitation of 391 nm radiation per unit area is reduced to 0.0005 of the value on axis at  $z = 0$ . When the contribution of the fast secondaries is calculated, no contribution is considered for  $z'$  or  $r'$  values beyond this range. This has the advantage of speeding the calculation by skipping those secondaries that will not contribute significantly to excitation because they are too far away, and it also means that it is seldom necessary to extrapolate  $r$  values beyond 150 mm.

As a result of the angular distributions, backscattered electrons are only important for electrons with  $E_0$  values less than 900 eV, and these electrons have only a modest range. Less than 12 percent of the original beam reaches



$z = -4$  cm. The electron scattering into negative  $z$  values is given to estimate the effect of backscattering.

The key physical inputs into the simulation are the values of absolute cross sections  $\sigma_{el}(E_0)$  and  $\sigma_j(E_0, E_j)$ , the relative cross sections for angular scattering  $\sigma_{el}(E_j, \theta)$  and  $\sigma_{inj}(E_0, E_j, \theta)$ , the relative cross section for producing a fast secondary electron at an angle  $\theta_s$ ,  $\sigma_{sec}(E_0, E_j, \theta_s)$ , and the relative cross sections for excitation of 391 nm radiation  $\sigma_{391}(E_0)$ . In the next subsections, we shall discuss our choices for each of these values.

#### 14.3 ABSOLUTE CROSS SECTIONS FOR ELASTIC AND INELASTIC SCATTERING

The absolute cross sections (together with the gas number density) are the parameters that determine the length of the path between collisions as well as the distribution of energy losses produced in inelastic collisions. We need a general prescription for determining  $\sigma_{el}(E_0)$ , and  $\sigma_{in}(E_0, j)$  for wide ranges of  $E_0$  and  $E_j$ . For this purpose we have used the expression from Jackman and Green (JG)<sup>169</sup> for  $\sigma_{el}$  and the expression given by Porter, Jackman, and Green (PJG)<sup>170</sup> for  $\sigma_{in}$ . These expressions give values that compare with the recommended values given by Itikawa, et al.<sup>171</sup> to within 10 to 20 percent, as shown in Figure 158. In the results section, we shall show that sensitivity studies indicate that changes of that magnitude for any one cross section have a relatively minor effect on the simulation. We have also compared the differential cross section,  $d\sigma_{ion}(E_0, E_j)/dE_j$ , for producing a secondary electron with an energy  $(E_j - 15.6)$  eV with Figure 9.8 in Itikawa et al.<sup>171</sup> Here our values usually are some 5 to 15 percent high. However at  $E_0 = 50$  eV, our calculations are as much as 100 percent larger than the recommended values for production of slow secondaries.

#### 14.4 ELASTIC SCATTERING ANGULAR DISTRIBUTION

The relative differential scattering cross section  $\sigma_{el}(E_0, \theta)$  determines the distribution of the angular scattering by elastic processes where the

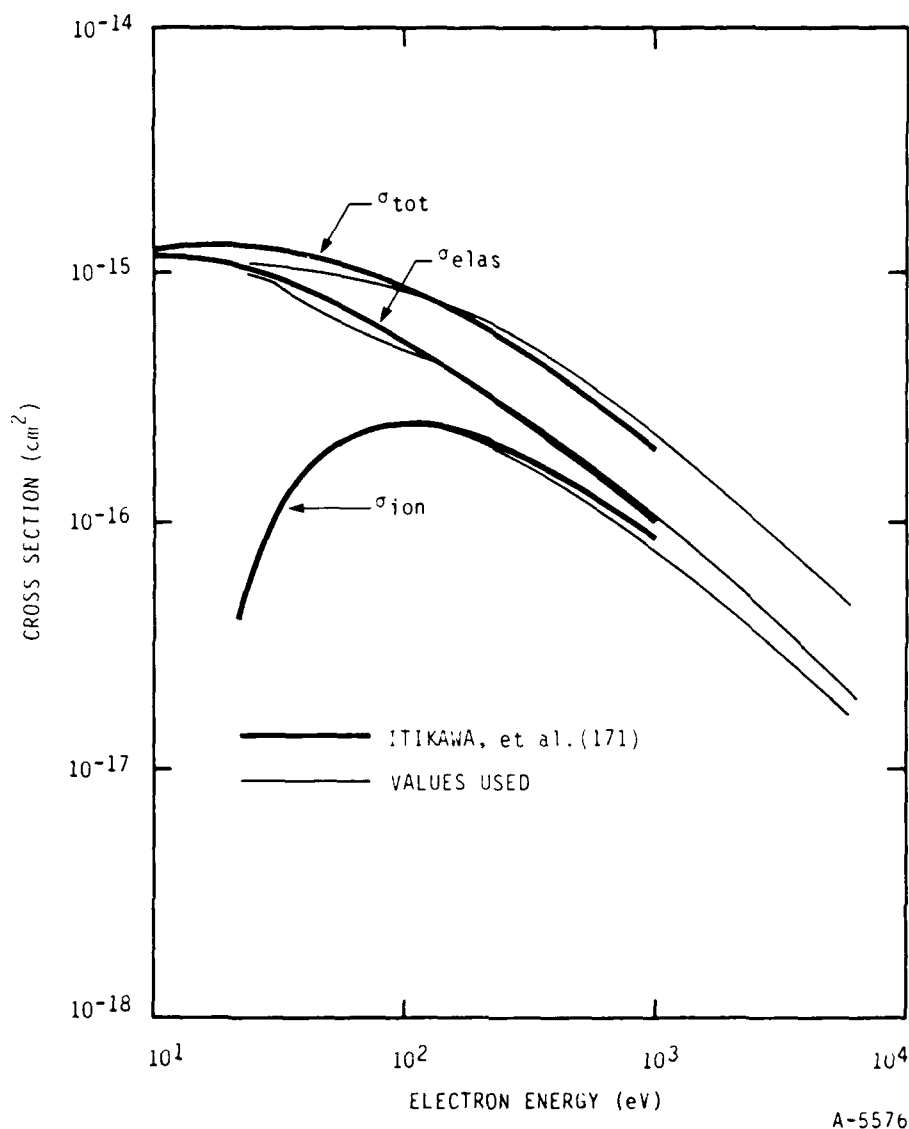
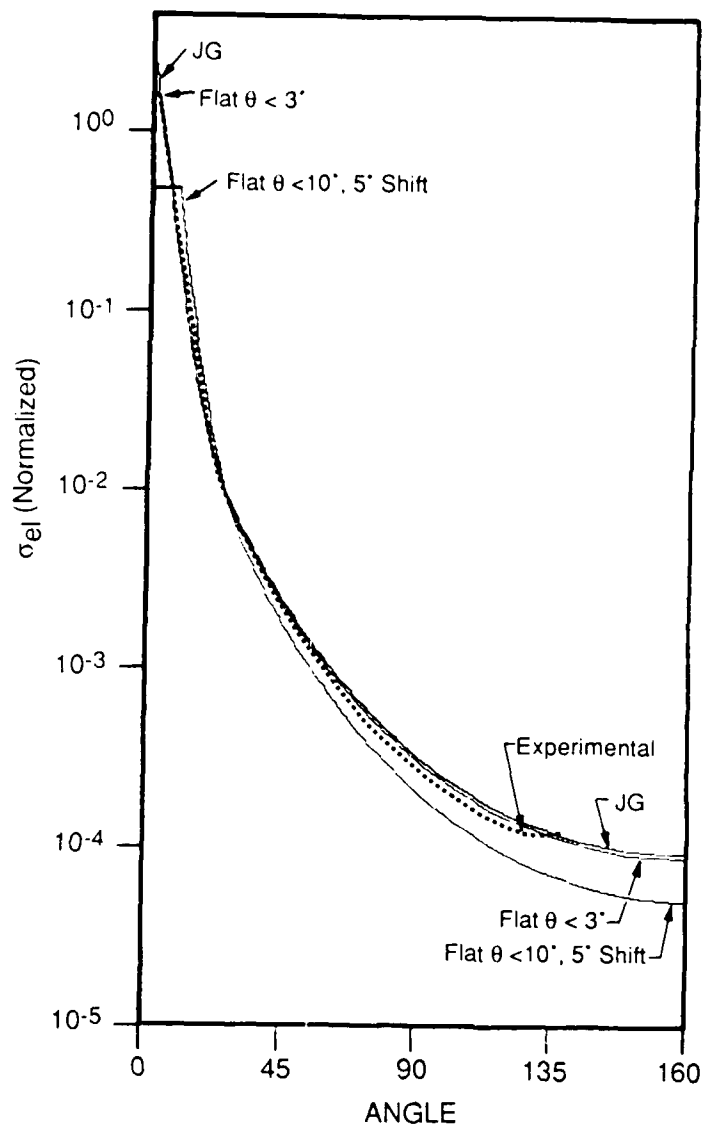


Figure 158. Summary of the cross sections for the electron collision with  $N_2$ .

electron energy  $E_0$  is unchanged during the collision. We have used either the general prescription for  $\sigma_{el}(E_0, \theta)$  given by Jackman and Green<sup>169</sup> or modifications of this distribution where the contribution from small angles is diminished. For fast electrons, the main feature of the distribution is a logarithmic decline of  $\sigma_{el}$  as the value of  $\theta$  increases, a result of Rutherford scattering of the incident electron from the positive nucleus of the nitrogen atom. This is shown in Figure 159, which compares experimental data at 1 keV (Herrmann et al.<sup>172</sup> and Jansen et al.<sup>173</sup>) with the JG formula results and with



A-5577

Figure 159. Differential elastic cross section at 1 keV. The dashed line shows data of Herrmann et al.<sup>172</sup> The bottom solid line is the form given by Jackman and Green,<sup>169</sup> and the other two lines are modifications used to test sensitivity to a flatter distribution.

modified versions. The modifications examined the sensitivity to changes in the relative shape of the angular distribution of  $\sigma_{el}$ . The changes both involved reducing the contribution from small-angle scattering. The experimental data are reported only for  $\theta \geq 3$  deg, and one modification was a minor change to simply cutoff the distribution so that  $\sigma_{el}$  is constant for  $\theta < 3$  deg and fits the JG formula for larger  $\theta$ . This choice is thus consistent with existing data. A more extreme flattening modification was to make  $\sigma_{el}$

constant for  $\theta < 10$  deg and to shift the JG formula by 5 deg; so that the calculation uses  $\sigma_{e1}(e_0, \theta-5 \text{ deg})$  for  $\theta \geq 10$  deg. The y axis for the experimental data has been arbitrarily adjusted in Figure 13. Shifting the y axis shows that the data also agree reasonably well with the 10 deg-flattened distribution, except for  $3 < \theta < 10$  deg.

#### 14.5 INELASTIC SCATTERING ANGULAR DISTRIBUTION

The inelastic scattering is also simulated by known cross section and the relative angular distribution. Here we focus on the relative values for  $\sigma_{inj}(E_0, E_j, \theta)$ . The inelastic scattering of electrons can be considered to result from two processes. One process is the small-angle scattering that occurs when the collision has a large impact parameter where the molecule is excited by an interaction with the time-varying electric field produced by the motion of the electron. Here the molecule responds to the motion of the electron in the same way that it interacts with a photon. This process is dominated by the optical oscillator strength  $df(E)/dE$  divided by  $E$ . These virtual-photon excitations correspond to small values of momentum transfer, which is also consistent with this process occurring at large impact parameters. The other process contributing to electron scattering is the hard collisions where the incident electron essentially has a binary collision with one of the electrons that surround the molecule. In the hard collision there is an exchange of momentum between the two electrons.

Both of these processes can be described in a consistent manner by extending the concept of the oscillator strength to allow for non-zero momentum transfer. Thus, we use the generalized oscillator strength (GOS) given by

$$df(E, Q)/dE = [(m/M)^2 / (4Z^2 a_0^2)] (1 - (m/M) (E/C_0))^{-0.5} Q .$$

$$(E/R^2) (d\sigma/d\omega) \tag{63}$$

where  $m$  is the mass of the electron,  $M$  is the molecular mass,  $Z$  is the charge on the nucleus,  $a_0$  is the Bohr radius,  $R$  is the Rydberg constant,  $Q = (Ka_0)^2$ ,  $\hbar k$  is the magnitude of the momentum transfer of the incident electron in the collision,  $\hbar$  is Planck's constant divided by  $2\pi$ , and  $\omega$  is the solid angle into which the electron is scattered in the center of mass coordinate system (Inokuti).<sup>174</sup> The square of the momentum transfer  $Q$  is related to the scattering angle by

$$Q = 2(E_0/R)(M/m)^2 \{1 - 0.5(m/M)(E/E_0) - [1 - (m/M)(E/E_0)]^{0.5} \cos\theta\}. \quad (64)$$

Inokuti<sup>174</sup> points out several interesting properties of GOS. A three-dimensional plot of the GOS versus the axes of  $E$  and the logarithm of  $Q$  gives the Bethe surface. The total cross section for transfer of an energy  $E$  is then given by the area under the Bethe surface at that value of  $E$ , with the limits of integration on the  $\ln(Q)$  axis determined by the energy and momentum conservation. These limits are given in Eq. (64) by using the values of 0 and  $\pi$  for  $\theta$ . Thus a knowledge of the GOS defines the angular scattering cross section.

Equation (63) can be considered to define an effective GOS when experimental  $\sigma$  values are substituted on the right hand side. These effective GOS are functions of  $E_0$ ; for large values of  $E_0$ , the effective GOS becomes independent of  $E_0$  and this is called the GOS. The GOS goes to the optical oscillator strength in the limit of  $Q \rightarrow 0$  and there are general sum rules for various moments. Porter, Jackman, and Green<sup>170</sup> considered these general properties when they fitted a parametrized form of the Massey-Mohr-Bethe surface (which is based on the theoretical form of  $df/dE$  that is correct for H atoms). The PJG fit is given in Eq. (14) and Table 2 of PJG,<sup>170</sup> with the following corrections as communicated by Professor Green: the argument of arctan is  $(\alpha^2/2)$ , a constant of 0.654 is added to  $\beta_2$  and a constant of 1.0 is added to  $\gamma$ . The PJG GOS can be improved in two areas: 1) there is now more data and 2) their GOS for large momentum transfer do not have the proper shape. PJG used the data of Silverman and Lassette<sup>175</sup> in fitting their Massey-Mohr-Bethe surface, and now there is additional data from Iida<sup>176</sup> and Shibata, et al.<sup>177</sup> As for the

shape of the PJG fit, the maximum in the GOS in the binary-encounter peak at the Bethe ridge should occur at higher values of momentum transfer than does the surface of PJG when the general considerations on the form of the Bethe surface discussed by Dillon, Inokuti, and Wang (DIW)<sup>178</sup> are considered. (The Bethe ridge corresponds to a binary collision with an electron in the valence shell of the molecule.) In addition, Dillon and Lassetre<sup>179</sup> have shown that the effective GOS are functions of  $E_0$  and that these effective GOS fall off more slowly with  $Q$  than would be predicted from the DIW considerations. Indeed, they show that the effective GOS falls off as  $Q^{-1}$ .

In practice we have used the absolute inelastic cross section  $\sigma_{in}(E_0, E_j)$  given by PJG together with two different relative angular distributions. One distribution of  $\sigma_{in}(E, E_0, \theta)$  is derived from the GOS surface given by PJG, and the other is derived from a modification of this surface. The purpose of the modification was to examine the effect of increasing the GOS at large momentum transfer, which will increase the relative contribution from scattering at larger angles. The changes involved using the PJG GOS at smaller values of  $Q$  and patching these values to modified values for large  $Q$ . The modification was to use GOS proportional to  $Q^{-1}$  for  $Q$  values larger than the value where GOS falls to 0.7 times the value at the maximum, and to simply broaden the maximum GOS to extend from the maximum in the PJG curve to the maximum predicted from the DIW form when the numerator function is  $Q - E/(3I)$ , which is the numerator function used by PJG ( $I$  is the ionization potential of  $N_2$ ). At  $E < 2I$ , the DIW form does not have a maximum, so the PJG form is used until GOS falls below 0.7 times the maximum GOS value. In order to approximate the observed dependence of the effective GOS on  $E_0$ , we also add the term  $0.8(E/E_0)[1 - (df/dE)_c / (df/dE)_0]$ , where  $(df/dE)_c$  represents the calculated value (using the PJG form with the modifications discussed above) and  $(df/dE)_0$  represents the value of the PJG form near the optical ( $Q = 0$ ) limit, which was evaluated using the minimum  $Q$  value when  $E_0 = 20$  keV. That is, we empirically adjust the calculated  $(df/dE)_c$  value by adding a term proportional to  $E/E_0$  (which goes to zero as  $E_0$  becomes large, where  $df/dE$  should be independent of

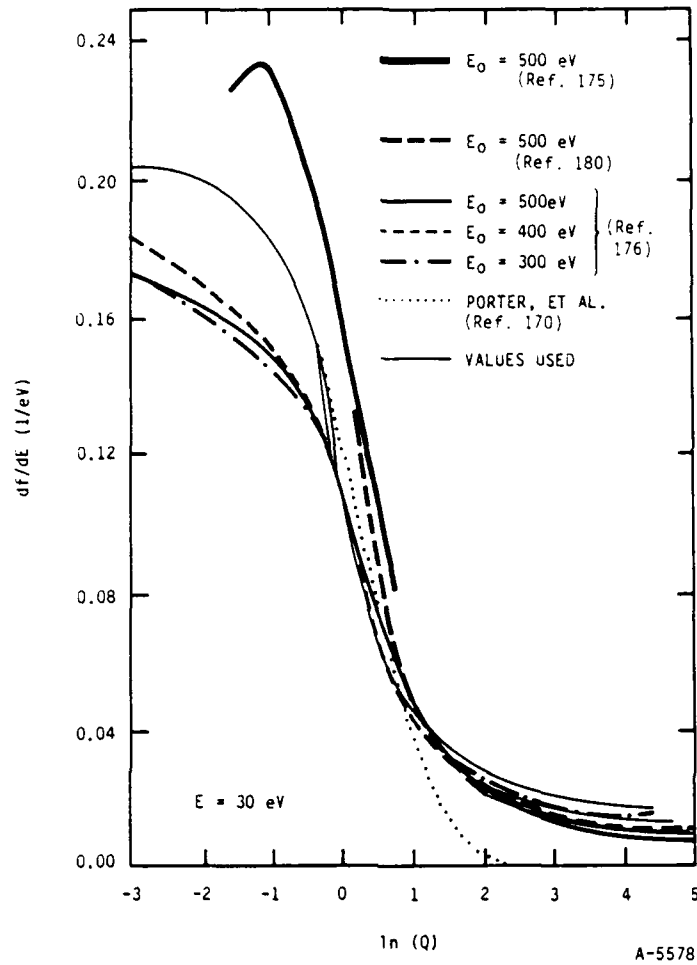


Figure 160. Generalized oscillator strength versus the square of the momentum transfer for 30 eV energy loss. The heavy lines represent experimental data. The dotted line and the light lines represent values used in simulations.

$E_0$ ). The adjustment increases or decreases  $df/dE$  depending on whether  $(df/dE)_c$  is less than or greater than  $(df/dE)_0$ , so that the adjustment will not interfere with the approach to the limit of the optical oscillator strength as  $Q$  goes to zero. In addition, the maximum decrease in the peak of the Bethe ridge was arbitrarily limited to  $-1.5 E/E_0$ . These GOS curves are compared with experimental data in Figures 160 through 162. The thin lines labeled "values used" show the modified GOS values. The values depend on  $E_0$  and when

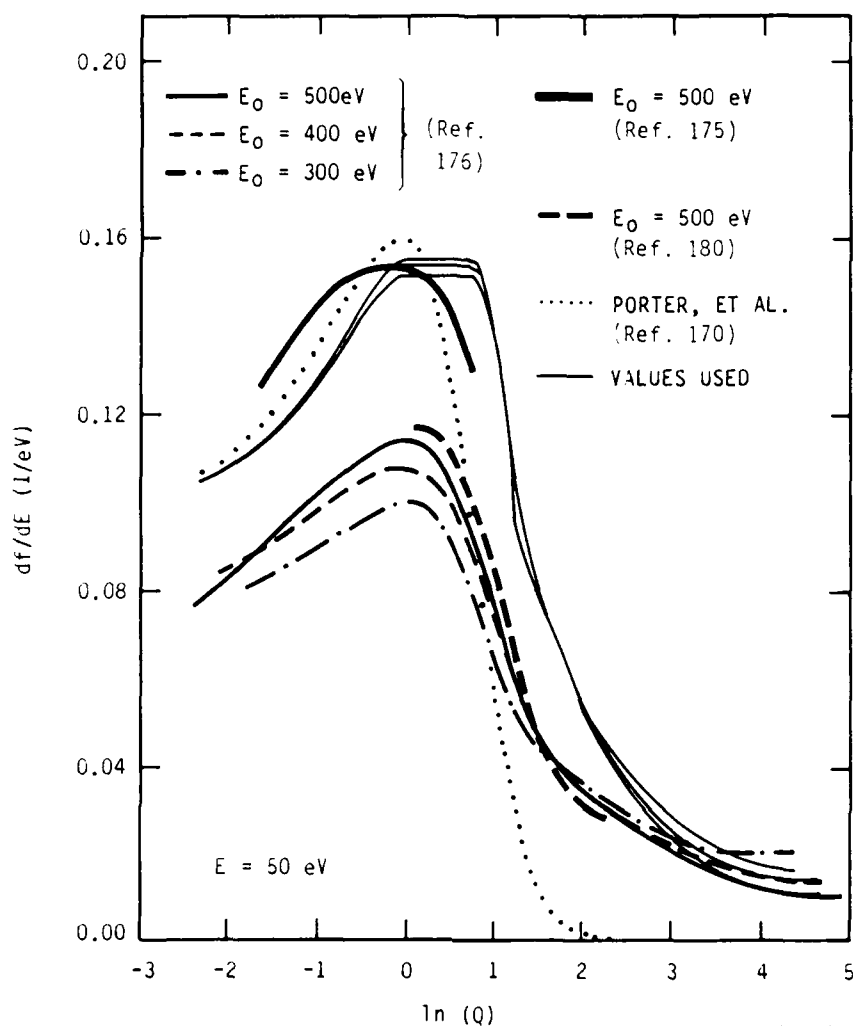


Figure 161. Generalized oscillator strength versus the square of the momentum transfer for 50 eV energy loss. The heavy lines represent experimental data. The dotted line and the light lines represent values used in simulations.

$df/dE$  is smaller than the  $df/dE$  value at low  $Q$ , the line for 300 eV has the largest values and the line for 500 eV has the lowest. In the peak of the Bethe ridge in Figures 161 and 162, the  $df/dE$  values are highest for the 500 eV data. The effect of the different GOS distributions is that the modified GOS gives an angular distribution that favors scattering at larger angles than that given by PJG. This difference is small for small  $E$  values, but it



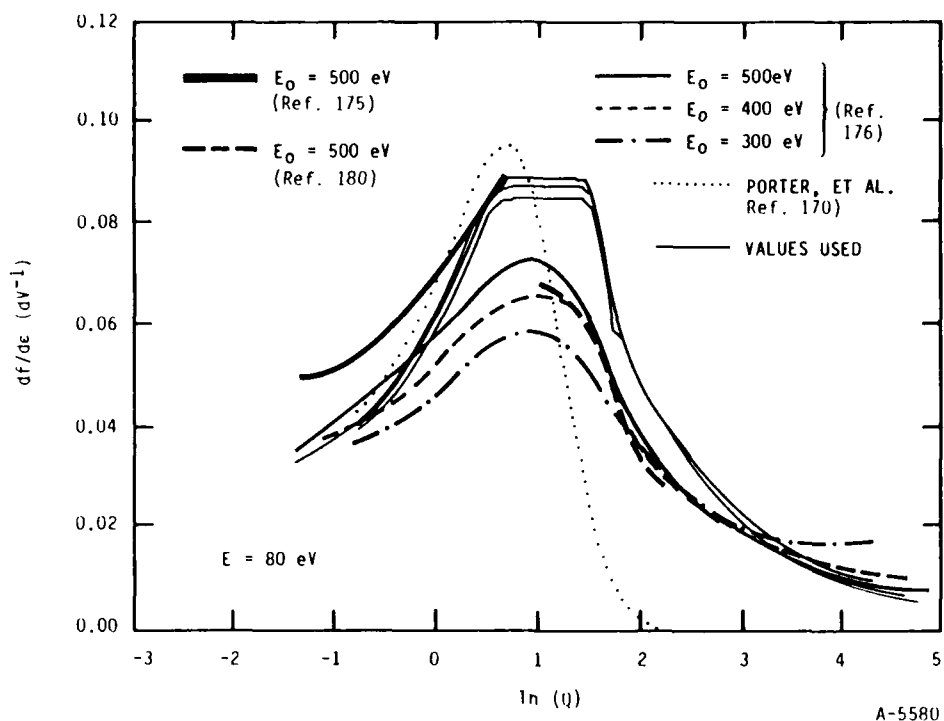


Figure 162. Generalized oscillator strength versus the square of the momentum transfer for 80 eV energy loss. The heavy lines represent experimental data. The dotted line and the light lines represent values used in simulations.

is significant for  $E > 2I$ . The relative  $\sigma(E_0, E_j, \theta)$  distribution for excitation collisions (where  $E_j = 12$  eV) is approximated by using the distribution calculated for  $E_j = 17.6$  eV.

#### 14.6 EXCITATION BY FAST SECONDARY ELECTRONS

We need to follow only the secondary electrons that have sufficient energy to excite 391 nm reduction, i.e., energies above 18.8 eV. These fast secondary electrons will lose energy by exciting and ionizing the nitrogen molecules. The total cross section for electronic excitation and ionization has a broad maximum around 100 eV, so that the range of the fast secondary electrons will be rather short for all except the highest-energy secondaries. These secondary electrons will tend to be produced with a velocity vector perpendicular to the primary beam. We have used the parameterization of PJG, their

Eq. (15), to describe the angular distribution of the secondary electrons formed when a primary electron loses an energy  $E$  in an ionization event. We have used  $I = 15.6$  eV to represent all ionizations, and this should be the most probable ionization event.

The calculation follows the trajectory of the primary electron as it undergoes elastic and inelastic scattering events. Each time an inelastic event occurs, we check if a fast secondary electron is formed. If a fast secondary is formed, we use the angular distribution of the angle of the secondary electron and a random number to find the direction cosines of the secondary. We then consider that the fast secondary electron will produce the same excitation as would a primary electron that has the same energy. Thus, we build up results by starting with low-energy primaries that do not produce any fast secondaries. As we increase  $E_0$ , we form fast secondaries whose initial energies correspond to  $E_0$  values used for low-energy primaries. The contribution of the fast secondaries depends on the distance from the position of the formation of the secondary to the point of interest. Thus for each formation of a fast secondary electron, we calculate the contribution to each radial value at several planes passing perpendicular to the initial beam direction. This is done by transforming the  $z, x, y$  coordinates of a point of interest (where the  $z$  distance is along the direction of the primary beam) into the  $z', r'$  cylindrical coordinates along the direction of the fast secondary electron and using the previously calculated 391 nm excitation for an electron that has the same kinetic energy as the secondary.

#### 14.7 CROSS SECTIONS FOR EXCITATION OF 391 nm RADIATION BY FAST SECONDARY ELECTRONS

As a result of exciting 391 nm radiation by electrons with different energies, we must correct for the different values of  $\sigma_{391}$ . We have used the  $\sigma_{391}$  values of Borst and Zipf.<sup>85</sup> The contribution to excitation for each secondary electron energy  $E_0'$  is computed by multiplication of the excitations produced by primaries at  $E_0$  by the ratio  $\sigma_{391}(E_{0i})/\sigma_{391}(E_0')$ , where  $E_{0i}$  is the

initial energy of the primaries at  $z = 0$ . In practice we changed the weighting factor for primary electrons only after they had been slowed so that their energy was reduced by approximately 30 percent. Changing the weighting factor at smaller energy steps would flatten the simulated  $G(r)$  distributions, because the electrons that are scattered to large  $r$  values have had more collisions than the electrons that remain at small  $r$  and because  $\sigma_{391}$  is larger for smaller  $E_0$ . However, the current steps are such that new  $\sigma_{391}$  values are used when they have changed by 25 to 37 percent, and the effect of increasing the number of steps should be rather less than this due to averaging effects. Also, this effect would be smaller for the 30 mtorr simulations, where in the case of 6 keV primaries, 98 percent of the electrons at  $z = 50$  cm have energies above 90 percent of the primary energy. For 2 keV primaries, the corresponding fraction is 71 percent.

#### 14.8 RESULTS

As discussed above, the experimental  $G(r)$  values are flatter than can be explained by the results of the simulations using only elastic scattering. However, inelastic scattering has a comparable cross section, so we should expect further broadening of the beam - even if the inelastic scattering is peaked in the forward direction. Furthermore, the broad wings of the distribution (where the  $G(r)$  values are down by 1 to 3 orders of magnitude from the values along the beam axis) have a significant contribution from fast secondaries.

Figures 163 through 165 show the results of the full simulation at the three primary energies of 2, 4.5, and 6 keV, respectively. In each figure the simulation results are shown for the two  $N_2$  pressures of 30 and 60 mtorr. For each energy the 60 mtorr simulation is flatter than the 30 mtorr simulation. However, the experimental data are consistently flatter than the simulated values. If we adjust the arbitrary  $y$  values in the figures so as to find which experimental data match the 60 mtorr simulations, we find that there is a fair match with the experimental data at 40 to 50 mtorr for each energy.

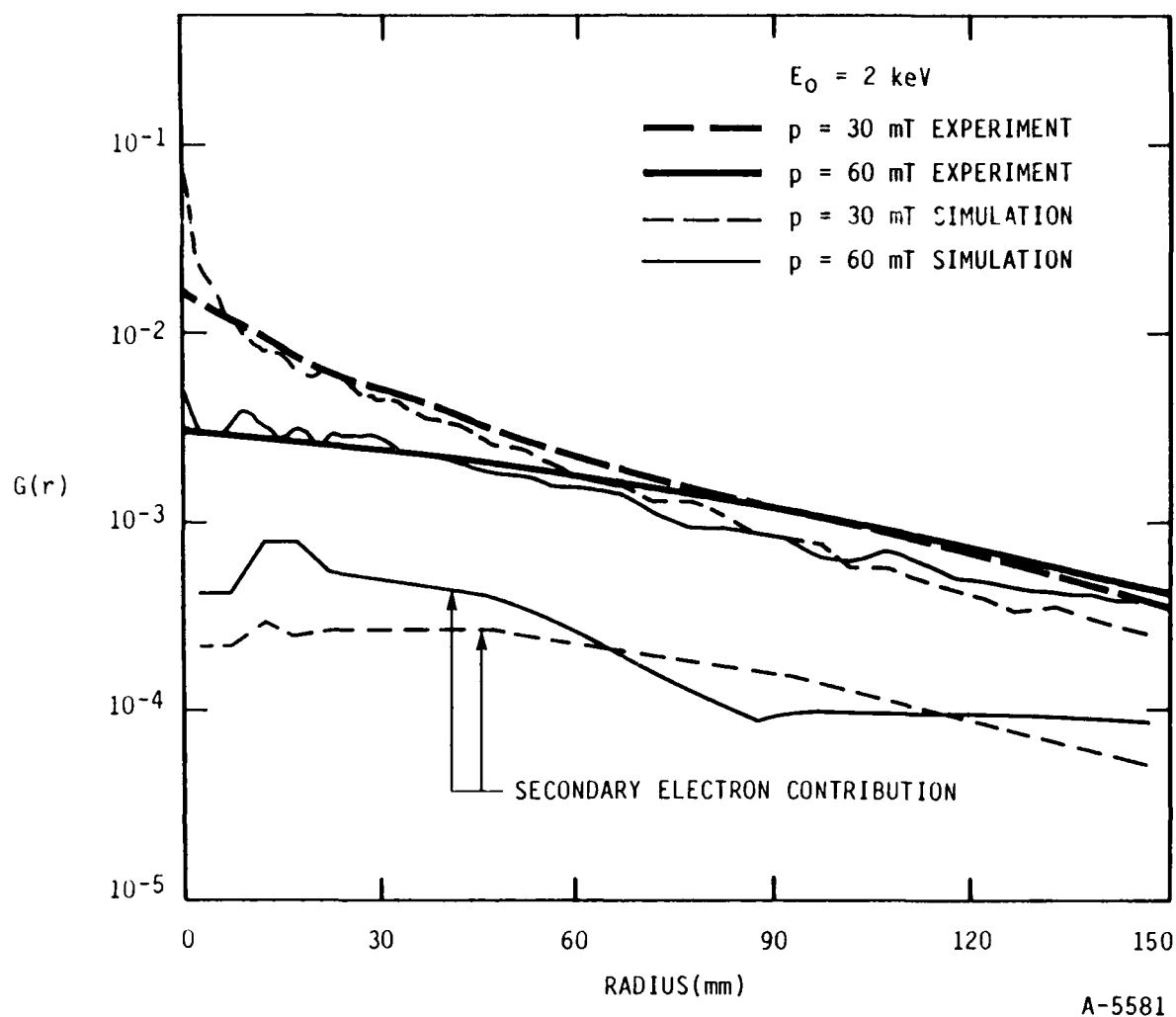


Figure 163. Comparison of simulated and experimental radial distribution for the two  $N_2$  pressures of 30 and 60 mtorr. The contributions from secondary electrons to the simulations are also shown. The primary electron energy is 2 keV.

Figures 163 through 165 also show the contribution of the fast secondaries at the two  $N_2$  pressures. These curves fall off more slowly with increasing  $r$  than do the contributions from the primary beam. Thus another way to achieve agreement between the simulations and the data would be to increase the contribution from the secondaries. This would occur if the cross section for excitation of the 391 nm radiation were decreased for the high-energy primary

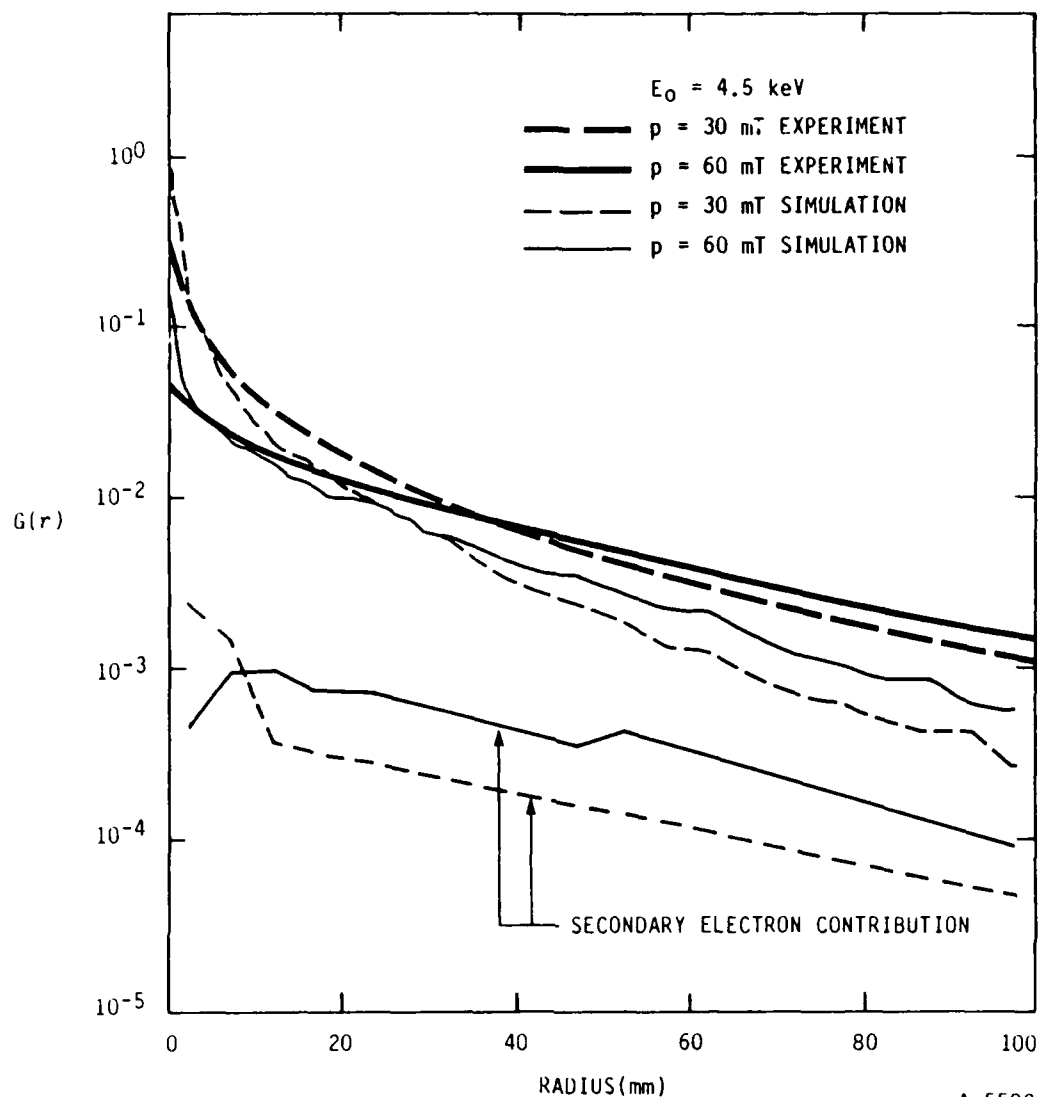


Figure 164. Comparison of simulated and experimental radial distributions for the two  $N_2$  pressures of 30 and 60 mtorr. The contributions from secondary electrons to the simulations are also shown. The primary electron energy is 4.5 keV.

secondary electrons relative to the cross sections for the low-energy electrons. The fast secondaries only contribute some 7 to 23 percent to the simulated results at large  $r$ , so a substantial change in the  $\sigma_{391}$  ratio would be necessary to make a significant effect. However an increase by a factor of two in the contribution from fast secondaries would bring the simulated curves nearly into agreement with the data for the case of 2 keV primary electrons. It would substantially reduce the disagreement for the higher-energy cases.

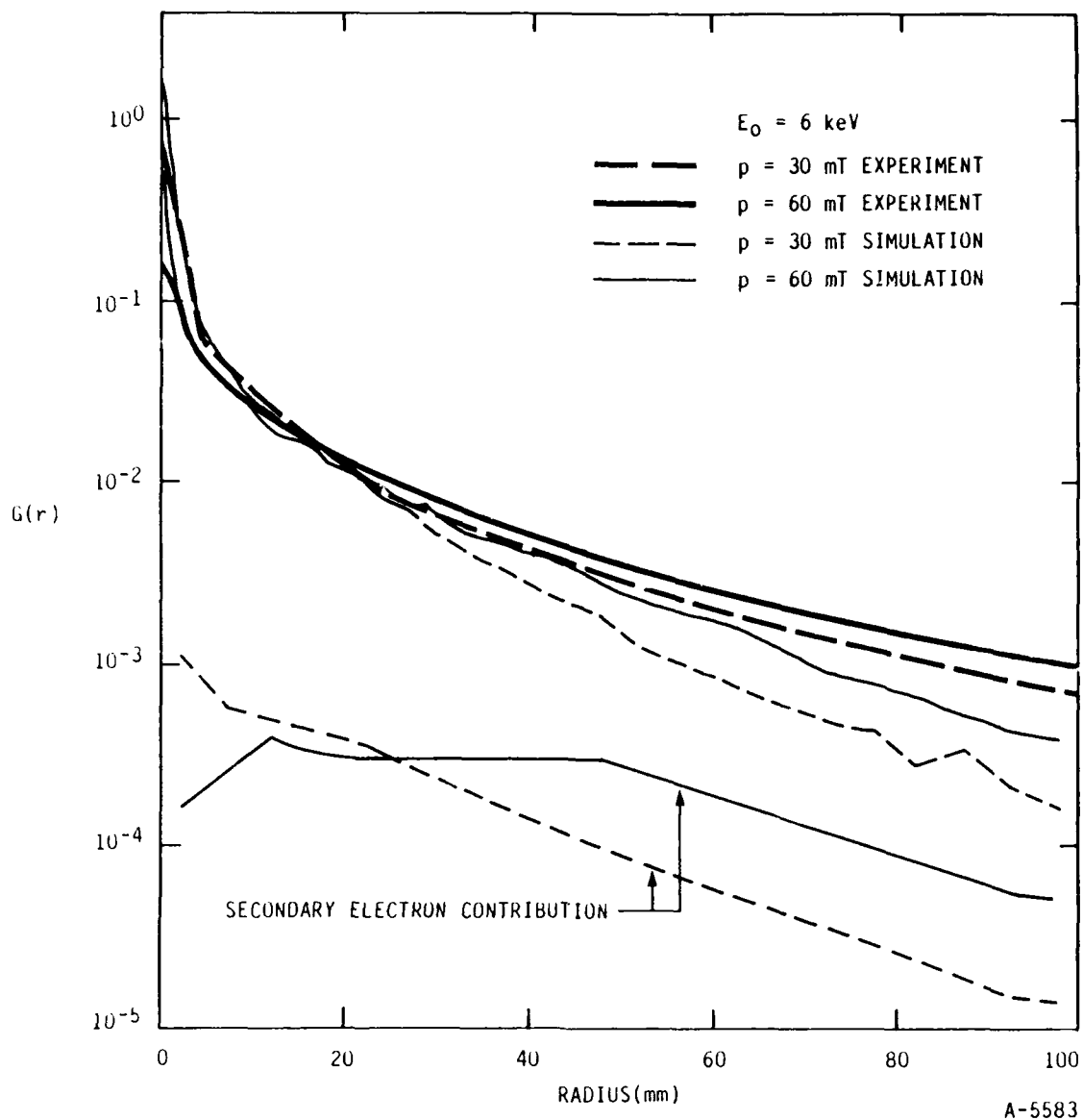


Figure 165. Comparison of simulated and experimental radial distributions for the two  $N_2$  pressures of 30 and 60 mtorr. The contributions from secondary electrons to the simulations are also shown. The primary electron energy is 6 keV.

#### 14.9 SENSITIVITY TO RELATIVE ANGULAR DISTRIBUTIONS

As discussed above, the original GOS surface of PJG has several deficiencies, but the results are not very sensitive to the exact form of the GOS used. Figure 166 shows a comparison of the simulations at 2 keV that result: a) from using the original PJG GOS values to estimate the inelastic scattering angular

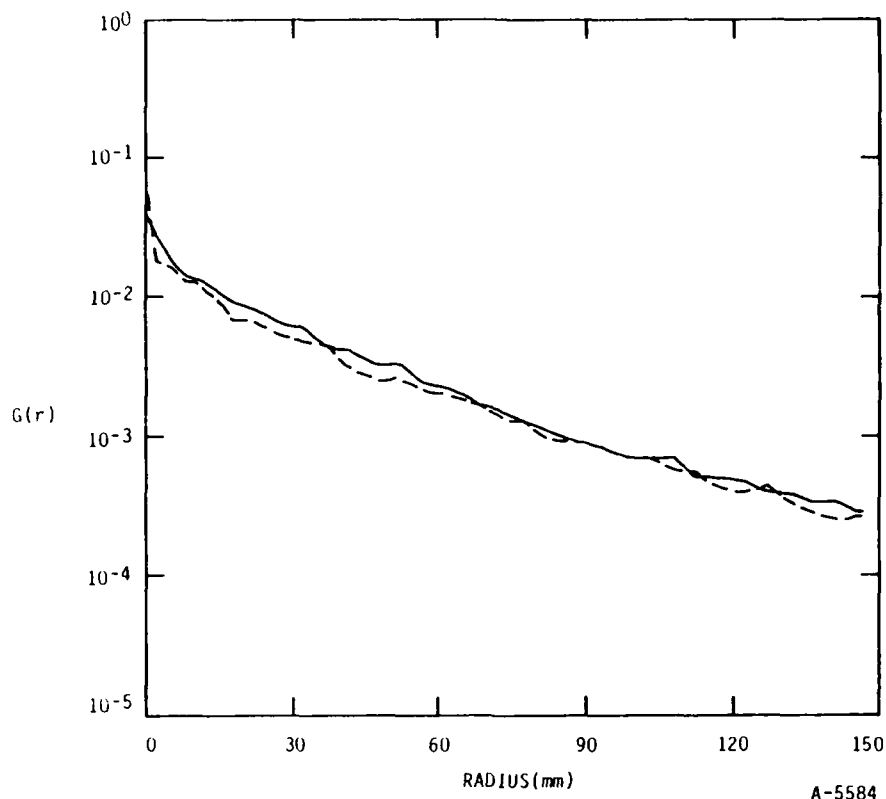


Figure 166. Comparison of different inelastic angular distributions to simulate the radial distribution for 30 mtorr  $N_2$  pressure at a primary energy of 2 keV. The solid curve uses the angular distribution derived from the Porter, Jackman, and Green<sup>170</sup> GOS distribution. The dashed curve uses the modifications discussed in the text.

distribution; or b) from using the modified GOS discussed above that gives the results shown in Figures 160 to 162. In both simulations, we used the elastic scattering angular distribution given by JG, and the absolute cross sections are the same. The simulations for the other energies are even closer than those in Figure 166. Thus the simulation is not sensitive to the shape of the GOS used, and further refinements of the GOS versus  $\ln(Q)$  curves are not likely to improve the fit very much.

The results are only moderately sensitive to the exact form of the the elastic scattering angular distribution. That is, the minor modification of changing  $\sigma_{el}(\theta)$  given by JG to make  $\sigma_{el}$  constant for  $\theta$  between 0 and 3 deg has only a minor effect on the simulations, as we would expect from Figure 159. However, a more drastic change of

$$\begin{aligned} &\text{for } E_0 > 900 \text{ eV,} \\ &\sigma_{el}(\theta) = \sigma_{el}(5^\circ), \quad \theta < 10^\circ \\ &\sigma_{el}(\theta) = \sigma_{el}(\theta - 5^\circ), \quad \theta > 10^\circ \end{aligned}$$

makes a large enough change to bring the simulations into fair agreement with the data, with the 2 keV case shown in Figure 167. Now the major disagreement is that the simulations are sharper than the data near the beam axis. Thus the simulation has enough sensitivity to the shape of the elastic scattering angular distribution that using distributions that are somewhat flatter than the measured values would be enough to bring the simulations and the data into agreement.

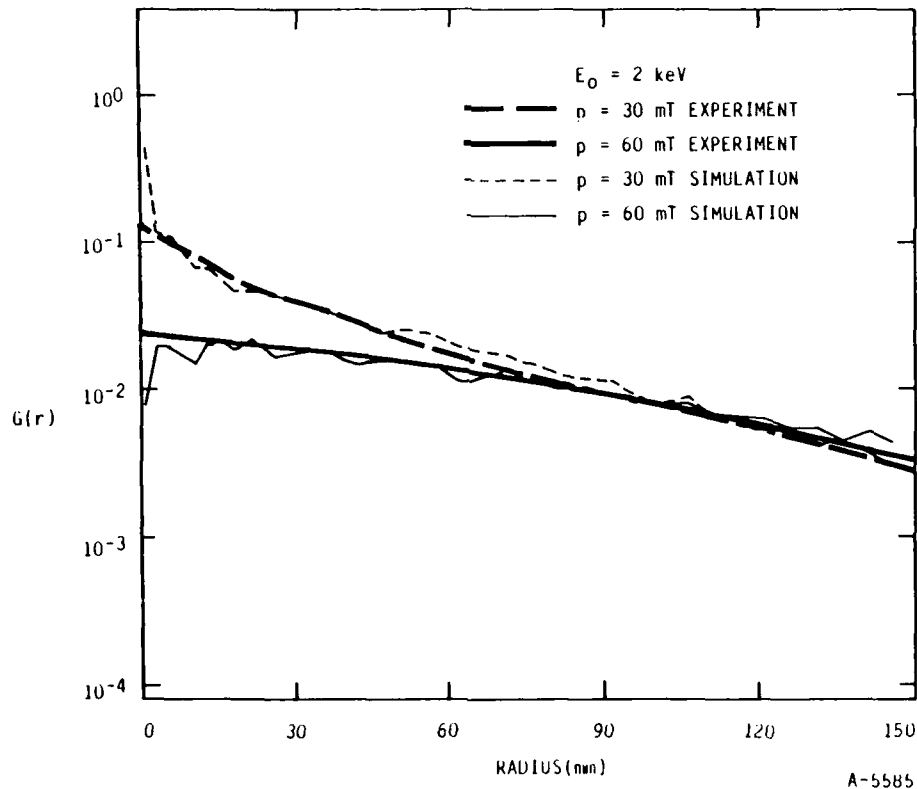


Figure 167. Comparison of simulated and experimental radial distribution for the two  $N_2$  pressures of 30 and 60 mtorr. The primary electron energy is 2 keV. These simulations used a flattened angular distribution for elastic scattering.



#### 14.10 SENSITIVITY TO ABSOLUTE CROSS SECTIONS

When the total cross section for any one process is changed by a value consistent with the 10 to 20 percent variation that we have between our calculated values and the recommended values show in Figure 158, then the simulated results are not changed very much. In Figure 168 we show the effects of increasing the total cross section by 20 percent for  $E_0$  values greater than 1 keV, while keeping  $\sigma_{\text{tot}}$  ( $E_0 < 1$  keV) the same. With larger changes in  $\sigma_{\text{tot}}$ , it is possible to make the simulations agree reasonably well with the data. However, this requires increasing  $\sigma_{\text{tot}}$  by about 50 percent. This adjustment is too large to be consistent with the uncertainties in the cross sections or in the experimental measurement of the pressure in the chamber. Note that the

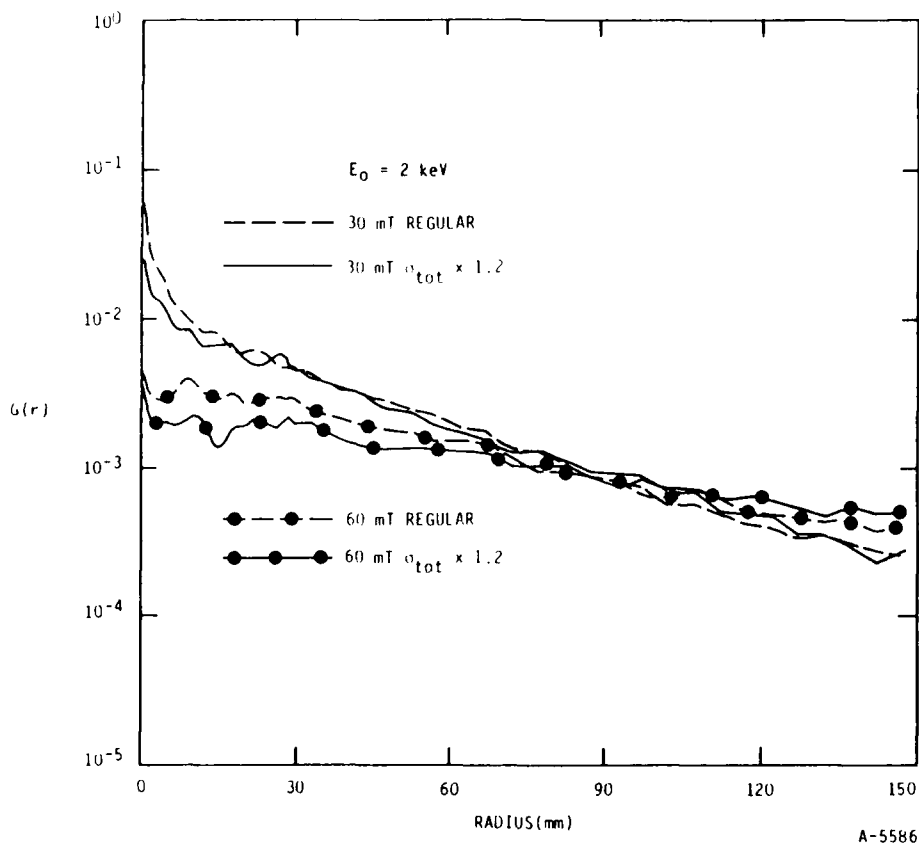


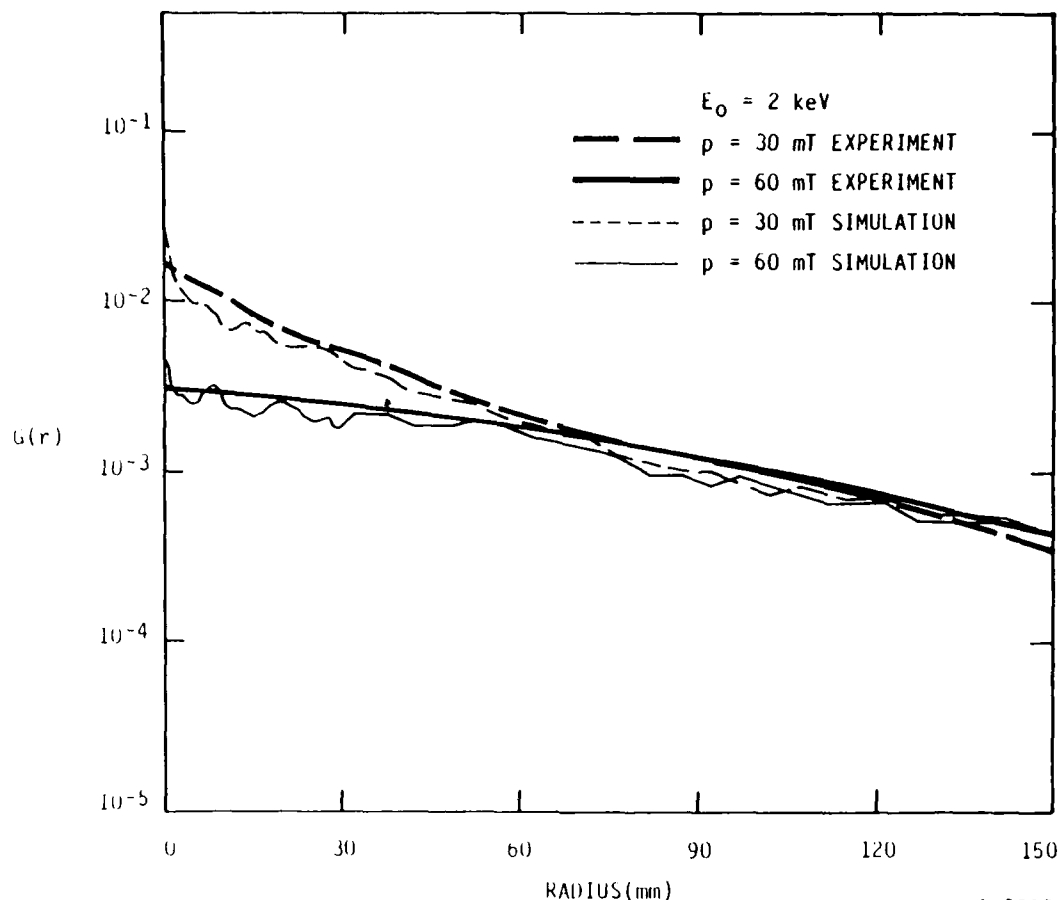
Figure 168. Effect of increasing the total cross section by 20 percent for the two  $N_2$  pressures of 30 and 60 mtorr at a primary energy of 2 keV.

presence of a significant pressure of gas in the electron-gun region of the chamber would contribute to the experimental error in the measure of the product of the number density times the pathlength. We estimate these effects to be 5 percent or less.

If we decrease  $\sigma_{391}$  for the higher  $E_0$  values, the effect is to increase the relative importance of the excitation of 391 nm radiation by the fast secondaries. As can be seen in Figures 163 through 165, such an increase will make the  $G(r)$  distributions flatter in the simulations, which will agree with the data better. Furthermore, if we increase  $\sigma_{e1}$  and  $\sigma_{in}$  at the same time that we decrease  $\sigma_{391}$  for the higher values of  $e_j$ , then we can get reasonable agreement between the simulations and the data. This is shown in Figures 169 and 170, where we compare the data with simulations where for  $E_0 > 1$  keV, the  $\sigma_{e1}$  values are increased by 20 percent, the  $\sigma_{in}$  values are increased by 30 percent, and the  $\sigma_{391}$  values are decreased by 20 percent. Note that the increase in  $\sigma_{in}$  by a larger amount than  $\sigma_{e1}$  has the effect of increasing the importance of secondary electrons. The comparisons show that the fit with the 2 keV data is good, but the simulations for the higher energies falls off too rapidly as  $r$  increases. Thus, we can begin to get fair agreement with the data if the measured pressure and/or the scattering pathlength are smaller than the actual values and/or the cross sections for  $\sigma_{e1}$  and  $\sigma_{in}$  are low while the relative shape of the Borst and Zipf<sup>85</sup>  $\sigma_{391}$  cross sections gives too large  $\sigma_{391}$  for the large  $E_0$  values.

#### 14.11 GENERAL FEATURES OF COMPARING THE SIMULATIONS AND THE DATA

In the comparisons presented above, there are some common features. One feature is that the simulations tend to show  $G(r)$  distributions that are sharper as  $r$  goes to zero than are the data. Another feature is that the simulations show a steeper  $r$  dependence than do the data for larger values of  $r$ . That is, the simulations correctly predict a large fall-off of  $G(r)$ , but the predicted fall-off is somewhat greater than what is observed. The discrepancies are about a factor of three in a decay that is more than a factor



A-5587

Figure 169. Comparison of simulated and experimental radial distributions for the two  $N_2$  pressures of 30 and 60 mtorr. The primary electron energy is 2 keV. The cross sections in the simulations have been adjusted to increase  $\sigma_{el}$  by 20 percent, increase  $\sigma_{in}$  by 30 percent, and decrease  $\sigma_{391}$  by 20 percent.

of 100. The simulations would match better if they included a larger contribution from the excitation of 391 nm radiation by fast secondary electrons. Alternatively, the simulations would agree better if the relative elastic scattering distributions for the primary electrons are significantly flatter than distributions given by JG. This flattened distribution matches experimental values reasonably well for larger scattering angles. Another factor that would contribute to a better match would be larger  $\sigma_{tot}$  values, especially for  $E_0 > 1 \text{ keV}$ , and especially if  $\sigma_{in}$  is larger. This effect could occur if the experimental pressure measurements or pathlength were low.

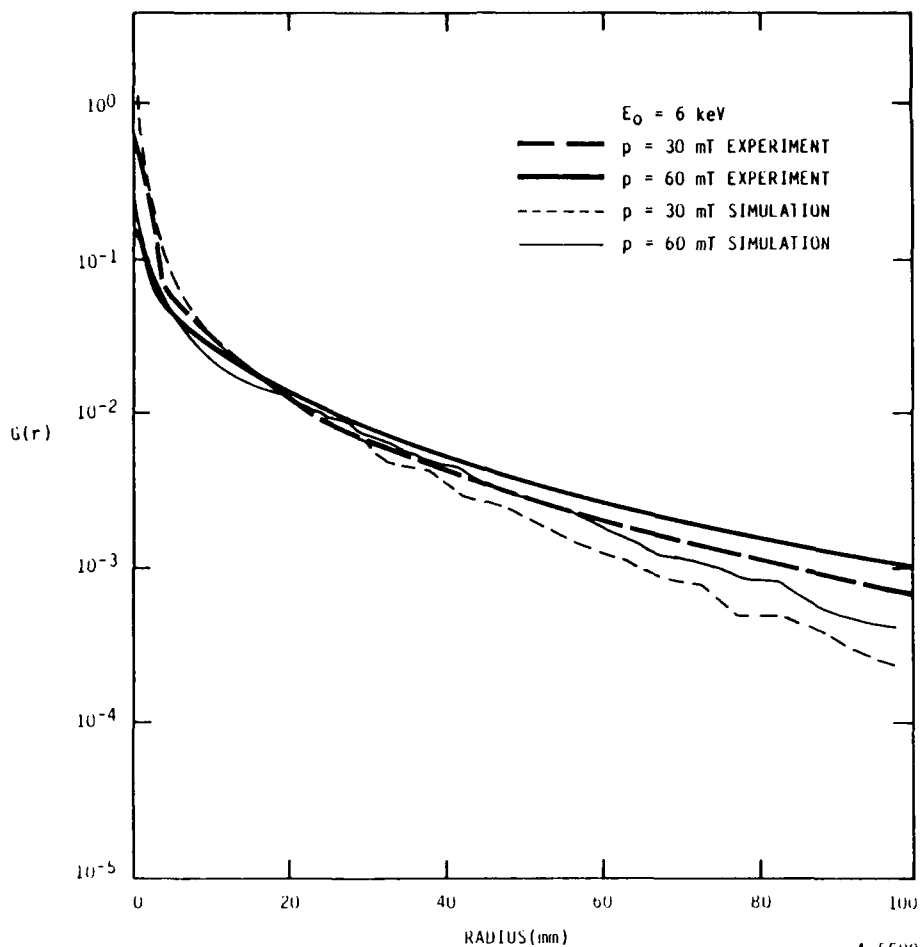


Figure 170. Comparison of simulated and experimental radial distributions for the two  $N_2$  pressures of 30 and 60 mtorr. The primary electron energy is 6 keV. The cross sections in the simulation have been adjusted to increase  $\sigma_{e1}$  by 20 percent, increase  $\sigma_{in}$  by 30 percent, and decrease  $\sigma_{391}$  by 20 percent.

#### 14.12 OTHER POSSIBLE CAUSES OF FLAT $G(r)$ DISTRIBUTIONS

The steeper  $G(r)$  distributions for the simulations may be a result of the many approximations that have been made. For example, our approximation to ignore fast secondaries beyond cut-off values of  $r'$  and  $z'$  will reduce the contribution from fast secondaries. Also, using finer grids for the various parameters (e.g., more angles for the contribution of each fast secondary, more values of the energies of the fast secondaries, more trajectories, etc.) may result in better agreement. We have investigated these effects over a limited

range. The residual differences between the simulations and the data could be the result of a combination of several approximations, as several effects tend to produce flatter distributions, e.g., lower energy electrons tend to have angular distributions that are less strongly peaked at forward scattering, so changing the angular distribution at closer energy spacings should contribute to a broader  $G(r)$  distribution, as would changing the  $\sigma_{391}$  values at smaller energy steps, or including secondary electrons formed beyond the cutoff ranges used for  $r'$  and  $z'$ .

The simulations include the effects of secondary electrons that are produced at  $z$  values greater than the 50 cm value where we compare with our measurements. The maximum  $z$  value considered is 50 cm for  $E_0 < 2$  keV, and 70, 80, and 90 cm for  $E_0 = 2, 4.5$ , and 6 keV, respectively. Secondaries formed at even larger  $z$  values will make only a small contribution, but this contribution would make the  $G(r)$  distribution flatter. We do not expect a significant contribution from electrons that travel the full 90 cm length of the chamber and then reflect so that they travel an additional 40 cm back to the  $z = 50$  cm plane.

We have investigated the effects on the simulations of using an electron beam with a wider Gaussian shape. As expected, the result is that the sharpness of the peak in  $G(r)$  at  $r=0$  can be reduced as we make the beam broader. At  $r$  values larger than 20 to 30 mm, the broader beam simply smooths the bumps on the curve. In the experiment, the photomultiplier travels nearly perpendicular to the direction of the primary beam, and although an error analysis of this viewing configuration on the Abel inversion yielded insignificant errors, the geometry of detector and beam may also contribute to a slower approach to  $r=0$ .

The simulation ignores the effects due to magnetic fields. The observed curvature of the electron beam indicates that there were residual magnetic fields on the order of 0.2 Gauss. Such a field will produce a 11.3m radius of curvature for an electron with an energy of 4.5 keV and a radius of curvature

of 1.13m for a 45 eV electron. As a 4.5 keV electron has a mean free path between collisions of about 16 cm and a 45 eV electron has a mean free path around 0.9 cm, we see that there will be very little curvature in the path between collisions. The curvature of the beam does cause the photomultiplier scan to be not exactly perpendicular to the beam direction, and this could contribute to reducing the sharpness of  $G(r)$  at small  $r$  values.

Another possible effect of a residual magnetic field would be to create a beam plasma discharge. Such discharges have been studied in the apparatus, and care was taken to avoid the parameter ranges where this occurs. That is, the experiments were done with combinations of lower magnetic fields, lower currents, and higher pressures than were used when a beam plasma discharge occurred. However, workers using lower gas pressures have observed that the electron beam develops broad wings at currents somewhat less than the threshold for a true beam plasma discharge (e.g., Bernstein, et al.).<sup>181</sup> Thus it is possible that there may be a slight broadening of the beam considerably below the beam plasma discharge onset. As the onset of the true beam plasma discharge occurs over a narrow current range, more evidence is necessary before assigning the extra broadening to an incipient beam plasma discharge. However, the primary beam will create ions along the central core, and this plasma may have instabilities excited that could perturb the electron radial distribution so as to broaden it enough to be detected. Recall that at large distances off-axis we are looking at excited state populations that are only 1 percent of the central beam.

#### 14.13 SUMMARY AND CONCLUSIONS

We report here experimental observation of 2 to 6 keV electron scattering by  $N_2$  in the 20 to 70 mtorr pressure regime. Our diagnostic of electron density is emission from the ionic B-state at 391 nm. A scanning photometer transversed the beam at several axial locations. In this configuration we observe the fluorescence from all processes occurring at these pressures, including

elastic and inelastic primary and secondary electron scattering. This experimental approach complicates the subsequent analysis, but permits assessment of the magnitudes of the relative processes. Previous data and modeling of the total and differential angular cross sections for both elastic and inelastic scattering processes were used as input into a detailed Monte Carlo simulation. This simulation permitted comparison with local electron densities derived from the data. Although some adjustments to literature values seem warranted, agreement was generally good. A sensitivity analysis was used to bound possible adjustments to the cross sections consistent with the data. Residual discrepancies in the width of the central core and in the magnitude of scattering at the wings could not be reconciled. The latter effect represented a factor of three discrepancy for electron concentration  $10^{-3}$  of the central core. Several potential sources for additional scattering at these large distances off axis are presented.

## 15. MODELING OF THE PRODUCTION OF VIBRATIONALLY EXCITED NH IN N<sub>2</sub>/H<sub>2</sub> MIXTURES

### 15.1 MODEL DESCRIPTION

To provide insight to the interpretation of experimental results on the emission from vibrationally excited NH radicals produced when 40-keV electrons interact with a mixture of N<sub>2</sub> and H<sub>2</sub>, we modeled the ongoing chemistry using the PSI kinetics code.<sup>182</sup> The PSI kinetics code is a driver program to use the CHEMKIN general purpose chemical kinetics software package of subroutines.<sup>183</sup> We solve the rate equations to find the concentrations of all species in the mechanism scheme as a function of time. This program takes as input the production rates of the species created by the action of the fast electrons. These production rates were estimated by calculating the initial yields of active species produced in pure N<sub>2</sub> by using a detailed microscopic calculation that uses electron impact cross sections to estimate the production of the various excited and ionized states.<sup>26</sup> The electron cross sections are from Jackman, et al.<sup>27</sup> We assume that most of the excited states of N<sub>2</sub> either dissociate or radiate rapidly enough that they have very low steady state concentrations and do not participate in the reaction scheme. Thus we follow N atoms, N(<sup>2</sup>D) atoms, N(<sup>2</sup>P) atoms, N<sub>2</sub><sup>+</sup>, N<sup>+</sup>, and N<sub>2</sub>(A<sup>3</sup>Σ<sub>u</sub><sup>+</sup>) species (in addition to the N<sub>2</sub> ground state). All other N<sub>2</sub> states are assumed to decay to form these species with some yield. The initial yields of the active nitrogen species are found by using a modification of the branching ratios given by Porter, Jackman, and Green,<sup>170</sup> (PJG), where the a<sup>1</sup>Π<sub>g</sub> state is assumed to be quenched, the yields of the Rydberg states are adjusted, and the yields of other states reduced to 30 percent of the PJG values to account for quenching by the nitrogen - adjustments that were necessary to explain the N production observed at pressures of 1 atm.<sup>182</sup> At the pressures of 4 to 30 torr of the present experiments, these adjustments may underestimate the N atom production rate, and this uncertainty adds to the uncertainty in the estimate of the dose rate. Table 27 gives the estimates of the g-values from the calculation, where the g-value for any species is the number produced when 100-eV of energy is



TABLE 27. Estimates of the initial yields of active species, expressed as g-values (number/100 eV).

Species	N	N( <sup>2</sup> D)	N( <sup>2</sup> P)	N <sub>2</sub> (A <sup>3</sup> Σ <sub>u</sub> <sup>+</sup> )	N <sub>2</sub> <sup>+</sup>	N <sup>+</sup>	e
9	0.86	0.66	0.049	0.69	2.15	0.54	2.70

absorbed. The hydrogen species g-values were estimated from the nitrogen species by assuming that  $g(H)$  is proportional to  $g(N) + g(N(^2D)) + g(N(^2P))$ , that  $g(H_2^+)$  is proportional to  $g(N_2^+)$ , and that  $g(H^+)$  is proportional to  $g(N^+)$ . The proportionality constant is taken as the electron fraction, i.e., 1/7th of the pressure ratio  $P_{H_2}/P_{N_2}$ . This crude estimate should be adequate, as the mixtures contain only a small amount of H<sub>2</sub>.

In order to estimate the dose rate, we need to know the energy absorbed per gram of gas. We do this by estimating the volume of gas that interacts with the electrons. As the electrons traverse the gas the primary electrons are scattered and fast secondary electrons are formed, so that the diameter of the beam grows. We consider that the overall shape of the electron-interaction volume is a cone, with the apex at the entrance to the gas cell. Two different methods were used to estimate the dose rate. One method was to assume that the power absorbed in the experimental chamber of length  $L_e$  was proportional to the cell length, with the fraction of the power absorbed equal to  $L_e/L_r$ , where  $L_r$  is the range that the electrons travel. The range was estimated from

$$L_r = 2.60 E^{1.75}/P \quad , \quad (65)$$

where  $L_r$  is in cm,  $P$  is the pressure in torr, and  $E$  is the electron energy in keV.<sup>184</sup> In addition, we assume that the radius of the cone with length  $L$  is equal to twice the radius  $r_{1/2}$ . Here  $r_{1/2}$  is the radius of the cone that encompasses 1/2 of the total beam current, which is calculated from the empirical relation found by Center,<sup>185</sup>

$$r_{1/2} = L \tan \theta_{1/2} \quad , \quad (66)$$

with  $\theta_{1/2}$  given by

$$\theta_{1/2} = A (NL)^{1.5} / (1 + B N L) \quad , \quad (67)$$

where  $N$  is the gas number density,  $A = 1.0 \times 10^{-28} \text{ cm}^3$  and  $B = 1.43 \times 10^{-18} \text{ cm}^2$ . Table 27 gives the values of  $L_T$ , as well as volume of the cone  $V(L_e)$ , when  $L_e$  is 16 cm. This volume increases as the pressure increases, approximately as  $P^{1.2}$ . The density of the gas increases as  $P$ , so that the mass of the absorbing gas increases as  $P^{2.2}$ . The energy absorbed in the experimental chamber increases as  $P$  [see Eq. (65)], so that the dose rate is approximately proportional to  $P/P^{2.2} = P^{-1.2}$  for this set of assumptions. In Table 28, these dose rates are labeled "lin.", as they result from the linear power absorption assumption. Table 28 gives dose rates in kGy/s (1 kGy = 1 J/g), for 2 mA, 40 keV electron pulses. Another way to estimate the dose rate is to assume that the energy absorbed in the chamber is proportional to the ratio of the volume of the cone at length  $L_e$  (the volume of absorbing gas in the experimental chamber) to the volume of the cone that represents the full range of the electrons. This has a length  $L_T$  and a cone radius that is twice the  $r_{1/2}$  given by Eq. (66) (the volume of the gas to absorb all of the electron energy). Table 28 gives these volumes  $V(L_T)$ , which are proportional to  $P^{-3}$ . Thus the absorbed energy is approximately proportional to  $P^{1.2}/P^{-3} = P^{4.2}$ , and the dose rate is proportional to  $P^{4.2}/P^{2.2} = P^2$ . This dose rate is labeled "vol.", as it represents the assumption that the dose is proportional to the volume. The two different assumptions give a wide range to the estimated dose rate. We expect to use experimental data on the relative signal levels at the different gas pressures to refine the dose rate estimates. Comparisons with data indicate that the dose rate is between the two estimates given. At the present time, we use a dose rate estimated as the linear assumption result multiplied by the pressure (normalized at 30 torr); these values are labeled "trial" in Table 28. Thus, the two assumptions give pressure dependences of  $P^{-1.2}$  and  $P^2$ , and the trial assumption has  $P^{-0.2}$ .

TABLE 28. Dose rate estimates for various N<sub>2</sub> pressures.

Quantity	4.0	7.5	10.0	15.0	20.0	30.0
$L_F$ , cm	414.0	221.0	165.0	110.0	82.7	55.1
$r_{1/2}(L_e)$ , cm	1.20	1.87	2.25	2.88	3.41	4.31
$V(L_e)$ , cm <sup>3</sup>	96.7	235.0	339.0	557.0	781.0	1231.0
Absorbed E/s, J/s	3.10	5.80	7.74	11.6	15.5	23.2
Lin. dose rate, kGy/s	5341.0	2202.0	1523.0	927.0	661.0	415.0
$r_{1/2}(L_F)$ , cm	228.0	122.0	91.2	60.8	45.6	30.4
$V(L_F)$ , 10 <sup>5</sup> cm <sup>3</sup>	900.0	137.0	57.6	17.1	7.20	2.13
Absorbed E/s, 10 <sup>-4</sup> J/s	0.860	13.7	47.1	261.0	868.0	4664.0
Vol. dose rate, kGy/s	0.148	0.522	0.927	2.09	3.71	8.34
Trial dose rate, kGy/s	712.0	550.0	508.0	464.0	441.0	415.0

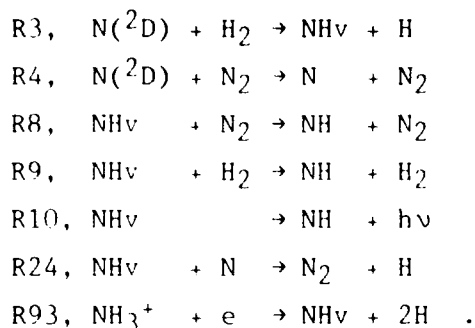
During the electron pulse, there is production of the active species of N, N(<sup>2</sup>D), N(<sup>2</sup>S), N<sub>2</sub>(A<sup>3</sup>Σ<sub>u</sub><sup>+</sup>), N<sub>2</sub><sup>+</sup>, N<sup>+</sup>, H, H<sub>2</sub><sup>+</sup>, and H<sup>+</sup>. These species then react to form other species. We considered around 95 reactions, and the rate constants for 50 of the more important are given in Table 29. In Table 29 we have assumed values for rate constants for reactions 8-10, and we have assumed that NHv reacts with the same rate constant as NH. The other rate constants come from the literature, from such sources as Duley and Williams,<sup>186</sup> Schofield,<sup>187</sup> Smith et al.,<sup>188</sup> Cohen and Westberg,<sup>189</sup> Piper et al.,<sup>190</sup> and Albritton.<sup>191</sup> The basic mechanism has the following reactions which dominate:

TABLE 29. Major reactions considered.

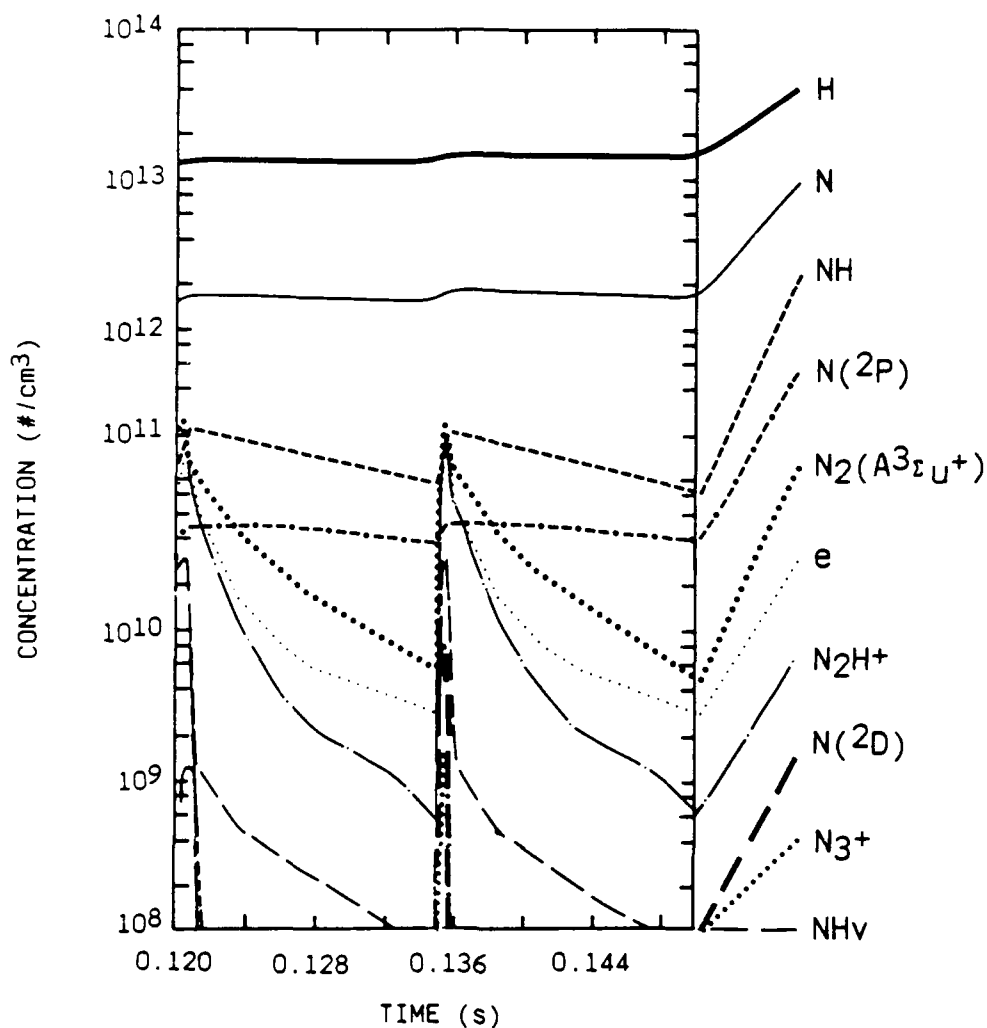
1.	2N	+ M	→ N <sub>2</sub>	+ M	8.30 × 10 <sup>-34</sup> exp(500./T)
3.	N( <sup>2</sup> D)	+ H <sub>2</sub>	→ NHv	+ H	2.30 × 10 <sup>-12</sup>
4.	N( <sup>2</sup> D)	+ N <sub>2</sub>	→ N	+ N <sub>2</sub>	9.40 × 10 <sup>-14</sup> exp(-510./T)
5.	N( <sup>2</sup> P)	+ N <sub>2</sub>	→ N	+ N <sub>2</sub>	2.00 × 10 <sup>-18</sup>
6.	N( <sup>2</sup> P)	+ N	→ 2N		1.00 × 10 <sup>-12</sup>
7.	N( <sup>2</sup> P)	+ H <sub>2</sub>	→ N	+ H <sub>2</sub>	1.50 × 10 <sup>-15</sup>
8.	NHv	+ N <sub>2</sub>	→ NH	+ N <sub>2</sub>	2.00 × 10 <sup>-14</sup>
9.	NHv	+ H <sub>2</sub>	→ NH	+ H <sub>2</sub>	2.00 × 10 <sup>-14</sup>
10.	NHv		→ NH	+ hv	1000.
21.	NH	+ H	→ N	+ H <sub>2</sub>	5.00 × 10 <sup>-11</sup> T <sup>0.5</sup> exp(-2400./T)
22.	NHv	+ H	→ N	+ H <sub>2</sub>	5.00 × 10 <sup>-11</sup> T <sup>0.5</sup> exp(-2400./T)
23.	NH	+ N	→ N <sub>2</sub>	+ H	2.89 × 10 <sup>-12</sup> T <sup>0.5</sup>
24.	NHv	+ N	→ N <sub>2</sub>	+ H	2.89 × 10 <sup>-12</sup> T <sup>0.5</sup>
25.	NH	+ N( <sup>2</sup> P)	→ N <sub>2</sub>	+ H	2.89 × 10 <sup>-12</sup> T <sup>0.5</sup>
26.	NHv	+ N( <sup>2</sup> P)	→ N <sub>2</sub>	+ H	2.89 × 10 <sup>-12</sup> T <sup>0.5</sup>
30.	NH <sub>2</sub>	+ H + M	→ NH <sub>3</sub>	+ M	6.10 × 10 <sup>-30</sup>
36.	NH <sub>2</sub>	+ N	→ 2NH		1.21 × 10 <sup>-10</sup>
38.	2H	+ H <sub>2</sub>	→ 2H <sub>2</sub>		2.76 × 10 <sup>-31</sup> T <sup>-0.6</sup>
40.	2H	+ N <sub>2</sub>	→ H <sub>2</sub>	+ N <sub>2</sub>	1.49 × 10 <sup>-29</sup> T <sup>-1.3</sup>
41.	N <sub>2</sub> A	+ N <sub>2</sub>	→ 2N <sub>2</sub>		2.00 × 10 <sup>-18</sup>
42.	N <sub>2</sub> A	+ H <sub>2</sub>	→ N <sub>2</sub>	+ H <sub>2</sub>	2.40 × 10 <sup>-15</sup>
43.	N <sub>2</sub> A	+ H	→ N	+ NH	3.50 × 10 <sup>-12</sup>
44.	N <sub>2</sub> A	+ N	→ N <sub>2</sub>	+ N( <sup>2</sup> P)	1.40 × 10 <sup>-11</sup>
45.	N <sub>2</sub> A	+ N	→ N <sub>2</sub>	+ N	2.60 × 10 <sup>-11</sup>
46.	2N <sub>2</sub> A		→ N <sub>2</sub> A	+ N <sub>2</sub>	3.00 × 10 <sup>-9</sup>
49.	N <sub>2</sub> A	+ NH <sub>3</sub>	→ NH <sub>2</sub>	+ H + N <sub>2</sub>	1.55 × 10 <sup>-10</sup>
54.	H <sub>2</sub> <sup>+</sup>	+ N <sub>2</sub>	→ N <sub>2</sub> H <sup>+</sup>	+ H	2.00 × 10 <sup>-9</sup>
55.	N <sup>+</sup>	+ N <sub>2</sub> + M	→ N <sub>3</sub> <sup>+</sup>	+ M	5.20 × 10 <sup>-30</sup>

TABLE 29. Continued.

56.	$N^+$	+ $H_2$	$\rightarrow NH^+$	+ $H$	$4.80 \times 10^{-10}$
65.	$N_2^+$	+ $N_2 + M$	$\rightarrow N_4^+$	+ $M$	$1.00 \times 10^{-29}$
66.	$N_2^+$	+ $H_2$	$\rightarrow N_2H^+$	+ $H$	$2.10 \times 10^{-9}$
67.	$N_3^+$	+ $H_2$	$\rightarrow N_2H^+$	+ $H + N$	$2.00 \times 10^{-13}$
68.	$N_3^+$	+ $NH_3$	$\rightarrow NH_3^+$	+ $N + N_2$	$2.10 \times 10^{-9}$
69.	$N_4^+$	+ $H_2$	$\rightarrow N_2H^+$	+ $H + N_2$	$5.80 \times 10^{-12}$
70.	$N_4^+$	+ $NH_3$	$\rightarrow NH_3^+$	+ $2N_2$	$1.80 \times 10^{-9}$
71.	$N_2H^+$	+ $NH$	$\rightarrow NH_2^+$	+ $N_2$	$6.40 \times 10^{-10}$
72.	$N_2H^+$	+ $NHv$	$\rightarrow NH_2^+$	+ $N_2$	$6.40 \times 10^{-10}$
74.	$N_2H^+$	+ $NH_3$	$\rightarrow NH_4^+$	+ $N_2$	$2.30 \times 10^{-9}$
75.	$NH^+$	+ $H_2$	$\rightarrow NH_2^+$	+ $H$	$9.50 \times 10^{-9}$
76.	$NH^+$	+ $N_2$	$\rightarrow N_2H^+$	+ $N$	$1.50 \times 10^{-8}$
77.	$NH_2^+$	+ $H_2$	$\rightarrow NH_3^+$	+ $H$	$1.20 \times 10^{-10}$
81.	$NH_3^+$	+ $H_2$	$\rightarrow NH_4^+$	+ $H$	$4.50 \times 10^{-13}$
83.	$N_2^+$	+ $e$	$\rightarrow N(^2D)$	+ $N$	$1.66 \times 10^{-6} \text{ T-0.39}$
84.	$N_4^+$	+ $e$	$\rightarrow 2N_2$		$1.50 \times 10^{-6}$
85.	$N_3^+$	+ $e$	$\rightarrow N$	+ $N_2$	$3.00 \times 10^{-7} \text{ T-0.5}$
86.	$N_2H^+$	+ $e$	$\rightarrow H$	+ $N_2$	$3.00 \times 10^{-7} \text{ T-0.5}$
91.	$NH_3^+$	+ $e$	$\rightarrow NH_2$	+ $H$	$3.00 \times 10^{-7} \text{ T-0.5}$
92.	$NH_3^+$	+ $e$	$\rightarrow NH$	+ $2H$	$1.50 \times 10^{-7} \text{ T-0.5}$
93.	$NH_3^+$	+ $e$	$\rightarrow NHv$	+ $2H$	$1.50 \times 10^{-7} \text{ T-0.5}$
94.	$NH_4^+$	+ $e$	$\rightarrow NH_3$	+ $H$	$3.00 \times 10^{-7} \text{ T-0.5}$
95.	$NH_4^+$	+ $e$	$\rightarrow NH_2$	+ $2H$	$3.00 \times 10^{-7} \text{ T-0.5}$



Thus the  $\text{N}(^2\text{D})$  atoms react with  $\text{H}_2$  to form  $\text{NHv}$ , where the  $\text{NH}$  is vibrationally excited into the  $v = 1, 2$ , or  $3$  level. The  $\text{NHv}$  can be quenched by  $\text{N}_2$ , and possibly by  $\text{H}_2$  or  $\text{N}$ , or it can emit an IR photon. The experimental data from the LABCEDE experiment measures the decay rate of  $\text{NHv}$  by observing these IR photons. Thus we wish to model the decay of the  $\text{NHv}$  species. In addition, some of the  $\text{N}(^2\text{D})$  atoms are quenched by  $\text{N}_2$  molecules. The  $\text{N}(^2\text{D})$  atoms are rather rapidly removed after the end of the electron pulse, and at longer times some  $\text{NHv}$  species are assumed to be produced by electron recombination with the  $\text{NH}_3^+$  ions that are formed by ion-molecule reactions. The dominant loss process for some of the beam created species is diffusion, so that their concentrations build up from sequential pulses. Figure 171 illustrates that the  $\text{N}$  and  $\text{H}$  concentrations still increase after eight pulses, but they are approaching a limiting value. In our mechanism we see that the  $\text{N}$  atom does some quenching of the  $\text{NHv}$ . Thus, we need to estimate the steady-state concentration of the  $\text{N}$  atoms after many pulses. To determine this we need to consider the loss of  $\text{N}$  atoms by diffusion and by removal with the gas flow out of the cell during the experiment. At this time we estimate these losses for all species by ignoring the diffusion losses and estimating the removal by gas flow by assuming that all active species in the gas chamber are removed with a time constant given by the chamber volume ( $\pi \times 10^2 \times 16 \text{ cm}^3$ ) divided by the flow rate ( $4 \text{ l-atm/min}$ ). Thus, a pressure of  $7.5 \text{ torr}$  corresponds to a time constant of  $0.75\text{s}$ . This time constant is an upper limit on the removal time constant of each species. In practice, other loss mechanisms will add to the removal rate and decrease the loss time constant. However, we need to follow pulses for a time period approaching  $1\text{s}$  before the concentrations of the  $\text{N}$



A-7581

Figure 171. Concentrations of major species for the ninth and tenth pulses in a mixture of 7.5 torr of N<sub>2</sub> and 0.2 torr of H<sub>2</sub>. The 0.6-ms pulses begin at 0.12 and 0.135s. The reaction mechanism for this calculation is similar to the mechanism used for the other calculations.

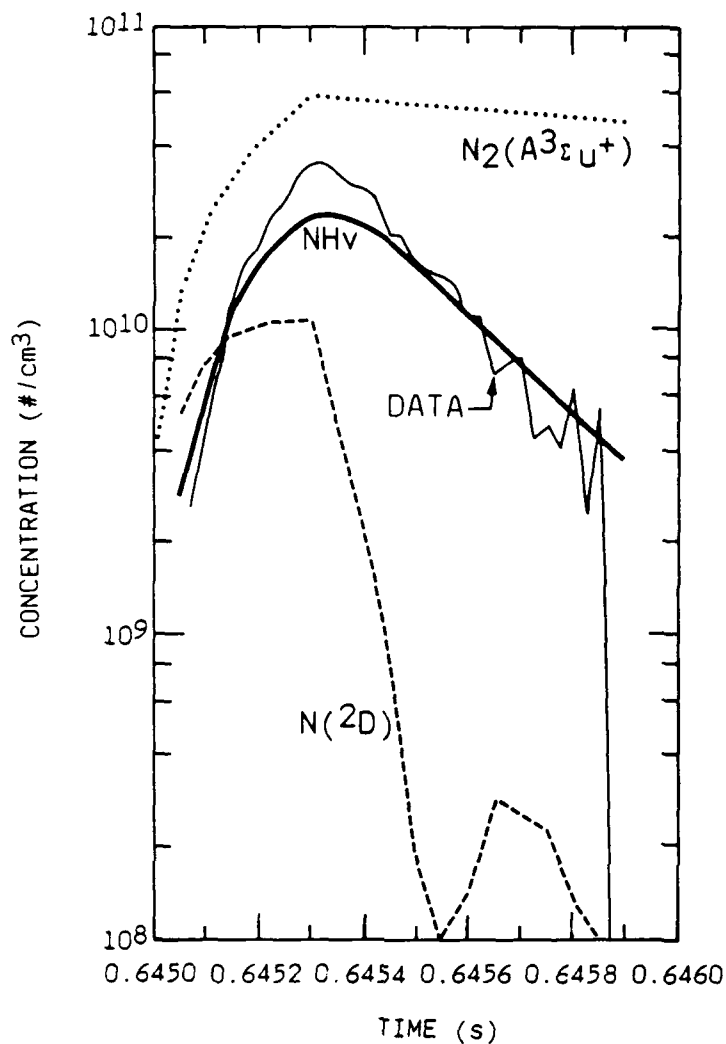
atoms will reach a steady-state value. Rather than doing such a computationally lengthy calculation directly, we found that we could make a reasonable estimate of the steady-state concentrations by following a few pulses (five) to settle the pulse-to-pulse change. We then used the change in concentration to estimate the change during a longer period (eight times the pulse period) as

the number of periods times the one-period change. This process was repeated until the concentrations become reasonably close to their steady-state values.

## 15.2 RESULTS

At the present time the model seems adequate to explain most of the experimental results except for the lowest pressure data. In the model we use rate constants from the literature and make reasonable assumptions that  $\text{NHv}$  is produced with a modest yield whenever an  $\text{NH}$ -formation reaction is exoergic enough to provide the excitation energy. We assume values for the  $\text{NHv}$  quenching by  $\text{N}_2$  and  $\text{H}_2$ , as well as the radiative rate constant. The high pressure LABCEDE data show that quenching by  $\text{N}_2$  is the most important loss for the range of partial pressures studied. Depending on the choice of the assumed rate constants we can get a reasonable fit for the data for  $\text{N}_2$  pressures from 10 to 30 torr. At 7.5 torr, the agreement is not as good, and at 4 torr the data show a more rapid build-up and fall-off than do the calculated values. The fit at low pressure is improved by including the pressure-independent radiative decay loss. The present calculations use an extreme upper limit for this rate constant of  $1000 \text{ s}^{-1}$ , and they use rate constants of  $1.6 \times 10^{-14} \text{ (cm}^3/\text{s)}$  and  $4 \times 10^{-14} \text{ (cm}^3/\text{s)}$  for quenching  $\text{NHv}$  by  $\text{N}_2$  and  $\text{H}_2$ , respectively. Future modeling will be performed with more accurate estimates of the Einstein coefficients for  $\text{NH}$ . Figures 172 through 175 show comparisons between the LABCEDE data and the calculations for three pressures. Figure 172 shows that at 4 torr the experimental data show a sharper pulse for  $\text{NHv}$ , as they buildup faster and decay faster than the calculated values. Figures 173 and 174 show a better match of the decay at 7.5 torr, with a reasonable agreement at low  $\text{H}_2$  pressure in Figure 173 and good agreement for both the buildup and decay at higher  $\text{H}_2$  pressure in Figure 174. Figure 175 illustrates that the good agreement persists at higher  $\text{N}_2$  pressures by showing the comparison at 30 torr. Table 30 shows a comparison of experimental decay rates with the maximum decay rate calculated for a 0.1-ms period. The third column gives the relative importance of the four most important  $\text{NHv}$ -removal processes: radiation, and quenching by  $\text{N}_2$ ,  $\text{N}$ , and  $\text{H}_2$ . The  $\text{N}_2$ -quenching reaction is always the most

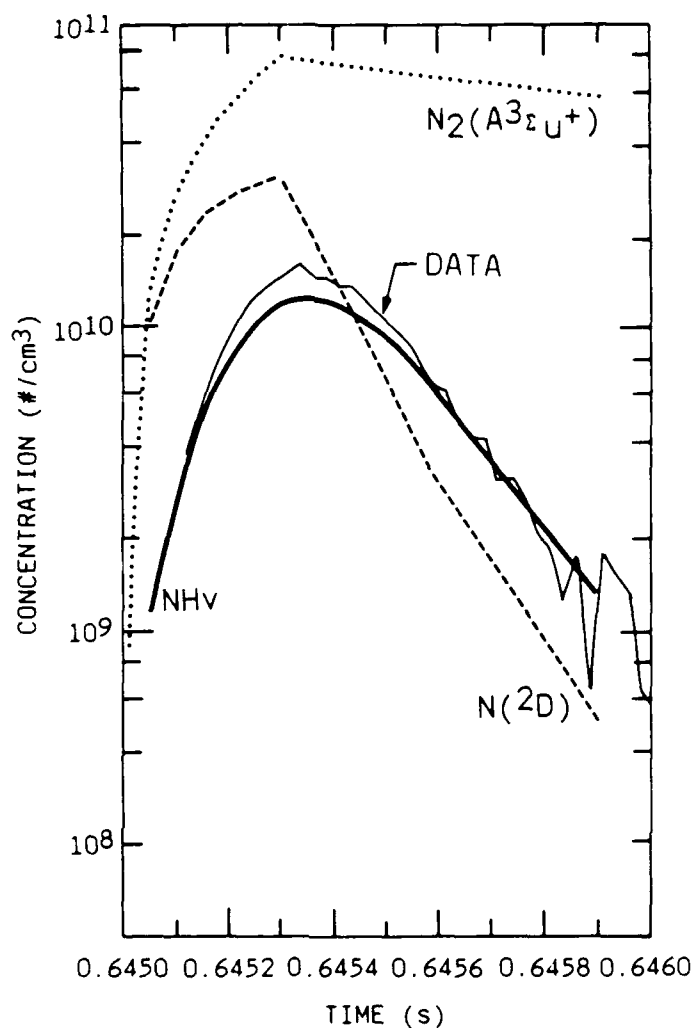




A-7582

Figure 172. Comparison with LABCEDE experimental data for  $\text{NH}\nu$  decay in a mixture of 4.05 torr of  $\text{N}_2$  and 0.2 torr of  $\text{H}_2$ . The 0.3-ms pulse begins at 0.645s. The calculated values of  $\text{N}(^2\text{D})$  and  $\text{N}_2(\text{A}^3\Sigma_u^+)$  are also shown.

important. The fast radiative decay helps to explain the 4-torr data, but Figures 172 and 173 suggest that some process is missing in our model at low pressures. Here the narrow electron beam and the more rapid diffusion may make diffusional losses play a more significant role.



A-7583

Figure 173. Comparison with LABCEDE experimental data for  $\text{NHv}$  decay in a mixture of 7.5 torr of  $\text{N}_2$  and 0.05 torr of  $\text{H}_2$ . The 0.3-ms pulse begins at 0.645s. The calculated values of  $\text{N}(^2\text{D})$  and  $\text{N}_2(\text{A}^3\Sigma_u^+)$  are also shown.

Another area of comparison between calculations and the LABCEDE data is the effect of changing electron pulse width. We performed a series of calculations to vary pulse width from 0.3 to 2.4 ms for a gas mixture with 15 torr  $\text{N}_2$  and 0.2 torr  $\text{H}_2$ . Table 31 results from slightly different values for the  $\text{NHv}$  quenching rate constant of  $1.6 \times 10^{-14}$  and  $4 \times 10^{-14} \text{ cm}^3/\text{s}$  for  $\text{N}_2$  and  $\text{H}_2$ , respectively. These results show that quenching by  $\text{N}$  becomes important at

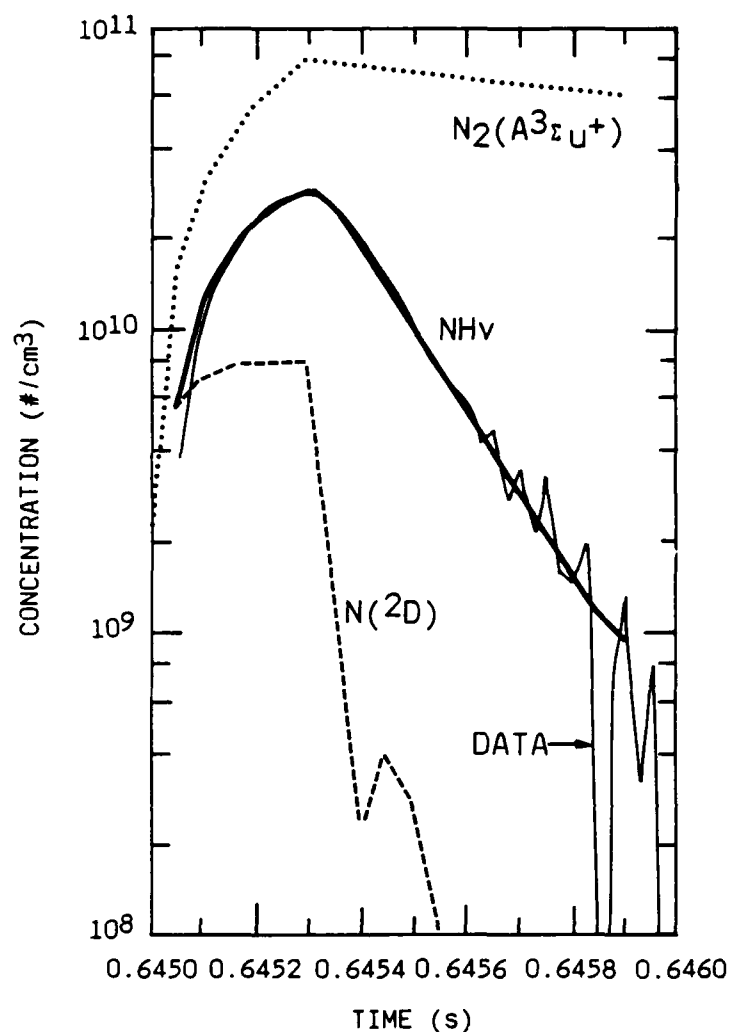
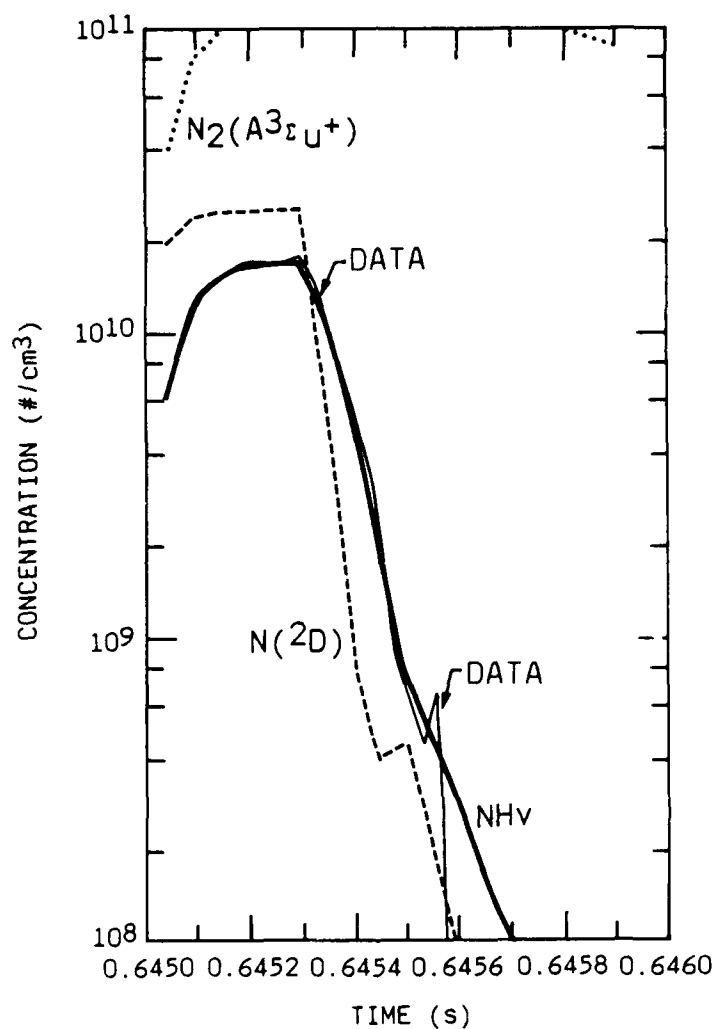


Figure 174. Comparison with LABCEDE experimental data for  $NHv$  decay in a mixture of 7.54 torr of  $N_2$  and 0.4 torr of  $H_2$ . The 0.3-ms pulse begins at 0.645s. The calculated values of  $N(^2D)$  and  $N_2(A^3\Sigma_u^+)$  are also shown.

longer pulse widths. As a result the maximum  $NHv$  concentration  $[NHv]_{\max}$  decreases, as shown in Table 31. Table 32 gives some experimental data for a similar range of pulse widths. The experimental  $[NHv]_{\max}$  has a maximum at 0.5 ms, which is similar to the calculated values for  $[NHv]_{\max}$  that go through a maximum at a pulse width of 0.6 ms. However the experimental data fall off faster than the calculated values for longer pulse widths. The experimental



A-7585

Figure 175. Comparison with LABCEDE experimental data for  $NH\nu$  decay in a mixture of 30.11 torr of  $N_2$  and 0.2 torr of  $H_2$ . The 0.3-ms pulse begins at 0.645s. The calculated values of  $N(^2D)$  and  $N_2(A^3\Sigma_u^+)$  are also shown.

decay at 0.25 ms pulse width is close to the calculated value at 0.3 ms. The experimental decays at pulse widths of 0.5 ms and longer are faster than the calculated decays. Table 31 gives the decay rate averaged over a 0.1-ms period. The time after the end of the pulse of this maximum decay is  $t_{\max-pw}$ . Table 30 also shows the relative contribution from the  $NH\nu+N_2$ ,  $NH\nu$  radiative, and  $NH\nu+N$  destruction reactions during a 0.15-ms interval near  $t_{\max}$ . These

TABLE 30. Calculated and experimental decay rates and reaction importance for 0.3-ms pulse width.

H <sub>2</sub> , torr	0.05			0.20			0.40		
	Decay Rate		Reaction Importance	Decay Rate		Reaction Importance	Decay Rate		Reaction Importance
N <sub>2</sub> Torr	Exptl 1/s	Calc 1/s	NHv+N <sub>2</sub> Radiative NHv+N NHv+H <sub>2</sub>	Exptl 1/s	Calc 1/s	NHv+N <sub>2</sub> Radiative NHv+N NHv+H <sub>2</sub>	Exptl 1/s	Calc 1/s	NHv+N <sub>2</sub> Radiative NHv+N NHv+H <sub>2</sub>
4.0	5446	3324	0.686 0.264 0.028	4579	4078	0.676 0.257 0.020 0.033			
7.5	5776	5097	0.783 0.161 0.040				7059	6639	0.769 0.157  0.041
10.1				8018	8043	0.817 0.124 0.032	7965	8398	0.810 0.124  0.032
30.1	17755	16795	0.892 0.046 0.057	20210	18935	0.898 0.046 0.045			

comparisons show that N atom appears to be a beam-generated quencher, which complicates the analysis of the experimental data. The present calculation needs a larger contribution from such quenching. Thus the calculations need a higher dose rate or a greater yield of N (which would increase the N concentration), and a faster N + NHv quenching rate constant. Also, there may be other beam generated quenchers.

TABLE 31. Calculated decay rates and reaction importance for different pulse widths (pulse period 15 ms for a mixture of 15 torr N<sub>2</sub> and 0.2 torr H<sub>2</sub>).

Pulse Width (ms)	[NHv] <sub>max</sub> (10 <sup>+10</sup> /cc)	Decay (1/s)	t <sub>max-pw</sub> (ms)	Destruction of NHv		
				NHv+N <sub>2</sub>	Radiation	NHv+N
0.3	2.67	9242	0.30	0.815	0.105	0.044
0.6	2.81	9351	0.30	0.777	0.100	0.085
1.2	2.64	9871	0.15	0.716	0.092	0.155
2.4	2.28	11350	0.15	0.620	0.080	0.262

TABLE 32. Experimental decay rates and relative NHv concentration for different pulse widths for 15 torr N<sub>2</sub>, 0.2 torr H<sub>2</sub>

Data Set	Pulse Period (ms)	Pulse Width (ms)	[NHv] <sub>max</sub> (Relative)
70623F	15	0.25	1320
70623C	15	0.5	1410
70623D	15	1.0	1078
70623E	15	2.0	756
70609C	10	0.5	1207
70626H	30	0.5	1425

In conclusion, we have identified the important reactions that appear to occur when an electron beam irradiates mixtures of N<sub>2</sub> and H<sub>2</sub>. Our present estimates of the dose rate are crude and some reaction rate constants are rather uncertain. When 0.3-ms electron pulses are used, the present model gives good estimates for the NHv concentration as a function of time for all except the

lowest pressures, as shown in Figures 172 through 175. The study of the effects of longer pulses shows that reaction with N atoms is the cause of the pulse-generated quenching of  $\text{NHv}$ . The present model needs a larger contribution from this in order to match the larger quenching observed in the experimental data for the longer pulses.

## 16. ELECTRON IRRADIATION OF CALCIUM FLUORIDE

### 16.1 INTRODUCTION

Data from the zenith-looking Field Widened Interferometer (FWI) Mission indicated the presence of a weak but broad spectral emission to the long wavelength side of the  $\text{CO}_2(\nu_3)$  4.3  $\mu\text{m}$  band. This feature had not been previously observed and no obvious atmospheric source could be suggested. This mission was flown into a region undergoing active auroral dosing. The possibility was raised that the broad emission feature resulted from the auroral electrons directly striking the Calcium fluoride window of the payload. The electron-induced fluorescence from most window materials (including  $\text{CaF}_2$ ) has been observed in the visible, but infrared observations are sparse. We therefore undertook a series of measurements under conditions representative of the upper atmosphere in terms of background pressure and primary electron energy. The large LABCEDE facility at AFGL provided an excellent test chamber for these experiments.

### 16.2 EXPERIMENTAL

The  $\text{CaF}_2$  window shards supplied by Ron Straka were placed inside the large LABCEDE facility operating at room temperature. Access was through the bottom port directly below the electron beam axis. The samples were positioned using a holder constructed to allow sample height and angle relative to the electron beam to be continuously variable, yet allow reproducible positioning. The sample was observed to be spatial stable during each experiment. At first, pure nitrogen gas was introduced into the chamber to permit the beam trajectory to be visually observed, thus permitting the window to be positioned in the beam. However, it was discovered that during irradiation, the window sample glowed brightly with a rich purple color with the edges being markedly brighter than the optical surface where impact occurred. We estimate this emission to be in the 450 to 470 nm region, but no visible spectra were obtained. This visual tracer permitted accurate sample positioning in the



beam and allowed several irradiation patterns (beam geometries to be utilized). During the observations described below the test sample was held at a small angle (nearly normal) to the electron beam axis.

The fluorescence resulting from this interaction was observed in the SWIR/MWIR regions with a 3 mm diameter round InSb detector (operated at 77 K) viewing the sample through the laboratory Michelson interferometer<sup>192</sup> operated at 20 cm<sup>-1</sup> resolution. The sample was irradiated with several currents of 4.5 keV electrons pulsed at 200 Hz so that phase-sensitive detection (PAR lock in amplifier) of the fluorescent signal could be employed. Effective gains as high as  $5 \times 10^5$  were used. This detection system had been recently checked and was operating at near NESR limited performance.

The interferometer field of view at the beam plane was roughly 10 cm in diameter. The test window fragments and the electron beam diameter were much smaller. Consequently, the instrumental field of view is not uniformly illuminated and absolute radiometric observations were not possible at this survey level. The interferometer looked in from the end of the test chamber and viewed the test sample nearly edge on.

Blank runs were made to ensure that there were no spurious signal sources. No background emission sources were observed. Spectra of a calibrated blackbody source at several temperatures between 150° and 1000°C were obtained to permit determination of the InSb/interferometer system relative spectral response.

The test samples were irradiated as delivered, after cleaning and after thinly coating different surfaces with a lubricant such as Apiezon grease (used for lubricating O-ring gaskets), Cutzol 711, and No. 1 Molydee (used as machining lubricants).

The CaF<sub>2</sub> sample (as delivered) was initially subjected to very low electron currents (< 1 mA total). No infrared signal within the system bandpass

(1.5 to 5.3  $\mu\text{m}$ ) was observed with the interferometer operating radiometrically. The dosing level was increased in two different manners: 1) the total current leaving the electron gun (and hitting the target) was increased by increasing filament temperature while maintaining the beam acceleration voltage constant at 4.5 keV; and 2) the primary beam electron density was increased as the beam was confined using the external magnetic coils. Both approaches produced similar effects. Below 4 mA for diffuse beams, no infrared fluorescence was detected by the detection system even operating radiometrically. Above this current (and above 2.5 mA for magnetically confined beams), blackbody emission from the  $\text{CaF}_2$  surface was observed, and the surface become visually marred. The signal level on the detector was optimized by varying the test sample orientation relative to beam and interferometer. A spectrum of this fluorescence is shown in Figure 176. A spectrum of a 596°C blackbody is shown in Figure 177 for comparison. The spectral shapes in the two figures are quite similar. The  $\text{CaF}_2$  data does not correspond exactly to a single blackbody temperature, but seems to have small contributions from surface areas of different temperatures as would be expected. Nevertheless, the spectrum is dominated by blackbody emission, and no broad spectral features in the 4.4 to 5.3  $\mu\text{m}$  region are observed above the noise level. The atmospheric absorption due to  $\text{CO}_2$  in the unpurged optical path is present in both spectra providing a convenient reference wavelength. The blackbody emission is observed only after the surface is destructively marred (giving a frosted or distorted appearance). After surface marring, blackbody emission could be observed at lower currents. Shown in Figure 178 is the fluorescence from previously marred  $\text{CaF}_2$  (as delivered) now irradiated by 1.6 mA of defocussed electrons. For comparison, a spectrum of a 150°C blackbody of 0.33  $\text{cm}^2$  area is shown in Figure 179. The spectral shapes are similar, but the  $\text{CaF}_2$  fluorescence has an emissivity/emitting area product of  $2 \times 10^{-3} \text{ cm}^2$ .

Thus post-flight visual inspection is a useful observable to see if significant electron irradiation has occurred. If it has not, then the LABCEDE observations would suggest that electron-induced fluorescence was not producing significant emission.

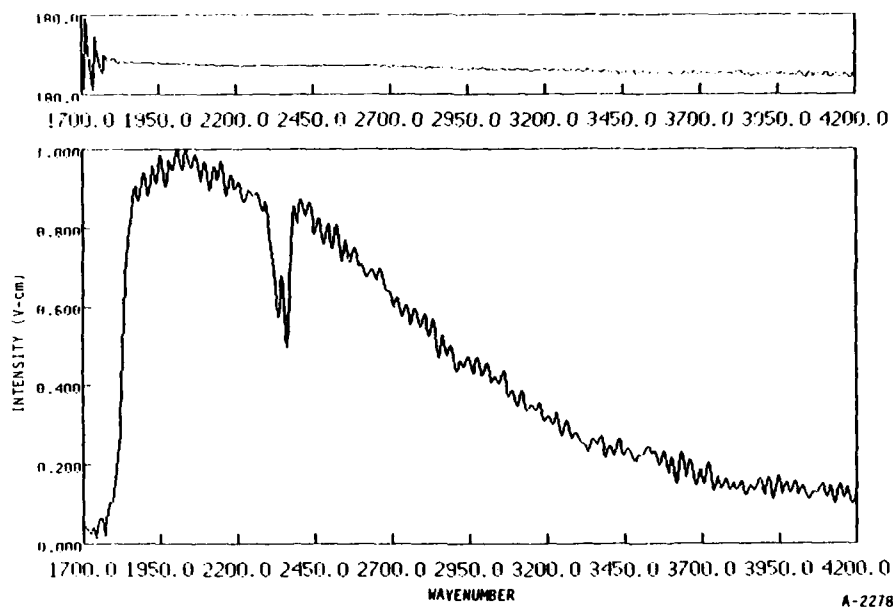


Figure 176. Spectrum of  $\text{CaF}_2$  (as delivered) irradiated by 2.5 mA of 4.5 keV electrons magnetically confined to irradiate a small portion of the window surface.

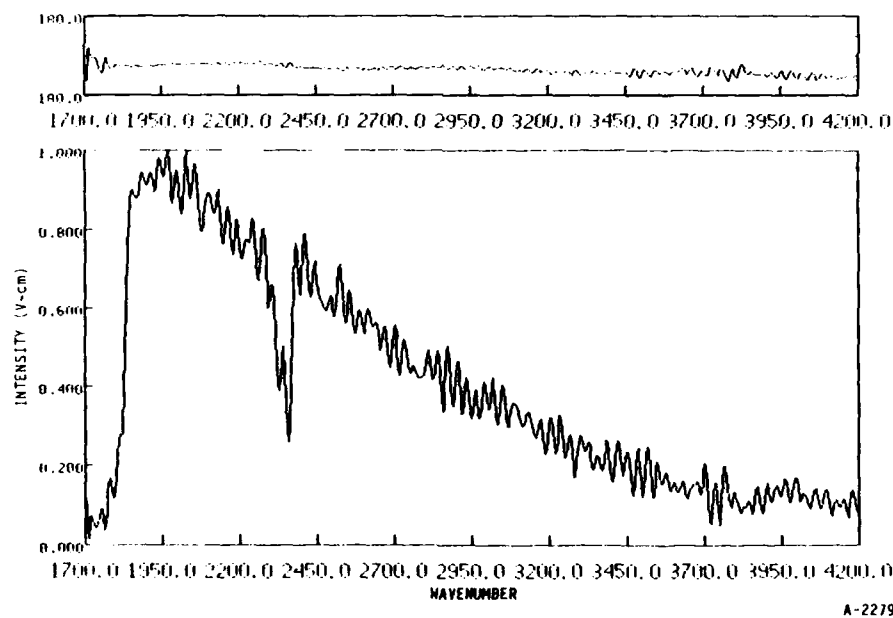


Figure 177. Spectrum of a  $596^\circ\text{C}$  blackbody of 0.65 mm diameter ( $3.3 \times 10^{-3} \text{ cm}^2$ ). The signal levels are identical to those in Figure 176.

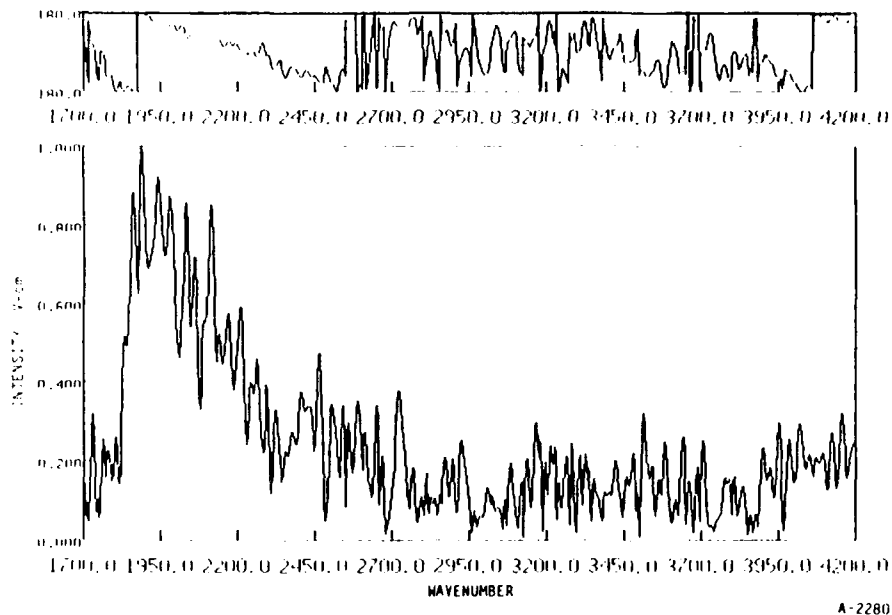


Figure 178. Emission from previously marred  $\text{CaF}_2$  (as delivered) irradiated by 1.6 mA of defocussed 4.5 keV electrons. The signal level is 1/160 of that of Figure 179.

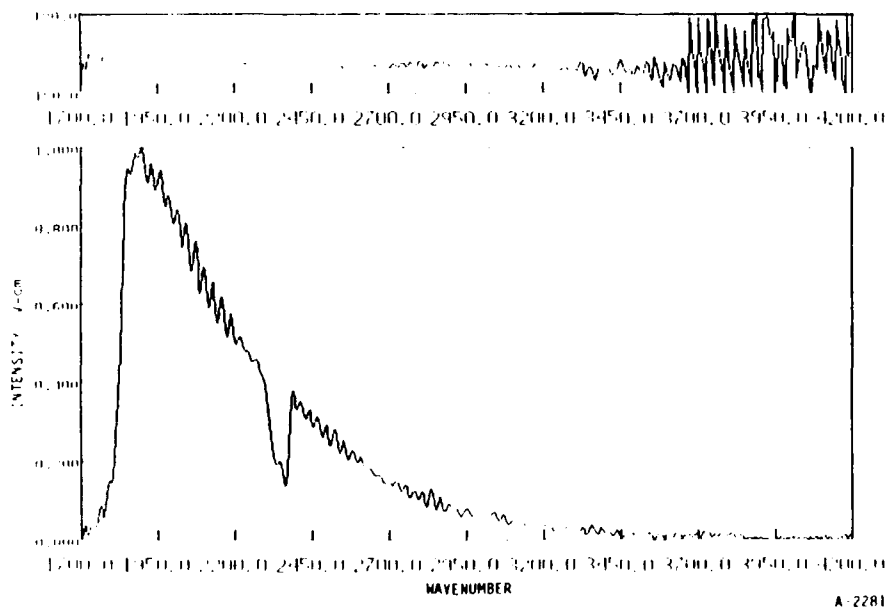


Figure 179. Emission from a blackbody of  $150^\circ\text{C}$  with an aperture of  $0.33\text{ cm}^2$  located 1m from interferometer.

The effects of geometry were considered also. Figure 180 displays a spectrum of the fluorescence when the electrons were striking the edge of  $\text{CaF}_2$  test samples. The emission also seems to be representative of a blackbody of higher temperature. The spectrum of a 1004 C blackbody is shown in Figure 181 for comparison. The emission of Figure 180 has an effective emissivity/area product of  $3.6 \times 10^{-5} \text{ cm}^2$  (0.007 cm diameter).

Thus, no discrete emission features were observed at dosing levels below those giving rise to blackbody emission and  $\text{CaF}_2$  sample marring. These dosing levels correspond to primary (4.5 keV) electron densities on the order of  $10^8/\text{cm}^3$ . By contrast the total electron density (including mostly low-energy thermal electrons) during the FWI Mission was about  $10^6/\text{cm}^3$ . Thus, it appears unlikely that electron-induced effects are present in the FWI data.

At the highest experimental currents and most focused beams, the test window was cleaved and disintegrated into several pieces. The possibility of surface contaminants giving rise to an electron-induced emission was also studied.

A  $\text{CaF}_2$  test sample was cleaned with ethanol then acetone. The cleaned sample was then irradiated and displayed a similar behavior to the as-delivered sample described above: no emission was observed below the marring threshold, blackbody emission was observed as above.

The unblemished side of the cleaned sample was coated with a thin coat of Apiezon grease. Upon irradiation the grease layer glowed white and was observed to boil off the surface. Again, there was no infrared fluorescence signal until surface heating occurred. The spectrum of 3.2 mA of confined electrons striking the Apiezon-coated surface is shown in Figure 182. This spectrum beautifully matches a 465 C blackbody spectrum plotted in Figure 183. No hint of additional emission features can be seen. The emissivity/emitting area product of the  $\text{CaF}_2$  flat is  $2.5 \times 10^{-3} \text{ cm}^2$ .

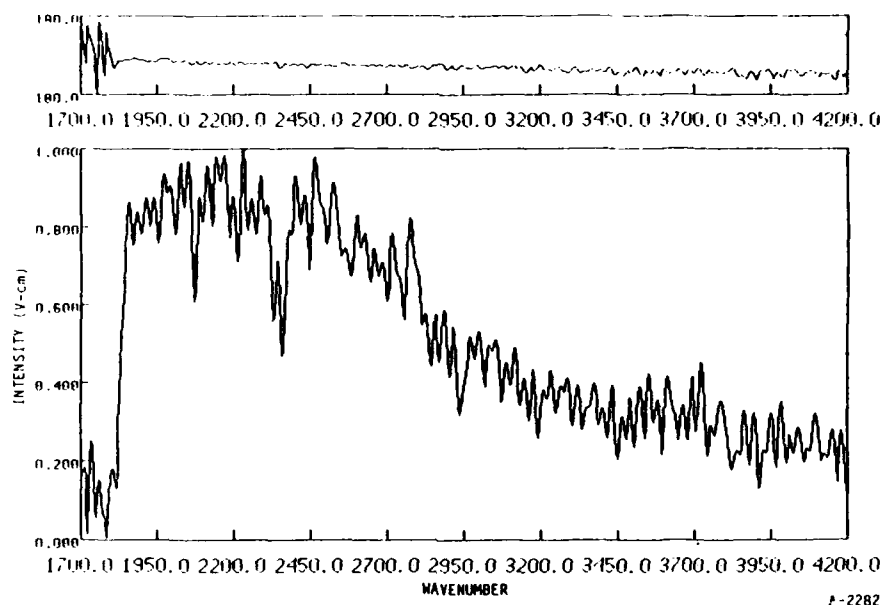


Figure 180. Spectrum of  $\text{CaF}_2$  (as delivered) irradiated by 4 mA of diffuse 4.5 keV electrons striking the edge corner of the window sample. This intensity scale is 4% of that of Figure 176.

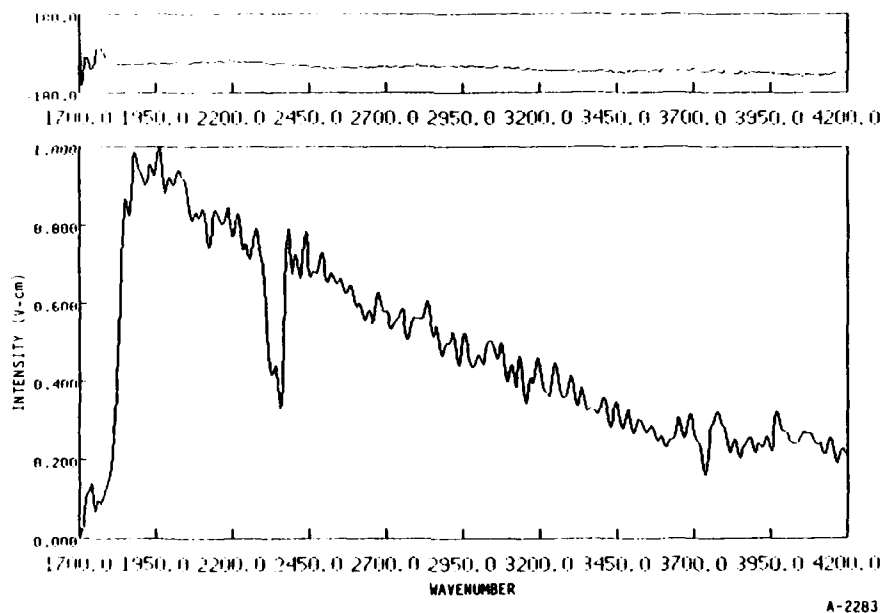


Figure 181. Spectrum of a  $1004^\circ\text{C}$  blackbody of  $1 \times 10^{-3} \text{ cm}^2$  area.

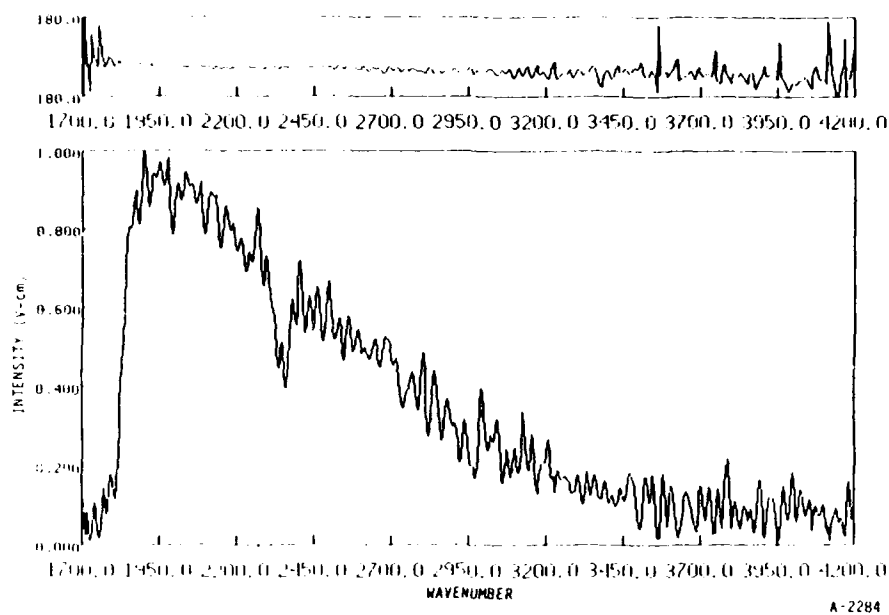


Figure 182. Fluorescence from Apiezon coated CaF<sub>2</sub> irradiated by 3.2 mA of confined electrons.

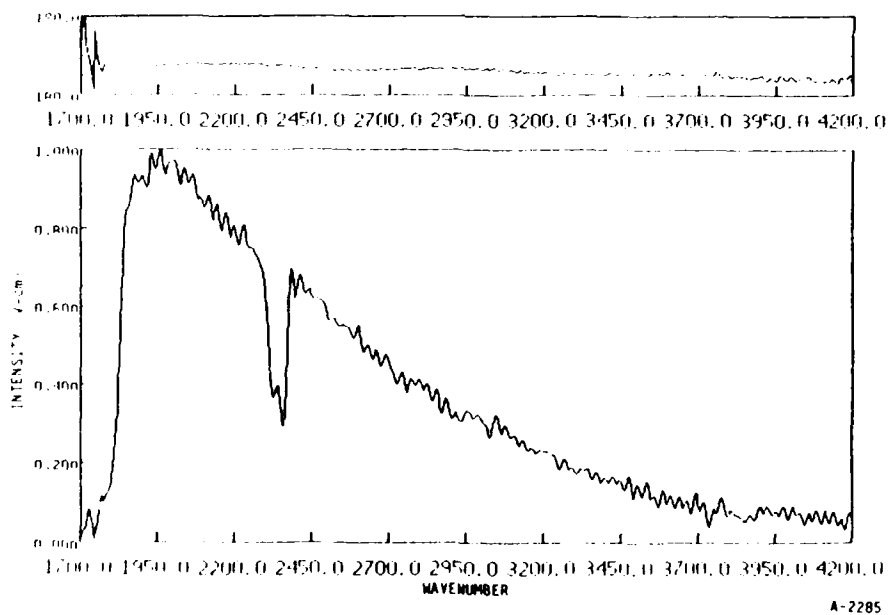


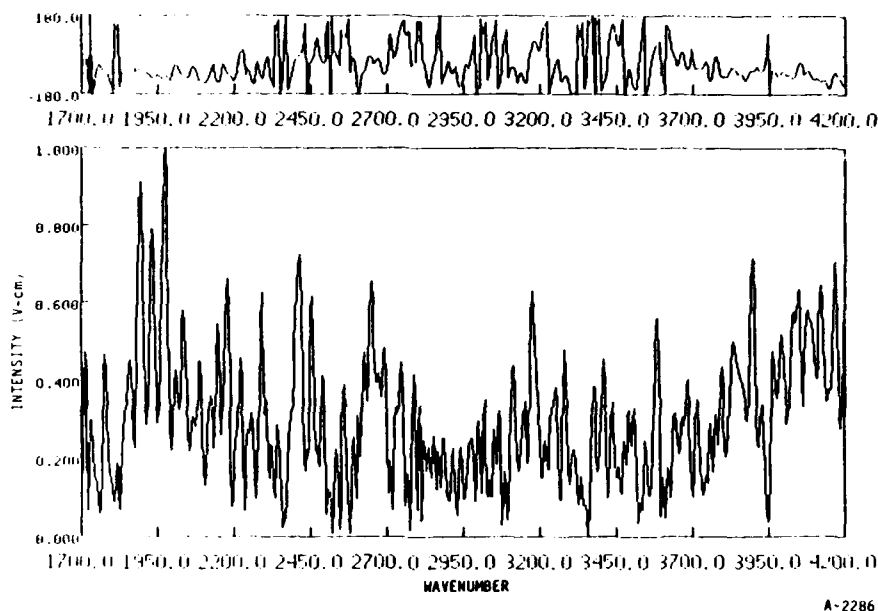
Figure 183. Emission through a 1 x 10<sup>-2</sup> cm<sup>2</sup> aperture viewing a 465°C blackbody.

Another  $\text{CaF}_2$  sample was coated with Molydee lubricant on one side and Cutzol on the other. Both these surface layers displayed spectral structure between 4 and 5.2  $\mu\text{m}$  and between 2.2 and 2.7  $\mu\text{m}$ , as displayed in Figures 184 through 187. Although the signal/noise levels are quite poor, the features appear to be quite structured even at  $20\text{ cm}^{-1}$  resolution. They appear to be from a diatomic species or hydrogenic species. Because this was not the behavior exhibited by the FWI data, we have not pursued this analysis further.

### 16.3 SUMMARY

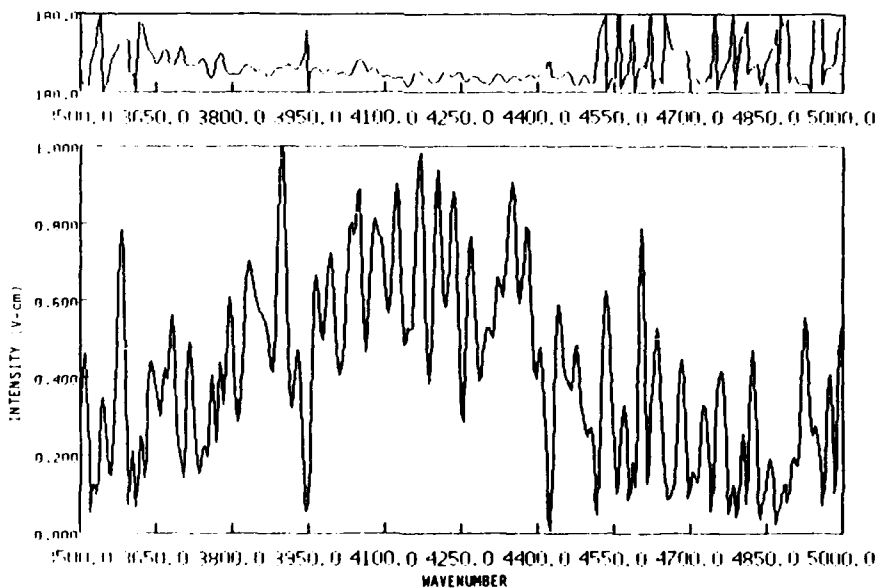
For clean  $\text{CaF}_2$  test samples, emission becomes detectable for the laboratory Michelson interferometer only when substantial surface heating of the sample has occurred. This is for current levels (dosing rates) far in excess of expected thermospheric auroral electron densities. It does not appear that electron-induced fluorescence gives rise to a 4.4 to 5.3  $\mu\text{m}$  broad feature in LABCEDE except as a blackbody surface heating phenomenon. None of the surface contaminants studied gave rise to an emission which could explain the field observations. This study raised several interesting questions regarding electron damage/heating thresholds and contamination-induced emission which should be addressed more carefully in later studies.





A-2286

Figure 184. Emission from a  $\text{CaF}_2$  test sample coated with Cutzol 711 lubricant upon irradiation by 5 mA of diffusion 4.5 keV electrons. Signal levels are comparable to Figure 180.



A-2287

Figure 185. SWIR emission from  $\text{CaF}_2$  test sample loaded with Cutzol 711 lubricant upon irradiation by 5 mA of diffusion 4.5 keV electrons.

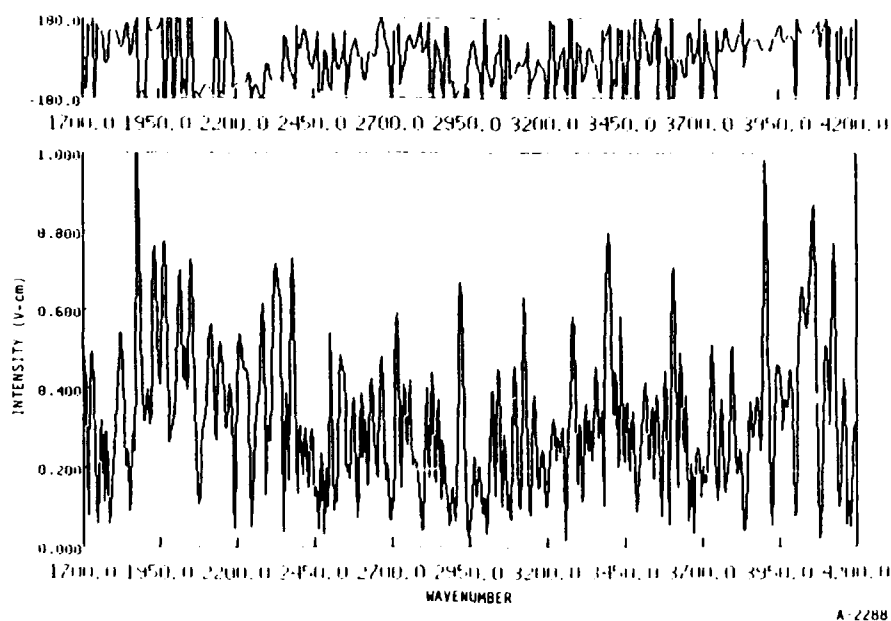


Figure 186. Emission from  $\text{CaF}_2$  test sample coated with MolyDee lubricant upon irradiation by 4 mA of 4.5 keV electrons. Signal levels are comparable to Figure 176.

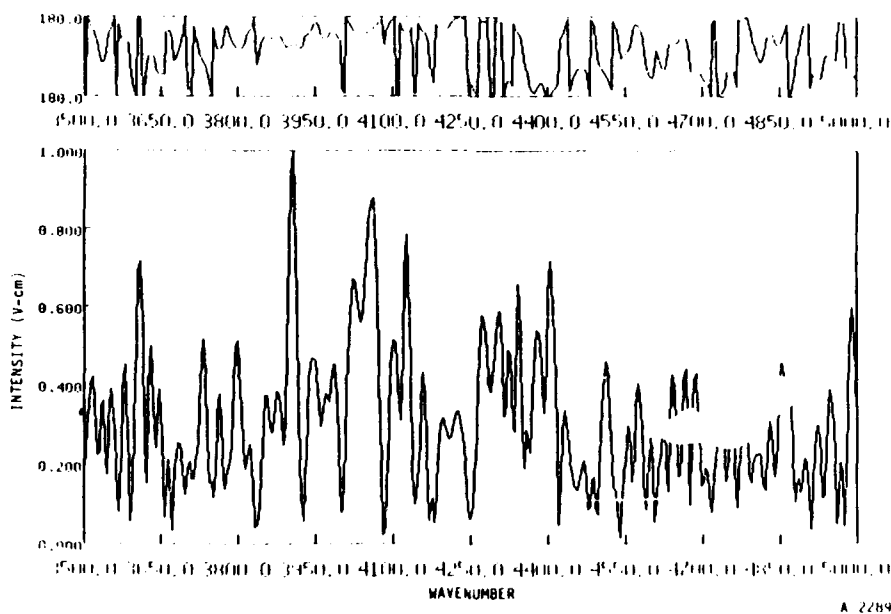


Figure 187. SWIR emission of same sample as Figure 186.

## 17. SPECTRAL SURVEY MEASUREMENTS

In this last section we present several interesting preliminary observations of the molecular fluorescence spectra arising from electron irradiated gases. These observations were often made as part of a separate measurements program. We present them here, with little analysis, as a guide for future measurements programs on these systems.

### 17.1 UV VISIBLE SPECTRA OF ELECTRON IRRADIATED NITRIC OXIDE (NO)

The spectrum shown in Figure 188 was taken with 1.5 mtorr of pure nitric oxide at a resolution of  $5.2\text{\AA}$  under beam plasma conditions. The electron energy and beam current were 4500 eV and 12.8 mamp. The  $\text{N}_2^+(\text{B}^2\Sigma_u^+ - \text{X}^2\Sigma_g^+)$ ,  $\text{N}_2(\text{C}^3\Pi_u - \text{B}^3\Pi_g)$  features arise from approximately 1 percent gas impurity and/or residual nitrogen from previous experiments. The major features of the  $\text{NO}(\text{A}_2\Sigma^+ - \text{X}^2\Pi)$   $\gamma$  bands have been identified. Contributions from a variety of other band systems,  $\text{N}_2(\text{a}^1\Pi_g - \text{X}^1\Sigma_g^+)$  LBH,  $\text{N}_2(\text{D}^3\Sigma_u^+ - \text{B}^3\Pi_g)$  Fourth Positive,  $\text{NO}(\text{B}^2\Pi - \text{X}^2\Pi)$   $\beta$  bands,  $\text{NO}(\text{C}^2\Pi - \text{X}^2\Pi)$   $\delta$ -bands, and  $\text{O}_2^+(\text{A}_2\Pi_u - \text{X}^2\Pi_g)$  Second Negative appear to be present. Preliminary attempts to fit this spectrum using a rotational temperature of 300 K for the transitions  $\text{N}_2^+(\text{B}^2\Sigma_u^+ - \text{X}^2\Sigma_g^+)$ ,  $\text{N}_2(\text{C}^3\Pi_u - \text{B}^3\Pi_g)$ , and  $\text{NO}(\text{A}_2\Sigma^+ - \text{X}^2\Pi)$  in the spectral generation code failed to properly reproduce the widths of the NO  $\gamma$ -bands, but at the same time adequately fit the  $\text{N}_2^+(\text{B-X})$ , and  $\text{N}_2(\text{C-B})$  band widths. The next attempt was to introduce, one at a time, then in combinations, the other possible band systems. (It was necessary at this point to generate approximate Einstein coefficients for the  $\text{NO}(\text{B-X})$ ,  $\text{NO}(\text{C-X})$ ,  $\text{O}_2^+(\text{A-X})$  band systems for incorporation into the fitting code. The details of each generation are described in subsequent paragraphs.) The overlap arising from many band systems also failed to fit the width of the NO  $\gamma$  band features.

The temperature of the NO  $\gamma$  bands in the generation code was then varied between 300 and 1500 K. From the variation it was possible to deduce a NO  $\gamma$  band rotational temperature,  $T_{\text{rot}}$ , upon electron impact excitation of

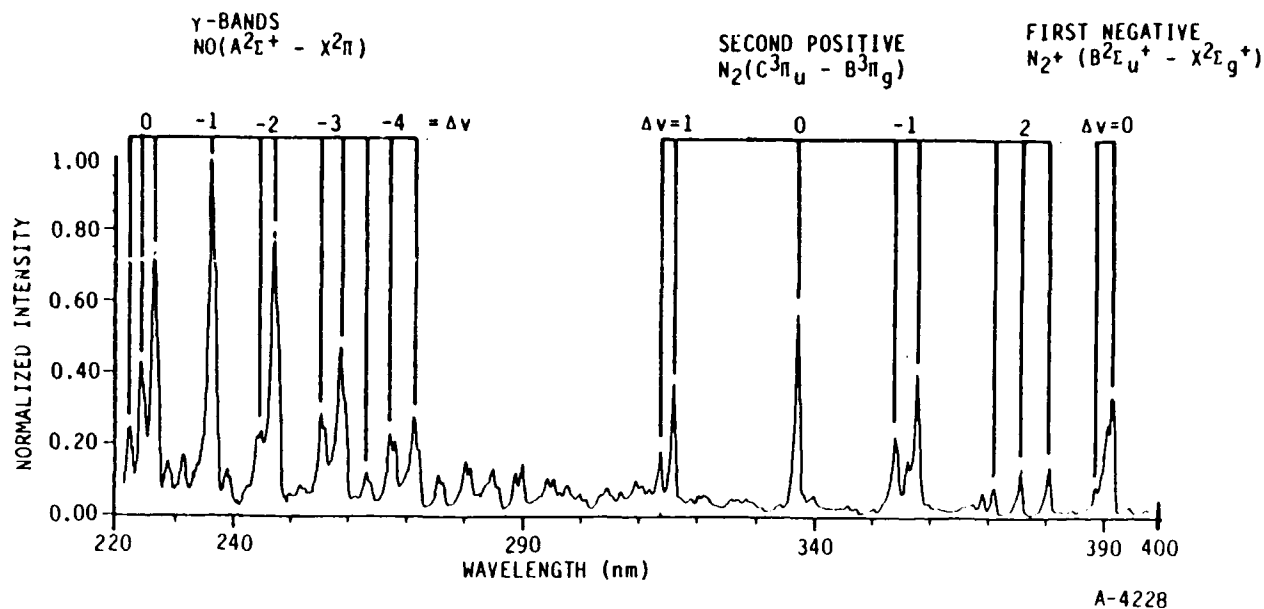


Figure 188. A 1.5 mtorr pure NO spectra at 5.2 Å resolution. The N<sub>2</sub> features represent approximately 1 percent impurity or residual gas from previous experiments. The N<sub>2</sub><sup>+</sup>(B-X), N<sub>2</sub>(C-B), NO(A-X) systems are easily identified.

1200 ± 100 K. The calculated spectra having 300 and 1200 K NO γ-bands are shown in Figure 189. The introduction of additional band systems was performed using 1200 K NO γ-bands. Figure 190 shows the introduction of b) NO(B<sup>2</sup>Π-X<sup>2</sup>Π), then c) O<sub>2</sub><sup>+</sup>(A<sup>2</sup>Π<sub>u</sub>-X<sup>2</sup>Π<sub>g</sub>), then d) both NO β-bands and O<sub>2</sub><sup>+</sup> Second Negative to the synthetic spectral fit. Figure 190d represents that best fit of the experimental data, although many narrow regions are poorly matched. The underfit between 220 and 240 nm is believed to arise from a Wood's anomaly in the grating. The effects of this anomaly have been observed previously (Section 6). The fitting region from 240 to 260 nm appears to be accurately assigned. The continuous overfit/underfit of the data between 260 and 310 nm is attributable to low signal intensity and band system overlap. Except for the small 369 nm feature the region from 310 to 400 nm is once again well determined.

The generation of Einstein coefficients for the NO(B-X), NO(C-X), O<sub>2</sub><sup>+</sup>(A-X) transition each required a slightly different treatment. The NO(B-X)

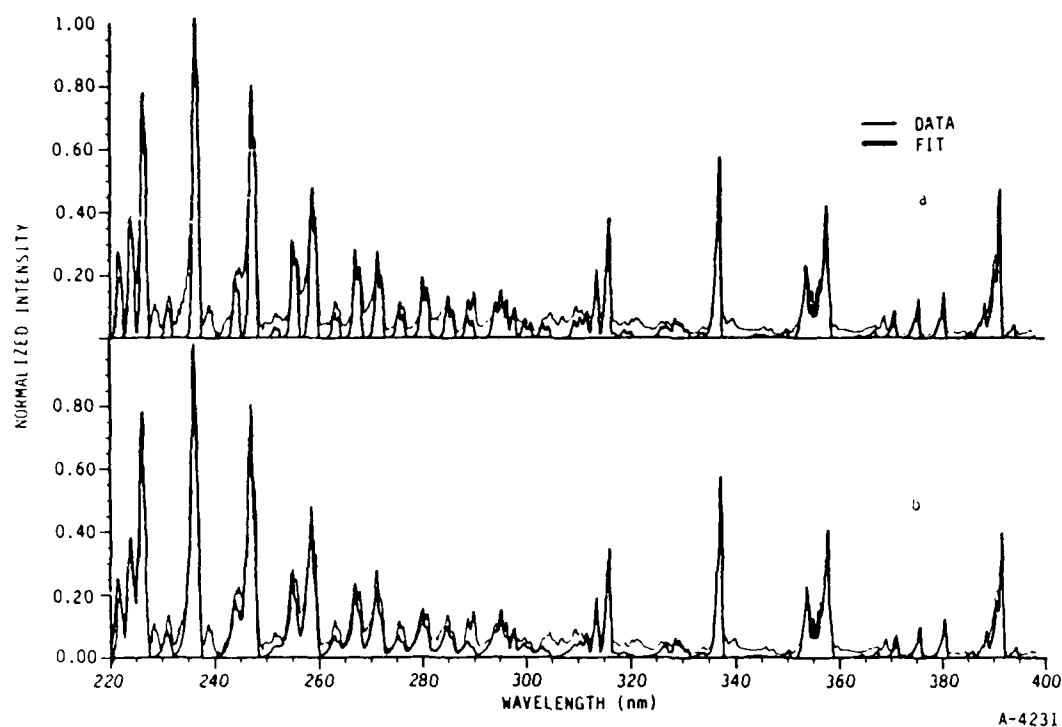


Figure 189. Synthetic spectra generated with NO  $\gamma$ -bands. a)  $T_{\text{rot}} = 300$  K; b)  $T_{\text{rot}} = 1200$  K and including  $\text{N}_2^+(\text{B}^2\Sigma_u^+ - \text{X}^2\Sigma_g^+)$  and  $\text{N}_2(\text{C}^3\Pi_u - \text{B}^3\Pi_g)$  systems at room temperature.

$\beta$ -bands were calculated by assuming no transition moment variation. The relevant equations:

$$A_{v',v''} = \frac{1}{\tau_{v'}} BR_{v',v''} \quad (68)$$

$$BR_{v',v''} = \frac{q_{v',v''} \nu_{v',v''}}{\sum_{v'} q_{v',v''} \nu_{v',v''}} = \text{Branching ratio} \quad (69)$$

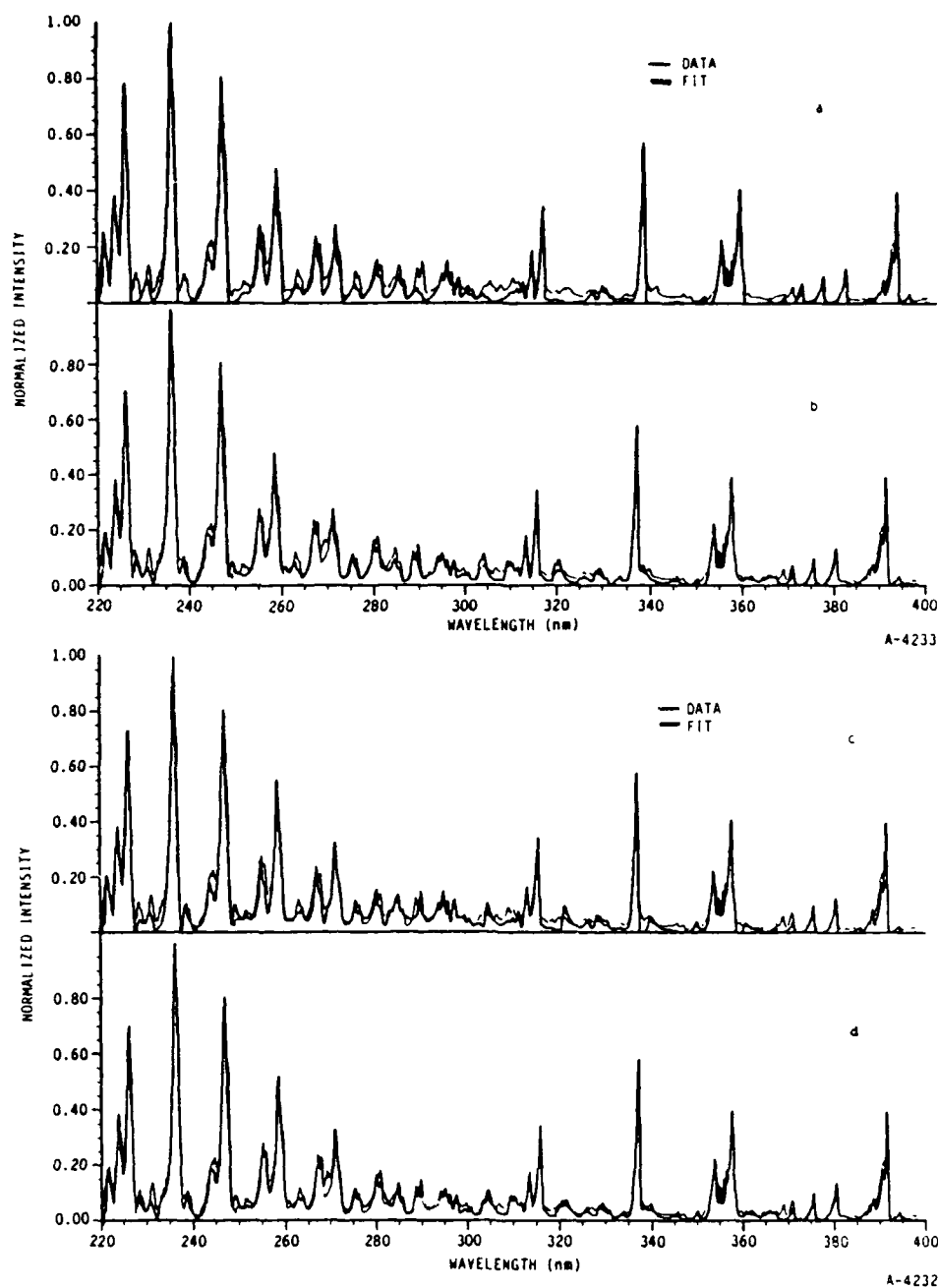


Figure 190. a) Synthetic spectrum generated using 1200 K  $\text{NO}(A^2\Sigma^+-X^2\Pi)$ , 300 K  $\text{N}_2(C^3\Pi_u-B^3\Pi_g)$ , and 300 K  $\text{N}_2^+(B^2\Sigma_u^+-X^2\Sigma_g^+)$ ; b) Addition of 300 K  $\text{NO}(B^2\Pi-X^2\Pi)$  to a); c) Addition of 300 K  $\text{O}_2^+(A^2\Pi_u-X^2\Pi_g)$  to a); d) Addition of both  $\text{NO}(B-X)$  and  $\text{O}_2^+(A-X)$  to a).

where:

$$\begin{aligned}\tau_{v'} &= \text{radiative lifetime,}^{193} \quad v'=0-7 \\ q_{v',v''} &= \text{Franck-Condon Factors}^{194} \\ \nu_{v',v''} &= \text{Transition frequency.}^{194}\end{aligned}$$

Implicitly we have assumed that the B-X transition is the dominant radiative process of the NO(B) state and that the summation over  $v''$  can be truncated at  $v'=16$ , the limit of existing Franck-Condon factors. By this procedure,  $A_{v',v''}$  values with  $v'$  ranging 0-6 and  $v''$  ranging 0-16 were calculated. The  $C^2X$ -state of NO is predissociating for  $v'=0$ ,  $J' \geq 4.5$ .<sup>193</sup> The lifetime of NO( $^2\Pi$ ,  $v'=0$ ) is in dispute. To our knowledge no direct measurement has been performed. Brozowski et al.<sup>193</sup> present relatively convincing arguments based on a measured absorption oscillator strength and C-X and C-A branching ratios that the radiative lifetime is 11.6 ns. In any case, most researchers agree the lifetime can be bounded between 10 and 60 ns. Using a radiative lifetime of 11.6 ns, Franck-Condon Factors of Nicholls<sup>195</sup> and the formulation presented earlier, the values of  $A_{0v''}$  for  $v''$  ranging 0-19 were calculated. The  $O_2^+(A^2\Pi-X^2\Pi)$  Second Negative Einstein coefficients were calculated via the oscillator strengths of Wetmore et al.,<sup>196</sup> those of Erman and Larsson,<sup>98</sup> the bandhead tables of Krupenie.<sup>197</sup>

Using the equation:

$$f_{v',v''} = \frac{m_e c \lambda_{v',v''}^2 A_{v',v''} d_u}{8\pi^2 e^2 d_l} = \text{Oscillator strength} \quad (70)$$

where:

$$\begin{aligned}m_e &= \text{mass of the electron} \\ c &= \text{speed of light} \\ d_u \text{ and } d_l &= \text{the degeneracies of upper state and lower state}\end{aligned}$$

$\lambda_{v',v''}$  = transition wavelength

$A_{v',v''}$  = calculated Einstein coefficient.

This series of experimental data was also collected in order to survey the prominent features arising from electron bombardment (4.5 keV) of nitric oxide. In this regard, it is important to reiterate not only which band systems were observed, i.e., NO(A-X), N<sub>2</sub>(C-B), N<sub>2</sub><sup>+</sup>(B-X), NO(B-X), O<sub>2</sub><sup>+</sup>(A-X), but the band systems which were considered and not observed: N<sub>2</sub>(LBH), N<sub>2</sub>(D-B), NO(C-X). The observation of rotationally hot NO(A-X), T<sub>rot</sub> = 1200 K, is not explained at present and further experiments should be performed with and without a beam plasma discharge occurring to verify this single observation. In addition, experiments should be performed to clearly determine if the nitrogen features arise from impurity in NO, residual gases or leaks, or a production mechanism initiated by electron impact on nitric oxide.

## 17.2 FLUORESCENCE FROM Ar/NO MIXTURES

Nitric oxide fundamental band fluorescence was observed to be quite weak in Argon/NO mixtures. The fluorescence was observed by a PbSe detector cooled to liquid nitrogen temperature viewing the center of the vacuum chamber through the Michelson interferometer. For these experiments 660 sccm of Argon and 140 sccm of NO were introduced into the chamber with the shroud at room temperature. A total pressure of 7.25 mt was achieved under these fast flow (flow throttling valve completely open) conditions. The confining magnetic field had a value ~ 60 Gauss. The fluorescence signal was observed to be quite weak. Two PAR113 preamplifiers were used in series to give a total gain of 10000. Even with this amplification, the time dependent fluorescent signal from pulsed beam operation was only 1.2V on the scope. A 1200 point interferogram was acquired and transformed to give the spectrum shown in Figure 191. The only feature present above the noise level is NO fundamental band emission. The distribution observed is quite peaked to low vibrational levels: in these mixtures substantial excitation of NO(v) does not occur upon electron irradiation. The weak signal levels prevented a systematic investigation under these



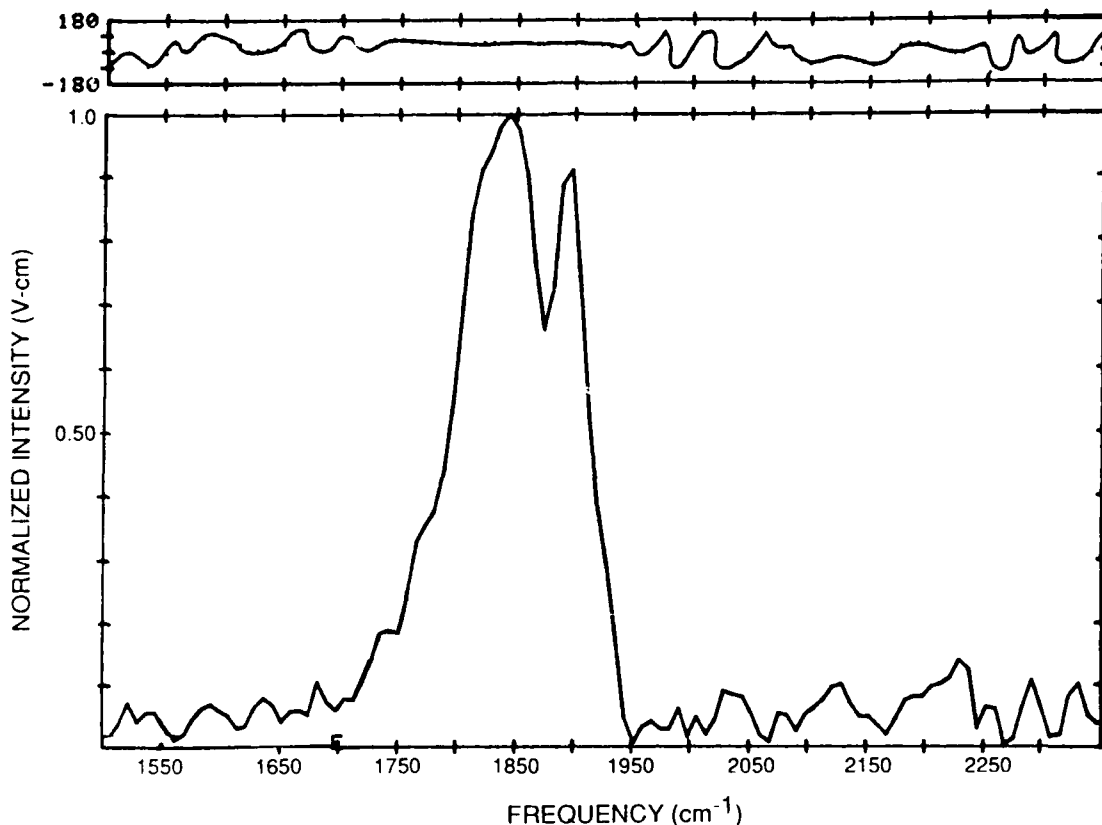


Figure 191. Fluorescence from irradiated Ar/NO mixture at 7 mt pressure. NO fundamental emission is the dominant spectral feature (Scan 4718D).

conditions. Future measurements with an improved sensitivity detection system will permit more accurate measurements of the excitation of pure NO and NO mixtures.

### 17.3 INFRARED EMISSION FROM N<sub>2</sub>/O<sub>2</sub> MIXTURES

These measurements were performed with the shroud operated at near liquid nitrogen temperatures. The fluorescence was detected by the liquid-He cooled As:Si detector in the CVF spectrometer. Mixtures of N<sub>2</sub> (1200 sccm) and O<sub>2</sub> (300 sccm) were introduced into the shroud through the porous tube array to give a total pressure of 35 mtorr. Electrons at 4.5 keV primary energy were operated in a pulsed mode (20 ms on, 84 ms period) with an average current of 6.6 mA. The applied magnetic field was 30 Gauss. Spectral data in the MWIR and SWIR spectral regions was acquired in the time-resolved mode. The fluorescence intensity at 15 ms after pulse onset (5 ms before termination) is shown

in Figure 192. The fluorescence signature is dominated by NO fundamental emission with substantial vibrational excitation. There is a hint of a feature at 4.75  $\mu\text{m}$ . In the same experiment at late times (20 ms after beam termination) the fluorescence spectrum has changed as shown in Figure 193. The total signal level has decreased by a factor of six to seven. This decay rate is far in excess of radiative and indicates quenching is occurring. The later time fluorescence indicated a more vibrationally relaxed distribution (peaking to shorter wavelength). Also the 4.5 to 4.8  $\mu\text{m}$  feature has increased in intensity relative to NO. This feature may be due to  $\text{O}_3$  ( $\nu_1 + \nu_3$ ) emission. The  $\text{O}_3(\nu_3)$  fundamental at 10  $\mu\text{m}$  is observed to be quite strong under these conditions.

NO overtone emission is observed in the SWIR under these conditions. The fluorescence of the same mixture near beam termination is displayed in Figure 194.  $\text{N}_2$  electronic transitions are also observed in this region. In order to lessen the effects of collisional quenching, lower pressure  $\text{N}_2/\text{O}_2$  mixtures at 4.9 mt total pressure were irradiated with 6.6 mA of 4.5 keV electrons. The observed NO fluorescence (Figure 195) was substantially vibrationally colder at all times during the pulse. Moreover there appears to be no evidence of rotational bandhead formation in these mixtures. The CVF resolution is barely adequate to detect bandheads if present. The strong signal level indicate that these studies can be performed at very low pressures in future cryogenic interferometer studies.

#### 17.4 MWIR EMISSION FROM Ar/ $\text{CO}_2$ MIXTURES

Strong fluorescence is observed when trace concentrations of  $\text{CO}_2$  (3 sccm) are added through the jet inlet into a bath of 30 mt of Ar (693 sccr) in the cryoshroud. Even with the applied magnetic field off, the pulsed electron beam produced large MWIR signals dominated by  $\text{CO}_2(\nu_3)$  with some  $\text{CO}(\nu)$  emission at 4.7  $\mu\text{m}$  at times near beam termination as shown in Figure 196. At late times the prompt ( $\tau = 2.5$  ms)  $\text{CO}_2\nu_3$  emission decays with the time constant of the detection system. CO fundamental band fluorescence persists decreasing to 50 percent of its beam termination value at 90 ms later (Figure 197). Because

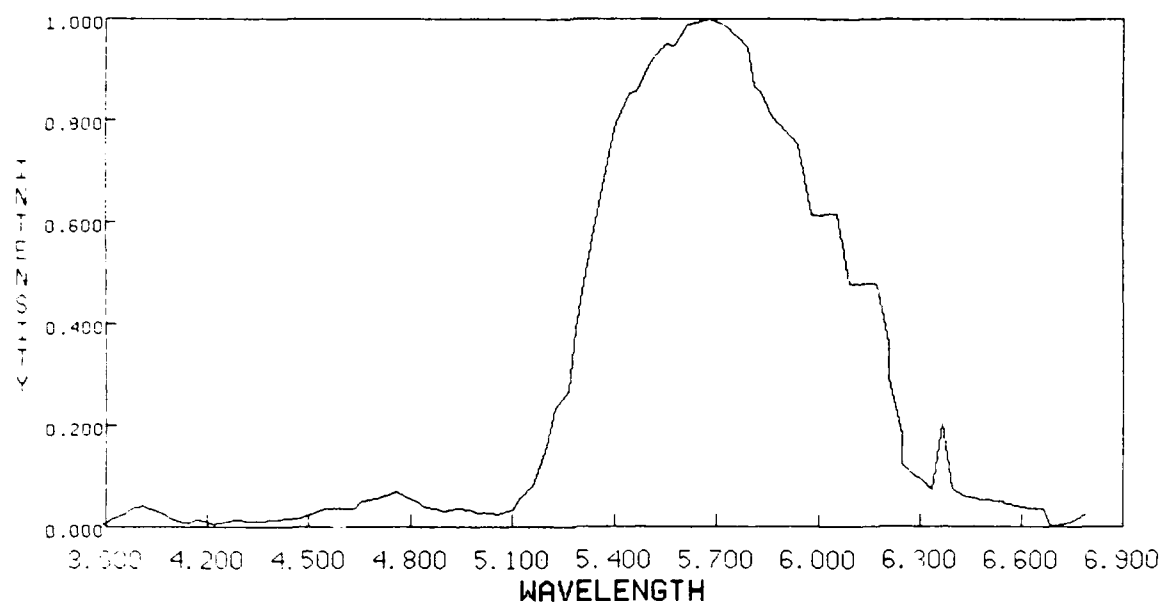


Figure 192. MWIR fluorescence from irradiated  $N_2/O_2$  mixtures ( $p=35$  mt) near beam termination. Maximum relative intensity is 45 mV (Scan H6029).

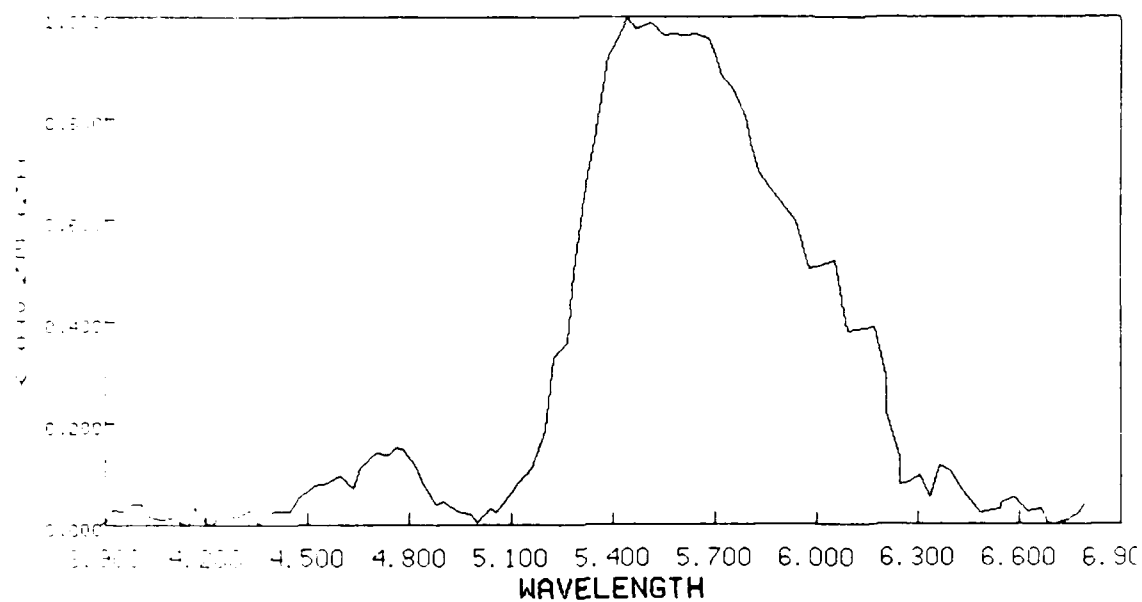


Figure 193. MWIR fluorescence from irradiated  $N_2/O_2$  mixtures ( $p=35$  mt) 20 ms after beam termination. Maximum relative intensity is 7 mV (Scan H6029).

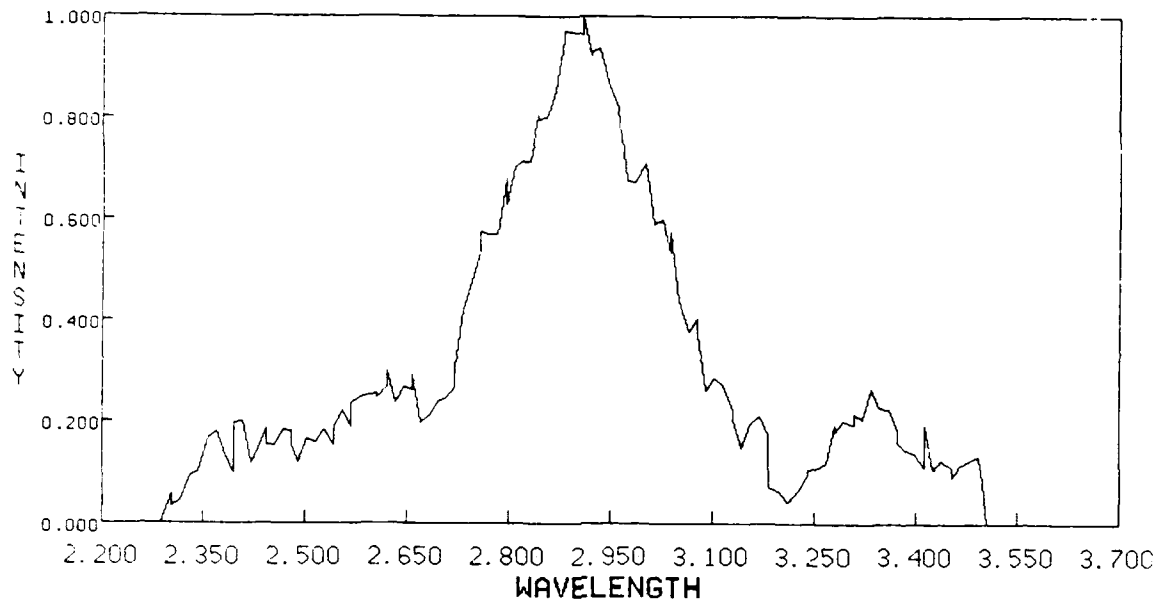


Figure 194. SWIR fluorescence from irradiated  $N_2/O_2$  mixtures ( $p=35$  mt) near beam termination. Maximum relative intensity is 5.3 mV (Scan J6029).

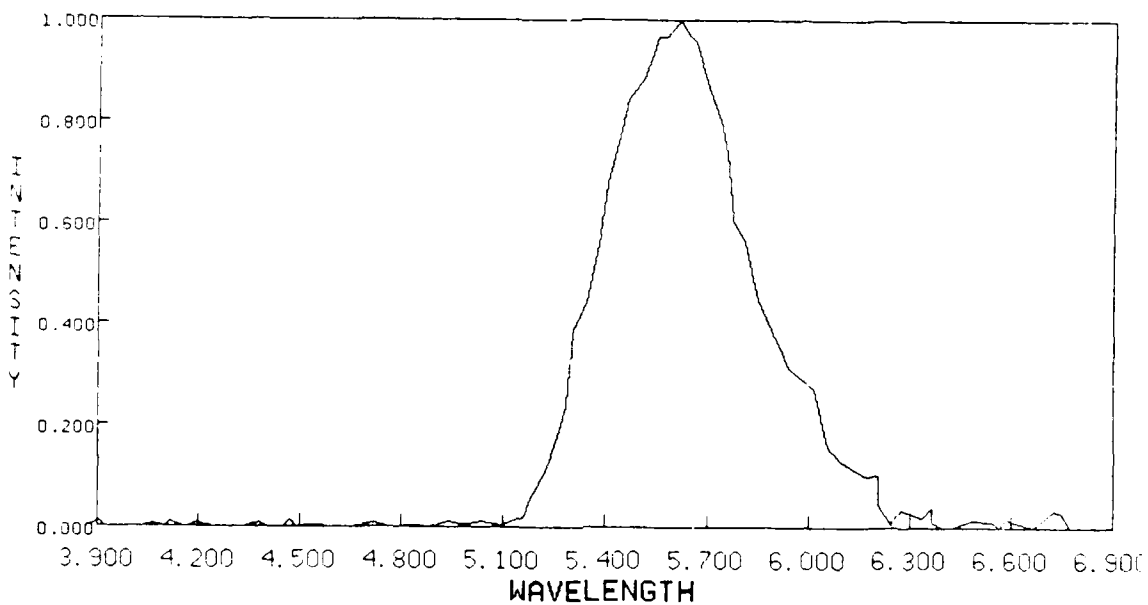


Figure 195. MWIR fluorescence from irradiated  $N_2/O_2$  mixtures ( $p=5$  mt) 45 ms after beam termination. Maximum relative intensity is 17 mV (Scan L6029).

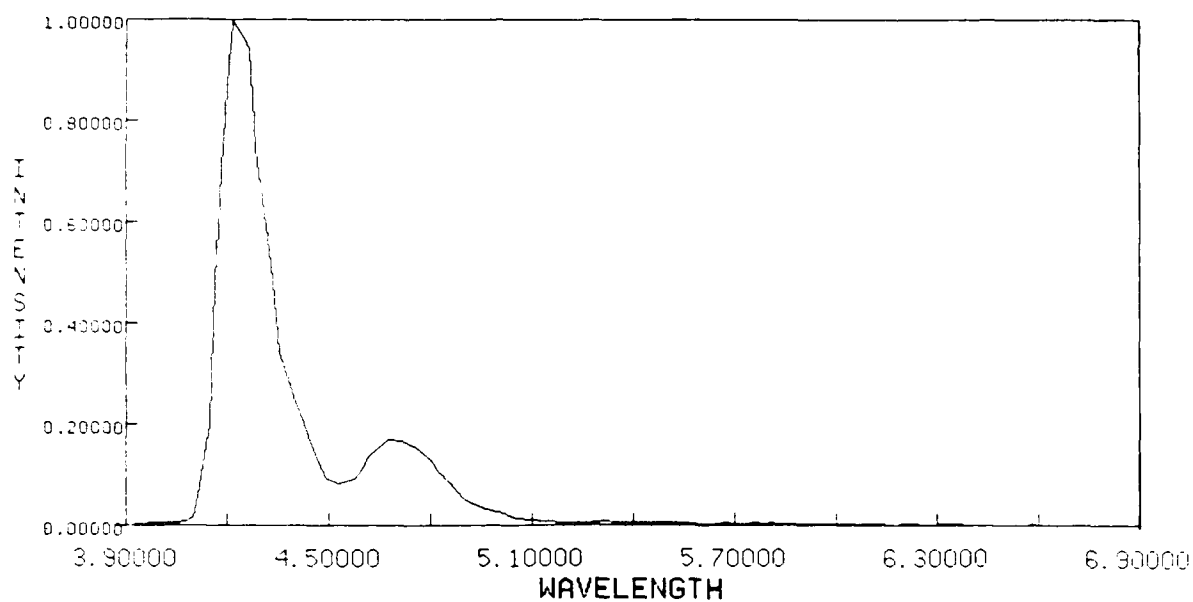


Figure 196. MWIR fluorescence from irradiated Ar/trace CO<sub>2</sub> mixtures at 30 ms at beam termination. Maximum relative intensity is 310 mV (Scan P7507).

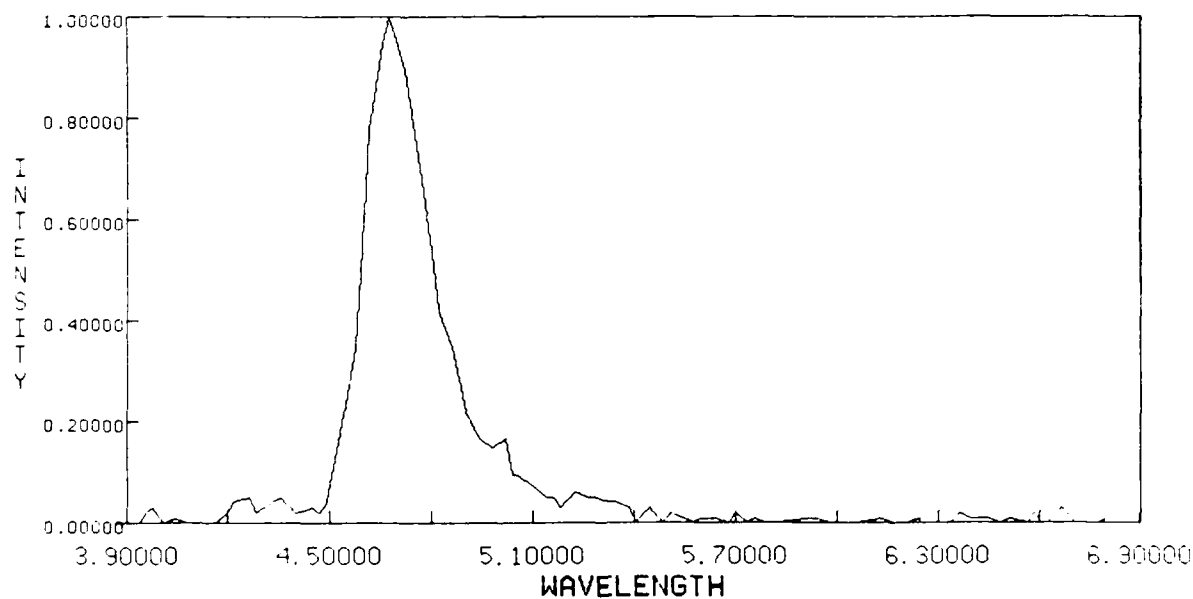


Figure 197. MWIR fluorescence from Ar/trace CO<sub>2</sub> mixtures 90 ms after beam termination. Maximum relative intensity is 9.5 mV. The CO feature is only a factor of two less than that in Figure 196.

this is a much slower decay rate than its radiative loss, substantial excitation must be occurring after beam termination.

Fluorescence was also observed from Ar/trace  $\text{CO}_2$  mixtures (277/9 sccm) at much lower pressures (2.9 mt) as shown in Figure 198. There is still no applied magnetic field. The spectrum is substantially altered. The gap between  $\text{CO}_2(\nu_3)$  and  $\text{CO}(\Delta v=1)$  has been filled with fluorescence. Moreover the fluorescence extends out to beyond 6  $\mu\text{m}$ . The  $\text{CO}_2(\nu_3)$  fluorescence is not substantially altered in width indicated little rotational excitation. The 4.4 to 4.7  $\mu\text{m}$  fluorescence can be attributed to hot bands of  $\text{CO}_2$  or to rotationally hot CO. Better spectral resolution is needed to understand these exciting observations.

#### 17.5 LWIR EMISSION FROM $\text{N}_2/\text{CO}_2$ MIXTURES

When trace amounts of  $\text{CO}_2$  were added to 36 mt of  $\text{N}_2$  in the cryoshroud, 13 to 15  $\mu\text{m}$  spectral features were observed using the CVF spectrometer. Figure 199 shows the presence of the  $\text{CO}_2(\nu_1 \rightarrow \nu_2)$  feature at 13.9  $\mu\text{m}$  as well as the R branch of the strong  $\nu_2$  feature. Vibrational temperatures can be determined from measurements of this type. Time-resolved fluorescence data was used to observe the vibrational relaxation of the  $\text{CO}_2\nu_2$  feature. With just 10 mt of  $\text{N}_2$  present, the  $\text{CO}_2(\nu_2)$  R branch fluorescence was observed to decay at a rate of about  $20 \text{ s}^{-1}$  as shown in Figure 200. When 2.5 mt of  $\text{O}_2$  was added, the relaxation rate increased substantially as indicated by the open symbols. It appears that collisional relaxation processes can be studied even for LWIR emitting states.

#### 17.6 OZONE 13 TO 15 $\mu\text{m}$ EMISSION

During the course of the studies of  $\text{O}_3(\nu_3)$  emission around 10  $\mu\text{m}$ , data were occasionally taken with all other CVF wheel segments. Under the highest signal conditions, there appeared to be a hint of emission of  $\text{O}_3\nu_2$  around 14.3  $\mu\text{m}$ . The spectrum shown in Figure 201 arises from an Ar (580 sccm)/ $\text{O}_2$

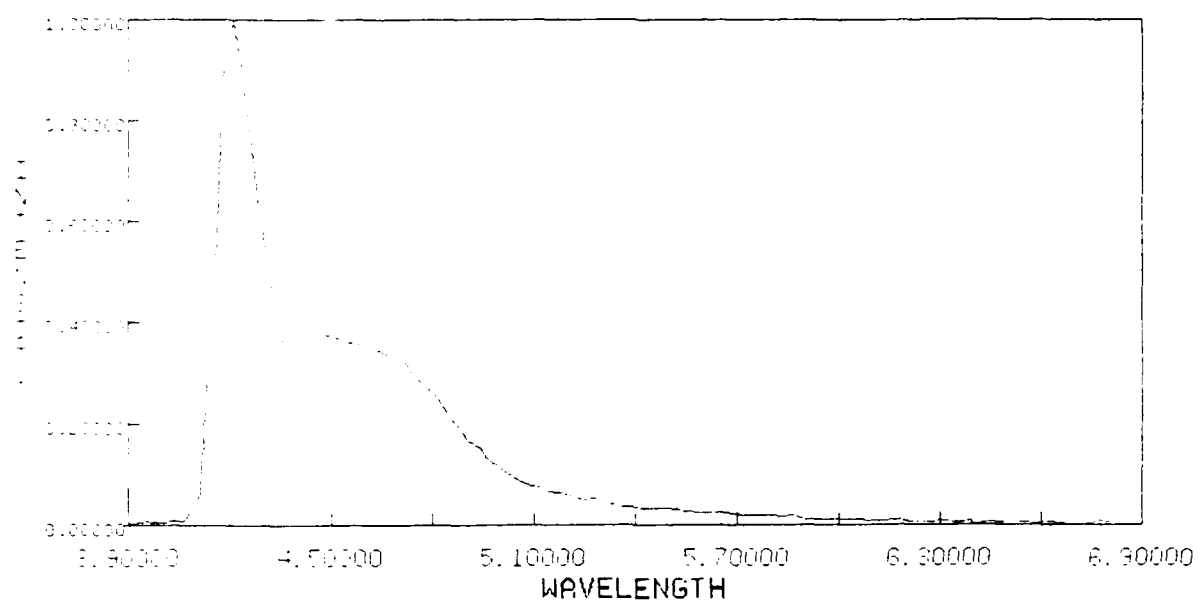


Figure 198. MWIR fluorescence from Ar/trace CO<sub>2</sub> mixture at 2.9 mt, 10 ms after beam termination. Maximum relative intensity is 150 mV (Scan T7616).

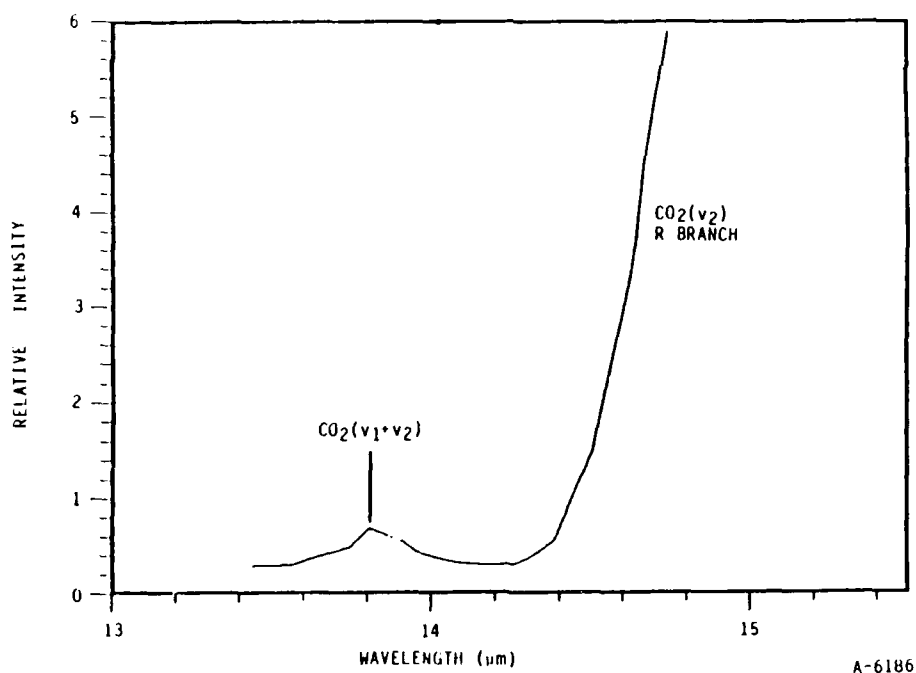


Figure 199. Fluorescence from 36 mt N<sub>2</sub>/trace CO<sub>2</sub> mixture at 25 ms after beam termination.

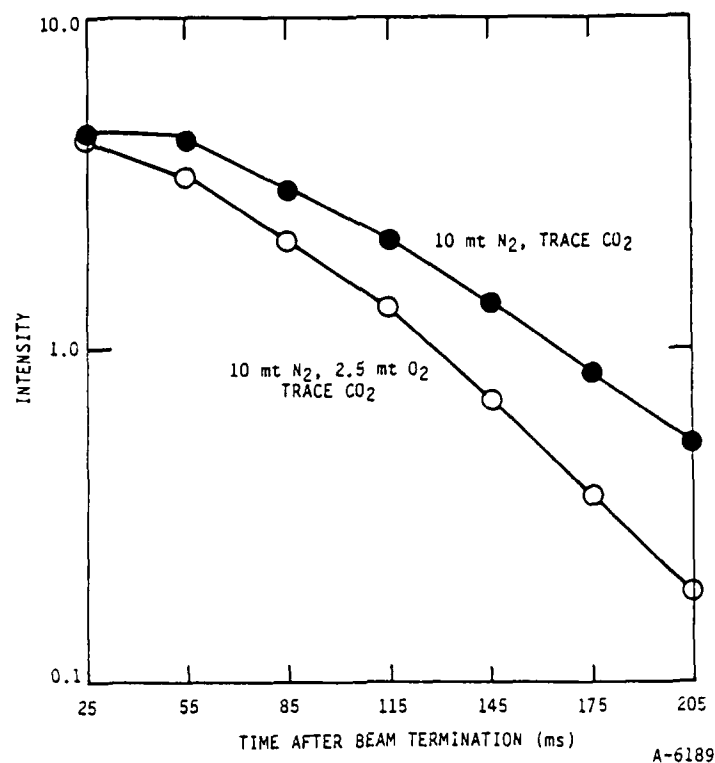


Figure 200. Intensity of  $\text{CO}_2(\nu_2)$  R branch fluorescence as a function of time after beam termination for  $\text{N}_2$  and  $\text{N}_2/\text{O}_2$  bath gases.

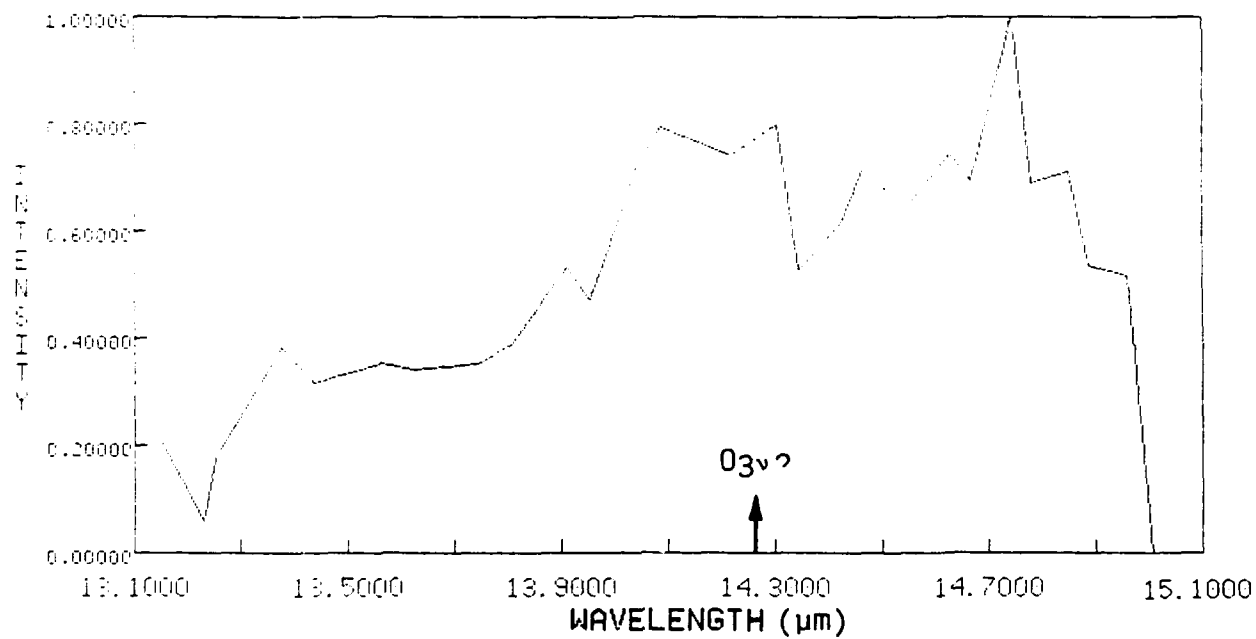


Figure 201. LWIR emission from  $\text{Ar}/\text{O}_2$  mixtures 15 ms after beam termination. Maximum relative intensity is 1.1 mV.



(100 sccm) mixture at 36 mt total pressure. The applied magnetic field was 7G. The 4.5keV electron beam was pulsed on for 17 ms and had a 328 ms period and had average currents of 1.7 mA. Even though the signal to noise is unity in this spectrum, persistent indications of an emission feature lead us to make this tentative assignment. To our knowledge this feature has never been observed, having a radiation lifetime of about a second. If future work on electron irradiated  $O_3$  supports this assignment, it will be a further demonstration of the sensitivity and versatility of the cryogenic LABCEDE facility.

## REFERENCES

1. Vallance-Jones, A. and Gattinger, R.L., "Quantitative Spectroscopy of the Aurora I: 7000-9000Å," Can. J. Phys., 50, 1833 (1972).
2. Gattinger, R.L. and Vallance-Jones, A., "Quantitative Spectroscopy of the Aurora II: 4500-8900Å," Can. J. Phys., 52, 2343 (1974).
3. Vallance-Jones, A. and Gattinger, R.L., "Quantitative Spectroscopy of the Aurora III: 3100-4700Å," Can. J. Phys., 53, 1806 (1975).
4. Cartwright, D.C., "Vibrational Populations of the Excited States of N<sub>2</sub> Under Auroral Conditions," J. Geophys. Res., 83, 517 (1978).
5. Gattinger, R.L. and Vallance-Jones, A., Can. J. Phys., 59, 480 (1981).
6. Lofthus, A. and Krupenie, P.H., "The Spectrum of Molecular Nitrogen," J. Phys. Chem. Ref. Data 6, 113 (1977).
7. Benesch, W., J. Geophys. Res., 86, 9065 (1981).
8. Benesch, W., J. Chem. Phys., 78, 2978 (1983).
9. Green, B.D., Piper, L.G., Caledonia, G.E., Lewis, P.F., Murphy, H.C., and Marinelli, W.J., "Fluorescence from Electron Irradiated Gases in Refurbished LABCEDE," AFGL-TR-84-0218 (Sept. 1985) ADA161674.
10. Piper, L.G., Green, B.D., Blumberg, W.A.M., and Wolnik, S.J., "Quenching of N<sub>2</sub><sup>+</sup> Meinel Band Emission by N<sub>2</sub> and O<sub>2</sub>," J. Chem. Phys., 82, 3139 (1985).
11. National Oceanic and Atmospheric Administration, U.S. Standard Atmosphere 1976 (U.S. Government Printing Office, Washington, DC) (1976).
12. Shemansky, D.E. and Broadfoot, A.L., "Excitation of N<sub>2</sub> and N<sub>2</sub><sup>+</sup> Systems by Electrons II: Excitation Cross-Sections and N<sub>2</sub>1PG Low Pressure Afterglow," J. Quant. Spectrosc. Radiat. Transfer 11, 1401 (1971).
13. Shemansky, D.E. and Broadfoot, A.L., "Excitation of N<sub>2</sub> and N<sub>2</sub><sup>+</sup> Systems by Electrons I: Absolute Transition Probabilities," J. Quant. Spectrosc. Radiat. Transfer 11, 1385 (1971).
14. Lewis, P.L. and Green, B.D., Physical Sciences Inc. Technical Report TR-413, Appendix C, June 1984.
15. Kovacs, J., Rotational Structure in the Spectra of Diatomic Molecules (American Elsevier, 1969).

16. Arnold, J.Q., Whiting, E.E., and Lyle, G.C., J. Quant. Spectrosc. Radiat. Transfer 9, 775 (1969).
17. Whiting, E.E. and Nicholls, R.W., Astrophys. J. Suppl. Ser. 235, 27, 1 (1974).
18. Huber, K. and Herzberg, G., Molecular Spectra and Molecular Structure: IV Constants of Diatomic Molecules, (Van Nostrand Reinhold, New York, 1979).
19. Vallance-Jones, A. and Gattinger, R.L., "Vibrational Development and Quenching Effects in the  $N_2(B-A)$  and  $N_2^+(A-X)$  systems in Aurora," J. Geophys. Res. 83, 3255 (1978).
20. Piper, L.G., "State-to-State  $N_2(A)$  Energy Pooling Reactions. II. The Formation and Quenching of  $N_2B$ ,  $v'=1-12$ ," J. Chem. Phys. 88, 6911 (1988).
21. Mitchell, K.B., J. Chem. Phys. 53, 1957 (1970).
22. Shemansky, D.E., " $A^3\Sigma_u^+$  Molecules in the  $N_2$  Afterglow," J. Chem. Phys. 64, 565 (1976).
23. Rotem, A. and Rosenwaks, S., Opt. Eng., 22, 564 (1983).
24. Cartwright, D.C., Chutjian, A., Trajmar, S., and Williams, W., "Electron Impact Excitation of the Electronic States of  $N_2$ . I. Differential Cross Sections at Incident Energies from 10 to 50 eV," Phys. Rev. A., 16, 1013 (1977).
25. Cartwright, D.C., Trajmar, S., Chutjian, A., and Williams, W., "Electron Impact Excitation of the Electronic States of  $N_2$ . II. Integral Cross Sections at Incident Energies from 10 to 50 eV," Phys. Rev. A., 16, 1041 (1977).
26. Peterson, L.R., Sawada, T., Bass, J.N., and Green, A.E.S., "Electron Energy Deposition in a Gaseous Mixture," Comp. Phys. Comm. 5, 239 (1973).
27. Jackman, C.H., Garvey, R.M., and Green, A.E.S., "Electron Impact on Atmospheric Gases. I. Updated Cross Sections," J. Geophys. Res. 82, 5081 (1977).
28. Piper, L.G., "State-to-State  $N_2(A)$  Energy Pooling Reactions. I. The Formation of  $N_2(C)$  and the Herman Infrared System," J. Chem. Phys. 88, 321 (1988).
29. Dreyer, J.W. and Perner, D., "Deactivation of  $N_2(A, v=0-7)$  by Ground State Nitrogen, Ethane and Ethylene Measured by Kinetic Absorption Spectroscopy," J. Chem. Phys. 58, 1195 (1973).

30. Sadeghi, N. and Setser, D.W., J. Chem. Phys., 79, 2710 (1983).
31. Pendleton, W.R., Espy, P., Steed, A., and O'Neil, R., Defense Nuclear Agency I.R. Data Review, September 20-23, 1983, Air Force Geophysics Laboratory, Bedford, MA.
32. Werner, H.J., Kalcher, J., and Reinsch, E.A., "Accurate and Initio Calculations of Radiative Transition Probabilities Between the  $A^3\Sigma_u^+$ ,  $B^3\Pi_g$ ,  $W^3\Delta_u$ ,  $B'^3\Sigma_u^-$  and  $C^3\Pi_u$  State of  $N_2$ ," J. Chem. Phys., 81, 2420 (1984).
33. Covey, R., Saum, K.A., and Benesch, W., J. Opt. Soc. Am., 63, 592 (1973).
34. Neuschaefer, D., Ottinger, C., and Sharma, A., "Observation of a Long-Lived Nitrogen Beam Afterglow and Lifetime Measurements on the  $N_2W$  State," J. Chem. Phys. 117, 133 (1987).
35. Brennen, W. and Shane, E.C., J. Phys. Chem., 75, 1552 (1971).
36. Carlson, T.A., Duric', N., Erdman, P., and Larsson, M., "Collisional Transfer to the B State in  $N_2$ ," Physica Scripta, 19, 25 (1979).
37. Gattinger, R.L., Harris, F.R., and Jones, A.V., Planetary and Space Sci., 33, 207 (1985).
38. Brown, N., Deehr, C., Halliman, T., Viereck, R., Hoch, E., Degin, V., "Emission Spectra of Type B Auroras," SA41C-212 EOS 68, 1397 (1987).
39. Erdman, P.W., Zipf, E.C., and Gorman, M.R., EOS 65, 247 (1984).
40. Gentieu, E.P., Feldman, P.D., and Meier, R.R., "Spectroscopy of the Extreme Ultraviolet Dayglow at 6.5Å Resolution: Atomic and Ionic Emissions between 530 and 1240Å," Geophys. Res. Lett., 6, 325 (1979).
41. Park, H., Feldman, P.D., and Fastie, W.G., "The Extreme Ultraviolet (750 to 1230Å) Spectrum of an Aurora," Geophys. Res. Lett., 4, 41 (1977).
42. Huffman, R.E., LeBlanc, F.J., Larrabee, J.C., and Paulsen, D.E., "Satellite Vacuum Ultraviolet Airglow and Auroral Observations," J. Geophys. Res., 85, 2201 (1980).
43. Takacs, P.Z. and Feldman, P.D., "Far Ultraviolet Atomic and Molecular Nitrogen Emissions in the Dayglow," J. Geophys. Res., 82, 5011 (1977).
44. Rottman, G.J., Feldman, P.D., and Moos, H.W., "Far Ultraviolet Spectra and Altitude Profiles of the Dawn Airglow, J. Geophys. Res., 78, 258 (1973).
45. Paresce, F., Lumpton, M., and Holberg, J., "Extreme Ultraviolet Emissions from an Aurora," J. Geophys. Res., 77, 4773 (1972).

46. Ajello, J.M. and Shemansky, D.E., "A Reexamination of Important N<sub>2</sub> Cross Sections by Electron Impact with Application to the Dayglow: The Lyman-Birge-Hopfield Band System and NI (119.99 nm)," J. Geophys. Res., 90, 9845-9861 (1985).
47. Torr, M.R., Torr, D.G., and Eun, J.W., "A Spectral Search for Lyman-Birge-Hopfield Band Nightglow From Spacelab 1," J. Geophys. Res., 90, 4427-4433 (1985).
48. McFarlane, R.A., "Precision Spectroscopy of New Infrared Emission Systems of Molecular Nitrogen," IEEE J. Quantum Electron., 2, 229-232 (1966).
49. Ogawa, M. and Tanaka, Y., "New Emission Bands of N<sub>2</sub> in the Vacuum Ultraviolet Region," J. Chem. Phys., 30, 1354-1355 (1959).
50. Ogawa, M. and Tanaka, Y., "New Emission Bands of Forbidden Systems of Nitrogen in the Vacuum Ultraviolet Region," J. Chem. Phys. 32, 754-758 (1964).
51. Tanaka, Y., Ogawa, M., and Jursa, A.S., "Forbidden Absorption-Band Systems of N<sub>2</sub> in the Vacuum-Ultraviolet Region," J. Chem. Phys., 40, 3690-3700 (1964).
52. Golde, M.F. and Thrush, B.A., "Vacuum Ultraviolet Emission by Active Nitrogen," Chem. Phys. Lett., 8, 375 (1971).
53. Golde, M.F. and Thrush, B.A., "Vacuum Ultraviolet Emission by Active Nitrogen I. The Formation and Removal of N<sub>2</sub>(a<sup>1</sup>Π<sub>g</sub>)," Proc. R. Soc. Lond. A., 330, 79-95 (1972).
54. Golde, M.F. and Thrush, B.A., "Vacuum Ultraviolet Emission by Active Nitrogen III. The Absolute Rates of Population of N<sub>2</sub>(a<sup>1</sup>Π<sub>g</sub>) and CO(A<sup>1</sup>Π)," Proc. R. Soc. Lond. A., 330, 109-120 (1972).
55. Golde, M.F., "Vacuum UV Emission by Electronically Excited N<sub>2</sub>: The Collision-Induced N<sub>2</sub>(a<sup>1</sup>Π<sub>g</sub>, v=0) - N<sub>2</sub>(a'<sup>1</sup>Σ<sub>u</sub><sup>-</sup>, v=0) Transition," Chem. Phys. Lett., 31, 348 (1975).
56. Freund, R.S., "Radiative Lifetime of N<sub>2</sub>(a<sup>1</sup>Π<sub>g</sub>) and the Formation of Metastable N<sub>2</sub>(a'<sup>1</sup>Σ<sub>u</sub><sup>-</sup>)," J. Chem. Phys., 56, 4344 (1972).
57. van Veen, N., Brewer, P., Das, P., and Bersohn, R., "Detection of the a<sup>1</sup>Π<sub>g</sub>(v'=0,1) ← X<sup>1</sup>Σ<sub>g</sub><sup>+</sup>(v'=0) Transition in N<sub>2</sub> by Laser-Induced Fluorescence," J. Chem. Phys. 77, 4326 (1982).
58. Shemansky, D.E., "Transition Probabilities and Collision Broadening Cross Section of the N<sub>2</sub> Lyman-Birge-Hopfield System," J. Chem. Phys., 51, 5487 (1969).

59. Krupenie, P.H., "The Band Spectrum of Carbon Monoxide," NSRDS-NBS5 (1966).
60. Piper, L.G. and Cowles, L.M., "Einstein Coefficients and Transition Moment Variation for the  $\text{NO}(\text{A}^2\Sigma^+-\text{X}^2\Pi)$  Transition," J. Chem. Phys. 85, 2419 (1986).
61. Huber, K.P. and Herzberg G., "Molecular Spectra and Molecular Structure. IV. Constants of Diatomic Molecules," Van Nostrand, New York (1979).
62. Holland, R.F., "Excitation of Nitrogen by Electrons: The Lyman-Birge-Hopfield System of  $\text{N}_2^*$ ," J. Chem. Phys. 51, 3940 (1968).
63. Pilling, M.J., Bass, A.M., and Braun, W., "A Curve of Growth Determination of the f-Values for the Fourth Positive System of CO and the Lyman-Birge-Hopfield System of  $\text{N}_2$ ," J. Quant. Spectrosc. Radiat. Transfer, 11, 1593-1604 (1971).
64. Tilford, S.G., Wilkinson, P.G., and Vanderslice, J.T., "The High Resolution Absorption Spectrum of Nitrogen from 1060 to 1520Å. II. The  $\text{a}'^1\Sigma_u^--\text{X}^1\Sigma_g^+$  System," Astrophys. J., 141, 427-442 (1965).
65. Yeager, D.L. and McKoy, V., "Transition Moments Between Excited Electronic States of  $\text{N}_2^*$ ," J. Chem. Phys., 67, 2473 (1977).
66. Piper, L.G., "Quenching Rate Coefficients for  $\text{N}_2(\text{a}'^1\Sigma_u^-)$ ," J. Chem. Phys. 87, 1625 (1987).
67. Piper, L.G., DeFaccio, M.A., and Rawlins, W.T., "Rate Coefficients for  $\text{N}(\text{D})$  and  $\text{N}_2(\text{a}'^1\Sigma_u^-)$  Reactions," American Geophysical Union Spring Meeting, 1986, EOS 67, 322 (1986).
68. Zipf, E.C. and McLaughlin, R.W., "On the Dissociation of Nitrogen by Electron Impact and by E.U.V. Photo-Absorption," Planet. Space Sci. 26, 449-462 (1977).
69. Filippelli, A.R., Chung, S., and Lin, C.C., "Electron-Impact Excitation of the  $\text{D}^3\Sigma_u^+$  and  $\text{c}_4'^1\Sigma_u^+$  Rydberg States of  $\text{N}_2$ ," Phys. Rev. A 29, 1709 (1984).
70. Meier, R.R., Conway, R.R., Feldman, P.D., Strickland, D.J., and Gentieu, E.P., "Analysis of Nitrogen and Oxygen Far Ultraviolet Auroral Emissions," J. Geophys. Res. 87, 2444-2452 (1982).
71. Conway, R.R., "Self-Absorption of the  $\text{N}_2$  Lyman-Birge-Hopfield Bands in the Far Ultraviolet Dayglow," J. Geophys. Res. 87, 859-866 (1982).
72. Feldman, P.D. and Gentieu, E.P., "The Ultraviolet Spectrum of an Aurora 530-1520Å," J. Geophys. Res. 87, 2453-2458 (1982).

73. Eastes, R.W. and Sharp, W.E., "Rocket-Borne Spectroscopic Measurements in the Ultraviolet Aurora: The Lyman-Birge-Hopfield Bands," J. Geophys. Res. 92, 10095 (1987).
74. Meier, R.R. and Conway, R.R., "On the N<sub>2</sub> Lyman-Birge-Hopfield Band Nightflow," J. Geophys. Res. 88, 4929-4934 (1983).
75. Conway, R.R., Meier, R.R., Strobel, D.F., and Huffman, R.E., "The Far Ultraviolet Vehicle Glow of the S3-4 Satellite," Geophys. Res. Lett. 14, 628 (1987).
76. Mandlebaum, D. and Feldman, P.D., J. Chem. Phys., 65, 672 (1976).
77. Skubenich, V.V. and Zapesochnyy, I.P., Geomag. and Aeronomy, 21, 355 (1981).
78. Holland, R.F. and Maier, W.B., II, J. Chem. Phys., 56, 5229 (1972).
79. Holland, R.F. and Maier, W.B., II, J. Chem. Phys., 58, 2672 (1973).
80. Simpson, F.R. and McConkey, J.W., Planet. Space Sci., 17, 1941 (1969).
81. Stanton, P.N. and St. John, R.M., J. Opt. Soc. Amer., 59, 252 (1969).
82. Srivastava, B.N. and Mizra, I.M., Phys. Rev., 168, 86 (1968).
83. Pendleton, W.R. and Weaver, L.D., Advanced Research Project Agency Report No. 1691 under Contract No. F33657-71-C-0174 to Utah State University (1973).
84. Piper, L.G., Green, B.D., Blumberg, W.A.M., and Wolnik, S.J., "Quenching of N<sub>2</sub><sup>+</sup> Meinel Band Emission by N<sub>2</sub> and O<sub>2</sub>," J. Chem. Phys., 82, 3139 (1985).
85. Borst, W.L. and Zipf, E.C., "Cross Section for Electron-Impact Excitation of the (0,0) First Negative Band of N<sub>2</sub><sup>+</sup> from Threshold to 3 keV," Phys. Rev. A, 1, 834-40 (1970).
86. Opal, C.B., Beaty, E.C., and Peterson, W.K. Atomic Data, 4, 209 (1972).
87. Wu, H.H. and Shemansky, D.E., J. Chem. Phys., 64, 1134 (1976) and private communication from D.E. Shemansky to L.G. Piper (1982).
88. Katayama, D.H., Miller, T.A., and Bondybey, V.E., J. Chem. Phys., 72, 5469 (1980).
89. Broadfoot, A.L., Planet. Space Sci., 15, 1801 (1967).
90. Lee, L.C. and Judge, D.L., J. Phys. B., 6, L121 (1973).

91. Shaw, M. and Campos, J., *J. Quant. Spectrosc. Radiat. Transfer*, 30, 73 (1983).
92. Srivastava, B.N. and Mizra, I.M., *Can. J. Phys.*, 47, 475 (1969).
93. Wyatt, Clair, L., "Infrared Spectrometer: Liquid Helium Cooled Rocketborne Circular-Variable Filter," *Applied Optics*, 14, 3086 (December 1975).
94. Huppi, Ray, E., *Spectrometric Technique*, Vol. 1, Ed. George A. Vanasse, A.P. New York, 1977, Chapter #4 and Appendix.
95. Marinelli, W.J., Green, B.D., DeFaccio, M.A., and Blumberg, W.A.M., "Vibrational Relaxation and Intersystem Crossing in  $N_2(a^1\Pi_g)$ ," *J. Phys. Chem.* 92, 3429 (1988).
96. Piper, L.G., Green, B.D., Blumberg, W.A.M., and Wolnik, S., "Electron Impact Excitation of the  $N_2^+$  Neinel Band," *Journal of Physics B: Atomic and Molecular Physics*, 19, 3327 (1986).
97. Fink, E.H. and Welge, K.H., "Lebensdauern und Löschquerschnitt elektronisch angeregter Zustände von  $N_2O^+$ , NO,  $O_2^+$ , CO,  $CO^+$ ," *Z. Naturforsch.* 23a, 358-376, p. 367 (1968).
98. Erman, P. and Larsson, M., "Lifetimes of Excited Levels in Some Important Ion-Molecules: Part II:  $O_2^+$ ," *Physica Scripta.*, 15, 335-338 (1977).
99. Green, B.D., Piper, L.G., Caledonia, G.E., Lewis, P.F., Murphy, H.C., and Marinelli, W.J., "Fluorescence from Electron Irradiated Gases in Refurbished LABCEDE," AFGL, Technical Report 84 0218 (1985) ADA161674.
100. Piper, L.G., Cowles, L.M., and Rawlins, W.T., "State-to State Excitation of  $NO(A^2\Sigma^+, v'=0,1,2)$  by  $N_2(A^3\Sigma_u^+, v'=0,1,2)$ ," *J. Chem. Phys.* 85, 3369 (1986).
101. Shemansky, D.E., " $N_2$  Vegard-Kaplan System in Absorption," *J. Chem. Phys.* 51, 689 (1969).
102. Shemansky, D.E., and Carleton, N.P., "Lifetime of the  $N_2$  Vegard-Kaplan System," *J. Chem. Phys.* 51, 682 (1969).
103. Carleton, N.P. and Oldenberg, O., "Lifetime of the Lowest Excited Level of  $N_2$ ," *J. Chem. Phys.* 36, 3460 (1967).
104. Weiner, B. and Öhrn, Y., "A Note on the Radiative Lifetimes of the  $B^3\Pi_g$  State of  $N_2$ ," *J. Chem. Phys.* 80, 5866 (1984).
105. Fraser, P.A., "A Method of Determining the Electronic Transition Moment for Diatomic Molecules," *Can. J. Phys.* 32, 515 (1954).



106. Grum, F. and Luckey, G.W., "Optical Sphere Paint and a Working Standard of Reflectance," Appl. Opt. 7, 2289 (1968).
107. Grum, F. and Wightman, T.E., "Absolute Reflectance of Eastman White Reflectance Standard," Appl. Opt. 16, 2775 (1977).
108. Fontijn, A., Meyer, C.B., and Schiff, H.I., "Absolute Quantum Yield Measurements of the NO-O Reaction and Its Use as a Standard for Chemiluminescent Reactions," J. Chem. Phys. 40, 64 (1964).
109. Sutoh, M., Morioka, Y., and Nakamura, M., "Absolute Rate Constant for the Chemiluminescent Reaction of Atomic Oxygen with Nitric Oxide," J. Chem. Phys. 72, 20 (1980).
110. Vanpee, M., Hill, K.D., and Kineyko, W.R., "Absolute Rate Constant Measurements for the Radiative Combination of Atomic Oxygen with Nitric Oxide," AIAA J. 9, 135 (1971).
111. Golde, M.F., Roche, A.E., and Kaufman, F., "Absolute Rate Constant for the O-NO Chemiluminescence in the Near Infrared," J. Chem. Phys. 59, 3953 (1973).
112. Stair, Jr., A.T. and Kennealy, J.P., "Infrared Chemiluminescence and Vibraluminescence in the NO-O-NO<sub>2</sub> Reaction System," J. Chim. Phys. Chim. Biol. 64, 174 (1967).
113. Bradburn, G. and Lilienfeld, H., J. Phys. Chem. 92, xxxx (1988).
114. The Einstein coefficients used in determining populations of the  $v' \geq 5$  overlapping first positive levels (overlap of the  $\Delta v = n$  and  $\Delta v = n-1$  sequences) as well as the infrared afterglow system are those found in Reference 5. Fitting involving the Meinel or Wu-Benesh bands did not require subtraction nor did more than one band from any  $v'$  occur in any fit, hence the values assumed for their Einstein coefficients are immaterial.
115. Marinelli, W.J. and Piper, L.G., "Franck-Condon Factors and Absolute Transition Probabilities for the IF ( $B^3\Pi_0^+ - X^1\Sigma^+$ ) Transition," J. Quant. Spectrosc. Radiat. Transfer 34, 121 (1985).
116. Roux, F., Michaud, F., and Verges, J., "High Resolution Fourier Spectrometry of <sup>14</sup>N<sub>2</sub> Infrared Emission Spectrum: Extensive Analysis of the  $B^3\Pi_g - A^3\Sigma_u^+$  System," J. Mol. Spectrosc. 97, 253 (1983).
117. Tellinghuisen, J., "A Fast Quadrature Method for Computing Diatomic RKR Potential Curves," Comput. Phys. Commun. 6, 221 (1974).
118. Eccles, J. and Malik, R., Quantum Chem. Prog. Exch. Bull. 13, 407 (1981).

119. Eyler, E.E. and Pipkin, F.M., "Lifetime Measurements of the B  $^3\Pi_g$  State of N<sub>2</sub> Using Laser Excitation," J. Chem. Phys. 79, 3654 (1983).
120. Jeunehomme, M., "Transition Moment of the First Positive Band System of Nitrogen," J. Chem. Phys. 45, 1805 (1966).
121. Holstein, M., Lorents, D.C., Peterson, J.R., and Sheridan, J.R., Can. J. Chem. 47, 1858 (1969).
122. Kuzmenko, N.E., Kuznetsova, L.A., Monyakin, A.P., Kuzyakov, Y.Y., J. Quant. Spectrosc. Radiat. Trans. 24, 29 (1980).
123. Curio, B.E. and Jansson, R.E.W., J. Quant. Spectrosc. Radiat. Trans. 8, 1763 (1980).
124. Jain, D.C., J. Quant. Spectrosc. Radiat. Trans. 12, 759 (1972).
125. Turner, R.G. and Nicholls, R.W., Can. J. Phys. 32, 468-475 (1954).
126. Fraser, M.E., Rawlins, W.T., and Miller, S.M., "Infrared (2 to 8  $\mu$ m) Fluorescence of the W $^3\Delta_u \rightarrow B^3\Pi_g$  and w $^1\Delta_u \rightarrow a^1\Pi_g$  Systems of Nitrogen," J. Chem. Phys., 88, 238 (1988).
127. Yamada, C. and Hirota, E., J. Chem. Phys. 11, 6434 (1987).
128. Freund, R.S., Chem. Phys. Lett. 31, 348 (1975).
129. Tilford, S.G. and Benesch, W.M., J. Chem. Phys. 64, 3370 (1976).
130. Casassa, M.P. and Golde, M.F., Chem. Phys. Lett. 60, 281 (1979).
131. Filseth, S.V., Wallenstein, R., and Zacharias, H., Opt. Commun. 23, 231 (1977).
132. Sha, G., Proch, D., and Kompa, K.L., J. Chem. Phys. 5, 2742 (1987).
133. Yardley, J.T., Introduction to Molecular Energy Transfer (1980).
134. Okabe, H., The Photochemistry of Small Molecules, (Wiley-Interscience, New York, 1978).
135. von Rosenberg, C.W. and Trainor, D.W., "Observations of Vibrationally Excited Ozone Formed by Recombination," J. Chem. Phys., 59, 2142 (1973).
136. von Rosenberg, C.W. and Trainor, D.W., "Vibrational Excitation of Ozone Formed by Recombination," J. Chem. Phys., 61, 2442 (1974).
137. von Rosenberg, C.W. and Trainer, D.W., "Excitation of Ozone Formed by Recombination, II," J. Chem. Phys., 63, 5348 (1975).

138. Rawlins, W.T., Caledonia, G.E., and Kennealy, J.P., "Observation of Spectrally Resolved Infrared Chemiluminescence from Vibrationally Excited  $O_3(v_3)$ ," J. Geophys. Res., 86, 5247 (1981).
139. Rawlins, W.T., Murphy, H.C., Caledonia, G.E., Kennealy, J.P., Robert, F.X., Corman, A., and Armstrong, R.A., "COCHISE: Laboratory Studies of Atmospheric Infrared Chemiluminescence in a Cryogenic Environment," Appl. Opt., 23, 3316 (1984).
140. Rawlins, W.T., Caledonia, G.E., Gibson, J.J., and Stair, A.T., Jr., "HIRIS Rocketborne Spectra of Infrared Fluorescence in the  $O_3(v_3)$  Band Near 100 km," J. Geophys. Res., 40, 2986 (1985).
141. Green, B.D., Rawlins, W.T., and Nadile, R.M., "Diurnal Variability of Vibrationally Excited Mesospheric Ozone as Detected by SPIRE," J. Geophys. Res. 91, 311 (1986).
142. Rawlins, W.T., "Chemistry of Vibrationally Excited Ozone in the Upper Atmosphere," J. Geophys. Res. 90, 12283 (1985).
143. Rothman, L.S., Gamache, R.R., Barbe, A., Goldman, A., Gillis, J.R., Brown, L.A., Toth, R.A., Flaud, J.M., and Camy-Peyret, C., "AFGL Atmospheric Absorption Line Parameters Compilation: 1982 Edition," Appl. Opt., 22, 2247 (1983).
144. Rothman, L.S., Gamache, R.R., Goldman, A., Brown, L.R., Toth, R.A., Pickett, H.M., Poynter, R.L., Flaud, J.M., Carney-Peyret, C., Barbe, A., Husson, N., Rinsland, C.P., and Smith, M.A.H., "The HITRAN Data Base: 1986 Edition," Appl. Opt., 26, 4058 (1987).
145. Adler-Golden, S.M. and Armstrong, R.A., "Spectroscopic Parameters for Ozone from Infrared and Ultraviolet Techniques," AFGL-TR-82-0231, Air Force Geophysics Laboratory, Hanscom AFB, MA (1982). ADA124315.
146. Caledonia, G.E., Green, B.D., and Murphy, R.E., "Vibrational Level Dependent Relaxation of  $CO(v=1-16)$  by  $CO_2$ ," J. Chem. Phys. 71, 4369 (1978). See also Green, B.D., Caledonia, G.E., and Murphy, R.E., "The Vibrational Relaxation of  $NO(v=1-7)$  by  $O_2$ ," J. Chem. Phys. 76, 2441 (1982).
147. Neil, R.R., Stair, Jr., A.T., Pendleton, Jr., W.R., and Burt, W., "The EXCEDE: Spectral Artificial Auroral Experiment: An Overview," in Artificial Particle Beams in Space Plasma Studies, ed. by B. Grandal, 505-523, Plenum, N.Y., 1982.
148. Bien, F., Gerish, M.E., O'Neil, R.R., Lee, E.T.P., Foley, C.I., and Grieder, W.R., "Analysis of the LWIR Signature from EXCEDE Spectral and OH Emission in EXCEDE Spectra," presented at the Defense Nuclear Agency IR Data Symposium, September 1983.

149. O'Neil, R.R., private communication (1987).
150. Green, B.D., Rawlins, W.T., and Caledonia, G.E., "Atmosphere Radiation Infrared Signature Analysis," Physical Sciences Inc. TR-366 (June 1983).
151. Rawlins, W.T., Caledonia, G.E., Gibson, J.J., and Stair, A.T., Jr., "Infrared Emission from  $\text{NO}(\Delta v=1)$  in an Aurora: Spectral Analysis and Kinetic Interpretation of HIRIS Measurements," J. Geophys. Res., 86, A3, 1313 (1981).
152. Kennealy, J.P., DelGreco, F.P., Caledonia, G.E., and Green, B.D., "Nitric Oxide Chemiexcitation Occurring in the Reaction Between Metastable Nitrogen Atoms and Oxygen Molecules," J. Chem. Phys., 69, 1574 (1978).
153. Grieder, W.R. and Foley, C.E., Analysis of Project EXCEDE II Circular Variable Filter Spectrometer Data, Space Data Analysis Laboratory, Boston College, AFGL-TR-81-0224, January 1981, ADA109894.
154. Piper, L.G., Marinelli, W.J., Rawlins, W.T., and Green, B.D., J. Chem. Phys., 83, 5602 (1985).
155. Whiting, E.E., Arnold, J.O., and Lyle, G.C., NASA TN-D5088, NASA/Ames, Distributed as Cosmic Program No. ARC-10221.
156. Hougen, J.T., The Calculation of Rotational Energy Levels and Rotational Line Intensities in Diatomic Molecules, NBS Monograph 115, National Bureau of Standards, Washington, D.C., June 1970.
157. Effantin, C., D'Incan, J., and Bacis, R., J. Mol. Spec., 76, 204 (1979).
158. Roux, F., Effantin, C., and D'Incan, J., J. Mol. Spec., 91, 238 (1982).
159. Cerny, D., Roux, F., Effantin, C., D'Incan, J., and Verges, J., J. Mol. Spec., 81, 216 (1980).
160. Effantin, C., Amoit, C., and Verges, J., J. Mol. Spec., 76, 221 (1979).
161. Green, B.D., Caledonia, G.E., Blumberg, W.A.M., and Cook, F.H., "Absolute Production Rates and Efficiencies of NO in Electron-Irradiated  $\text{N}_2/\text{O}_2$  Mixtures," J. Chem. Phys., 80, 773 (1984).
162. Green, B.D., Caledonia, G.E., and Murphy, R.E., "A Determination of the Nitric Oxide Einstein Coefficient Ratios," J. Quantitative Spectros. and Radiat. Transfer, 26, 215 (1981).
163. Wu, H.L. and Benesch, W., Phys. Rev., 172, 31 (1968).
164. Saum, K.A. and Benesch, W.M., "Infrared Electronic Emission Spectrum of Nitrogen," Applied Optics, 9, 195 (1970).

165. Green, B.D., Upschulte, B.L., Holtzclaw, K.W., and Blumberg, W.A.M., "Spectra Measurements of  $N_2$  Electronic Emission Between 0.8 and 7  $\mu m$ ," EOS 63, 1397 (1987), presentation at Am. Geophys. Union.
166. McClatchey, R.A., Benedict, W.S., Clough, S.A., Burch, D.E., Calfee, P.F., Fox, K., Rothman, L.S., and Goring, J.S., AFCRL Atmospheric Absorption Line Parameters Compilation, Air Force Cambridge Research Laboratories, AFCRL-TR-73-0096, January 1973 ADA962904.
167. Luie, J.B., Miller, S.M., and Armstrong, R.A., SWIR and Visible Atomic Emission from Laser Produced Oxygen and Nitrogen Plasmas, AFGL TR 84-0161 (June 1984). ADA147528
168. Rawlins, W.T. and Fraser, M.E., "COCHISE: NO Einstein Coefficient Ratios for  $V \leq 12$ ," manuscript in preparation.
169. Jackman, C.H. and Green, A.E.S., "Electron Impact on Atmospheric Gases 3. Spatial Yield Spectra for  $N_2$ ," J. Geophys. Res., 84, 2715-24 (1979).
170. Porter, H.S., Jackman, C.H., and Green, A.E.S., "Efficiencies for Production of Atomic Nitrogen and Oxygen by Relativistic Proton Impact in Air," J. Chem. Phys., 65, 154-67 (1976).
171. Itikawa, Y., Hayashi, M., Ichimura, A., Onda, K., Sakimoto, K., Takayanagi, K., Nakamura, M., Nishimura, H., and Takayanagi, T., "Cross Sections for Collisions of Electrons and Photons with Nitrogen Molecules," J. Phys. Chem. Ref. Data, 15, 985-1010 (1986).
172. Herrmann, D., Jost, K., Kessler, J., and Fink, M., "Differential Cross Sections for Elastic Electron Scattering. II. Charge Cloud Polarization in  $N_2$ ," J. Chem. Phys., 64, 1-5 (1976).
173. Jansen, R.H.J., de Heer, F.J., Luyken, H.J., Van Wingerden, B., and Blaauw, H.J., "Absolute Differential Cross Sections for Elastic Scattering of Electrons by Helium, Neon, Argon and Molecular Nitrogen," J. Phys. B, 9, 185-212 (1976).
174. Inokuti, M., "Inelastic Collisions of Fast Charged Particles with Atoms and Molecules - The Bethe Theory Revisited," Rev. Mod. Phys., 43, 297-347 (1971).
175. Silverman, S.M. and Lassettre, E.N., "Generalized Oscillator Strengths and Electronic Collision Cross Sections for Nitrogen at Excitation Energies Above 10 eV," J. Chem. Phys., 42, 3420-29 (1965).
176. Iida, T., "Measurements of Energy-Loss Cross Sections for 300, 400, and 500 eV Electrons in the Continuum of  $N_2$ ," Japan. J. Appl. Phys., 18, 1667-77 (1979).

177. Shibata, H., Kuroki, K., Nishimura, F., and Oda, N., "Partial Generalized Oscillator Strengths for Ionization of the Nitrogen Molecule by 1 keV Electron Impact," J. Phys. B. 17, L739-44 (1984).
178. Dillon, M.A., Inokuti, M., and Wang, Z.-W., "Analytic Representation of the Generalized Oscillator Strength for Ionization," Rad. Res., 102, 151-64 (1985).
179. Dillon, M.A. and Lassetre, E.N., "A Collision Cross Section Study of the  $1s \rightarrow 2^1p$  and  $1s \rightarrow 2^1s$  Transitions in Helium at Kinetic Energies from 200 to 700 eV. Failure of the Born Approximation at Large Momentum Changes," J. Chem. Phys., 62, 2373-90 (1975).
180. Tisone, G.C., "Low-Resolution Study of the Inelastic Continuum of  $N_2$ ," J. Chem. Phys., 56, 108-12 (1972).
181. Bernstein, W., Leinback, H., Kellogg, P.J., Monson, S.J., and Hallinan, T., "Further Laboratory Measurements of the Beam-Plasma Discharge," J. Geophys. Res., 84, 7271-78 (1979).
182. Person, J.C., Ham, D.O., and Boni, A.A., A Unified Projection of the Performance and Economics of Radiation-Initiated  $NO_x/SO_x$  Emission Control Technologies, Report PSI-252/TR-542, Physical Sciences Inc., Andover, MA (1985).
183. Kee, R.J., Miller, J.A., and Jefferson, T.H., CHEMKIN: A General-Purpose Problem-Independent, Transportable, FORTRAN Chemical Kinetics Code Package, Report SAND 80-8003, Sandia Laboratories, Albuquerque, NM (1980).
184. Cohn, A. and Caledonia, G., "Spatial Distribution of the Fluorescent Radiation Emission Caused by an Electron Beam," J. Appl. Phys., 41, 3767-75 (1970).
185. Center, R.E., "Plural and Multiple Scattering of Fast Electrons in Gases," Phys. Fluids, 13, 79 (1970).
186. Duley, W.W. and Williams, D.A., Interstellar Chemistry, Academic Press, New York, 1984.
187. Schofield, K., "Critically Evaluated Rate Constants for Gaseous Reactions of Several Electronically Excited Species," J. Phys. Chem. Ref. Data, 8, 723-98 (1979).
188. Smith, D., Adams, N.G., and Miller, T.M., "A Laboratory Study of the Reactions of  $N^+$ ,  $N_2^+$ ,  $N_3^+$ ,  $N_4^+$ ,  $O^+$ ,  $O_2^+$ , and  $NO^+$  Ions with Several Molecules at 300 K," J. Chem. Phys., 69, 308-18 (1978).

189. Cohen, N. and Westberg, K.R., "Chemical Kinetic Data Sheets for High-Temperature Chemical Reactions," J. Phys. Chem. Ref. Data, 12, 531-90 (1983).
190. Piper, L.G., Donahue, M.E., and Rawlins, W.T., "Rate Coefficients for N(<sup>2</sup>D) Reactions," J. Phys. Chem., 91, 3883-88 (1987).
191. Albritton, D.L., "Ion-Neutral Reaction Rate Constants Measured in Flow Reactors Through 1977," Atomic Data and Nuclear Data Tables, 22, 1, 1-101 (1978).
192. Murphy, R.W., Cook, F.H. and Sakai, H., "Time Resolved Fourier Spectroscopy," J. Opt. Soc. Amer. 65, 600 (1975).
193. Brzozowski, J., Erman, P., and Lygra, M., "Predissociation Rates and Perturbations of the A, B, B', C, D, and F States in NO Studied Using Time Resolved Spectroscopy," Physica Scripta., 14, 290-297 (1976).
194. Albritton, D.L., private communication (1978).
195. Nicholls, R.W., "Franck-Condon Factors to High Vibrational Quantum Numbers IV: NO Band Systems," J. Research, 68A, 5, September-October (1964).
196. Wetmore, R.W., Fox, J.L., and Dalgarno, A., "Radiative Lifetimes of the Second Negative System of O<sub>2</sub><sup>+</sup>," Planet. Space. Sci., 32, 1111-1113 (1984).
197. Krupenie, P.H., "The Spectrum of Molecular Oxygen," J. of Phys. Chem. Ref. Data, 1, 423-534 (1972).

## APPENDIX A

### LIST OF JOURNAL PUBLICATIONS AND PRESENTATIONS AT SCIENTIFIC CONFERENCES DURING THIS PROJECT

#### JOURNAL PUBLICATIONS

1. Green, B.D., Caledonia, G.E., Blumberg, W.A.M., and Cook, F.H., "Absolute Production Rates and Efficiencies of NO in Electron-Irradiated N<sub>2</sub>/O<sub>2</sub> Mixtures," Journal of Chemical Physics 80 (2), 773 (1984).
2. Piper, L.G., Green, B.D., Blumberg, W.A.M., and Wolnik, S.J., "Quenching of N<sub>2</sub><sup>+</sup> Meinel Band Emission by N<sub>2</sub> and O<sub>2</sub>," Journal of Chemical Physics 82, 3139 (1985).
3. Piper, L.G., Green, B.D., Blumberg, W.A.M. and Wolnik, S.J., "Electron Impact Excitation of the N<sub>2</sub><sup>+</sup> Meinel Band," Journal of Physics B, 19, 3327 (1986).
4. Marinelli, W.J., Green, B.D., Defaccio, M.A., and Blumberg, W.A.M., "Vibrational Relaxation and Intersystem Crossing in N<sub>2</sub> a(<sup>1</sup>Π<sub>g</sub>)," Journal of Physical Chemistry 92, 3429 (1988).
5. Piper, L.G., Holtzclaw, K.W., Green, B.D., and Blumberg, W.A.M., "Experimental Determination of the Einstein Coefficients for the N<sub>2</sub>(B-A) Transition," to be submitted to Journal of Chemical Physics (1988).
6. Marinelli, W.J., Kessler, W.J., Green, B.D., and Blumberg, W.A.M., "Quenching of N<sub>2</sub>(a<sup>1</sup>Π<sub>g</sub>, v'=0) by N<sub>2</sub>, O<sub>2</sub>, CO, CO<sub>2</sub>, CH<sub>4</sub>, H<sub>2</sub>, and Ar," to be submitted to Journal of Chemical Physics (1988).
7. Green, B.D., Marinelli, W.J., Piper, L.G., and Blumberg, W.A.M., "Excitation and Quenching of the Vibrationally Excited N<sub>2</sub>B(Π<sub>g</sub>) State in Electron-Irradiated Nitrogen," to be submitted to the Journal of Chemical Physics (1988).

#### SCIENTIFIC CONFERENCE PRESENTATIONS

1. Green, B.D., Piper, L.G., Pugh, E.R., and Blumberg, W., "Beam Plasma Discharge Studies on the LABCEDE Apparatus," Fall Meeting, American Geophysical Union (Dec. 1983).
2. Caledonia, G.E., Green, B.D., and Blumberg, W.A.M., "Absolute Production Rates and Efficiencies in NO in Electron-Irradiated N<sub>2</sub>/O<sub>2</sub> Mixtures," American Geophysical Union Fall Meeting (San Francisco, 1983).
3. Piper, L.G., Green, B.D., Blumberg, W.A.M., and Wolnik, S.J., "N<sub>2</sub><sup>+</sup> Meinel Band Excitation and Quenching," Int. Conf. Atom. Phys., Seattle, July 1984.



4. Marinelli, W.J., Green, B.D., and Blumberg, W.A.M., "Measurement of Excitation and Quenching of  $N_2(B^3\Pi_g)$ ," Fall Meeting, American Geophysical Union (Dec. 1984).
5. Green, B.D., Marinelli, W.J., Weyl, G., and Blumberg, W.A.M., "Laboratory Measurements of Beam Plasma Discharge Thresholds," Fall Meeting, American Geophysical Union (Dec. 1984).
6. Green, B.D., Caledonia, G.E., Blumberg, W.A.M., and Wolnik, S.J., "Formation and Relaxation of High Levels of Atomic Oxygen," International Chemical Congress of Pacific Basin Societies (ACS) (Dec. 1984).
7. Green, B.D., Marinelli, W.J., Caledonia, G.E., and Blumberg, W.A.M., "Vibrational Relaxation of  $NO(v)$  by  $NO$ ," International Chemical Congress of Pacific Basin Societies (Dec. 1984).
8. Green, B.D., Marinelli, W.J., and Blumberg, W.A.M., "Laboratory Observations of  $N_2$  Electronic Emissions Between 180 nm and 5  $\mu$ m," Spring Meeting, American Geophysical Union (May 1985).
9. Green, B.D., Marinelli, W.J., and Blumberg, W.A.M., "Relative Excitation Efficiencies of  $N_2$  Electronic States," 38th Gaseous Electronics Conference (Oct. 1985).
10. Green, B.D., Marinelli, W.J., and Blumberg, W.A.M., "Excitation and Quenching of the Lowest Vibrational Levels of  $N_2(B)$  and  $N_2^+(A)$  States," Fall Meeting, American Geophysical Union (Dec. 1985).
11. Marinelli, W.J., Green, B.D., and Blumberg, W.A.M., "Quenching of  $N_2(a^1\Pi_g)$  by  $N_2$ ," Fall Meeting American Geophysical Union Meeting, (Dec. 1985).
12. Green, B.D., Marinelli, W.J., Piper, L.G., and Blumberg, W.A.M., "Excitation and Quenching of  $N_2B(^3\Pi_g)$  in Electron-Irradiated Nitrogen," Conf. on Dynamics of Molecular Collision, Utah, 1986.
13. Green, B.D., Marinelli, W.J., and Blumberg, W.A.M., "Electron Excitation and Intersystem Quenching of  $N_2(a)$  by  $N_2$ ," 39th Gaseous Electronic Conference (Oct. 1986).
14. Upschulte, B.L., Green, B.D., and Marinelli, W.J., "Nitrogen Infrared Electronic Emissions Representative of the Aurora," Fall Meeting, American Geophysical Union (Dec. 1986).
15. Green, B.D., Fraser, M.E., Defaccio, M.A., Lee, E.T.P., and O'Neil, R.R., "Analysis of EXCEDE: Spectral 2-8  $\mu$ m Data," Fall Meeting American Geophysical Union, (Dec. 1986).

16. Marinelli, W.J., Kessler, W.J., Green, B.D., and Blumberg, W.A.M., "Quenching and Intersystem Crossing in  $N_2$   $a(^1\Pi_g)$ ," American Physical Society, AMOP Division (May 1987).
17. Green, B.D., Upschulte, B.L., and Blumberg, W.A.M., "Observation of Infrared Fluorescence from  $O_3$  Created by a Two-Body Process," Int'l Union of Geodesy and Geophysics (July 1987).
18. Green, B.D., Upschulte, B.L., Holtzclaw, K.W., and Blumberg, W.A.M., "Laboratory Studies of the Electron Excitation of Singlet and Triplet Electronic States of  $N_2$ ," 40th Gaseous Electronics Conference (Oct. 1987).
19. Piper, L.G., Holtzclaw, K.W., Green, B.D., and Blumberg, W.A.M., "Experimental Determination of the Einstein Coefficients for the  $N_2(B-A)$  Transition," 40th Annual Gaseous Electronics Conference, October 1987, Bull. APS 33, XXXX (1988).
20. Green, B.D., Upschulte, B.L., Holtzclaw, K.W., and Blumberg, W.A.M., "Spectral Measurements of  $N_2$  Electronic Emissions Between 0.8-7.0  $\mu m$ ," Fall Meeting, American Geophysical Union (Dec. 1987).
21. Marinelli, W.J., Kessler, W.J., Green, B.D., and Blumberg, W.A.M., "Quenching of  $N_2(a^1\Pi_g, v'-0)$ ," Fall Meeting American Geophysical Union (Dec. 1987).
22. Upschulte, B.L., Green, B.D., and Blumberg, W.A.M., "Investigations of Ozone: Two-Body Production and Vibrational Quenching," Fall Meeting American Geophysical Union (Dec. 1987).

## APPENDIX B

### LABCEDE STARTUP PROCEDURE

Step 1: Check the current state of vacuum inside the LABCEDE shroud ("the tank") and within the electron beam formation chamber ("e-beam chamber").

For the Tank, use the convectron gauge (cold cathode) located above the multichannel chart recorder on the window side of the tank. This gauge is normally left on all the time and can read pressures from 5 mtorr to 999 torr. If the tank pressure is below ~ 1.4 torr, the baratron head pressure readout on the MKS flow controller provides a more accurate measurement. This flow controller (positioned above the gas cylinders) is normally shut off at the end of the day, so it will be necessary to turn it on, and select a pressure range x1 or X10 representing a 1 or 10V maximum signal level. A flashing readout means the readout is overranged. A leak rate of a couple of torr per week is common.

For the e-beam chamber use the thermocouple gauge meter mounted in the equipment rack directly behind the e-beam chamber. Note the TC-gauge is positioned in the vacuum line between the mechanical pump (normally on) and the diffusion pump (normally off). The equipment rack is normally powered down and is turned on with the topmost toggle switch (obvious). Next turn on the TC gauge power switch and select "TC #2." A 1 to 5 mtorr reading represents the mechanical pump minimum.

Step 2: Proceed to the pump room and turn on compressed air, water flow, oil flow and close the vacuum backfill/vent valve.

The compressed air line valve is located within the "Rat Hole" of the pump room (at the junction of the welding supply wall and

window wall). This valve points up and to the window side of the horizontal pipeline near the Rat Hole's left edge and at a depth into the hole of about 1 ft. A brass dogtag stamped "Air" can be used to positively identify the valve. (A flashlight may be required to read the dogtag.) This valve should be opened completely. An audible hiss of air flow should immediately be perceptible. A strain gauge pressure dial, located ~ 12 ft height between the welding supply and the diffusion pump, should read a pressure of about 75 psi or about 11:00 o'clock on the dial. If the building air supply is off a cylinder of compressed air/N<sub>2</sub> is normally located nearby and can be connected up using polyflow tubing (~ 100 psi rating).

The water flow control system hangs on the hallway side of the diffusion pump at about chest level. Locate the water booster pump in this area and follow the pipelines to find the inlet valve (orange/red handle lever action) and the outlet valve (blue metal handle with rotation action). Open these valves, listen for waterflow and note the rise of the float type water flow meters. Reading the top edge of the float should show a flow of about 2-1/4 GPM (1/3 column rise) into and out of the diffusion pump. Currently, the float to the Kinney mechanical pump is stuck up! Closing the lever action inlet valve should produce an audible clank and flow stoppage. To start the water booster pump, locate the "Monitor" panel box with start/stop/reset switches. Press start and release; the booster pump should come on (sound of the motor) and the floats should read 5 GPM (near the column top). Do not shut the water valves with the booster pump running. Note sweating of all water pipes is common, particularly during 3H weather.

The oil flow valve (orange handle lever action) on the window side of the Kinney mechanical pump must be opened (parallel to

the pipeline). Failure to open this valve produces a loud clanking noise and low pump capacity, i.e., high tank pressure, and will lead to pump damage.

On the vacuum line between the gate valve and the L-H Roots blower pump is a Swagelock terminated 1/2 in. copper line open to the room air. The valve on this line (small green handle 90 deg pivot action) must be closed/crossing the pipeline. This valve is used to backfill/vent the pumps to atmosphere on shutdown.

Step 3: The pump start up is controlled at the equipment racks just inside the LABCEDE single door entrance (see e-beam chamber pump down).

Pressing the start button above "Mechanical Pump #1" should produce a red light, an audible pump rumble and a perceptible floor vibration. Wait five minutes then rotate the "Gate Valve #2" switch to open. A buzzing/hissing sound lasts ~ 5s. The pressure in the tank should drop and asymptote to the 1 torr range (taking 5 min for a several torr starting pressure).

Below 15 torr the roots blower can be started. The start/stop panel switch is on the wall near the windows and the  $\text{LN}_2$  overflow tank. The pressure should drop more rapidly with the Roots blower on and asymptote to the 2 mtorr range (5 min).

Below 0.1 torr the "Diffusion Pump #2" can be turned on. The red light will glow, but no other perceptible phenomena will occur until the pump becomes hot in about 40 min. Typical operating pressures into the middle  $10^{-7}$  torr range reflect reasonably clean walls.

The operation of the diffusion pump can be checked by adding  $10^3$  sccm  $\text{N}_2$  with the flow conductance valve (pump end of tank)

open (000). This normally produces a pressure of 4.8 mtorr  $\pm$  0.2 mtorr.

Step 4: Cryogenic LABCEDE operation should begin now, but is optional! (Skip to the next step if a warm shroud is adequate.).

The outdoor reservoir should have a minimum dial position of  $\sim$  9:00 o'clock for an adequate supply for cooling LABCEDE. The tank holds  $\sim$  1250 gal at the 12:30 1:00 o'clock (full) position. The dial moves counterclockwise as the tank empties. To begin cooling the shroud open valves 110, 107, 111, 109 (the "Regulator" fraction open), 106 (the main inlet valve located below the LN<sub>2</sub> overflow tank); and close all other valves. The "Regulator" valve #109 has a string that marks its position. The string should be positioned at 11:00 12:00 o'clock ( $\sim$  1/2 turn open) for a standard cooldown. Additional opening/closing will produce quicker/slower cooling. Turn on the 30 channel thermocouple chart recorder and mark it with the date and time. Pay careful attention to the tank pressure reading. At least once, possibly twice, large pressure bursts will occur due to leakage from expansion/contraction strain in the cooling system. These pressure bursts are halted by closing the "Regulator" valve #109 until the pressure drops, then reopening for LN<sub>2</sub> flow. Once the temperature has begun a steady decline  $\sim$  1 hr these bursts should stop. Total cooldown time is variable, but normally requires 3 to 5 hr at the standard flow rate. Quicker cool downs  $\sim$  30 min have been accomplished once the pressure burst region is passed. Cut back on LN<sub>2</sub> flow when the temperature begins to asymptote to the 90 K range to avoid filling the overflow tank.

Step 5: The e-beam chamber can be pumped down simultaneous with the tank because the 1 in. throat gate valve separating these tanks is normally closed.

Open the water flow valve (blue metal handle rotation action) located below the roots blower start/stop switch. This valve points into the room on a horizontal pipeline and can be identified by a paper dogtag labeled "7." Start the mechanical pump, (if not already on) wait for the foreline pressure to reach 0.1 torr. The red push button "Diffusion Pump #2" illuminates when the pump is toggled on. Immediately fill the LN<sub>2</sub> cold trap. In about 30 min the ion gauge (move cables) will reach the middle 10<sup>-6</sup> torr range.

Step 6: Warm up the e beam filament slowly. The high voltage power supply near the bottom of the e beam equipment rack should be switched AC on, but HV off to allow it to warm up. The e beam filament power supply inside the plexiglass box should be on and the box fan at the rear of this plexiglass enclosure should be operating. Rotate the voltage control (plastic tube extension) many turns clockwise and observe about 2A filament current. Rotate the current control (plastic tube extension) clockwise in 2 to 3A increments every 5 min to warm up the filament do not exceed 18A on the filament supply at this time.

Step 7: Warm up the e beam focusing electromagnet. Beside the e-beam equipment rack is an additional power supply and digital volt meter used to operate the focusing magnet. Turn these units on and rotate the current/voltage controls to set a current limit above 6A (light over the current control). Rotate the voltage control to set an operating voltage of 2V (corresponds to about 6A) in constant voltage mode.

Step 8: Start B-Field water cooling system. Near the junction of the windows and the sink is located a set of water filters for the B-Field water cooling line. Trace the lines and locate the small green handle 90 deg pivot bleed valve with plastic tube line to the sink. Close this valve/crossing the tubeline. Open the water inlet and outlet valves to the water filters (change every 3 months). The water pressure should be 65 psi. On the back flange of the LABCEDE tank (window side) is a switch to the B-Field water coil booster pump. Toggle this switch to on and the pressure should rise to 130 psi. Note, a pressure sensor in the water line prevents B Field startup unless the water pressure is high.

Step 9: Introduce gas/mixtures into the tank. The MKS Flow Controller handles three lines of gas introduction A,B,C. Line C can be routed to a 1/4 in. tube outlet or into the heat exchanger/porous plug on the shroud via a three way valve on the tank above the flow controller. Lines A, B always go to the porous plug. The flow readouts are always in sccm, the decimal point on line C is marked in pen. Maximum total flow is 1500 sccm. Note, by closing the pump conductance valve at the end of the shroud (max closed is 138, full open is 000) it is possible to obtain high pressure even at low flow rates. Also, two ranges are available on the flow control lines; be careful not to overload the diffusion pump. If the pressure continues to climb monotonically, then the gas load is too high (settling times of  $\leq 2$  min are reasonable).

Step 10: Open 1 in. aperture gate valve between tank and e beam chambers.

Step 11: Electron beam turn on is next. If pulsing is required attach Wavetek at "minimum" attenuation or the General Radio at 30% full amplitude (~ 20V out). Turn high voltage power supply HV switch to the on position and select the e-beam energy. Hold the temporary contact switch to the ma position while rotating the filament power



supply current control (plastic extension) to obtain 10 mA CW emission current (max is 25 mA). Be careful never to exceed 20A total filament heating current. To begin pulsing rotate potentiometer dial reading (located inside plexiglass enclosure) from 998 to 110 using the insulated screwdriver. If the emission current falls to zero reduce attenuation on the Wavetek or increase output amplitude on the General Radio. Adjust filament current to obtain desired emission current (30 mA peak current max). Note emission current is average and must be divided by duty cycle to obtain peak current.

Step 12: Turning on the large magnetic coils: check/select the hi/lo range of the Miller Welding Power Supply in the pump room. This switch is located just above the large multipin MS remote control cable connection. Returning upstairs; near the gas cylinders is the on/off/control box. The maximum continuous operation is at a dial valve of 40 on the high range. Always dial down to zero prior to turning on or off.

Step 13: The e-beam alignment is adjusted using the focusing magnet power supply (2.5V/8A max); the small external steering magnet below the 1 in. gate valve and the B-Field dial valve. A change in any of the above and/or pressure/flow/pump conductance will effect the e-beam size and trajectory. The e-beam is adjusted visually via the window port near the e-beam chamber.

Step 14: Make the detector operational and begin experiments.

### LABCEDE Shutdown

- Step 1: Nitrogen (3 to 5 mtorr, pump conductance valve open) should always be introduced to a CW e-beam for 10 min at the end of the day; this is thought to extend the filament lifetime.
- Step 2: Shut off: the tank "Diffusion Pump #2," the red light should go out. Note this shut off time because this diffusion pump will cool in about 55 min. Turn the high voltage to 0V and the HV switch to the off position. The e-beam should not be observable. Close the 1 in. gate valve between chambers. Turn the B-Field dial to zero then switch power off, but continue water flow to cool the coils. Reduce then shut off focusing magnet power supply and voltage meter. Shut off all gas flows and open pump conductance valve. Fill LN<sub>2</sub> trap of e beam chamber.
- Step 3: Close the main LN<sub>2</sub> access valve #106 below the overflow tank, then open all other LN<sub>2</sub> valves. A fast flow may persist for several minutes to clear the lines but 15 min should produce an audible/observable boiloff gas flow reduction.
- Step 4: Slowly reduce filament current i.e., 2 to 3A decrements/5 min. The last 2A current decrement requires the voltage control to be turned fully counterclockwise.
- Step 5: Turn off the e-beam diffusion pump once the filament current is reduced below ~ 6A. This diffusion pump cooling time is about 30 min.
- Step 6: When the B-Field cooling water temperature is below 60°F and stabilizes, shut off the booster pump then the water inlet and outlet valves and bleed the water line.

- Step 7: When the e-beam diffusion pump exhaust arm is cool to the touch shut off the cooling water to the pump.
- Step 8: When the tank pressure rises to 30 mtorr turn off the roots blower and observe a more rapid pressure rise to ~ 60 mtorr before closing "Gate Valve #2." A 5s buzz/hiss, maybe a thud, is perceptible. This sound marks the closing of gate valve. The pressure in the tank should now be nearly constant. If it isn't the valve may not be closed. This is important. If uncertain repeat or add gas and observe no pumping. Now turn off the "Mechanical Pump #1" (red light/noise/vibration halts).
- Step 9: In the pump room, shut off the water booster pump, close the inlet and outlet water valves, close the "Rat Hole" compressed air line. The hiss of compressed air will continue for several minutes note the pressure dial decline. Next close (cross pipeline) the Kinney oil flow valve and vent the pumps. Be sure to close the vent valve afterwards to avoid a startup headache. Lock the door.
- Step 10: Check that the tank pressure is stabilized; shut off flow controller; shut off equipment rack; check all water flows are off; check all electronics are off; shut down computer/air conditioning; check LN<sub>2</sub> flow is stopped. Lock door.

### Recommendations/Upgrades

1. TC gauge/remote readout on foreline between Kinney and Roots
2. Ion gauge/controller/readout/cables for e-beam chamber
3. Emission current monitor/readout/regulator with limits
4. Pump room cleanup
5. Compressed air line valve repositioning
6. LN<sub>2</sub> flow meter
7. E-beam chamber/water flow meter.

## APPENDIX C

### COMPUTATION OF ELECTRONIC SPECTRA OF DIATOMIC MOLECULES

#### C.1 INTRODUCTION

When analyzing spectral data for the purposes of determining populations (or relative populations) of various radiators, it is often necessary to predict the relative intensities and shapes of the various transition spectra, especially where overlap is severe. In this report we describe a method which we have used to perform such predictions for electronic transitions of diatomic molecules.

The model is based upon the work of Kovacs<sup>C-1</sup> and is implemented through a major modification and extension of the computer code of Whiting, et al.<sup>C-2,C-3</sup> The current model considers singlet-singlet, doublet-doublet, and triplet-triplet dipole transitions in the optically thin limit. Lambda doubling is not considered. The code is constructed in such a way that extensions are easily implemented. Some possible extensions will be discussed in Subsections C.5.4 and C.6.

The method of distributing the line intensities over wavelength is only slightly modified from that of the original code. For our purposes we have used a trapezoidal (as opposed to Voight) line shape but have retained the original algorithm for convolution with slit functions.

At present the code has been written, debugged and partially validated. It has been adapted to our immediate needs and is not currently "user-friendly." Necessary validation and refinements are currently in progress.

#### C.2 THEORY OF LINE INTENSITY

The intensity of a spectral line in emission from state  $u = (n', v', J', i')$  to state  $l = (n'', v'', j'', i'')$  is

$$I_1^u = N_u h c \omega_1^u A_1^u \times 10^{-7} / 4\pi \quad (C-1)$$

where

$n$  designates the electronic state  
 $v$  designates the vibrational level  
 $J$  designates the total angular momentum  
 $i$  designates the spin-spin component of the angular momentum state  
 $I$  is  $W/\text{cm}^3\text{-sr}$   
 $N_u$  is particles  $\text{cm}^{-3}$   
 $A$  is the Einstein coefficient in  $(s)^{-1}$   
 $h$  is Planck's constant  
 $c$  is the speed of light.

and  $\omega_1^u$  is the wavenumber of the transition:

$$\omega_1^u = \omega_u - \omega_1$$

where

$$\omega(n', v', J', i') = T_e + G'(v') + F_i'(v', J') \quad (C-2)$$

Here,  $T_e$  and  $G(v)$  have their usual meaning and  $F_i'(v', J')$  is the usual rotation/spin part.

This and the next section are concerned with the computation of the rotation/spin distribution of a particular electronic/vibrational transition. If it is assumed that the spin and rotational states are given by a single temperature,  $T_r$ , then:

$$N_u = \frac{N_v (2J+1) \exp(-F_{i'}(v', J') hc/kt)}{Q_R} \quad , \quad (C-3)$$

$$A_l^u = A_{n''v''}^{n'v'} \frac{\cancel{S} \begin{matrix} J' i' \\ J'' i'' \end{matrix}}{(2J'+1)(2S'+1)} \quad (C-4)$$

and thus

$$I_l^u = N_v' A_{n''v''}^{n'v'} hc \omega_u \frac{10^{-7}}{4\pi} \cancel{S} \begin{matrix} J' i' \\ J'' i'' \end{matrix} \frac{\exp(-F_{i'}(v', J') hc/kT_r)}{(2S'+1) Q_R} \quad . \quad (C-5)$$

The transition frequency is

$$\omega_l^u = \omega_{0l}^u + F'_{i'}(v', J') - F''_{i''}(v'', J'') \quad (C-6)$$

where  $\omega_{0l}^u$  is the band origin.

$\cancel{S} \begin{matrix} J' i' \\ J'' i'' \end{matrix}$  is the line intensity factor normalized that

$$\sum_{J'' i''} \cancel{S} \begin{matrix} J' i' \\ J'' i'' \end{matrix} = (2J'+1)(2S'+1) \quad . \quad (C-7)$$

$\cancel{S}$  and  $F$  are found in an accepted manner<sup>C-4, C-5</sup> by describing the eigenfunctions of the states as a linear combination of eigenfunctions of hypothetical pure Hund's case (a) eigenstates. In pure Hund's case (a), the eigenvalues and transition intensity factors (Hönl-London factors) are known from separation of the wave equation:

$$(H^a - F_i^a) \psi_i^a = 0 \quad . \quad (C-8)$$

The case (a) eigenvalues,  $F_i^a$ , are known as a function of total (J) and axial component ( $\Omega$ ) of the angular momentum and will be given in the next section. The intensity factors are given in Table C-1 for the three branches.

TABLE C-1. Hund's case (A) line strengths.

Branch	$\Delta\Omega = 0$	$\Delta\Omega = \pm 1$
$P(J''=J'+1)$	$\frac{(J'+1)^2 - \Omega^2}{(J'+1)}$	$\frac{(J'+1+\Omega')(J'+2+\Omega')}{2(J'+1)}$
$Q(J''=J')$	$\frac{\Omega_2(2J'+1)}{J(J+1)}$	$\frac{(J'+1+\Omega')(J'+\Omega')(2J'+1)}{2J'(J'+1)}$
$R(J''=J'-1)$	$\frac{J'^2 - \Omega^2}{J'}$	$\frac{(J'+\Omega')(J'+\Omega'-1)}{2J'}$
	$\Delta\Omega = \Omega' - \Omega''$	

The real eigenfunctions and eigenvalues are found from

$$(H^a + H' - F_i)\psi_i = 0 \quad (C-9)$$

by writing

$$\psi_i = \sum_k S_{ki} \psi_k^a \quad (C-10)$$

and substituting in Eqs. (C-8) and (C-9) to give

$$S_{li}(F_l^a - F_i) + \sum_k S_{ki} H_{ik} = 0 \quad (C-11)$$



$F_i$  are the desired energy levels. The transition amplitudes are given by the transformation of the dipole moment between the upper and lower states,

$$\langle J' i' | J'' i'' \rangle = \left| \sum_l S'_{li'} \sqrt{J_l^a} S''_{li''} \right|^2. \quad (C-12)$$

The index  $l$  sums over the case (a) spin configurations and the matrix element  $J_l^a$  is of course the given function of  $J', J'', \Omega' = \Sigma'(l)$ , and  $\Omega''$ .

The treatment presented so far is exact. Any basis set could be used even for  $\Lambda = 0$ . The case (a) basis set allows one to specify

$$H_{lk} = \psi_l^a H' \psi_k^a. \quad (C-13)$$

These matrix elements and the  $F_l^a$  are given by Kovacs including spin orbit, spin-spin, spin-rotation, and centrifugal distortion. Interactions with other electronic states have not been considered in our work.

### C.3 COMPUTATION OF TRANSFORMATION MATRICES AND ENERGIES

In this section we discuss the solution of Eq. (C-11) for the transformation matrix  $S$  and for the eigenvalues  $F$ . The solution for singlet is just Table C-1 for the amplitudes and

$$F = B_v J_\Lambda^2 + D_v J_\Lambda^4 \quad (C-14)$$

and

$$J_\Lambda^2 = J(J+1) - \Lambda^2. \quad (C-15)$$

### C.3.1 Doublets

The eigenvalues for doublets found from solution of Eq. (C-11) are rewritten as

$$\begin{pmatrix} F_1^a + H_{11} & H_{12} \\ H_{21} & F_2^a + H_{22} \end{pmatrix} \begin{pmatrix} S_{1i} \\ S_{2i} \end{pmatrix} = F_i \begin{pmatrix} S_{1i} \\ S_{2i} \end{pmatrix} \quad (C-16)$$

By subtracting one half the trace,  $F$ , of the matrix from both sides we obtain, using Kovacs' values for  $F^a$  and  $H_{ij}$ ,

$$\begin{pmatrix} \delta & H \\ H & -\delta \end{pmatrix} \begin{pmatrix} S_{1i} \\ S_{2i} \end{pmatrix} = \lambda_i \begin{pmatrix} S_{1i} \\ S_{2i} \end{pmatrix} \quad (C-17)$$

where

$$\begin{aligned} \delta &= \frac{\Lambda}{2} \left\{ 2B_v - A_v - 4D_v J_\Lambda^2 \right\} \\ H &= \left( B_v - \frac{\gamma}{2} - 2D_v J_\Lambda^2 \right) J_\Lambda \\ J_\Lambda^2 &= \left( J + \frac{1}{2} \right)^2 - \Lambda^2 \\ \lambda_i &= F_i - F \end{aligned} \quad (C-18)$$

$$\text{and } \bar{F} = B_v J_\Lambda^2 - \frac{\gamma}{2} - D_v \left( J_\Lambda^4 + J_\Lambda^2 + \Lambda^4 \right) \quad .$$

The solution to Eq. (C-17) is:

$$\left. \begin{aligned} \lambda_i &= \pm \left( \delta^2 + H^2 \right)^{1/2} \\ S_{1i} &= H/D \\ S_{2i} &= (\lambda_i - \delta)/D \\ D^2 &= 2\lambda_i(\lambda_i - \delta) \end{aligned} \right\} \quad (C-19)$$

These are given in slightly different form by Kovacs<sup>C-1</sup> (pg. 61), for  $D_V = 0$  and  $\gamma = 0$ . Kovacs chooses to treat  $D_V$  and  $\gamma$  as perturbations; however, there is no numerical reason for doing this. It is, in fact, numerically easier to solve as shown above. We note that at  $J = \Lambda - 1/2$ ,  $J_\Lambda = 0$  and there is only one eigenvalue,  $\lambda = -\delta$  for which the  $S$ 's are non-zero. This solution gives  $S_1 = 0$  and  $S_2 = 1$  as expected. Thus, Eq. (C-11) is valid for all  $J$ . Application of these results in Eq. (C-12) is discussed in Subsection C.5.2.

### C.3.2 Triplets

For triplets, Eq. (C-11) is written as

$$\begin{pmatrix} F_1^a + H_{11} & H_{12} & H_{13} \\ H_{21} & F_2^a + H_{22} & H_{23} \\ H_{31} & H_{32} & F_3^a + H_{33} \end{pmatrix} \begin{pmatrix} S_{1i} \\ S_{2i} \\ S_{3i} \end{pmatrix} = F_i \begin{pmatrix} S_{1i} \\ S_{2i} \\ S_{3i} \end{pmatrix} \quad (C-20)$$

where the  $F_i^a$  and  $H_{ij}$  are taken from Kovacs.<sup>C-1</sup> The matrix can be reduced for computation by first subtracting  $\bar{F}$ , one third the trace from the diagonal of each side of the equation. Then the  $S_1$  and  $S_3$  are transformed to

$$\left. \begin{aligned} s'_{1i} &= \frac{H_{12}S_{1i} + H_{23}S_{3i}}{H} \\ s'_{2i} &= S_{2i} \\ s'_{3i} &= \frac{H_{23}S_{1i} - H_{13}S_{3i}}{H} \end{aligned} \right\} \quad (C-21)$$

with

$$\left. \begin{aligned} H^2 &= H_{12}^2 + H_{23}^2 = 4J_{\Lambda}^2 \{ b_1^2 + 4D_v \Lambda^2 - 8b_1 D_v \Lambda^2 / J_{\Lambda}^2 \} \\ H_{21} &= H_{12} = (b_1 - 2D_v \Lambda) \left( 2(J_{\Lambda}^2 - \Lambda) \right)^{1/2} \\ H_{32} &= H_{23} = (b_1 + 2D_v \Lambda) \left( 2(J_{\Lambda}^2 - \Lambda) \right)^{1/2} \\ J_{\Lambda}^2 &= J(J+1) - \Lambda^2 \\ b_1 &= B_v - 2D_v (J_{\Lambda}^2 + 1) - \gamma/2 \\ H_{13} &= H_{31} = -2D_v \left( 2(J_{\Lambda}^2 + \Lambda) - 2(J_{\Lambda}^2 - \Lambda) \right)^{1/2} \\ \bar{F} &= B_v (J_{\Lambda}^2 + 2/3) - D_v (J_{\Lambda}^4 + 4J_{\Lambda}^2 + 8/3 \Lambda^2 + 4/3) - 4/3 \gamma \end{aligned} \right\} \quad (C-22)$$

The new matrix will then have zero for the 2,3 and 3,2 components, thus

$$\begin{pmatrix} \delta + \eta & H & G \\ H & -2\delta & 0 \\ G & 0 & \delta - \eta \end{pmatrix} \begin{pmatrix} S'_{1i} \\ S'_{2i} \\ S'_{3i} \end{pmatrix} = \lambda_i \begin{pmatrix} S'_{1i} \\ S'_{2i} \\ S'_{3i} \end{pmatrix} \quad (\text{C-23})$$

where

$$\left. \begin{aligned} \delta &= -2/3 B_v + 2D_v \left( J_\Lambda^2 - 2/3 \Lambda^2 + 2/3 \right) + \varepsilon + 1/3 \gamma \\ \lambda_i &= F_i - \bar{F} \\ G &= -H_{13} h + b t_h \\ \eta &= b h + H_{13} t_h \\ t_h &= \frac{2H_{12}H_{23}}{H^2} = (1 - h^2)^{1/2} \\ b &= \Lambda \left( 2B_v - A_v - 2D_v \left( 2J_\Lambda^2 + 1 \right) \right) \\ H^2 h &= 4\Lambda \left\{ b_1^2 + 4D_v^2 \Lambda^2 - 8b_1 D_v J_\Lambda^2 \right\} \\ &= H_{12}^2 - H_{23}^2 \end{aligned} \right\} \quad (\text{C-24})$$

Equation (C-23) is solved for the  $S'_{1i}$  and  $\lambda_i$  to determine  $S_{1i}$  and  $F_i$ . The solution method depends upon whether  $G = 0$  which will be true for  $\Lambda = 0$ , and some other specific cases: e.g.,  $D_V = 0$  and  $2B_V = A_V$ . The solutions are found in Attachment A.

Kovacs has given (pg. 69) expressions for the  $S_{1i}$  and  $F_i$  in approximate form for  $\gamma = 0$ ,  $D_V = 0$ , and  $\epsilon = 0$ . As with the doublet states, he chose to treat these terms as a perturbation. His expressions for  $F_i$  agree with those of Herzberg<sup>C-6</sup> and originate from the work of Budo.<sup>C-7</sup> The  $S_{1i}$  are the same for  $\Lambda = 1$  as those given by Budo.<sup>C-7</sup> However, in both cases, the  $S_{1i}$  are not orthogonal unless  $\Lambda = 0$  or  $A_V = 0$ . We have checked our  $S_{1i}$  against those of Kovacs for several cases and find small differences; however, these small differences give detectable changes in the spectral shapes. Whiting, et al.<sup>C-8,C-9</sup> have also checked the results of Kovacs and find little difference with their numerical results except at low  $J$ .

The limiting low  $J$  for which the above equations can be solved is  $J = \Lambda$ , for which  $J_{\Lambda}^2 = \Lambda$ ,  $H_{23} = 0$ ,  $H_{13} = 0$ , and thus  $G = 0$ . For this case we get three solutions. The first is  $S_1 = S_2 = 0$  and  $S_3 = 1$  for  $F = -F_0 = -\Lambda(B_V - A_V) + \dots$

For the other two roots we get  $S_3 = 0$  and  $F = +e$  and  $F = -e$ . These two eigenvalues correlate with  $\Omega = \Lambda - 1$  and  $\Lambda$  as  $S_3 = 0$  implies. The first eigenvalue,  $-F_0$ , has  $S_3 = 1$ . Thus must be true for it to be orthogonal to the other two.

Kovacs equations give values at  $J = \Lambda$  such that all three eigenvalues have  $S_3 = 0$  and one of them also has  $S_2 = 0$ . In fact, all of his given  $S$  values have the same sign for  $J = \Lambda \neq 0$  and thus cannot be orthogonal.

There is a rotational level with  $J = \Lambda - 1$  which is not split and cannot be readily determined from the above formula. For this case  $H_{12} = 0$  and  $N_{13} = 0$  and we will get one eigenvalue with  $S_1 \approx 1$  and  $S_2 = S_3 = 0$  with

$F = \Lambda(B_V - A_V) + \dots$  Since  $H_{23}$  is imaginary the other two values are meaningless.

#### C.4 DISTRIBUTION OF SPECTRAL INTENSITY

The intensity of a spectral line is given by Eq. (C-5) along with Eq. (C-10) and the results of Section C.3. The line centers are given by Eq. (C-6) and the results of Section C.3.

This intensity is distributed over a wavelength indexed array, ELAM, whose index,  $i$ , corresponds to wavelengths

$$\lambda_i = \lambda_{\min} \exp((i-1)\delta) \quad (C-25)$$

where  $\delta = \Delta\lambda/\lambda$  and  $\lambda_{\min}$  (and  $\lambda_{\max}$ ) are code inputs. If  $\lambda$  falls between  $\lambda_{i-1}$  and  $\lambda_i$  then the intensity is distributed between the two values of  $i$  and a trapezoidal manner thusly;

$$E_{(i-1)} = I \frac{(\lambda_i - \lambda)}{(\lambda_i - \lambda_{i-1})^2}$$

$$E_{(i)} = I \frac{(\lambda - \lambda_{i-1})}{(\lambda_i - \lambda_{i-1})^2} \quad (C-26)$$

where  $I$  is a line strength in  $W/cm^3$  sr and  $E$  is in  $W/cm^3$  sr  $\mu m$ .

The exponential distribution of wavelength was chosen because of the desire to cover a wide range of wavelength space. The trapezoidal distribution of spectral intensity was chosen because there was no immediate need for a more sophisticated method and because when convolved with a piecewise linear slit function it will conserve energy with trapezoidal integration over a slit

function. Interferometrically acquired spectra may be treated as long as the  $\Delta\lambda$  interval is less than the interferometer's resolution element, as described below.

Computation of the  $E_\lambda$  array is performed in the code called RAD for a particular band system where a separate  $E_\lambda$  array is produced and filed for each upper state. The upper state density is taken as  $10^{16}$  particles per  $\text{cm}^3$ . A separate code, SPEC, then uses these  $E_\lambda$  arrays to compute synthetic spectra for specified upper state densities, instrument slit functions, and calibrations. These convolved synthetic spectra can then be compared with experimental observations.

The integration over the slit function is performed in the same manner as the NASA Code,<sup>C-3</sup> that is

$$I_\lambda = \frac{R(\lambda) \int_{-\epsilon}^{\epsilon} E_{\lambda+\epsilon'} f(\epsilon') d\epsilon'}{\int_{-\epsilon}^{\epsilon} f(\epsilon') d\epsilon'}, \quad \text{W/cm}^3 \text{ sr } \mu\text{m} \quad (\text{C-27})$$

Where  $R(\lambda)$  is the instrument calibration,  $f(\epsilon')$  is the slit function, and  $\epsilon$  gives the range of the slit function.

## C.5 APPLICATION TO SPECTRAL SYNTHESIS

### C.5.1 Singlet-Singlet Transitions

As examples of calculations of singlet-singlet transitions, we present two sets of spectra which correspond not to singlet-singlet transitions but to transitions which for our purposes were reasonably approximated by a singlet-singlet intensity distribution. They are the first negative bands of  $\text{N}_2^+$  ( $B^2\Sigma \rightarrow X^2\Sigma$ ) and the Vegard-Kaplan bands of  $\text{N}_2$  ( $A^3\Sigma \rightarrow X^1\Sigma$ ).



a.  $N_2^+ B^2\Sigma \rightarrow X^2\Sigma$ ,  $v'=0$ ,  $v''=0$  at 391.4 nm

This band is treated as a singlet-singlet transition since the spin-splitting constant,  $\gamma = 0.002 \text{ cm}^{-1}$ , of Eq. (C-18) is much less than any resolution of current interest.

The spectroscopic data for  $N_2^+$  are taken from Huber and Herzberg.<sup>C-10</sup> Einstein coefficients were taken from the compilation of Loftus and Krupenie.<sup>C-11</sup> The computed spectrum is shown in Figure C-1 for  $T_r = 85 \text{ K}$  and a triangular slit of width 0.2 nm.

Since the doppler line width is typically  $10^{-6}$  of the line position ( $4 \times 10^{-4} \text{ nm}$ ) and the lines are typically two rotational constants apart ( $4 \times 10^{-2} \text{ nm}$ ), the 0.2 nm resolution masks the detailed structure. In ELAM,  $\Delta\lambda/\lambda$  was  $10^{-4}$ , about one-fifth the resolution.

b.  $N_2 (A^3\Sigma \rightarrow X^1\Sigma)$

The Vegard-Kaplan bands of  $N_2$  are spin forbidden and will be discussed again in Subsection C.5.4; however, for our purposes we have calculated the spectrum assuming a singlet-singlet type intensity distribution. The slit function applied is a 0.66 nm wide triangle. Because the R branch band head is at  $J = 3$ , the branches overlay each other and we need not use a more sophisticated computational technique.

The spectroscopic constants were taken from Loftus and Krupenie<sup>C-11</sup> and the Einstein coefficients from Shemansky.<sup>C-12</sup> A portion of the resultant spectrum for  $N_0: N_1: N_2 = 1:0.15:0.03$  and  $T_r = 300 \text{ K}$  is shown in Figure C-2 for  $\Delta v = -2$  to 11 for  $v'=0, 1$  and 2.

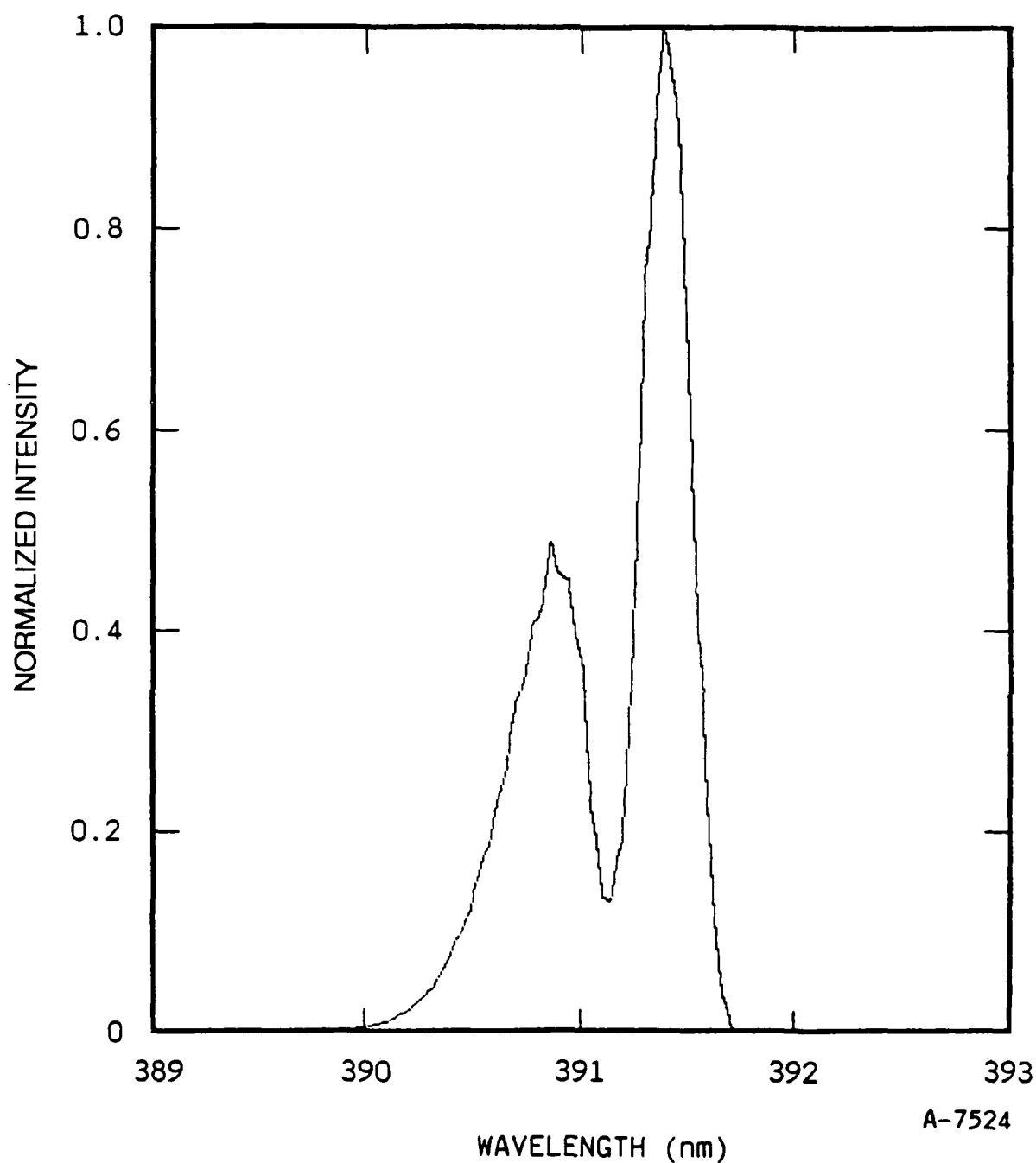


Figure C-1. Synthetic spectrum of  $N_2^+(B, v'=0) \rightarrow N_2^+(X, v''=0)$  with a rotational temperature of 85 K. The dominant features are the R and P branches since spin-splitting is small. Maximum intensity is  $4.6 \times 10^{-17}$  W/molecule-sr- $\mu\text{m}$ . Resolution is 0.2 nm.

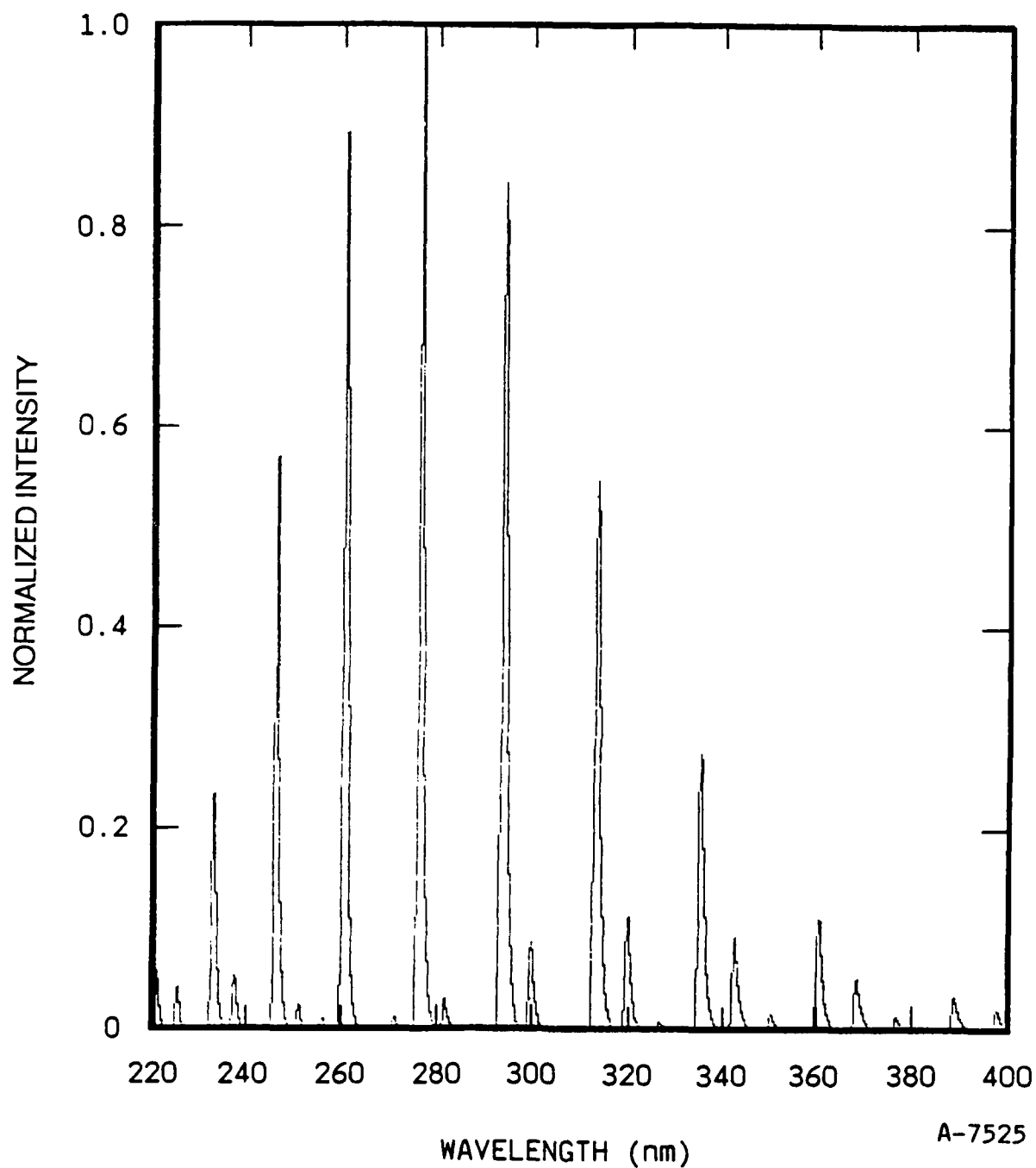


Figure C-2. Synthetic spectrum of  $N_2(A, v' \leq 2) \rightarrow N_2(X, v'' \leq 13)$  "Vegard-Kaplan" system at 300 K. The A-state,  $v' = 0, 1, 2$  have populations of 1:0.15:0.03. Resolution is 0.66 nm. Maximum intensity is  $7.2 \times 10^{-18}$  W/molecule-sr- $\mu$ m. Each spectral feature is comprised of an unresolved P and R branch.

### C.5.2 Doublet Doublet Transitions

To date we have investigated two doublet-doublet transitions: the NO- $\gamma$  system ( $A^2\Sigma \rightarrow X^2\Pi$ ) and the  $N_2^+$  Meinel system ( $A^2\Pi \rightarrow X^2\Sigma$ ). In doublet-doublet transitions there can be twelve branches. For both of the transitions of interest one of states is a sigma state for which  $F_1(J) = F_2(J-1)$ . Thus there are, to a first approximation, only eight branches. There is however, no need to use this approximation in the computation.

#### a. NO( $A^2\Sigma \rightarrow X^2\Pi$ )

The spectroscopic constants were taken from Huber and Herzberg<sup>C-10</sup> and the Einstein coefficients from Mohlman et.al.<sup>C-13</sup> with total lifetimes of the  $v=0,1$  and 2 state taken as 210, 205 and 200 ns respectively to take into account the slightly longer lifetime found by McGee et.al.<sup>C-14</sup> for the  $v=0$  state.

The spectra are shown in Figures C-3 and C-4 for  $T_r = 1200$  K and  $N_0:N_1:N_2 = 1:0.35:0.03$  for the upper state. The intensity of Figure C-4 is about seven times exaggerated compared to that of Figure C-3. In both cases the slit function is triangular of width at half height of 0.08 nm. The overlap of the branches and the rotational structure is apparent. At this temperature, the bands from the same value of  $\Delta v$  are close enough that they significantly overlap.

#### b. $N_2^+(A^2\Pi \rightarrow X^2\Sigma)$

The spectroscopic data for the Meinel system was taken from Huber and Herzberg.<sup>C-10</sup> The Einstein coefficients were taken from the compilation of Loftus and Krupenie.<sup>C-11</sup>

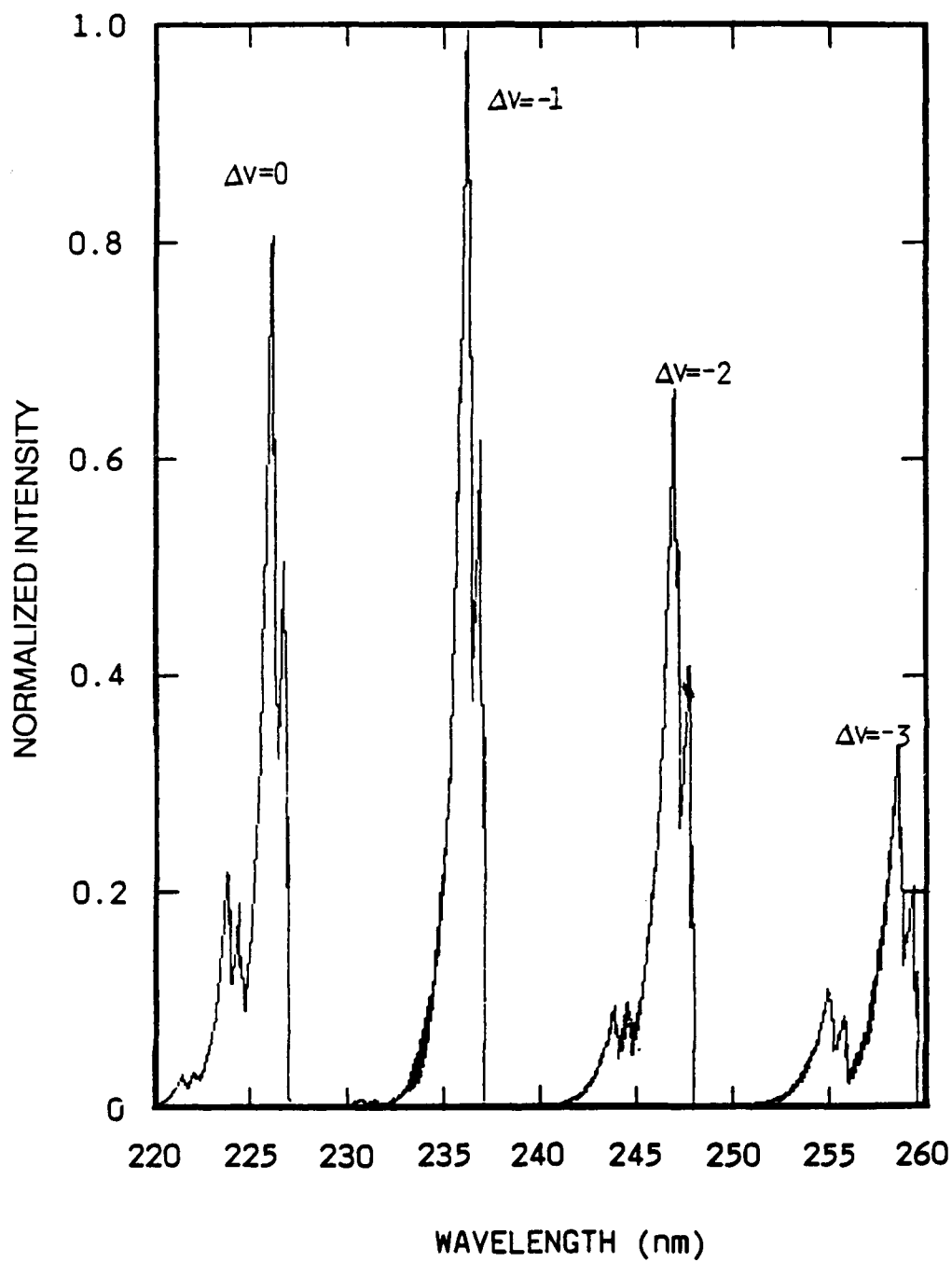


Figure C-3. The synthetic spectrum of  $\text{NO}(\text{A}^2\Sigma) \rightarrow (\text{X}^2\Pi)$  between 220 and 260 nm. See text for details.  $T_r = 1200$  K, resolution is 0.08 nm. Maximum intensity is  $7.4 \times 10^{-11}$  W/molecule/sr- $\mu\text{m}$ .

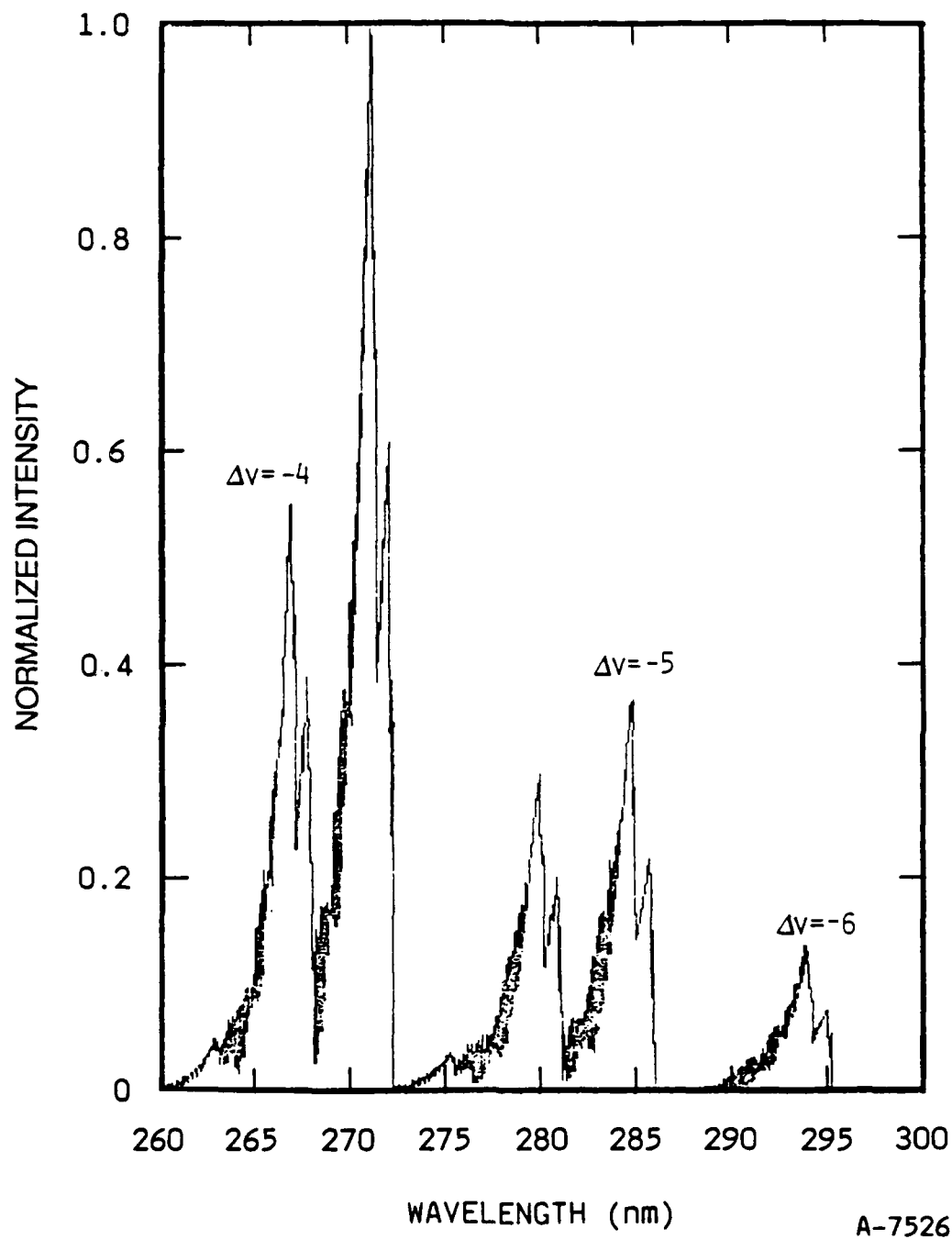


Figure C-4. The synthetic spectrum of NO(A→X) between 260 and 300 nm for the same conditions as Figure C-3. Maximum intensity is  $1.06 \times 10^{-11}$  W/molecule-sr- $\mu\text{m}$ .

Computed Meinel spectra are shown for  $T_r = 300$  K in Figure C-5 for the  $\Delta v=3$  sequence where  $N_3:N_4:N_5:N_6:N_7 = 1:0.44:0.18:0.068:0.026$  and the resolution is triangular with a full width at half height of 0.52 nm.

### C.5.3 Triplet-Triplet Transitions

Computations for triplet-triplet transitions were performed for the  $N_2$  Wu-Benesch bands ( $W^3\Delta \rightarrow B^3\Pi$ ) and the  $N_2$  first positive system ( $B^3\Pi \rightarrow A^3\Sigma$ ).

#### a. $N_2(B^3\Pi \rightarrow A^3\Sigma)$

The data for the first positive system were taken from the collection of Loftus and Krupenie.<sup>C-11</sup> Because the A-state is a sigma state, there are only 15 branches instead of the possible 27. This is because the transitions to the spin-split states of adjacent lower state J's have nearly the same frequency, i.e.,  $F_1(J+1) \sim F_2(J) \sim F_3(J-1)$ . There is also near coincidence of various bands. For example, the 2-6 and 5-10 transitions are both at 2.1  $\mu\text{m}$  and the 1-5 and 4-9 both at 2.3  $\mu\text{m}$ . The 7-13 appears at 2.2  $\mu\text{m}$  and the 6-12 at 2.5  $\mu\text{m}$ .

These features are shown in Figure C-6 for  $T_v = 80$  K and equal populations of  $v=1-7$  and a triangular resolution of 5 nm. Figure C-7 shows results with  $N_0:N_1:N_2:N_3:N_4:N_5:N_6:N_7 = 1:0.8:0.6:0.4:0.2:0.1:0.05:0.025$ . The normalization of the spectra of Figures C-6 and C-7 are such that the peak intensity of Figure C-6 is 2.3 times the peak intensity of Figure C-7.

#### b. $N_2(B^3\Pi \rightarrow W^3\Delta)$

The Einstein Coefficients for the Wu-Benesch system were taken from Covey et.al.<sup>C-15</sup> Their given value for  $V_B = 6 \rightarrow V_W = 5$  has been changed from the given  $1.14 \text{ s}^{-1}$  to  $640 \text{ s}^{-1}$  scaling with the Franck-Condon factors given in Ref. C-11. The spectroscopic constants were taken from Loftus and Krupenie<sup>C-11</sup> with corrections to  $T_e$  and  $A_v$  of the W-state from Cerny et al.<sup>C-15</sup>

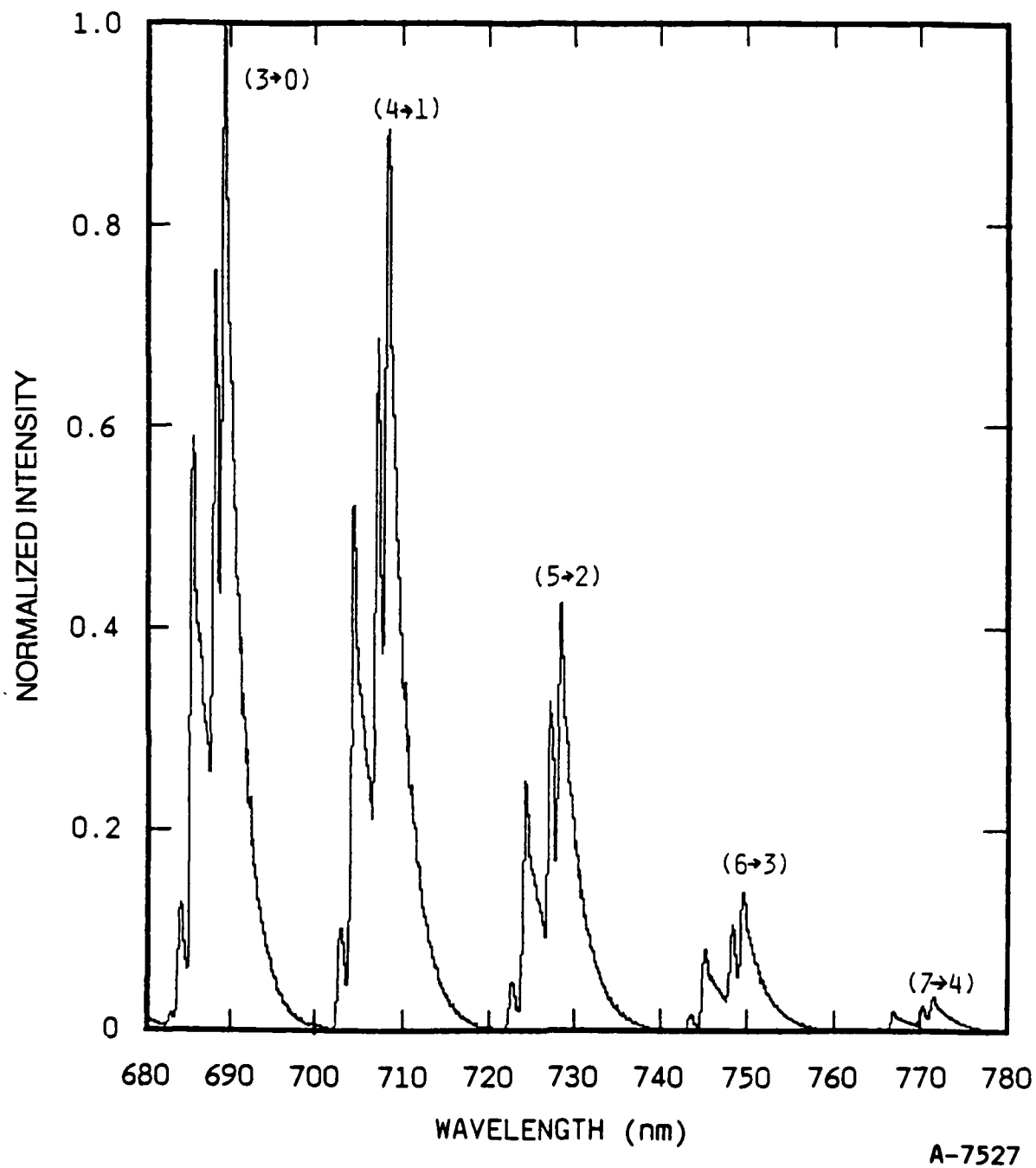
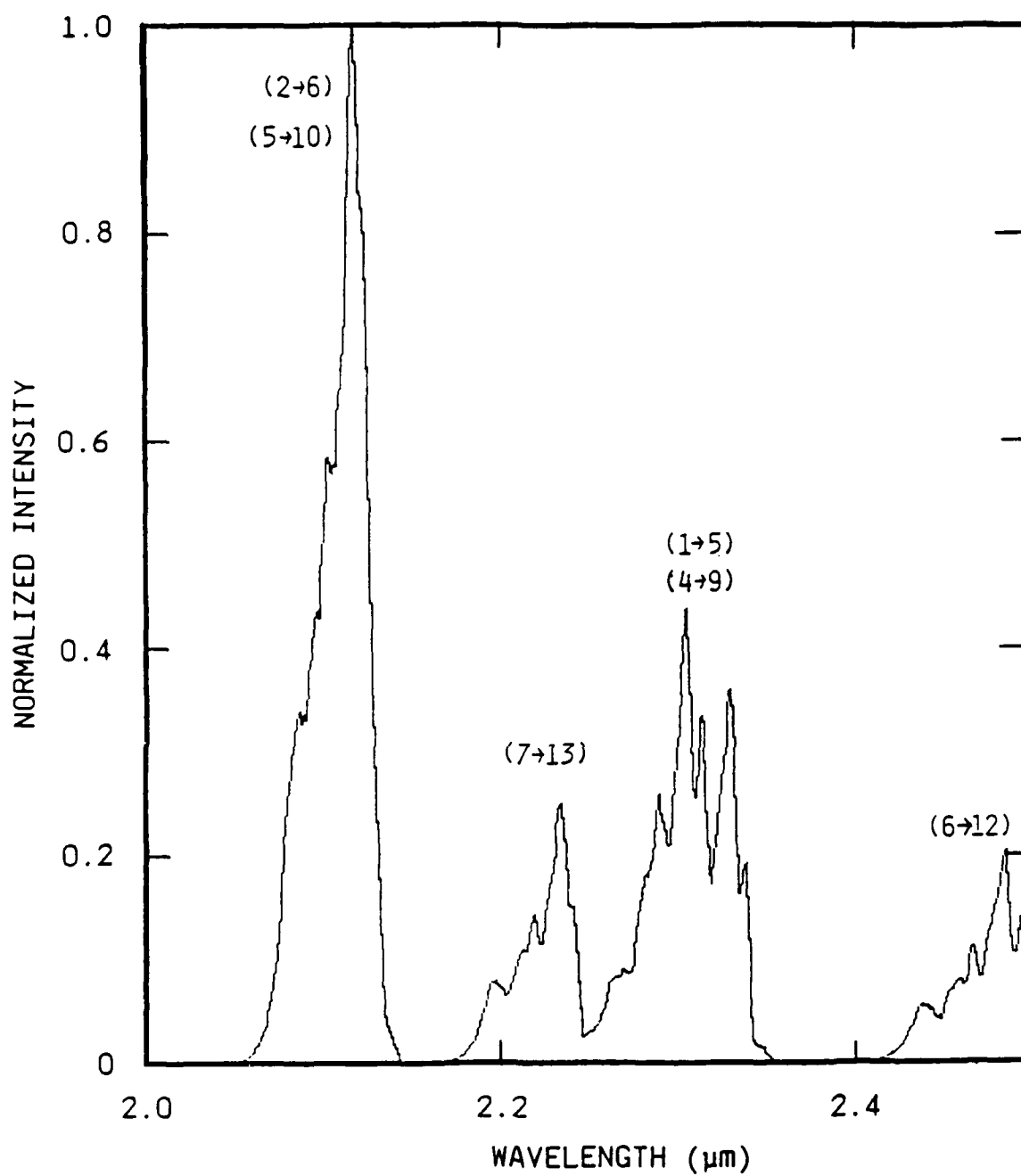


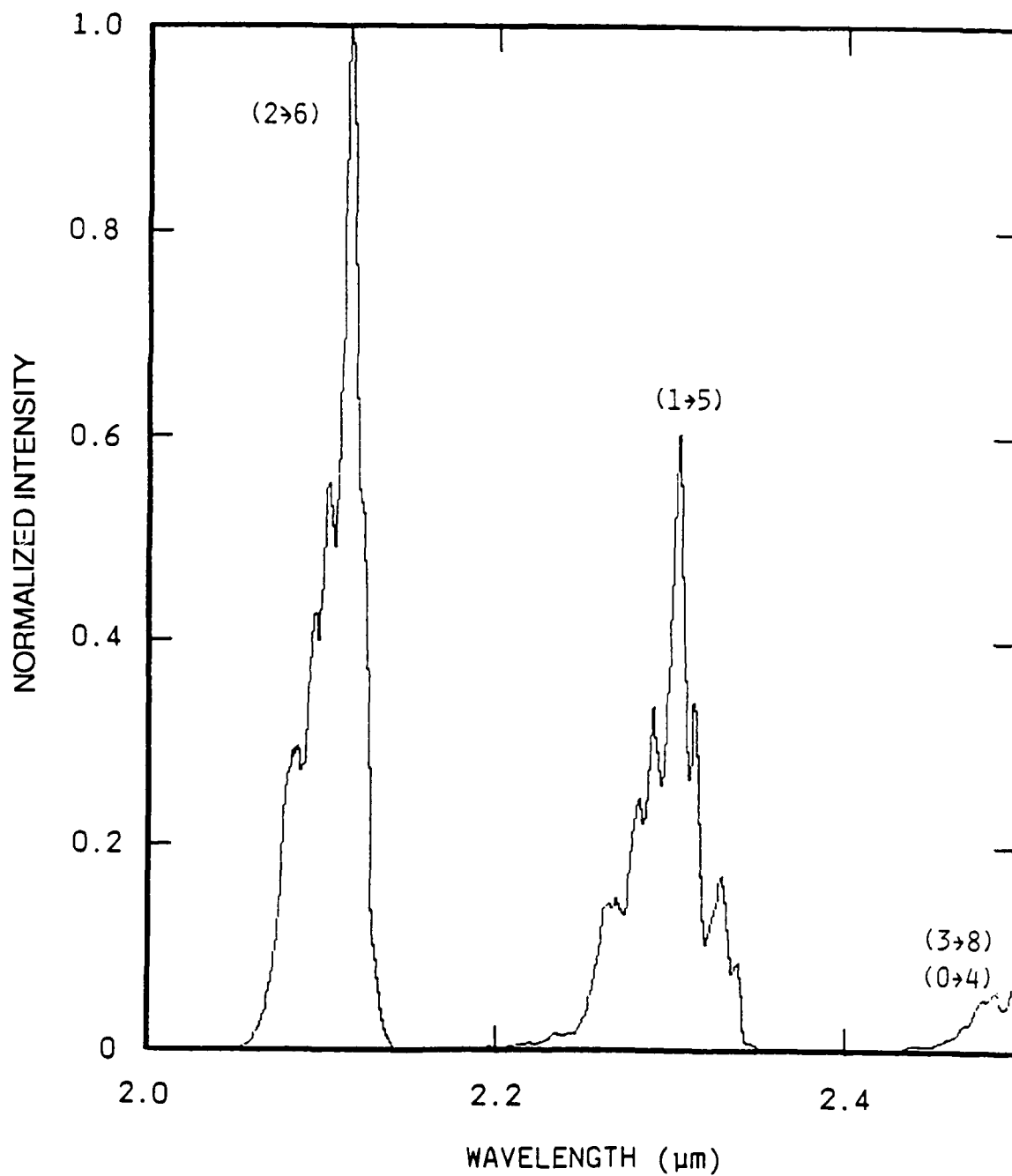
Figure C-5. Synthetic spectrum of  $N_2^+(A^2\Pi \rightarrow X^2\Sigma)$  "Meinel" system in  $\Delta v=3$  sequence  $T_r = 300$  K, populations as given in text. Individual bands in sequence and branch structure are resolved. Maximum intensity is  $1.4 \times 10^{-14}$  W/molecule-sr- $\mu\text{m}$ .





A-7528

Figure C-6. Synthetic infrared spectrum of  $N_2(B \rightarrow A)$  "First Positive" system between 2.0 and 2.5  $\mu m$  for a resolution of 5 nm. See text for details. Maximum intensity is  $1.3 \times 10^{-15}$  W/molecule-sr- $\mu m$ .  $T_r = 80$  K.



A-7529

Figure C-7. Synthetic spectrum of  $N_2(B \rightarrow A)$  for a different population distribution than Figure C-6 as described in text. Maximum intensity is  $5.8 \times 10^{-15}$  W/molecule-sr- $\mu m$ .

Computed spectra are shown in Figure C-8 for the 2-0 and 3-1 transitions of the W $\rightarrow$ B. These are computed with  $T_v = 80$  K and a triangular resolution of 13 nm. Figure C-9 shows the same spectra at 5 nm resolution. The structure indicates the complexity of the 27 band system.

#### C.5.4 Other Transitions

In Subsection C.4.1, spectra of the Vagard-Kaplan bands,  $N_2(A^3\Sigma-X^1\Sigma)$ , were shown as computed from a singlet-singlet transition distribution. This transition is an electric dipole-spin forbidden transition. The line strength factors have been the subject of much discussion over the years and appear to be resolved by the work of Watson<sup>C-7</sup> (see also Hougen<sup>C-5</sup> and Kovacs<sup>C-1</sup>). The values used by Shemansky<sup>C-12</sup> were incorrect.

For  $3\Sigma^+ \rightarrow 1\Sigma^+$ , there are four branches  $Q_1$ ,  $Q_3$ ,  $P_2$ , and  $R_2$ . The rotational distribution of the intensity is given by the equivalent of Eq. (C-12) except we no longer restrict ourselves to  $\delta\Sigma = 0$ .

$$S_{J''i''}^{J'i'} = \left| \begin{matrix} \Sigma \\ l'l'' \end{matrix} S_{l'l'} \sqrt{\frac{a}{l'l''}} S_{l''i''} \right|^2 \quad (C-28)$$

where the sign of square root must now be taken carefully and is dependent upon the symmetry of the eigenfunction.

More generally we can write

$$S_{J''i''}^{J'i'} = \left| \begin{matrix} \Sigma \\ l'l'' \end{matrix} \alpha_{l'l'} S_{l'i'} \sqrt{\frac{a}{l'l''}} S_{l''i''} \right|^2 \quad (C-29)$$

where  $\alpha_{l'l''}$  is a unit upper and lower state and of the transitions of interest. Since there are in general multiple unallowed transitions with

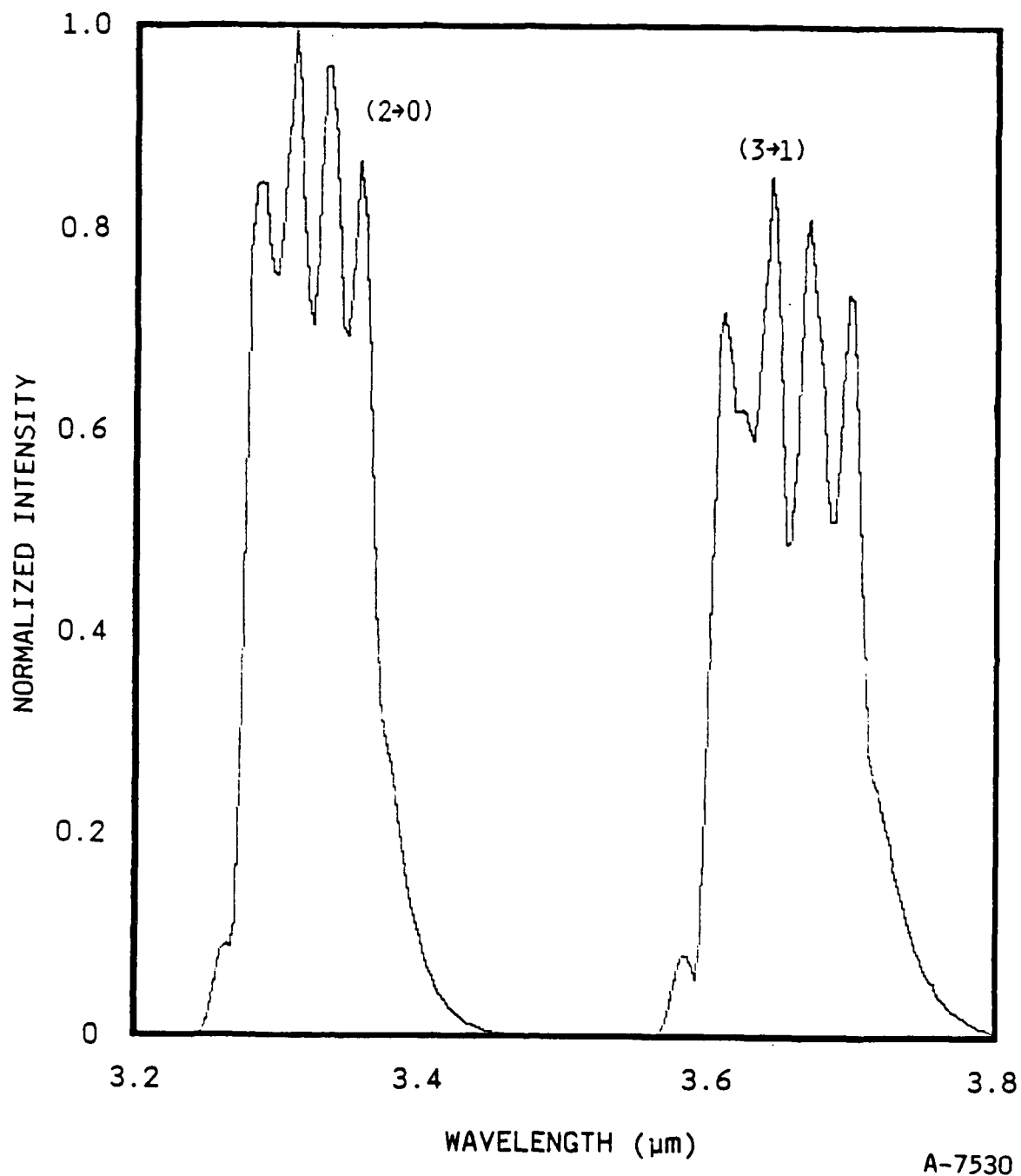


Figure C-8. Synthetic infrared spectrum of  $N_2(W^3\Delta) \rightarrow B(3\Pi)$  "Wu-Benesch" system at  $T_r = 80$  K and 13 nm resolution. The (2→0) and (3→1) bands are shown. Maximum intensity is  $9.4 \times 10^{-17}$  W/molecule-sr- $\mu\text{m}$ .

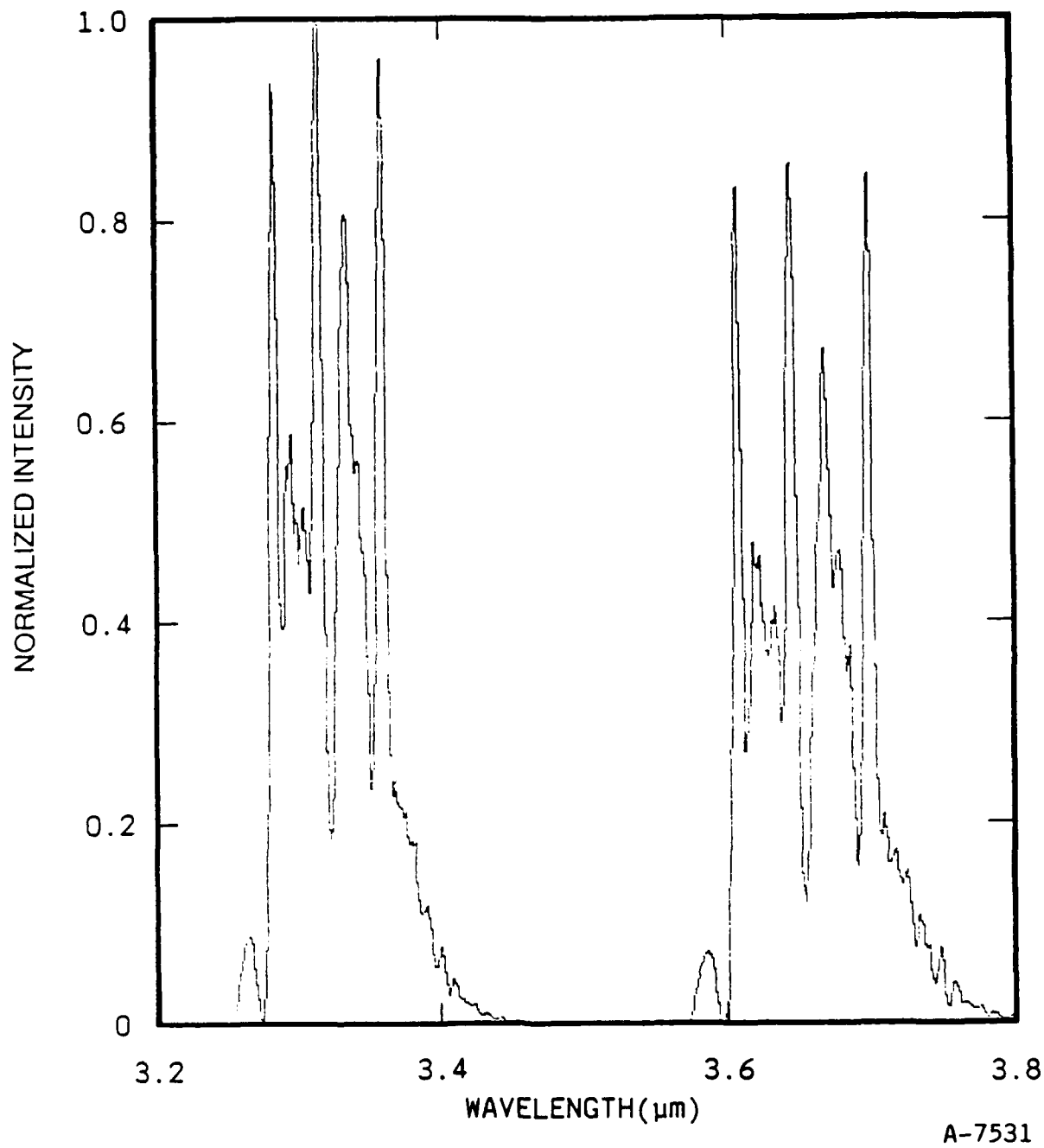


Figure C-9. Synthetic spectrum for  $N_2$  ( $W \rightarrow B$ ) as in Figure C-8 except for 5 nm resolution.  $I_{\max} = 1.4 \times 10^{-16}$  W/molecule-sr- $\mu\text{m}$ . Considerable branch structure is evident.

different transition moments, these will be multiple A values for Eq. (C-5), each having a different  $\alpha$  matrix. Whiting, et al. discuss this problem in Ref. C-4 and present useful tables in Ref. C-8.

Also of interest are quadrupole transitions. For example, one component of the Lyman-Birge-Hopfield system is quadrupole,<sup>C-18</sup> and is nearly as large as the dipole component (i.e. the quadrupole Einstein coefficient is about one tenth the dipole value). Kovacs<sup>C-1</sup> presents results for some quadrupole transitions.

## C.6 FUTURE EXTENSIONS

The code must be rigorously validated before it can be used as a routine spectroscopic analysis tool. This validation will be performed by comparison with experimental spectra for all bands of interest to see if band widths, branch structure, relative intensities are consistent for known systems. Aside from these exercises, additional refinement of the code will be necessary.

From Subsection C.5.4, we see that there is need for an algorithm for calculating the "symmetry matrix"  $\alpha$  of Eq. (C-29) for forbidden transitions. For quadrupole transitions, there is a need for a set of case (a) intensity factors as in Table C-1.

Perturbation by adjacent states has not been included in the model and could be important for some transitions. An approach such as that outlined by Kovacs<sup>C-1</sup> and used by Beiting et al.<sup>C-19</sup> would seem appropriate.

In some cases such as the N<sub>2</sub> First Positive system, transitions are observed for which no Einstein coefficients are given in the literature. Schader<sup>C-20</sup> shows quite convincingly that

$$A_{v',v''} \approx q_{v',v''} f(\lambda) \quad (C-30)$$

where  $q_{v',v''}$  is the Franck-Condon factor and  $f$  is a function of wavelength only and can be found from known values of  $A_{v',v''}$ . Thus when the Franck-Condon factors are known,  $A_{v',v''}$  can be extended by Eq. (C-30). We would use this approach in determining populations from IR transitions. Multiple emissions from the same radiating upper state would allow  $f(\lambda)$  determination or direct Einstein coefficient determination for these states. The unique capabilities of LABCEDE and COCHISE may permit us to carry out quantitative spectroscopy on previously unobserved or weakly observed molecular electronic states.

To a first approximation, we can uncouple the spin and rotational temperatures in Eq. (C-5) by replacing the exponent,

$$F_{i'}(v', J') \quad hc/kT_r ,$$

by

$$\bar{F}(v', J') \quad jc/kT_r + \lambda_{i'}(v, J') \quad hc/kT_s ,$$

where  $\bar{F}$  and  $\lambda_{i'}$  are defined in Subsections C.3.1 and C.3.2 and are computed in subroutines FSn. A careful analysis is necessary to examine the validity of this approximation. But under the single collision conditions of the cryogenic facilities spin-equilibration may not be achieved.

#### C.7. REFERENCES

- C.1 Kovacs, Istvan, Rotational Structure in the Spectra of Diatomic Molecules, American Elsevier (1969).
- C.2 Arnold, J.O., Whiting, E.E., and Lyle, G.C., JQSRT, 9, 775 (1969).
- C.3 Whiting, E.E., Arnold, J.O., and Lyle, G.C., NAS Distributed as Cosmic Program #ARC-10221.
- C.4 Whiting, E.E. and Nicholls, R.W., Astro. J., Sup. 235, 27, 1 (1974).

- C.5 Hougén, J.T., NBS Monograph 115, June 1970.
- C.6 Herzberg, G., Molecular Spectra and Molecular Structure; I. Spectra of Diatomic Molecules, Second Edition, D. van Nostrand, 1950.
- C.7 Budo, A., Z. Phys. 105, 579 (1937).
- C.8 Whiting, E., Patterson, J., Kovacs, I., and Nicholls, R., J. Mol. Spec., 47, 84 (1973).
- C.9 Whiting, E.E., NASA TN D-7269, Ames Research Center, September 1973.
- C.10 Huber, K. and Herzberg, G., Molecules Spectra and Molecular Constants of Diatomic Molecules, Van Nostrand Reinhold, New York, 1979.
- C.11 Loftus, A. and Krupenie, P., J. Phys. Chem. Ref. Data, 6, 113 (1977).
- C.12 Shemansky, D., J. Chem. Phys., 51, 689 (1969).
- C.13 Hohlman, G., van Spring, H., Bloeman, E., and deHeer, F., Chem. Phys., 32, 239(1978).
- C.14 McGee, T., Miller, G., Bruuis, J., and McIlrath, F., J. Quant. Spectrosc. Radiat. Transfer, 29, 333(1983).
- C.15 Covey, R., Saum, K., and Benesch, W., J. Opt Soc. Amer., 63, 592 (1973).
- C.16 Cerny, D., Roux, F., Effantin, C., D'incan, J., and Verges J., J. Mol. Spec., 81, 216 (1980).
- C.17 Watson, J.K.G., Can. J. Phys., 46, 1637 (1968).
- C.18 Shemansky, D., J. Chem. Phys., 51, 5487 (1969).
- C.19 Beiting, E.J., III, Jones, C.C., and Benesch, W., J. Mol. Spec., 70, 108 (1978).
- C 20 Schader, A., JQSRT, 7, 169(1976).



# ATTACHMENT A

## Solution of the Triplet Transformation Matrix

We wish to solve the matrix equation

$$\begin{pmatrix} \delta+\eta & H & G \\ H & -2\delta & 0 \\ G & 0 & \delta-\eta \end{pmatrix} \begin{pmatrix} S'_{1i} \\ S'_{2i} \\ S'_{3i} \end{pmatrix} = i \begin{pmatrix} S'_{1i} \\ S'_{2i} \\ S'_{3i} \end{pmatrix}$$

for  $S'_{1i}$  and  $\lambda_i$ . We discuss cases separately.

A.  $G = 0$

The  $\lambda_i$  can be found from  $\delta-\eta$  and the quadratic for  $G = 0$ .

$$i) \quad \lambda_2 = \delta-\eta$$

$$S'_1 = 0, S'_2 = 0, S'_3 = 1$$

$$ii) \quad \lambda_{1,3} = -\frac{(\delta-\eta)}{2} \pm \sqrt{\left(\frac{\delta-\eta}{2}\right)^2 + B^2 + 2\delta(\delta+\eta)}$$

$$S'_1 = H/D$$

$$S'_2 = (\lambda - (\delta-\eta))/D$$

$$S'_3 = 0$$

$$D^2 = (2H^2 - 3(\delta-\eta)(\lambda - (\delta-\eta)))$$

B.  $G \neq 0$

For  $G \neq 0$  we use the cosine rule to get the  $\lambda_i$  from

$$\lambda^3 - a^- \lambda + b' = 0$$

where

$$a^- = 3\delta^2 + H^2 + G^2 + \eta^2$$

$$b' = 2\delta(\delta^2 - \eta^2 - G^2) + (\delta - \eta)H^2 \quad .$$

Given

$$f = \sqrt{a^-/3}$$

$$\cos \theta = -3/2 b'/(a^- f)$$

Then

$$\lambda_1 = -2 f \cos ((\Pi - \theta)/3) = -f \alpha - f(3(1 - \alpha^2))^{1/2}$$

$$\lambda_2 = -2 f \cos ((\Pi - \theta)/3) = -f \alpha - f(3(1 - \alpha^2))^{1/2}$$

$$\lambda_3 = -2 f \cos (\theta/3) = 2f\alpha \quad .$$

Define

$$T_1 = \lambda - (\delta + \eta)$$

$$T_2 = \lambda + 2\delta$$

$$T_3 = \lambda - (\delta - \eta) \quad .$$

When for  $\lambda_1$  and  $\lambda_3$

$$S'_1 = H T_3 T_2 / D$$

$$S'_2 = H^2 T_3 / D$$

$$S'_3 = H G T_2 / D$$

$$D^2 = H^2 \{ T_2^2 T_3^2 + G^2 T_2^2 + H^2 T_3^2 \} \quad .$$

For  $\lambda_2$ ;  $T_1$  and  $T_3$  especially will be small compared to  $H$ , so we use

$$S'_1 = T_3 H / D$$

$$S'_2 = (T_1 T_3 - G^2) / D$$

$$S'_3 = G H / D$$

$$D^2 = T_3^2 H^2 + G^2 H^2 + (T_1 T_3 - G^2)^2 \quad .$$

APPENDIX D

PARTICLE BOMBARDMENT OF ATMOSPHERIC GASES

Final Report

to

Physical Sciences, Inc.

Contract: SC 9579

Contract Manager: Dr. David Green

by

Professor Stanley Bashkin

Principal Investigator

Department of Physics

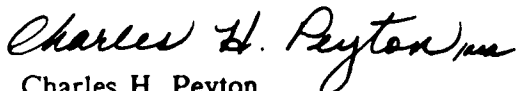
University of Arizona

Tucson, Arizona 85721

(602)621-2322

Date of Report: September 25, 1986

Approved for the University:

  
Charles H. Peyton  
Associate Vice-President for Research

## INTRODUCTION

We bombarded nitrogen gas with projectiles of  $H^+$ ,  $H_2^+$ , and  $H_3^+$ . The particle energy was varied from 0.5 to 1.5 MeV and the gas pressure was controlled at various pressures from 2 to 20 millitorr. The light generated in the gas was spectrally analyzed with an air spectrometer and detected with a photomultiplier tube. The spectra extended from 350 to 650 nm, and several dozen individual lines were detected, two of which were studied in detail. Our search of the literature indicates that ours is the first bombardment of nitrogen gas which used  $H_3^+$  as a projectile.

The ultimate goal of the experiments was to determine the absolute cross section for the excitation of individual states of the emitting systems. Therefore, an immediate goal was to establish what alterations in the experimental arrangement would be needed in order to meet that ultimate goal.

Another purpose of the experiments was to find out whether and in what direction further experimental work would be worth doing.

It will be seen from the following report that a great deal of data of the desired nature was obtained, and that we were able to reach significant conclusions regarding the other matters mentioned above. On the other hand, the shortage of time made it impossible to engage in more than a cursory analysis of our results; a more complete study remains to be done in the near future. We expect that the work to date will be suitable for preparation of a paper for submission to a major research journal.

## PERSONNEL

The people who were engaged in this effort were:

a) From the University of Arizona -

Professor Stanley Bashkin, Principal Investigator

Mr. Bijan Dezfouly-Arjomandy, graduate student

Mr. Peter Sercel and Mr. David Durkin, undergraduate students

b) From the University of Nevada - Reno -

Professor Reinhard Bruch

Mr. Stephen Fuelling and Mr. David De Witt, graduate students

Note on personnel: Partly because of the uncertainty of long-term funding, Mr. Dezfouly-Arjomandy has elected to join another research group. The visitors from Nevada participated in the work for periods ranging from a few days to a month.

## EXPERIMENTAL PARAMETERS

The experimental parameters available for this work were the type of gas in the target chamber, the gas pressure, the type of incident particle, the particle energy, and the spectral range over which the observations could be made. Each of these parameters merits some discussion.

1. The target gas chosen was nitrogen, for nitrogen is an important constituent of the atmosphere and preliminary measurements showed that it emits strong signals in the spectral region appropriate to our apparatus. The cross section for the formation of  $N_2^+$  by protons has a maximum near the bombarding energy we used, which helps to provide a satisfactory fluorescence yield.

2. The gas pressure was controlled by an MKS device, and was measured with an MKS capacitance manometer. With this equipment, we could control the pressure to within a few per cent at the lowest pressure (2 millitorr) and to better than that at the highest pressure we used (20 millitorr).

3. As noted in the introduction, we used three different ions of hydrogen as the incident particles. The particles were extracted from a 2 MV Van de Graaff accelerator equipped with an RF ion source. The emergent particles were mass-analyzed with a precision-controlled magnetic spectrometer, and the appropriate particles were directed into the target arm we were using.

4. For much of the work, we maintained the same velocity for the incident particles, which meant running at 0.5 MeV for protons, 1.0 MeV for the diatomic hydrogen ions, and 1.5 MeV for the triatomic hydrogen ions. However, some data were also taken for a particular ion as a function of particle energy. For the data taken at constant particle velocity, we used pressures from 2 to 20 millitorr in steps of 2 millitorr.

A factor which is implicit in the work is that the particle energy was constant for all data taken at a particular nominal value. That was the case, the energy fluctuation being of the order of 10 keV or less. This stability of the energy was accomplished by means of a slit system which, on receiving current from the particle beam, sent a signal back to the accelerator which adjusted the machine voltage either up or down as required to balance the current to the two slits. This system worked very well.

5. The spectral range of the spectrometer was nominally 180 to 900 nm. However, the actual effective range was limited by the blaze of the diffraction grating and the response characteristics of the photomultiplier tube that detected the optical signal. In our case, the grating was blazed at 500 nm, which meant that the reflectivity fell off rapidly below 350 and above 650 nm. Within these limits, the S-20 response of the photomultiplier tube was satisfactory.

We used a standard lamp, calibrated by the Bureau of Standards, to measure the response function of our optical system. That was not an entirely satisfactory measurement, because the lamp operated with a kilowatt of power. Consequently, it was so hot (thermally) that it couldn't be put inside the target chamber. Its actual position was in the air, and a blower was needed to keep everything in the vicinity from catching fire. As a result, two reflecting surfaces and a transparent window were omitted from the path of light from the standard lamp, and the light from the lamp did not enter the spectrometer along the optic axis. Because of these factors, we estimate that the spectral response function is probably not known to better than 30%.

## EXPERIMENTAL LIMITATIONS

The main limitation of our measurements was in the determination of the number of particles incident on the target gas as the particle type, particle energy, and gas pressure were altered. The difficulty arises from fundamental physical processes, which we may describe as follows:

The number of incident particles is most directly measured in terms of the electric charge which is collected in a Faraday cup. Nominally there is one electronic charge per particle, so the correlation of charge and particle number is one-to-one. The measurement is generally complicated by the possibility that the incident beam will graze a slit edge somewhere and liberate electrons, which are also collected by the cup, thereby introducing an error into the measurement. It is also possible for electrons to be ejected from the cup, which again causes the measured incident charge to be inaccurate.

These effects may be avoided, in principle, by inserting a repeller ring between the entrance to the cup and the collector proper. This ring is biased negatively, which prevents electrons from either entering or leaving the collector.

However, the situation becomes more difficult when a gas target is used, because some of the gas inevitably enters the cup, and then ionization occurs by virtue of collisions with the incident particles. Such ionizations, taking place between the repeller ring and the collector, cause electrons to be accelerated to the collector, and, again, an error is made in the collected charge. We actually took our data without biasing the ring.

Furthermore, charge-changing events occur in the target gas itself, so that some of, for instance, the incident molecular ions, which enter the target with a single electronic charge, may emerge with two (or three) charges, while protons may pick up electrons and enter the cup as neutral particles, which are not counted. In addition, ions created or electrons liberated in the gas target may drift to the collector. A final consideration is that the incident beam undergoes scattering in the target.

These effects are serious functions of the kind of incident particle, the particle energy, the kind of gas in the target, the target pressure, and the geometry of the target/collecting system. These factors were especially awkward for our arrangement. What we had to do within the time available to us was to insert a high-impedance channel in the beam pipe, well ahead of the observation region. Pumps were located on the entrance to this channel and on the rear of the target chamber. However, there was a long beam path which contained the target gas, so that the charge-exchange and scattering effects took place over a distance of about a meter. The region of observation was only 2.5 cm. long.

This means that the measurement of the number of incident particles was necessarily unsatisfactory. We have carried out some measurements in order to reduce the uncertainties inherent in work such as ours. Thus we measured the current to our collector with and without gas in the target cell, for all three incident particles at a common velocity. We have used those data to normalize the measured yields as a function of pressure and also of particle type. We look upon these data, which are presented in the form of graphs, as preliminary, only.

Another limitation which also affects measurements of cross sections is that the density of particles in the target is not simply given by the gas pressure. The reason is that the beam heats the gas, so that the density of targets along the beam axis is not the same as that of the gas as a whole. Again, it is not a simple matter to make a precise correction for this effect.

A further limitation has to do with the spectral resolution and spectral range. In principle, one wants to work at the highest possible instrumental resolution over the entire spectral range. In practice, that takes far too long a time to be sensible. Instead, one uses low-to-moderate resolution over broad portions of the spectrum, and restricts the high-resolution studies to relatively small regions. That is what we did, and the data we present reflect the choices made as regards resolution.

Still other problems, which are present even if relative cross sections are to be found, have to

do with the possible presence of cascades. If the level whose decay is being observed is repopulated by cascades from higher-lying levels, the detected intensity is no longer a direct measure of the degree to which the level of interest has been excited. If, furthermore, the level of interest branches into a number of lower levels, it is necessary to know the branching ratios in order to relate the intensity of a particular branch to the population of the initial level. The lifetime of the level, a feature which is virtually unknown for most levels in the molecular systems we have investigated, is another factor which must be known if cross sections are to be deduced. If the emitted radiation is polarized, further corrections to the observed intensity are needed. Finally, it is obvious that to find absolute cross sections, one must know the absolute collecting efficiency of the experimental system.

It should be clear from the foregoing that a great effort is needed to produce meaningful approximations to cross section measurements: we have taken some of the essential early steps.

## EXPERIMENTAL RESULTS

We present our findings in terms of a set of figures, which are essentially spectra obtained under different conditions. These graphs may be summarized as follows:

Fig. 1. Low-resolution survey of the spectral region from 360 to 520 nm. The incident particle was  $H_3^+$  at 0.5 MeV, and the target pressure was 20 millitorr. This figure shows that a considerable number of individual transitions were detected. The strongest lines came from  $N_2^+$ , and were  $1N(0,0)$ ,  $1N(0,1)$ , and  $1N(0,2)$ , at 391.4, 427.8, and 471.0 nm., respectively. We paid particular attention to the band heads at 391.4 and 427.8 nm, which belong to the molecular ion,  $N_2^+$ .

Fig. 2. An expanded part of Fig. 1, showing the  $2P(2,4)$  and  $2P(1,3)$  band heads in  $N_2$ , at 370.9 and 375.5 nm, respectively.

Fig. 3. A further expanded part of Fig. 1, showing the  $2P(0,2)$ ,  $2P(2,5)$ , and  $2P(1,4)$  band heads, at 380.4, 394.4, and 399.8 nm, respectively.

Fig. 4. A further expanded part of Fig. 1, showing the  $2P(0,3)$  band head in  $N_2$  at 405.9 nm and the  $1N(2,3)$  band head in  $N_2^+$  at 419.9 nm.

Fig. 5. A further expanded part of Fig. 1, which shows only very strong features better seen in Fig. 1. An interesting point is that the second Balmer line, which should appear at 434.1 nm is probably not present.

Fig. 6. A further expanded part of Fig. 1, showing  $2P(3,8)$  and  $GK(0,10)$  at 441.7 and 443.3 nm., respectively. The figure also shows  $1N(3,5)$  and  $1N(2,4)$  in  $N_2^+$ , at 455.4 and 460.0 nm, respectively.

Fig. 7. A further expanded part of Fig. 1, showing  $1N(1,3)$  at 465.2 nm. There is possible blending with  $2P(4,10)$  and  $VK(4,16)$ , both at 464.9 nm.

Fig. 8. A further expanded part of Fig. 1, showing  $2P(1,7)$  at 491.7 nm.

Fig. 9. A further expanded part of Fig. 1, showing  $1N(3,6)$  and  $1N(1,4)$  at 501.3 and 514.9 nm, respectively.

Unidentified features appear at: 398.5, 402.6, 403.6, 404.2, 411.0, 417.6, 442.8, 444.2, 453.2, 489.7, 493.7, and 501.0 nm.



Fig. 10. As in Fig. 1, but for a gas pressure of 6.5 millitorr, and an upper wavelength limit of 570 nm.

Figs. 11-20. Moderate-resolution spectra for protons with an energy of 0.5 MeV incident on nitrogen for target pressures from 2 to 20 millitorr. The main feature is the band head at 391.4 nm from the 1N(0,0) level in  $N_2^+$ .

Figs. 21-29. As in Figs. 11-20, but for incident particles of  $H_2^+$  at an energy of 1.0 MeV. These incident particles have the same velocity as the protons mentioned above.

Figs. 30-39. As in Figs. 11-20, but for incident particles of  $H_3^+$  at an energy of 1.5 MeV. These incident particles have the same velocity as the protons mentioned above.

Figs. 40-49. As in Figs. 11-20, but in the vicinity of the 1N(0,1) band head at 427.8 nm in  $N_2^+$ . The proton energy is again 500 keV.

Figs. 50-58. As in Figs. 30-39, but for the band head at 427.8 nm.

Figs. 59-68. As in Figs. 40-49, but for the band head at 427.8 nm.

Fig. 69. Study of the band head at 391.4 nm with incident particles of  $H_2^+$  at 0.5 MeV and a target pressure of 14 millitorr.

Fig. 70. As in Fig. 69, but with an energy of 1 MeV, and better resolution. Here the peak which is furthest to the left (390.83 nm) corresponds to the peak in Fig. 69 which is just to the left of the valley. The improvement in resolution in Fig. 70 is evident.

Fig. 71. Study of the line at 391.4 nm from 1N(0,0) in  $N_2^+$ , excited with incident particles of  $H_3^+$  at 0.5 MeV, and a target pressure of 6.5 mT.

Fig. 72. As in Fig. 71, but for a target pressure of 20 mT.

Fig. 73. As in Fig. 72, but for an incident energy of 1 MeV.

Fig. 74. A high-resolution study (second order) of the band at 391.4 nm.

Fig. 75. Study of the band head at 427.8 nm with incident particles of  $H_2^+$  at 0.5 MeV and a target pressure of 14 millitorr.

Fig. 76. As in Fig. 75, but with improved resolution (second order).

Figs. 77-79. Normalized yields as a function of pressure for the line at 391.4 nm, for all three incident particles at the same velocity.

Figs. 80-82. Normalized yields as a function of pressure for the line at 427.8 nm, for all three incident particles at the same velocity.

## INTERPRETATION

We have not had the time to attempt a theoretical interpretation of our data. That will be done when a paper is prepared for submission to a research journal. However, it is worth pointing out that the incident particles have so large a mass that they carry considerable angular momentum into the collisions. This means that there are essentially no limitations in the interactions because of any angular-momentum selection rules. According to C. Y. Fan

(private communication), it is likely that the dominant mechanism in the excitation of the nitrogen molecular ion involves a direct interaction between the projectile and the target, rather than electron detachment from the target followed by capture of that electron by the incident particle. This possibility lends itself to direct experimental investigation, because, should electron capture be significant, we ought to see the Balmer lines, several of which lie within our spectroscopic capability. In fact, the second Balmer line, if present, would overlap with  $2P(0,4)$ , which is very weak in our spectra.

The overall spectrum (see Fig. 1) indicates that a considerable number of spectral lines were generated. It is interesting to look at these in terms of the quantum characteristics of the states involved. In the first place, the lines from the molecular ion are far more prominent than those from the neutral molecule. In the  $1N$  system of  $N_2^+$ , the strongest lines belong to transitions which start on a level with vibrational quantum number 0. This is not surprising, since the ground term of the ion has that same vibrational quantum number, and the overlap of the wave function for the excited state is greatest when the vibrational quantum number doesn't change. We see the  $1N(0,0)$ ,  $(0,1)$ , and  $(0,2)$  transitions, the apparent relative intensities of the first two being about the same, and greater than that of  $(0,2)$ . However, before one can draw a physically significant conclusion from this, the data have to be corrected for the wavelength response function of the optical system, and that we have not yet done.

It is worth pointing out that we also generated lines which start on levels with higher vibrational quantum numbers. Thus,  $1N(1,2)$  is quite strong, and  $1N(3,6)$  is readily detected. We did not have the time to look at these features in any detail.

Another comment can be made: Figures 77-82 show that the intensities at 391.4 and 427.8 nm do not show the same pressure dependence, although all yields are linear with pressure. Thus the yield of 391.4 is proportional to that of 427.8, but the proportionality constants are not the same for all incident particles. Specifically, taking ratios of 391.4 to 427.8 for the three particles, we have 1.9 for protons, 1.7 for diatomic ions, and 1.6 for the triatomic ions. This variation might not be physically significant, since the uncertainties are about as large as the apparent differences. It would be hard to understand such a variation, since the lines come from the same initial state, so their relative intensities should be independent of the manner of excitation.

As Figs. 1-10 show, we saw a number of features belonging to the neutral molecule, but, again, there was no opportunity to follow their behavior as a function of our various parameters. In the following discussion, we restrict our remarks to the lines at 391.4 and 427.8 nm.

The yield from what is nominally the same number of incident charges is the same for protons and  $H_2^+$  particles. This suggests that the cross section for excitation by protons is twice that for the diatomic molecular ions. The yield from incident  $H_3^+$  particles is only  $2/3$  that for the same collected proton charge, which implies that the proton excitation cross section is 4 to 5 times larger than for the triatomic ions.

It is worthwhile to point out that comparison of our results with those in the literature is virtually impossible, because:

1. To our knowledge, nobody else has ever used the triatomic hydrogen ion as the incident particle in the excitation of nitrogen.
2. Most of the other work has been carried out for incident energies of a few keV, at most, so that we are in a novel energy regime.

## FUTURE WORK

Although the present contract has come to an end, the work done with its help has pointed the way to a major improvement in the kinds of data already taken and to new experiments of a broadened nature. A brief discussion of our intentions for the future follows.

We do not lose sight of the ultimate goal of measuring absolute cross sections for the excitation of individual states. To reach this goal, our present results emphasize the necessity of improving the determination of the number of incident particles and the density of target particles. For the first of these, we have designed a novel Faraday cup, which, along with corrections due to the energy-dependence of charge-changing events in thin foils, should provide the desired information. The second matter is more difficult, and no satisfactory solution has yet been found. We will continue to look for ways of circumventing this problem.

Improvements are needed in the gas-handling system. We are now using old-fashioned diffusion pumps with liquid nitrogen traps. This has two serious drawbacks. For one, the pumping speed is too low to permit as wide a range of target pressures as would be desirable. Second, the cost of liquid nitrogen is so great that new-style pumps, which don't require trapping, would be amortized quite quickly. The modern pumps would also provide perhaps 3 or 4 times the pumping speed we can now get. Third, the need to keep target gas out of the collector region is severe, and better pumps would be of material assistance in achieving this.

A new target chamber is also needed. The present chamber doesn't have as good coupling to the pumping system as desired, and this also affects the range of pressures over which data can be taken. The special Faraday cup would be connected to a new target chamber.

There is an entirely different target chamber which appears to offer substantial advantages over the present design, as regards certain kinds of observations. In this chamber, the optic axis of the spectrometer would look right along the particle beam, in contrast to the present - and customary - arrangement in which the light from the excited gas is seen at right angles to the particle beam. It happens that the recoil particles emerge at right angles to the incident direction, which means that looking at right angles to that beam gives rise to the maximum Doppler broadening that occurs. On the other hand, looking along the beam eliminates the linear Doppler effect, and the broadening from that cause is virtually eliminated. At the same time that the resolution is enhanced, the total amount of light collected by the spectrometer is greatly increased, and the sensitivity of the experiment is made much better than before. The mirrors now in use would also be eliminated from the optical system.

This target chamber would be terminated with a transparent window, through which the spectrometer would receive the light. However, one cannot allow the particles to strike that window, since that would cause an inevitable blackening of and radiation-induced damage to that window. The way in which to avoid this problem is to use a magnetic field to sweep the charged particles to the side. This would protect the window, and all one need do is insert a particle detector before the gas chamber, so as to measure the number of incident particles.

Another interesting possibility with observations made along the line of the particle beam is to replace the spectrometer with a variable dye laser. Such a laser would permit us to pump from whatever low-lying states were generated to higher ones, whence the fluorescence could be simply detected with a photomultiplier tube. We already possess a variable dye laser, and an argon ion laser which pumps the dye laser. Thus it is attractive to think in terms of such work. One interesting feature is that spectral resolutions far higher than any we have used

so far could be obtained, perhaps even to the extent of seeing hyperfine effects.

With additional diffraction gratings for the spectrometer, blazed closer to the ultraviolet and infrared spectral regions, we could examine spectral features now concealed from us. The spectrometer also needs a better encoder to give better wavelength reproducibility of the drive. A grating blazed at, say, 700 or 750 nm would make it easier to see the first Balmer line, should electron capture result in its presence.

A final desirable modification of the equipment would be a new mount for the spectrometer. The present structure, which was inherited from a previous user, is massive and awkward. In fact, despite the delicate nature of the optical components, the alignment of the spectrometer along the beam axis requires manipulation with a crow bar! Furthermore, the mount is so made that it is impossible to achieve a simple rotation about, say, the entrance slit, although that is badly needed in setting up the experiment. We hope to build a more suitable mount in the near future.

The data presented in Figs. 1-10 show that the investigations we have already made on 391.4 and 427.8 nm could be easily extended to the other strong lines. It would be especially valuable to examine 423.7 nm, which derives from  $1N(1,2)$ , to see if its dependence on the various physical parameters mirrors or differs from that shown by the two lines we did study. The lines from the neutral molecule present another interesting field of investigation. What is important to keep in mind is that we could exploit our present equipment without any change whatsoever in looking at those spectral features, and there is clearly a lot of appeal to taking good data instead of improving the apparatus.

It is relatively simple to extend the variety of incident particles, and this will be done in the near future. Similarly, it is an easy matter to change target gas. We are especially interested to use  $O_2$ ,  $CO_2$ , and air.

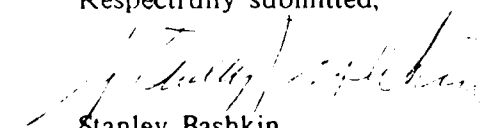
Turning to new kinds of experiments, we think especially in terms of looking into the chemistry which accompanies the formation of molecular ions in the vicinity of neutral species. For example, with air as the target gas, we could attempt to determine the yield of NO, which presumably results from the interaction of nitrogen molecular ions with neutral oxygen. Such measurements could have significant application to the upper atmosphere of the earth.

Still other inviting experiments involve the use of target gases similar to those which exist in the atmospheres of non-terrestrial components of the solar system. Thus, bombarding methane, ammonia, sulfur, and other substances with energetic protons could shed light on events taking place in various objects in the solar system. While such experiments would not necessarily be of direct interest to the Air Force, it is nonetheless the case that techniques learned in the course of such investigations could well have a positive impact on those matters which are of immediate concern to the Air Force.

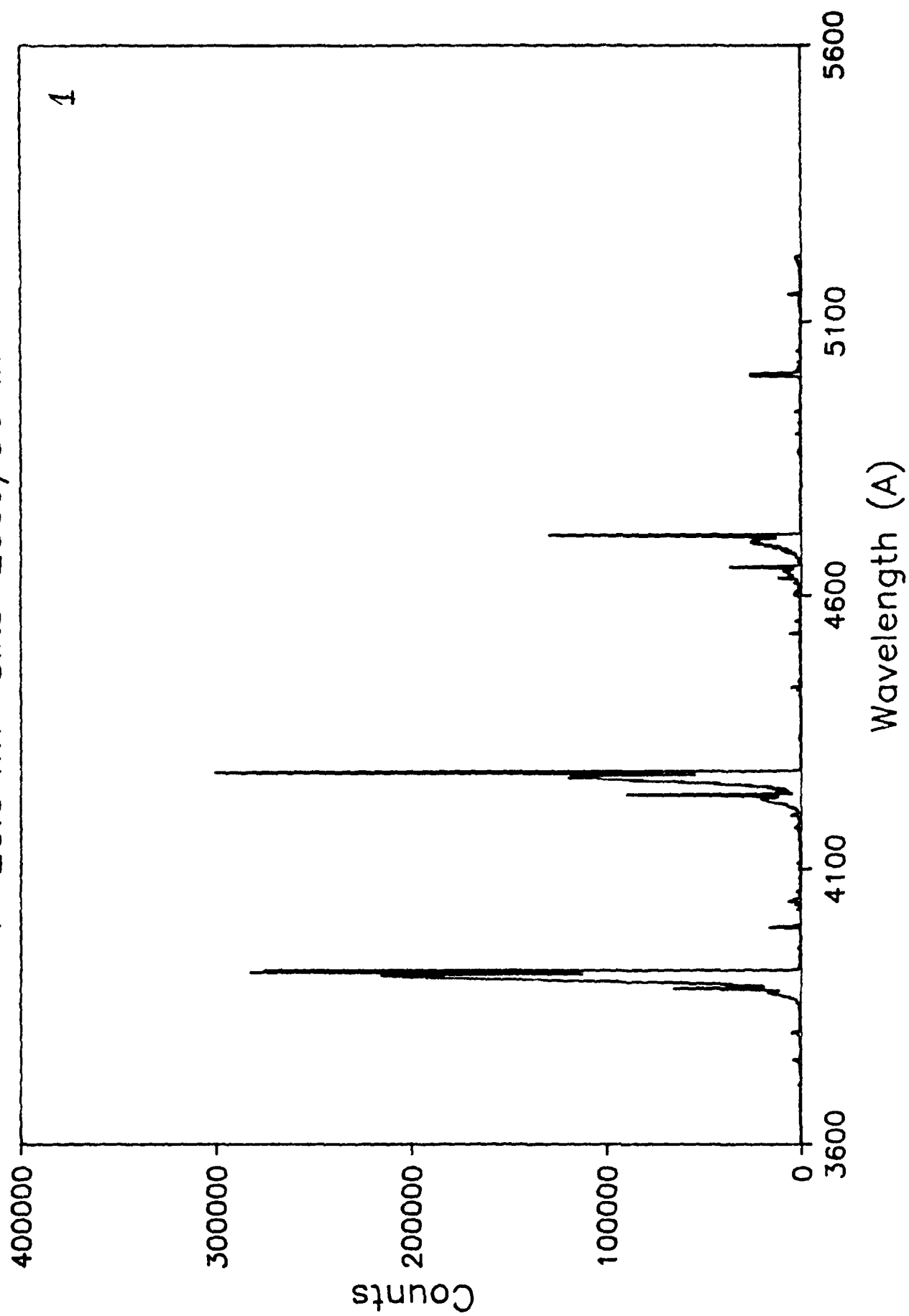
#### BUDGET

All funds allocated under this contract were spent during the contract period.

Respectfully submitted,

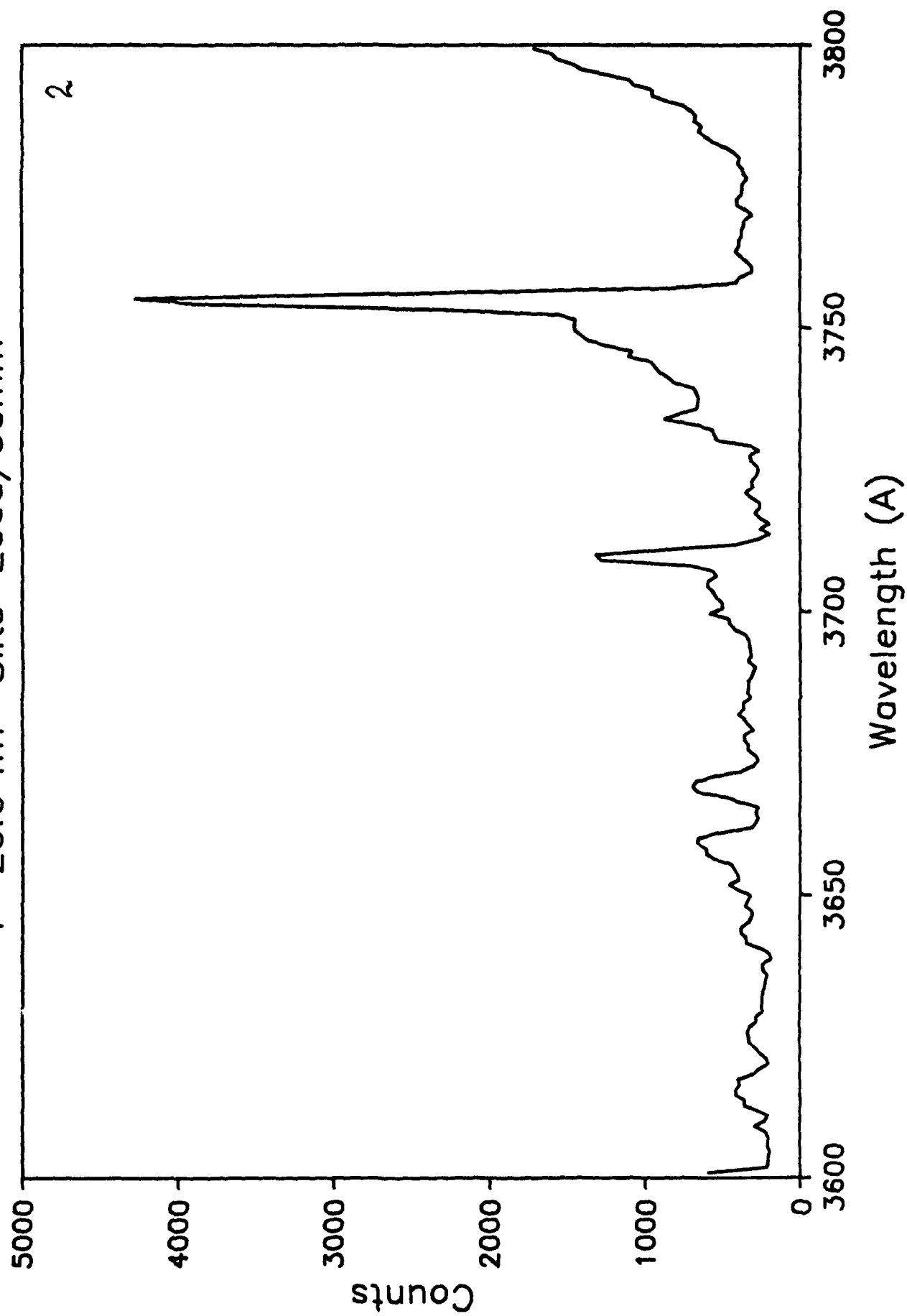
  
Stanley Bashkin  
Principal Investigator

H3+ at 0.5 MeV on N2  
P=20.0 mT Slits=200u/50mm

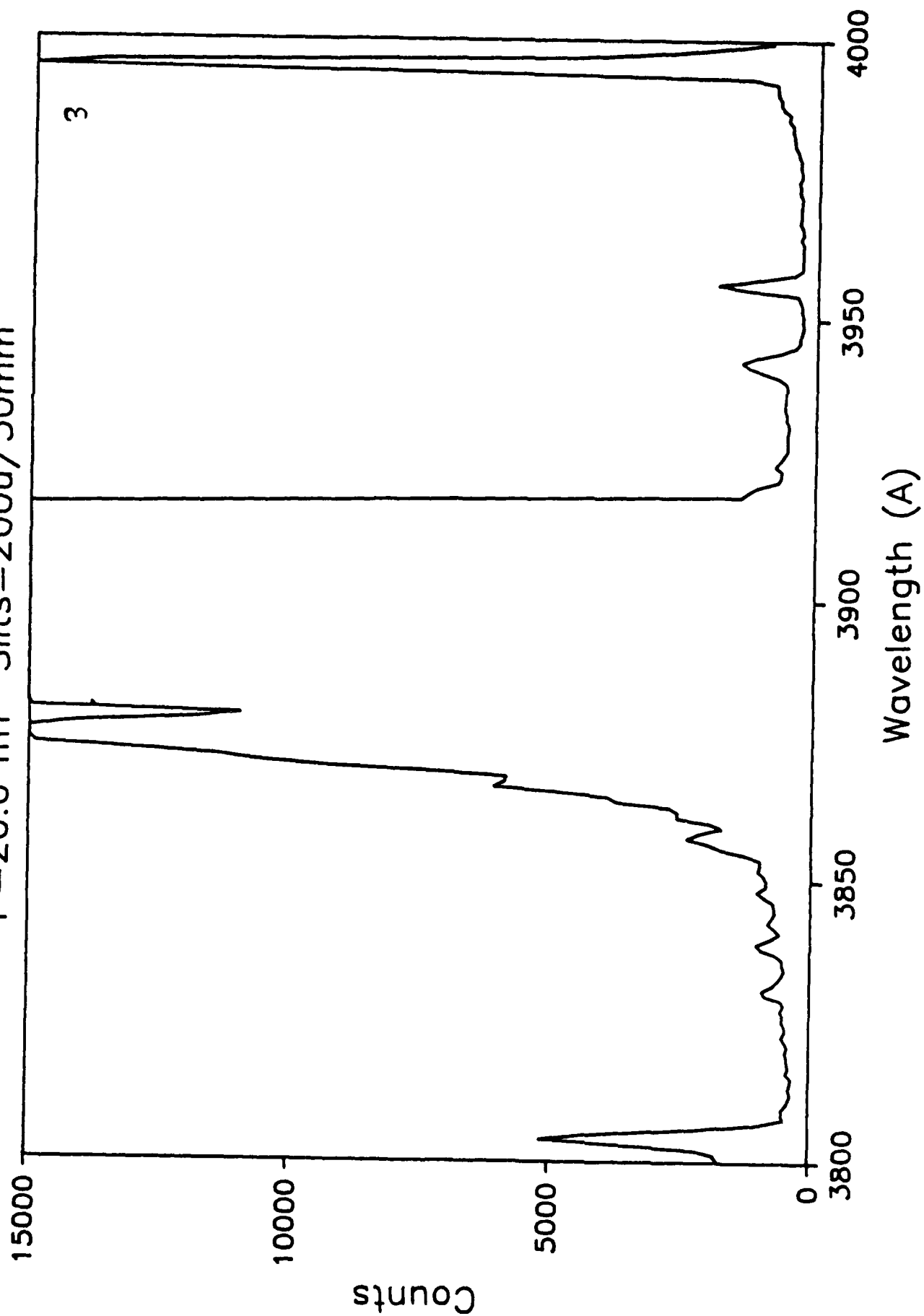


H3+ at 0.5 MeV on N2

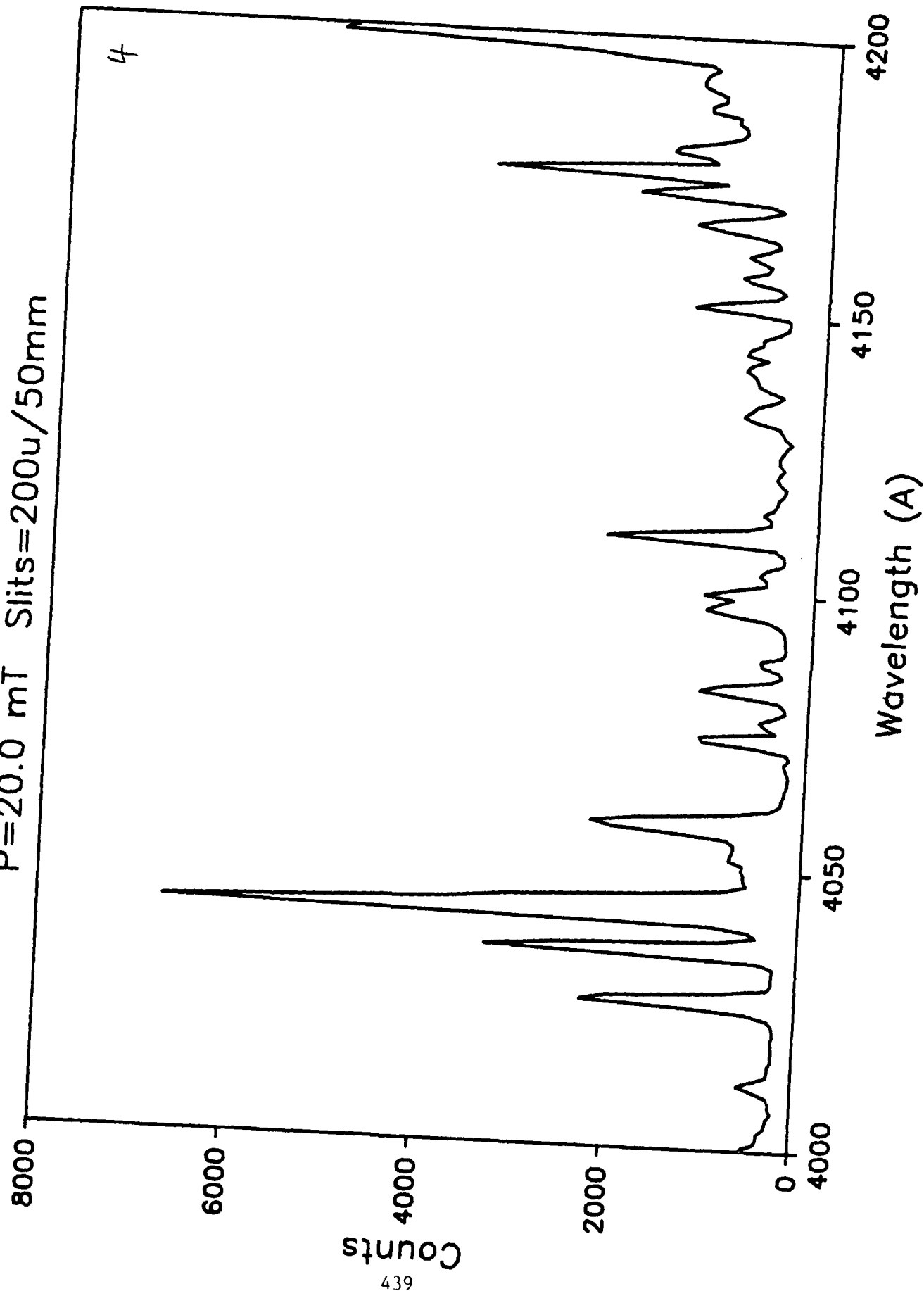
P=20.0 mT Slits=200u/50mm



H3+ at 0.5 MeV on N2  
P=20.0 mT Slits=200u/50mm

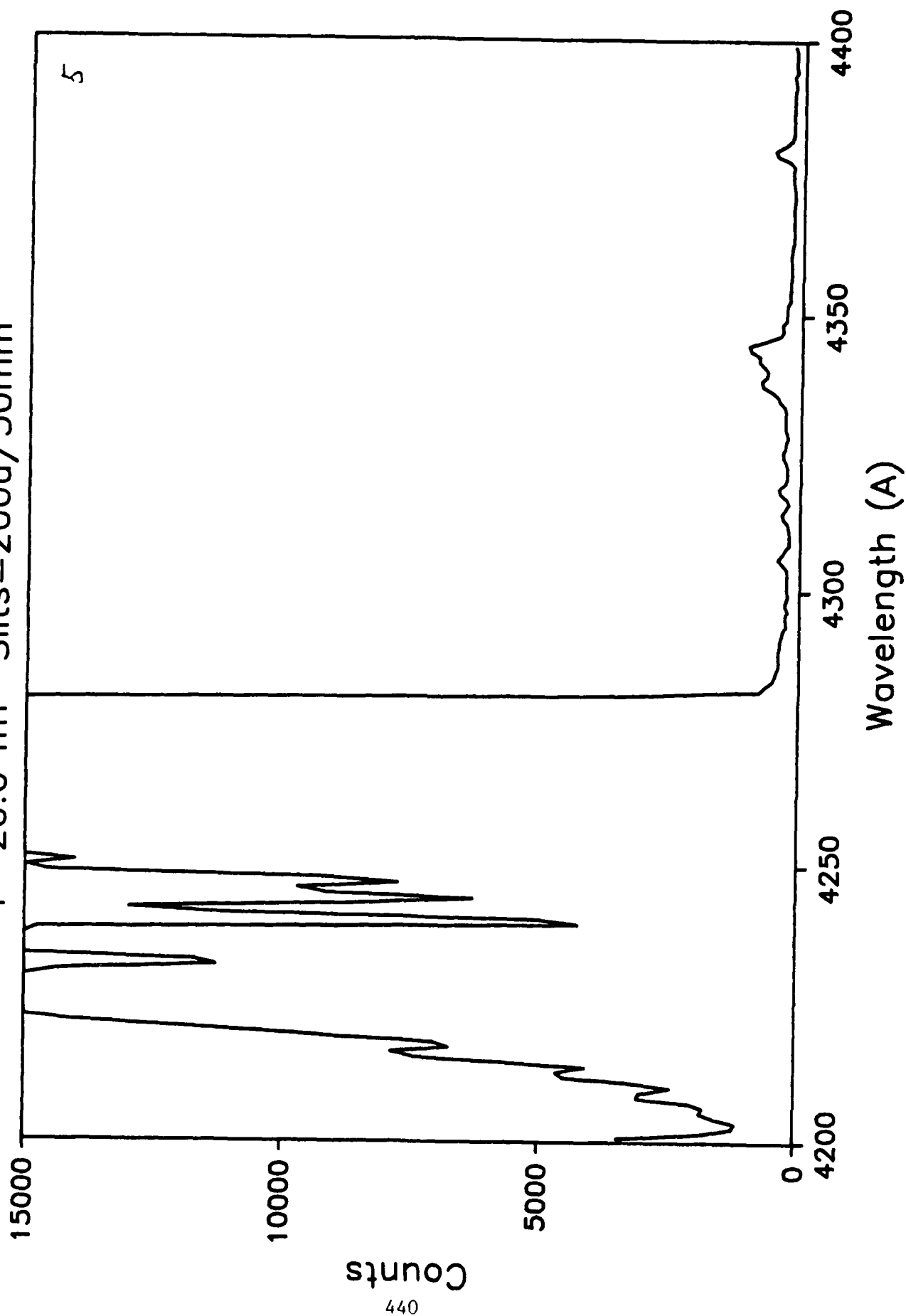


H3+ at 0.5 MeV on N2  
P=20.0 mT Slits=200u/50mm

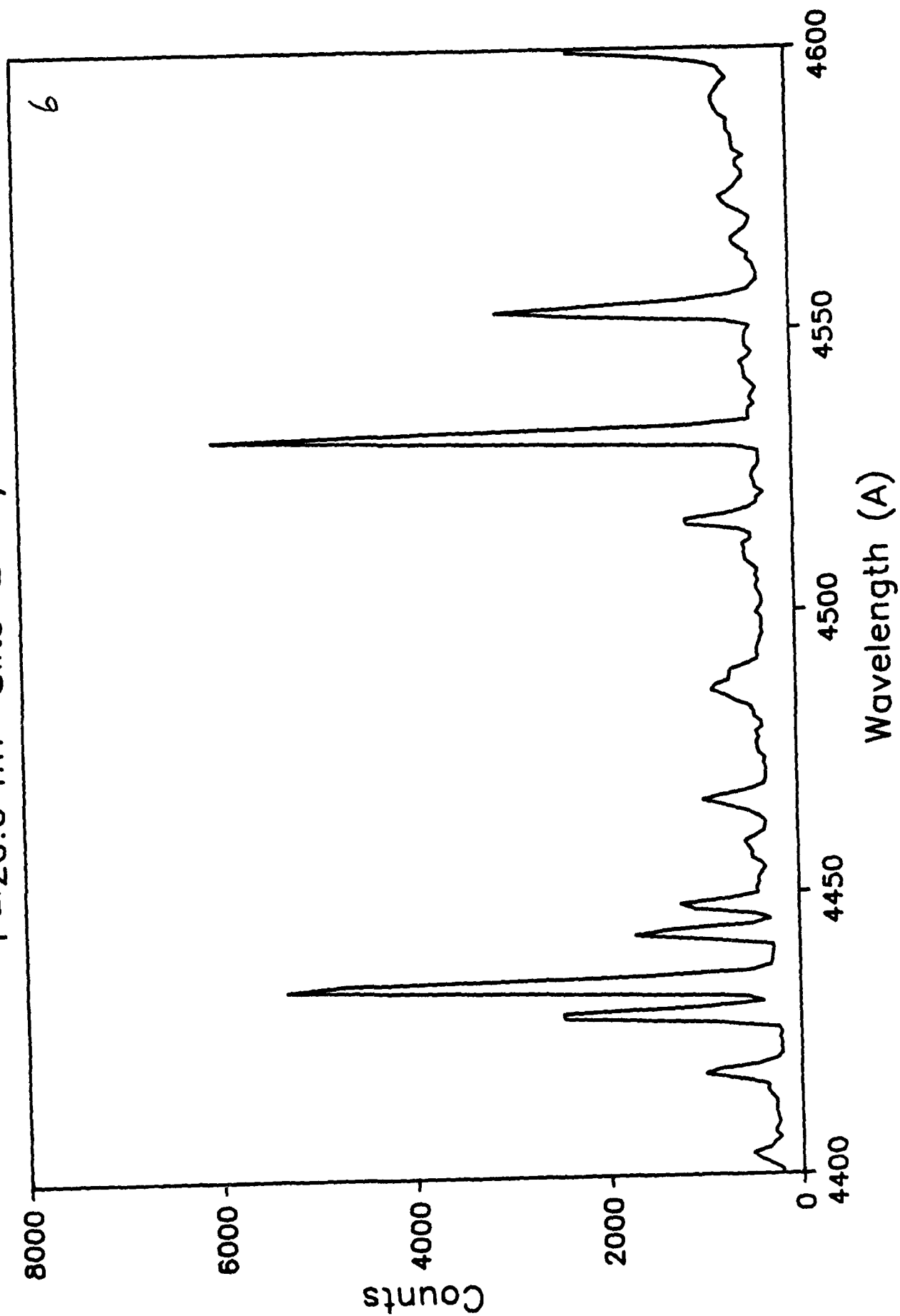




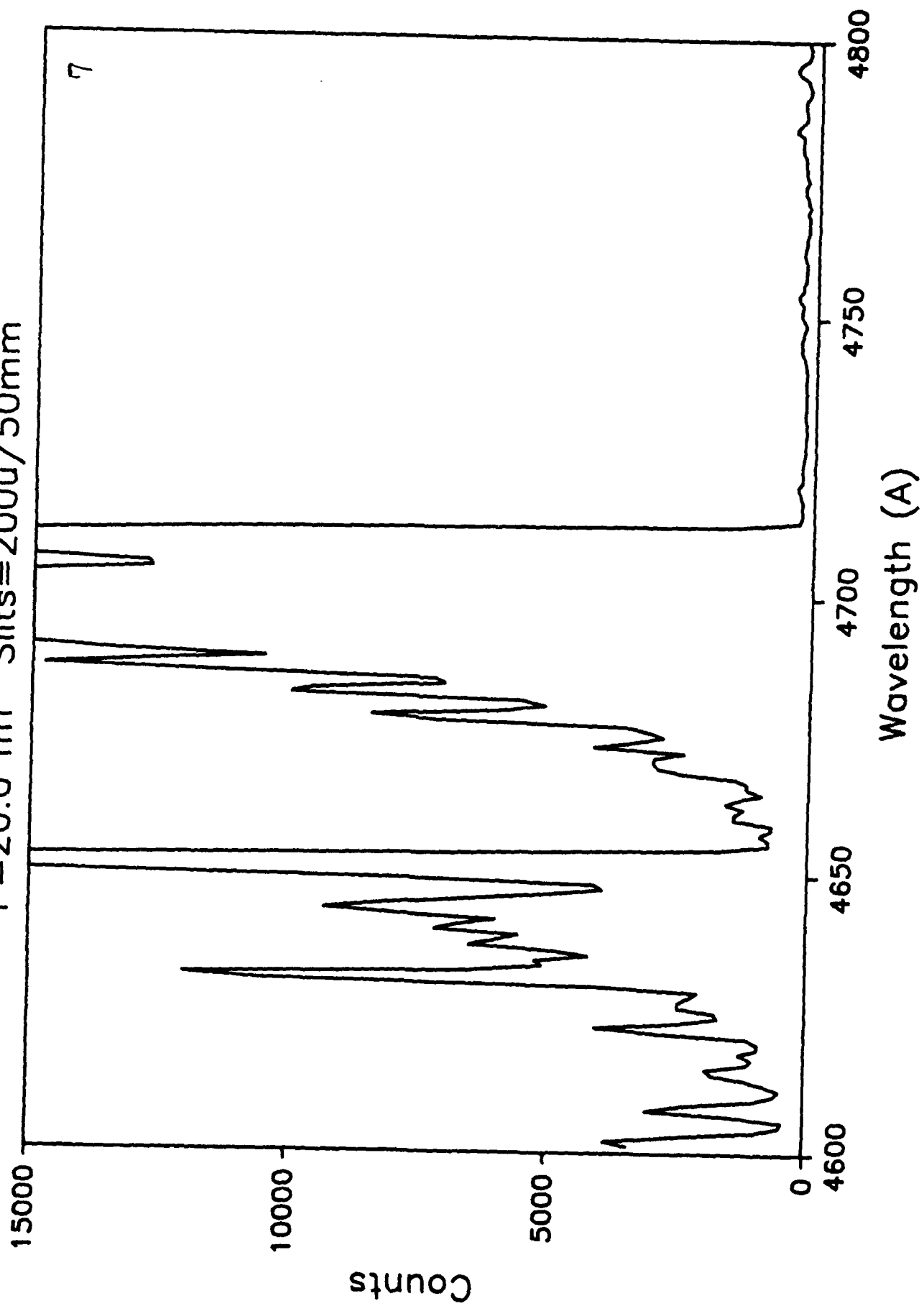
H3+ at 0.5 MeV on N2  
P=20.0 mT Slits=200u/50mm



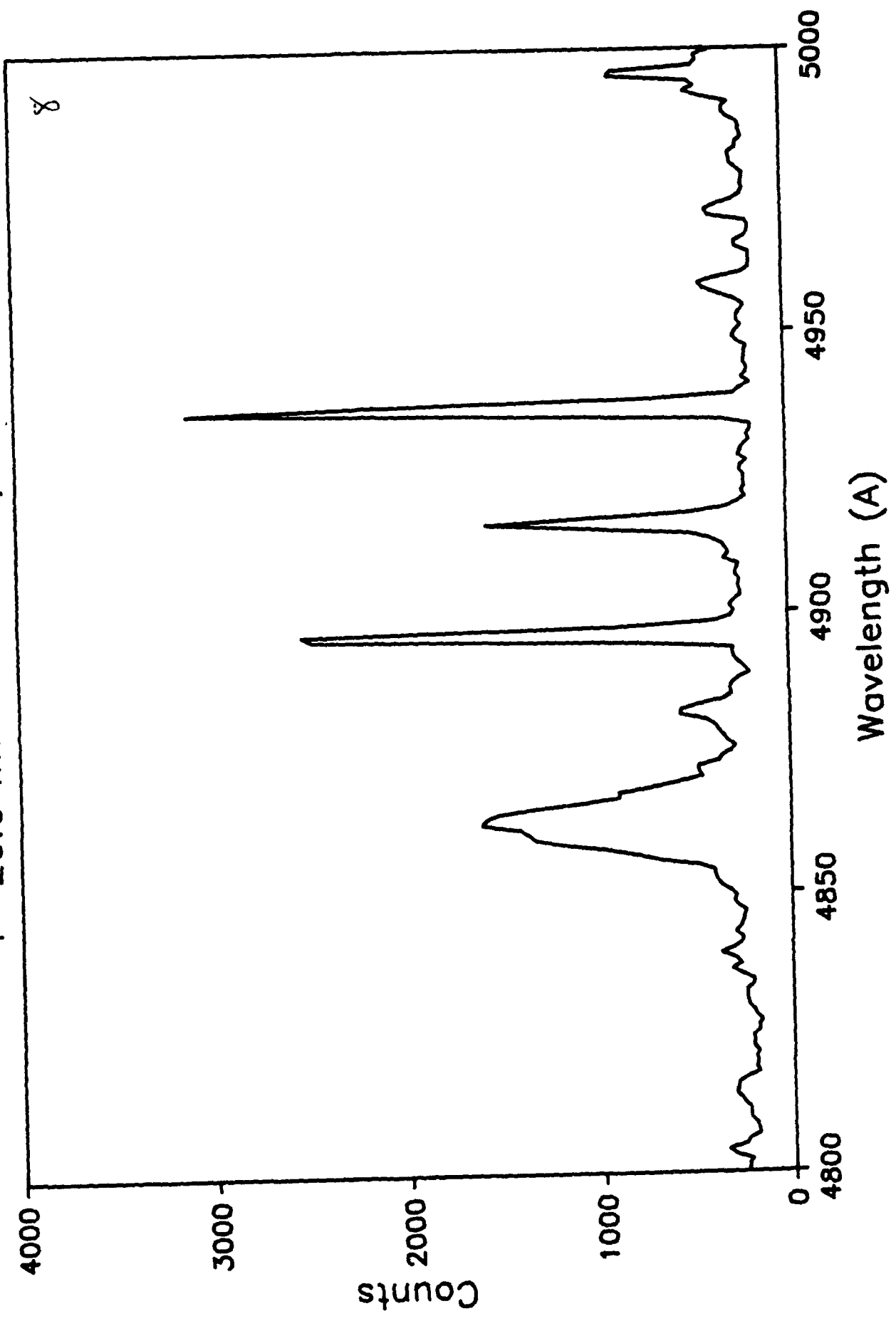
H3+ at 0.5 MeV on N2  
P=20.0 mT Slits=200u/50mm



H3+ at 0.5 MeV on N2  
P=20.0 mT Slits=200u/50mm

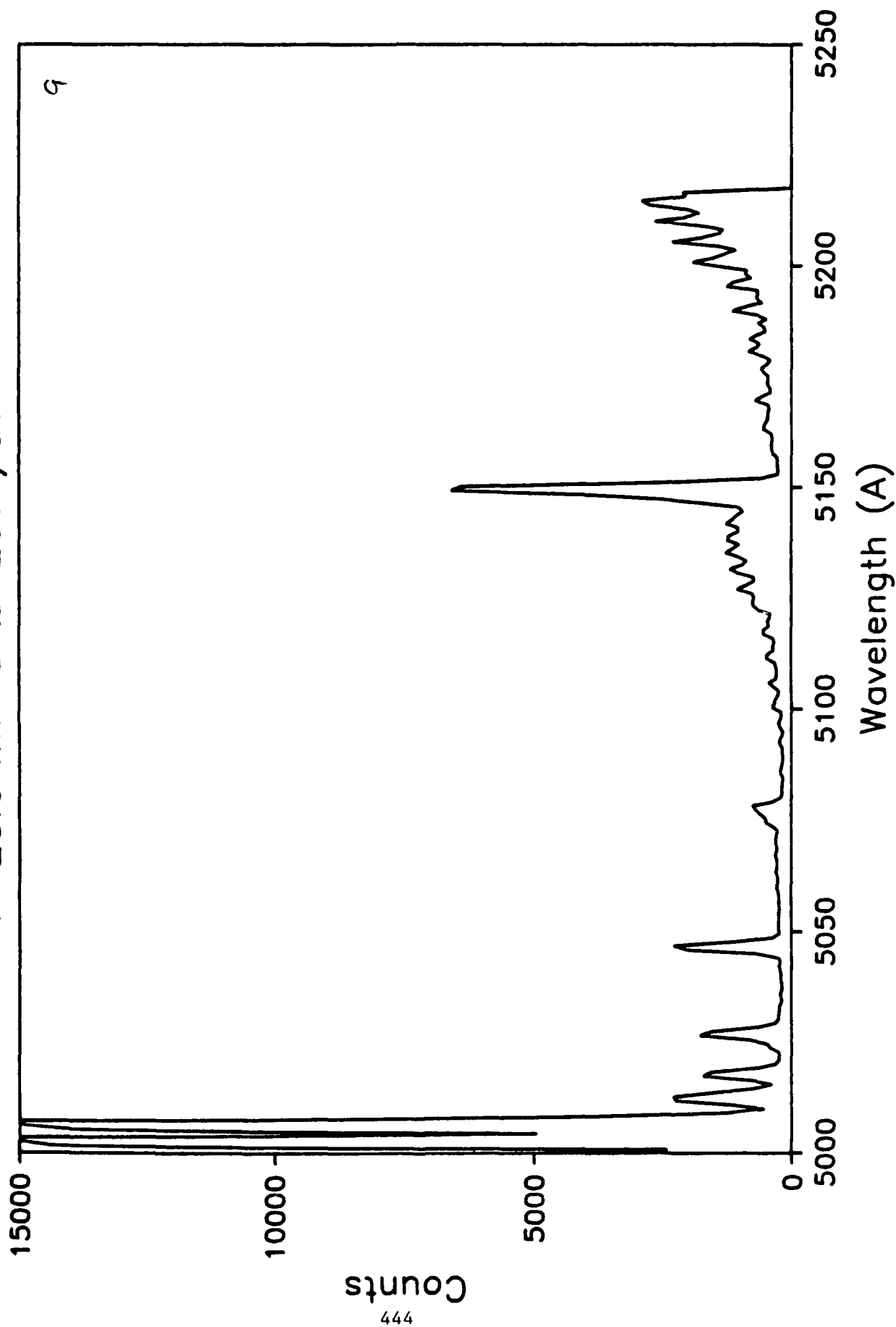


H3+ at 0.5 MeV on N2  
P=20.0 mT Slits=200u/50mm

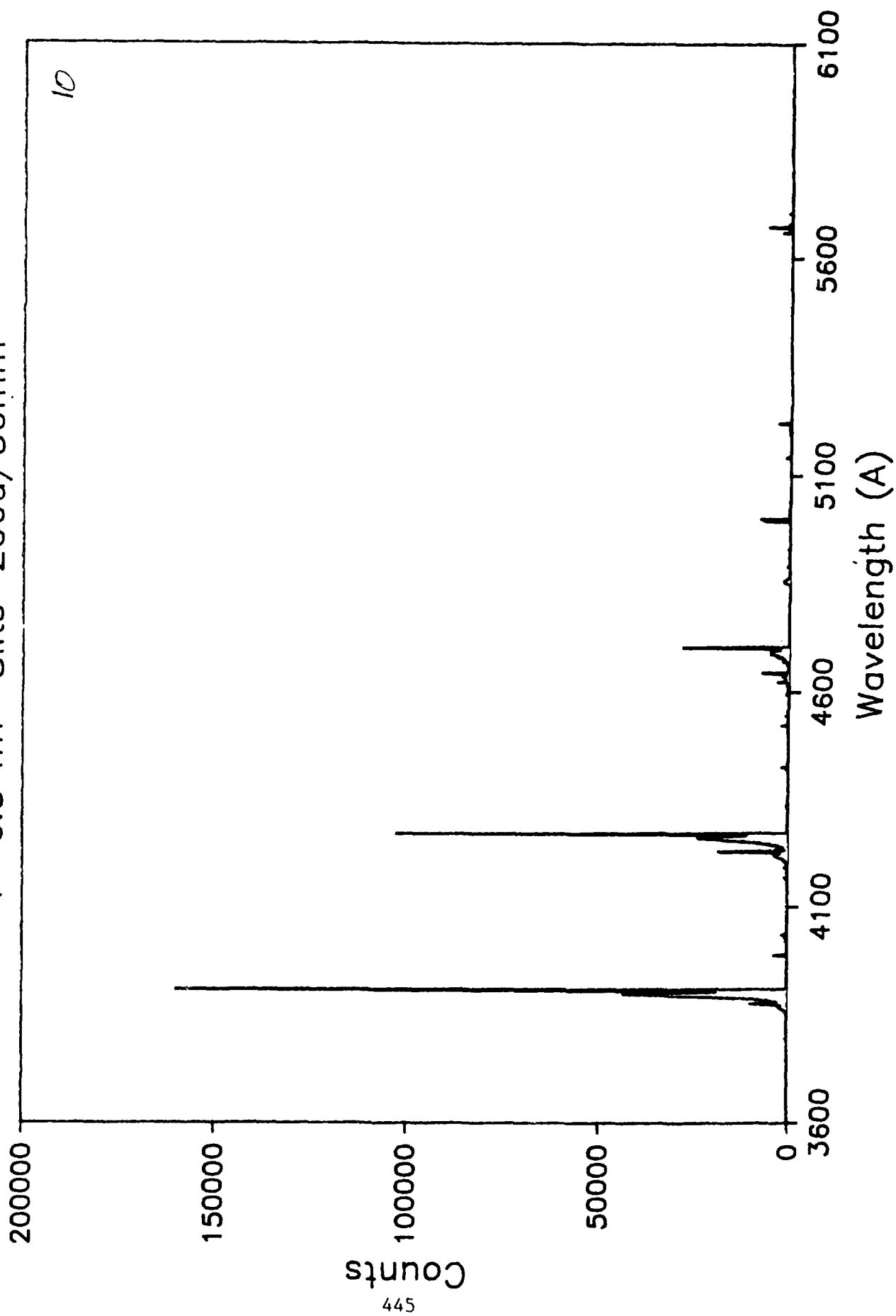


H3+ at 0.5 MeV on N2

P=20.0 mT Slits=200u/50mm

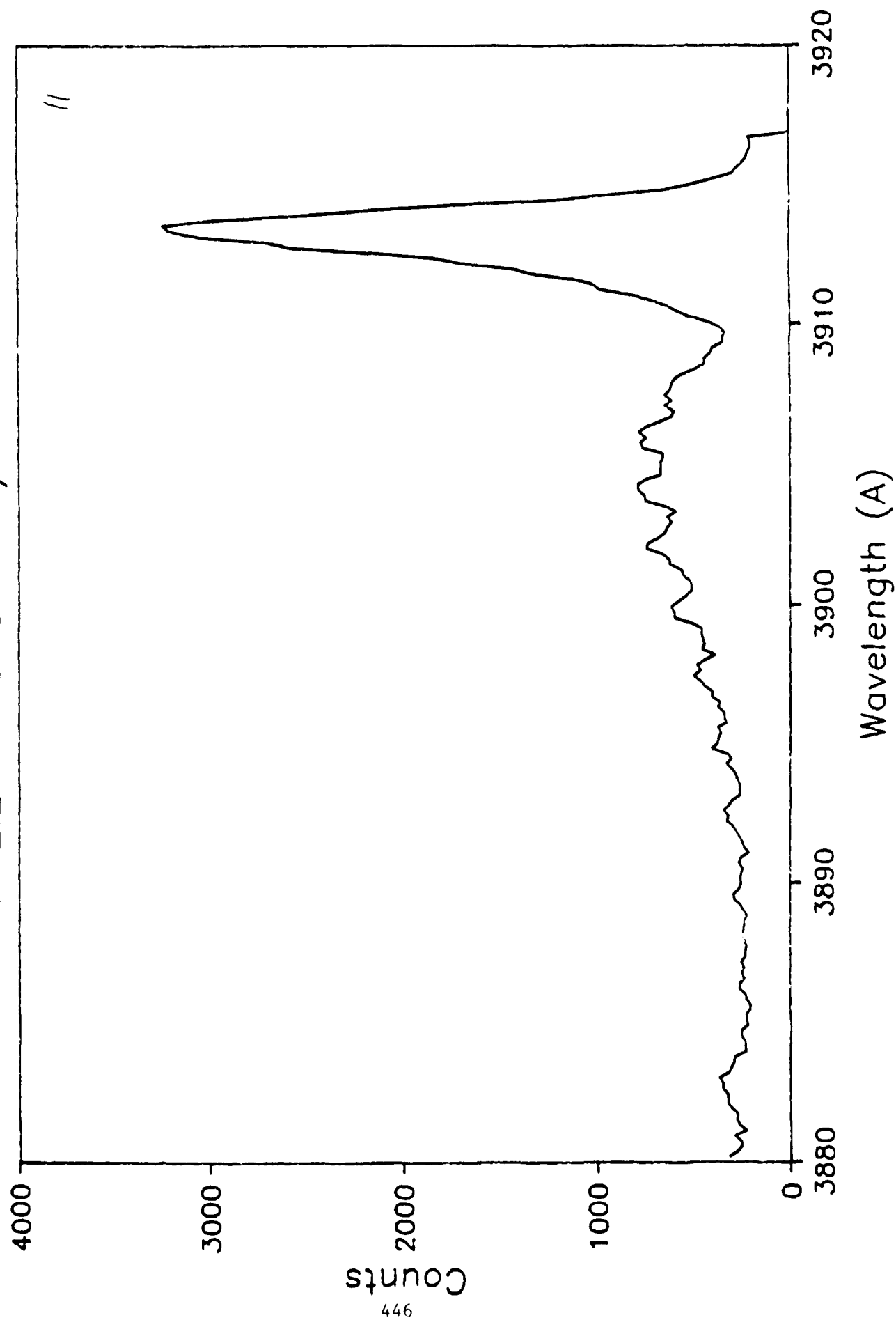


H3+ at 0.5 MeV on N2  
P=6.5 mT Slits=200u/50mm

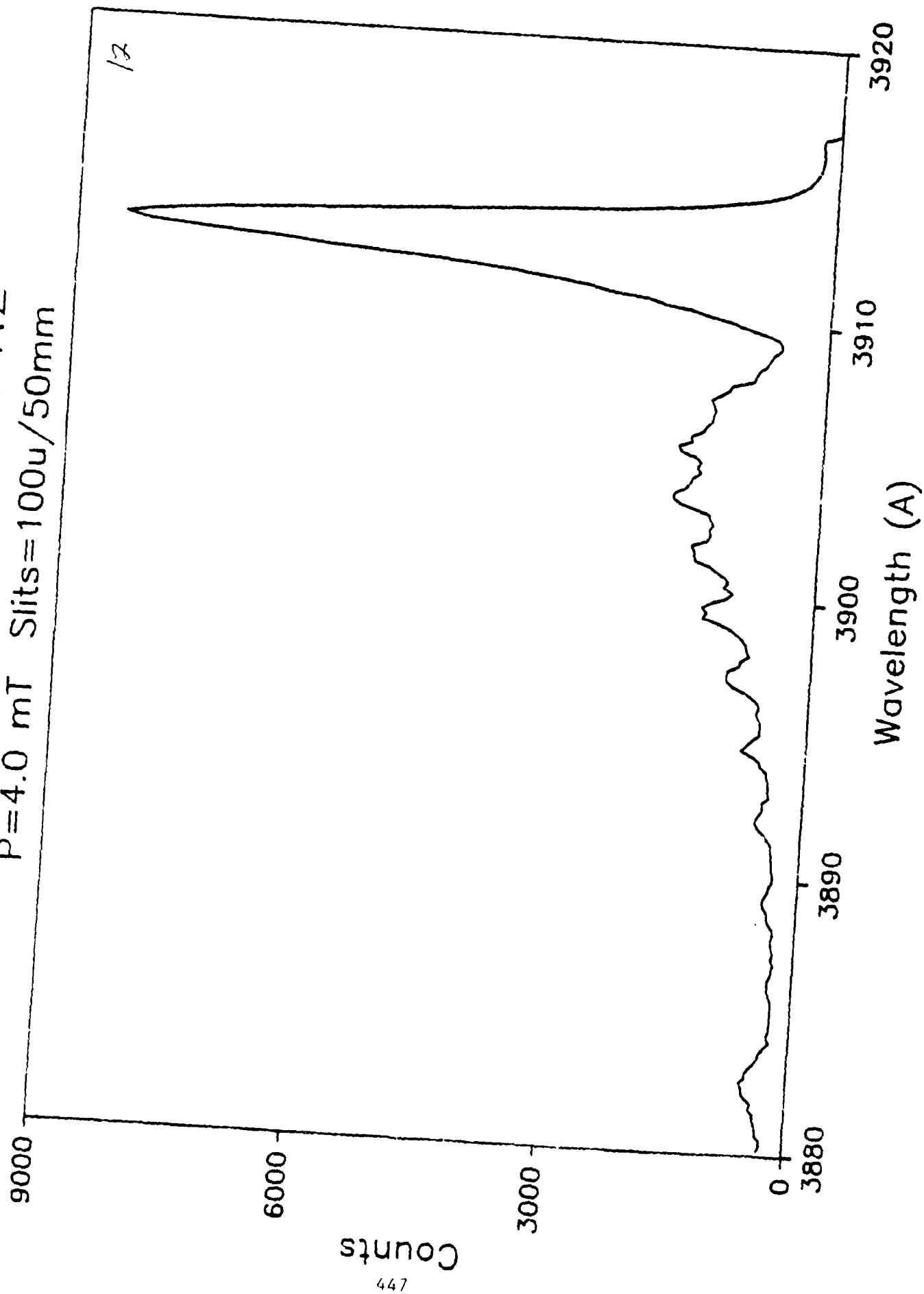


H+ at 0.5 MeV on N2

P=2.2 mT Slits=100u/50mm

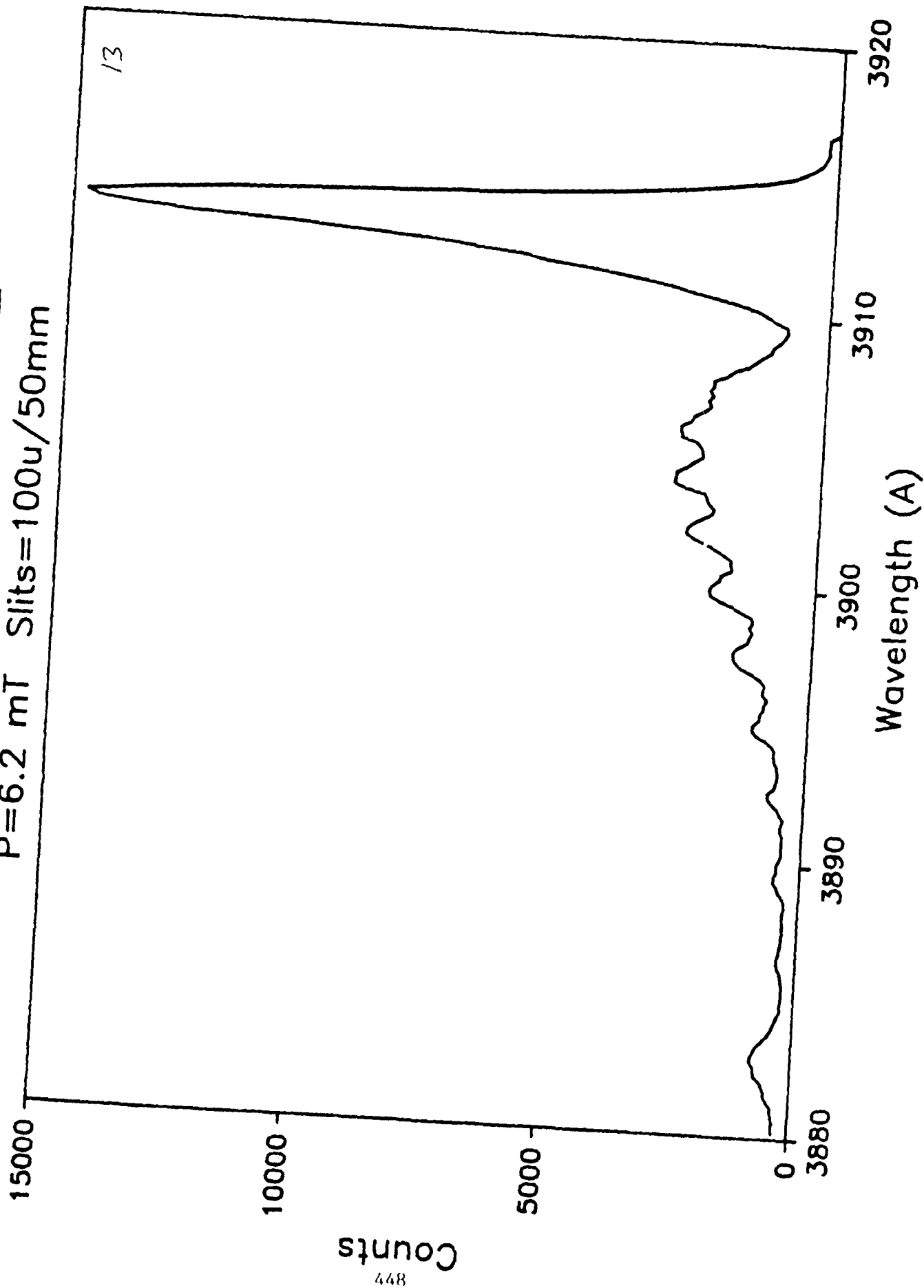


H+ at 0.5 MeV on N2  
P=4.0 mT Slits=100u/50mm

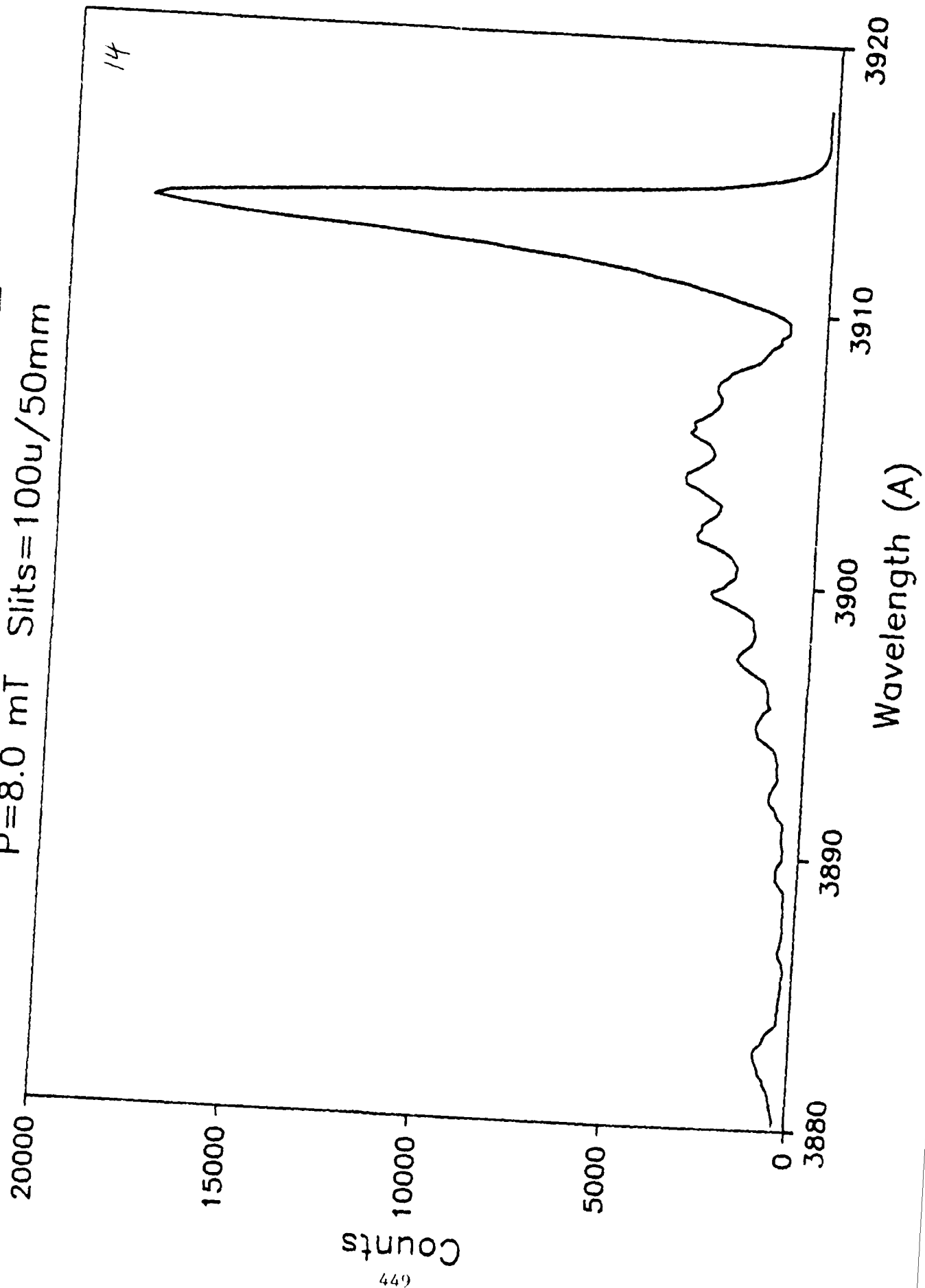




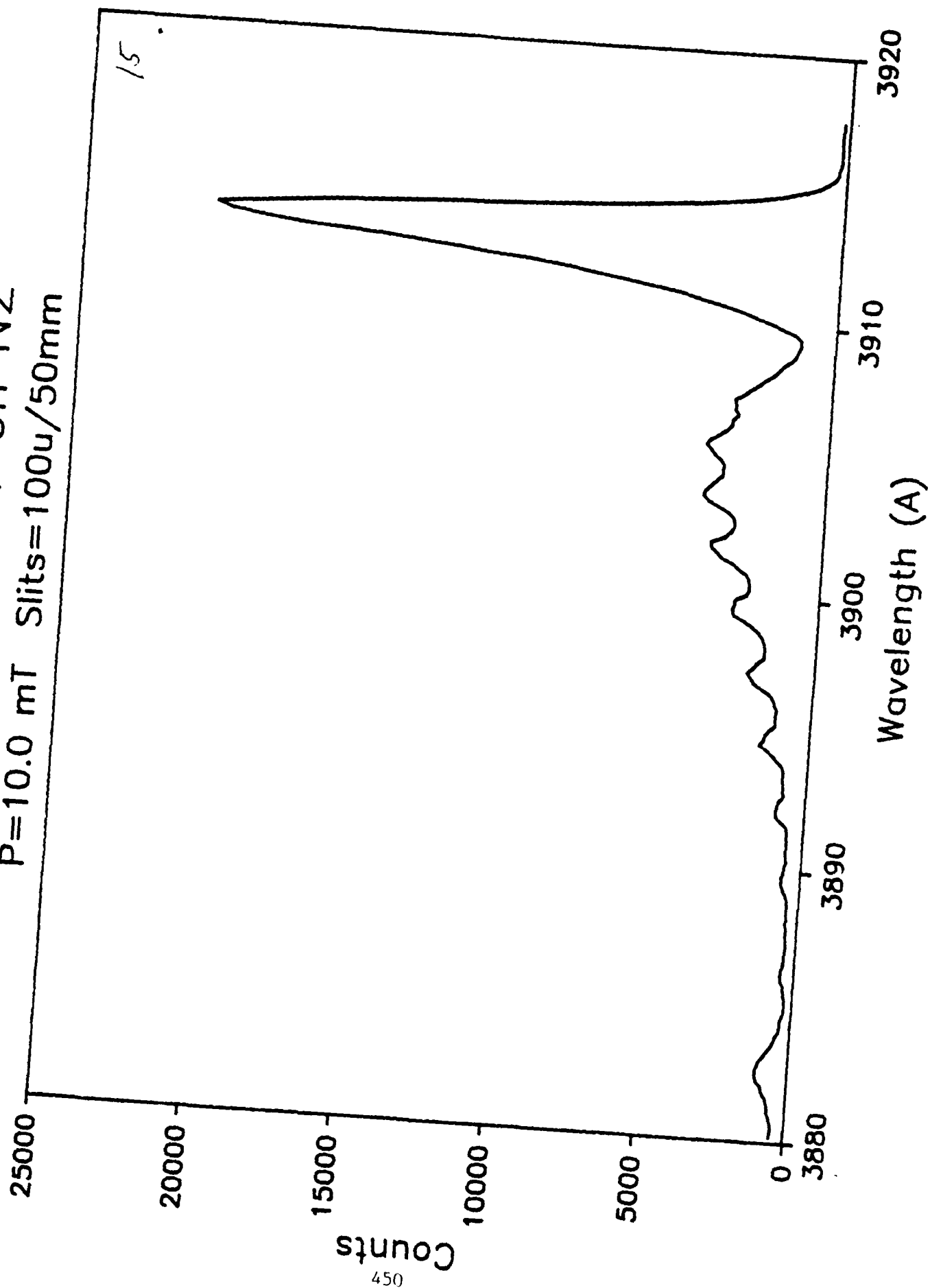
H+ at 0.5 MeV on N2  
P=6.2 mT Slits=100u/50mm



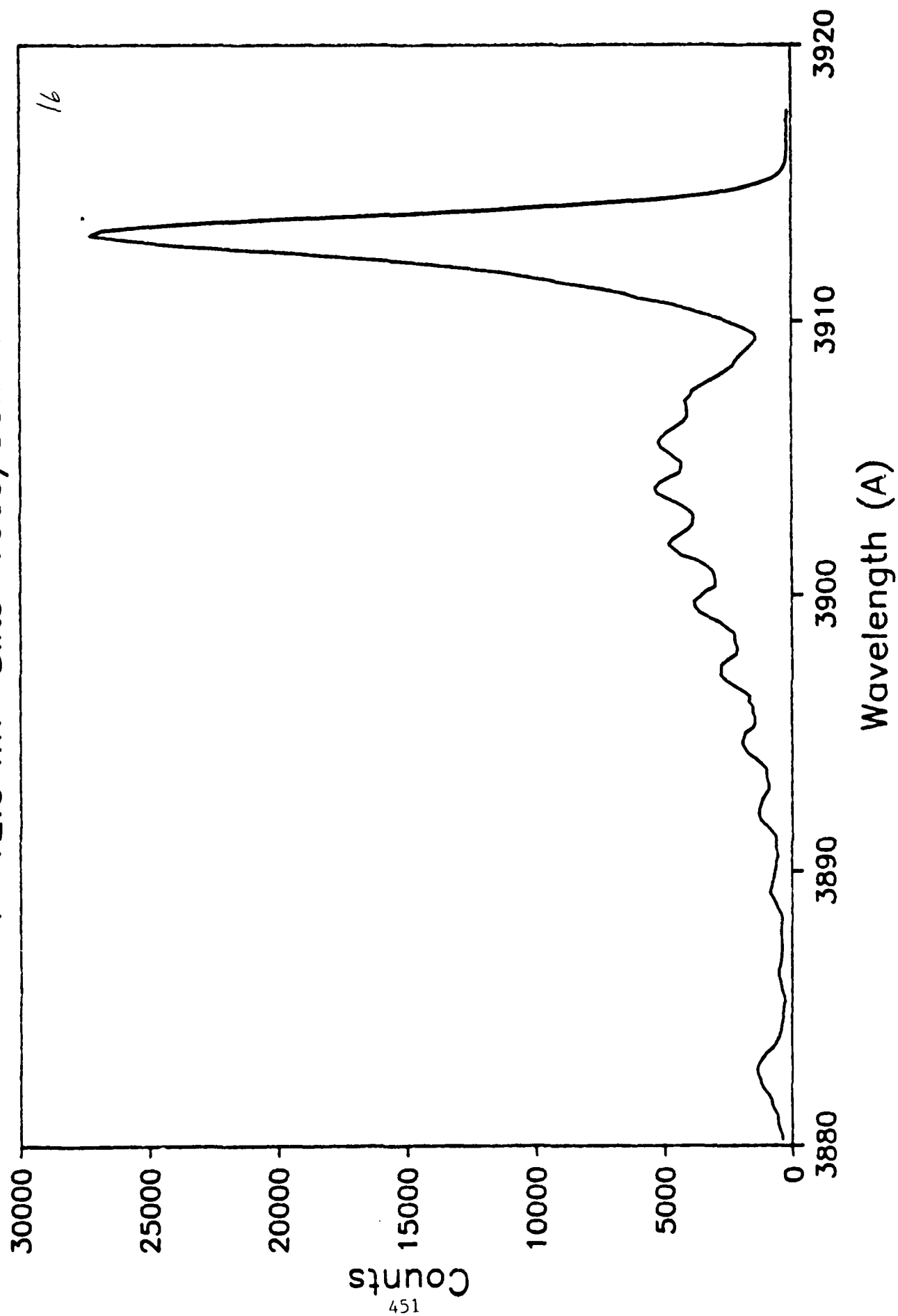
H+ at 0.5 MeV on N2  
P=8.0 mT Slits=100u/50mm



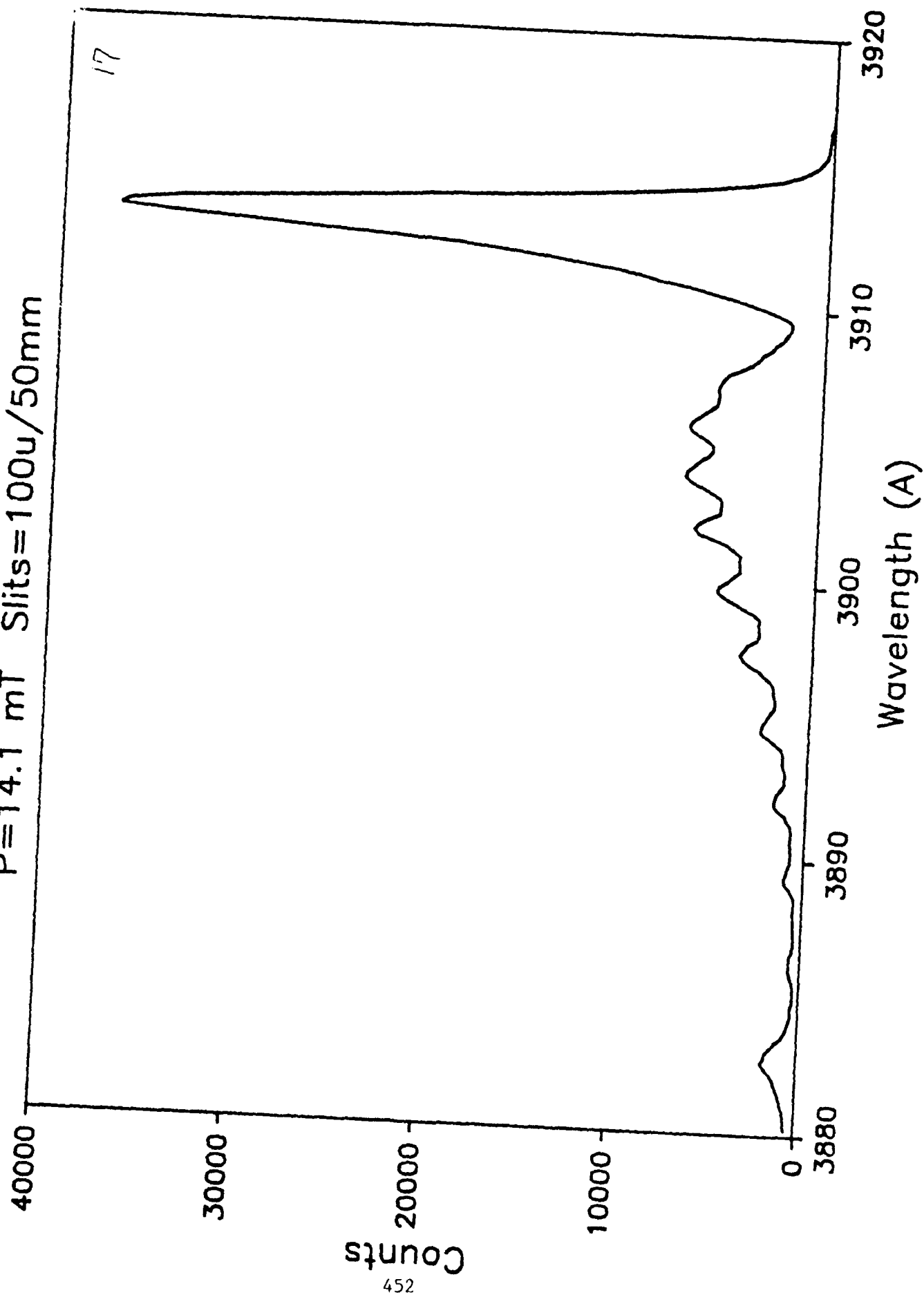
H<sup>+</sup> at 0.5 MeV on N<sub>2</sub>  
P=10.0 mT Slits=100 $\mu$ /50mm



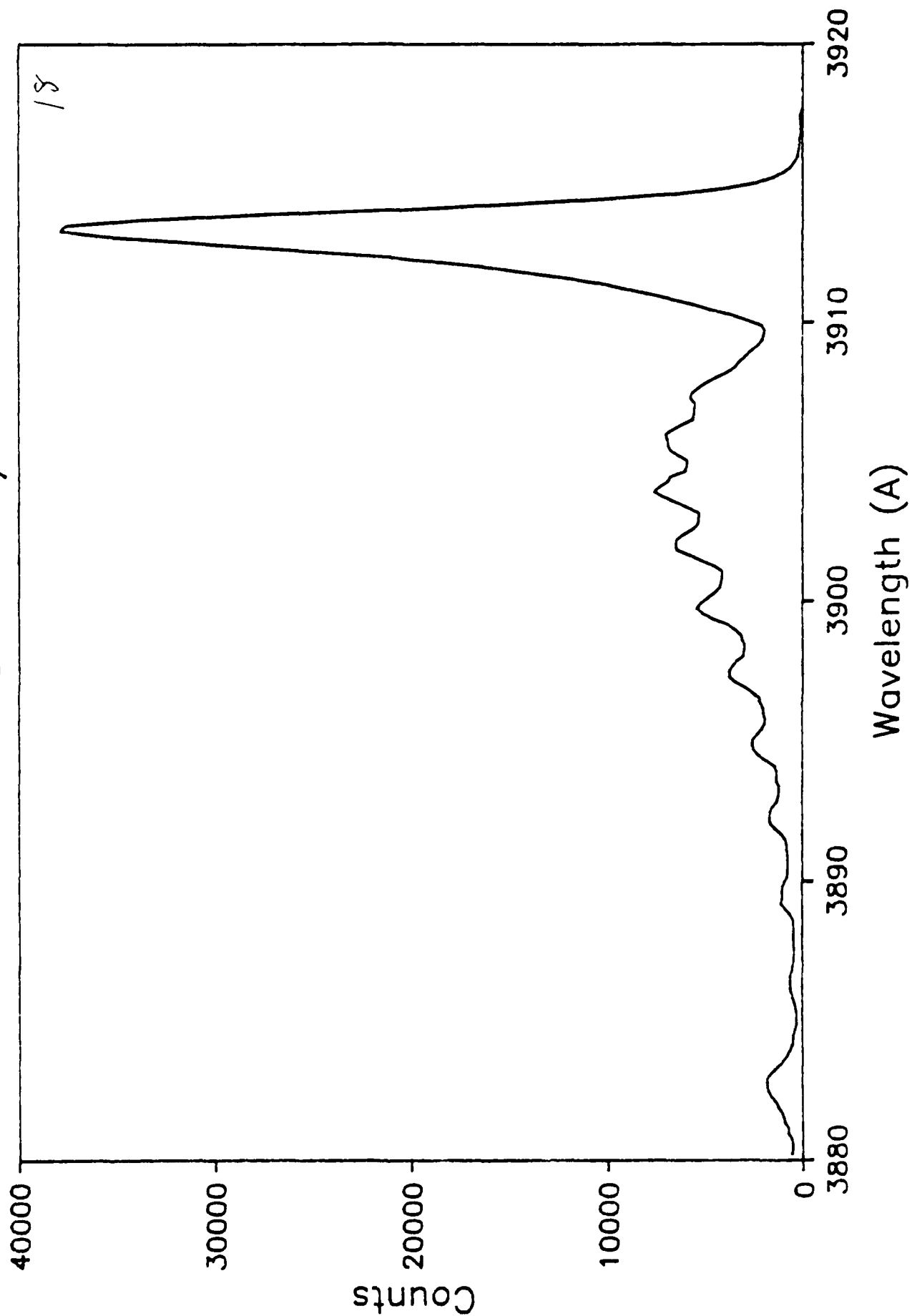
H+ at 0.5 MeV on N2  
P=12.0 mT Slits=100u/50mm



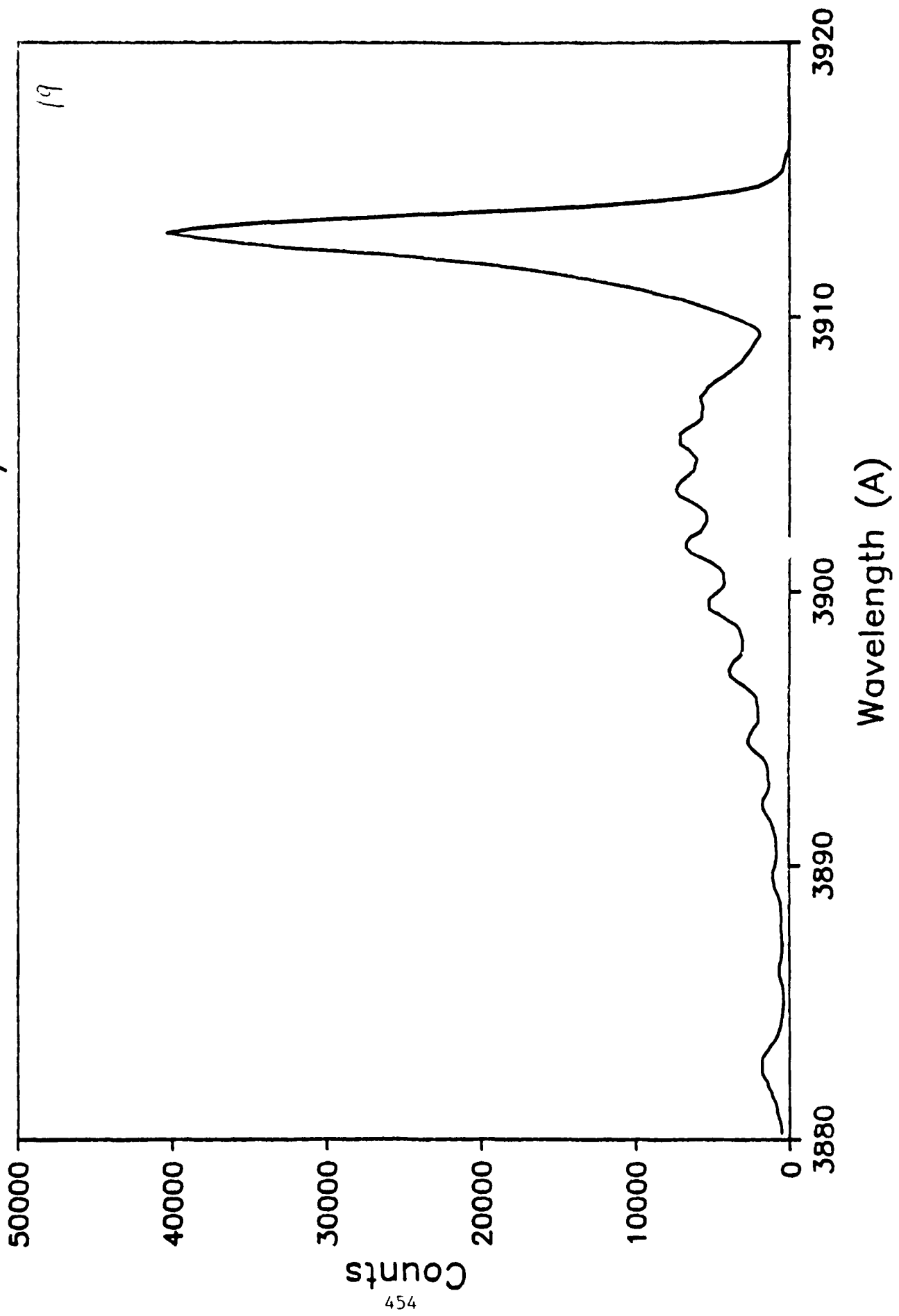
H+ at 0.5 MeV on N2  
P=14.1 mT Slits=100u/50mm



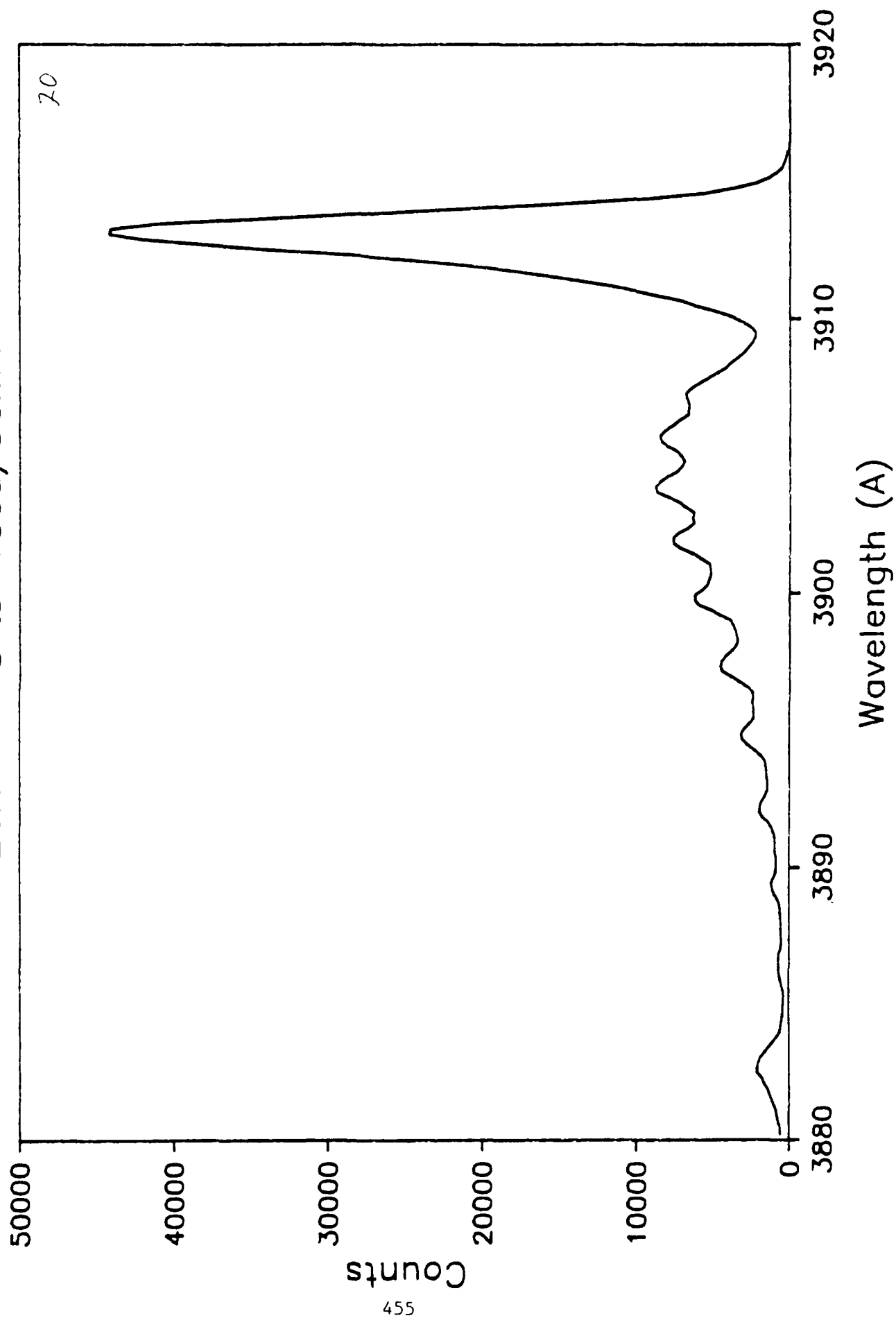
H+ at 0.5 MeV on N2  
P=16.0 mT Slits=100u/50mm



H+ at 0.5 MeV on N2  
P=18.0 mT Slits=100u/50mm

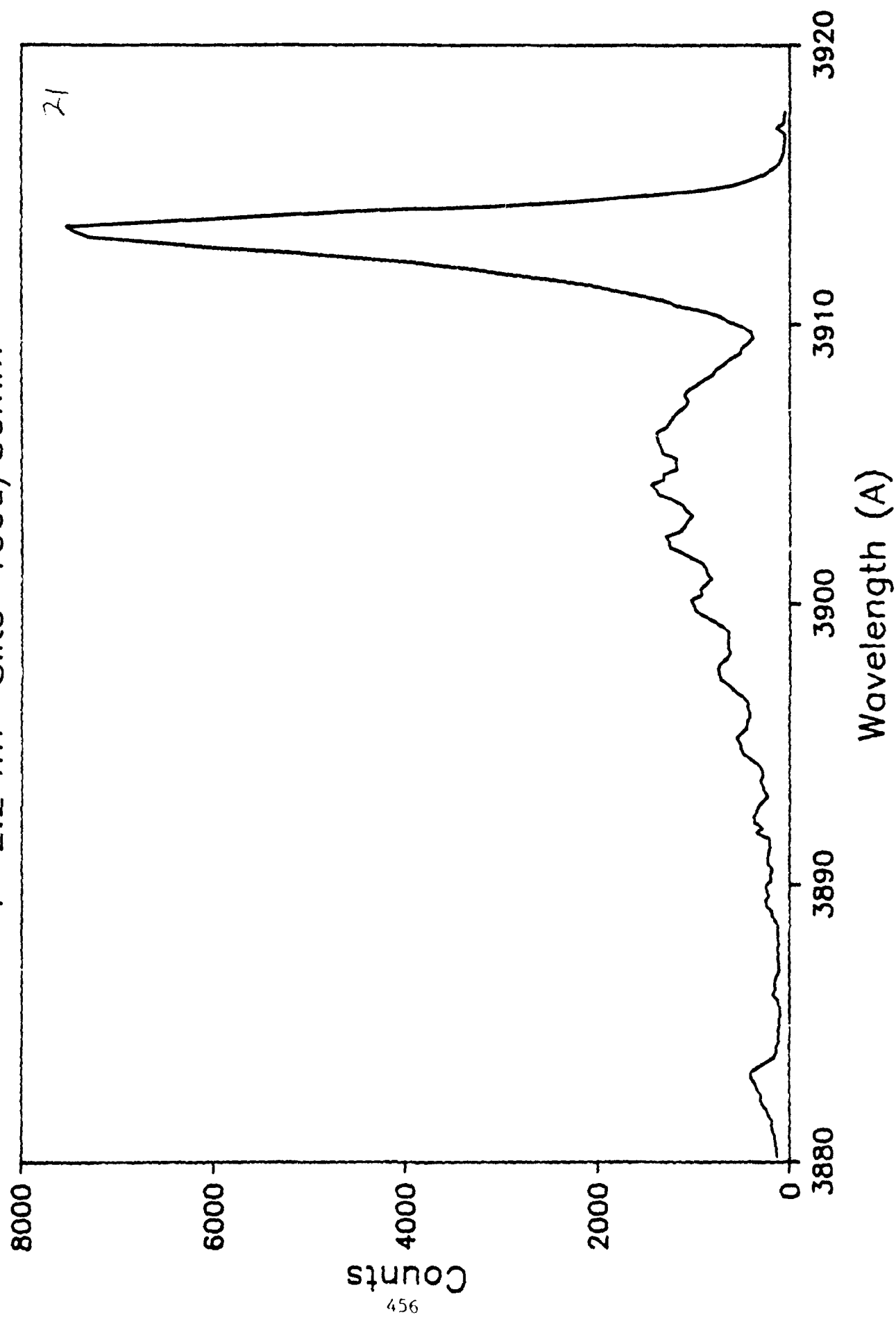


H+ at 0.5 MeV on N2  
P=20.0 mT Slits=100u/50mm

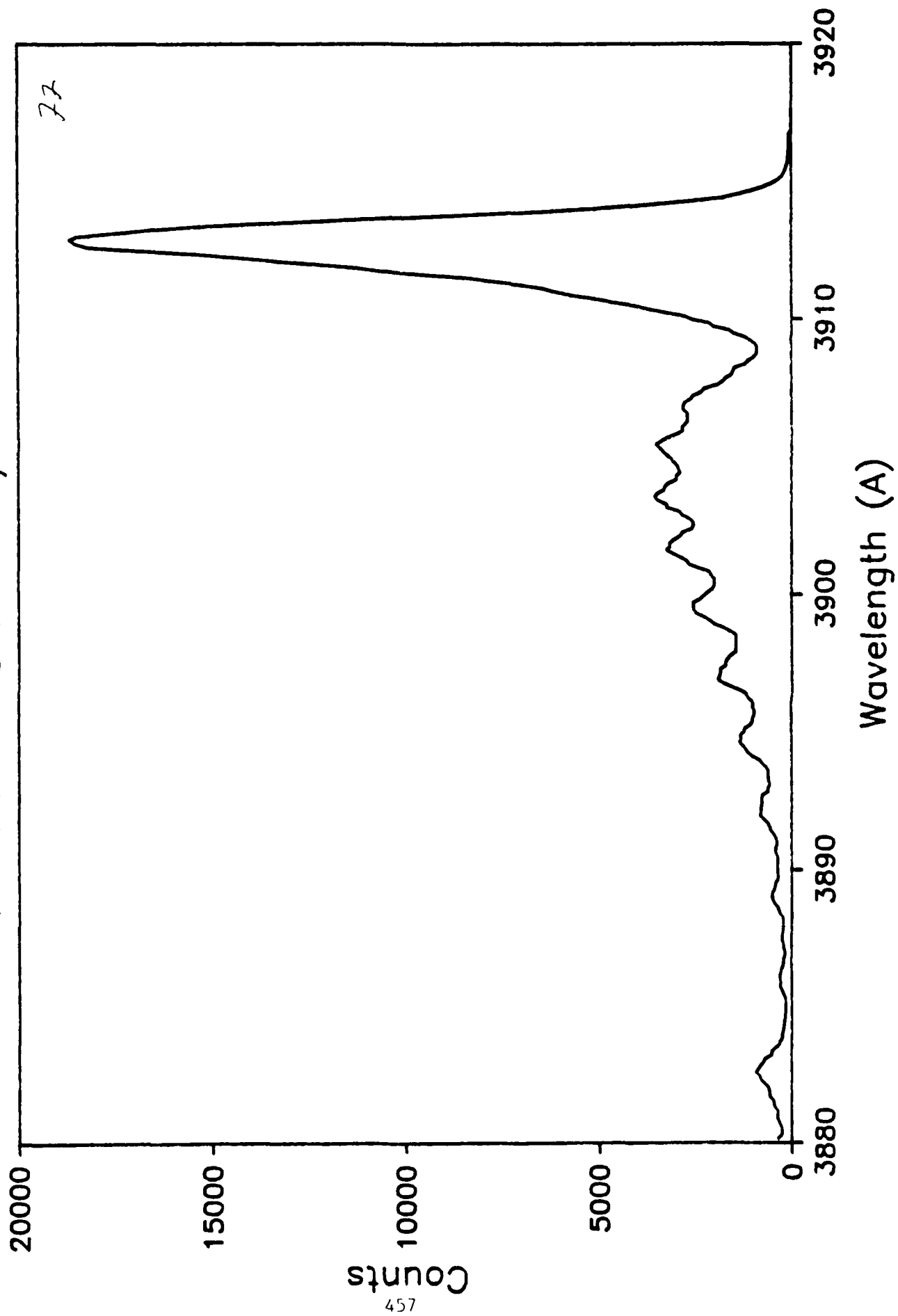




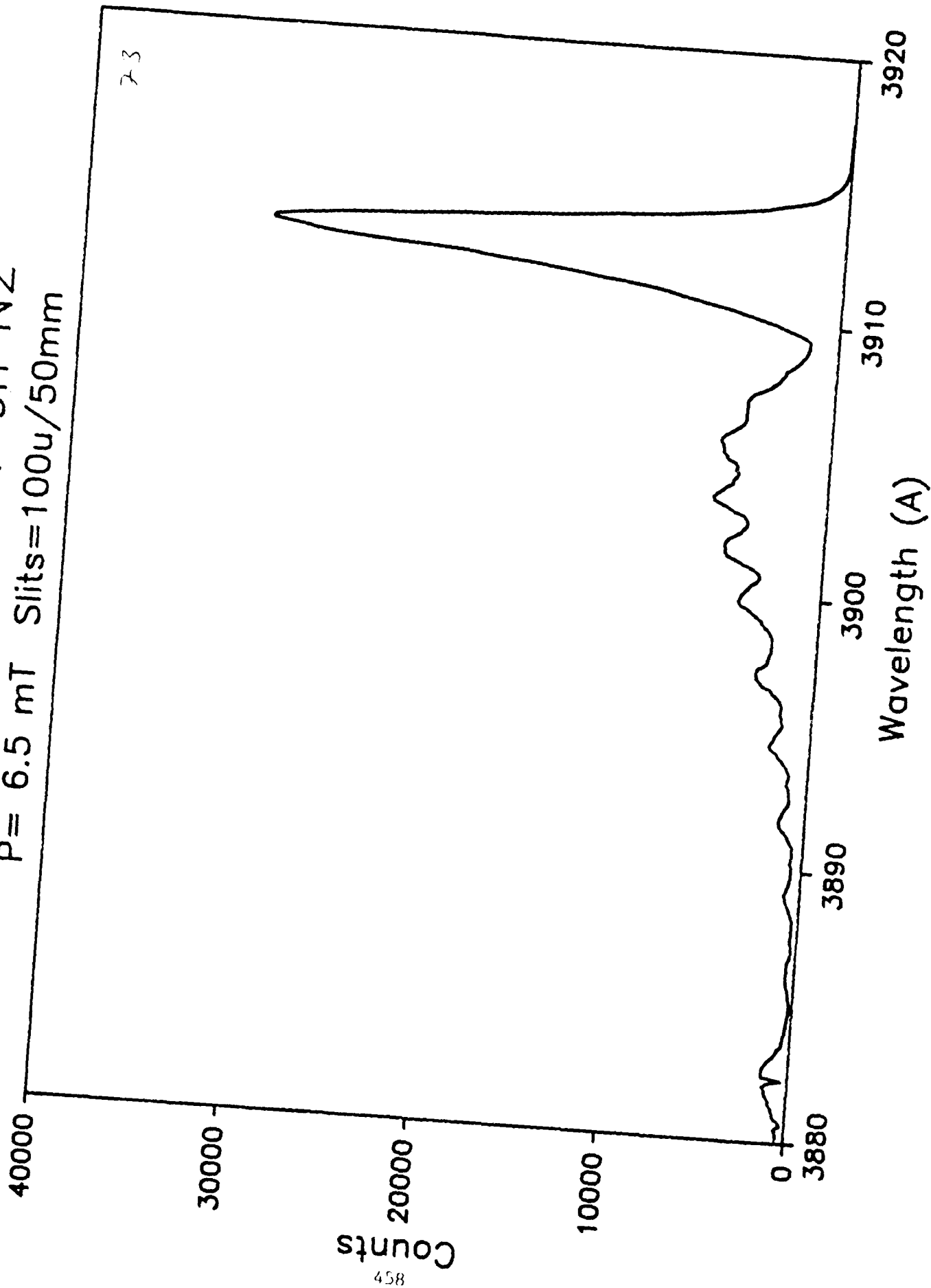
H2+ at 1.0 MeV on N2  
P=2.2 mT Slits=100u/50mm



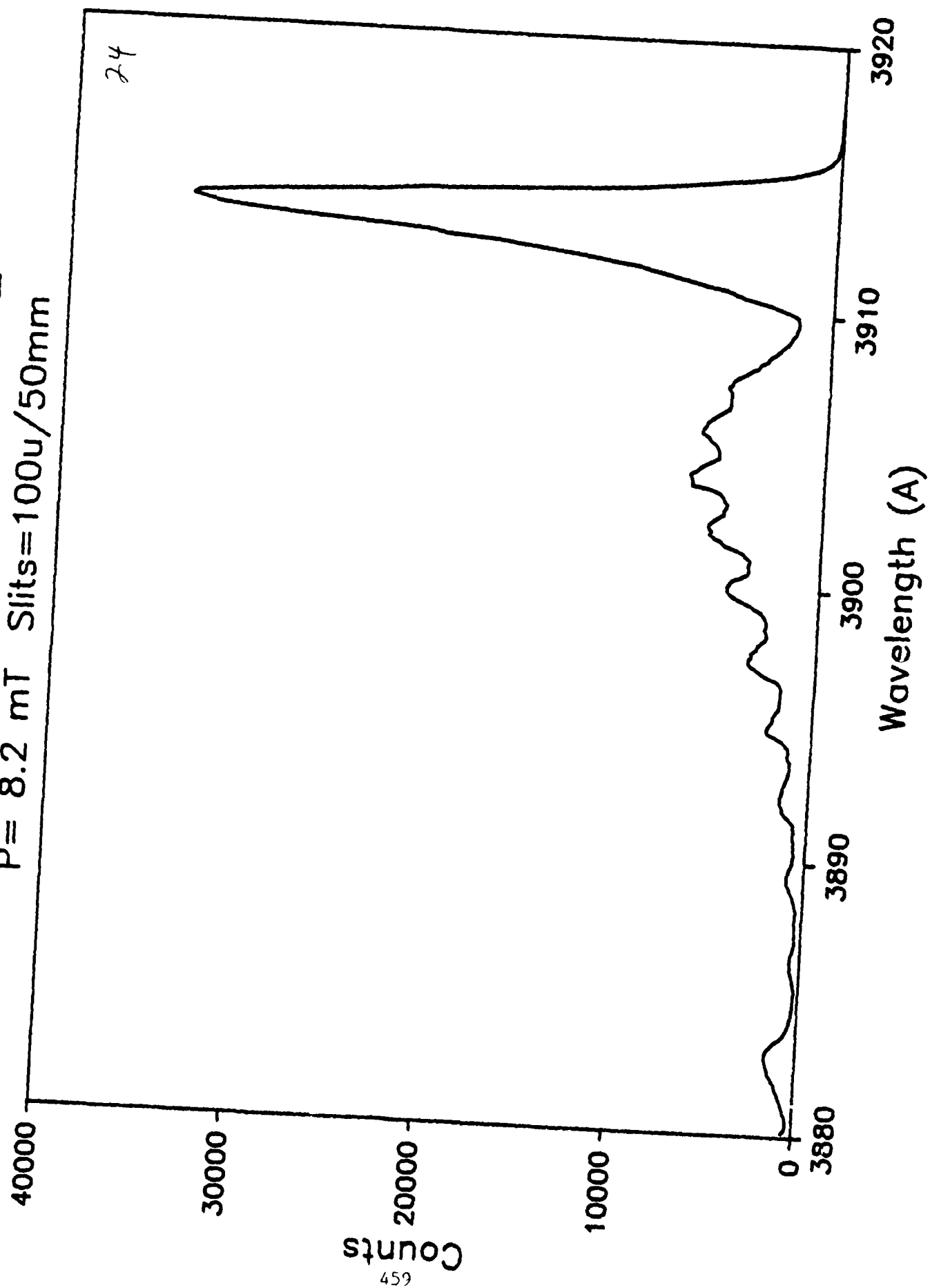
H2+ at 1.0 MeV on N2  
P= 4.1 mT Slits=100u/50mm



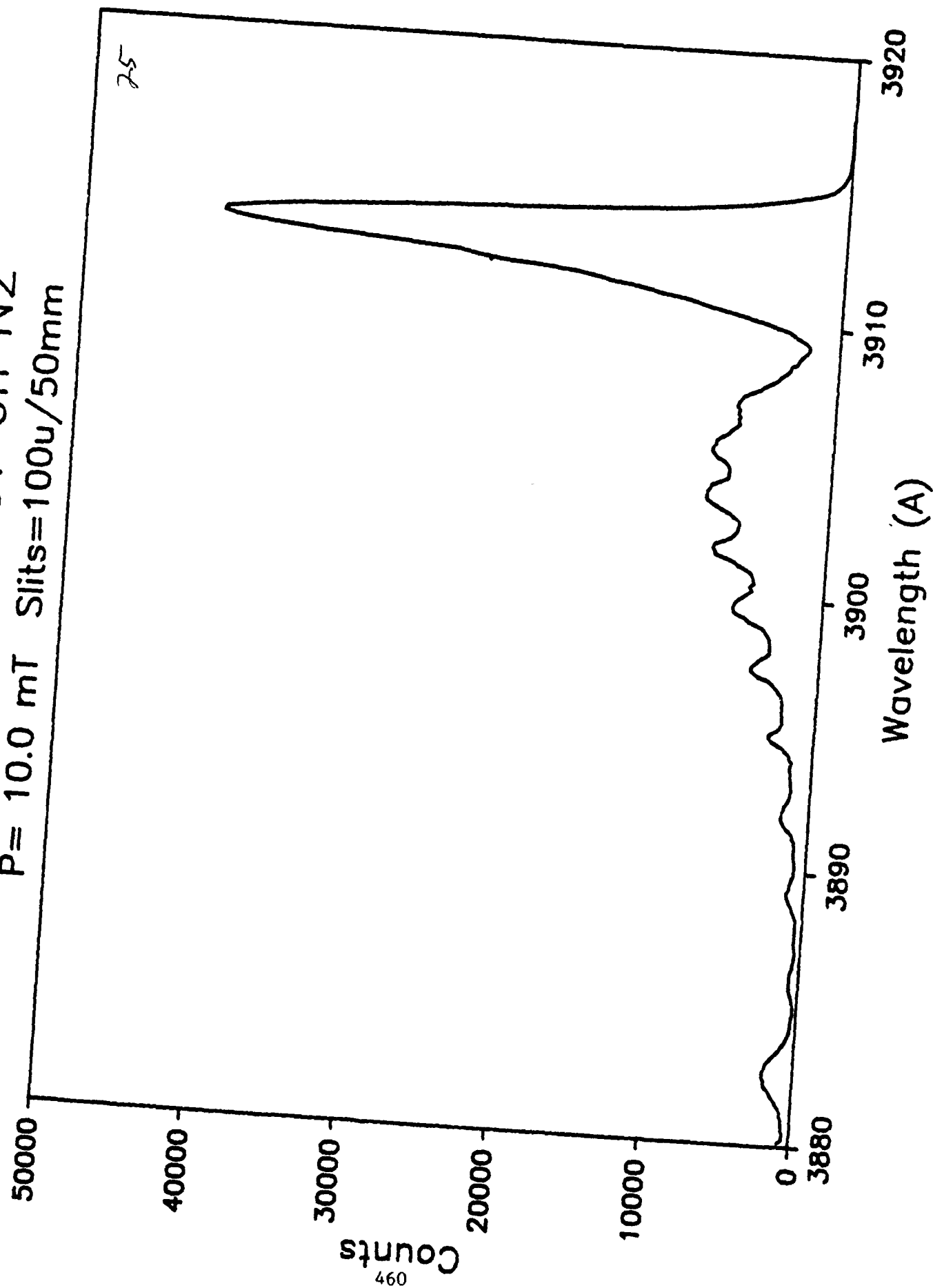
H2+ at 1.0 MeV on N2  
P= 6.5 mT Slits=100u/50mm



H2+ at 1.0 MeV on N2  
P= 8.2 mT Slits=100u/50mm

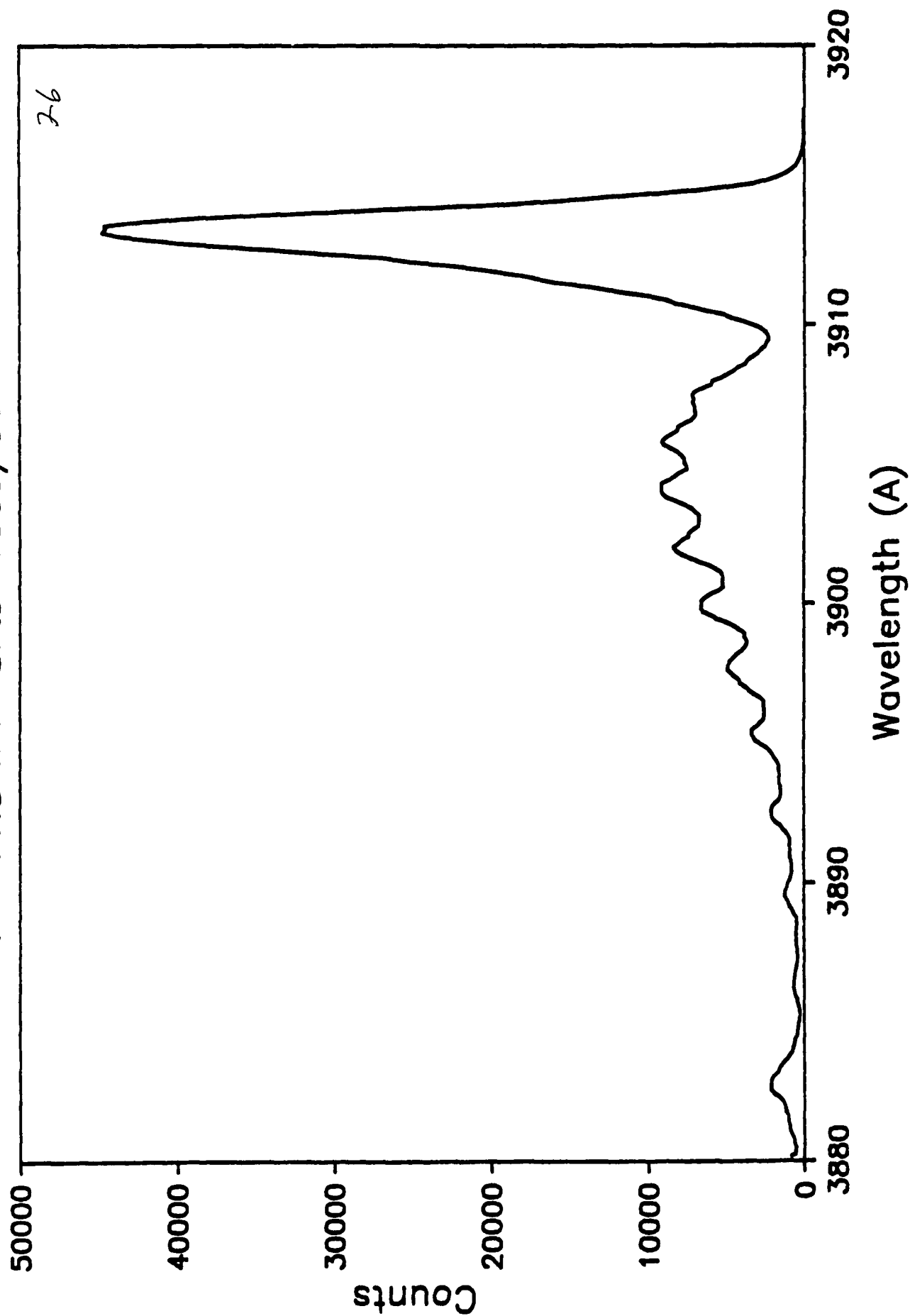


H2+ at 1.0 MeV on N2  
P= 10.0 mT Slits=100u/50mm

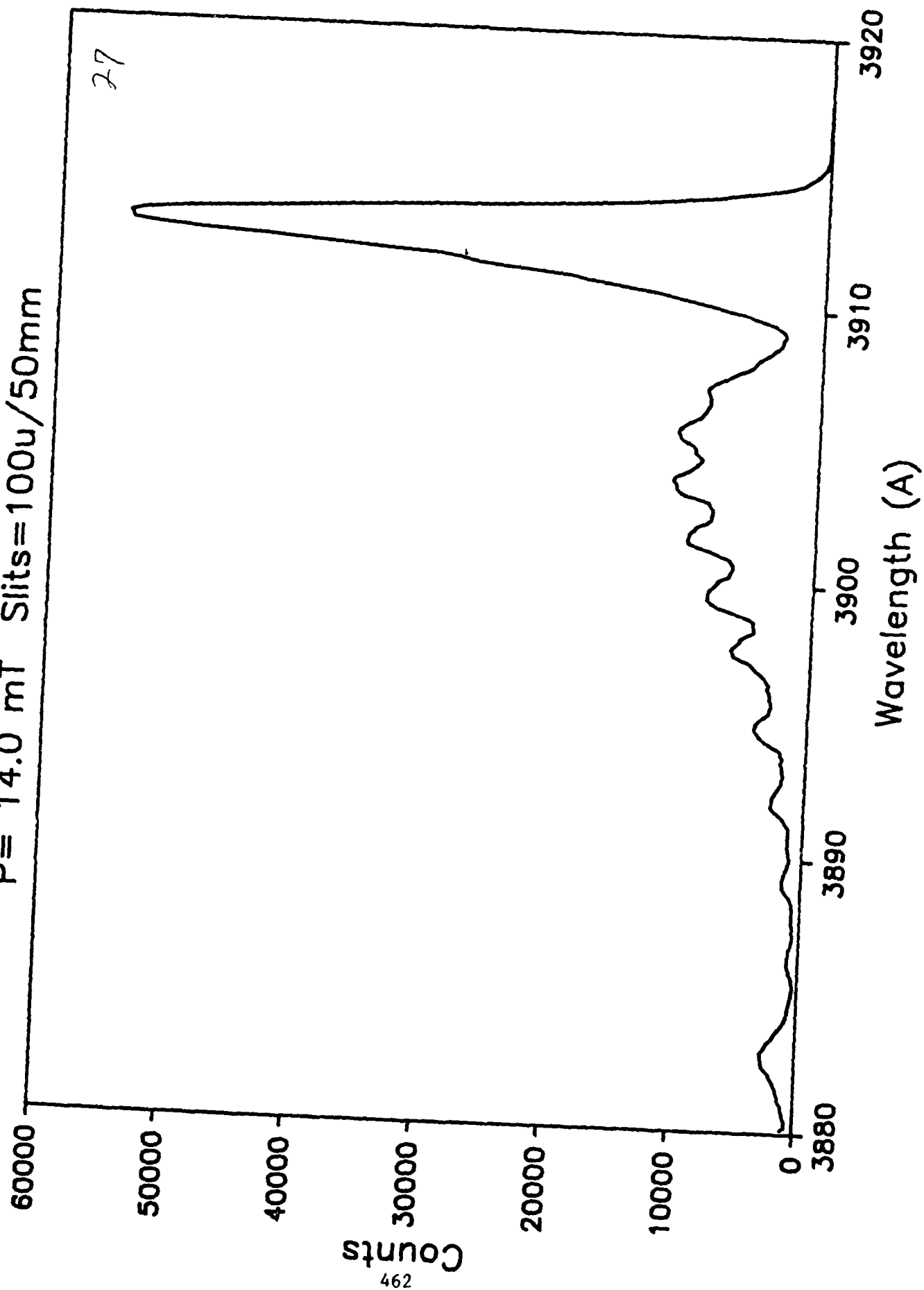


H2+ at 1.0 MeV on N2

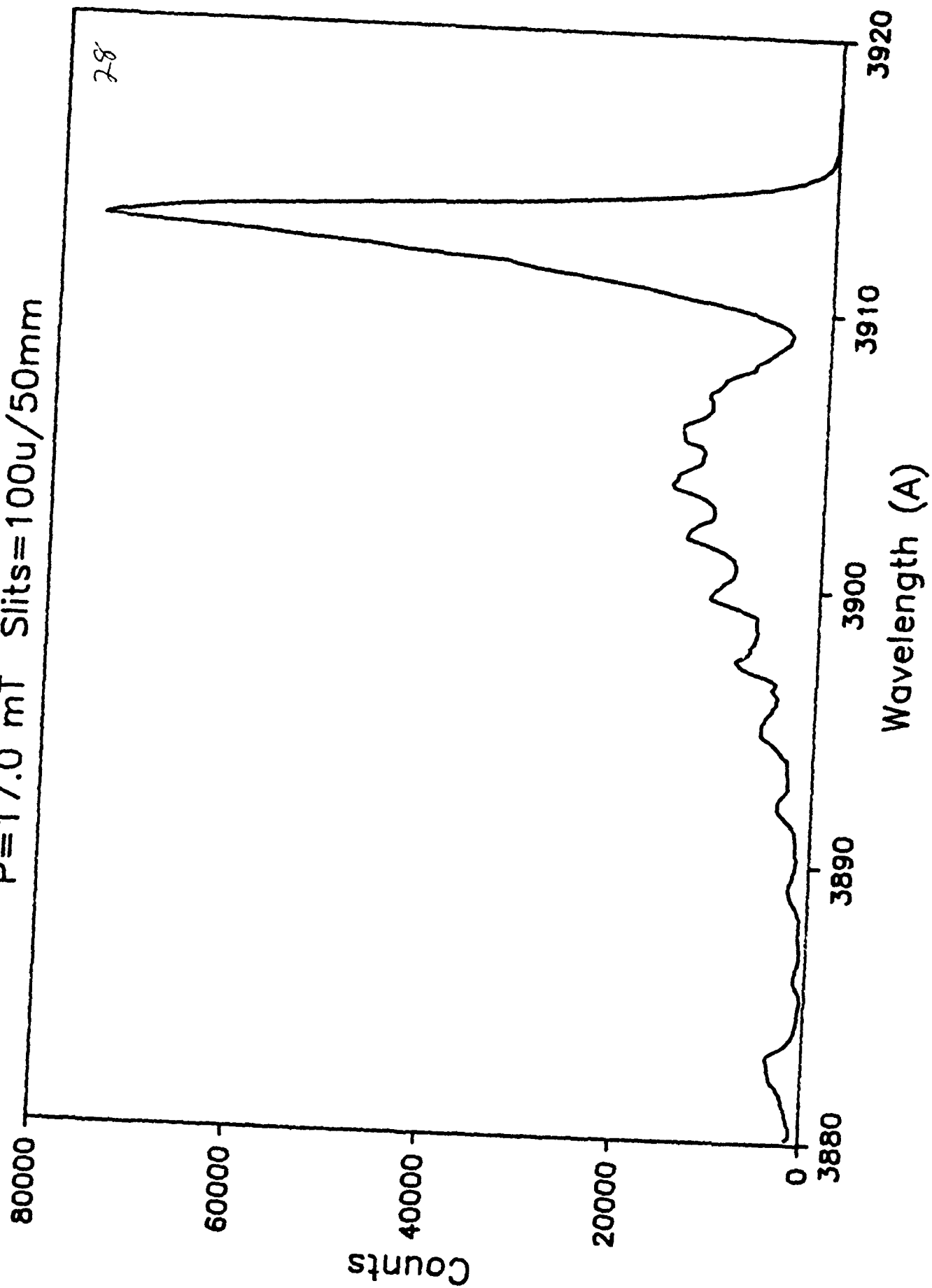
P= 11.8 mT Slits=100u/50mm



H2+ at 1.0 MeV on N2  
P= 14.0 mT Slits=100u/50mm

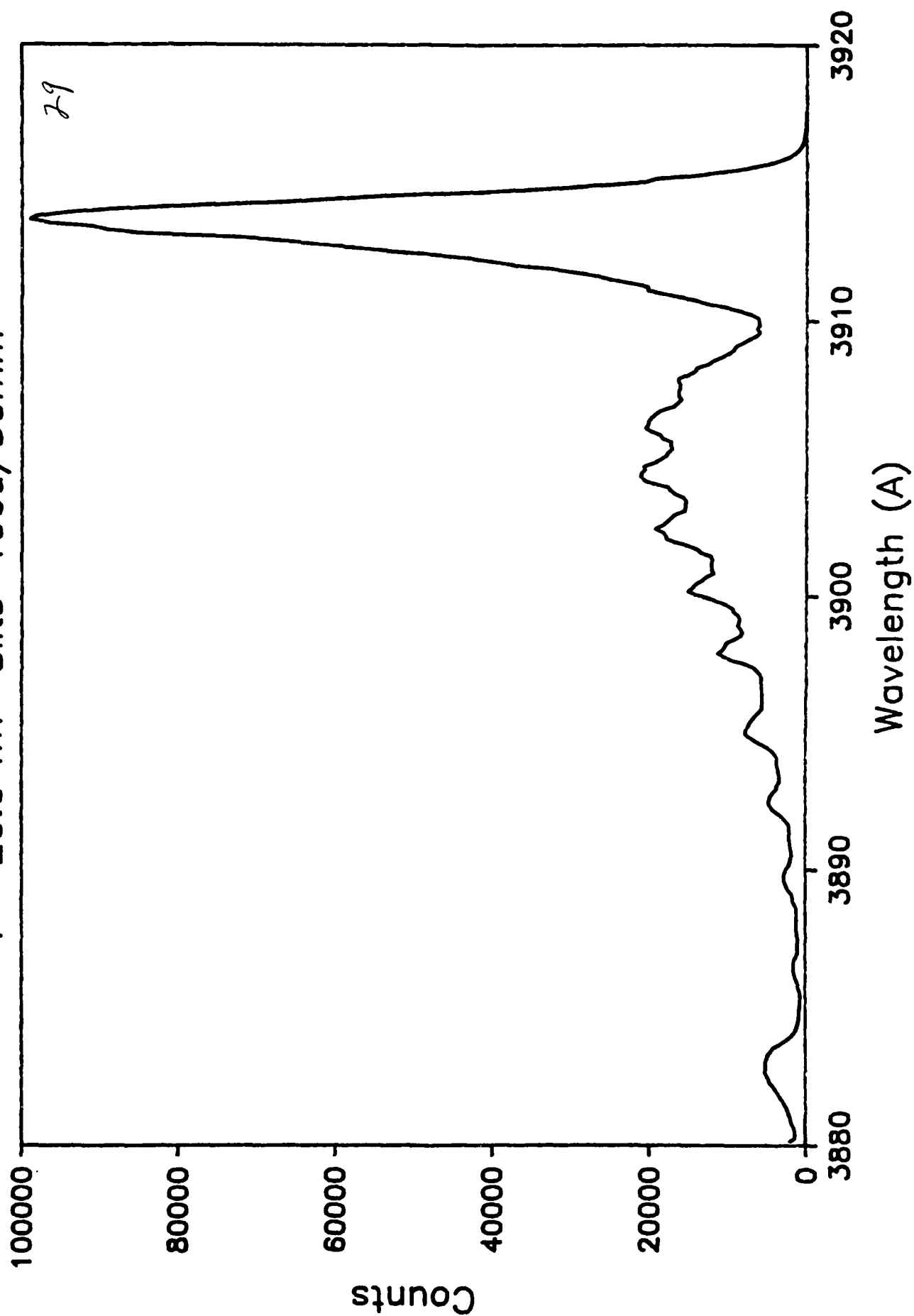


H2+ at 1.0 MeV on N2  
P=17.0 mT Slits=100u/50mm



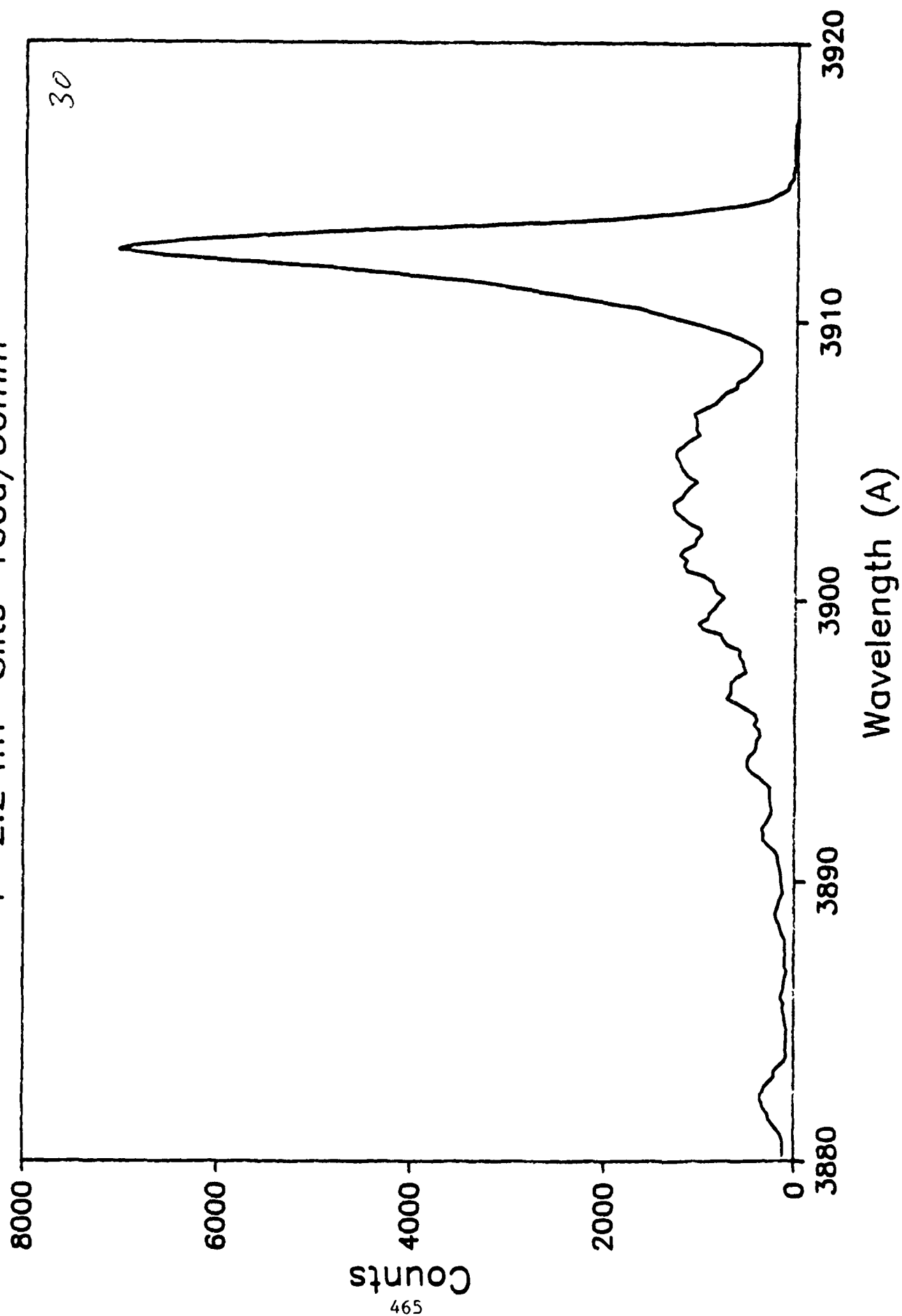


H2+ at 1.0 MeV on N2  
P= 20.0 mT Slits=100u/50mm

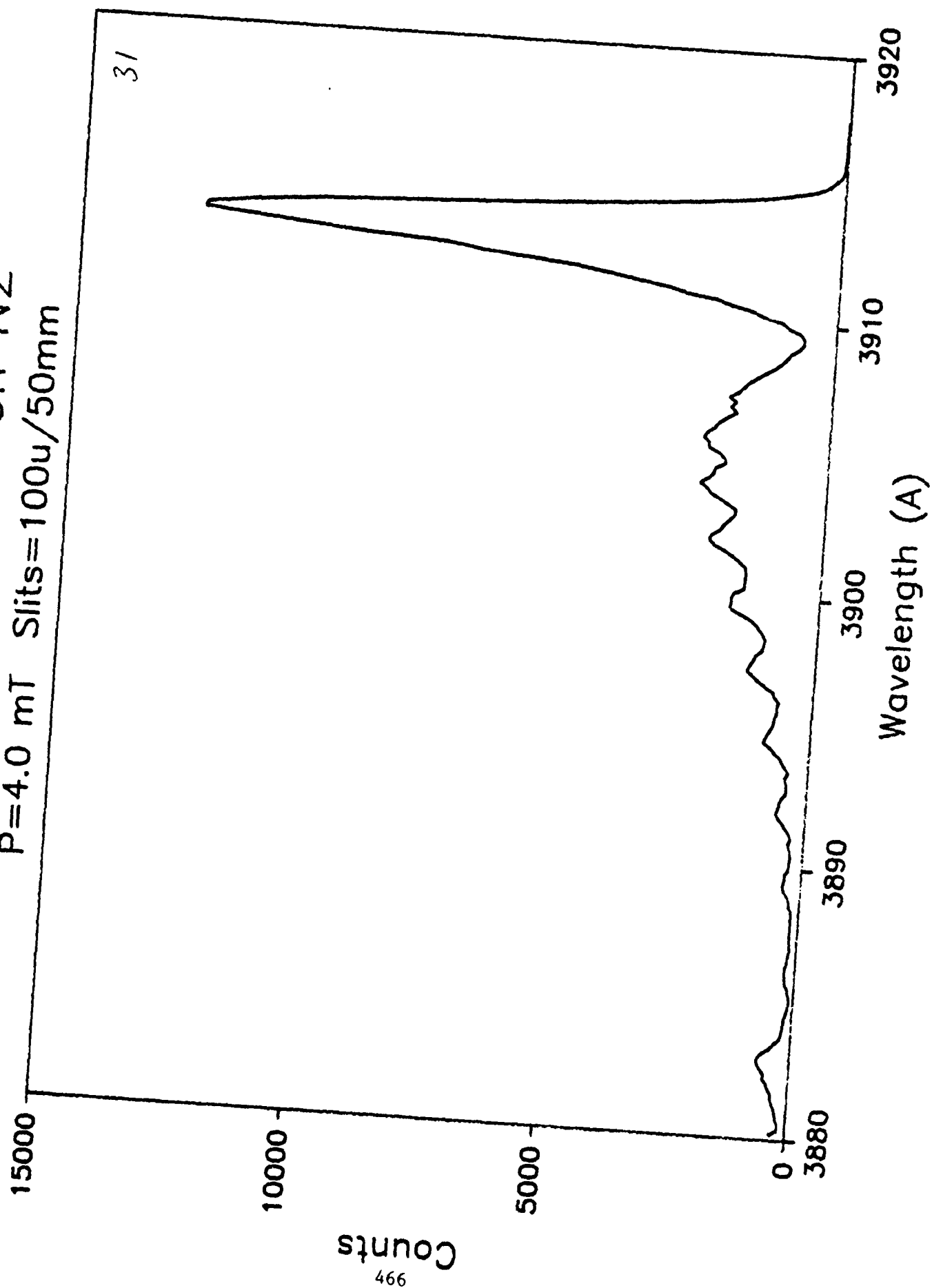


H3+ at 1.5 MeV on N2

P=2.2 mT Slits=100u/50mm

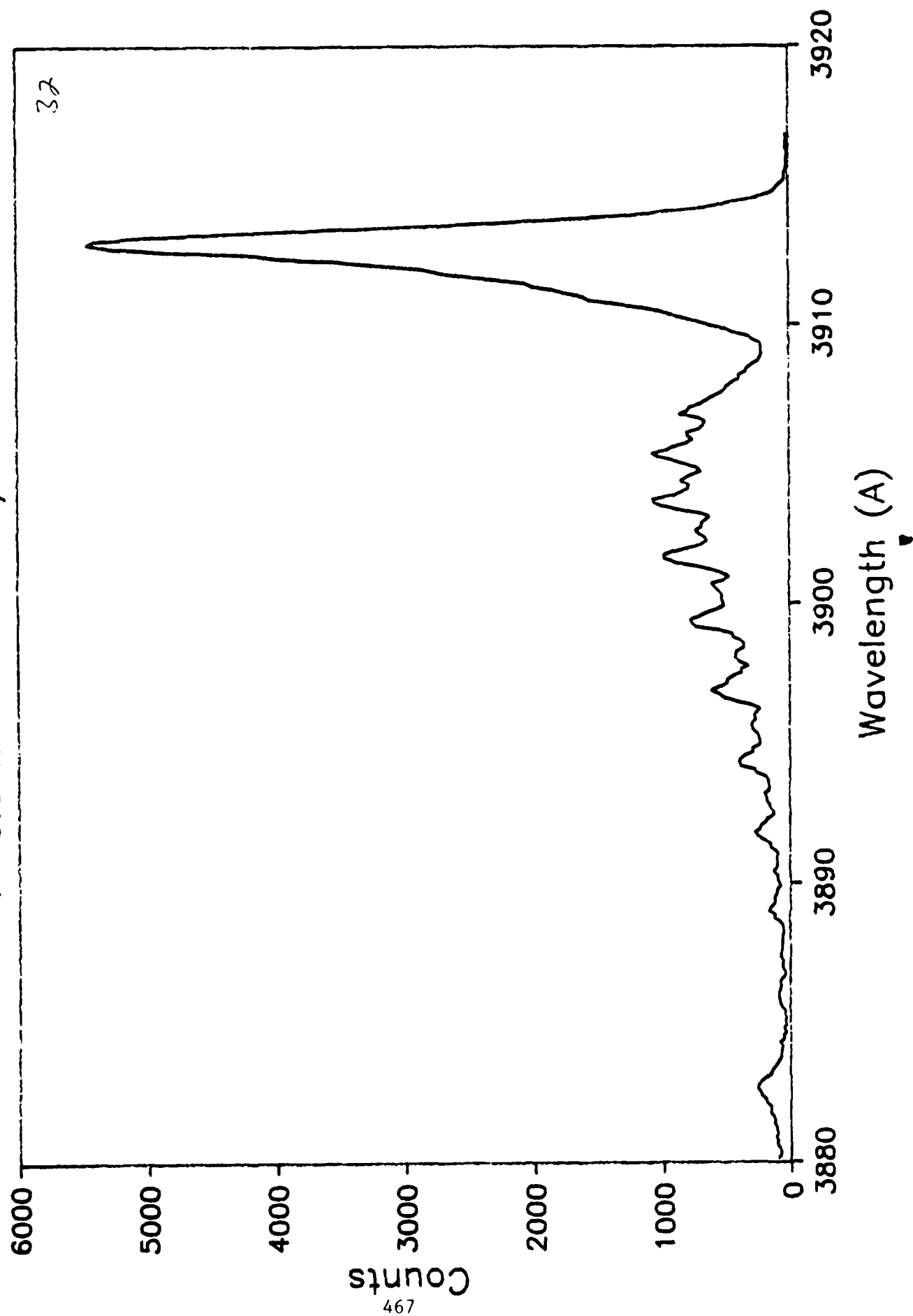


H3+ at 1.5 MeV on N2  
P=4.0 mT Slits=100u/50mm

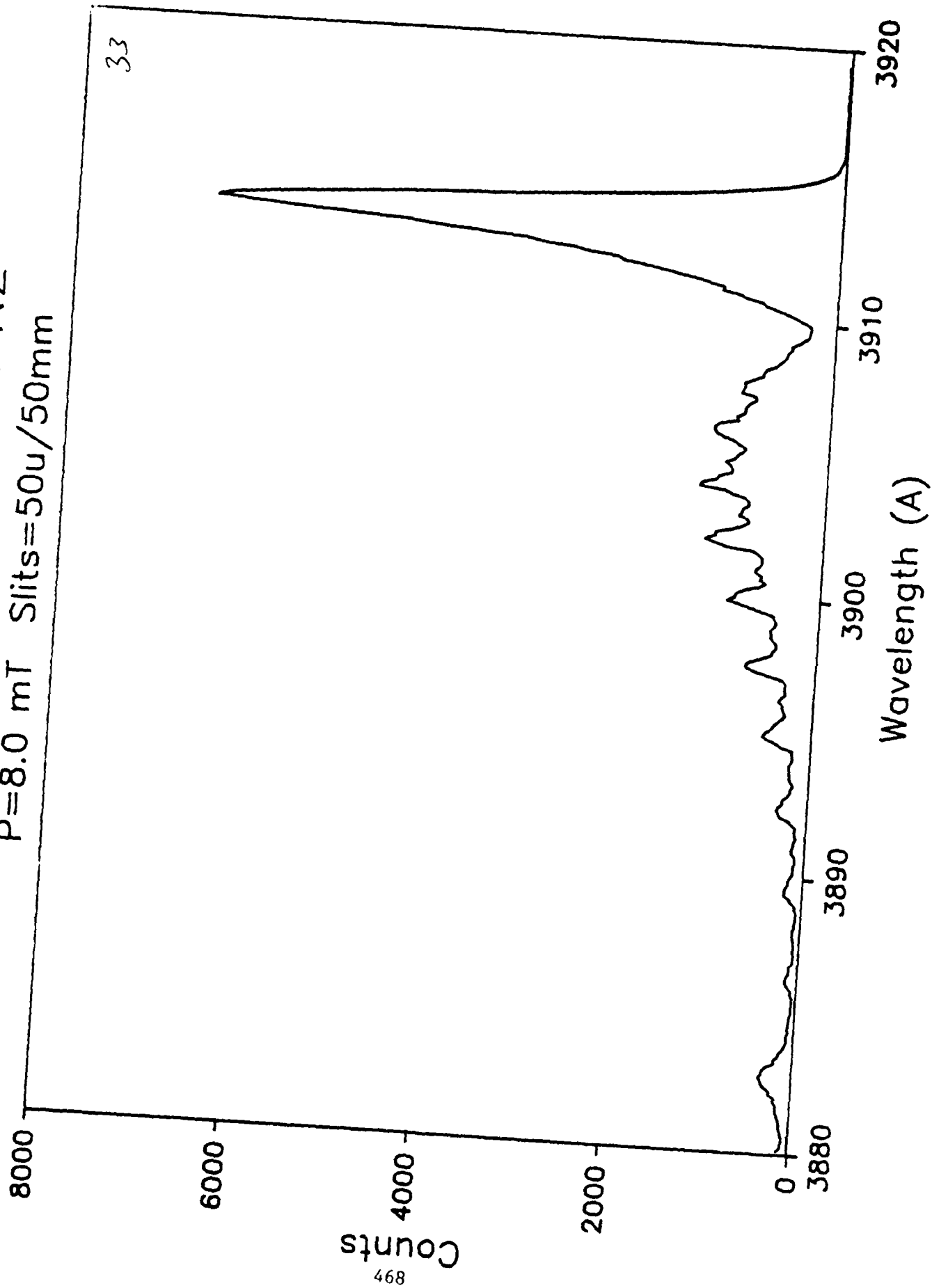


H3+ at 1.5 MeV on N2

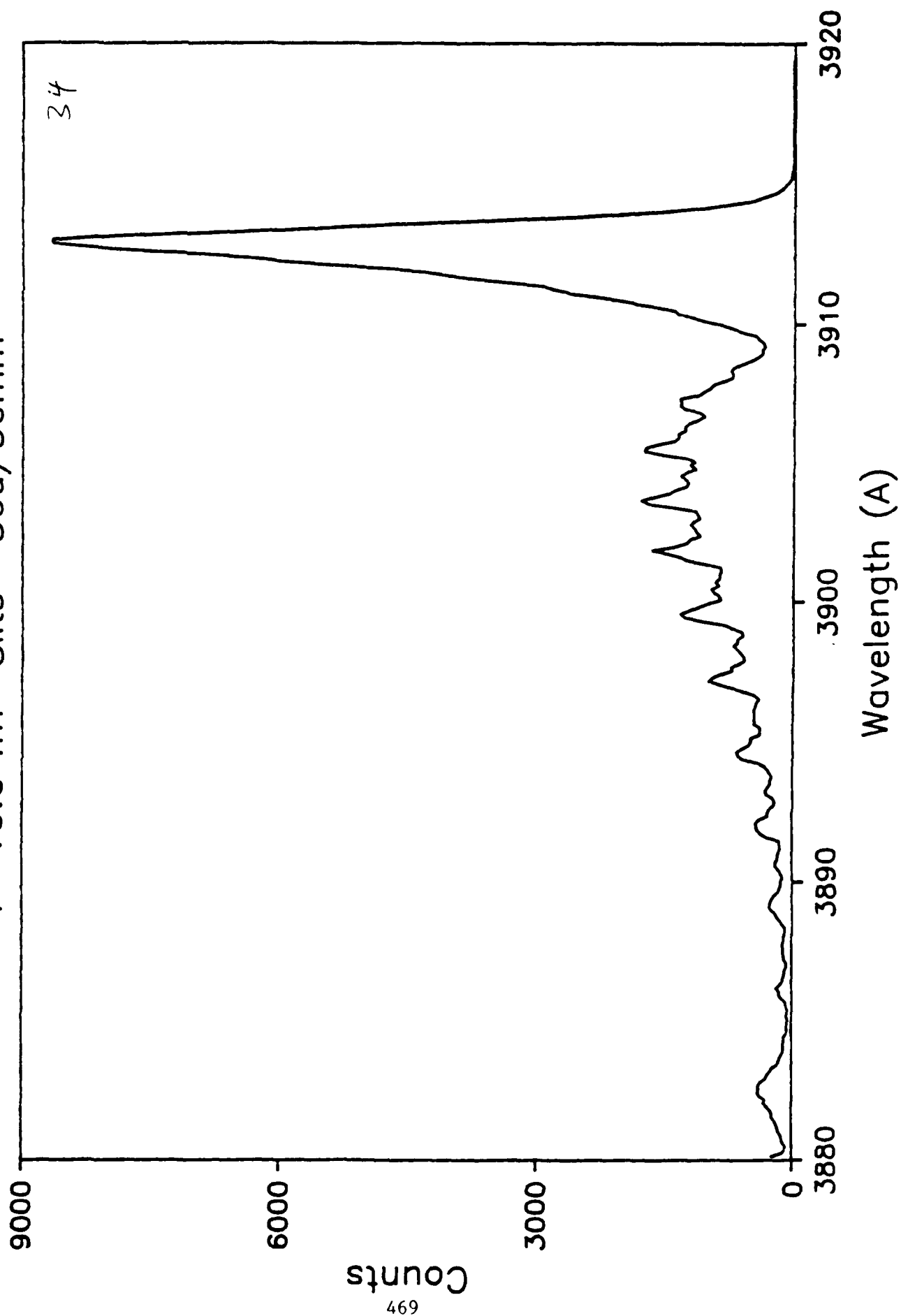
P=6.0 mT Slits=50u/50mm



H3+ at 1.5 MeV on N2  
P=8.0 mT Slits=50u/50mm

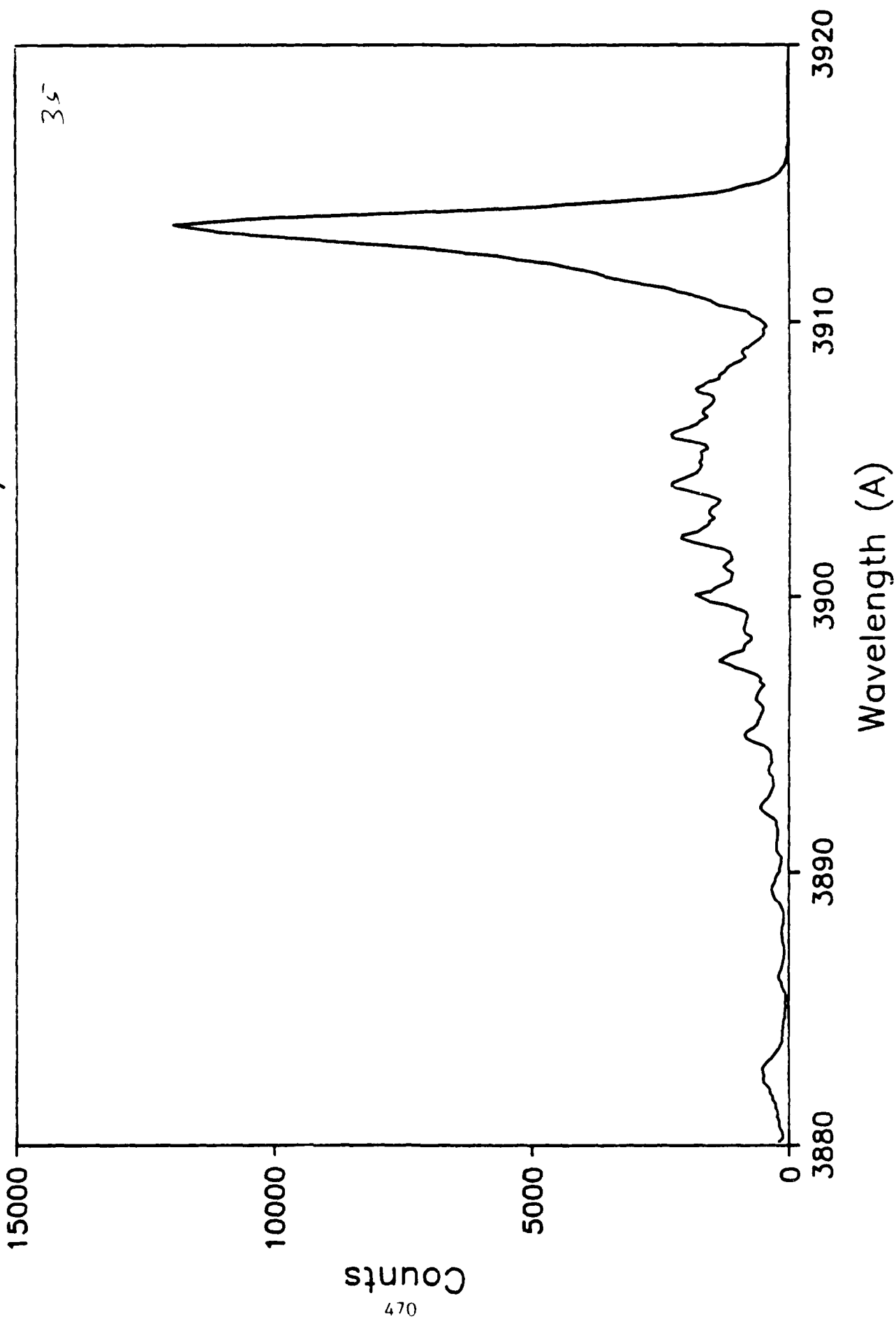


H3+ at 1.5 MeV on N2  
P=10.0 mT Slits =50u/50mm

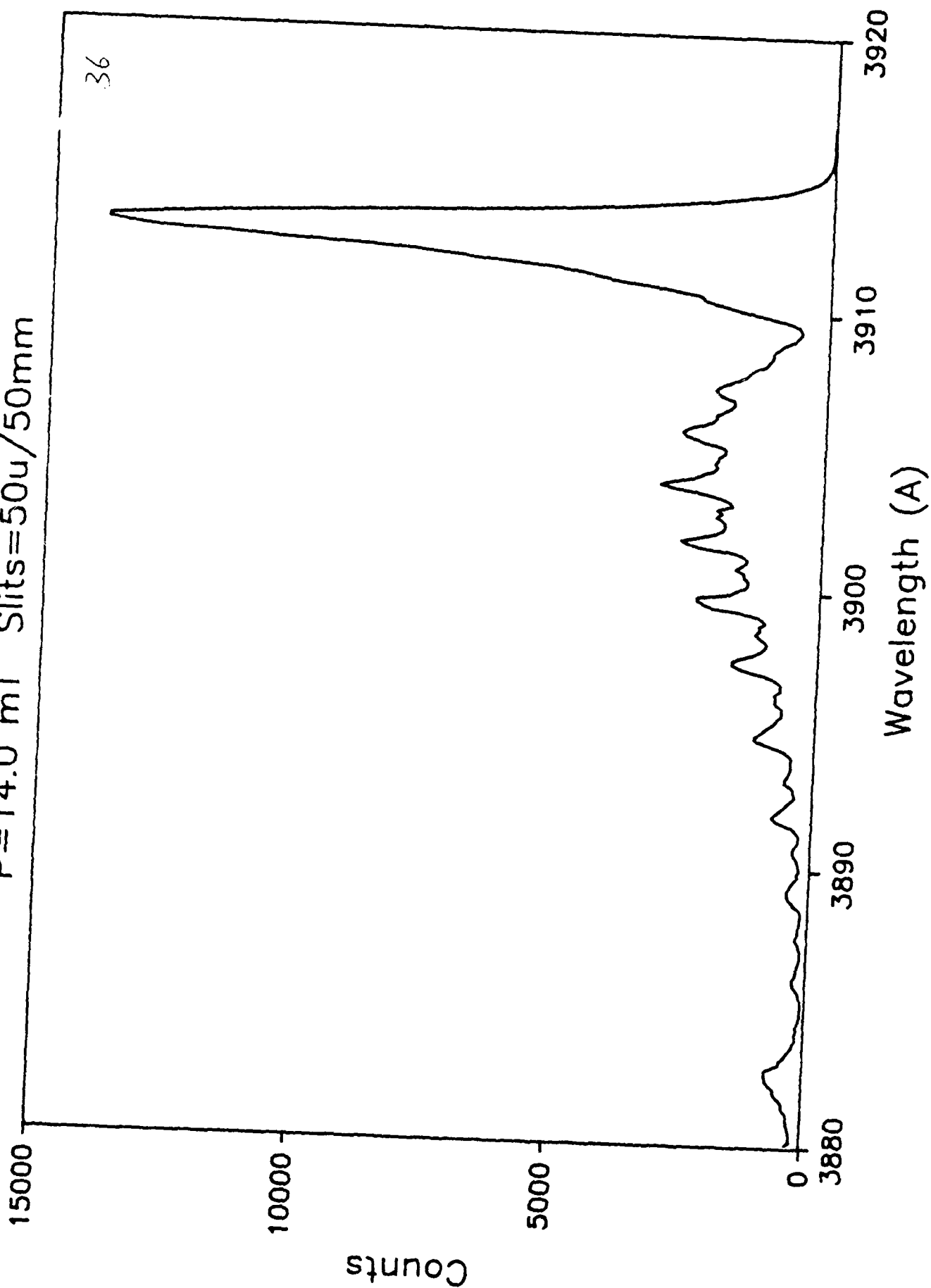


H3+ at 1.5 MeV on N2

P=12.0 mT Slits=50u/50mm

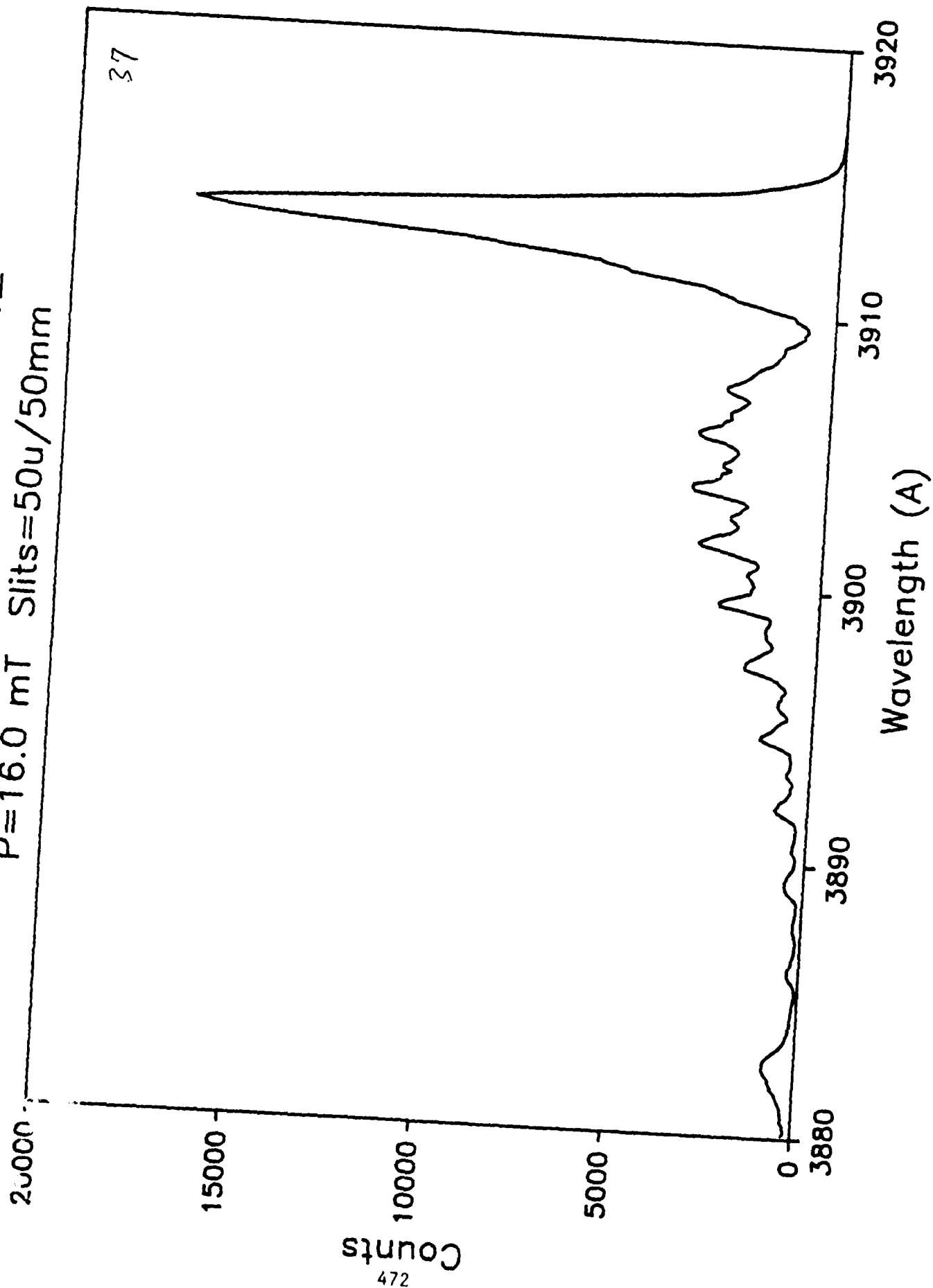


H3+ at 1.5 MeV on N2  
P=14.0 mT Slits=50u/50mm

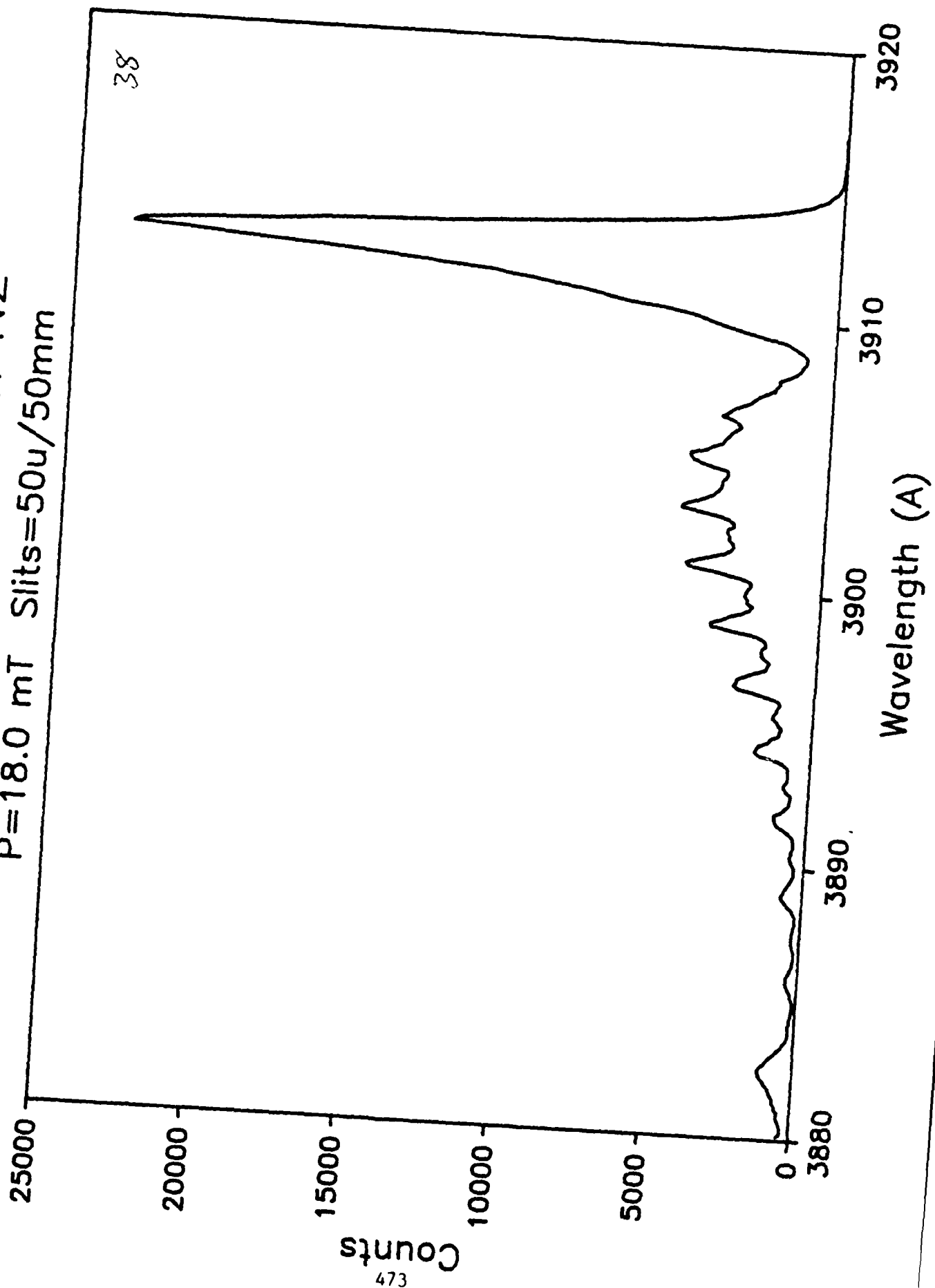




H3+ at 1.5 MeV on N2  
P=16.0 mT Slits=50u/50mm

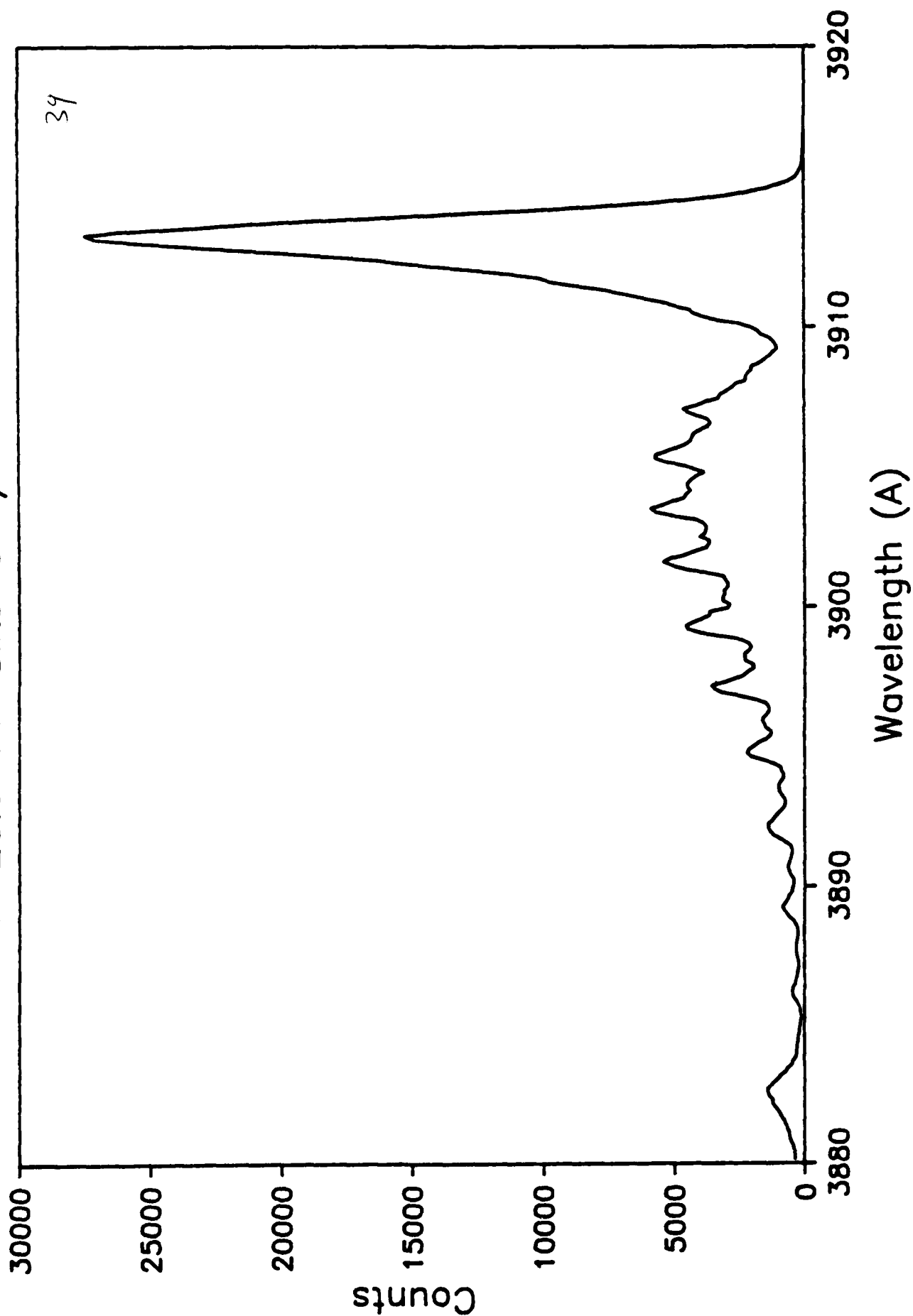


H3+ at 1.5 MeV on N2  
P=18.0 mT Slits=50u/50mm

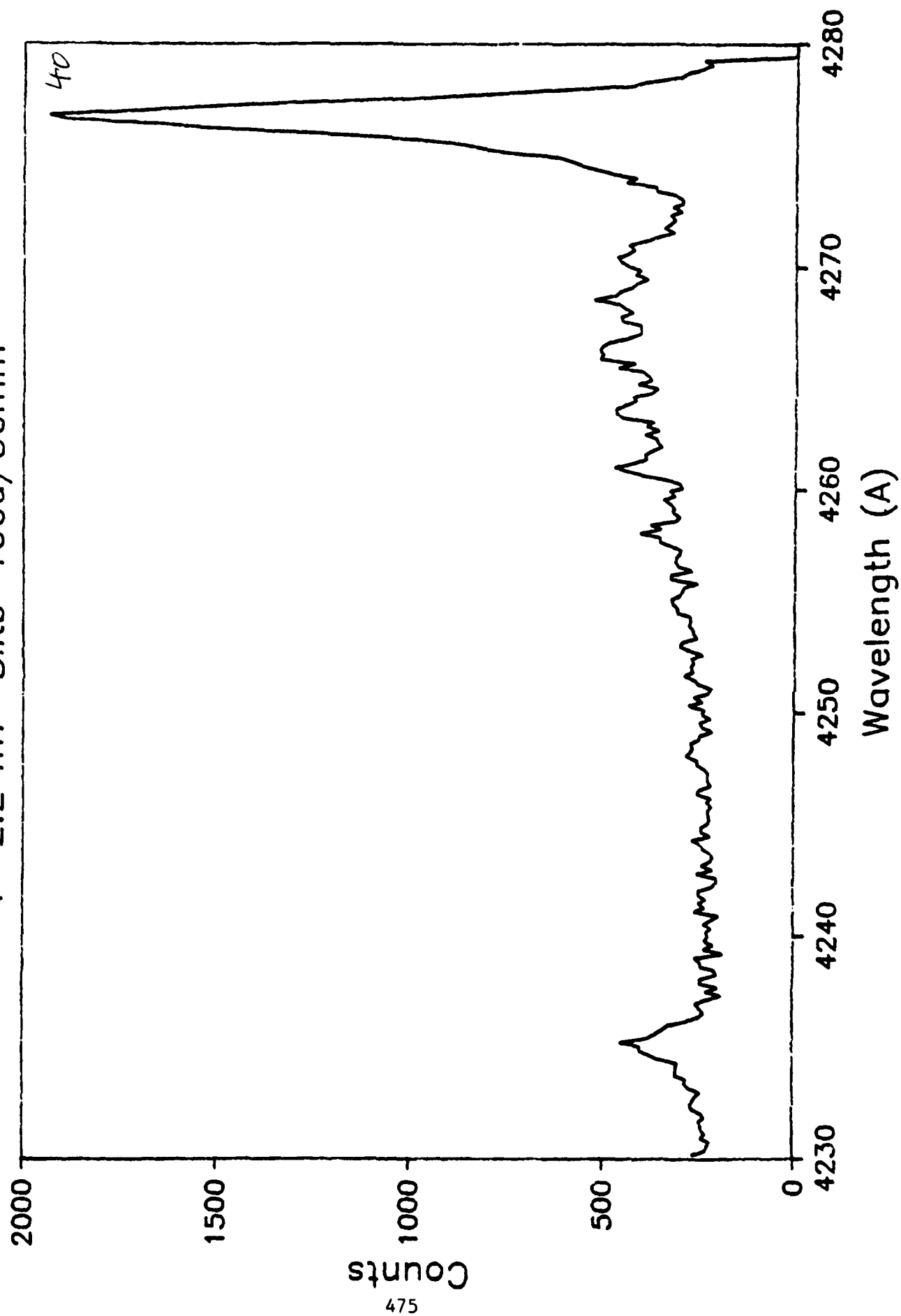


H3+ at 1.5 MeV on N2

P=20.0 mT Slits=50u/50mm

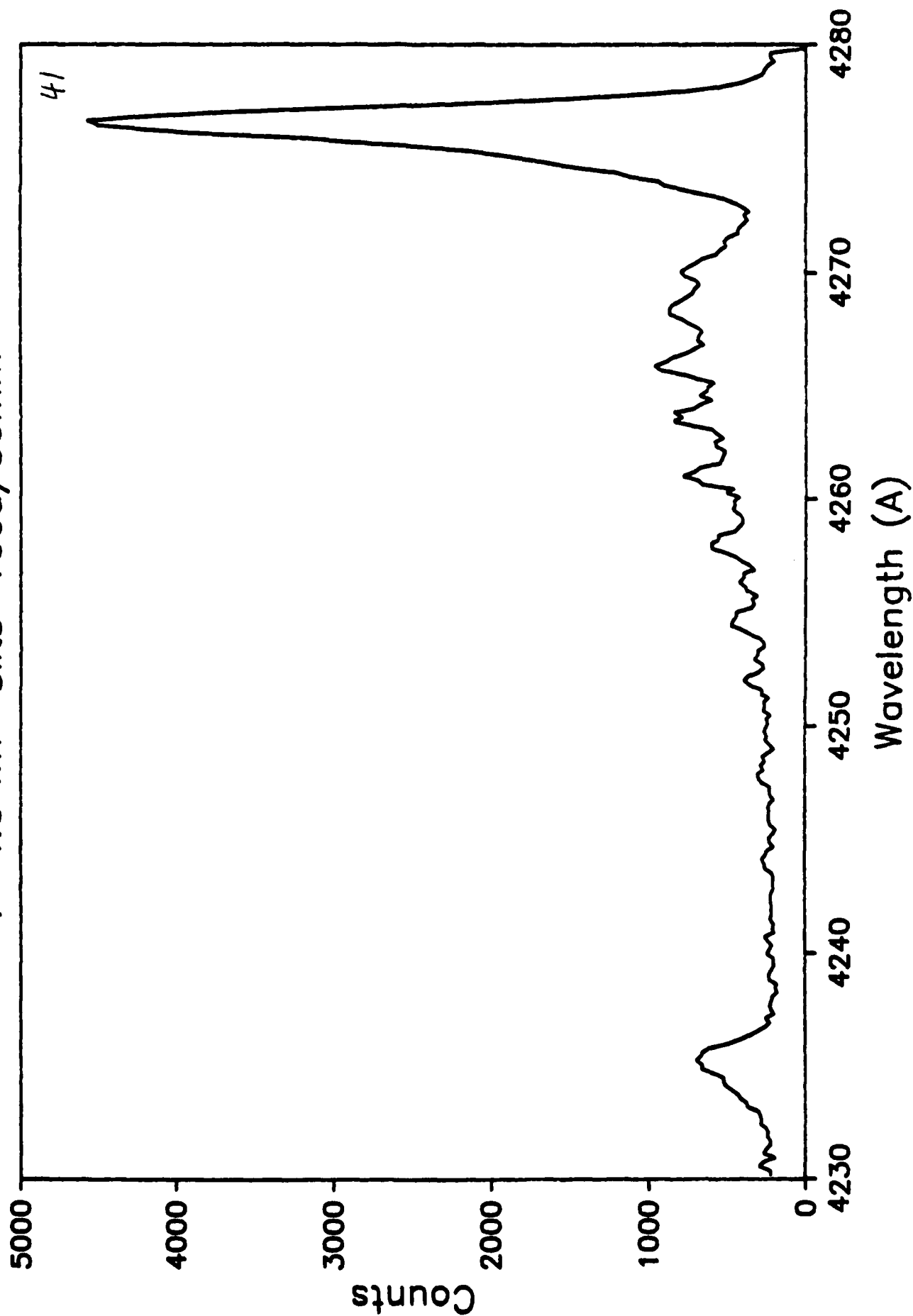


H+ at 0.5 MeV on N2  
P=2.2 mT Slits=100u/50mm

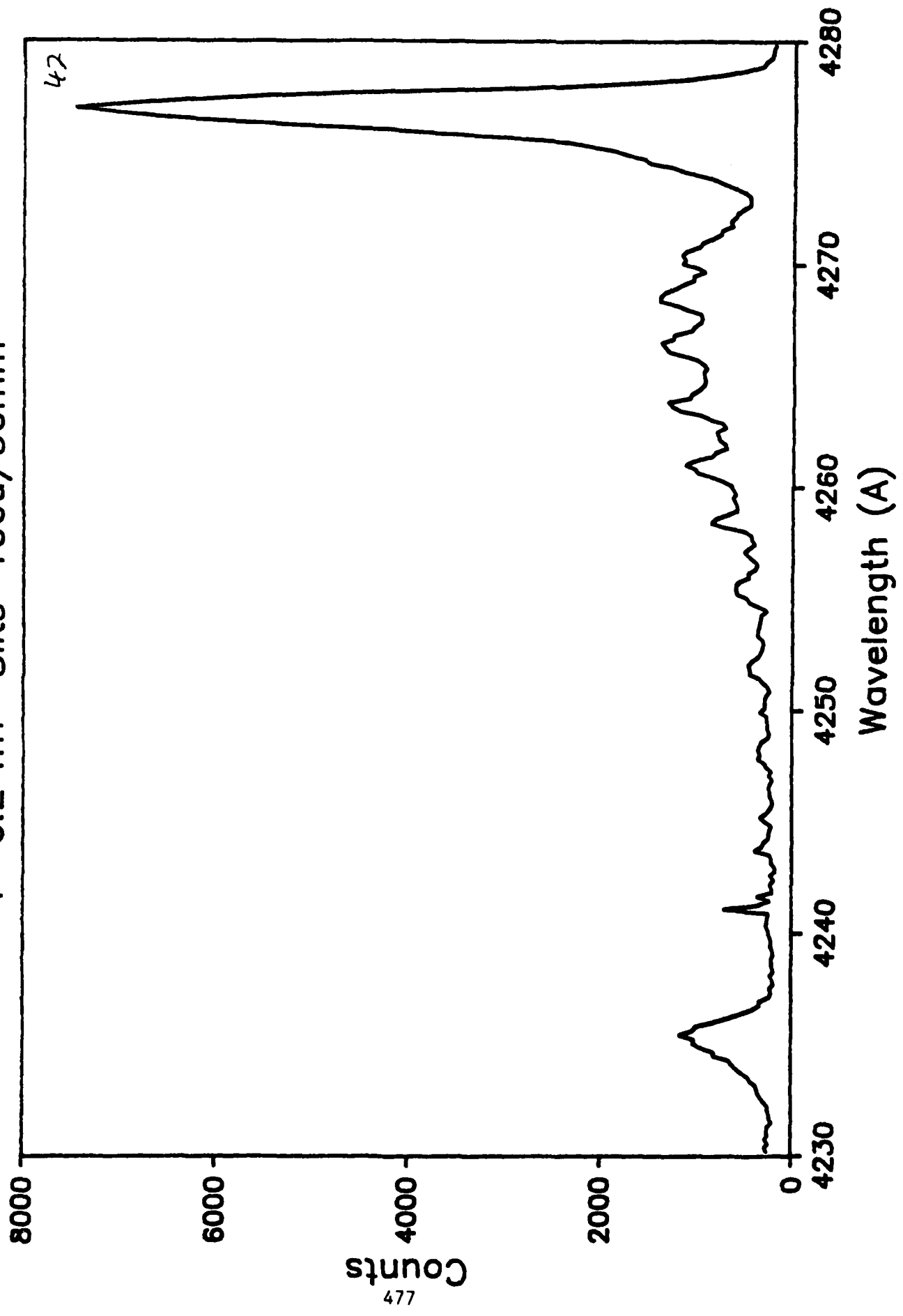


H+ at 0.5 MeV on N2

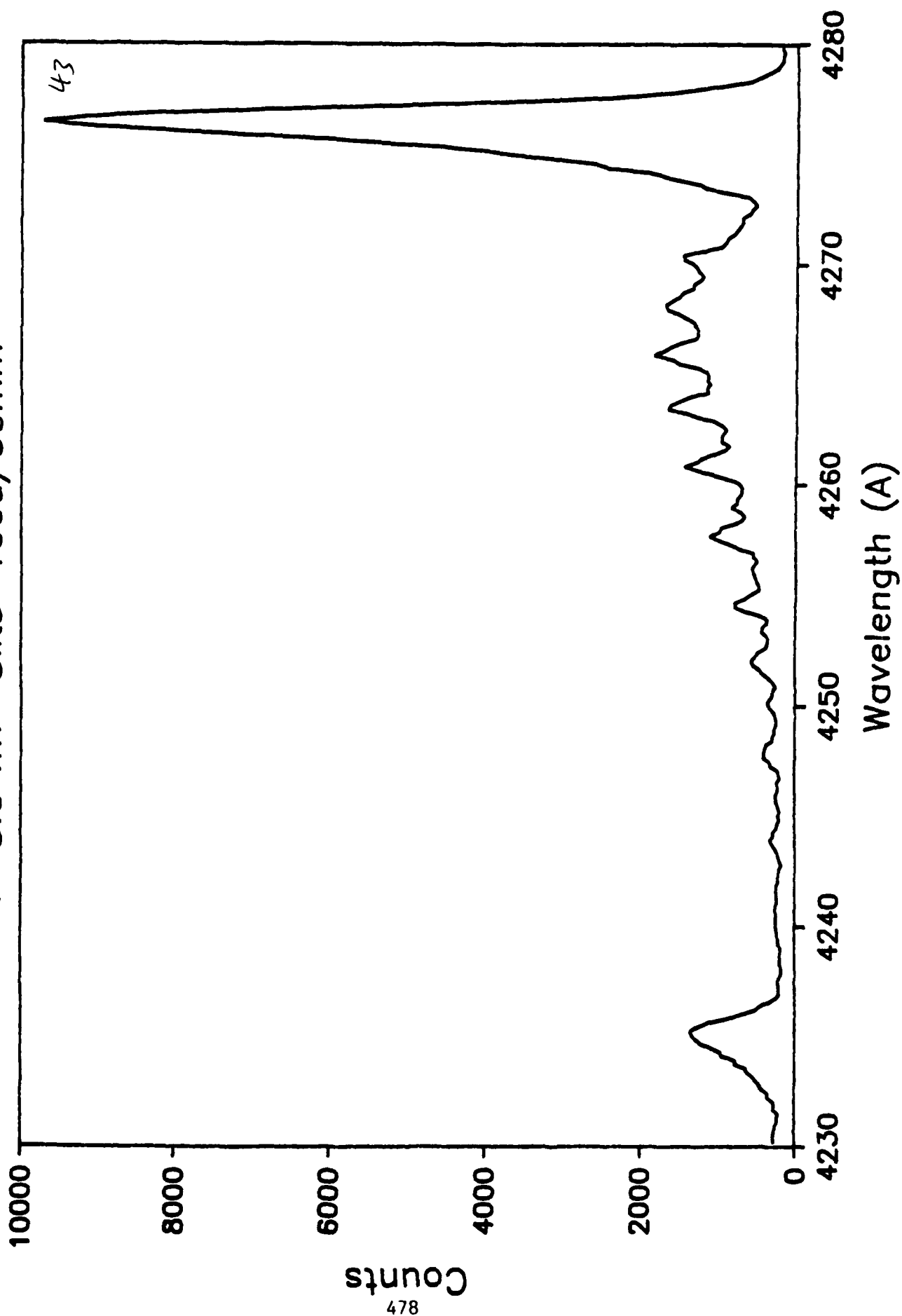
P=4.0 mT Slits=100u/50mm



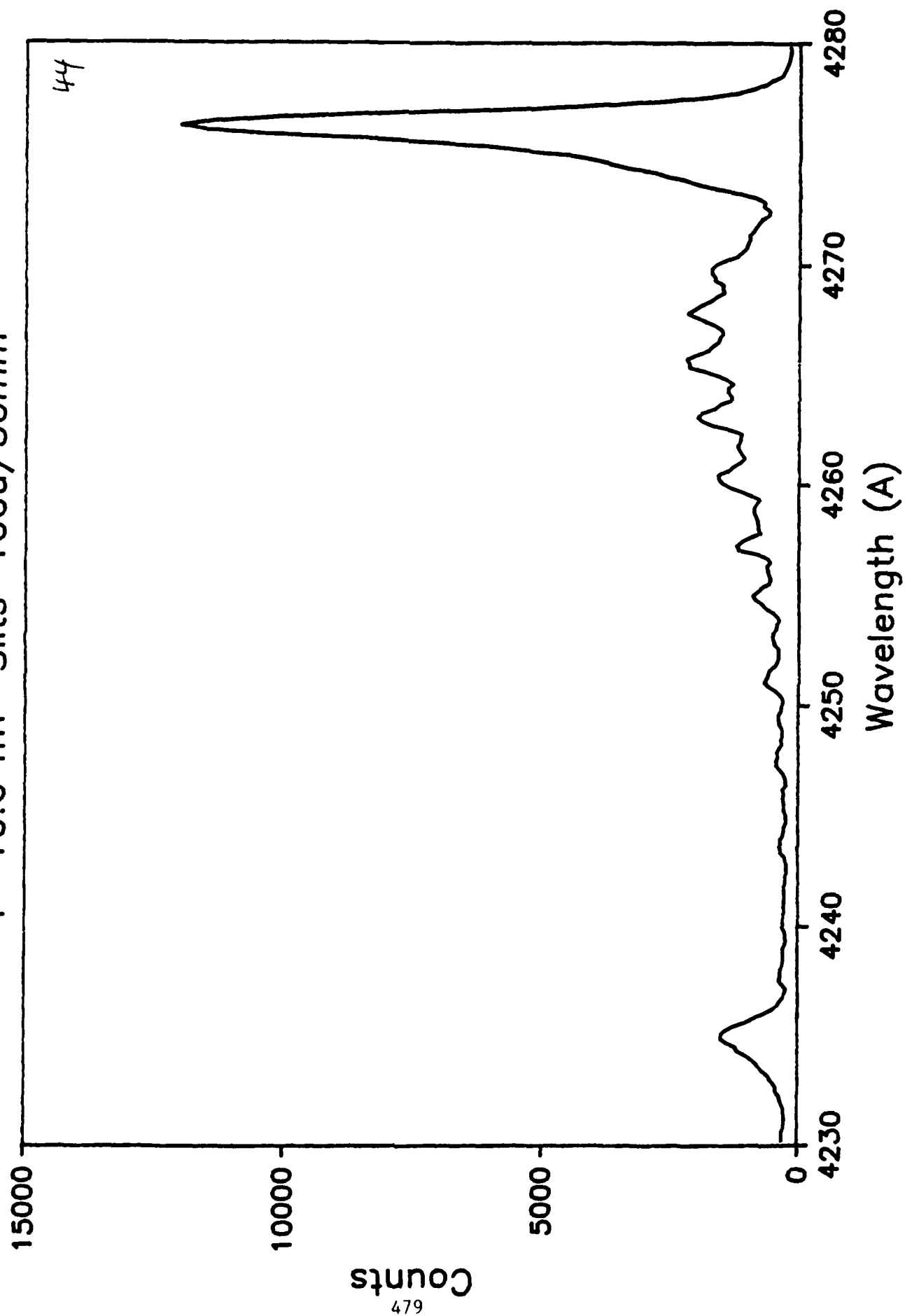
H+ at 0.5 MeV on N2  
P=6.2 mT Slits=100u/50mm



H+ at 0.5 MeV on N2  
P=8.0 mT Slits=100u/50mm

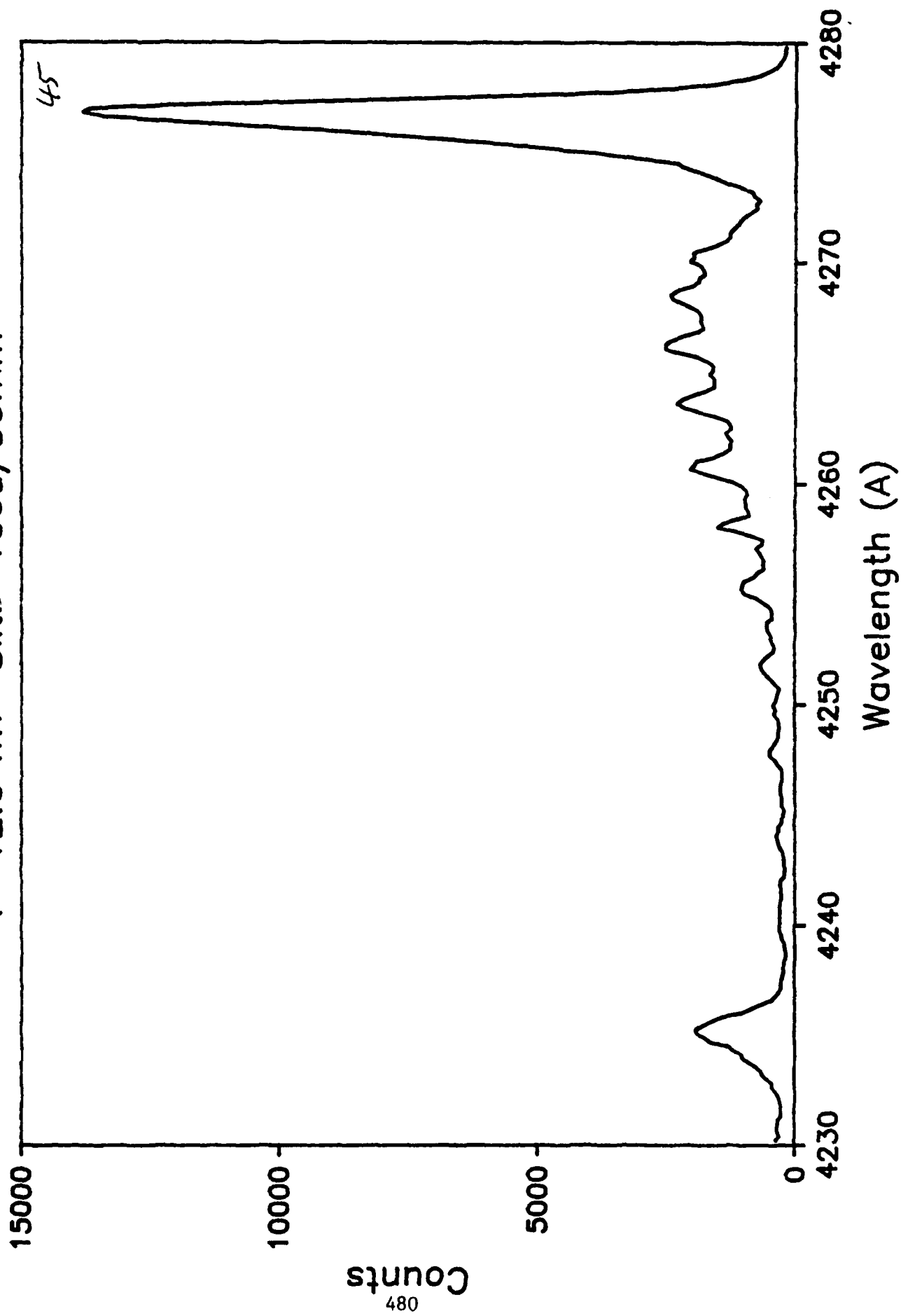


H+ at 0.5 MeV on N2  
P=10.0 mT Slits=100u/50mm

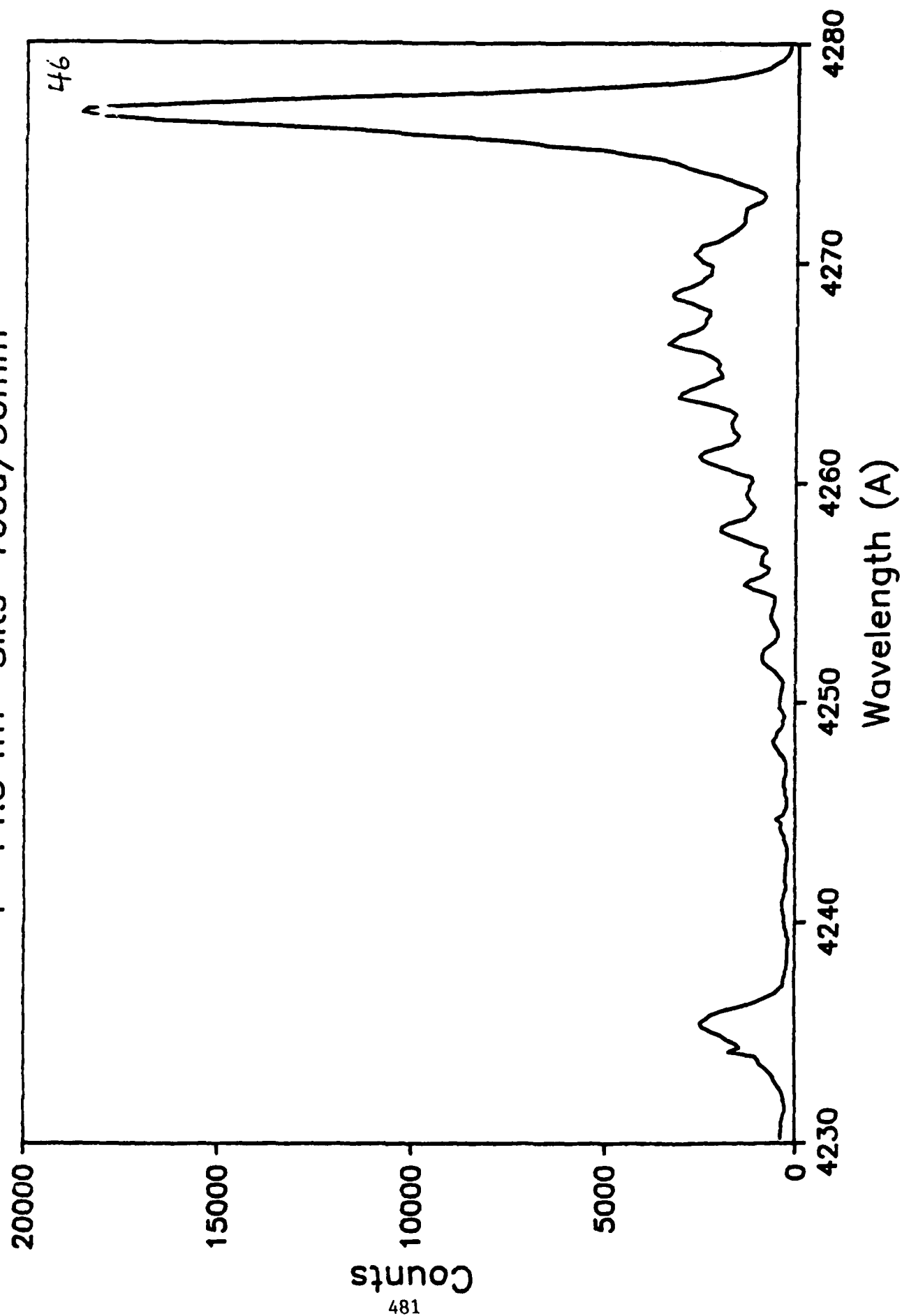




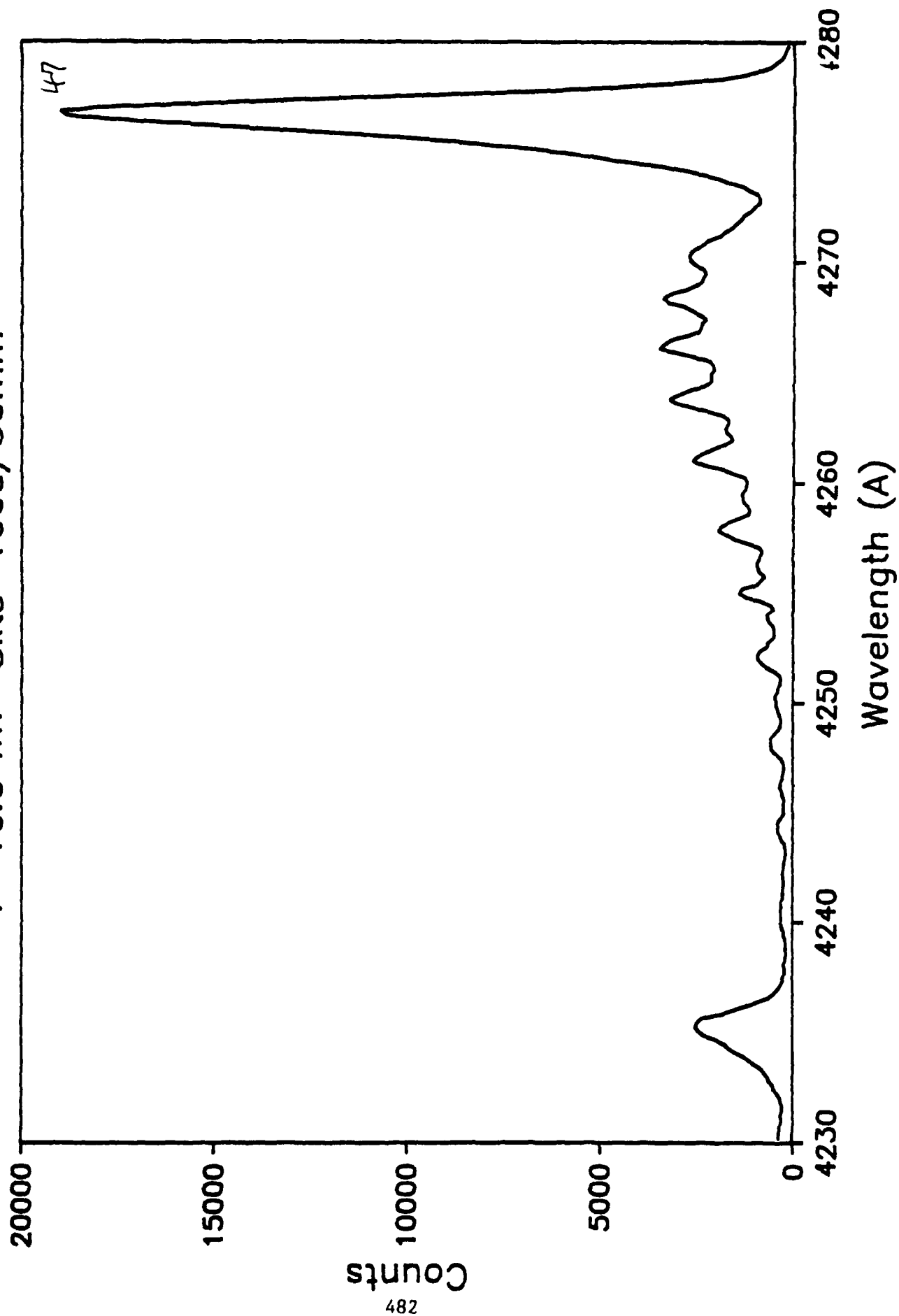
H+ at 0.5 MeV on N2  
P=12.0 mT Slits=100u/50mm



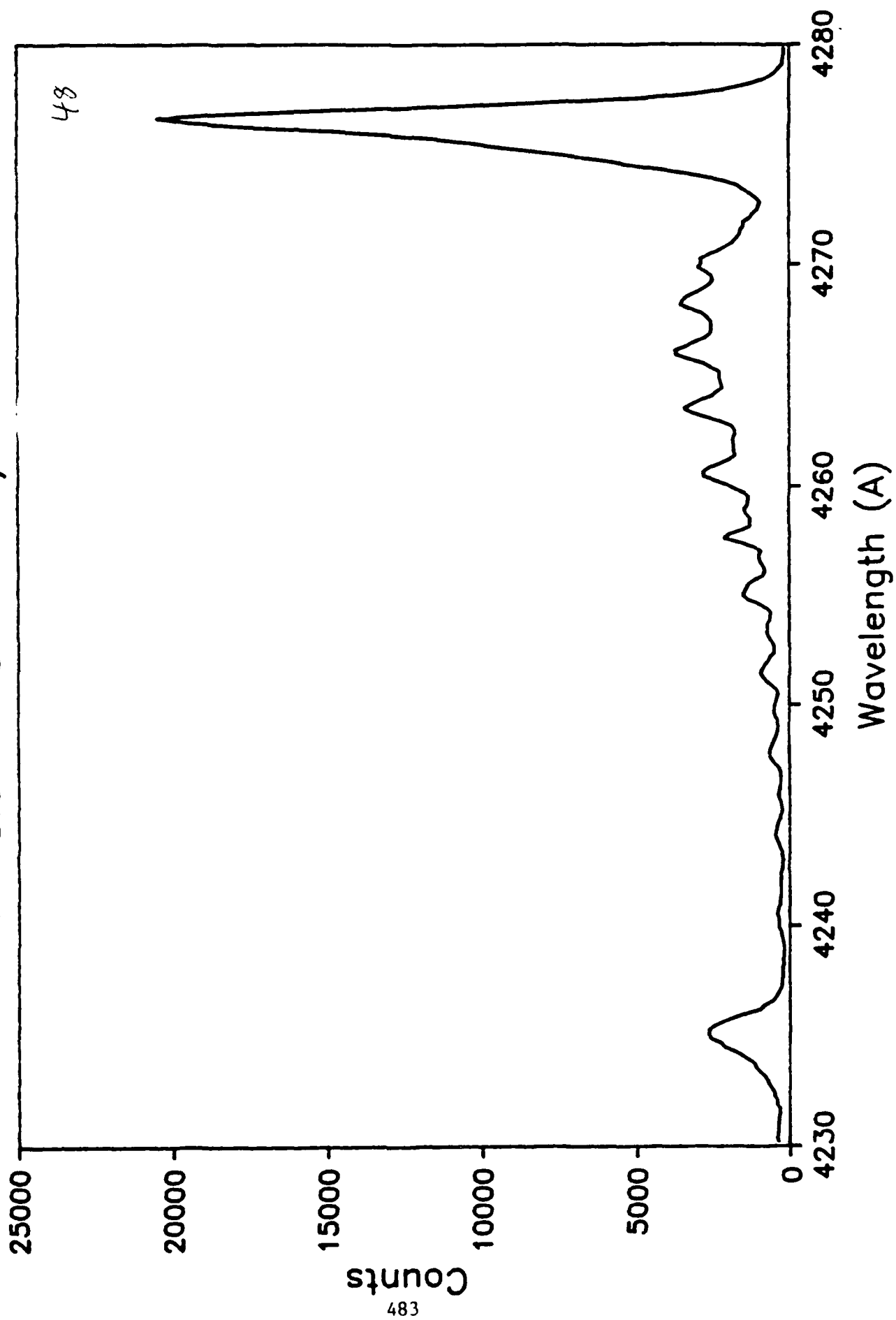
H+ at 0.5 MeV on N2  
P=14.3 mT Slits=100u/50mm



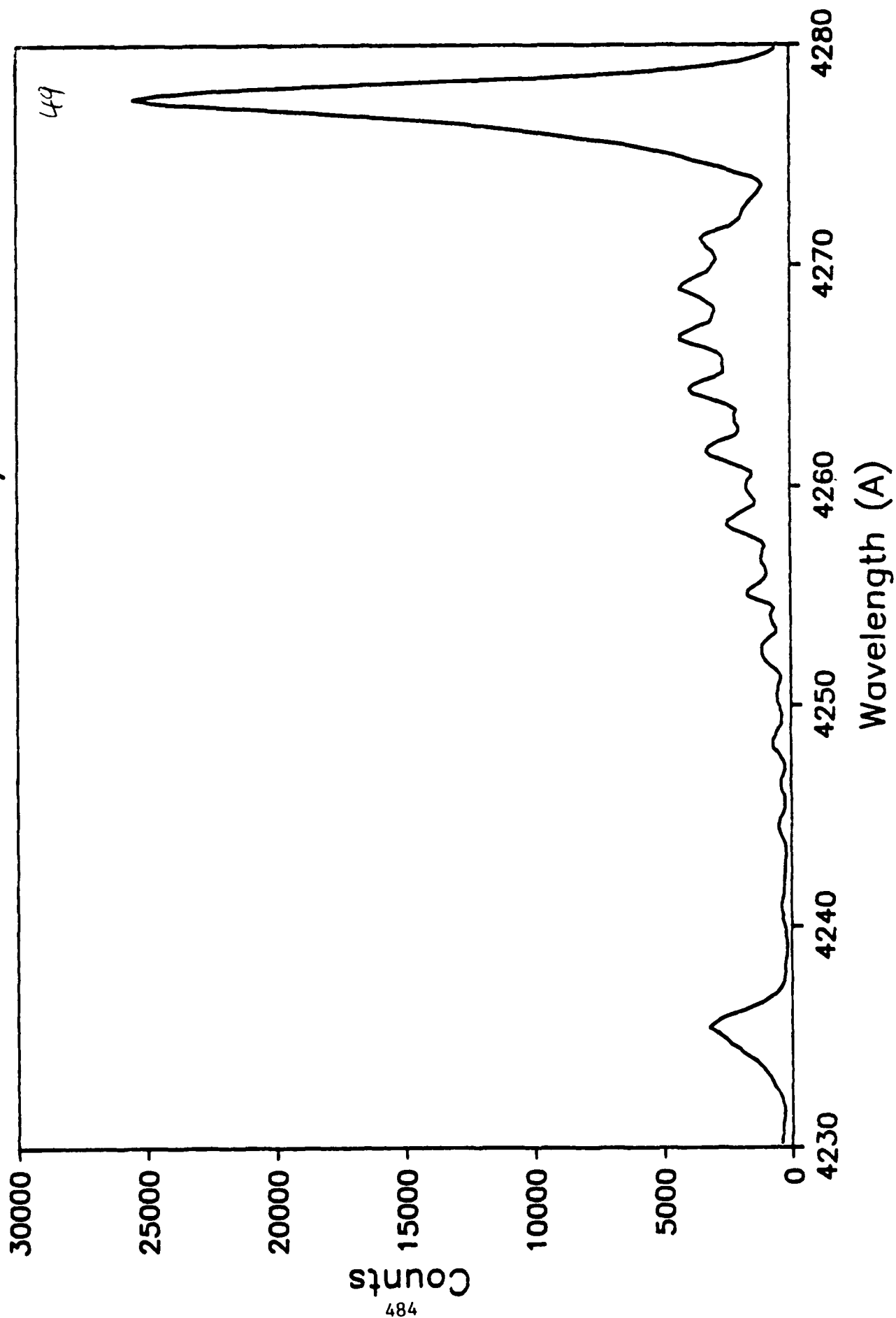
H+ at 0.5 MeV on N2  
P=16.0 mT Slits=100u/50mm



H+ at 0.5 MeV on N2  
P=18.0 mT Slits=100u/50mm

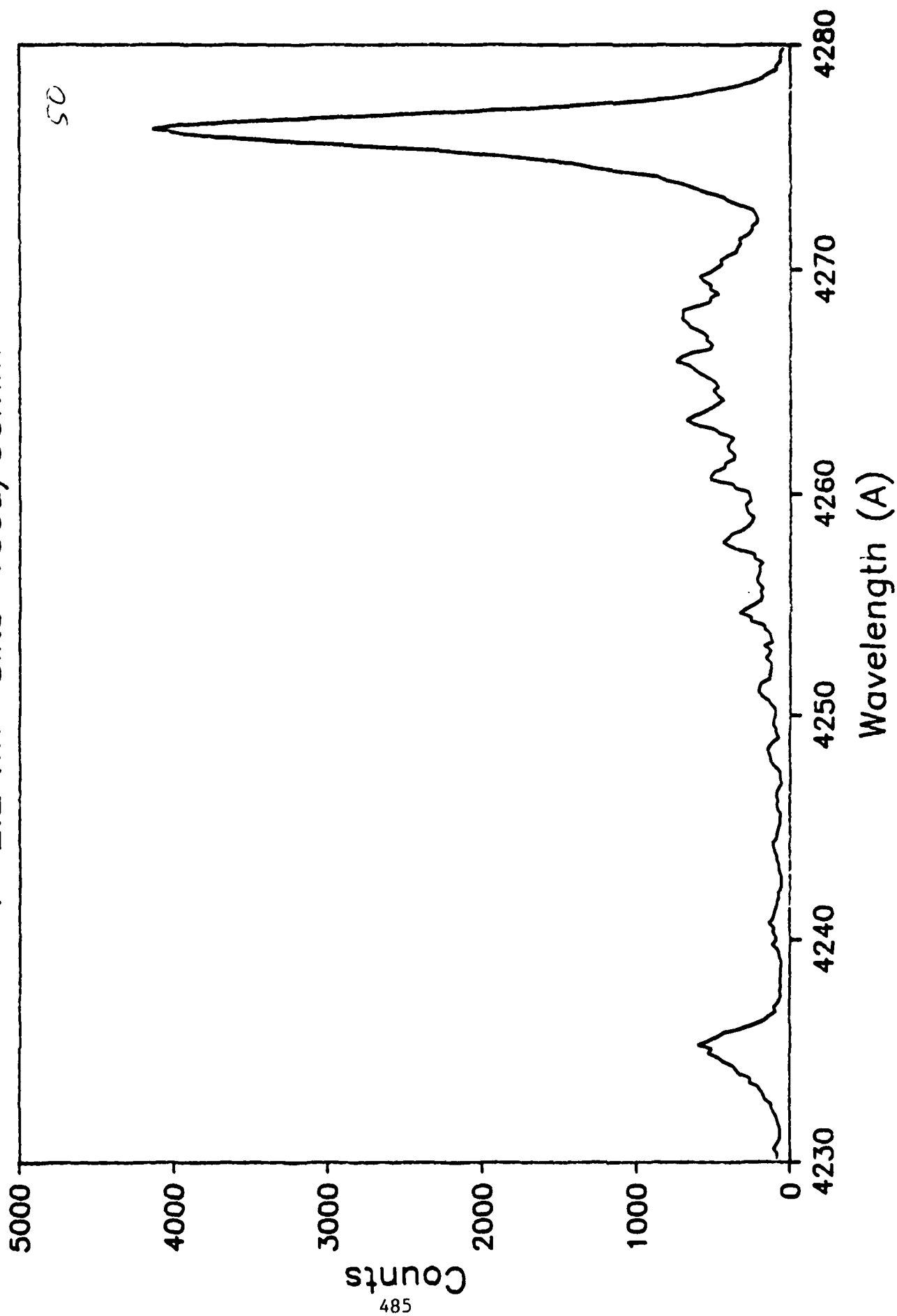


H+ at 0.5 MeV on N2  
P=20.0 mT Slits=100u/50mm

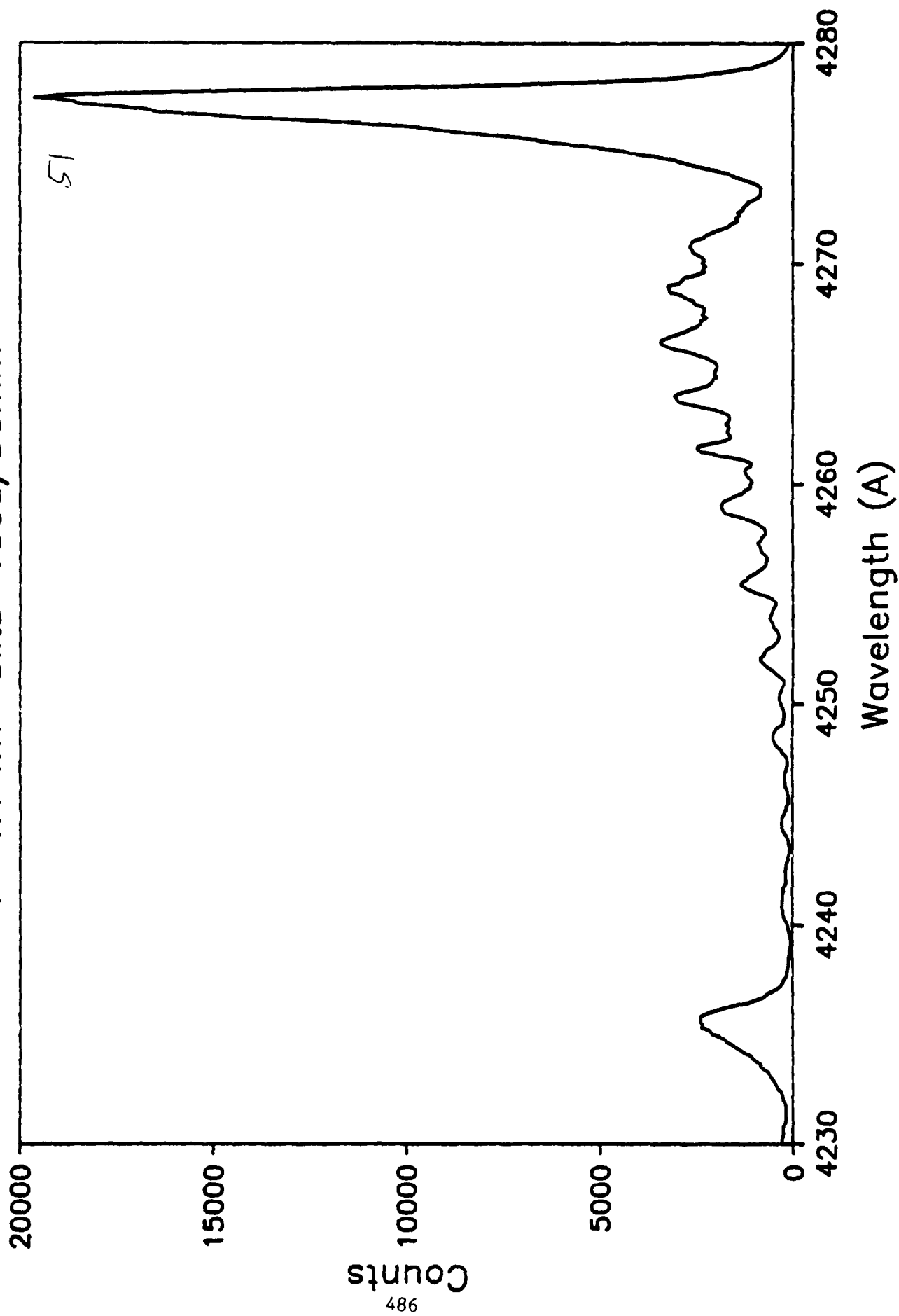


H2+ at 1.0 MeV on N2

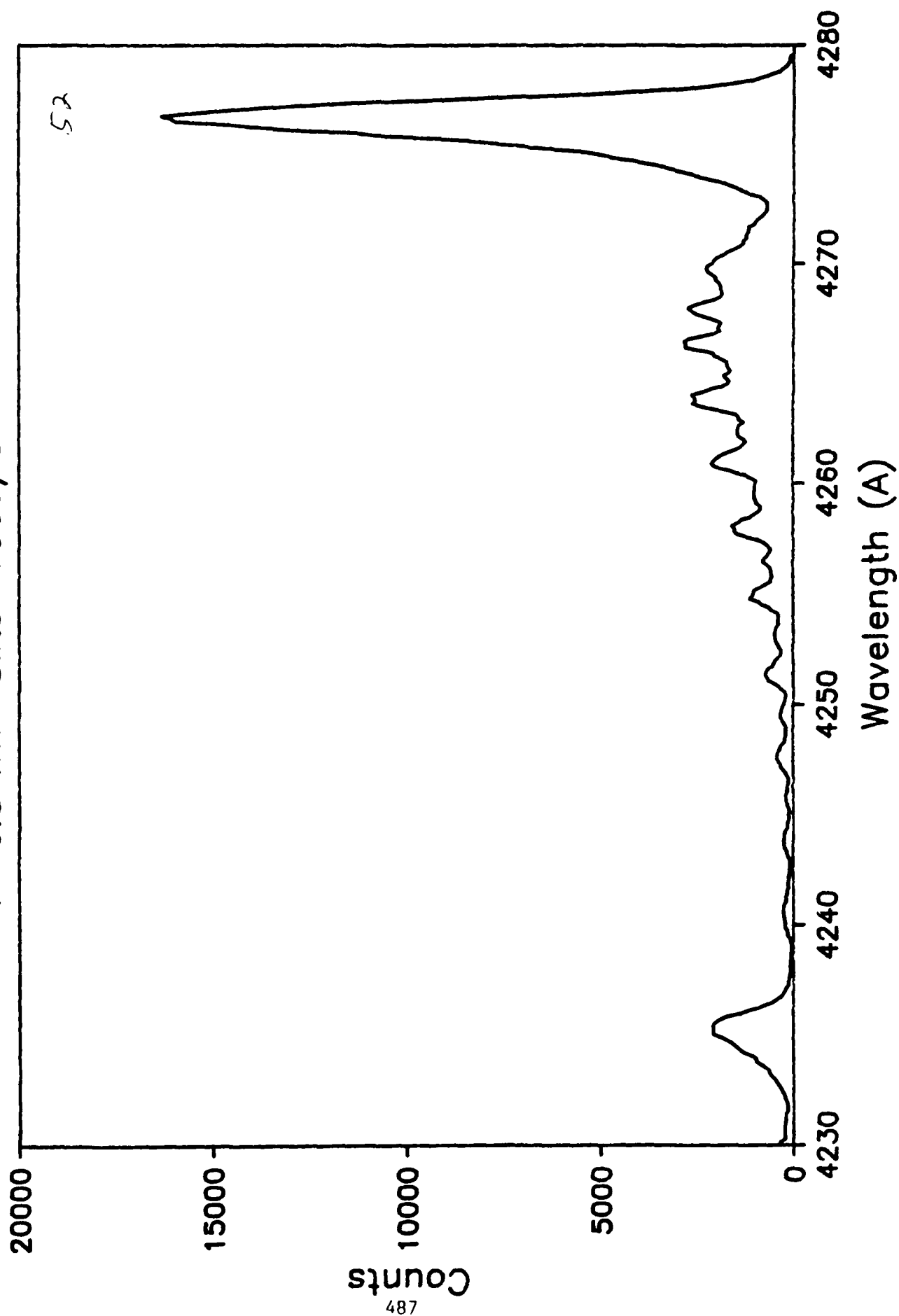
P=2.2 mT Slits=100u/50mm



H2+ at 1.0 MeV on N2  
P=4.1 mT Slits=100u/50mm

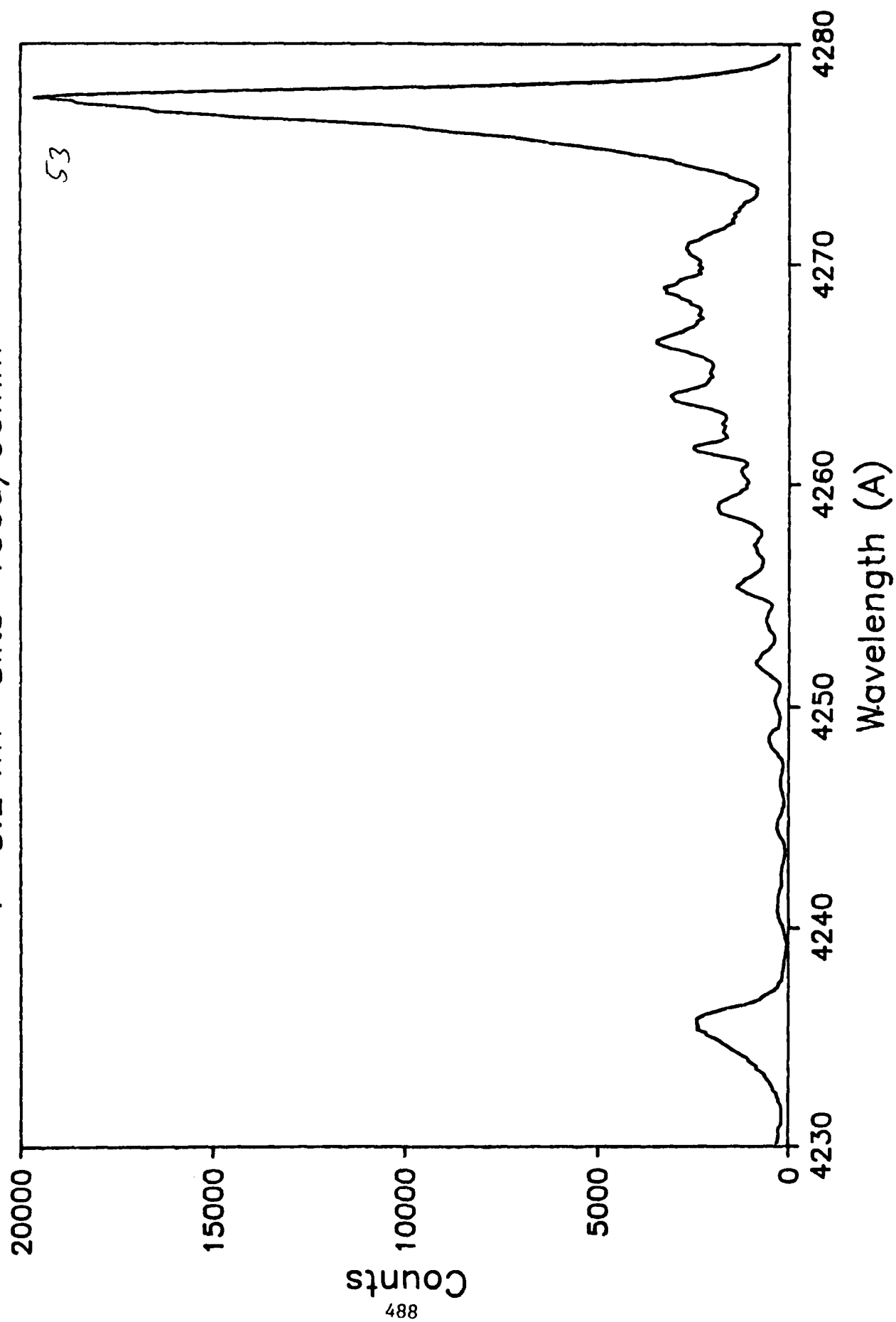


H2+ at 1.0 MeV on N2  
P=6.5 mT Slits=100u/50mm

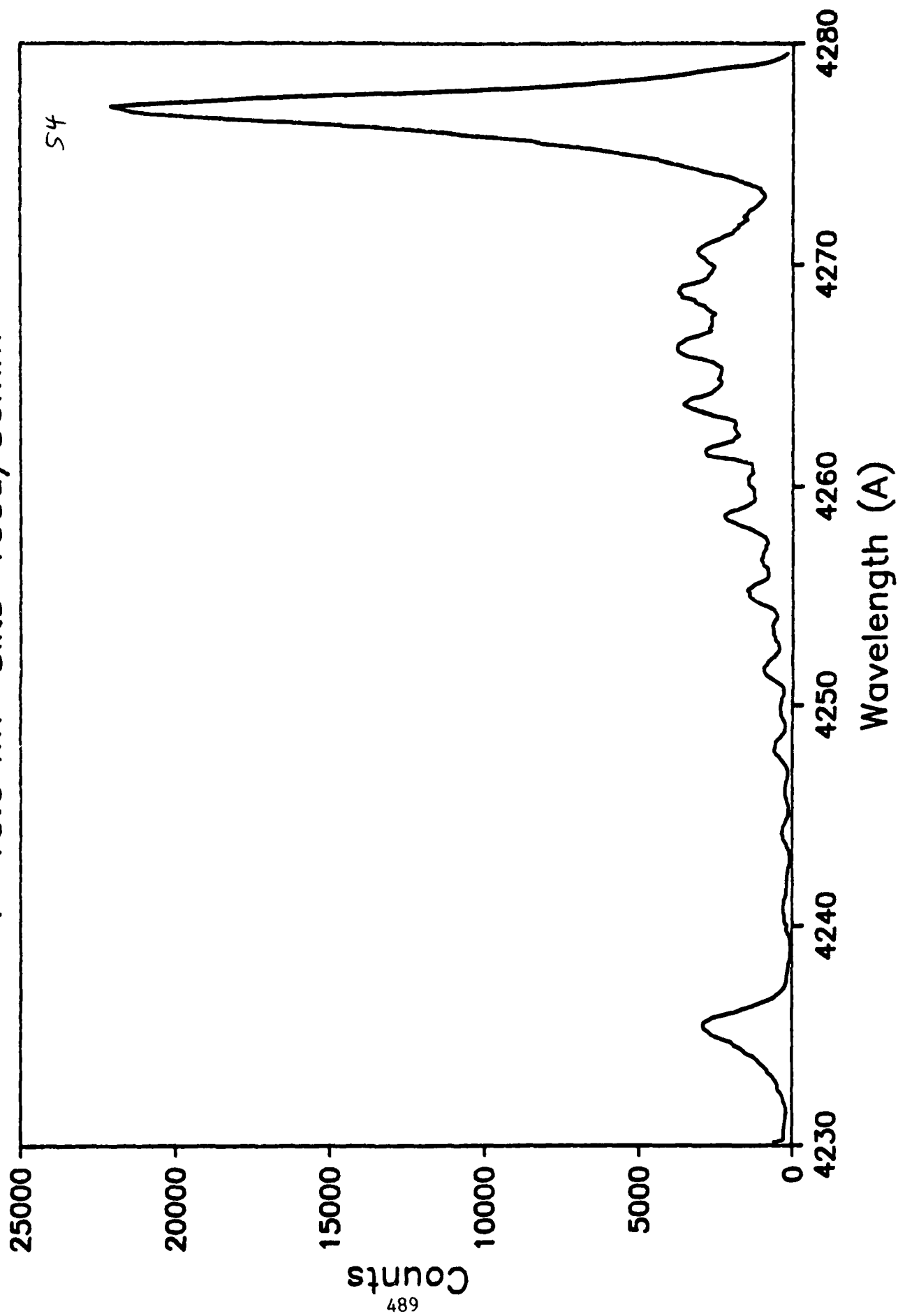




H2+ at 1.0 MeV on N2  
P=8.2 mT Slits=100u/50mm

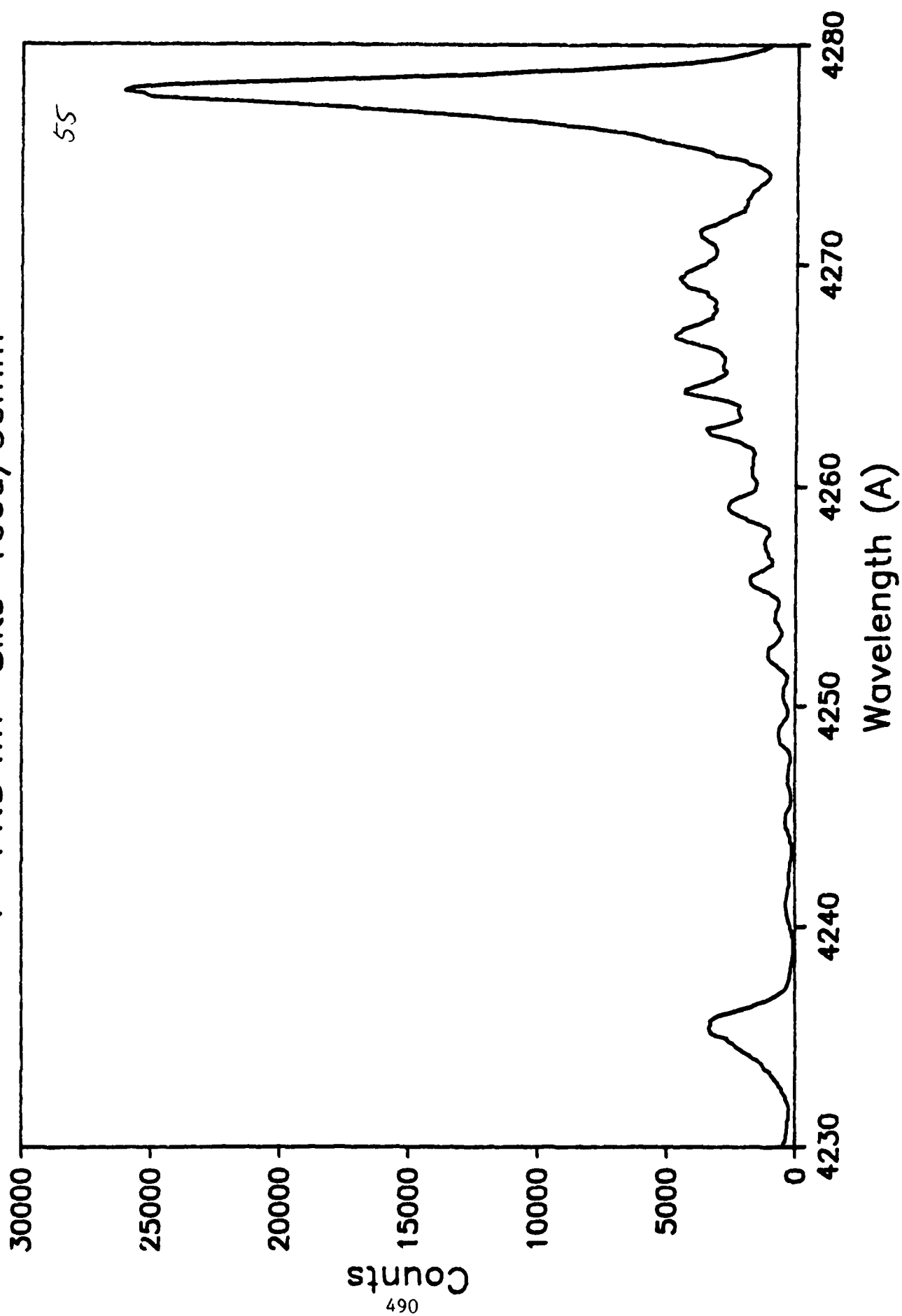


H2+ at 1.0 MeV on N2  
P=10.0 mT Slits=100u/50mm

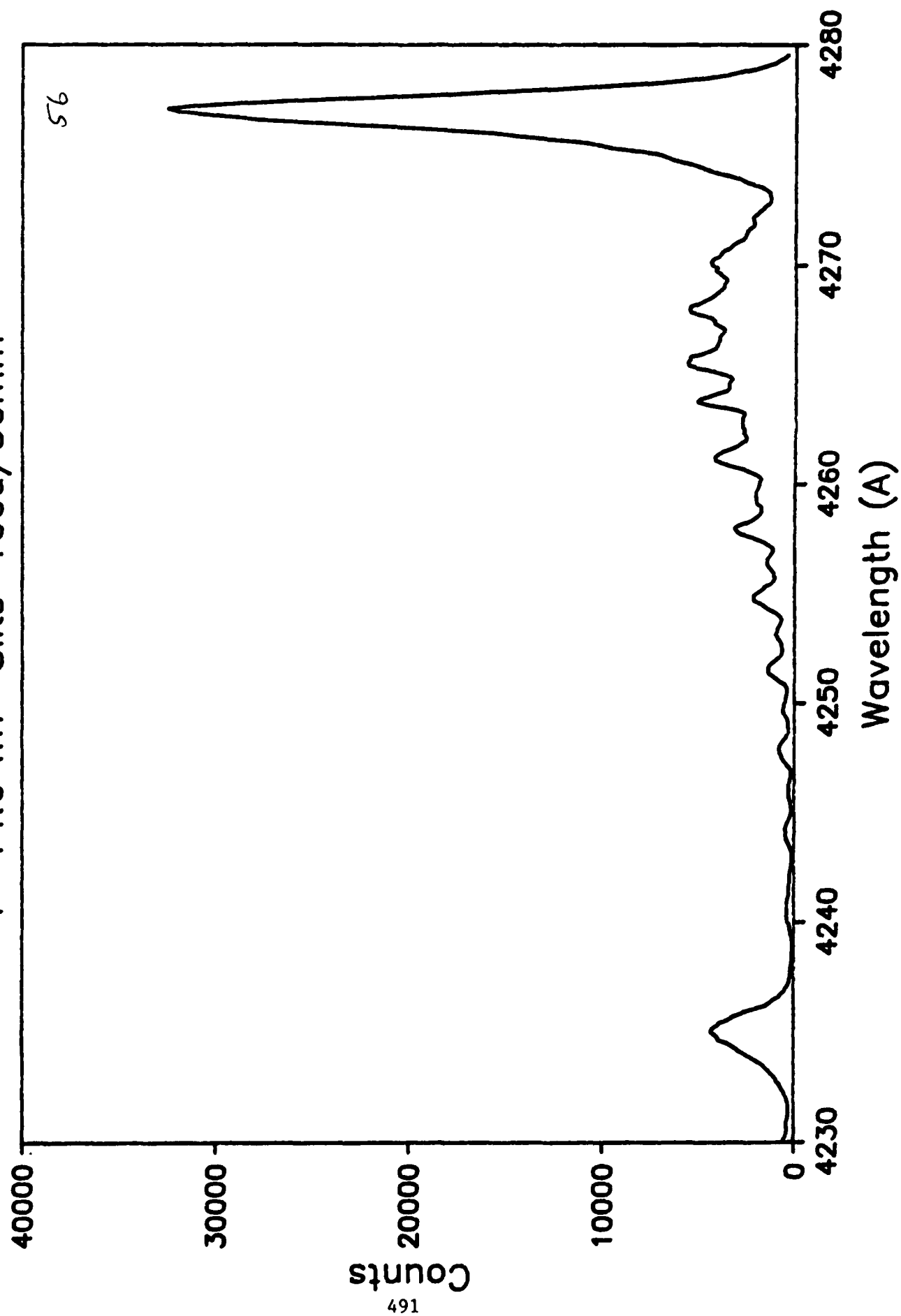


H2+ at 1.0 MeV on N2

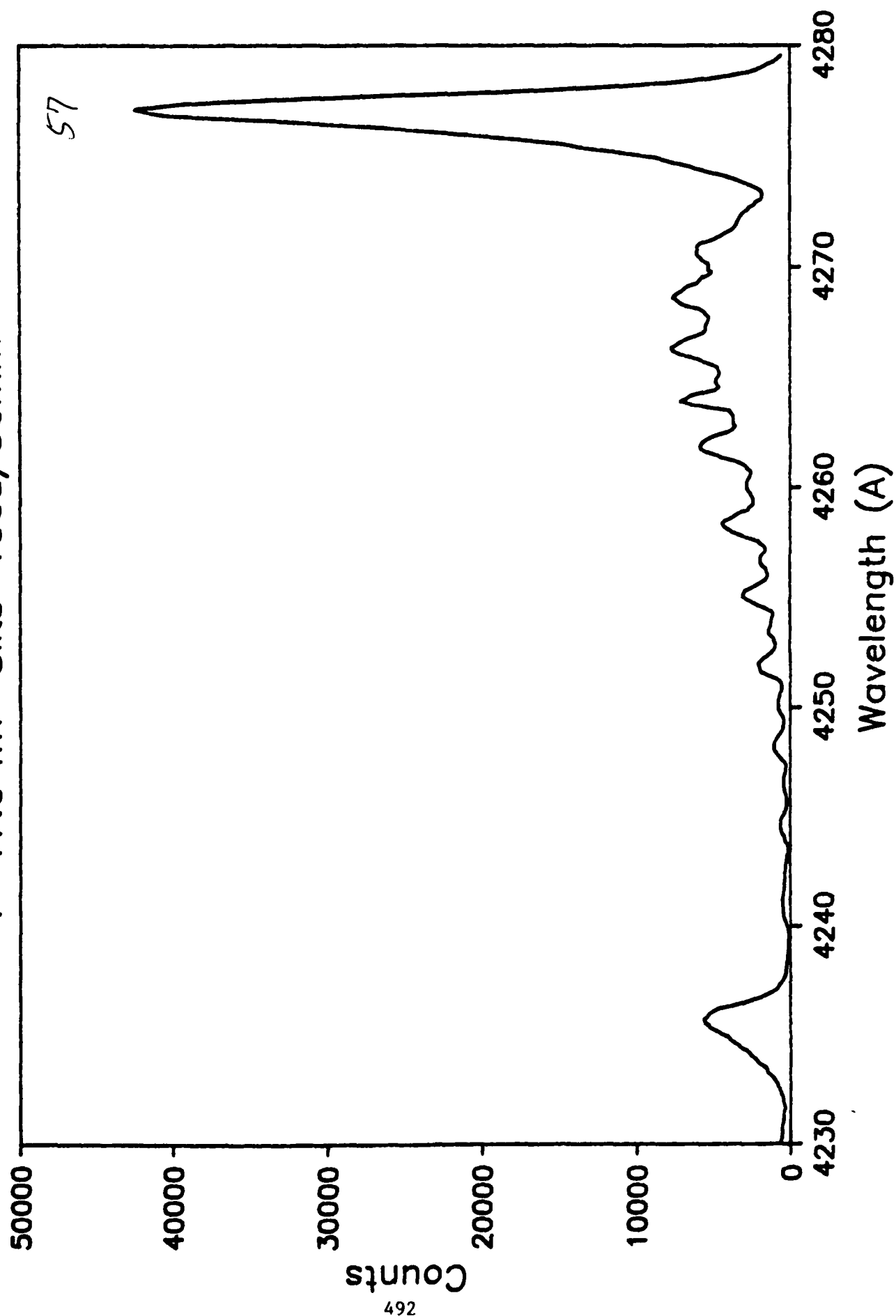
P=11.8 mT Slits=100u/50mm



H2+ at 1.0 MeV on N2  
P=14.0 mT Slits=100u/50mm

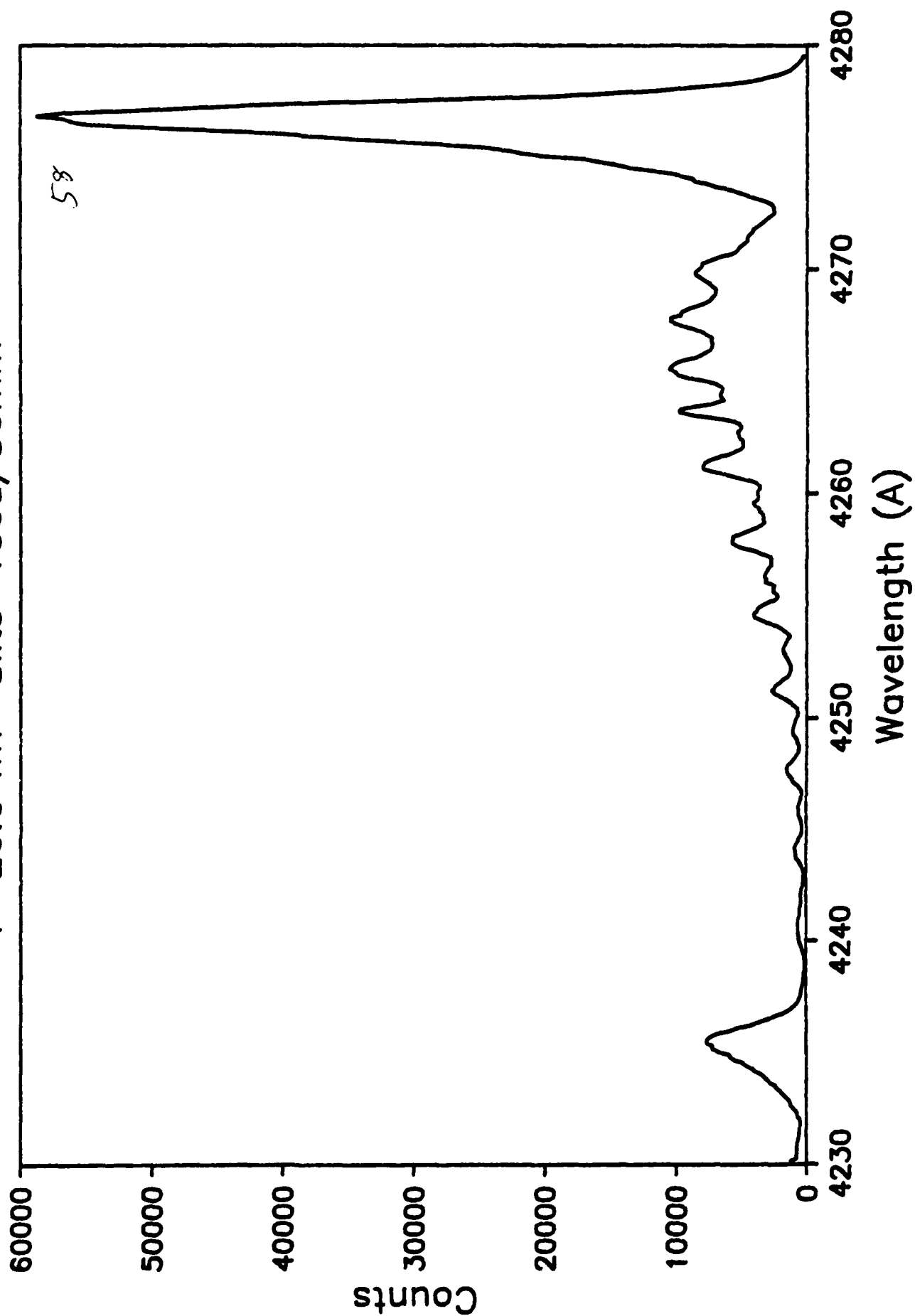


H2+ at 1.0 MeV on N2  
P=17.0 mT Slits=100u/50mm



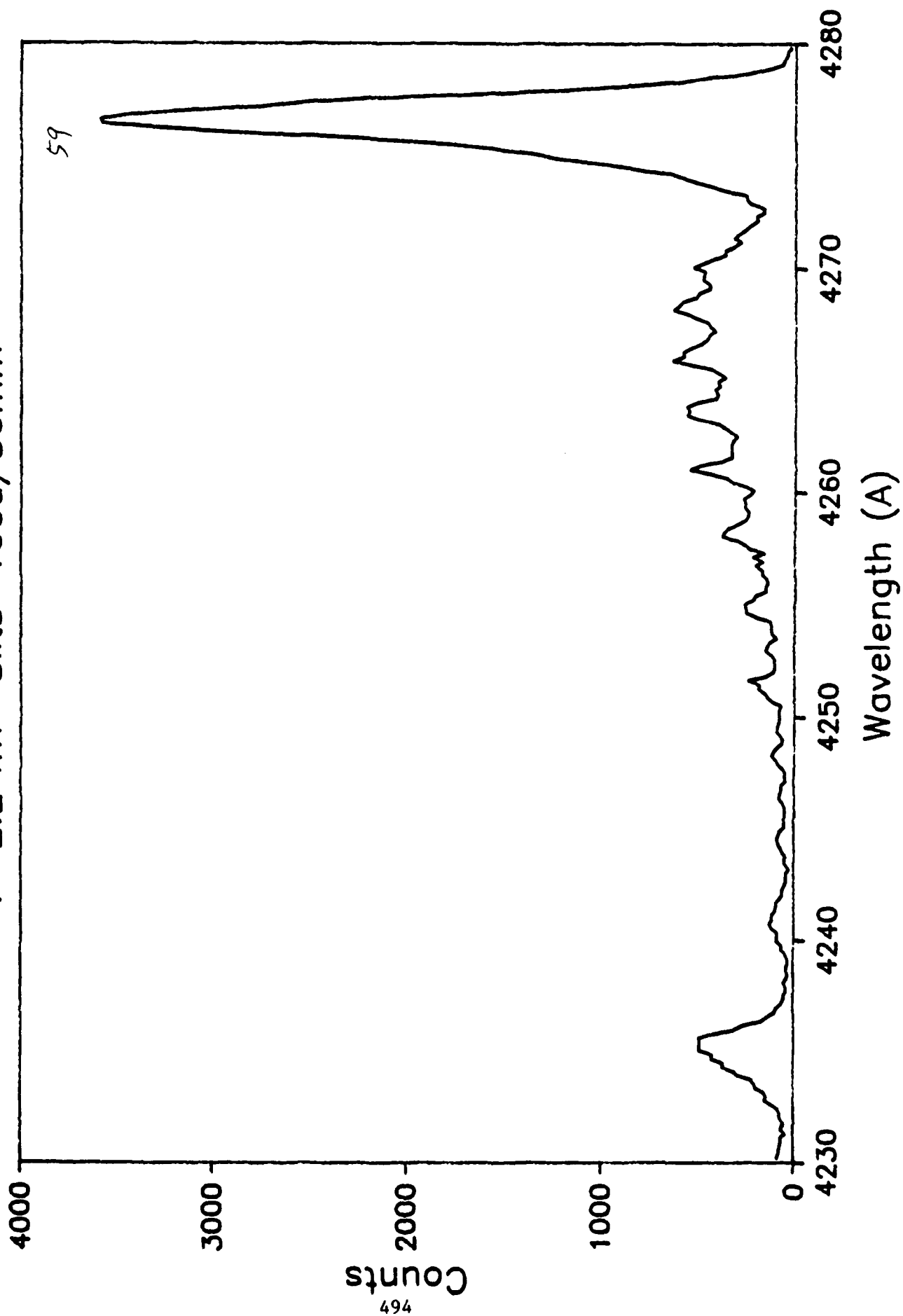
H2+ at 1.0 MeV on N2

P=20.0 mT Slits=100u/50mm

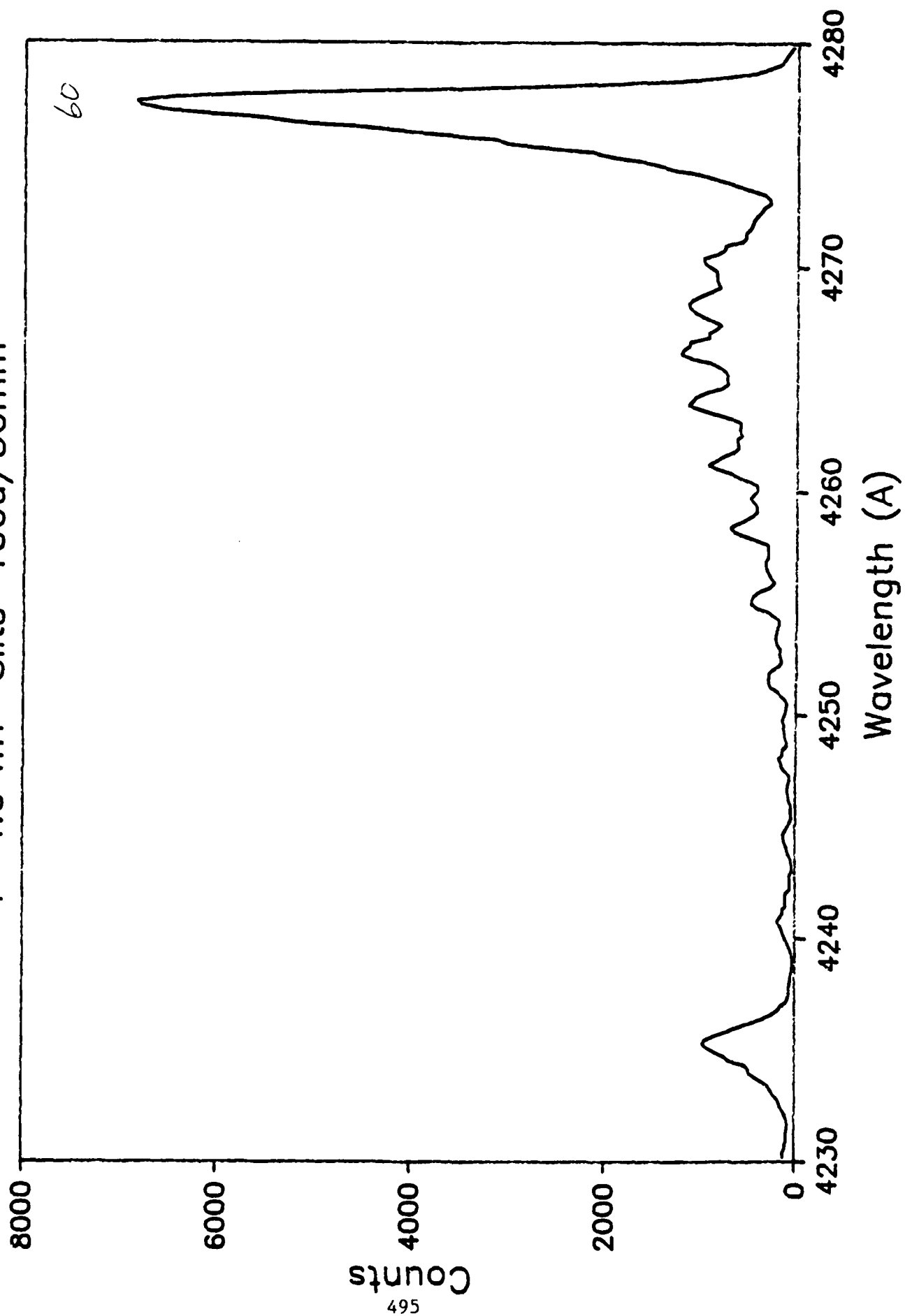


H3+ at 1.5 MeV on N2

P=2.2 mT Slits=100u/50mm



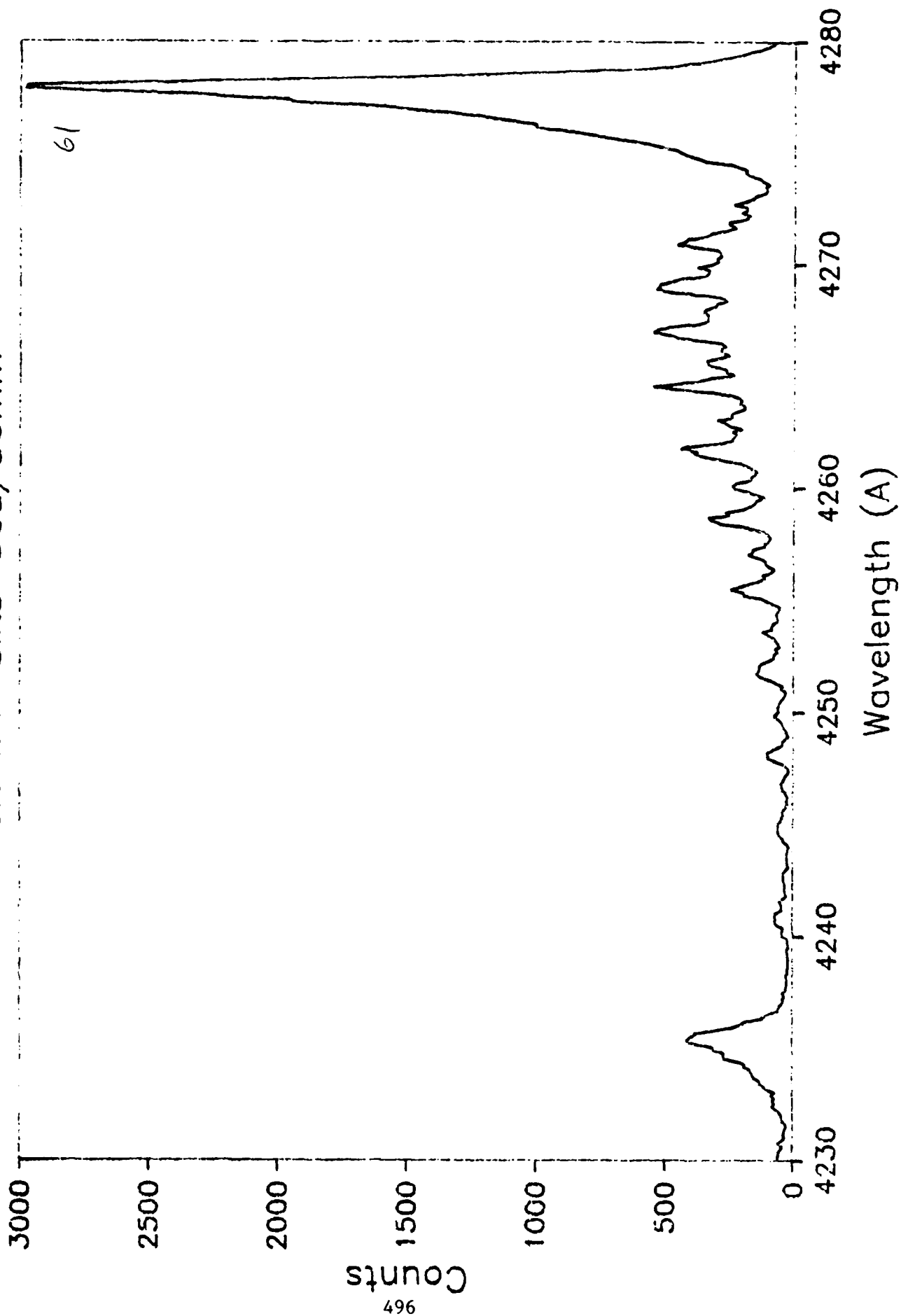
H3+ at 1.5 MeV on N2  
P=4.0 mT Slits=100u/50mm



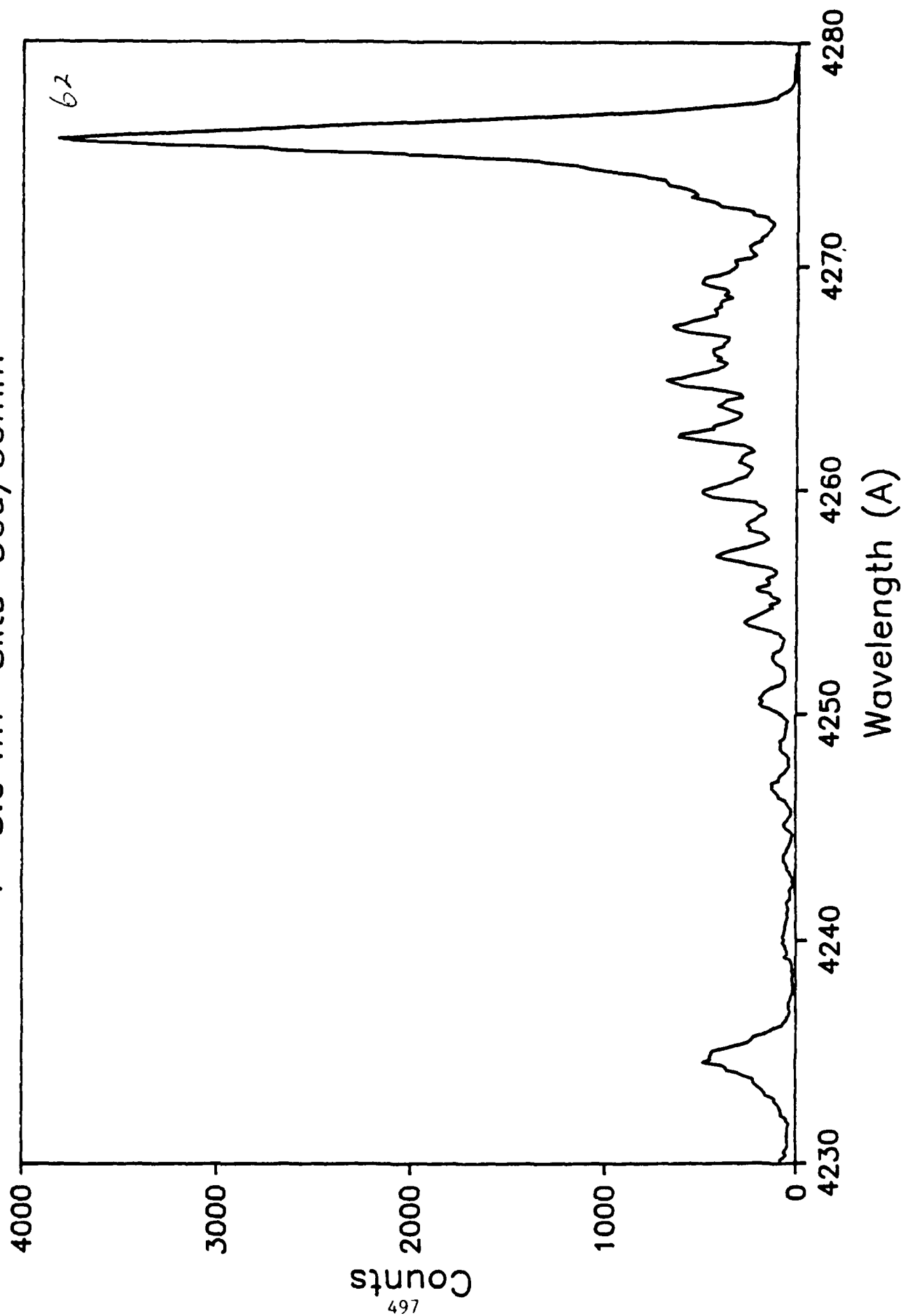


H3+ at 1.5 MeV on N2

P=6.0 mT Slits=50u/50mm

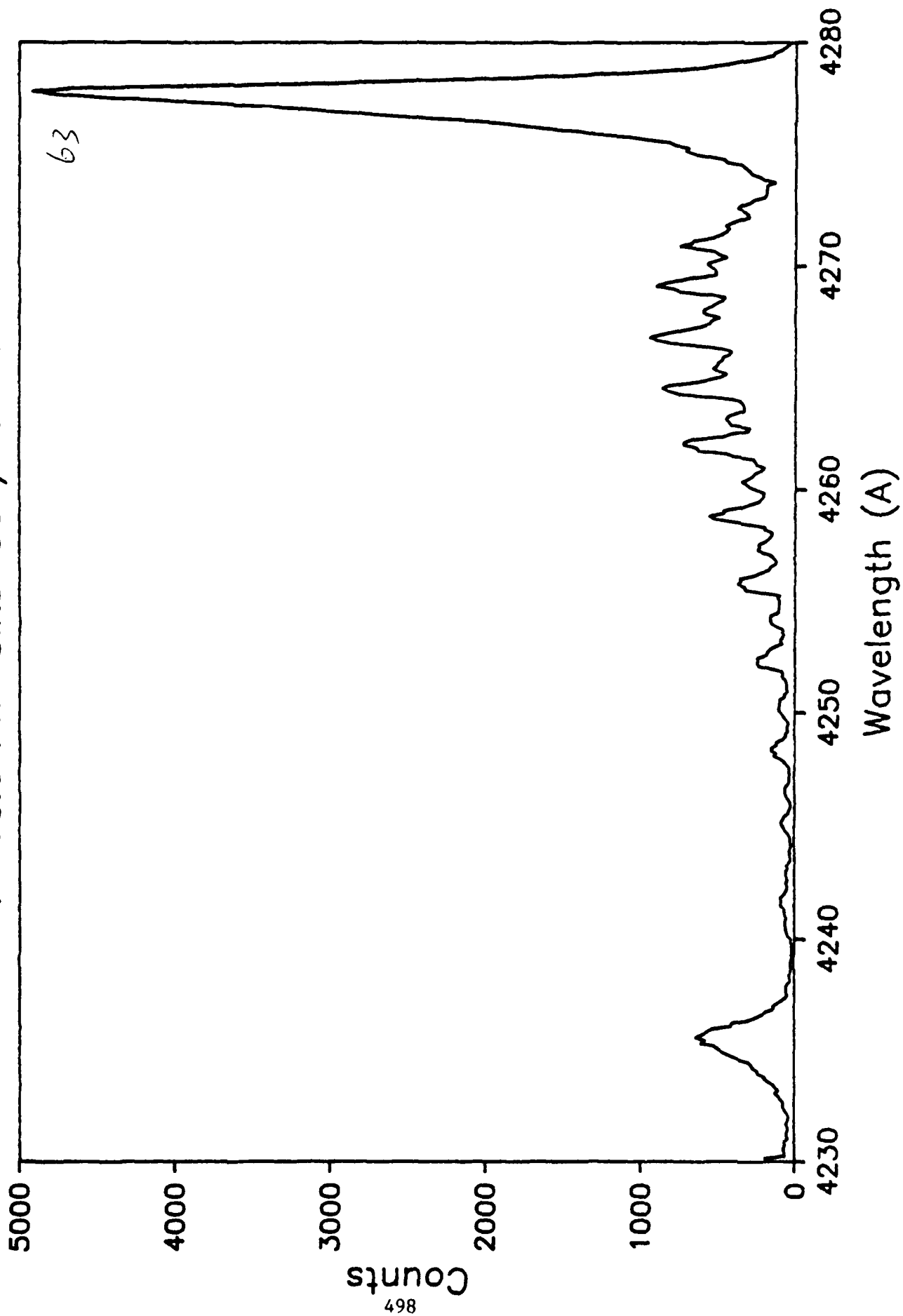


H3+ at 1.5 MeV on N2  
P=8.0 mT Slits=50u/50mm



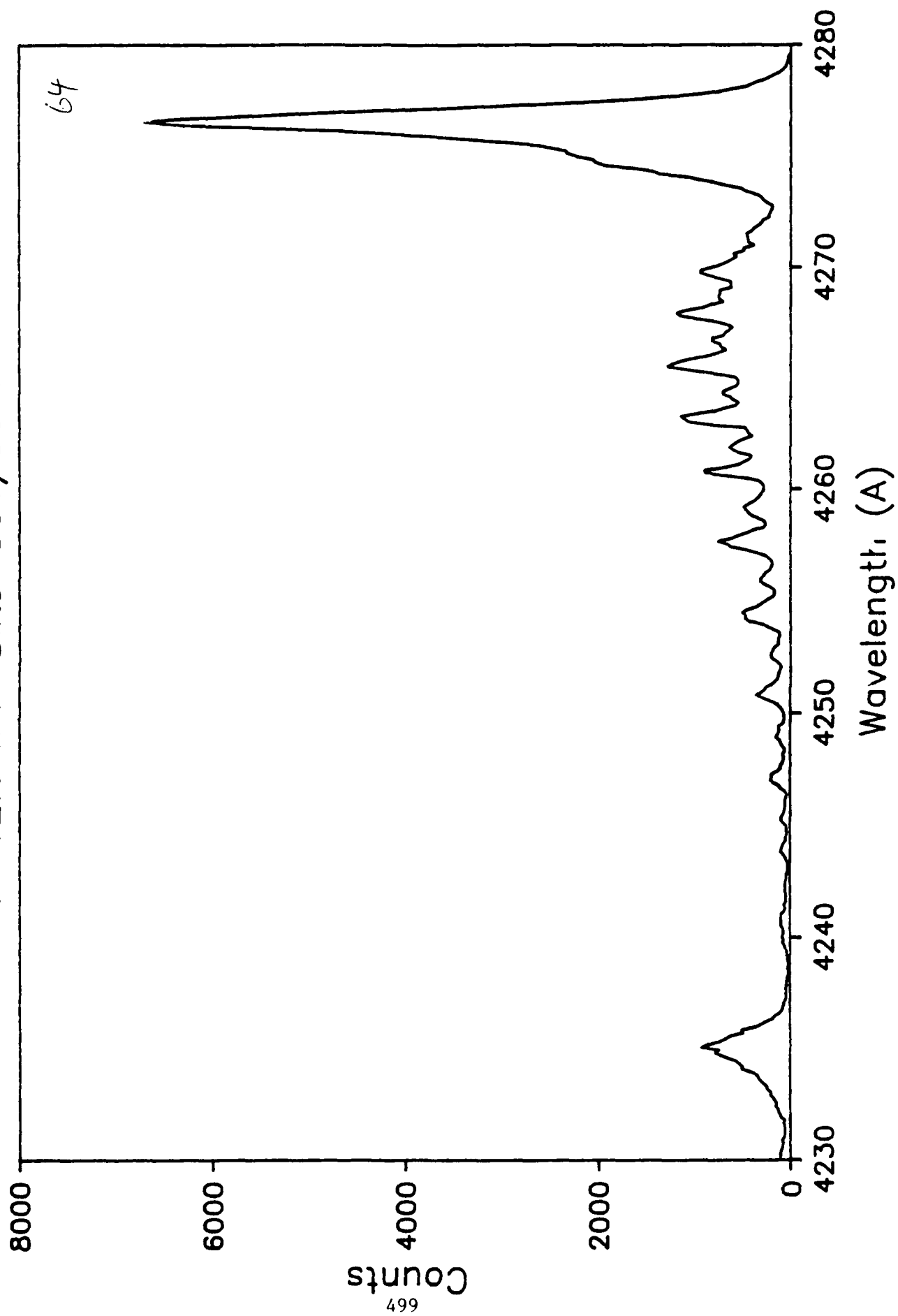
H3+ at 1.5 MeV on N2

P=10.0 mT Slits=50u/50mm



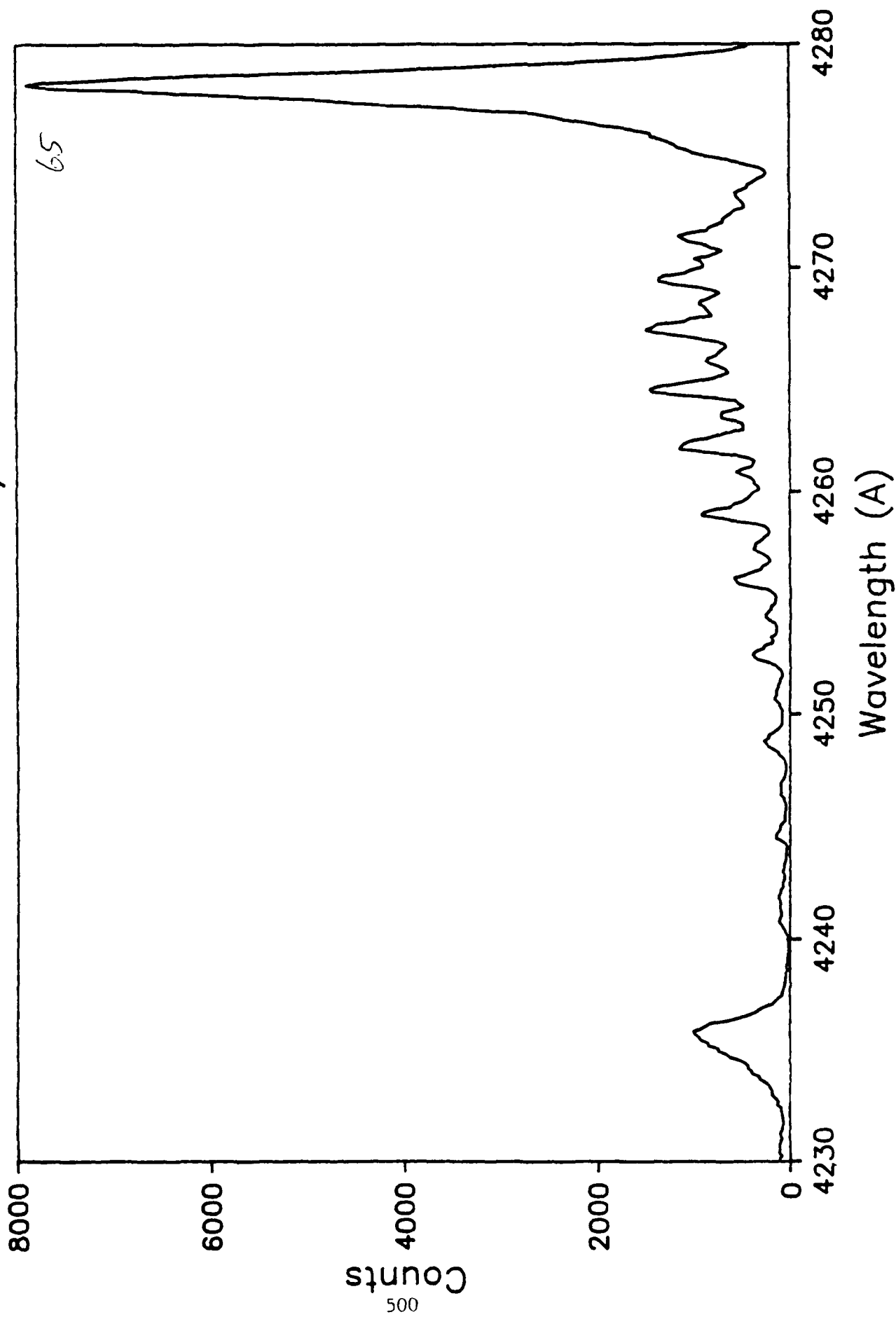
H3+ at 1.5 MeV on N2

P=12.0 mT Slits=50u/50mm

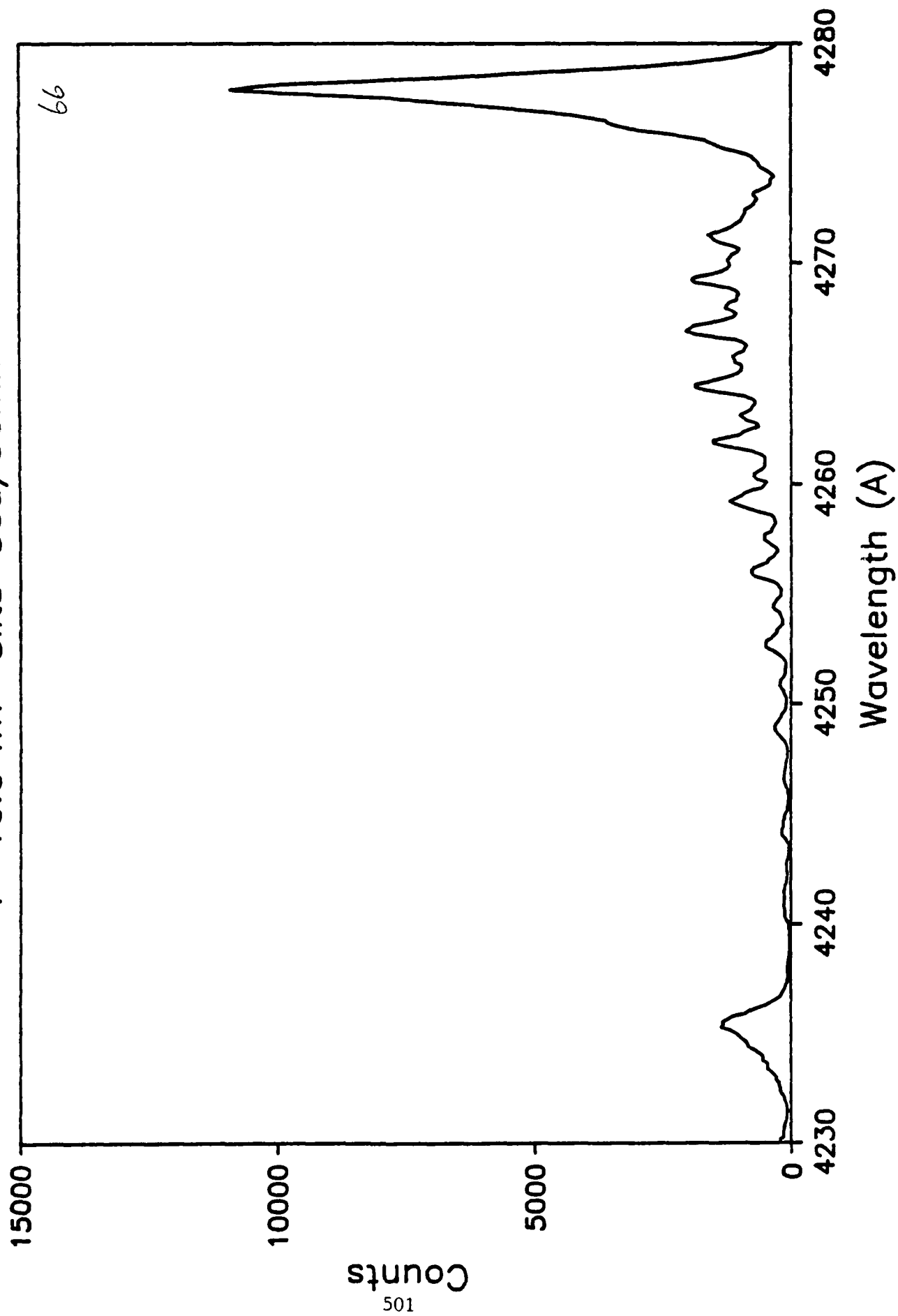


H3+ at 1.5 MeV on N2

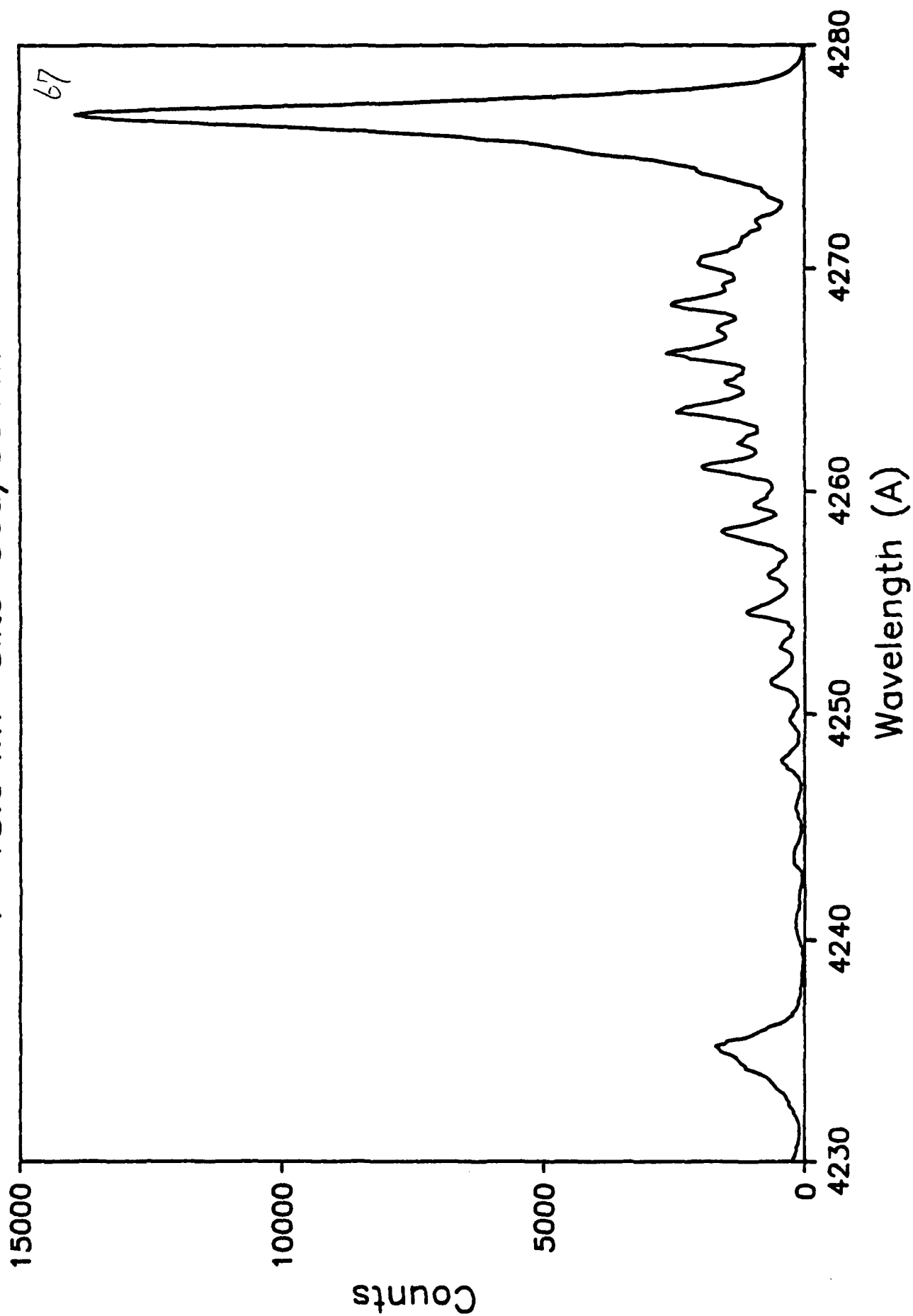
P=14.0 mT Slits=50u/50mm



H3+ at 1.5 MeV on N2  
P=16.0 mT Slits=50u/50mm

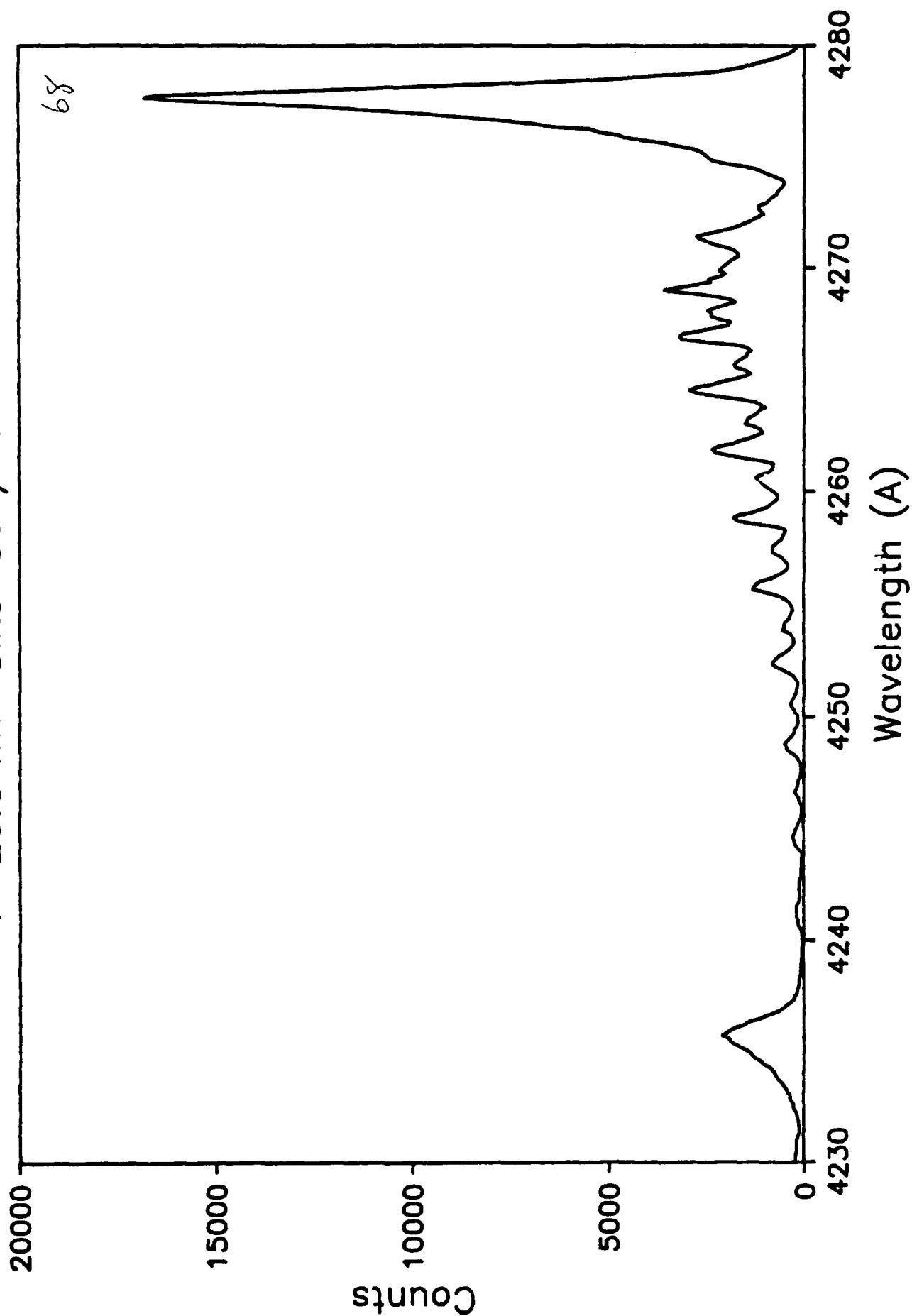


H3+ at 1.5 MeV on N2  
P=18.0 mT Slits=50u/50mm



H3+ at 1.5 MeV on N2

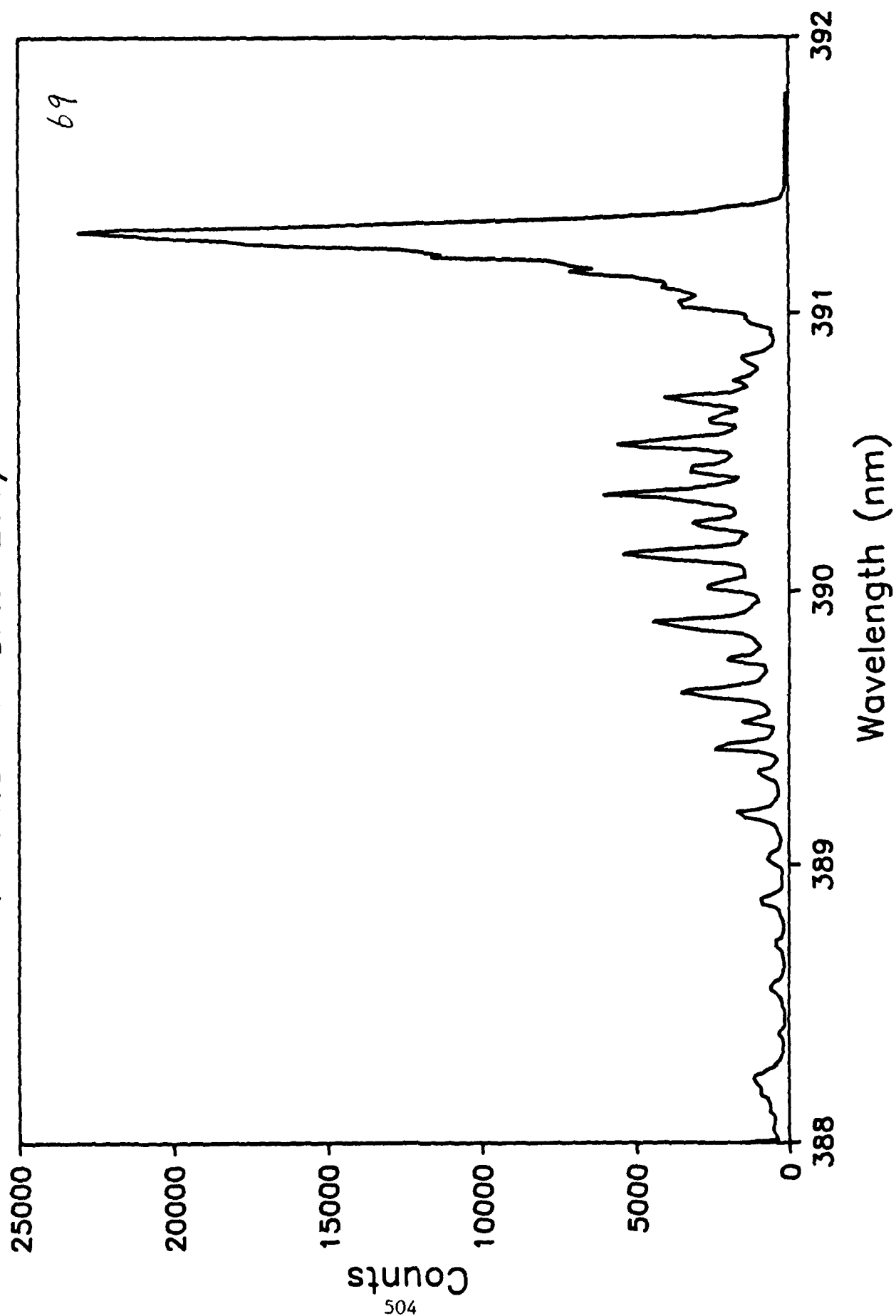
P=20.0 mT Slits=50u/50mm



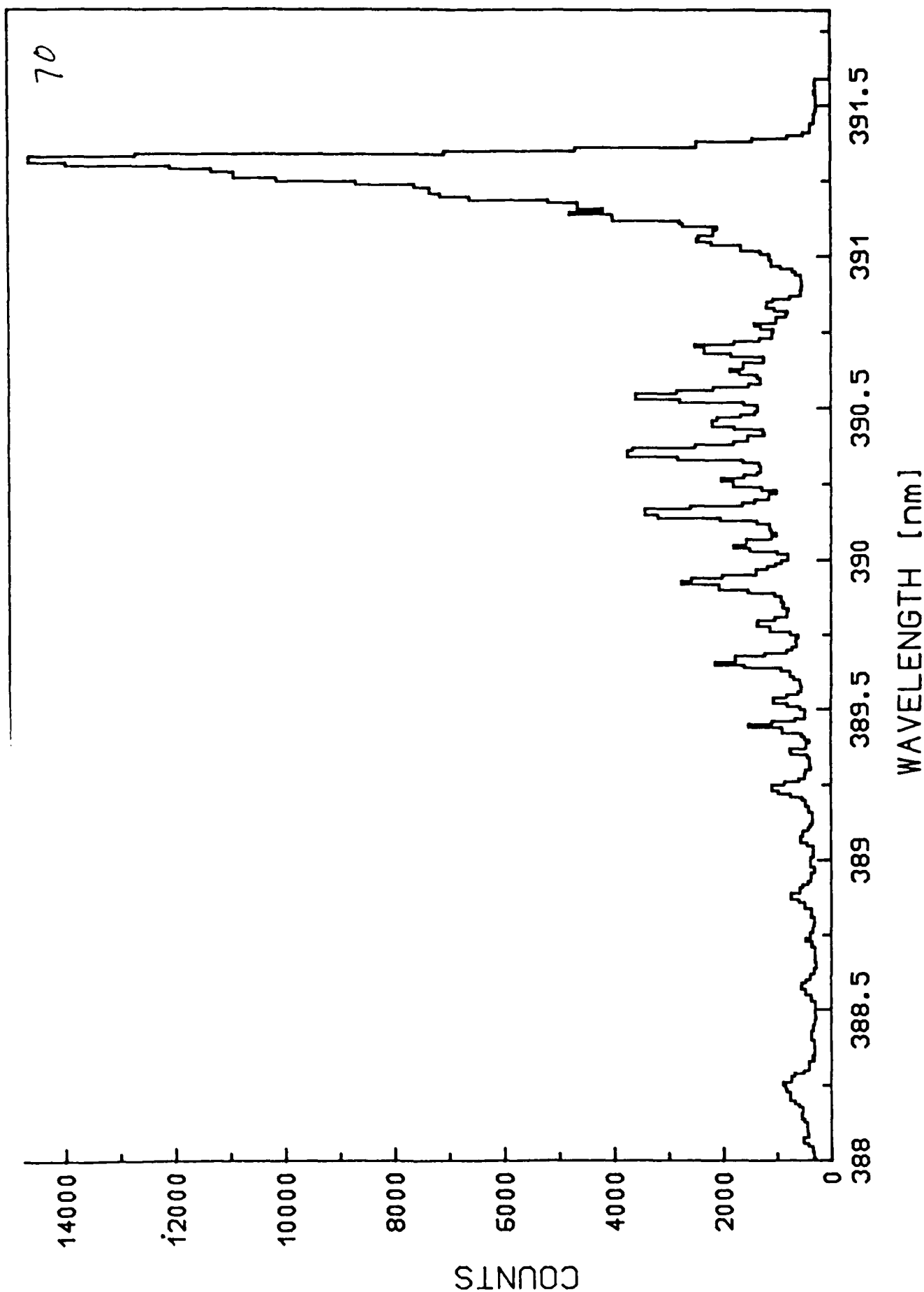


H2+ at 0.5 MeV on N2

P=14.0 mT Slits=25u/20mm

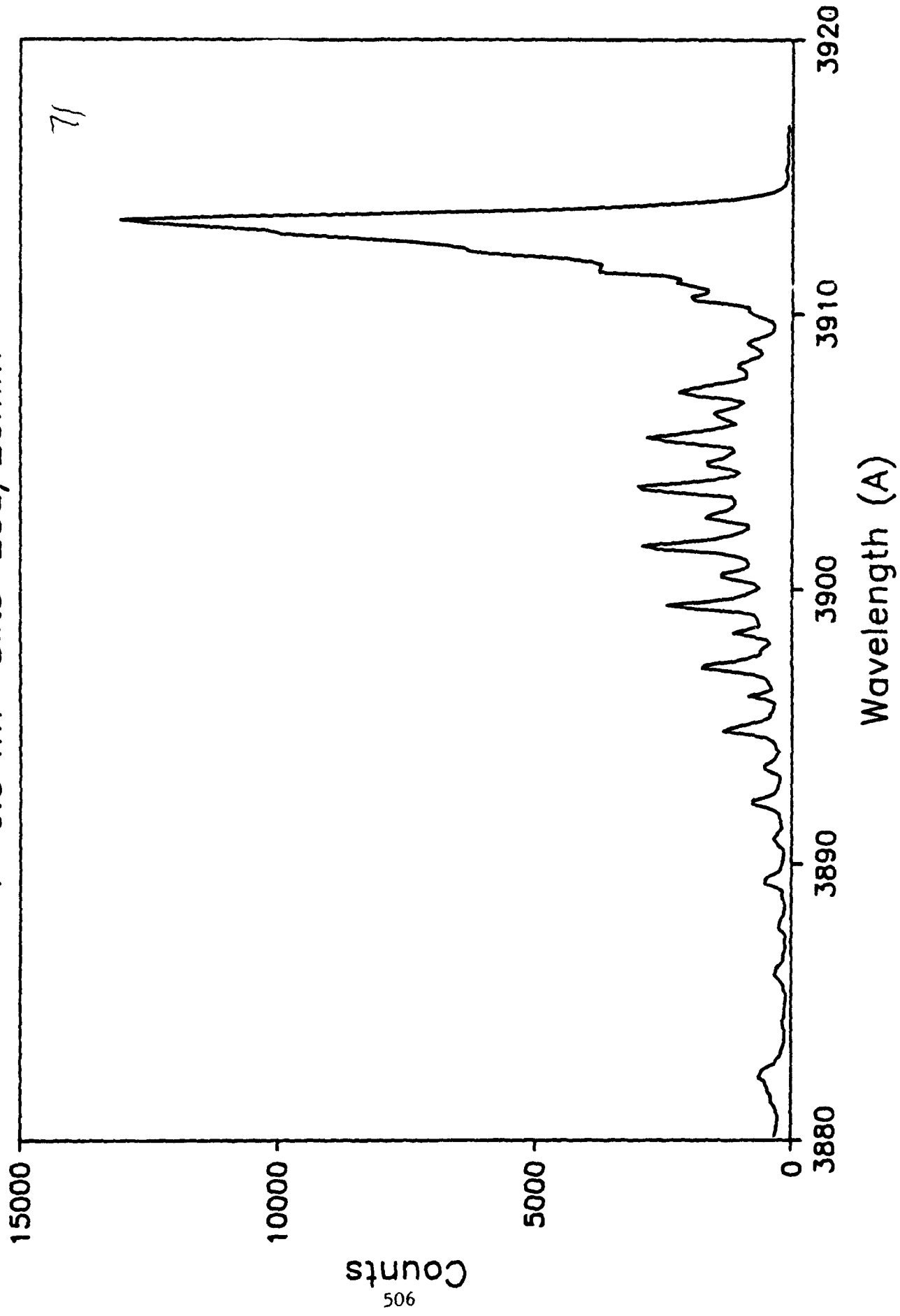


H2+ at 1.0 MeV on N2  
P=14.3 mT slits=25u/20mm

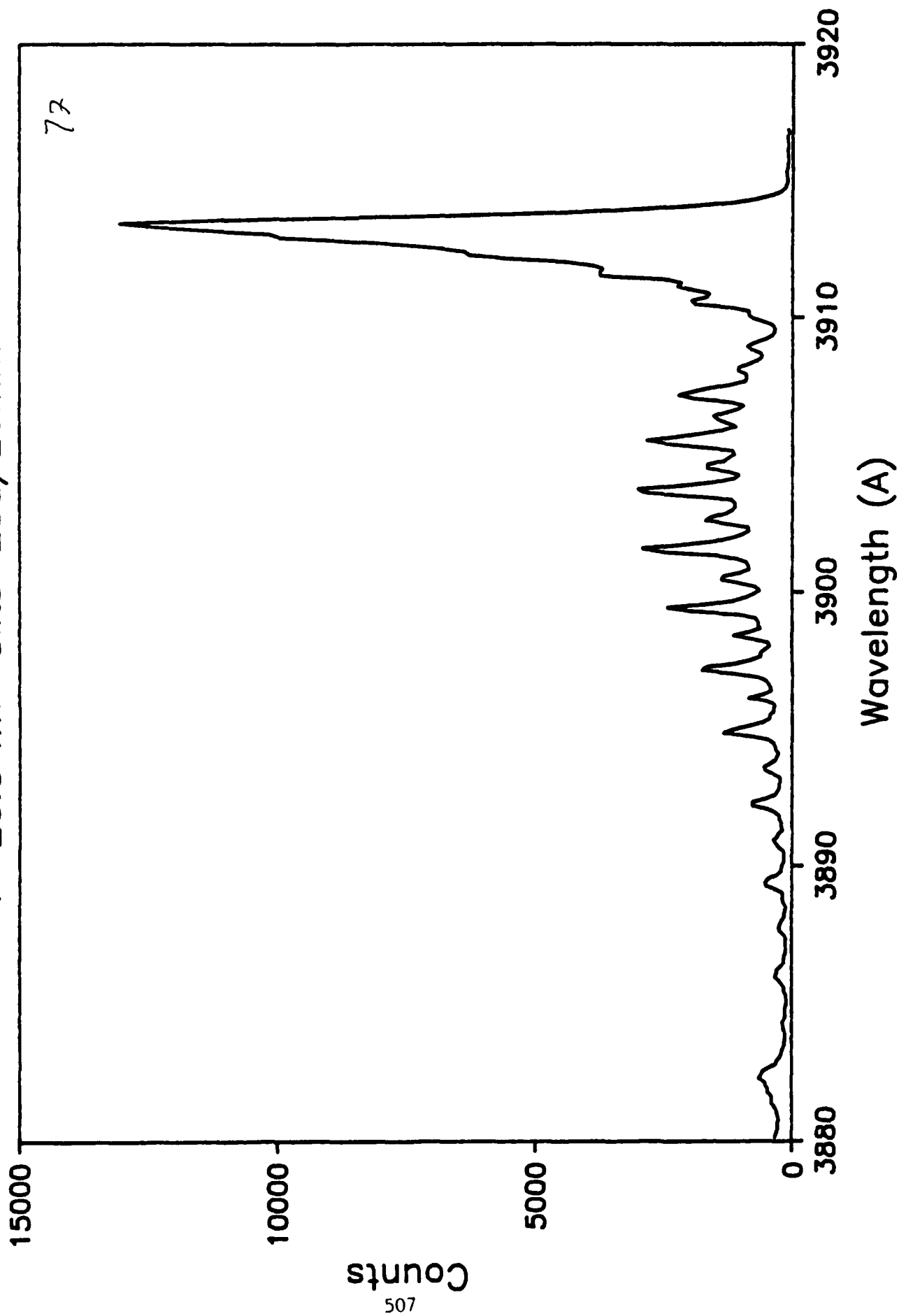


H3+ at 0.5 MeV on N2

P=6.5 mT Slits=25u/20mm

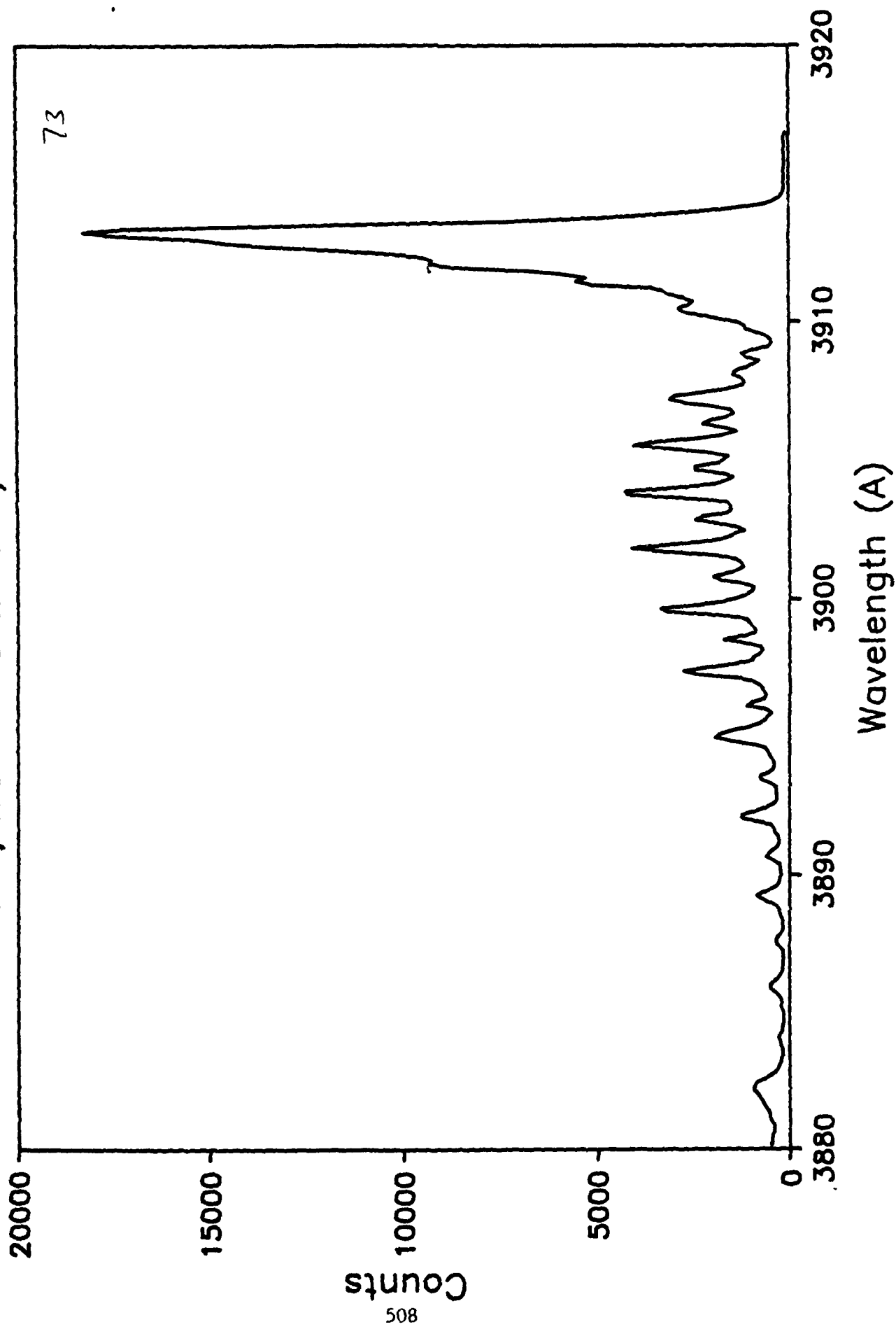


H3+ at 0.5 MeV on N2  
P=20.0 mT Slits=25u/20mm

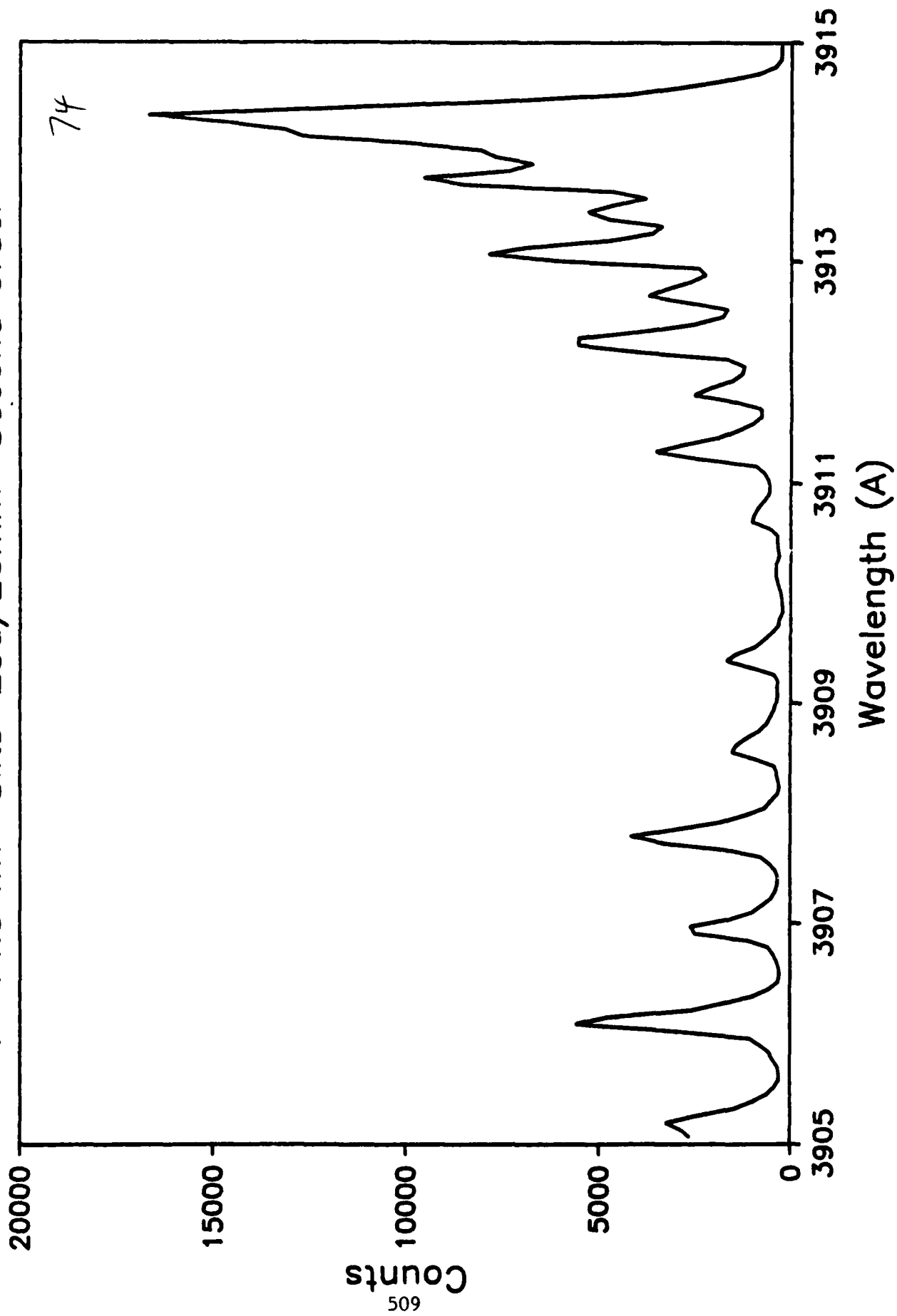


H3+ at 1.0 MeV on N2

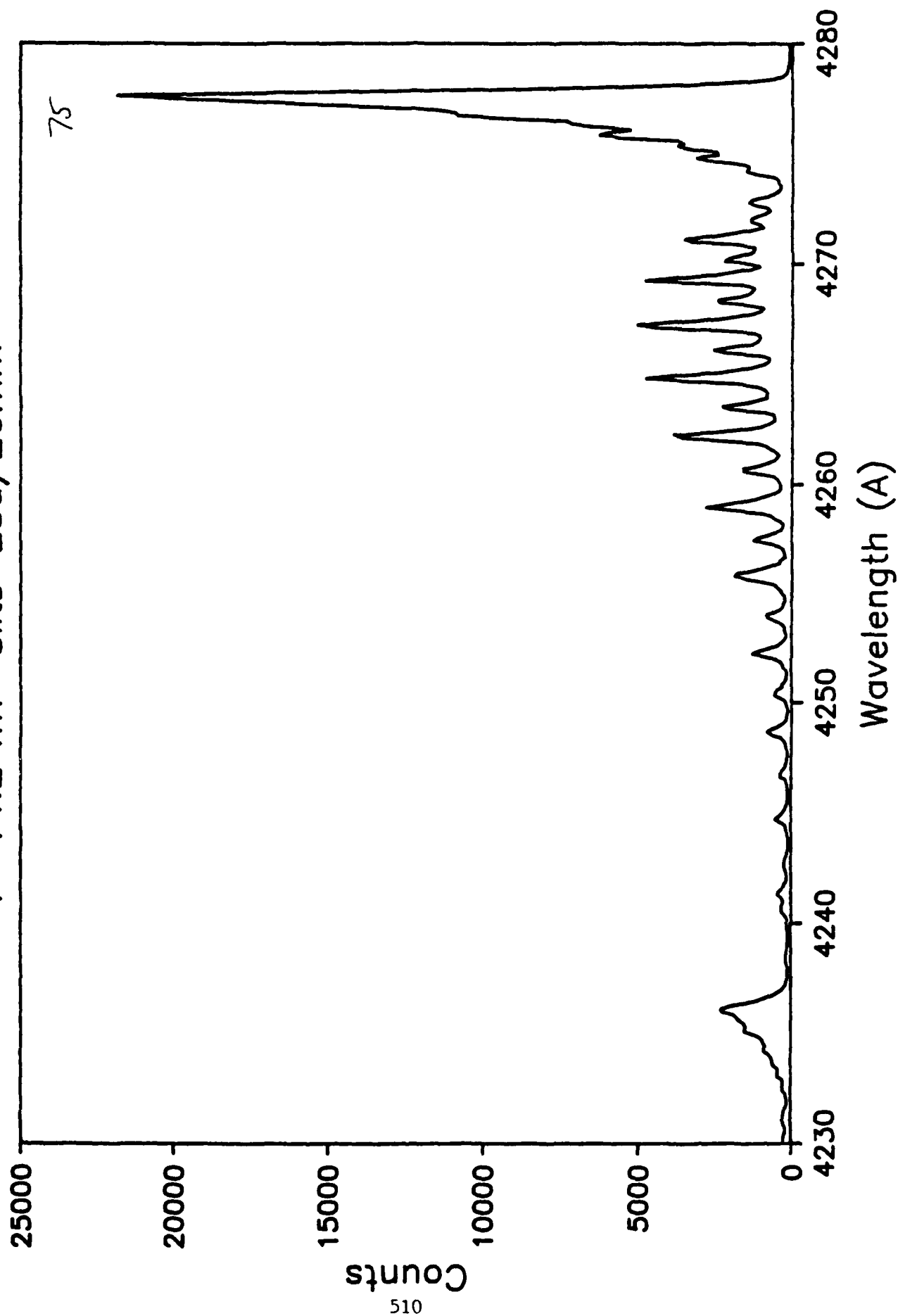
P=14.2 mT Slits=25u/20mm



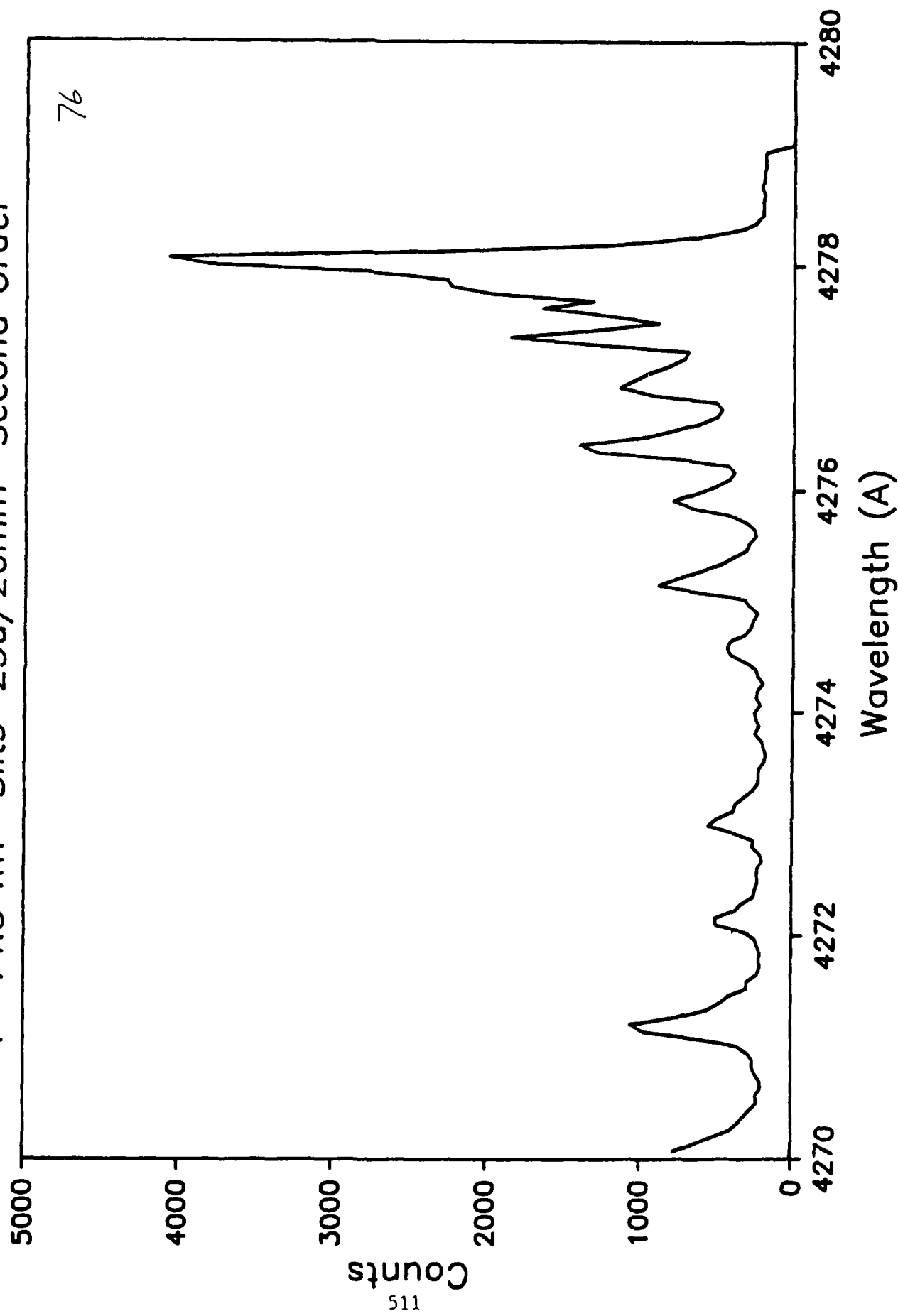
H3+ at 0.5 MeV on N2  
P=14.3 mT Slits=25u/20mm Second Order



H3+ at 0.5 MeV on N2  
P=14.2 mT Slits=25u/20mm



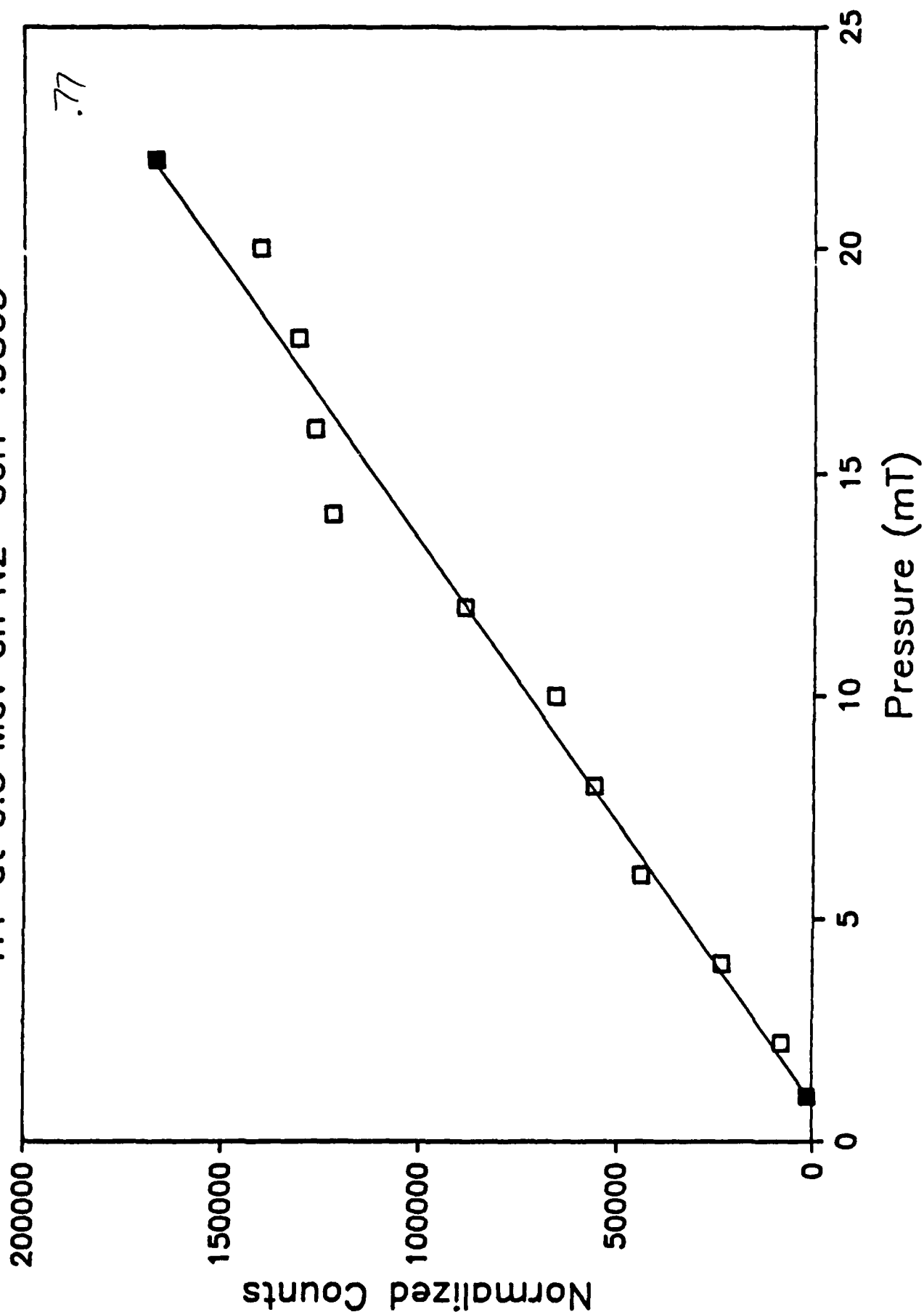
H3+ at 0.5 MeV on N2  
P=14.3 mT Slits=25u/20mm Second Order





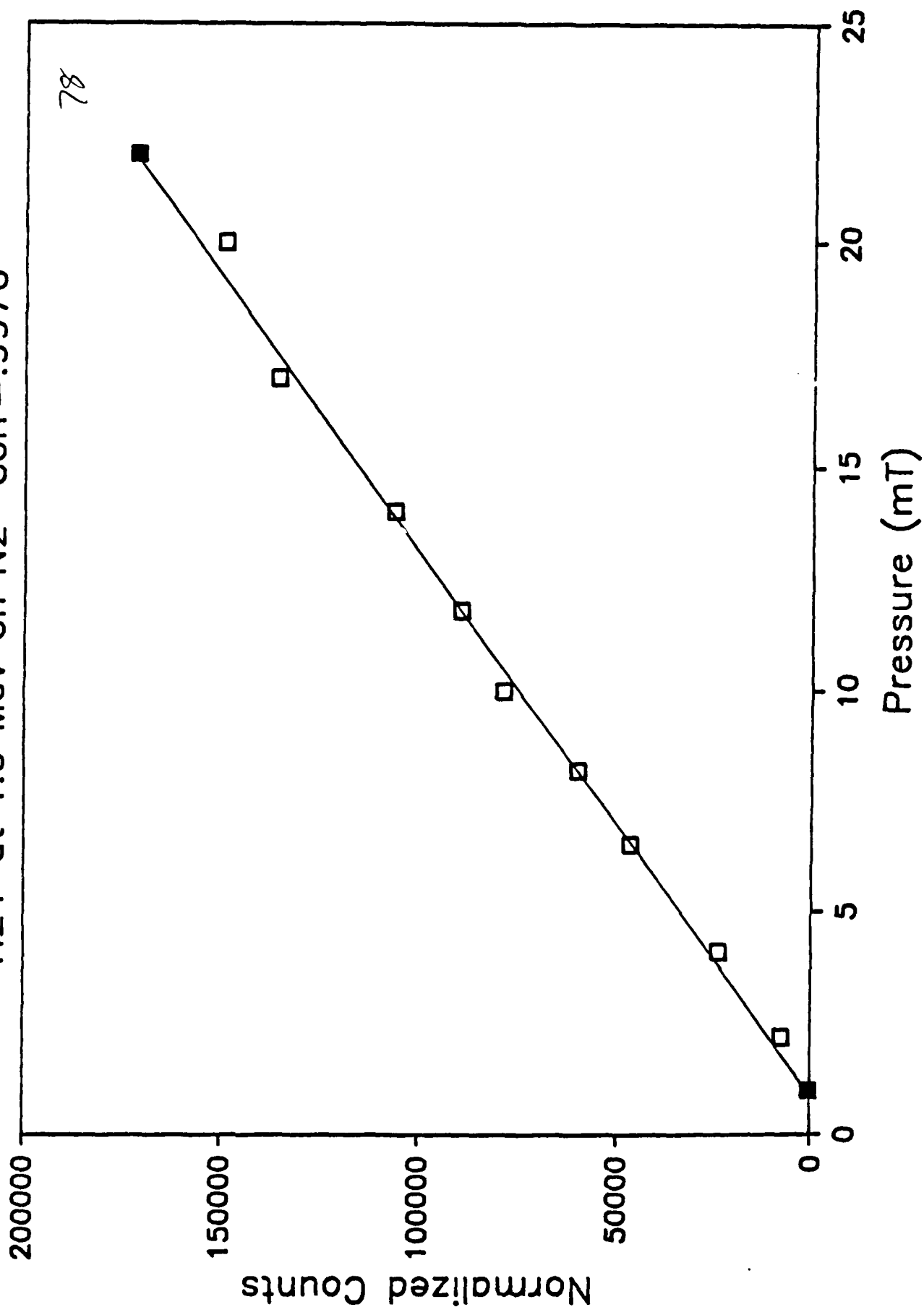
# Normalized Yield vs. Pressure: 391.4 nm

H+ at 0.5 MeV on N2 Corr=.9865



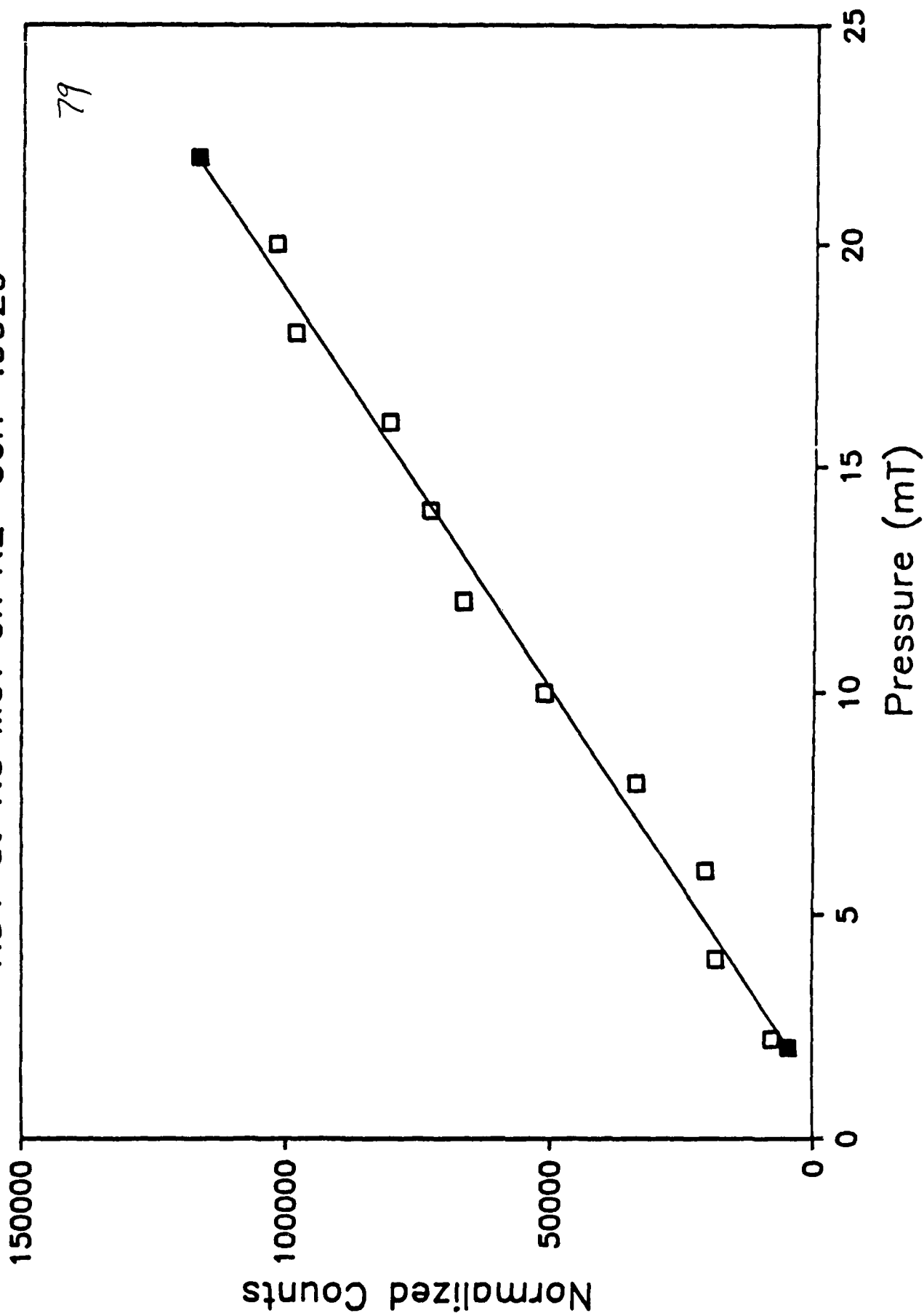
# Normalized Yield vs. Pressure: 391.4 nm

H2+ at 1.0 MeV on N2 Corr=.9976



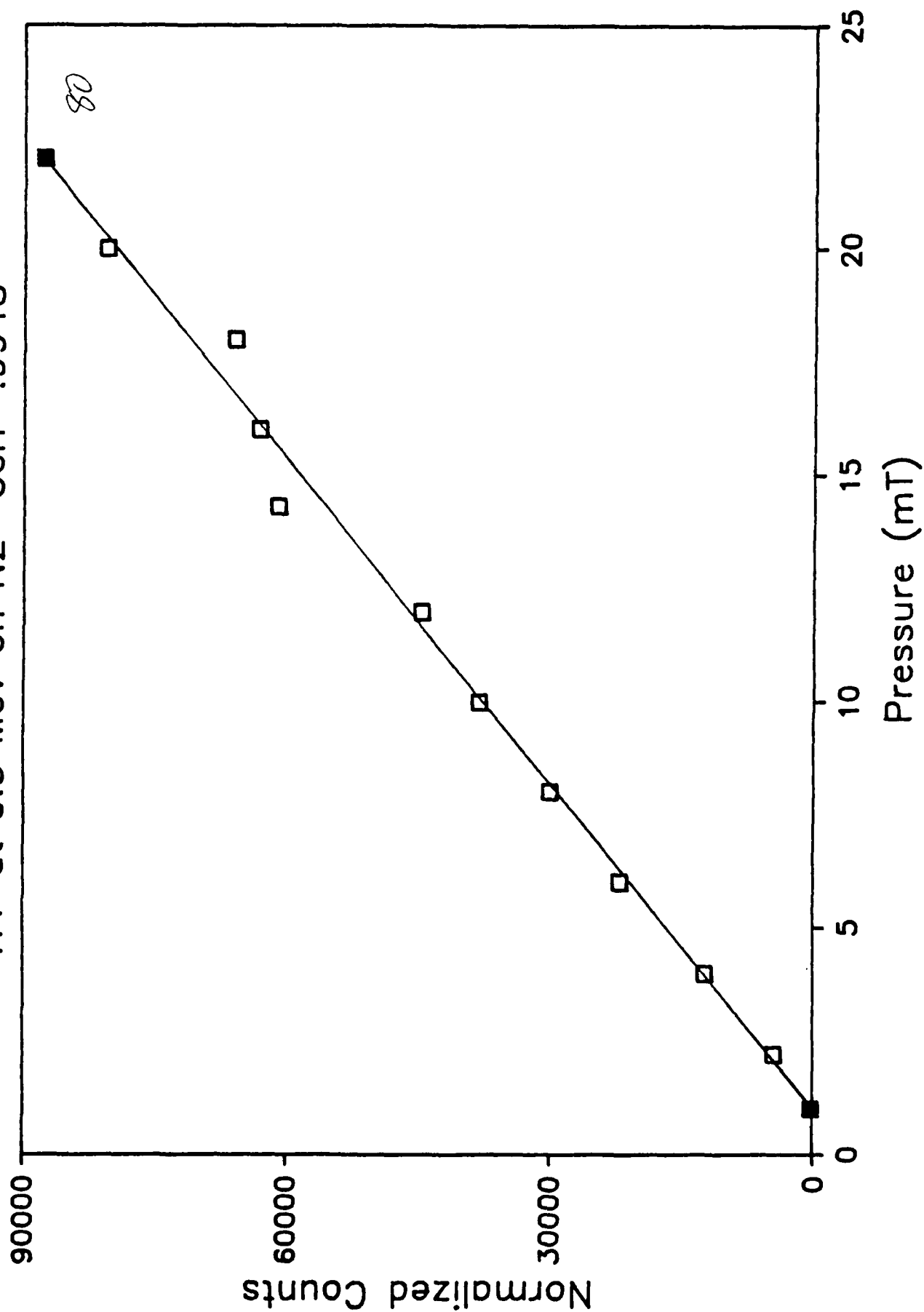
# Normalized Yield vs. Pressure: 391.4 nm

H3+ at 1.5 MeV on N2 Corr=.9929

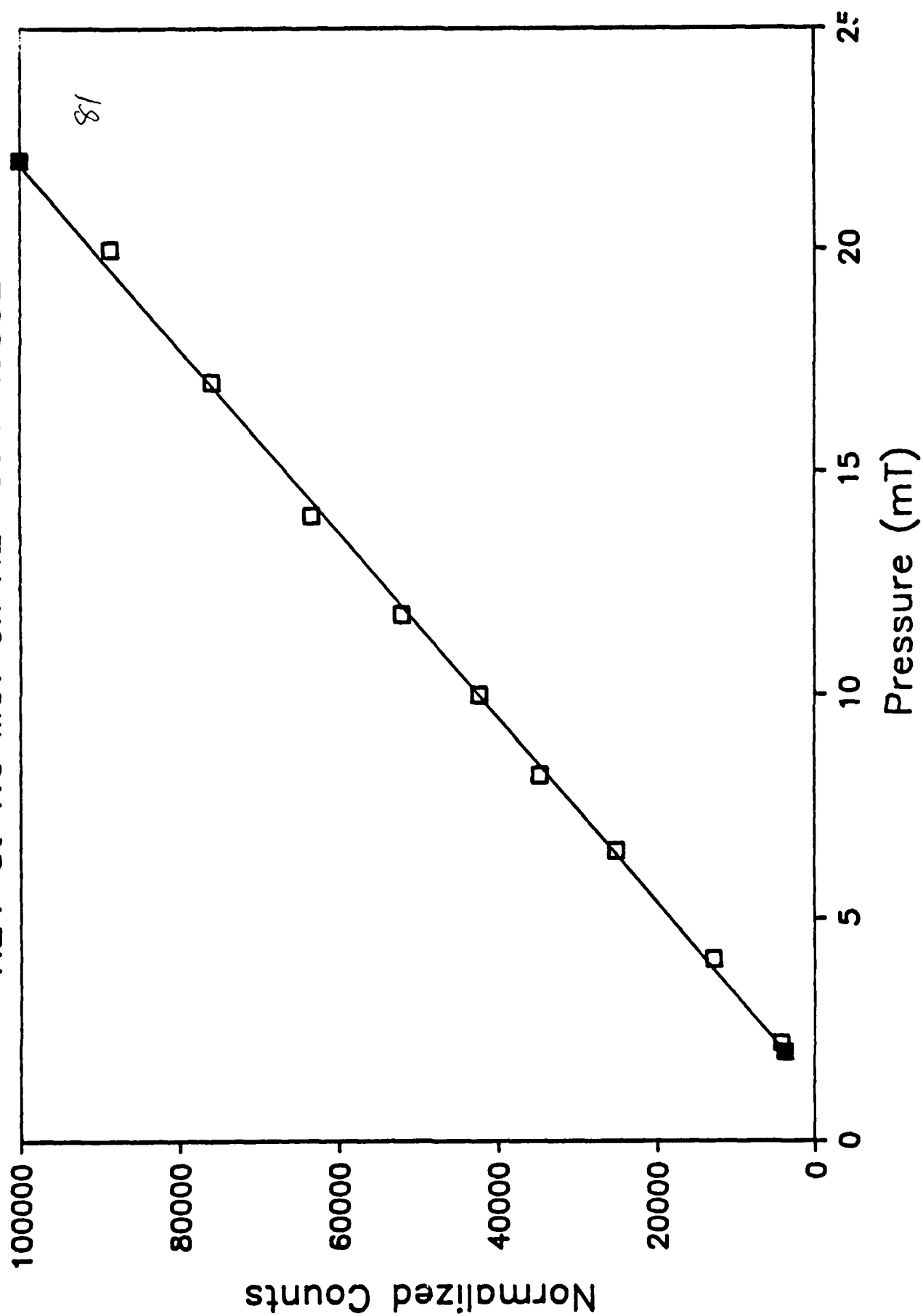


# Normalized Yield vs. Pressure: 427.8 nm

H+ at 0.5 MeV on N2 Corr=.9948

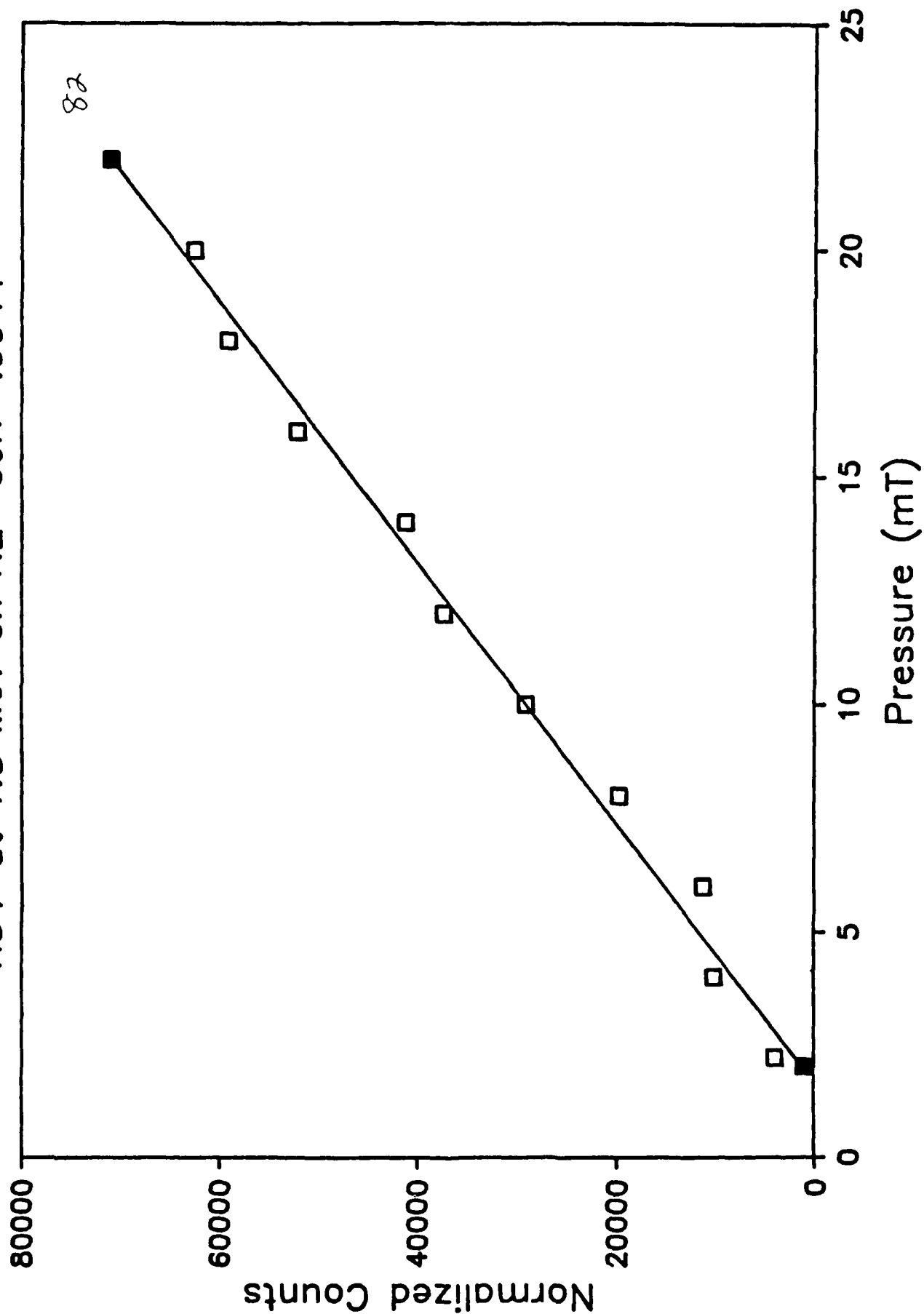


# Normalized Yield vs. Pressure: 427.8 nm H2+ at 1.0 MeV on N2 Corr=.9992



# Normalized Yield vs. Pressure: 427.8 nm

H3+ at 1.5 MeV on N2 corr=.9944



## APPENDIX E

### O-ATOM EMISSION IN FAIRCEDE

The recent exciting LINUS observations<sup>E-1</sup> reminded us of the 1974 observations by Murphy, Fairbairn, Rogers, and Hart of the infrared spectrum of atomic emission in a hollow cathode discharge (FAIRCEDE) using time resolved interferometry. Their results were presented at the DARPA Fourth Strategic Space Symposium<sup>E-2</sup>. They observed that in pure oxygen at high currents the spectrum was dominated by atomic line emissions. In nitrogen, the First Positive bands (B→A) are observed with atomic features being very weak. The band emissions increase with increasing pressure and current. Murphy observed that under their conditions, "the oxygen lines are much more easily excited than nitrogen lines" even though the dissociation cross section of N<sub>2</sub> is as large as for O<sub>2</sub> and the N-atom transition moments in the infrared are just as large as the O-atom moments. N-atom level depopulation by strong visible transitions may be the cause. In air mixtures molecular emission dominated with NO  $\Delta v=1,2$  bands and N<sub>2</sub>O( $v_3$ ) being observed. Formation of NO and charge transfer (N<sub>2</sub><sup>+</sup>+O<sub>2</sub>, NO) will also keep N-atom concentrations low.

We report here a re-examination of the rich O-atom spectrum of FAIRCEDE to see if trends in the populations of the emitting states can lead to information on excitation mechanisms. On September 27, 1974, 9 torr of O<sub>2</sub> was passed through a 2 amp discharge. The time resolved spectrum (from an 8 K interferogram) near pulse termination is shown in Figure E-1. Spectral intensities are in V-cm and are not corrected for InSb detector spectral response which peaks at 2000 cm<sup>-1</sup> and drops rapidly beyond 1800 cm<sup>-1</sup>. The beamsplitter RT product (which is unknown) probably limits the short wavelength response. The InSb detector size limits resolution to 15 cm<sup>-1</sup> and its temporal response (~ 1  $\mu$ s) limits the observed decays. Murphy et al.<sup>E-2</sup> observed the line emission to decay near this rate.

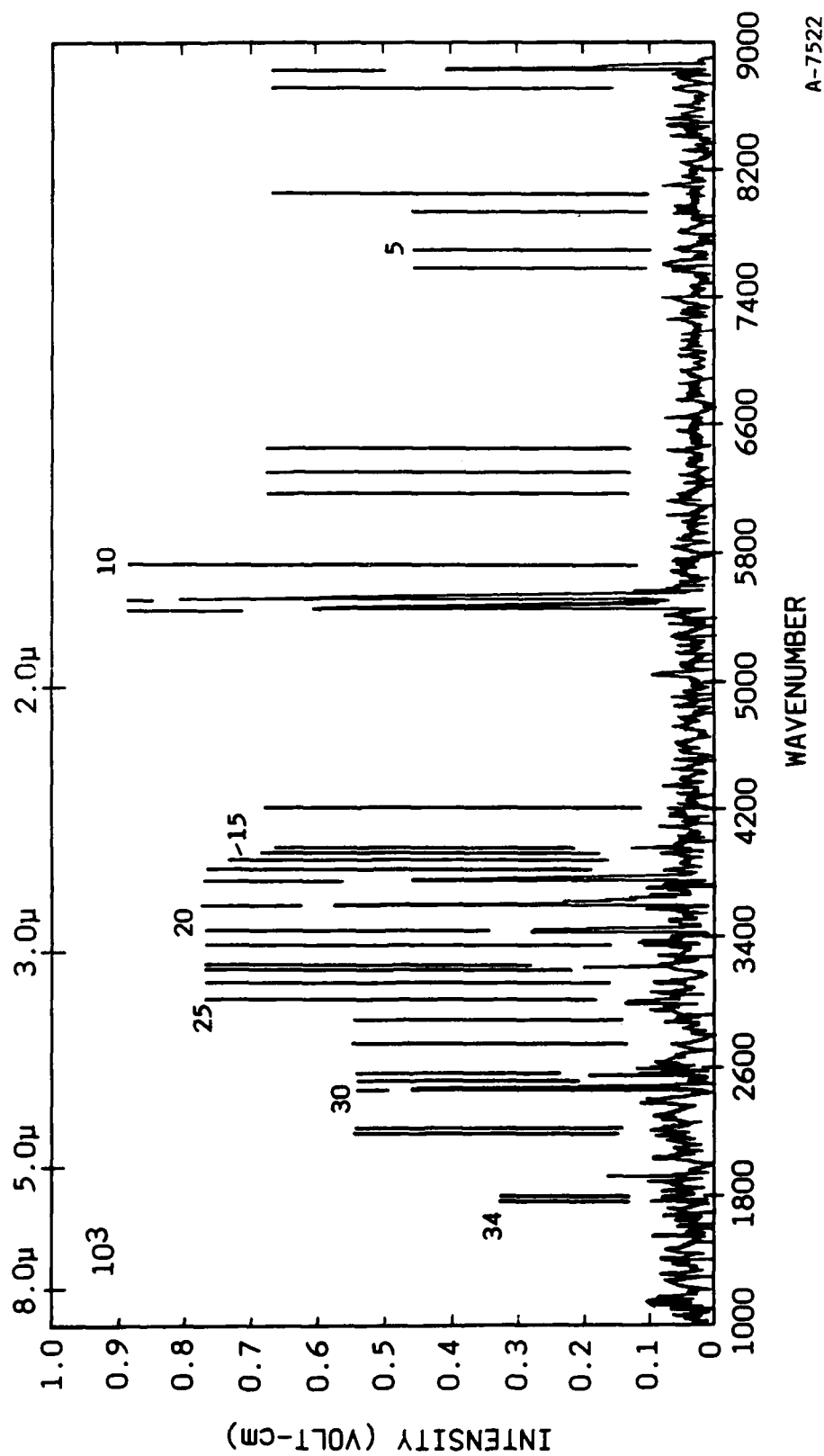


Figure E-1. Data from 27 September 1974 observation of hollow cathode emission using time resolved interferometry pressure = 9 torr, current 2 amps. Lines are numbered as in Table E-1.

A-7522



Relative emitting state populations are obtained by dividing the observed intensities (V-cm) by gf factors. We made use of the oscillator strengths of Biemont and Grevesse<sup>E-3</sup> calculated using Coulomb wave functions as represented by the Bates-Damgaard method. They do not cite accuracies but they note that the  $np\ 3p$ ,  $4d\ 3D$ ,  $ns'\ 3D^0$ ,  $nd'\ 3p^0$ , and  $nd'\ 3D^0$  levels are perturbed and thus less accurately treated. Transitions from these levels are present in the spectrum of Figure E-1. Calculations of argon gA factors by Gelb and Rawlins<sup>E-4</sup> were cited as being accurate to only a factor of three. Oxygen more closely approaches l-s and IR transitions are between high lying levels remote from the core. Both these factors make the Coulomb approximation more accurate. Biemont and Grevesse use C. Moore's energy levels<sup>E-5</sup> and not the more recent work of Bashkin and Stoner<sup>E-6</sup> and thus may have missed some levels and perturbations. Consequently we apply only a factor of three accuracy to their numbers. The intensities of all the lines of multiplets which fall within a resolution element ( $15\text{ cm}^{-1}$ ) have been summed.

The strong lines tentatively identified by Murphy et al.<sup>E-2</sup> exhibited similar populations - their intensities being in the ratios of their gf factors. We then went through Biemont and Grevesse's compilation to identify all multiplets which are strongly allowed. The largest gf in this spectral region (25) was for the  $4f\ 5F \rightarrow 3d\ 5D$  transition at  $5547\text{ cm}^{-1}$ . This feature had a signal to noise of 20. The noise level should be fairly constant across the interferometer's spectrum. Thirty-four transitions with gf-factors down to 0.5 (1/50 of the strongest) are listed in Table E-1 and their positions indicated in Figure E-1. In that figure we see that these transitions correlate with a number of features which were previously unassigned. Several conclusions can be drawn:

The observed spectrum can be explained by equal populations of all highly excited states of the atoms. No strongly allowed transitions are missing.

TABLE E-1. Infrared line intensities and population.

Line Position (cm <sup>-1</sup> )	Upper State	Lower State	Upper State Energy	Observed Intensity	gf	Population
1. 8850 {8857 8848}	3D3D 4S5S	3P3P 3P5P	97488 95476	74	8.5 2.3	9) 32) } 7 each
2. 8710	4S' 3D	3P' 3F	122420	10	3.1	3
3. 8021	5F5F	3D5D	105442	<3	4.1	<0.7
4. 7953	5F3F	3D3D	105442	<5	2.4	<2
5. 7696	3D' 1F	3P' 1D	124326	9	2.6	3
6. 7594	4S3S	3P3P	96225	9	1.5	6
7. 6430	5D' 3D	4P' 3D	132210	10	1.1	9
8. 6292	5D5D	4P5P	99093	8	1.8	4
9. 6168	4S' 1D	3P' 1D	122798	8	1	8
10. 5728	5D3D	4P3P	105409	<8	0.8	<10
11. 5547	4F5F	3D5D	102968	145	25	6
12. 5480	4F3F	3D3D	102968	110	15	7
13. 4195	4D' 3P	4P' 3D	129980	10	1.2	8
14. 3950 {3956 3947}	4D' 3S 7D5D	4P' 3D 5P5P	129737 107572	23	* 0.8	? ) <30)
15. 3920 {3919 3916}	6F5F 4D' 3D	4D5D 4P' 3D	106785 129690	13	4.6 5	3) 3) } 1.5 each
16. 3877	6F3F	4D3D	106788	7	3.2	2
17. 3819	6G3, 5G	4F3, 5F	106788	10	10	1

TABLE E-1. Continued.

Line Position ( $\text{cm}^{-1}$ )	Upper State	Lower State	Upper State Energy	Observed Intensity	gf	Population
18. 3772	4D5D	4P5P	102866	82	17	5
19. 3617	4P5P	4S5S	99093	105	7.2	14
20. 3456	4P3P	4S3S	99681	49	4.5	11
21. 3350	4P' 3D	4S' 3D	125780	19	6.6	3
22. 3227	4D3D	4P3P	102908	36	11	3
23. 3210	5S' 3D	4P' 3D	128990	6	4	1.5
24. 3125	6D5D	5P5P	106751	13	2.4	5
25. 3023	5S5S	4P5P	102117	21	4.4	5
26. 2896	6D3D	5P3P	106766	9	1.2	8
27. 2731	5S3S	4P3P	102412	10	3	3
28. 2576	5F5S	4D5D	105442	34	21	1.6
29. 2533	5F3F	4D3D	105442	6	13	0.5
30. 2470	4P' 3D	3D' 3P	125780	82	*	?
31. 2210	7F5F	5D5D	107595	13	4.7	3
32. 2190 { 2193 2186}	4P3P	3D3D	99681	13	2.7	5) } 2 each
	7F3F	5D3D	107595		2.9	
33. 1785	7D5D	6P5P	107573	12	2.9	4
34. 1759	5D5D	5P5P	105385	17	19.5	0.9
*Not tabulated in Ref. E-2.						

- The majority of the lines are in the ground state core configuration  $2p^3 (4s^0)$ ,  $nl \rightarrow 2p^3 (4s^0)$ ,  $n'l'$ . Both triplet and quintet transitions are observed and are indicated in Figure E-2.
- Eight lines (two of which are not in Biemont and Grevesse's tables) are observed from the  $(^2D^0)$  core triplet manifold,  $2p^3 (^2D^0 nl \rightarrow 2p^3 (^2D^0) n'l')$ . They are indicated in Figure E-3.
- Two transitions in the  $(^2D^0)$  core singlet manifold are observed:

$$\begin{array}{l} 4s' \ ^1D^0 \rightarrow 3p' \ ^1D \\ 3d' \ ^1F^0 \rightarrow 3p' \ ^1D \end{array}$$

(see Figure E-4).

- No transitions in the  $2p^0$  core or between cores was observed.
- The  $2470 \text{ cm}^{-1}$  feature has been reassigned as  $4p' \ ^3D \rightarrow 3d' \ ^3p$ .
- All levels in all cores and manifolds have roughly the same relative populations between 1 and 10. The  $^2D^0$  core lines are weaker due to smaller gf, not lower populations.
- In the ground state core, the quintet states are slightly more populated than the triplets. Collisional process at 9 torr will collisionally partition energy in these nearly degenerate states. For levels with  $n + l \geq 5$  the triplet-quintet splittings are less than  $kT$ . Thus for these experiments preferential formation in a specific manifold is obscured.
- The strongest three lines around  $3 \mu\text{m}$  in FAIRCEDE are the three features observed in LINUS<sup>-1</sup> with comparable relative intensities.

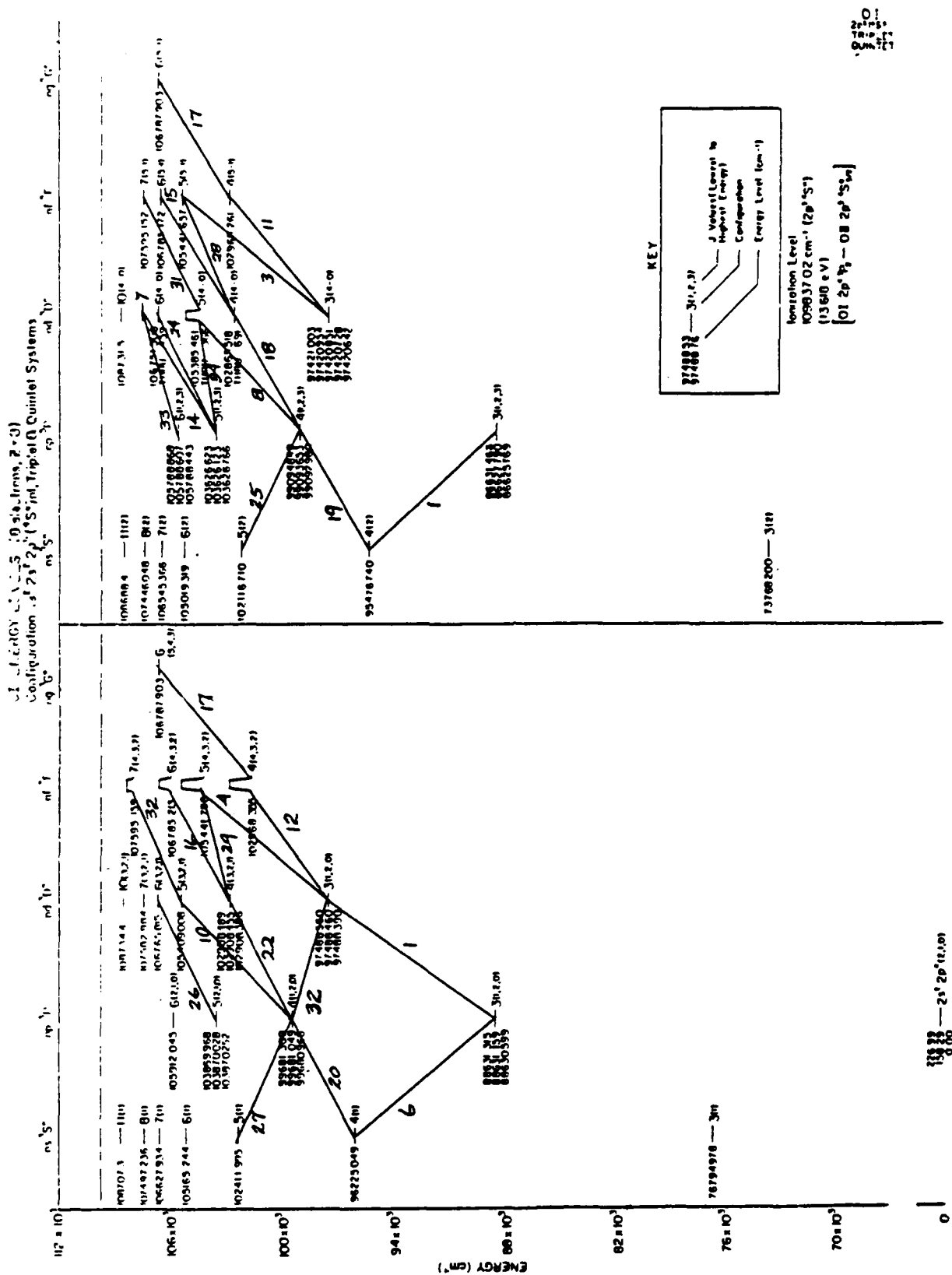


Figure E-2. Grotrian diagram of  $02p^3 (4s^0)$  core triplet and quintet systems. Numbers correspond to listing in Table E-1 as observed in FAIRCEDE. Figure taken from Ref. E-6.

# O I ENERGY LEVELS (8 electrons, $Z=8$ ) (Configuration: $1s^2 2s^2 2p^4 (D^3) n'l$ Triplet System)

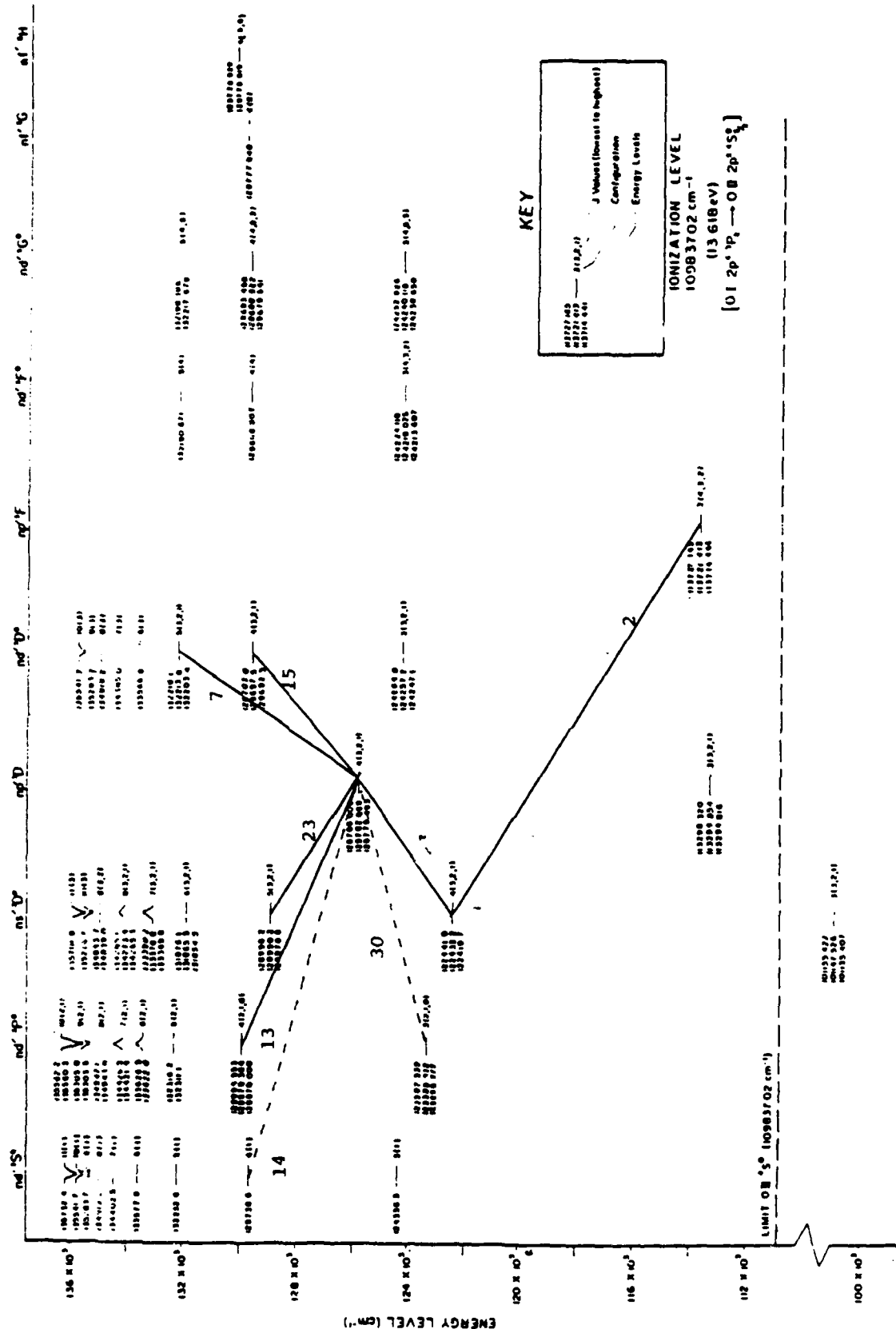


Figure E-3. Grotrian diagram of  $02p^3 (2D^0)$  core triplet system. Numbers are listed in Table E-1. Solid lines are transitions in Biemont and Grevesse tabulation, dashed lines are not but correspond to strong features observed in FAIRCEDE spectrum. Figure taken from Ref. E-6.

O I ENERGY LEVELS (8 electrons, Z = 8)  
Configuration  $1s^2 2p^3 3p^3 4d^1$ , Singlet System

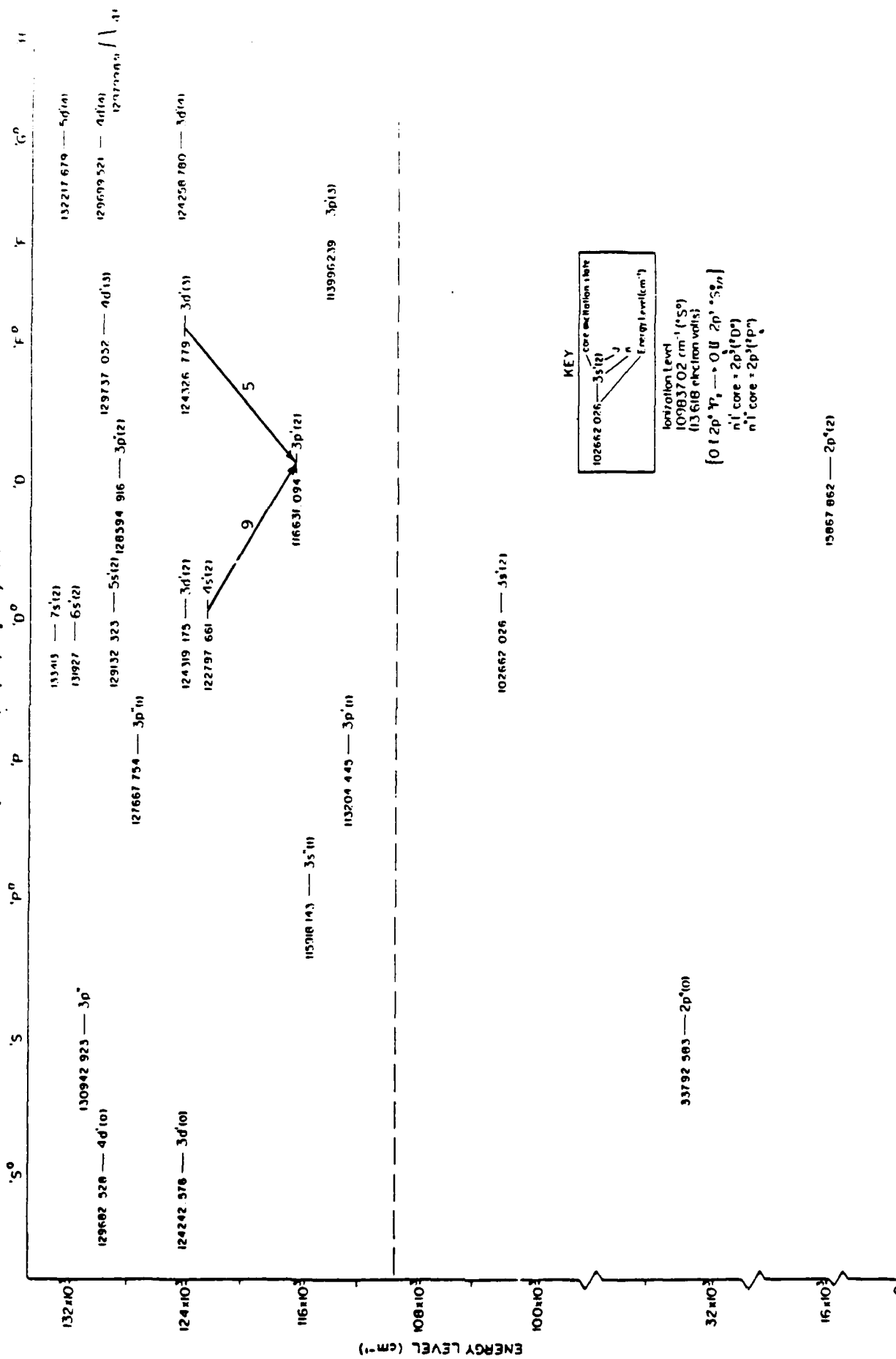
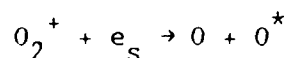
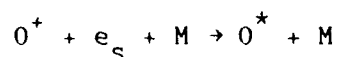


Figure E-4. Grotrian diagram of  $0 2p^3 (2p^0, 2p^0)$  cores singlet manifold. From Ref. E-6.

- There are still several weak features which are unassigned in the spectrum. Since Ref. E-3 missed two features in the  $2D^0$  core, a more refined treatment of O and N transitions may be required if future SWIR-LWIR line emission observations are not completely assignable.
- The next factor of 50 weaker gf factors (0.01 to 0.5) from Biemont and Grevesse have only random overlaps with residual spectral features: 6 matches for 12 transitions - notably the 8480, 3712, and  $3500\text{ cm}^{-1}$  features. Thus no definite assignments are made.

The degree of collisional coupling in these experiments precluded specific formation mechanism isolation. Possible excitation mechanisms include:

- 1) direct dissociation to form  $O^*$ ; 2) dissociative ionization; and
- 3) ionization followed by dissociative recombination:



All three processes can occur without change of the inner shell configuration since the ground state of  $O_2$  and  $O_2^+$  correlate with a  $4s$  inner shell configuration. The  $O_2^+$  b  $4\epsilon_g^-$  state, however, is readily excited by electron impact (mechanism 3). It has large Franck-Condon factors since its equilibrium internuclear separation is the same as the ground state. The  $O_2^+$  b-state



correlates to the excited  $2D^0$  core. The  $O_2^+ b \rightarrow X$  system is the dominant visible emission in LABCEDE at low pressures. Thus the excited core can be created by process (E-3).

From Kieffer<sup>E-7</sup> processes 1-3 peak at  $e_p \sim 100$  eV with dissociation having by far the smallest cross section. Total ionization is three times dissociative ionization so that either processes 2 or 3 could dominate. Of course in the FAIRCEDE discharge, electrons can further interact with the products of processes 1-3 and further cloud the physics.



Thus lower pressure experiments would considerably ease mechanism determination. Nevertheless, these observations serve to encourage further IR observations. Biemont and Grevesse<sup>E-3</sup> predict quite strong emission out into the LWIR (including a very strong feature at  $7.4 \mu m$ ). These lines are listed in Table E-2. These LWIR transitions arise from the same levels as transitions observed in FAIRCEDE and thus should be observable in higher pressure (collisionally coupled) experiments such as LINUS. Lower pressure visible and SWIR observations of oxygen and nitrogen will provide insight into formation mechanisms and can be used to guide low pressure LWIR observation programs.

TABLE E-2. Strong LWIR O-atom lines.

Line Position (cm <sup>-1</sup> )	Upper State	Lower State	Upper State Energy (cm <sup>-1</sup> )	gf
1539	5D3D	5P3P	105409	13
1509	5P5P	5S5S	105385	9
1458	5P3P	5S3S	103870	6
1400	6F5F	5D5D	106785	19
1393	6S5S	5P5P	105019	6
1376	6F3F	5D3D	106785	15
1346	6G5G	5F5F	106787	62
1295	6S3S	5P3P	105165	4
963	6D5D	6P5P	106751	22
854	6D3D	6P3P	106765	14
844	7F5F	6D5D	107595	18
829	7F3F	6D3D	107595	11
769	6P5P	6S5S	105789	12
761	5P5P	4D5D	103626	8
757	7S5S	6P5P	106545	8
747	6P3P	6S3S	105912	7
716	7S3S	6P3P	106628	5
503	6P3P	5D3D	105912	8
403	6P5P	5D5D	105789	11

## REFERENCES

- E-1. Lurie, J., Miller, S., and Armstrong, R., (1984), Private Communication
- E-2. Murphy, R.E., Fairbairn, A.R., Rogers, J.W., and Hart, A.M., "Near IR Nuclear Spectra: Interpretation by Recent Laboratory Results," DARPA Strategic Space Symposium, 23 September 1975 (Monterey, CA).
- E-3. Biemont, E. and Grevesse, N., "Infrared Wavelengths and Transition Probabilities by Atoms,  $3 \leq Z \leq 20$ ," Atomic Data and Nuclear Data Tables 12, 217 (1973).
- E-4. Rawlins, W.T., Gelb, A., and Armstrong, R.A., COCHISE Observations of Argon Rydberg Emission from 2 to 16  $\mu$ m, AFGL TR-83-0201. ADA137916
- E-5. Moore, C.E., Atomic Energy Levels, Vol. I, NSRDS-NBS35 (1971).
- E-6. Bashki, S. and Stoner, Jr., J.O., Atomic Energy Level and Grotrian Diagrams, Vol. I (North-Holland, Amsterdam, 1978).
- E-7. Kieffer, L.J., A Compilation of Electron Collision Cross Section Data for Modeling Gas Discharge Lasers, JILA Information Center Report 13 (1973).